

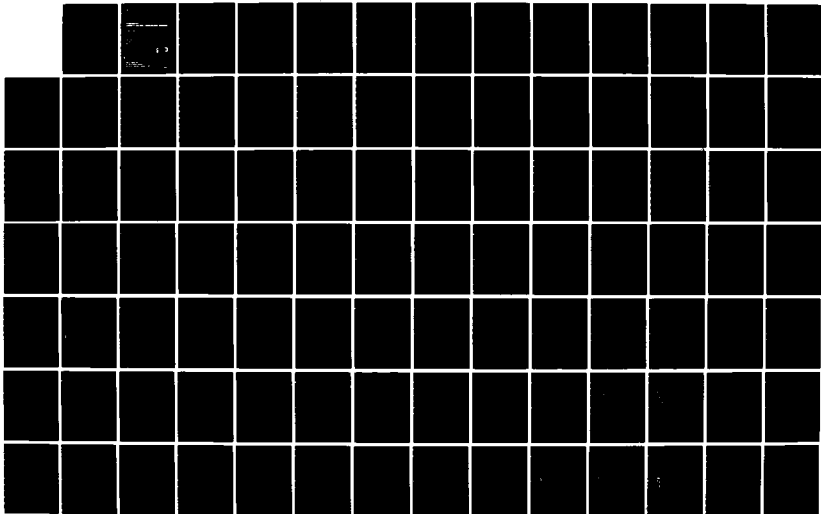
AD-A146 222

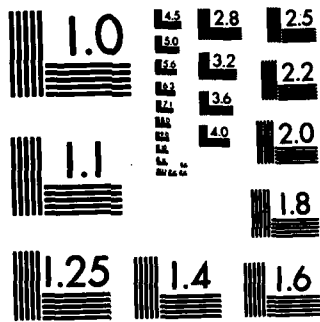
PEACEKEEPER QUANTITY-DISTANCE VERIFICATION PROGRAM AND
ADDENDUM(U) TRN DEFENSE SYSTEMS GROUP REDONDO BEACH CA
B SUSSHOLZ JUN 84 TRW-43597-6001-UT-00 BMO-TR-84-17
F04704-83-C-0045 F/G 16/1

1/4

UNCLASSIFIED

NL





MICROCOPY RESOLUTION TEST CHART

DDO-TR-84-17

②

AD-A146 222

**PEACEKEEPER
QUANTITY-DISTANCE VERIFICATION PROGRAM**

JUNE 1984

Prepared by
TRW Defense Systems Group
One Space Park
Redondo Beach, California 90278

DTIC FILE COPY

DTIC
ELECTE
OCT 2 1984
S A D

Approved for public release; distribution unlimited.

Ballistic Missile Office
Air Force Systems Command
Barton Air Force Base, California 92409

9 09 21 02.2

BMO-TR-84-17A

**ADDENDUM
TO
PEACEKEEPER QUANTITY-DISTANCE VERIFICATION PROGRAM**

August 1984

**Prepared by
TRW Defense Systems Group
One Space Park
Redondo Beach, CA 90278**

**Ballistic Missile Office
Air Force Systems Command
Norton Air Force Base, CA 92409**

**ADDENDUM
TO
PEACEKEEPER QUANTITY-DISTANCE VERIFICATION PROGRAM**

During the course of the study, a comprehensive effort was initiated to determine appropriate drag coefficients for the fragments of interest. High speed photography for the 1/4-scale test indicated substantial tumbling among fragments of all sizes. A literature survey yielded considerable data for drag effects associated with constant cross-sectional areas for bodies of various shapes; however, there appeared to be no information regarding tumbling fragments. Discussions with several sources indicated a consensus that the drag effect for a tumbling fragment was most probably comparable to that of a sphere. Therefore, for the purpose of the study an assumption was made to apply scale factors based on a drag coefficient of 0.5 toward development of Q-D estimates.

During a presentation to the Department of Defense Explosives Safety Board (DDESB) in July 1984 regarding results of the Peacekeeper Quality-Distance Verification Program, an interest was expressed in determining the sensitivity of the Q-D estimates to variations in the drag coefficient parameter from 0.5 to 1.0. An evaluation was performed indicating that the average full-scale range corresponding to a drag coefficient of 1.0 was 1644 feet, which is a factor of only 4.9% greater than the value of 1567 feet established for a drag coefficient of 0.50. Details of the analyses are presented in the following discussion.

A comparison is shown in Table A-1 of the upper bound range multiplication factors that were developed on the basis of the trajectory limitation approach for drag coefficients of 0.5 and 1.0. The average value of 2.29 determined for a C_D of 1.0 is a factor of 2.2% greater than the value of 2.24 associated with a C_D of 0.50.

A calculation was performed for Case 13 based on the statistical simulation technique with the following assumptions: (a) skewed distribution for launch velocities and angles, (b) QDT-3 shape factors, (c) fragment size gradient of 2/3, and (d) drag coefficient of 1.0. These parameters are similar to those of Case 11 in the study except that the drag coefficient is 1.0 instead of 0.5. Results of the analysis for Case 13 are presented in Table A-2 in comparison with the associated data for the other 12 cases.

The debris scaling factor based on the ratio of full-scale range to 1/4-scale range at a density of 1 per 600 sq ft was evaluated to be 1.90 for Case 13 as compared to 1.75 for Case 11, or an enhancement by about 8.6% for an increase in C_D from 0.5 to 1.0.

Tables A-3 and A-4 present Q-D estimates based on C_D values of 0.5 and 1.0, respectively. The average full-scale range for $C_D = 0.5$ was determined to be 1567 feet, whereas the corresponding value for $C_D = 1.0$ was evaluated as 1644 feet. The difference of 4.9% indicates that Q-D estimates are relatively insensitive to drag coefficient parameters.

Table A-1. Upper Bound Range Multiplication Factors for $C_D = 0.5$ and 1.0

Fragment Length (in.)		R_{4L}/R_L	
1/4 Scale	Full Scale	$C_D = 0.5$	$C_D = 1.0$
0.50	2	2.36	2.41
0.75	3	2.24	2.28
1.00	4	2.22	2.26
1.50	6	2.21	2.25
2.00	8	2.18	2.23
	Average	2.24	2.29

Table A-2. Comparison of Debris Scaling Evaluations by Statistical Simulation Method

Case	Launch V_0 and θ_0 Spectrum	Drag Coefficient	Number Gradient	Scaling Approach A			Scaling Approach B			Scaling Approach C					
				$R_{1/4}$ for 1/600 ft ² (ft)	$(R_{PS})_1$ for 1/600 ft ² (ft)	$(R_{PS})_1 / R_{1/4}$	Scale Factor λ	λ^2	$R_{1/4}$ for 1/600 ft ² (ft)	$(R_{PS})_1$ for 1/600 ft ² (ft)	$(R_{PS})_1 / R_{1/4}$	Scale Factor λ	λ^2	$(R_{1/4})_c$ for 1/600 ft ² (ft)	$(R_{PS})_c$ for 1/600 ft ² (ft)
1*	Uniform	1/2	1/2	848	1644	1.93	2.72	7.4	604	1644	2.72	16	512	2048	1.24
2	Uniform	1/2	2/3	1020	1999	1.96	2.88	8.3	694	1999	2.88	16	593	2322	1.19
3	Uniform	1/2	3/8	732	1446	1.98	2.74	7.5	528	1446	2.74	16	453	1812	1.25
4	Skewed	1/2	1/2	773	1572	2.03	2.88	8.3	546	1572	2.88	16	475	1900	1.21
5	Uniform	1	1/2	553	1249	2.26	3.11	9.7	402	1249	3.11	16	367	1468	1.18
6	Skewed	1	1/2	516	1150	2.23	3.11	9.7	370	1150	3.11	16	336	1340	1.16
7	Uniform; Scaling 2:1	1/2	1/2	848	1704	2.01	2.88	8.3	591	1704	2.88	16	512	2048	1.20
8	Uniform; 2N ₀	1/2	1/2	932	1889	2.03	2.76	7.6	684	1889	2.76	16	596	2348	1.26
9	Uniform; 1/2N ₀	1/2	1/2	764	1398	1.83	2.64	7.0	530	1398	2.64	16	427	1708	1.22
10**	Average	1/2	1/2	670	1159	2.03	2.86	8.2	552	1159	2.86	16	450	1800	1.21
11	Skewed	1/2	2/3	750	1310	1.75	2.12	4.5	616	1310	2.12	16	504	2016	1.54
12	Uniform	1/2	2/3	712	1140	1.60	2.14	4.6	531	1140	2.14	16	384	1536	1.35
13	Skewed	1	2/3	456	865	1.90	2.21	4.9	391	865	2.21	16	343	1373	1.59

*Cases 1-9; Distant Runner shape factors - pretest calculations
 **Cases 10-13; QDT-3 shape factors - post-test calculations

**Table A-3. Full-Scale Quantity-Distance Estimates
Based on a Drag Coefficient of 0.5**

Debris Scaling Method	QDT-3 Radials	Total Fragment Number	Fragments per 600 ft ²	QDT-3 Range (ft)	Scale Factor	Full Scale Range (ft)
Statistical Simulation	S, NE, NW	N ₀	1	812	1.75	1421
		2N ₀	1	901	1.75	1577
	NW	N ₀	1	896	1.75	1568
		2N ₀	1	977	1.75	1710
Trajectory Limitation	S, NE, NW	N ₀	5	604	2.24	1353
		2N ₀	5	694	2.24	1554
	NW	N ₀	5	706	2.24	1581
		2N ₀	5	790	2.24	1770
Average						1567

**Table A-4. Full-Scale Quantity-Distance Estimates
Based on a Drag Coefficient of 1.0**

Debris Scaling Method	QDT-3 Radials	Total Fragment Number	Fragments per 600 ft ²	QDT-3 Range (ft)	Scale Factor	Full Scale Range (ft)
Statistical Simulation	S, NE, NW	N ₀	1	812	1.90	1543
		2N ₀	1	901	1.90	1712
	NW	N ₀	1	896	1.90	1702
		2N ₀	1	977	1.90	1856
Trajectory Limitation	S, NE, NW	N ₀	5.24	598	2.29	1369
		2N ₀	5.24	688	2.29	1575
	NW	N ₀	5.24	701	2.29	1605
		2N ₀	5.24	782	2.29	1791
Average						1644

2

BMO-TR-84-17

PEACEKEEPER
QUANTITY-DISTANCE VERIFICATION PROGRAM

June 1984

Prepared by
TRW Defense Systems Group
One Space Park
Redondo Beach, California 90278

Approved for public release; distribution unlimited.

SECRET
OCT 2 1984
A

Ballistic Missile Office
Air Force Systems Command
Norton Air Force Base, California 92409

PREFACE

The Peacekeeper Quantity-Distance Verification Program was sponsored by the Ballistic Missile Office (BMO/AWS) of the Air Force Systems Command, Norton Air Force Base, California. Technical assistance was furnished by the TRW Defense Systems Group. The BMO Program Manager was Maj. John Hammond and the TRW Program Manager was Mr. Roy W. Harris. The BMO Project Officer was Lt. Steve Mattern and the TRW Project Engineer was Mr. Richard Thibedeau. Overall program technical direction was provided by Dr. Benjamin Sussholz of TRW, who prepared the report.

The test program was conducted by the Structures Laboratory of the U.S. Army Engineer Waterways Experiment Station (WES), Vicksburg, Mississippi, under the direct supervision of Dr. Jimmy P. Balsara, Program Manager, Structural Mechanics Division (SMD). The SMD work was performed under the supervision of Mr. Gayle E. Albritton, Project Manager. The project engineers were Mrs. Patricia S. Jones (SL) and Mr. David L. Tilson (SMD). Work performed by the Explosion Effects Division (EED) was under the supervision of Mr. Landon K. Davis, Project Manager. Material property tests were conducted under the supervision of Dr. Joseph S. Zelasko, Project Manager, Geomechanics Division (GD). Structural designs and details were furnished to WES by TRW.

Field support was provided to WES by the Field Command Defense Nuclear Agency, under the direction of Maj. Mike Evinrude, and the White Sands Missile Range, under the supervision of Mr. Lee Meadows. Photographic data reduction was provided by Dr. John Wisotski of the Denver Research Institute, Denver, Colorado.

The analytical program was performed under the direction of Dr. Benjamin Sussholz, TRW Defense Systems Group, Redondo Beach, California. Principal investigators in several of the key technical areas were Mr. Martin P. Bronstein and Mr. Stanton F. Fink, responsible for the airblast analysis, Mr. James V. Schumacher, conducting the structural fragmentation studies, and Dr. Benjamin Sussholz, developing the debris scaling methodology.

CONTENTS

	Page
EXECUTIVE SUMMARY	1
1.0 INTRODUCTION	1-1
1.1 Background	1-1
1.2 Objectives	1-2
2.0 PROGRAM DEFINITION	2-1
2.1 Test Requirements	2-1
2.2 Theoretical Investigations	2-2
3.0 TEST DESCRIPTION	3-1
3.1 Introduction	3-1
3.2 Test Site Description	3-2
3.3 Soil Backfill Description	3-2
3.4 Test Concept for 1/10-Scale Structures	3-2
3.5 Test Concept for 1/4-Scale Structure	3-4
3.6 Debris/Ejecta Studies	3-7
3.7 Documentary Photography	3-9
4.0 AIRBLAST PHENOMENA	4-1
4.1 Hydrocode Description	4-1
4.2 Tangent Sphere Calibration	4-2
4.3 Rigid Silo Calculations	4-2
4.4 Scale Model Computations	4-4
4.5 Test Predictions	4-8
5.0 SOIL EJECTA CHARACTERISTICS	5-1
5.1 Ejecta Data Review	5-1
5.2 Safe Distance	5-2
5.3 Test Predictions	5-5
6.0 STRUCTURAL DEBRIS	6-1
6.1 Early Time Break Up	6-1
6.2 Surface Spallation	6-3
6.3 Fragment Launch Characteristics	6-9
6.4 Test Predictions	6-14
7.0 FRAGMENT SCALING METHODOLOGY	7-1
7.1 Impact Energy Criterion	7-1
7.2 Statistical Simulation Model	7-3
7.3 Trajectory Limitation Technique	7-8
8.0 TEST RESULTS	8-1
8.1 Airblast	8-1
8.2 Debris/Ejecta	8-2
8.3 Strain Gage	8-4
8.4 Technical Photography	8-4

9.0	TEST DATA ANALYSIS	9-1
9.1	Airblast Scaling	9-1
9.2	Soil Ejecta Considerations	9-3
9.3	Structural Break-Up Characteristics	9-4
9.4	Debris Density Distribution	9-9
9.5	Dust Cloud Considerations	9-11
10.0	QUANTITY DISTANCE VERIFICATION	10-1
10.1	Airblast	10-1
10.2	Soil Ejecta	10-2
10.3	Structural Debris	10-2
11.0	SUMMARY AND CONCLUSIONS	11-1
12.0	REFERENCES	12-1
 APPENDICES		
A	Photographic Sequence of 1/4-Scale Silo Construction and QDT-3 Test Site Preparation	A-1
B	QDT-1 Airblast Records	B-1
C	QDT-2 Airblast Records	C-1
D	QDT-3 Airblast Records	D-1
E	Calibration Shot Airblast Records	E-1

TABLES

	Page
Executive Summary	
1	Comparison of Fragment Scaling Evaluations by Statistical Simulation Method 9
2	Scaling Comparison of Positive Duration and Arrival Time of Airblast Waveforms 10
3	QDT-3 Structural Debris Data Summary 11
4	Full-Scale Quantity-Distance Estimates for Structural Debris 12
5	Quantity-Distance Ranges for All Environments 12
 Section 3	
3-1	Pentolite Test Charges 3-9
3-2	Airblast Instrumentation Locations for 1/10-Scale Tests on Each Radial 3-10
3-3	Airblast Instrumentation Locations for 1/4-Scale Test on Each Radial 3-10
3-4	Strain Gage Locations for 1/4-Scale Silo 3-11
3-5	QDT Instrumentation Measurement List 3-12
3-6	Camera Requirements for Peacekeeper 1/4-Scale Test 3-12
 Section 5	
5-1	Summary of Ejecta Data for Selected Buried Bursts 5-6
5-2	Areal Density Functions for Danny Boy and Dry Soil Events 5-7
 Section 6	
6-1	Input Parameter Values Used in Headworks SDOF Analysis 6-16
6-2	Calculated Sequence of Headworks Failure 6-17
6-3	Particle Size Distribution for Debris from Spalling of Top Layer 6-17
6-4	Structure Fragmentation Summary 6-18
 Section 7	
7-1	Debris Scaling Analyses by Statistical Simulation Method 7-10
7-2	Number of Fragments Per Length Category 7-11
7-3	Case 4 - Maximum Range Distribution for 0.5-Inch Fragments 7-12
7-4	Case 4 - Maximum Range Distribution for 2-Inch Fragments 7-13
7-5	Case 4 - Number Density for 0.5-Inch Fragments 7-16
7-6	Case 4 - Number Density for 2-Inch Fragments 7-17

7-7	Case 4 - 1/4-Scale Debris Density Distribution	7-19
7-8	Upper Bound Range Multiplication Factors	7-21

Section 8

8-1	QDT-1 and QDT-2 Airblast Test Results	8-5
8-2	QDT-3 Airblast Test Results	8-6
8-3	QDT-3 Meteorological Data	8-7
8-4	Calibration Shot Airblast Test Results	8-8
8-5	QDT-3 Structural Debris Data Summary	8-9
8-6	QDT-3 Debris Data Acquisition at 400 ft Range	8-10
8-7	Artificial Missile Data	8-11
8-8	Soil Ejecta Test Data	8-13

Section 9

9-1	Scaling Comparison of Positive Duration and Arrival Time of Airblast Waveforms	9-13
9-2	Comparison of Cratering Effects	9-13
9-3	Debris Distribution Symmetry Evaluation at 400-Foot Range	9-14
9-4	Enhancement of Maximum Ranges Due to Downwind Velocity of 10 mph	9-15
9-5	Variation of Fragment Distribution with Size	9-16
9-6	QDT-3 Debris Density Variation with Range	9-17
9-7	Dust Cloud Growth Characteristics	9-18
9-8	Evaluation of Dust Cloud Impact	9-19

Section 10

10-1	Comparison of Fragment Scaling Evaluations by Statistical Simulation Method	10-5
10-2	Full-Scale Quantity-Distance Estimates for Structural Debris	10-6

FIGURES

		<u>Page</u>
Executive Summary		
1	Test Bed Configuration for 1/4-Scale Structure	13
2	Locations of Areas Requiring Brush Clearing for Airblast Gages and Fragment Surveys	14

3	Comparison of Maximum Range Ratios Corresponding to QDT-3 Fragment Shape Factors and Drag Coefficient of 0.5	15
4	Comparison of Airblast Data Predictions and Test Data	16
5	QDT-3 Structural Debris Density Versus Range	17
6	Peak Overpressure Versus Scaled Range	18
7	QDT-3 Debris Density Scaling for Data on S, NE, and NW Radials	19

Section 3

3-1	Soil Gradation Data for Minuteman Sites	3-13
3-2	Acceptable Gradation Range for QDT Test Bed	3-14
3-3	One-Tenth Scale Structure	3-15
3-4	Test Site Layout for QDT-1, QDT-2, and QDT-3	3-16
3-5	Test Bed Configuration for 1/10-Scale Structure	3-17
3-6	One-Quarter Scale Structure	3-18
3-7	Test Bed Configuration for 1/4-Scale Structure	3-19
3-8	Locations of Areas Requiring Brush Clearing for Airblast Gages and Ejecta Surveys	3-20
3-9	Camera, Locations and Coverages for Debris/Ejecta Photography	3-21

Section 4

4-1	TNT Tangent Sphere Configuration	4-9
4-2	Overpressure Versus Range Curve for Tangent Sphere	4-9
4-3	Model-Geometry for the Full-Scale Rigid Wall Silo Calculation	4-10
4-4	Comparison of Initial CSQ Calculations with DNA Results for Rigid Silo Detonation	4-11
4-5	Zoning Sensitivity for Rigid Silo Calculation	4-12
4-6	Final Result of TRW Full-Scale Rigid Silo Calculation	4-13
4-7	One-Tenth Scale Structure Used for Calculation	4-14
4-8	Material Boundaries for 1/10-Scale Calculation at 1.2 msec	4-15
4-9	Material Boundaries for 1/10-Scale Calculation at 1.9 msec	4-16
4-10	Material Boundaries for 1/10-Scale Calculation at 2.4 msec	4-17
4-11	Pressure Contours for 1/10-Scale Calculation at 1.2 msec	4-18
4-12	Pressure Contours for 1/10-Scale Calculation at 1.9 msec	4-19
4-13	Pressure Contours for 1/10-Scale Calculation at 2.4 msec	4-20
4-14	One-Quarter Scale Structure Used for Calculation	4-21
4-15	One-Quarter Scale Silo with Closure at 0.4 msec	4-22

4-16	One-Quarter Scale Silo with Closure at 3 msec	4-23
4-17	One-Quarter Scale Silo with Closure at 10.7 msec	4-24
4-18	One-Quarter Scale Silo with Closure at 12.9 msec	4-25
4-19	One-Quarter Scale Silo with Closure at 15.9 msec	4-26
4-20	One-Quarter Scale Silo without Closure at 0 msec	4-27
4-21	One-Quarter Scale Silo without Closure at 0.5 msec	4-28
4-22	One-Quarter Scale Silo without Closure at 3 msec	4-29
4-23	One-Quarter Scale Silo without Closure at 6 msec	4-30
4-24	Pressure Contours for 1/4-Scale Silo without Closure at 0.5 msec	4-31
4-25	Pressure Contours for 1/4-Scale Silo without Closure at 3 msec	4-32
4-26	Pressure Contours for 1/4-Scale Silo without Closure at 6 msec	4-33
4-27	Pressure-Time History at Ground Range of 42 Feet	4-34
4-28	Pressure-Time History at Ground Range of 78 Feet	4-35
4-29	Pressure-Time History at Ground Range of 110 Feet	4-36
4-30	Pressure-Time History at Ground Range of 130 Feet	4-37
4-31	Overpressure Versus Range for 1/4-Scale Silo Calculation Without Closure	4-38

Section 5

5-1	Scaled Range to 1 Particle per 600 Square Feet Versus Scaled Depth of Burst	5-8
5-2	Comparison of Stagecoach and Scooter Effective Velocity Fields	5-9
5-3	QDT-3 Soil Ejecta Density Predictions	5-10

Section 6

6-1	Freebody Diagram of Headworks Element	6-21
6-2	Hoop Stress Distribution in Headworks	6-22
6-3	Recommended Blast Loadings for Spalling Analysis of 1/4-Scale Test	6-23
6-4	Spring-Mass Check of Top Headworks Stirrup Failure Due to Spalling Phenomenon	6-24
6-5	QDT-3 LER Plan View	
6-6	QDT-3 LER Cross-sections	6-26
6-7	General SDOF Model for Fragmentation Analyses	6-27
6-8	Loading Functions for QDT-3 Fragmentation Studies	6-28
6-9	Closure Plan and Section	6-29
6-10	SDOF Modeling of Closure Shear	6-30

6-11	Failure Mode of Level B Headworks	6-31
6-12	Results of SDOF Analyses of Level B Headworks	6-32
6-13	Nonsafe Model and Results for Level B Headworks in the Horizontal Plane	6-33
6-14	Nonsafe Model for Response of QDT-3 LER Below Level B Headworks	6-34
6-15	Nonsafe Results at 10 msec	6-35
6-16	Cumulative Probability Distribution of Fragment Weight	6-36
6-17	QDT-3 Debris Density Predictions	6-37

Section 7

7-1	Fragment Size Limitation for Impact Energy Criterion of 58 ft-lb and Drag Coefficient of 0.5	7-21
7-2	Fragment Size Limitation for Impact Energy Criterion of 58 ft-lb and Drag Coefficient of 1.0	7-23
7-3	Debris Number Distribution for Distant Runner Event 5 Front Wall	7-24
7-4	Velocity and Angle Distribution for Scaling Analyses	7-24
7-5	Case 4A - 1/4-Scale Debris Density Variation with Range	7-25
7-6	Case 4B - Full-Scale Debris Density Variation with Range	7-26
7-7	Representative Fragment Density Scaling Procedure	7-27
7-8	Case 4 - Analytical Function Modification for Scaling Approach B	7-28
7-9	Comparison of Maximum Range Ratios for Fragment Lengths L and 4L for Drag Coefficient of 0.5	7-29
7-10	Comparison of Maximum Range Ratios for Fragment Lengths L and 4L for Drag Coefficient of 1.0	7-30

Section 8

8-1	Profiles of QDT-3 Apparent Crater	8-14
8-2	As-Built Charge for Calibration Shot	8-15
8-3	Photographic Sequence of QDT-3 Explosion	8-16

Section 9

9-1	Comparison of QDT Airblast Data	9-20
9-2	Airblast Waveform Comparison	9-21
9-3	QDT-3 Pressure-Time History Prediction at 110-Foot Range	9-22
9-4	QDT-3 Blast Pressure Data	9-23
9-5	Elevation Histogram at Wing V Sites	9-24
9-6	Calibration Shot Airblast Data	9-25

9-7	Gradation Characteristics of QD Soil Delivered to Test Site	9-26
9-8	Comparison of QDT-3 Far Field Large Fragment Survey with Pretest Predictions	9-27
9-9	QDT-3 Headworks Level B and Level C Fragment Recovery	9-28
9-10	Fragment Occurrence Frequencies for Various Structural Elements	9-29
9-11	Scaling of Large Fragment Distribution	9-30
9-12	Scaling of Small Fragment Distribution	9-31
9-13	Analysis of QDT-3 Strain Gage Data	9-32
9-14	Fragment Density Variation with Azimuth at 400-Foot Range	9-33
9-15	QDT-3 Debris Size Distribution	9-34
9-16	QDT-3 Mass Distribution for 1-Inch Structural Fragments	9-35
9-17	Occurrence Frequency of Other Dimensions of 1-Inch Fragments	9-36
9-18	QDT-3 Fragment Shape Factor Variation with Length	9-37
9-19	QDT-3 Debris Density Distribution	9-38
9-20	Comparison of Fragment and Dust Cloud Velocities	9-39
9-21	Fragment Angles After Exit from Dust Cloud	9-40

Section 10

10-1	Peak Overpressure versus Scaled Range	10-7
10-2	Energy Distribution versus Time	10-8
10-3	Case 11 - Debris Density Scaling by Statistical Simulation Method	10-9
10-4	Comparison of Maximum Range Ratios Corresponding to QDT-3 Fragment Shape Factors and Drag Coefficient of 0.5	10-10
10-5	QDT-3 Debris Density Scaling for Data on S, NE, and NW Radials	10-11
10-6	QDT-3 Debris Density Scaling for Data on NW Radial Only	10-12

EXECUTIVE SUMMARY

Introduction

The Department of the Air Force Inspector General had established, for planning purposes, an estimate of 1750 feet as the quantity-distance (Q-D) for Peacekeeper missiles in Minuteman silos, with the requirement that rigorous analyses and testing would be performed to verify the planning criteria. The Peacekeeper Quantity-Distance Verification Program was established to satisfy this requirement with the principal objective of verification of the adequacy of 1750 feet as the quantity-distance for the Peacekeeper system. *(to piii)*

Requirements for quantity-distance verification, based on safety criteria specified in the Air Force Regulation (AFR) 127-100, consist essentially of determination of (1) the ground range for a peak overpressure level of 1 psi and (2) the ground range for a hazardous fragment areal density of one fragment per 600 square feet with impact energy of 58 ft-lb or greater as associated with an in-silo explosion of a Peacekeeper missile or equivalent TNT charge.

An upper bound value of 202,000 pounds of TNT had been assumed in the present investigation for the net equivalent weight (NEW) of TNT corresponding to an explosion of a Peacekeeper missile. This value is based on a conservative estimate of 1.20, 1.20, and 1.25 times the propellant weights of Stages I, II, and III, respectively, as the NEW for each stage assuming full order sympathetic detonation of progressive stages following initiation of Stage III.

Program Definition

Considerations were directed toward establishing a minimum test program adequate for verifying the Q-D criteria. The tests are briefly outlined as follows:

- Two 1/10-Scale tests of steel structures scaled to volume and mass of a Minuteman Wing V silo; explosive charge 202 pounds of TNT; blast measurements only.
- One 1/4-scale test of reinforced concrete structure with detailed representation of a Minuteman Wing V silo; explosive charge 3156 pounds of TNT; blast and debris/ejecta measurements.
- One 1000-pound TNT surface tangent sphere as a calibration shot; blast measurements only.

In the analytical program, attention was focused principally on three aspects: airblast phenomena, structural fragmentation characteristics, and debris scaling procedures. The airblast analytical model was calibrated by means of a calculation for a rigid silo configuration similar to an analysis by S-Cubed of Albuquerque for DNA, and determination of the blast effects associated with a selected previous experiment for correlation with empirical results. Test predictions were to be developed for the airblast and fragment distributions associated with the scale model tests. An evaluation was performed of the quantity-distance corresponding to a full scale operational event.

Test Description

The schedule for the Q-D test program was as follows:

<u>Test</u>	<u>Date</u>
QDT-1	26 Jan 84
QDT-2	01 Feb 84
QDT-3	29 Feb 84
Calibration	07 Mar 84

The quantity-distance tests (QDT) were conducted at the Permanent High Explosive Test Site, White Sands Missile Range, New Mexico. This site was selected for the flatness and area of cleared real estate. The water table was approximately 130 feet in depth so that interference with the test beds was of no concern.

Figure 1 indicates the test bed layout for the 1/4-scale structure. The select backfill was incorporated out to a distance of 7 feet at the depth of 159 inches corresponding to the charge center of gravity (CG) and increased in radial extent linearly up to a range of 20 feet at ground surface. The explosive charge consisted of Pentolite rather than TNT, with appropriate modification in weight and dimensions due to the energy density of Pentolite being 13% greater than TNT.

With reference to the test configuration, several of the most significant considerations are noted as follows:

- Cylindrical explosive charges with diameter scaled to missile diameter of 92 inches; charge depths with CG same as scaled CG of missile propellants; charge initiation point at scaled CG of Stage III propellant; steel containers for charges simulating missile canister.

- Closures included in all tests.
- Backfill soil specifications for 1/4-scale test similar to characteristics for Wing V operational sites.
- High speed photography for 1/4-scale test.

Blast measurements for the 1/10-scale tests, QDT-1 and QDT-2, were along two radials with 90° separation. Both tests were conducted with the same ground zero in order to economize with only one set of instrumented blast lines. Three radials with 120° separation, as depicted in Figure 2, were the zones for blast and debris/ejecta measurements for the 1/4-scale test QDT-3.

Characteristics of the structural debris and soil ejecta in relation to dimensions, weight, color, and location were measured in the three sectors for fragments with a maximum dimension of 1/2 inch and greater. Distinctive dye coloring was added to the various structural elements of the 1/4-scale model in order to permit post-test identification of fragment sources.

Analytical Investigations

Results of the analytical program may be briefly summarized as follows:

Airblast

- Good correlation was observed between analytical results and empirical data for the detonation of a 1000 pound TNT sphere tangent to ground surface.
- Comparison of S-Cubed and TRW results for the rigid silo calculations indicated certain anomalies which could not be resolved.
- Computation of airblast predictions for the 1/10-scale tests was not completed due to time constraints.
- A ground range of 202 feet corresponding to a pressure level of 1 psi was predicted for QDT-3.

Soil Ejecta

- Soil ejecta calculations for gradations, such as pebbles and rocks, estimated a ground range of 390 for an ejecta density of 1 per 600 sq ft resulting from the QDT-3 test.
- A very conservative estimate of the occurrence probability of large earth clumps indicated a maximum range of 1600 feet for a full-scale density of 1 per 600 sq ft.

Structural Debris

- Breakup of the 1/4-scale structural model was analyzed in detail with predictions developed for a broad spectrum of fragment sizes, launch parameters and impact ranges.
- Predictions for the QDT-3 debris distributions indicated a range of 721 feet for a density of 1 per 600 sq ft.
- Two independent analytical models, namely, a statistical simulation technique and a trajectory limitation approach, were developed for the purpose of debris scaling from the QDT-3 results to a full-scale operational event.

Results of the debris scaling evaluations associated with the statistical simulation method are shown in Table 1. Pretest calculations for Cases 1 to 9 were based on shape factors determined from the Distant Runner test data. Post-test calculations for Cases 10 to 12 were based on the QDT-3 shape factors. The various assumptions associated with Case 11 appeared to be a reasonable representation of the parameters associated with the QDT-3 results. Scaling approach A was selected for the purpose of establishing full-scale estimates. In essence, it appeared reasonable to assume that the full-scale range for a density of 1 per 600 sq ft may be determined by multiplication of the corresponding 1/4-scale QDT-3 range by a factor of 1.75.

The debris scaling approach based on trajectory limitation is demonstrated by the family of contours plotted in Figure 3. The abscissa values represent the maximum range R_L for a fragment of length L , whereas the ordinate values indicate the ratio of maximum ranges R_{4L}/R_L for fragments of lengths $4L$ and L , corresponding to ballistic trajectories associated with the designated launch velocities and launch angles. An ordinate value of 2.24 was selected as a reasonable upper bound to encompass the broad spectrum of launch parameters. The debris scaling procedure consists of determining the range corresponding to a density of $(2.24)^2$ or 5 per 600 sq ft and multiplying this range by 2.24 in order to determine the full-scale range for a density of 1 per 600 sq ft.

Test Results and Analyses

Figure 4(a) presents a comparative plot of the QDT airblast measurements of peak overpressures as a function of range. The ranges corresponding to the QDT-1 and QDT-2 data have been multiplied by a range scaling factor of 2.5 to coincide with the QDT-3 ranges in order to evaluate the applicability of cube root scaling on a common frame of reference. The agreement is excellent indicating that the cube root law is effective for

peak pressures over the domain of the 1/10- and 1/4-scale tests. The scaling comparison of positive duration and arrival time presented in Table 2 similarly shows good agreement, as also determined by a comparison of airblast waveforms.

In Figure 4(a), a comparison is also shown of the analytical prediction for QDT-3 with the observed results. Although the analytical curve is somewhat lower than the test data, the agreement is considered good, since it was anticipated that the predicted peak pressures would be lower due to a rounding of the sharp shock front caused by the computer zoning process. The analytical curve predicted a ground range of 202 feet for a pressure level of 1 psi. The QDT-3 data in Figure 4(a) indicates a ground range of 270 feet corresponding to an overpressure of 1 psi.

A calibration shot consisting of a surface burst of a 1000-pound tangent sphere was conducted for the purpose of evaluating the reliability of the QDT sensors and recording system as a total integrated system. This test was conducted at the same ground zero as QDT-3, permitting utilization of the same blast gage array. Excellent agreement is observed between the recorded blast data and the pretest predictions as shown in Figure 4(b).

A summary of the QDT-3 debris distribution for fragments of maximum dimension ranging from 1/2 to 7 inches is shown in Table 3. The test data consisted of 4732 fragments covering an area of 190,000 sq ft. The total number of fragments of 1/2 inch diameter or greater was estimated to be about 76,000 for the circumferential zone extending in radius from 125 to 1000 feet.

At QDT-3 shot time, there existed at ground zero a surface wind of 10 mph with azimuth of 110° relative to True North. Post-test analysis of the debris data indicated significantly higher quantities along the Northwest radial than along the other two. The data asymmetry was attributed to the influence of wind conditions.

Analysis of the QDT-3 data yielded the debris density distributions shown in Figure 5(a) for the case of all of the data from the South, Northeast, and Northwest radials being given equal weight, and in Figure 5(b) for the case of the data only from the Northwest radial being assumed as representative for all radials as an upper bound. A least squares analysis was performed for several analytic functions with the result that a minimum standard deviation was obtained for the following exponential functions:

$$\text{S, NE, and NW radials: } N_{1/4} = e^{6.3 \left(1 - \frac{R}{812}\right)}$$

$$\text{NW radial only: } N_{1/4} = e^{7.6 \left(1 - \frac{R}{896}\right)}$$

where $N_{1/4}$ is the number of fragments per 600 square feet and R is the range in feet.

For the first relation, the range corresponding to a density of 1 per 600 sq ft is 812 feet, and for the second relation, the range is 896 feet. There appears to be reasonably good correlation with the test prediction of 721 feet. For the soil ejecta distribution, the test data indicated a range of about 300 feet for a density of 1 per 600 sq ft as compared to the prediction of 390 feet.

It is readily apparent that structural debris is the major contributor to the fragment hazards with negligible influence by the soil ejecta.

Quantity-Distance Verification

Results of the evaluation of the QDT airblast data, indicated the applicability of cube root scaling for 1/10- and 1/4-scale tests. The computer analyses indicated a similarity of effects at scaled times and scaled distances for the 1/10- and 1/4-scale results implying the suitability of cube root scalings for all scale factors. As far as can be judged from the analytical and experimental results, it appears reasonable to conclude that cube root scaling would be applicable for a full-scale event. The ground range to 1 psi for the QDT-3 data was 270 feet. Therefore, the corresponding distance for a full scale event is estimated as 4×270 feet or 1080 feet.

A comparative plot is shown in Figure 6 of the peak overpressure versus scaled distance for a TNT surface burst, results of the C-Cubed rigid silo analysis and QDT-3 test results. For a value of $R = 1080$ feet and $W = 202,000$ pounds, the scaled range is $R/W^{1/3} = 18.4 \text{ ft/lb}^{1/3}$ for a Peacekeeper event. For the case of the Q-D planning range of 1750 feet, the scaled range is $29.8 \text{ ft/lb}^{1/3}$.

The early calculations leading to the planning estimate of 1750 feet, were based on a rigid silo model with 5% reduction in range to account for flexible walls, launcher equipment room (LER) configuration, and closure. This range reduction corresponds to an

1/4-scale events indicated in both cases an energy loss of 65% to the concrete and soil within a period of several milliseconds. It is quite probable that this major reduction at a very early stage in the energy available for airblast effects contributed significantly to the relative low Q-D range of 1080 feet.

A scaling evaluation of structural fragmentation characteristics indicated that geometric scaling of the QDT-3 fragments was most probable with an upper bound estimate that the total number of fragments may be enhanced by a factor of 2.

Figure 7(a) indicates the results of scaling the QDT-3 data for the S, NE, and NW radials by means of the statistical simulation method. Scaling results by the trajectory limitation approach are presented in Figure 7(b). A summary tabulation of the Q-D debris ranges based on the various assumptions and procedures is presented in Table 4. As an upper bound, it appears reasonable to assume the overall average value of 1567 feet.

Summary and Conclusions

Results of the study may be briefly summarized as follows:

Airblast

- The airblast data for the 1/10-scale and 1/4-scale tests verified applicability of cube root scaling.
- Excellent agreement between test data and predictions for a calibration shot validated the reliability of the airblast measurements.
- Analytical predictions for the 1/4-scale test were in agreement with the empirical data.
- The ground range to a peak pressure level of 1 psi for the 1/4-scale test was determined to be 270 feet, with a corresponding full-scale value of 1080 feet.

Soil Ejecta

- The ejecta distribution for the 1/4-scale test extended out to relatively limited ranges.
- The impact of ejecta on quantity-distance considerations was considered to be negligible.

Structural Debris

- There was good correlation between predictions of structural fragmentation characteristics and test results.

- Geometric scaling of fragment dimensions was considered applicable for a full-scale event.
- A rationale was established for an increase in the fragment number by a factor of 2 as an upper limit for a full scale explosion.
- Application of statistical simulation and trajectory limitation scaling methods to the 1/4-scale test data results in an estimate of 1567 feet as a conservative upper bound for the required quantity-distance.

Table 5 indicates the Q-D ranges for the various hazardous environments. Based on the analytical and experimental results of the present study, it is concluded that the adequacy of 1750 feet as the quantity-distance for the Peacekeeper system has been verified.

Table 1. Comparison of Fragment Scaling Evaluations by Statistical Simulation Method

Case	Launch V_0 and θ_0 Spectrum	Drag Coefficient	Number Gradient	Scaling Approach A			Scaling Approach B			Scaling Approach C					
				$R_{1/4}$ for $1/600 \text{ ft}^2$ (ft)	$(RFS)_{1/4}$ for $1/600 \text{ ft}^2$ (ft)	Scale Factor λ	λ^2	$R_{1/4}$ for $\lambda^2/600 \text{ ft}^2$ (ft)	$(RFS)_{1/4}$ for $1/600 \text{ ft}^2$ (ft)	Scale Factor λ	λ^2	$(R_{1/4})_{1/4}$ for $1/600 \text{ ft}^2$ (ft)	$(RFS)_{1/4}$ for $1/600 \text{ ft}^2$ (ft)	$(RFS)_{1/4}$ for $1/600 \text{ ft}^2$ (ft)	
1*	Uniform	1/2	1/2	848	1644	1.93	2.72	7.4	604	1644	4	16	512	2048	1.24
2	Uniform	1/2	2/3	1020	1999	1.96	2.88	8.3	694	1999	4	16	593	2322	1.19
3	Uniform	1/2	3/8	732	1446	1.98	2.74	7.5	528	1446	4	16	453	1812	1.25
4	Skewed	1/2	1/2	773	1572	2.03	2.88	8.3	546	1572	4	16	475	1900	1.21
5	Uniform	1	1/2	553	1249	2.26	3.11	9.7	402	1249	4	16	367	1468	1.18
6	Skewed	1	1/2	516	1150	2.23	3.11	9.7	370	1150	4	16	336	1340	1.16
7	Uniform; Scaling 2:1	1/2	1/2	848	1704	2.01	2.88	8.3	591	1704	4	16	512	2048	1.20
8	Uniform; $2N_0$	1/2	1/2	932	1889	2.03	2.76	7.6	684	1889	4	16	596	2348	1.26
9	Uniform; $1/2N_0$	1/2	1/2	764	1398	1.83	2.64	7.0	530	1398	4	16	427	1708	1.22
	Average					2.03	2.86	8.2							1.21
10**	Skewed	1/2	1/2	670	1159	1.73	2.10	4.4	552	1159	4	16	450	1800	1.55
11	Skewed	1/2	2/3	750	1310	1.75	2.12	4.5	616	1310	4	16	504	2016	1.54
12	Uniform	1/2	2/3	712	1140	1.60	2.14	4.6	531	1140	4	16	384	1536	1.35

*Cases 1-9: Distant Runner shape factors - pretest calculations

**Cases 10-12: QDT-3 shape factors - post-test calculations

Table 2. Scaling Comparison of Positive Duration and Arrival Time of Airblast Waveforms

Range* (ft)	Positive Duration (msec)		Arrival Time (msec)	
	Average Value QDT-1 and -2*	QDT-3	Average Value QDT-1 and -2*	QDT-3
42	11.6	12.5	25	22
78	18.2	15.7	48	48
110	20.8	20.7	74	70
130	22.9	22.3	93	90
160	24.2	23.6	120	115
200	25.4	24.9	156	148
250	26.6	26.7	194	191
325	28.7	28.9	260	259
400	30.5	30.9	326	324
500	32.5	32.8	415	415
610	33.7	34.8	515	513
740	35.0	36.1	627	629
880	36.0	37.7	750	752
1080	37.1	39.4	931	931
1320	39.0	40.7	1155	1147

*QDT-1 and QDT-2 values scaled to QDT-3 by multiplication by factor of 2.5.

Table 3. QDT-3 Structural Debris Data Summary

Range (ft)	Radial			Range (ft)	S Radial		NE Radial		NW Radial	
	Area 3 (10 ft x 10 ft)				Area 57.5 ft x 50 ft		Area 57.5 ft x 50 ft		Area 57.5 ft x 50 ft	
	S	NE	NW		Left Segment	Right Segment	Left Segment	Right Segment	Left Segment	Right Segment
125	135	122	126*	130-187	143	---	273	---	---	---
250	67	49	188	187-245	395	---	179	---	---	---
375	18	15	60	255-312	179	---	130	---	410	---
500	11	2	42	312-370	90	---	91	---	721	---
625	0	1	7	380-437	70	54	39	37	271	---
750	0	0	4	437-495	68	20	32	8	227	---
875	0	0	2	505-562	43	15	16	11	---	103
1000	2	0	2	562-620	13	12	4	10	---	52
Total	233	189	431	630-687	15	9	2	5	---	33
Number of Fragments 4732				687-745	4	5	2	2	---	12
Area $A_0 = 190,900 \text{ ft}^2$				755-812	6	4	0	2	8	9
Total Area				812-870	1	5	4	2	13	5
$A_T = \pi (1000^2 - 125^2)$				880-938	1	1	0	2	3	2
$A_T = 3,090,000 \text{ ft}^2$				938-995	0	0	0	1	2	3
$\frac{A_0}{A_T} = 6.2\%$				Total	1028	125	772	80	1655	219
Total Number of Fragments										
$N_T = \frac{4732}{0.062} = 76,300$										
*Data for two witness sheets										

Table 4. Full-Scale Quantity-Distance Estimates for Structural Debris

Debris Scaling Method	QDT-3 Radials	Total Fragment Number	Fragments per 600 ft ²	QDT-3 Range (ft)	Scale Factor	Full Scale Range (ft)
Statistical Simulation	S, NE, NW	N ₀	1	812	1.75	1421
		2N ₀	1	901	1.75	1577
	NW	N ₀	1	896	1.75	1568
		2N ₀	1	977	1.75	1710
Trajectory Limitation	S, NE, NW	N ₀	5	604	2.24	1353
		2N ₀	5	694	2.24	1554
	NW	N ₀	5	706	2.24	1581
		2N ₀	5	790	2.24	1770
Average						1567

Table 5. Quantity-Distance Ranges for All Environments

HAZARDOUS ENVIRONMENT		Q - D RANGE (FEET)					
		0	500	1000	1500	1750	2000
BLAST OVERPRESSURE				▽			
FRAGMENTS	SOIL EJECTA	▽					
	STRUCTURAL DEBRIS				▽		

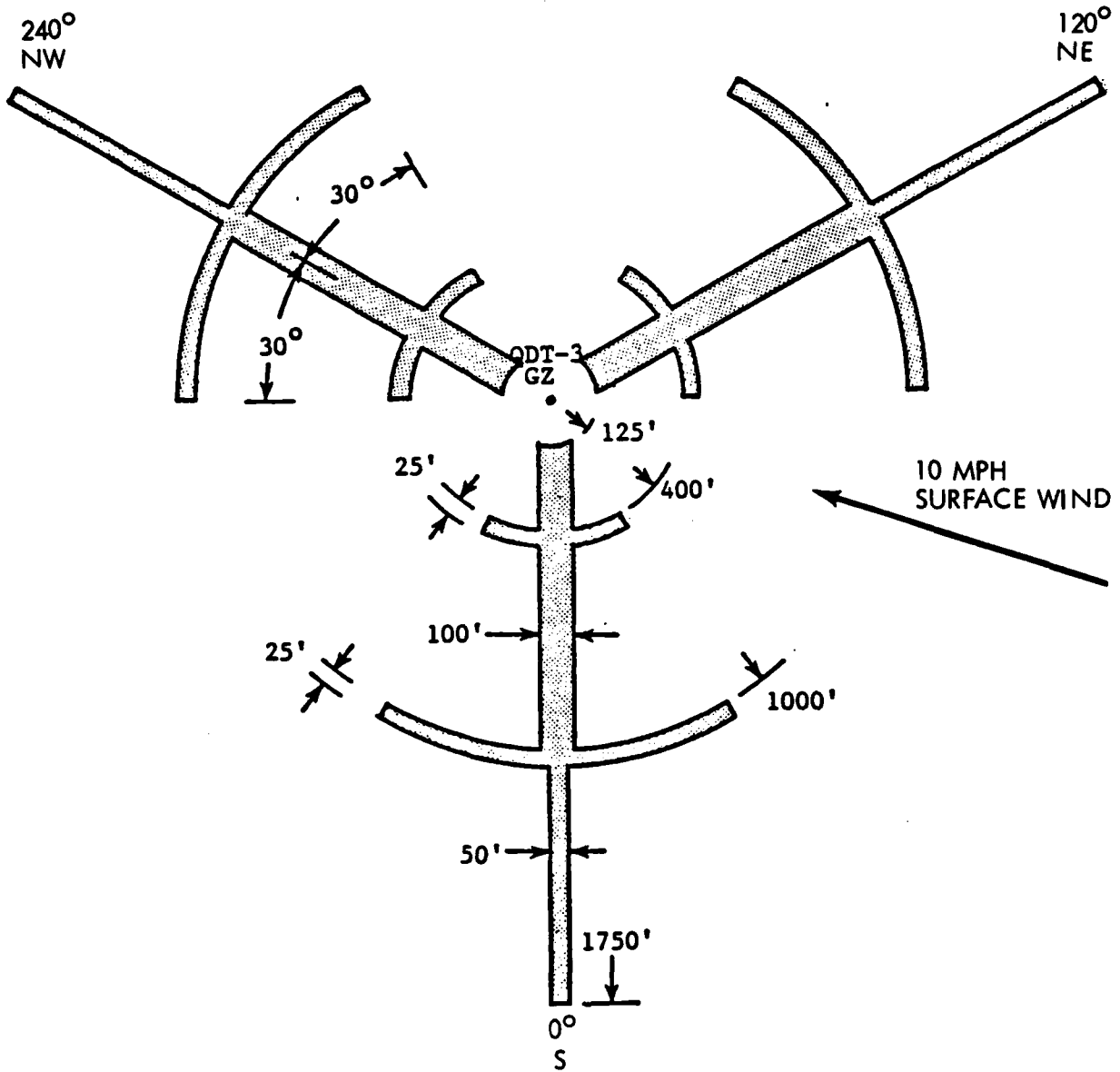
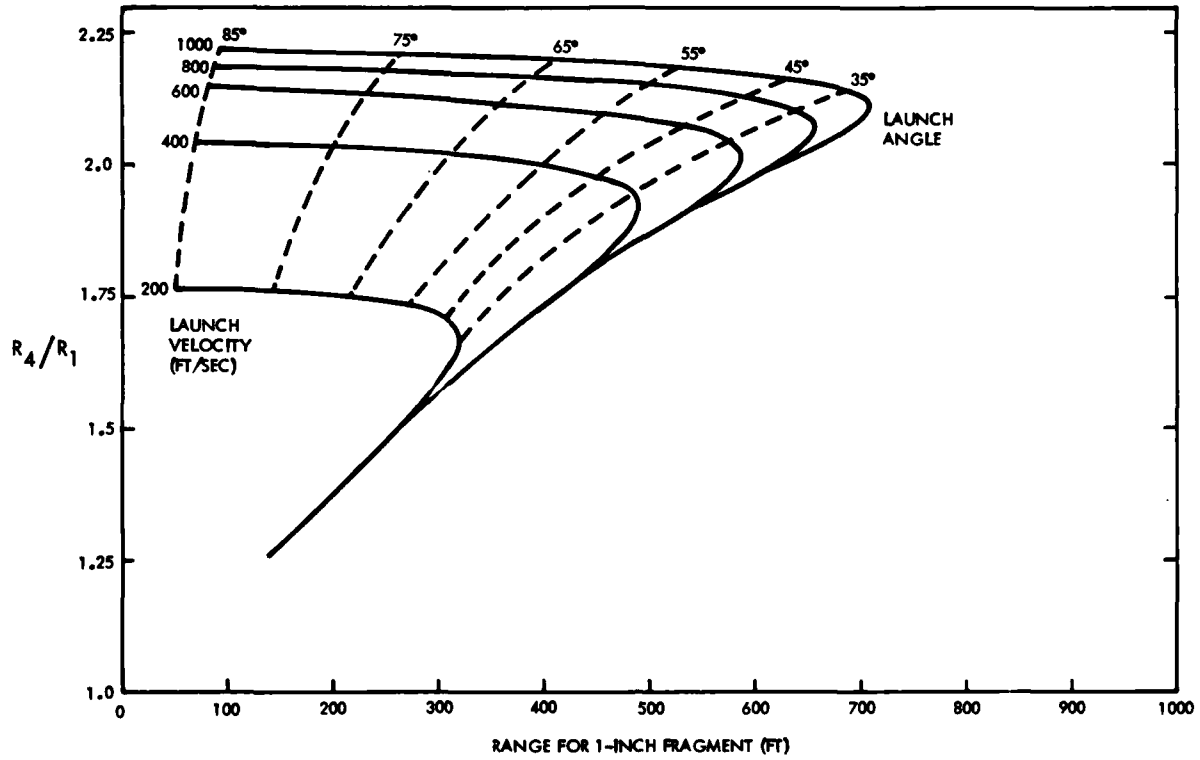


Figure 2. Locations of Areas Requiring Brush Clearing for Airblast Gages and Fragment Surveys

(a) FRAGMENT LENGTHS OF $L = 1''$, $4L = 4''$



(b) FRAGMENT LENGTHS OF $L = 2''$, $4L = 8''$

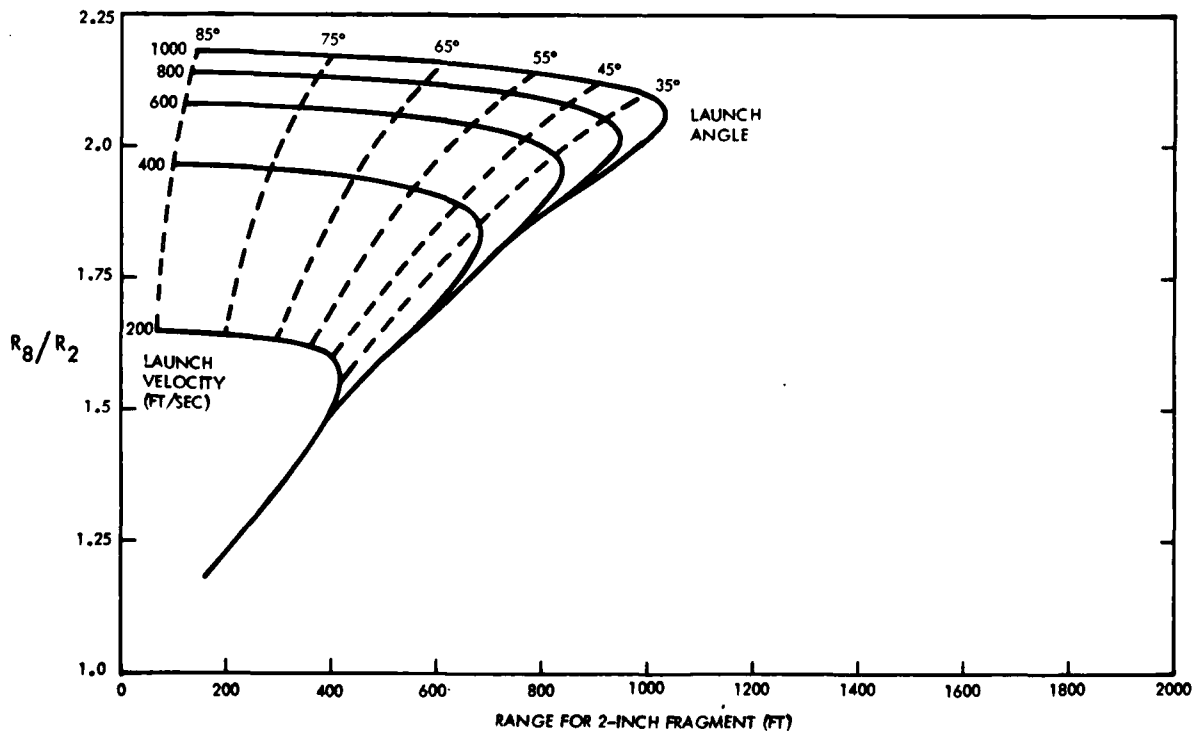


Figure 3. Comparison of Maximum Range Ratios Corresponding to QDT-3 Fragment Shape Factors and Drag Coefficient of 0.5

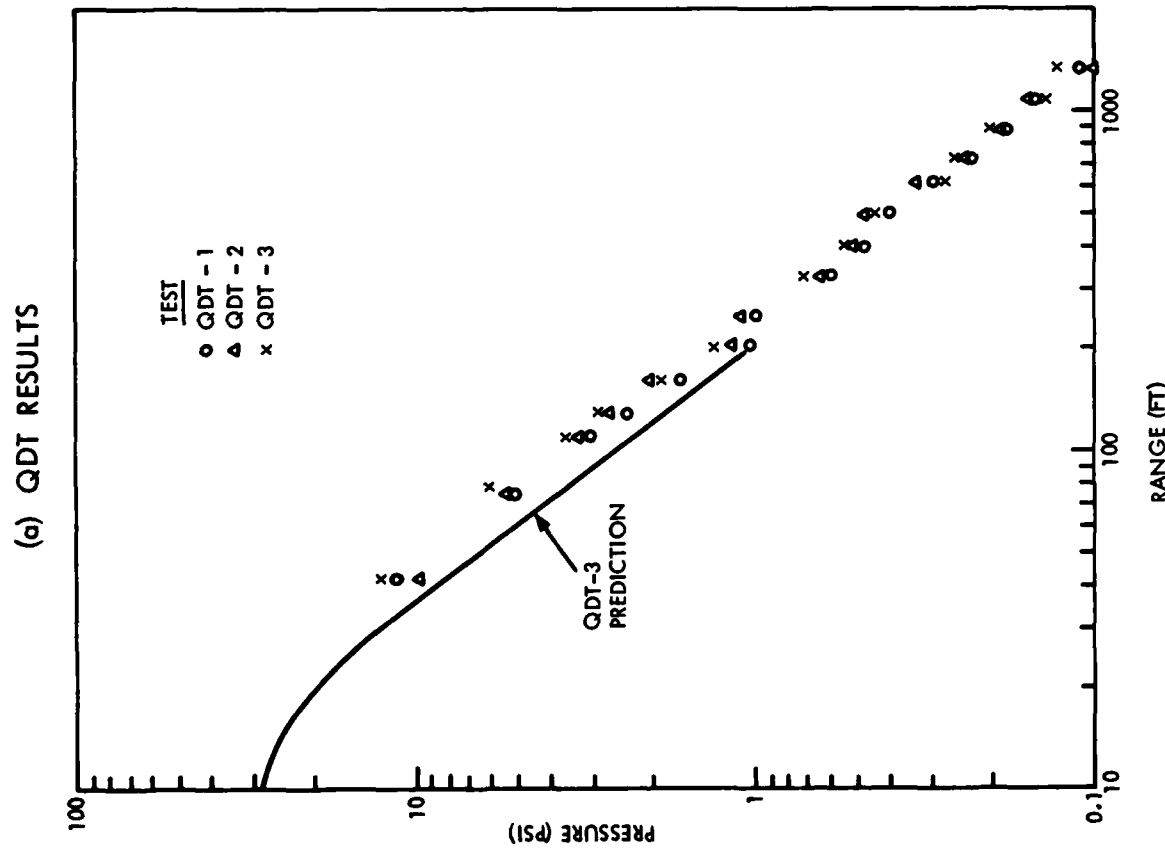
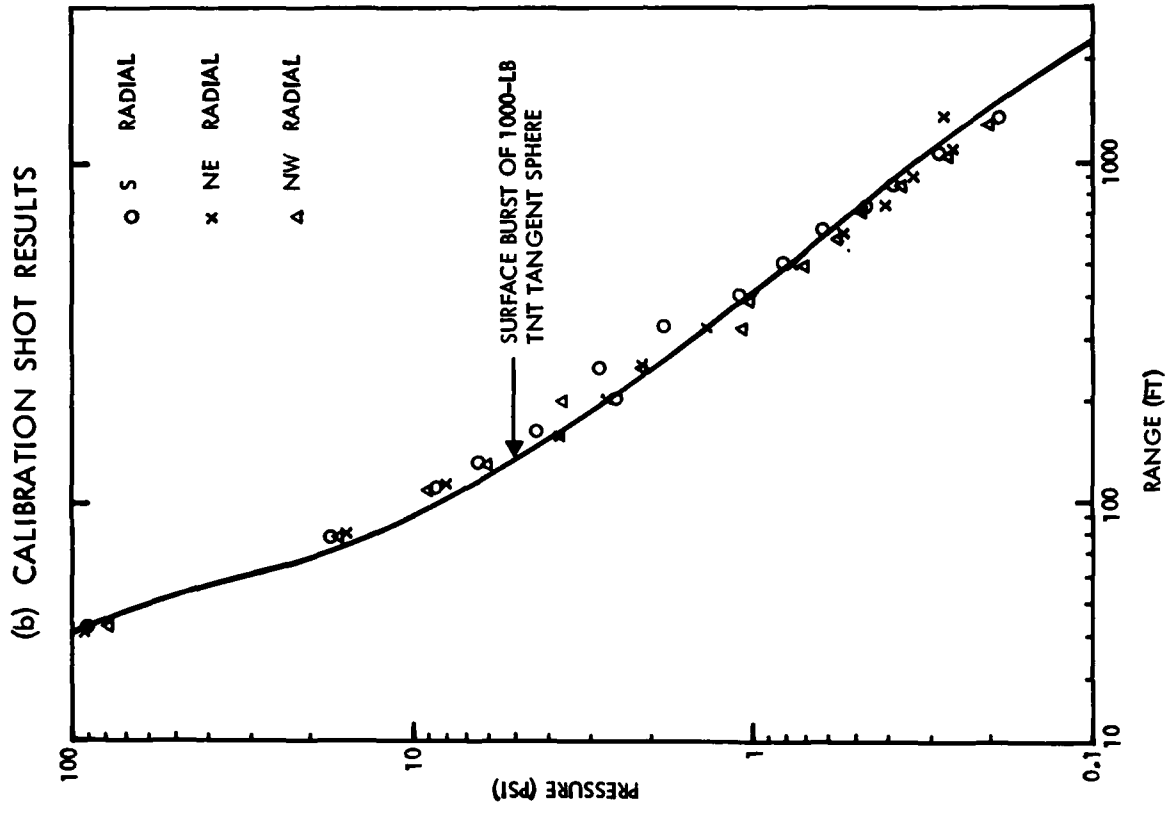
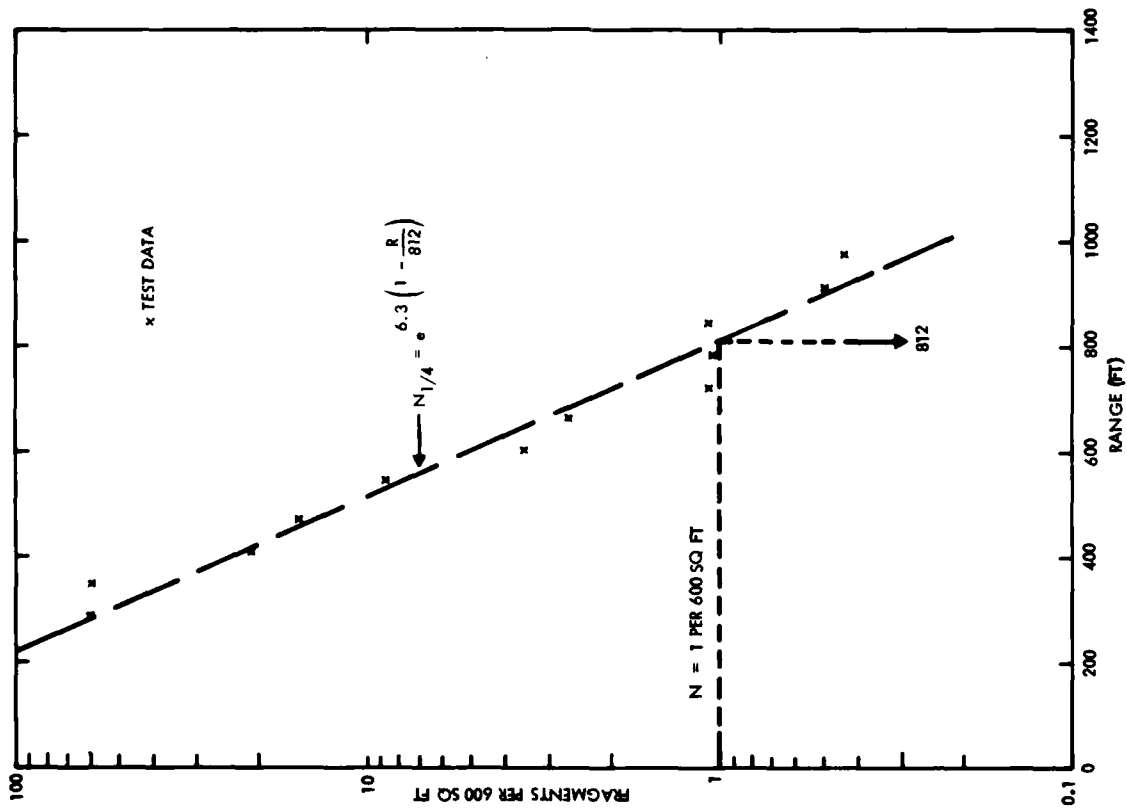


Figure 4. Comparison of Airblast Data Predictions and Test Data

(a) S, NE, AND NW RADIALS



(b) NW RADIAL ONLY

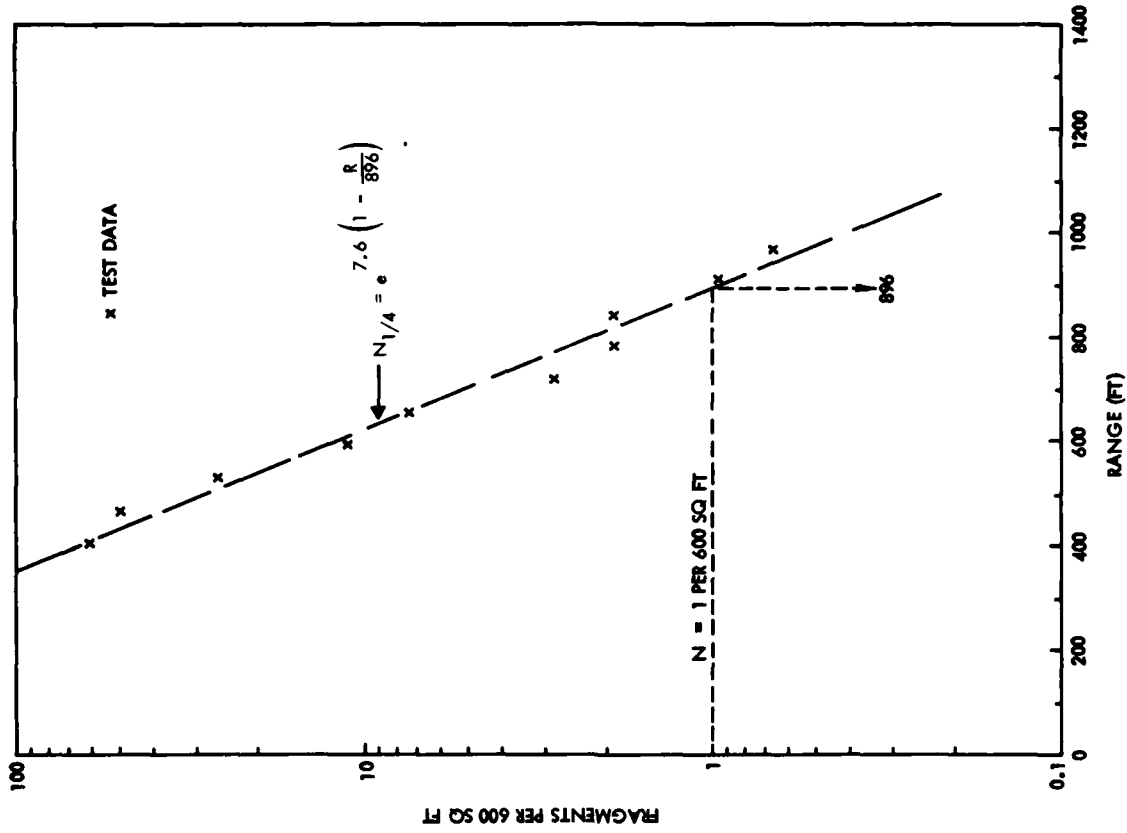


Figure 5. QDT-3 Structural Debris Density Versus Range

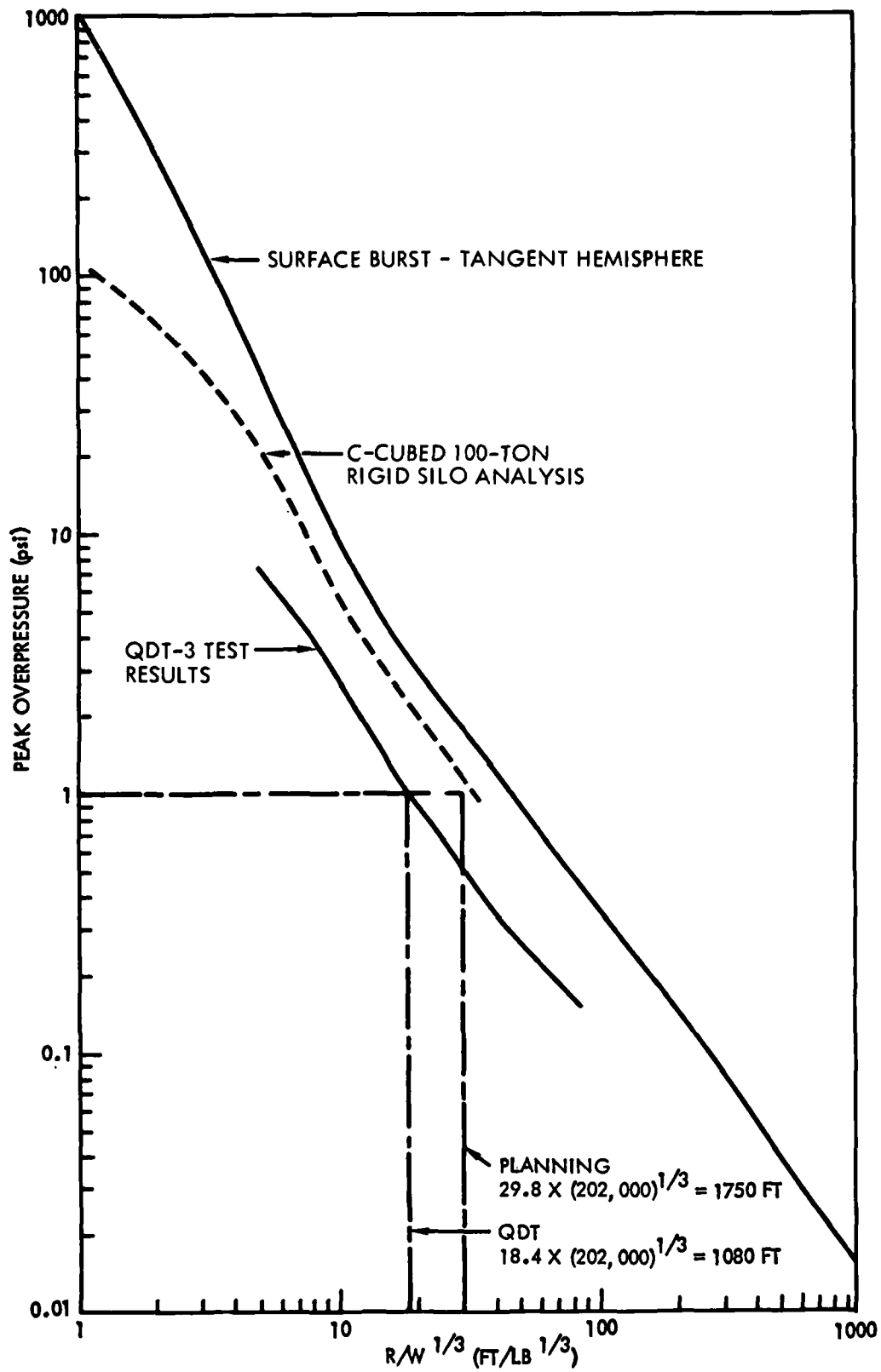
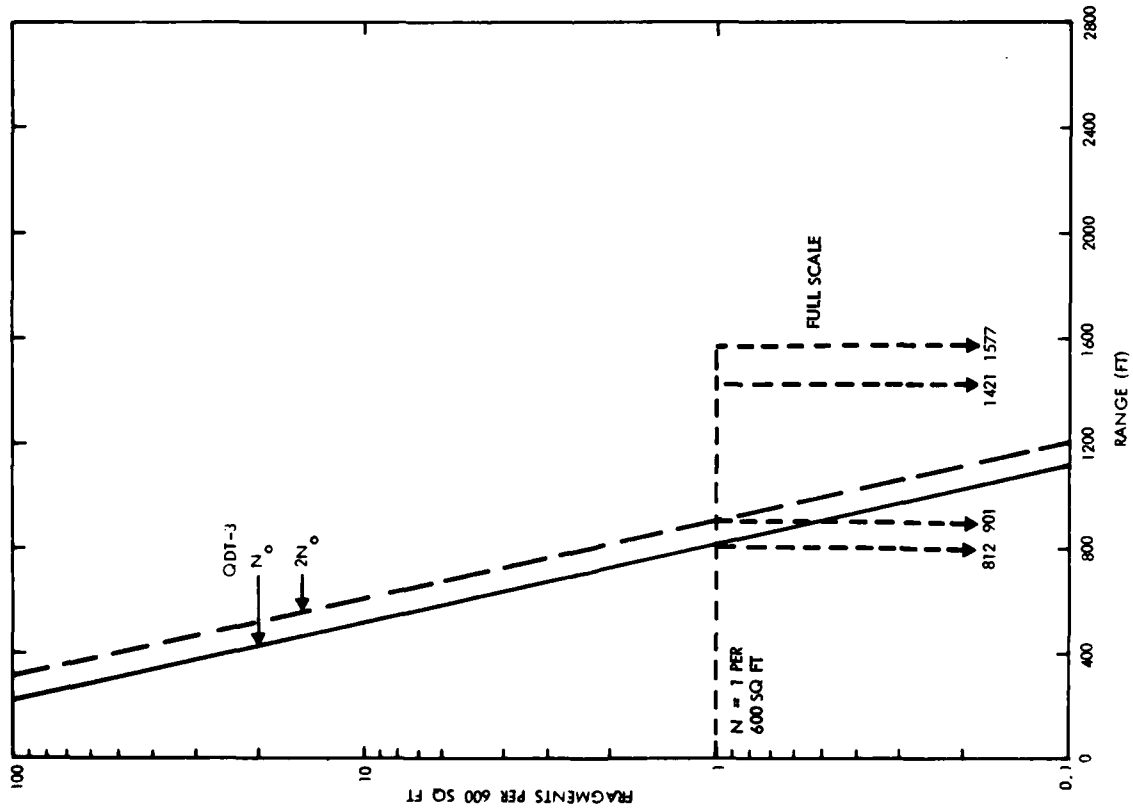


Figure 6. Peak Overpressure Versus Scaled Range

(a) STATISTICAL SIMULATION METHOD



(b) TRAJECTORY LIMITATION METHOD

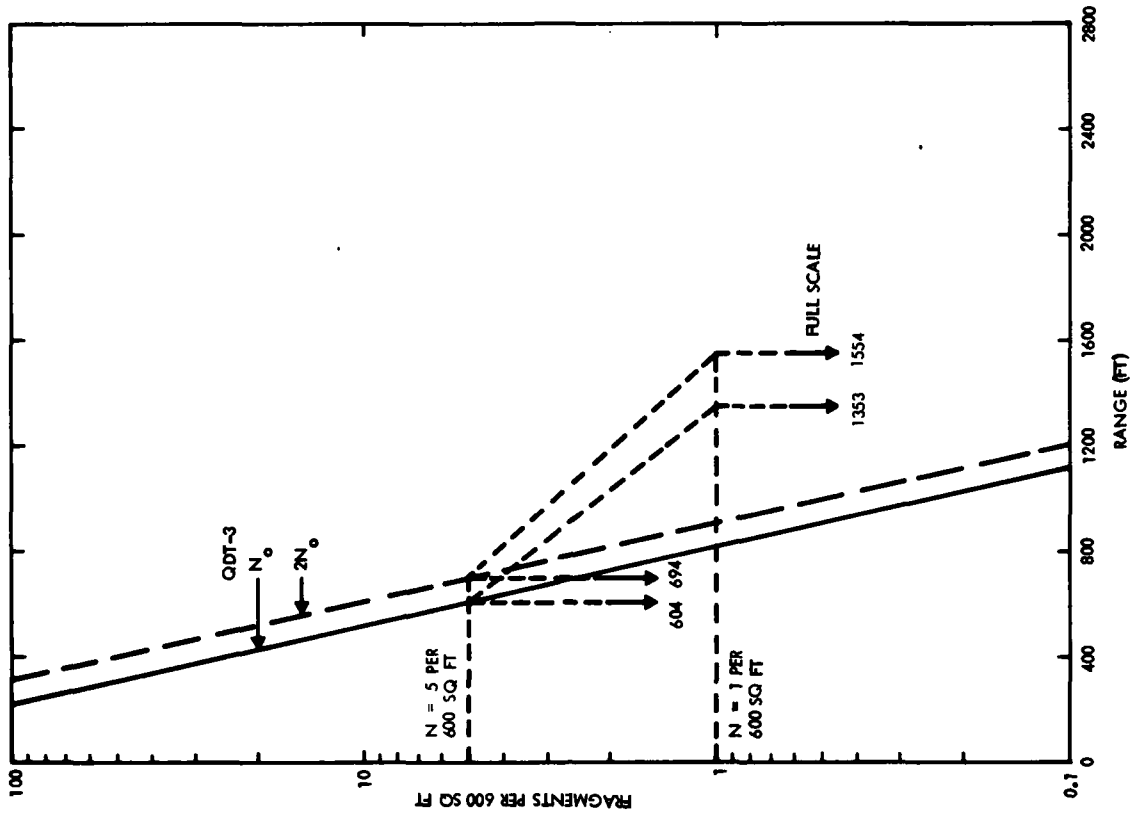


Figure 7. QDT-3 Debris Density Scaling for Data on S, NE, and NW Radials

1.0 INTRODUCTION

1.1 Background

When the decision was made to base 100 Peacekeeper missiles in Minuteman silos, the Department of the Air Force Inspector General established, for planning purposes, an estimate of the quantity-distance requirements as 1750 feet from inhabited buildings and 1050 feet from public traffic routes. The IG further stated that rigorous analyses and testing would be performed to verify the planning criteria. The implementing direction in PMD No. 0075(13)/64312F/11215F, dated 14 September 83, Section 3a(1)(b)(r) directs AFSC to "Verify, through analysis and testing, the quantity-distance criteria established by the HQ USAF/IG for planning purposes for Peacekeeper in Minuteman silos."

The basic issues associated with Q-D that were addressed in the Q-D Verification Program are:

- Determine blast and fragment distribution characteristics for an explosion of a Peacekeeper missile installed in an operational Minuteman launch facility.
- No experimental data exist on blast or debris effects associated with an in-silo explosion corresponding to the charge geometry and location within a reinforced concrete structure of the nature of the operational configuration.

Requirements for Q-D verification based on safety criteria specified in AFR 127-100 consist essentially of determination of (a) the ground range for 1 psi peak overpressure level and (b) the ground range for a hazardous fragment areal density of one fragment per 600 square feet with impact energy of 58 ft-lb or greater, as associated with an in-silo explosion of a full-scale missile or equivalent TNT charge.

An analytical effort could be performed toward investigation of the probability of sympathetic mass detonation of Stages I and II as a result of initiation of Stage III by some arbitrary unspecified means. Detailed considerations would be directed toward evaluation of the effect of interstage separation, canister constraint, propellant geometry, and fragment characteristics. The purpose of the analytical program would be to determine whether sympathetic detonation between stages is probable or not, which would result in a significant difference in estimates of missile TNT equivalence. However, the capability of achieving a reduction in NEW from upper limits purely by theoretical analysis was not considered feasible due to the extreme complexity of the associated phenomena. Therefore, for the purpose of the Q-D verification program, it was conservatively

assumed that sympathetic detonation would occur, leading to of an upper bound of 202,000 lb as the NEW for the Peacekeeper missile. This value is base on a conservative estimate of 1.20, 1.20, and 1.25 times the propellant weights of Stages I, II, and III, respectively, as the NEW for each stage assuming full order sympathetic detonation of progressive stages following initiation of Stage III.

With reference to the blast and debris phenomenology, efforts were directed toward solely formulating analytical program which would be considered adequate for the purpose of verification of the Q-D criteria. However, one limitation to this approach was that no empirical blast or debris data exist for in-silo explosions corresponding to the charge geometry or silo configuration of interest. The technical community have indicated that in singular types of events where only analytical data may be available, it is essential that at least one meaningful test be performed for correlation in order to eliminate the possibility of unforeseen effects that may occur due to the complexity of the real world which often cannot be adequately modeled in theoretical investigations. Supplementary analyses would be essential where experimental programs were limited to subscale tests in order to establish required estimates of effects associated with full-scale events. Analytical models would be evaluated for the purpose of developing scaling laws for blast and debris phenomenology associated with explosions in subsurface structures like the reinforced concrete Minuteman silos.

Scaling of blast overpressure has generally been based on the cube root law, such that the ratio $R/W^{1/3}$, where R is the ground range to a specified overpressure level and W is the charge weight, is conserved for a specified pressure level. No specific criteria for debris scaling are currently available. Each configuration of charge and structure requires an independent ejecta distribution evaluation.

1.2 Objectives

The principal objective of the present program was to verify the adequacy of 1750 feet as the quantity-distance criteria for an explosion associated with a Peacekeeper missile within a Minuteman silo.

2.0 PROGRAM DEFINITION

An effort was made to identify the minimum testing required to supply an empirical frame of reference adequate to supplement an analytical program toward the required Q-D verification. It appeared that a subscale silo test (approximately 1/10-scale) would be sufficient to establish the necessary blast scaling data assuming the applicability of cube root scaling. A simplified cylindrical pit with commercial pipe liner was considered satisfactory for the purpose of obtaining the required empirical data point.

However, for the basic debris dispersal information, a minimum requirement consisted of a 1/4-scale test of a reinforced concrete Minuteman Wing V silo. The blast data associated with the 1/4-scale test would have been sufficient by itself for a scaling analysis based on the cube root law. However, it was considered advisable to incorporate both the 1/10-scale and 1/4-scale tests in the verification program in order to determine the applicability of the cube root law over this domain of scaling. Two identical 1/10-scale tests were planned for the purpose of evaluating the reproducibility of complex phenomena associated with an event of this nature.

2.1 Test Requirements

The test requirements are briefly outlined as follows:

- Two 1/10-scale tests
 - Steel structures scaled to volume and mass of Minuteman Wing V silo
 - Explosive charge of 202 pounds TNT
 - Blast measurements only on two radials at 90 degree separation
- One 1/4-scale test
 - Reinforced concrete structure simulating detailed representation of Minuteman Wing V silo
 - Explosive charge of 3156 pounds TNT
 - Blast and debris/ejecta measurements on three radials at 120 degree separation
 - Debris/ejecta measurements of dimensions, weight and location for fragments of 1/2-inch maximum diameter or greater

- High speed photography of explosion effects
- General
 - Closures included on all tests
 - Cylindrical explosive charges with center of gravity at scaled CG of missile propellants during Peacekeeper operational alert stage
 - Charge initiation at charge center with depth corresponding to scaled CG of Stage III propellant
 - Steel containers for charges to simulate missile canister

2.2 Theoretical Investigations

Requirements for the analytical program were as follows:

- Airblast
 - Calibrate analytical model by two methods
 - Calculation for rigid silo configuration similar to DNA/S³ analysis
 - Determination of blast effects associated with a selected previous experiment for correlation with empirical results
 - Develop test predictions for the 1/10- and 1/4-scale tests
 - Determine quantity-distance for full-scale operational event
- Debris/ejecta
 - Develop test predictions based on analytical and empirical models
 - Investigate structural fragmentation characteristics under high internal blast pressure loading
 - Develop debris scaling methodology
 - Determine quantity-distance for full-scale operational event.

3.0 TEST DESCRIPTION

The following description of test procedures consists of segments reproduced from the Test Plan prepared by the Waterways Experiment Station (WES), Test Conductor (Reference 3-1).

3.1 Introduction

The tests associated with the Peacekeeper Quantity-Distance Verification Program consisted of a series of three scaled tests (two at 1/10-scale and one at 1/4-scale) using high explosives to simulate the blast and ejecta effects associated with an explosion of a Peacekeeper missile within an operational Minuteman silo.

3.1.1 Objectives

The overall objective of the test program was to provide experimental data to be used as a basis for verification of the quantity-distance criteria corresponding to a full-scale operational event. The primary objective of the 1/10-scale tests was to measure airblast and corresponding distance associated with an explosion within a scaled buried silo to verify airblast scaling relations. The primary objective of the 1/4-scale test was to measure airblast, ejecta, and fragmentation with respect to distance due to an explosion in a scaled silo to provide specific data to aid in the development of airblast and ejecta scaling relations between the model test and a full-scale detonation.

3.1.2 Scope

The QDT program consisted of tests on two 1/10-scale structures and one 1/4-scale structure. The 1/10-scale structures were a volumetric representation of the Minuteman silo, constructed of steel plate, with a length of 8 feet 2-3/4 inches. The 1/4-scale structure was a detailed representation constructed of concrete and steel, with an overall length of 23 feet 7-1/2 inches. A high-explosive charge was placed in each structure to simulate the airblast, ejecta, and fragmentation associated with an explosion in a Minuteman silo.

The airblast measurements during the 1/10-scale tests were made on two radial lines (15 gages on each line) out to 530 feet. During the 1/4-scale test, airblast was measured on three radial lines (15 gages each) out to approximately 1320 feet, with debris/ejecta

measured out to 1750 feet. The 1/4-scale structure was placed in an 80 by 80-foot wide test bed and backfilled with a simulated Wing V soil consisting of a blend of sand and gravel. The crater ejecta and concrete fragmentation resulting from the explosion were measured using plastic sheets. Colored sand columns and special ejecta pieces were placed in the test bed for more accurate identification. The silo was instrumented with 16 strain gages to determine when the structure broke apart. High-speed photography of the explosion events was incorporated in the 1/4-scale test program.

3.2 Test Site Description

The QDT tests were conducted on the Permanent High Explosive Test Site located at the White Sands Missile Range, New Mexico. This site was selected because of its flatness and lack of established real estate. The water table is approximately 130 feet deep and would not interfere with the test beds.

3.3 Soil Backfill Description

A search was conducted to determine how many of the Minuteman sites in Wing V had soil (as opposed to rock) in the upper 130 feet of the profiles for correlation with the available soil gradation data (Figure 3-1). This information is given in Reference 3-2. It was required that the backfill around the scaled structures should meet the limits of the gradation curve shown in Figure 3-2 plus 1/2% of total mass distribution consisting of 3/4-inch particles up to 12-inch particles. In order to obtain such material, it was necessary to blend both sand and aggregate in proportions and check gradations until the objective was satisfied. After the backfill had been selected, laboratory tests were performed to determine the compaction required to achieve a relatively dense state. This number was used as a guideline during field placement.

Once the backfill material had been blended and was on site, bag samples were obtained for the purpose of laboratory tests. These tests included uniaxial strain tests up to 1 kbar as well as triaxial tests. One bag sample was taken from every 100 yd³ of material.

3.4 Test Concept for 1/10-Scale Structures

The 1/10-scale structures were designed to simulate the scaled volume of a Minuteman silo. In addition, the volume and configuration of the LER was modeled so the airblast exiting the structure would be correctly simulated.

3.4.1 Structure Description and Fabrication

The 1/10-scale structure, shown in Figure 3-3, consisted of three sections: a launch tube (LT), LER, and closure. The LT had an internal diameter of 1 foot 3 inches and a length of 5 feet 10 inches. The LT was fabricated from 1/8-inch thick steel plate. The plate was sheared and rolled to the correct diameter and then welded with full penetration welds.

The LER had an internal diameter of 2 feet 6 inches and an internal height of 2 feet. Steel plate, 1/2-inch thick, was used to build the LER. The plate was sheared and rolled to form the side of the LER and joined by full penetration welds. A flat ring was torch cut having an inside diameter of 1 foot 3 inches and an outside diameter of 2 feet 7 inches and then welded to the top of the LER. Another 1-inch thick ring in eight segments was welded to the top as shown in Figure 3-3, to more closely scale the mass at the top of the LER.

The closure consisted of 1-inch and 1-3/4-inch thick steel plates torch cut to a diameter of 1 foot 6 inches. The closure, which weighed 200 pounds, covered the opening atop the LER.

3.4.2 Field Preparation

The field preparation at the test site began by laying out the first of the 1/10-scale silo locations (QDT-1) and two 530-foot radial lines extending from ground zero at 90 degrees separation (Figure 3-4). The ground surface of the radials was smoothed over a 100-foot width to 500 feet and a 50-foot width to 530 feet. Next, an 8-foot 2-3/4-inch hole, 9 feet square, was excavated at ground zero. The bottom of the excavation was leveled and the LT lowered into place, the top opening covered, and the backfill soil placed around the LT. The backfill (recompacted native material) was placed in 6-inch lifts and approximately two vibration passes were made to achieve the desired density. Density and moisture content readings were obtained at 1-foot intervals. When the backfill reached the top of the LT, the LER was emplaced and backfill continued. A test bed layout for the 1/10-scale structure is shown in Figure 3-5.

Cables for the airblast gages were run from the instrumentation trailer to each gage location on the two radial lines, and a gage mount within a 1-foot diameter concrete pad placed at each gage position. Once the gages were installed and checked, the test

explosive and simulated closure were placed. This field operation procedure was repeated for the second 1/10-scale silo (QDT-2) at the same location.

3.4.3 Explosive Charge

The explosive charges for the tests were Pentolite 50/50 (energy density 13% greater than TNT) due to higher reliability than TNT, and were in a cylindrical form as shown in Table 3-1. The 179-pound charges for the 1/10-scale silo tests were cast in a single integral cylinder made from 16-gage steel plate. The bottom of the cylinder had a permanent base. The charges had a well in the center of the top of the cylinder to place the detonator. Charge detonation was 0.4 feet below the top. For each test, the charge was suspended by a harness and cables in the LT so the center of gravity of the charge was 58.2 inches below the ground surface (Figure 3.5).

3.4.4 Airblast Instrumentation

The instrumentation for each 1/10-scale test consisted of two radial lines of airblast gages extending from ground zero at 90 degrees separation. Airblast instrumentation locations are given in Table 3-2. There were 15 gages on each radial (total of 60 gages for QDT-1 and -2) extending from 17 feet out to 530 feet from ground zero.

3.5 Test Concept for 1/4-Scale Structure

The 1/4-scale structure was designed to be a detailed scale model of an operational Minuteman Wing V Silo. The mass of the structure, including concrete and steel, was scaled and also included a scaled closure.

3.5.1 Structure Description

The 1/4-scale Minuteman model consisted of three structures: the LT, LER, and closure (Figure 3-6). The LT was an axisymmetric reinforced concrete structure with an inner steel liner with an internal diameter of 3 feet and an overall length of 18 feet 9 inches. The LER was an asymmetric reinforced concrete structure with an inner steel liner with an internal diameter of 6 feet 3 inches and an overall length of 8 feet 1-1/2 inches. The asymmetry was due to the personnel access hatch (PAH) included in the LER. The closure was constructed from reinforced concrete in a pie pan container with a depth of 10.5 inches. A 2-1/2-inch layer of concrete was placed on top of the closure and LER. All steel was ASTM A-36, or Grade 40, with the exception of the Number 2 bars

which were Grade 60. The concrete had a compressive strength of 7,000 psi at 28 days. The model LER is shown in Figure 3-6.

3.5.2 Structure Fabrication

The construction drawings for the model were prepared by TRW. The model was fabricated at WES to these specifications.

The liner for the LT was sheared, rolled, and welded to the correct diameter with concrete anchors welded to it. The hoop and longitudinal bars were tied to form the wall reinforcing. The concrete for the LT was placed continuously in the walls with a cold joint at the base.

The liner for the LER was sheared, rolled, and welded to the correct dimensions. The reinforcing was placed in the structure according to drawings. Concrete, in four stages was placed with each level having a different color. After the LER was completed, the top of the structure was painted a contrasting color.

The steel container for the closure was fabricated and reinforcing bars placed inside. Concrete, with another color added, was placed in the pie pan container. A 2-1/2-inch layer of concrete was bonded to the top of the LER and closure by means of epoxy.

3.5.3 Test Bed Description

The test bed layout for the 1/4-scale structure is shown in Figure 3-7. An excavation was made down to a depth of 25 feet. The top of the test bed was 80 by 80 feet.

3.5.4 Field Preparation

The method for constructing the test bed is shown in Figure 3-7. The test bed was constructed to provide an 80 by 80-foot wide by 20-foot deep open pit with the sides having a one-to-one slope. The final excavation was a 10 by 10 by 5-foot deep inner bed, making the total depth of excavation 25 feet. A ramp was dug to the north side of the test bed to allow machinery to move in and out of the pit.

In the inner bed, all necessary work was completed before placing the LT. A 14-inch life of native material backfill was added to bring the test bed to the proper depth of 23 feet 10 inches. The LT was placed and native material was backfilled in lifts of 2 feet up

to the 12-foot mark. The material was compacted by means of a vibratory roller and hand compacters.

Beginning at the 12-foot level, the simulated backfill was used to backfill around the structure. This procedure was accomplished in a stair-step method so that the native material and sand mixture would remain separate and the side would resemble a one-to-one slope. When the backfilling procedure reached the 15-foot 6-inch level, the LT liner extension was welded to the inner liner and the LER lowered into position with the PAH aligned to the northeast (120-degree radial).

After reaching the 16-foot 6-inch level, the instrumentation cables were connected and buried. These cables were protected by 6-inch PVC pipe and foam padding. Backfill placement continued to the 21-foot 6-inch level, where track footing for the closure was installed. The three tracks were then positioned and grouted into place. The remaining structure was buried and the test bed cleared.

Instrumentation cables for the airblast gages were run from the instrumentation trailer to each gage location on the three radial lines and a gage mount positioned. Once the gages were installed and checked, the test explosive, held in place by a harness, was positioned and the closure placed on the LER.

3.5.5 Explosive Charge

The explosive charge for the test was Pentolite 50/50 in a cylindrical form as given in Table 3-1. The 2,790-pound charge was cast in a single integral cylinder made from 1/8-inch thick steel plate. The charge had a well point in the center top of the container in which to place a detonator for firing. Charge detonation was one foot below the top. The charge was suspended by a harness and cables so its center of gravity was a distance of 159 inches below the ground surface (Figure 3-7).

3.5.6 Instrumentation

Test QDT-3 had 45 channels of airblast and 16 channels of strain on the silo. Airblast gage locations are given in Table 3-3. Locations of the strain gages in the 1/4-scale structure (QDT-3 test) are given in Table 3-4. Structure north is the positive x-direction and structure east is the positive y-direction.

A summary of the instrumentation for the three tests is given in Table 3-5.

3.6 Debris/Ejecta Studies

The objective of the ejecta studies was to document the ejecta/debris hazard produced by a 1/4-scale model test of a missile detonation in a Minuteman silo. A supporting objective was to provide specific ejecta/debris data to aid in the development of ejecta scaling relations between the model test and a full-scale detonation.

The approach to this study involved both active and passive measurements of ejecta/debris produced by a simulated missile detonation in a 1/4-scale model of a Minuteman silo.

Active measurements of ejecta/debris consisted of motion picture photography of both the early and terminal velocities of ejecta and debris missiles, and their early ejection and final impact angles. Limitations due to dust cloud obscuration were to be determined from the test results

Passive measurements consisted of searching, surveying, and recording the terminal locations of ejecta/debris missiles in three sectors and two circumferential rings (or portions thereof). One sector also included "seeded" artificial missiles, color-coded to identify their exact origins. Figure 3-8 shows the general layout of these survey areas at the test site. The ground surface within the surveyed radial sectors was cleared of brush and smoothed over a maximum 100-foot width out to 1000 feet for QDT-3. The 400-foot and 1000-foot rings were cleared to a 25-foot width in a 60-degree sector about each radial. The 1750-foot ring was identified with flagging.

3.6.1 Active Measurements

Technical motion picture coverage of the 1/4-scale missile/silo detonation included high-speed camera coverage of the initial rise and growth of the crater mound, early trajectories of material thrown out by the detonation, and impact of ejecta/debris pieces beyond the continuous ejecta field. Table 3-6 describes the camera coverage. Camera stations and coverages are depicted in Figure 3-9.

The 70-mm film records gave information on particle ejection angles and velocities, impact angles and velocities, and particle sizes. The exposure time of about 0.3 msec allowed a slur factor of approximately 0.7 inch for particles having velocities around 200 ft/sec. The 16-mm film records were used to record and analyze initial silo cap and exit-hole breakup symmetry and initial velocities of ejecta throwout.

The ejecta parameters were determined from tracking records obtained from 16- and 70-mm Vanguard Motion Analyzers. The trajectories of selected ejecta/debris missiles were analyzed for initial ejection and terminal impact parameters.

Gridded reference boards were used as backgrounds for determining the size of and distance to falling missiles. To reduce dust obscuration produced by ground shock and airblast, the ground surface between detonation and the camera position was sprinkled with oil, water, or other dust palliatives.

3.6.2 Passive Measurements

The passive measurements included the following activities:

- a. Seeded debris. During construction of the 1/4-scale Minuteman silo, the concrete of the structure was color-coded by adding concrete dye to the concrete mix.
- b. Sand columns. After the model silo was constructed, an array of sand columns was emplaced in one sector of the backfill area. A total of 90 linear feet of columns were emplaced, ranging from 20 feet deep at 10 feet from the silo axis to 10 feet deep at a range of 40 feet from the axis.

The columns were constructed as the backfill was placed around the completed silo. Prior to placing the first lift of backfill, the lower portion of the 6-inch diameter columns was drilled into the native soil and backfilled with colored sand. Two-foot-long sections of PVC pipe were placed over the columns. After two feet of fill had been placed around the structure, the pipes were filled with colored sand and then raised another two feet to accommodate the next lift of surrounding fill. Different colors of sand were used for different columns, and colored plastic beads were mixed in the sand to code the hole elevations at 3-foot intervals.

- c. Seeded ejecta. In order to determine the origin of natural missiles impacting beyond the continuous ejecta region, the backfill and in situ soil in the expected crater area were seeded with artificial missiles along the sand column radial. Two types of artificial missiles were used. One-inch cubes of colored plastic, each stamped with an identification number, were placed in the sand columns at 6-inch vertical intervals as they were backfilled. The second type of artificial missiles were aluminum cubes measuring one, two, four, and eight inches on a side. These cubes also were stamped with identification numbers corresponding to their emplacement locations. Clusters of cubes were buried at 15 locations adjacent to the sand column radial, before and during placement of backfill soil around the silo. Each cluster contained 16 one-inch, 8 two-inch, 4 four-inch, and 2 eight-inch cubes.
- d. Plastic witness sheets. Plastic sheets measuring approximately 10 by 10 feet in area (100 sq ft) were installed on the ground surface at selected locations in all ejecta/debris survey areas for use in determining missile impact densities. The edges of the sheets were staked or covered with soil to prevent their damage or removal by wind or airblast. They were spaced in groups of three at intervals of 125 feet out to a range of 1000 feet, and then

placed in pairs at intervals of 250 feet out to a range of 1750 feet. In addition, collector sheets were located at 10-degree intervals around each survey ring. After the shot, each witness sheet was examined for artificial missiles, debris, and ejecta in that order.

- e. Ground survey. Immediately after the test, a survey was made of ejecta/debris missiles lying within the three survey sectors and rings. The survey was conducted using to the following procedures:
- 1) Beginning at the outer edge of the continuous ejecta region, one sector was searched for artificial missiles. When located, the I.D. number was recorded, as well as the range at which it was found.
 - 2) After all artificial missiles and natural ejecta lying on the surface were recorded and collected, a search was made for seeded pieces of concrete debris. When found, the size and weight, cement color, and bead color were recorded along with the range and/or azimuth. Although the search for seeded concrete debris was concentrated in the survey sectors and rings, it included the entire cleared area surrounding the silo test.
 - 3) After all artificial missiles and seeded debris were recorded, the three survey sectors and rings were systematically searched for any other missiles with a maximum dimension of 1/2-inch or more.
 - 4) The maximum missile range was determined by carefully searching the survey sectors for ejecta/debris missiles lying at the greatest ranges from the detonation, first within the ejecta sectors, and then around the perimeter of the entire ejecta field. The survey was limited to missiles having a maximum dimension of at least 1/2-inch.

3.7 Documentary Photography

Photographs, presented in Appendix A, indicate various stages in the construction of the 1/4-scale model of the Minuteman silo and preparation of the QDT-3 test site (Reference 3-3).

Table 3-1. Pentolite Test Charges

Test	Charge Weight (lb)	Charge Diameter (in.)	Charge Length (in.)	Charge CG Below Ground Surface (in.)	Charge Container
1/10	179	8.7	50*	58.2	16 gage steel plate
1/4	2793	21.8	125**	159	1/8-in. steel plate

Note: Charge detonation was on center at 1-foot below top for 1/4-scale charge and 0.4-foot below top for 1/10-scale charge.

* Charge built as five cylinder lengths for 10 in. each.

** Charge built as five cylinder lengths of 25 in. each.

Table 3-2. Airblast Instrumentation Locations for 1/10-Scale Tests on Each Radial

Gage No.	Distance from GZ (ft)
BP1	17
BP2	30
BP3	44
BP4	52
BP5	65
BP6	82
BP7	100
BP8	130
BP9	160
BP10	200
BP11	245
BP12	295
BP13	350
BP14	430
BP15	530

Table 3-3. Airblast Instrumentation Locations for 1/4-Scale Test on Each Radial

Gage No.	Distance from GZ (ft)
BP1	42
BP2	78
BP3	110
BP4	130
BP5	160
BP6	200
BP7	250
BP8	325
BP9	400
BP10	500
BP11	610
BP12	740
BP13	880
BP14	1080
BP15	1320

Table 3-4. Strain Gage Locations for 1/4-Scale Silo

Gage No.	X (in.)	Y (in.)	Z (in.)	Item
Circumferential/Strain Gages* (8)				
E1	+30.76	-30.76	+58.5	LER wall
E2	-30.76	-30.76	+58.5	LER wall
E3	-30.76	+30.76	+58.5	LER wall
E4	+47	+15	+58.5	PAS wall
E5	+18	+41	+58.5	PAS wall
E6	+30.76	-30.76	+91.5	LER footing
E7	-30.76	-30.76	+91.5	LER footing
E8	-30.76	+30.76	+91.5	LER footing
Axial Strain Gages** (6)				
E9	+29	-29	20	LER headworks to wall joint
E10	-29	-29	20	
E11	-29	+29	20	
E12	+29	-29	88	LER wall to foundation joint
E13	-29	-29	88	
E14	-29	+29	88	
Closure Strain Gages*** (2)				
E15	0	0	3.25	X direction
E16	0	0	3.50	Y direction
<p>*The circumferential strain gages were placed on or in the vicinity of the outer LER wall hoop or PAS wall rebar.</p> <p>**These gages were in the vertical or "X" direction.</p> <p>***These gages were attached in the vicinity of the closure upper rebar and located near the center of the closure.</p>				

Table 3-5. QDT Instrumentation Measurement List

Test No.	Type Measurement	No. of Gages	Manufacturer	Model No.	Gage Range
QDT-1	Airblast	30	Kulite	XT-190	5, 25, 100 psi
QDT-2	Airblast	30	Kulite	XT-190	5, 25, 100 psi
QDT-3	Airblast	45	Kulite	XT-190	5, 25, 100 psi
	Strain	16	Micromasurements	EA-06-250BZ-350	50,000 μ in./in.

Table 3-6. Camera Requirements for Peacekeeper
1/4-Scale Test

No.	WSMR Camera Number	Purpose	Format	FOV (HXW)	Frame Rate	Resolution	Exposure (ms)	Run Time (sec)	Aim Point Range X Elevation
1	3714	Initial silo breakup (ambient)	Fastax II 16mm	25' x 33'	6000	2"	0.1 VNF	0.6	0 x 8'
2	3715	Initial ejecta parameters	Photosonic 70mm	375' x 375'	64.0	4"	0.1 VNF	30	0 x 150'
3	3716	Initial ejecta parameters	Photosonic 70mm	750' x 750'	60.0	8"	0.1 VNF	30	0 x 300'
4	3717	Ejecta impact parameters	Photosonic 70mm	180' x 180'	60.5	2"	0.1 VNF	15	80'S x 80'
5	3718	Ejecta impact parameters	Photosonic 70mm	180' x 180'	64.0	2"	0.1 VNF	15	80'NE x 80'
6	3719	Ejecta impact parameters	Photosonic 70mm	180' x 180'	63.9	2"	0.1 VNF	15	250'S x 80'
7	3720	Ejecta impact parameters	Photosonic 70mm	180' x 180'	62.3	2"	0.1 VNF	15	420'S x 80'
8	3721	Initial silo	Hycam 16mm	25' x 33'	6000	2"	0.05 IR EKTA	0.6	0 x 8'
9	--	Ejecta impact along 0° radial	Locam 16mm	150' x 200'	48	-	0.1 VNF	45	SGZ
10	3722	Ejecta impact parameters	Photosonic 70mm	180' x 180'	63.0	2"	0.1 VNF	15	590'S x 80'
11	3723	Ejecta impact parameters	Photosonic 70mm	180' x 180'	61.0	2"	0.1 VNF	15	760'S x 80'
12	--	Ejecta impact along 120° radial	Locam 16mm	150' x 200'	48	-	0.1 VNF	45	SGZ
13	3725	Ejecta impact parameters	Photosonic 70mm	180' x 180'	63.4	2"	0.1 VNF	15	250'NE x 80'

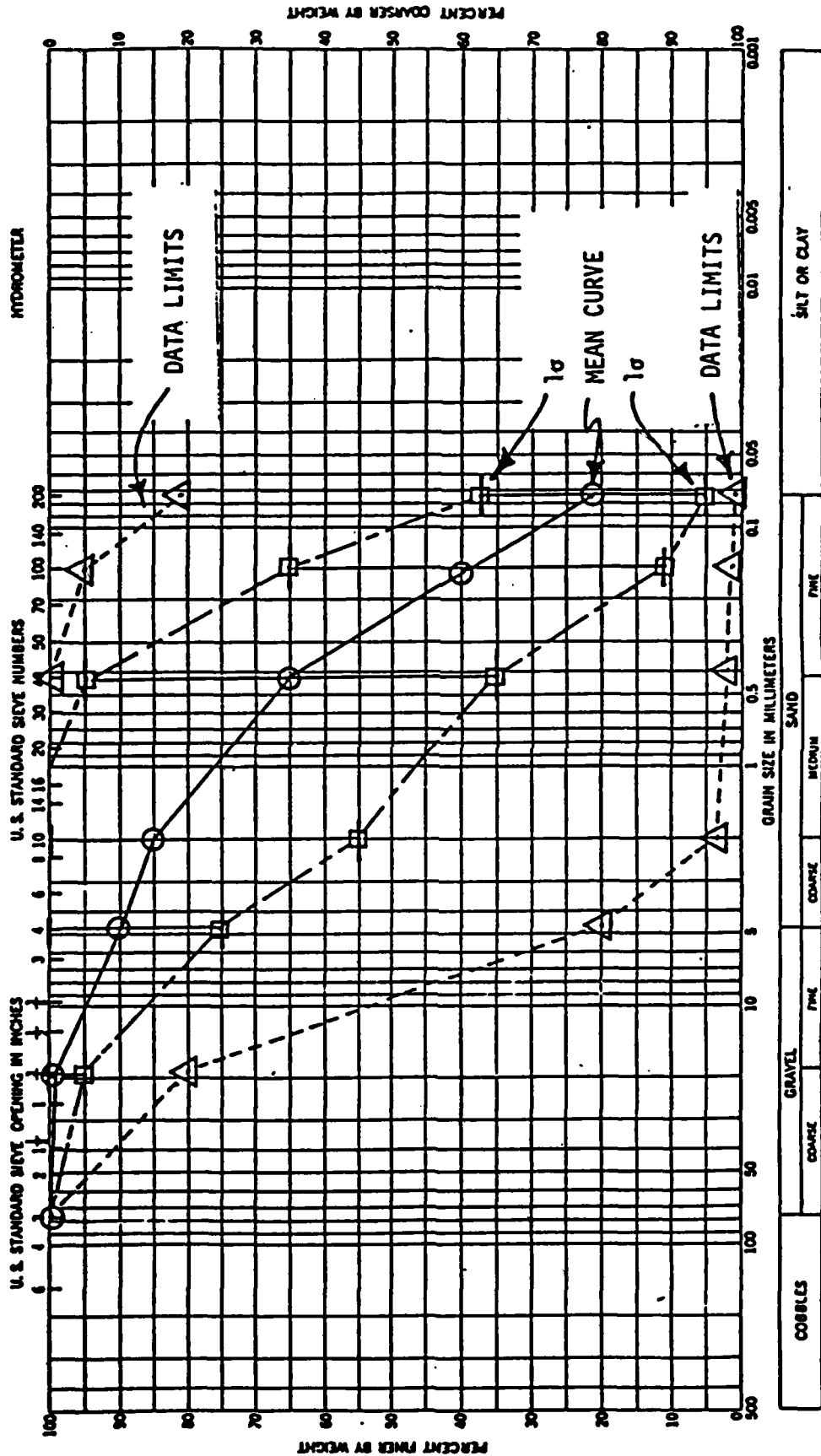


Figure 3-1. Soil Gradation Data for Minuteman Sites

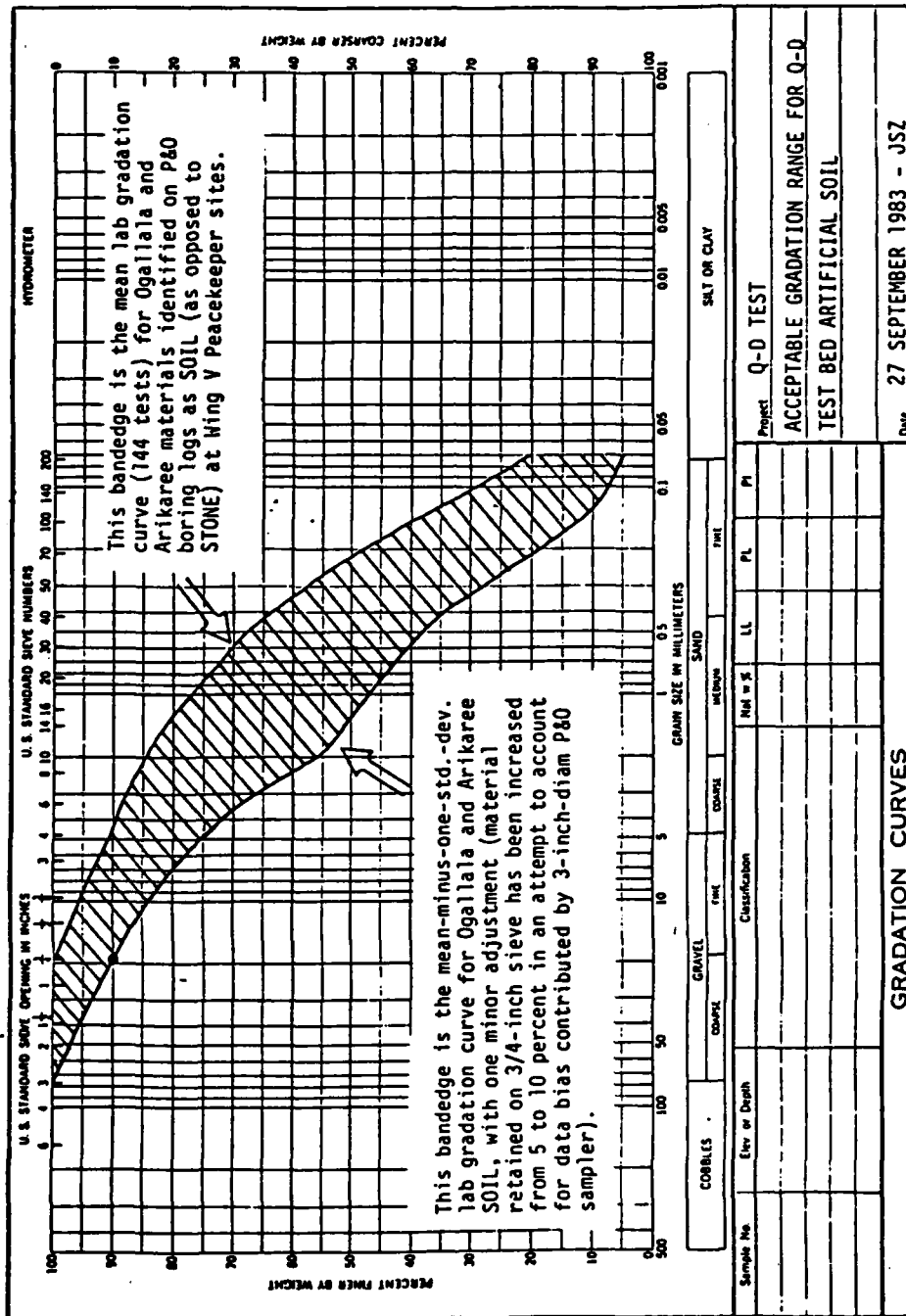


Figure 3-2. Acceptable Gradation Range for QDT Test Bed

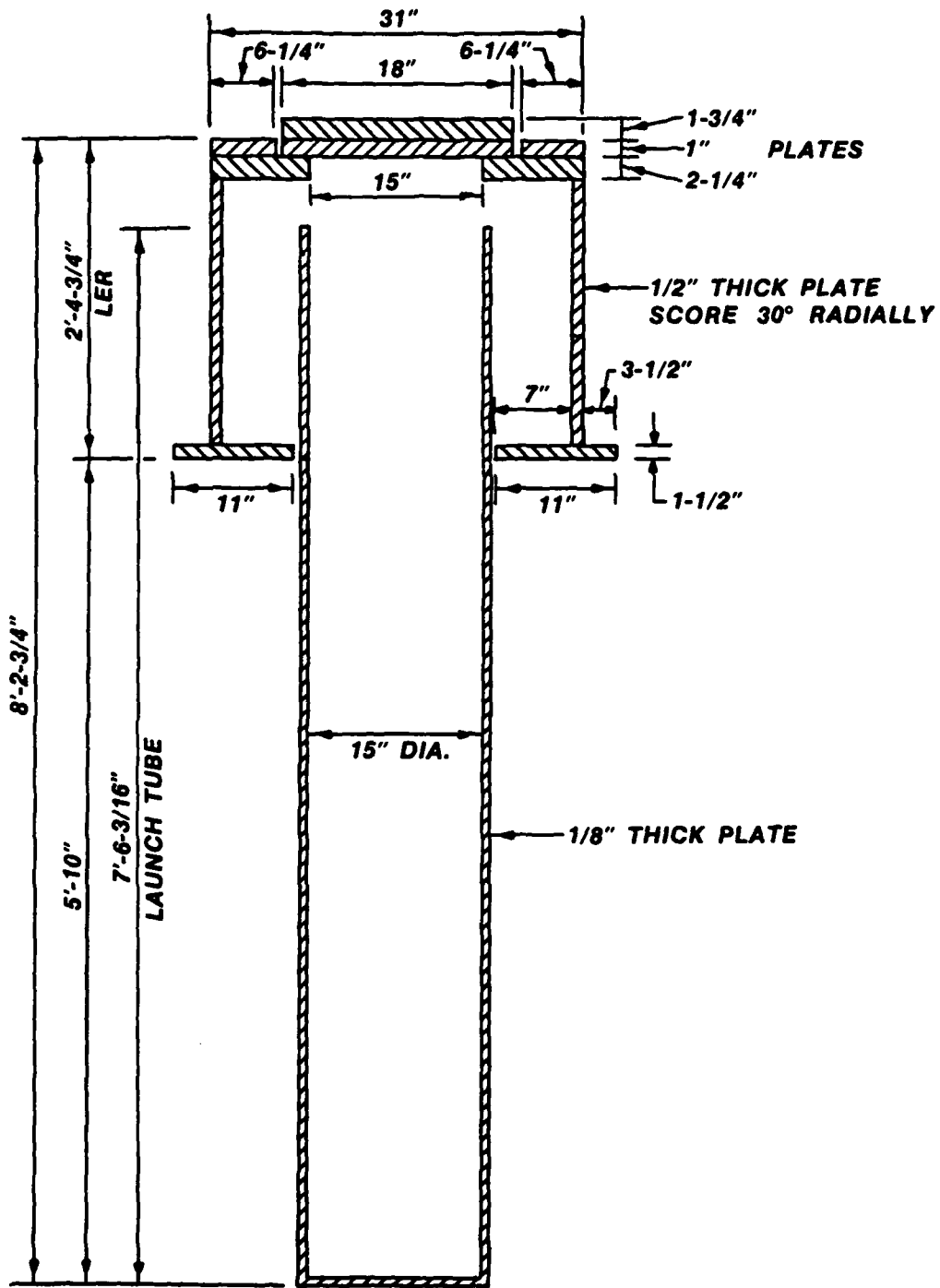


Figure 3-3. One-tenth Scale Structure

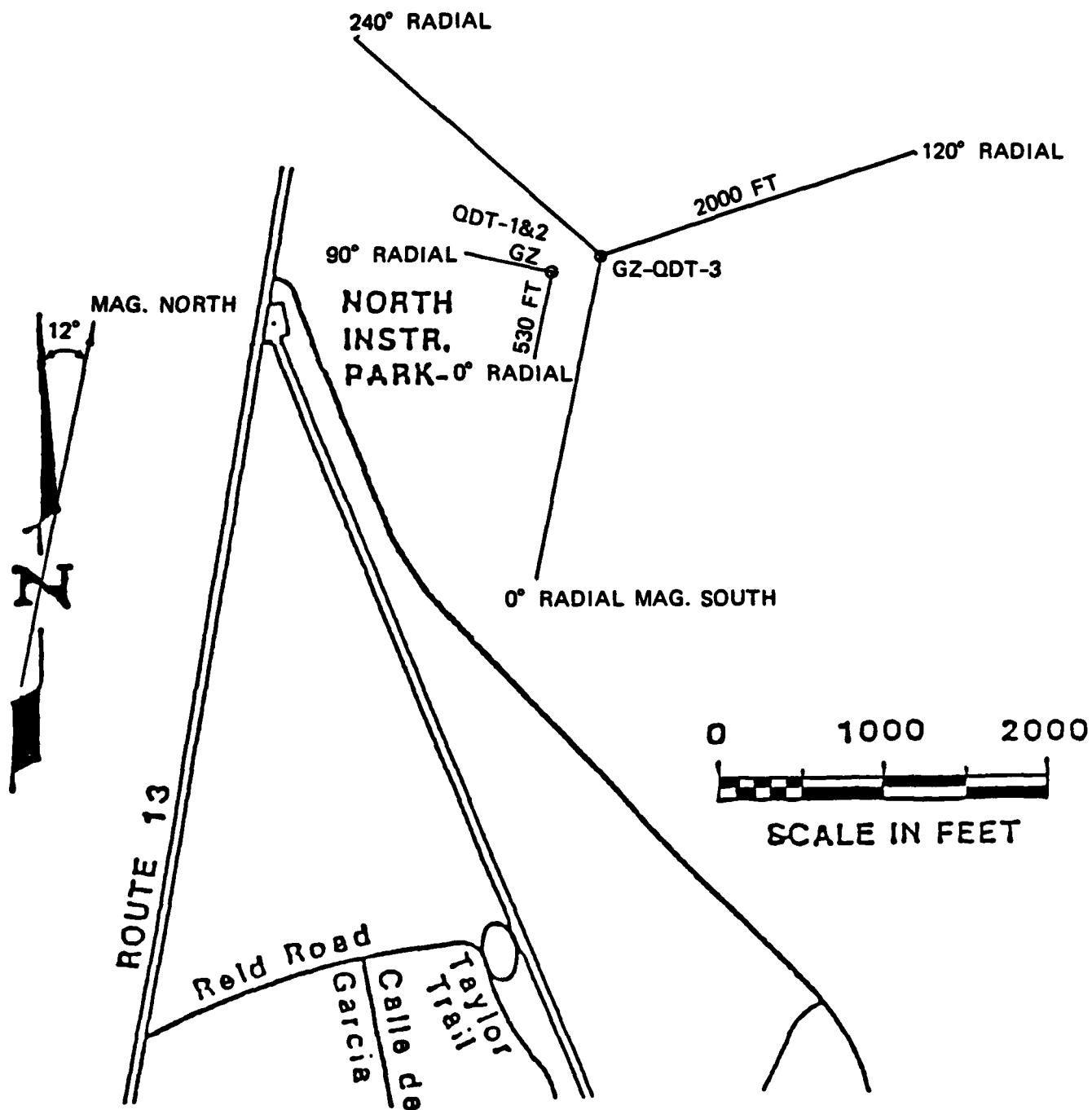


Figure 3-4. Test Site Layout for QDT-1, QDT-2, and QDT-3

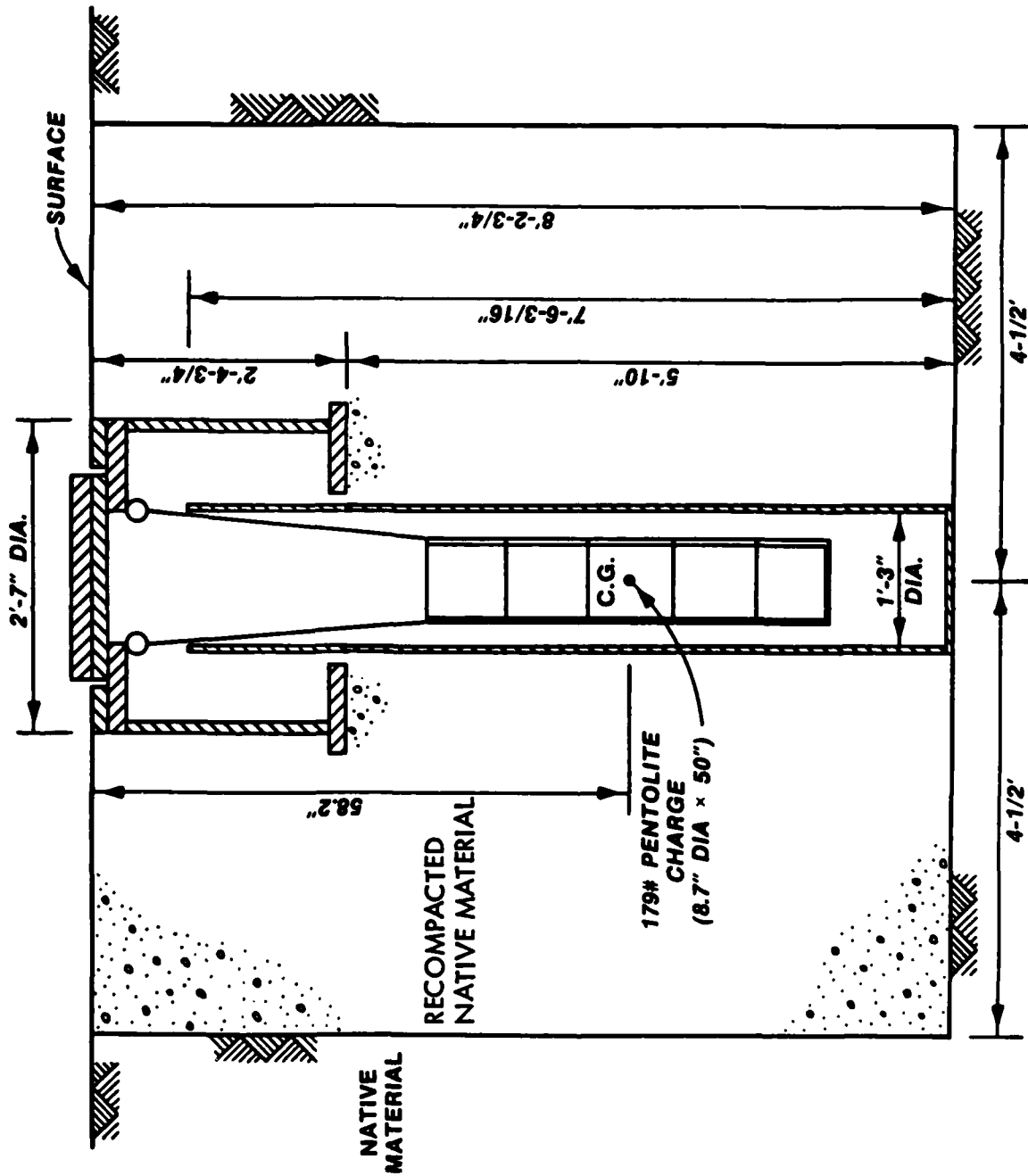


Figure 3-5. Test Bed Configuration for 1/10-Scale Structure

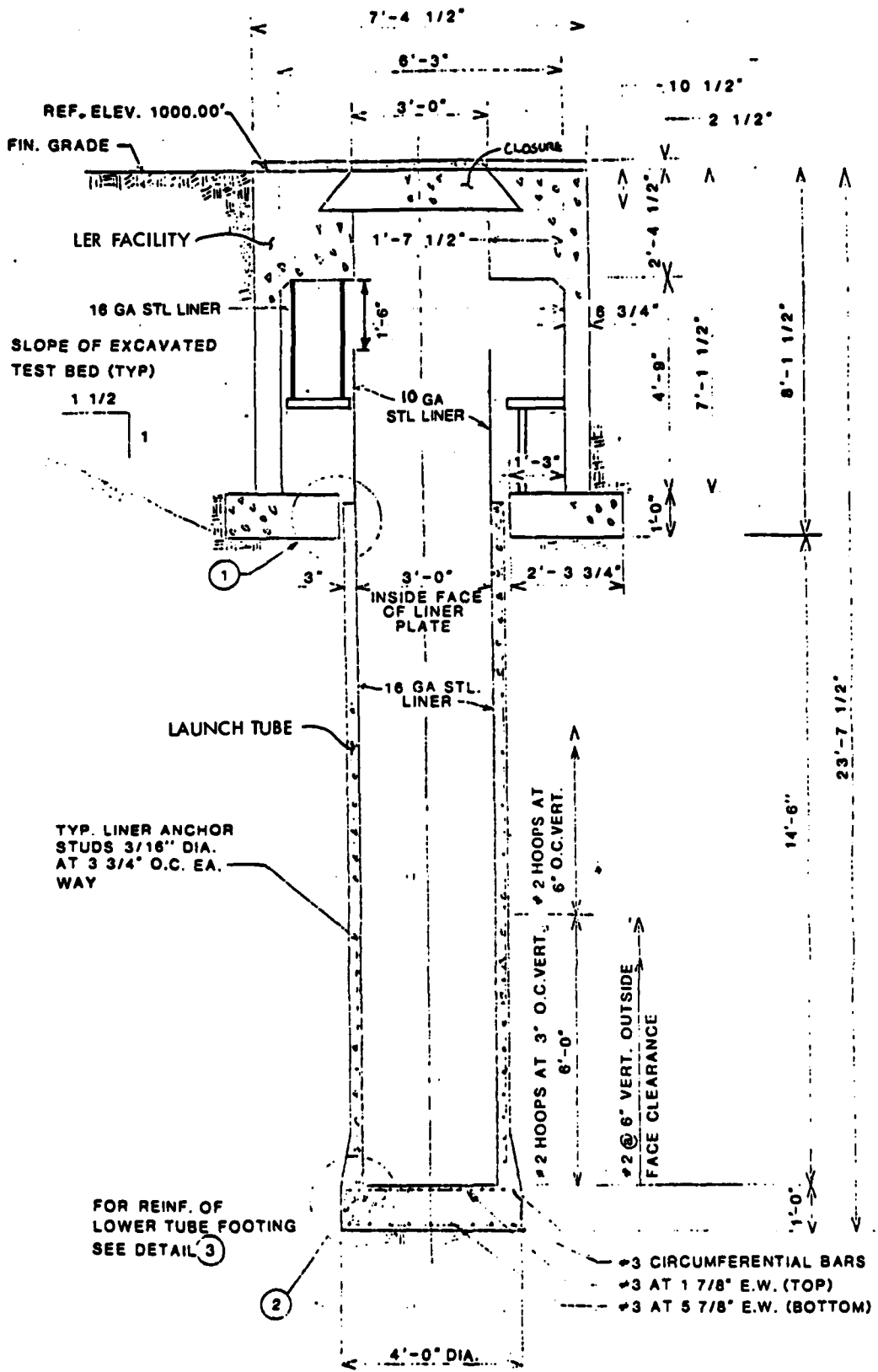


Figure 3-6. One-Quarter Scale Structure

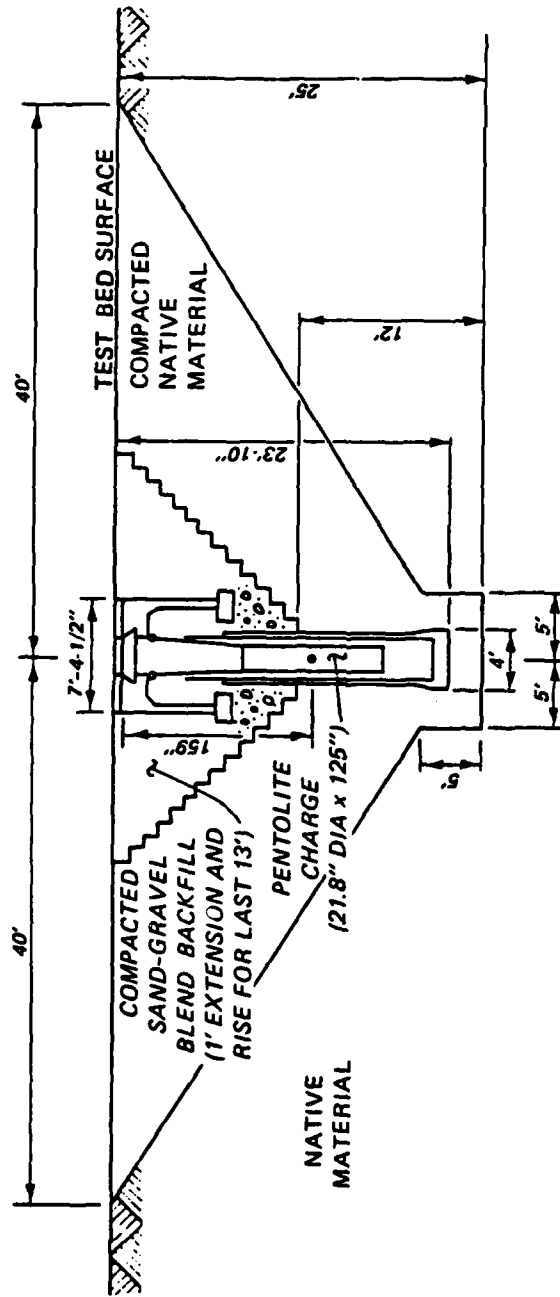


Figure 3-7. Test Bed Configuration for 1/4-Scale Structure

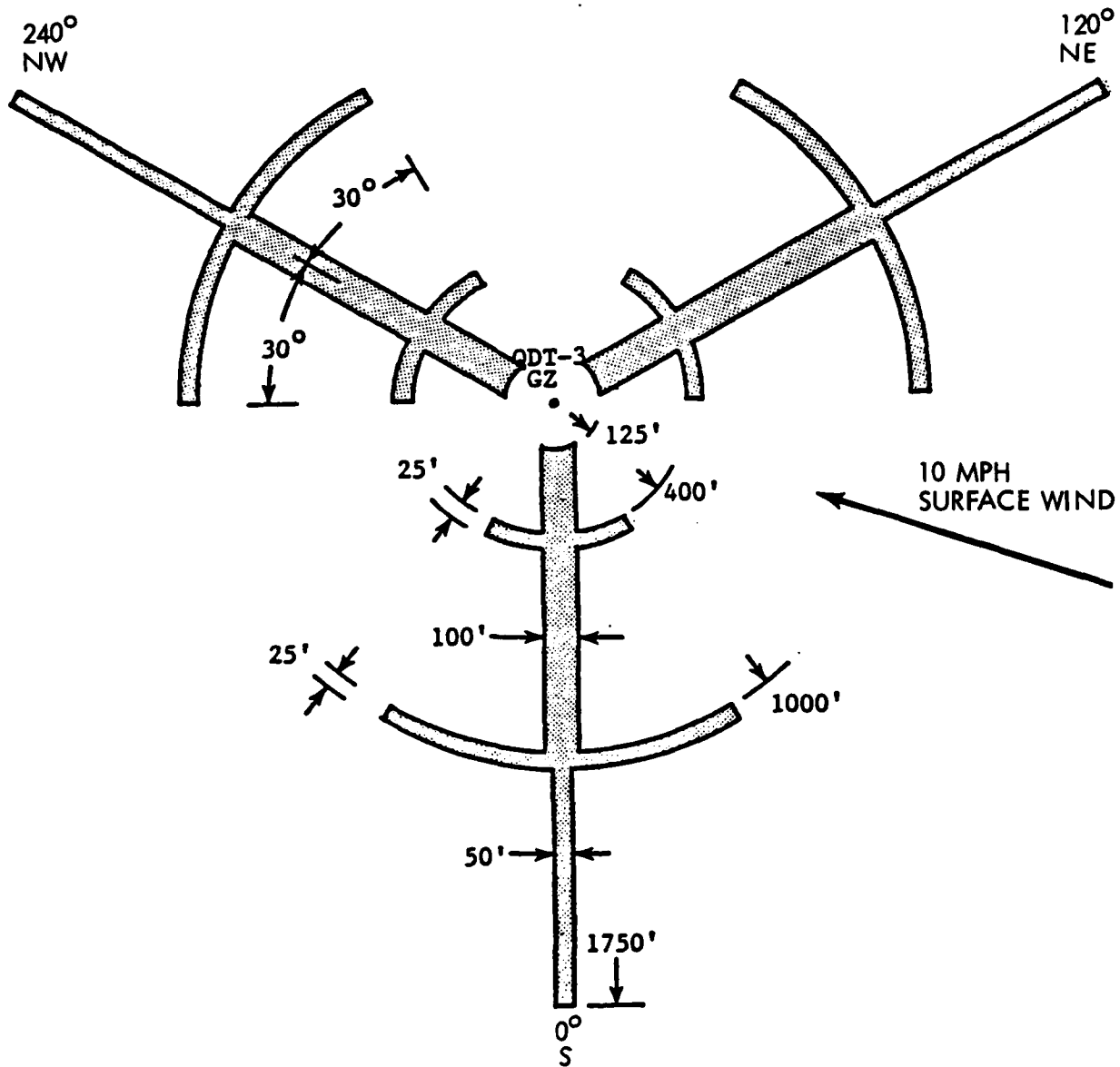
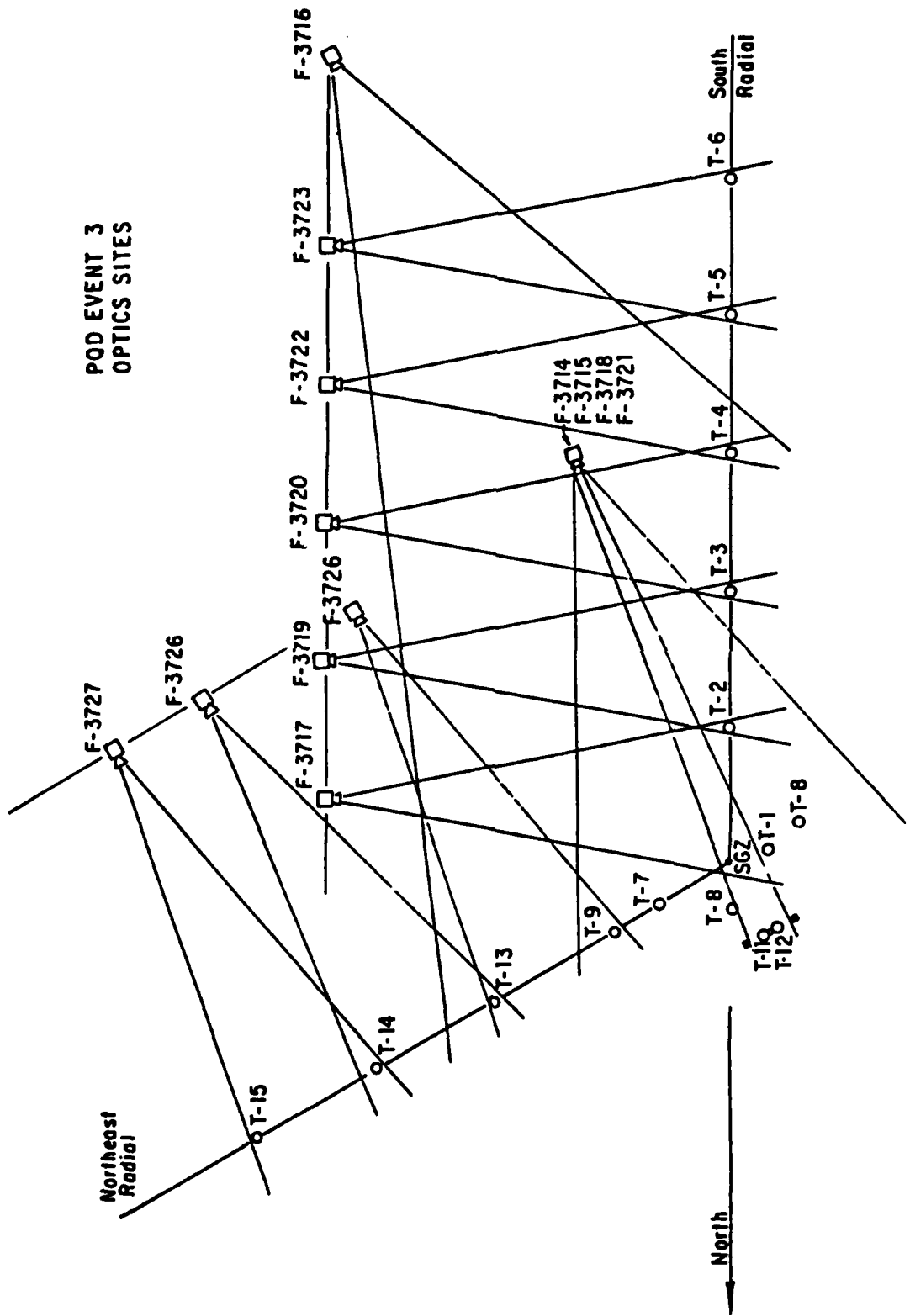


Figure 3-8. Locations of Areas Requiring Brush Clearing for Airblast Gages and Fragment Surveys



POD EVENT 3
OPTICS SITES

Figure 3-9. Camera, Locations and Coverages for Debris/Ejecta Photography

4.0 AIRBLAST PHENOMENA

In support of the planned scale model test program, an analytical effort was initiated to determine by means of a computer program the nature of airblast phenomena associated with the high explosive detonations within the 1/10-scale and 1/4-scale silo structures.

Calculations performed by S-Cubed/Albuquerque at the direction of DNA (Reference 4-1) were used to help establish the guidelines presented by AF/IG for a quantity-distance of 1750 feet. A detonation of a 101-ton TNT charge in an open rigid cylindrical silo was used to estimate the range to 1 psi for an explosion of a Peacekeeper missile in a Minuteman silo. These computations were based on the HULL code developed by AFWL, whereas calculations in the present report were undertaken with the CSQ II hydrocode developed by Sandia Laboratories/Albuquerque. It was of interest to determine whether similar conclusions would result for solutions of the same problem by the substantially different computer programs.

A brief summary is presented of the computational results related to code calibration for the case of a surface burst of a TNT tangent sphere, determination of airblast characteristics for a detonation within an open rigid silo, and evaluation of blast pressure distributions corresponding to explosions within the scale model facilities.

4.1 Hydrocode Description

CSQ II hydrocode was used for calculations of the DNA rigid silo configuration, tangent sphere configuration, 1/10-scale and 1/4-scale Minuteman silo configurations.

CSQ II is a FORTRAN program for computation of two-dimensional material response. It employs a finite difference method to solve the conservation equations of mass, momentum and energy in either rectangular or cylindrical coordinates. CSQ II is basically an Eulerian code. It also adopts a unique method to overcome distorted meshes and avoid the small time steps and large numerical errors associated with two-dimensional flow problems.

CSQ II can treat detonation of high explosives (HE) such as Pentolite and TNT. Equations-of-state for high explosives, and other materials including soil, concrete and air, are available in the code. One of the useful features of the code is a restart capability. At any time, the problem can be stopped, and material can be added or deleted from the problem, input parameters can be changed, and a new computational grid can be defined. In this way, different features of interest at different times can be modeled with reasonable cost and computation time.

4.2 Tangent Sphere Calibration

A tangent sphere computation was performed to check the CSQ II code against a known solution. A 101-ton sphere of TNT high explosive was placed on a rigid surface as shown in Figure 4-1. The sphere had an initial diameter of 473 cm, and initial density of 1.65 gm/cm^3 . The detonation point was the center of the sphere, with a detonation velocity of 6.93 km/sec, and Chapman-Jouguet pressure of $2.10 \times 10^{11} \text{ dynes/cm}^2$. The initial grid size was $\Delta x = \Delta y = 25 \text{ cm}$. This calculation was run until the shock had propagated to a distance about 200 feet along the ground with an overpressure about 180 psi. Figure 4-2 compares the overpressure versus range from the CSQ II calculation and the data taken from the scaled Prairie Flat test results. (Reference 4-2)

The shock overpressure is underpredicted at ground ranges less than 100 feet from ground zero. Finer zoning would be needed at close range to resolve the interaction of the shock wave emerging from the TNT high explosive and reflecting off the rigid surface. However, the overpressures predicted by CSQ II code agree with the Prairie Flat test data at ground ranges greater than 150 feet.

4.3 Rigid Silo Calculations

A calculation was performed for the same configuration used in the DNA calculation. This calculation consists of the detonation of 101 tons of TNT in a rigid wall silo without a closure. The geometry for this problem is shown in Figure 4-3. The purpose of this comparison was to verify the CSQ II code, which was to be used for later calculations with an operational silo with yielding walls and a closure.

The Jones-Wilkens-Lee (JWL) equation-of-state was used for the TNT high explosive. A uniform sea-level atmosphere occupies the space above ground level and inside the silo. The HE was detonated at $t = 0$ at the initiation point four feet below the top of the charge corresponding to the third stage ignition of the Peacekeeper as indicated in Figure 4-3. Figure 4-4 shows the results of this calculation.

The most obvious differences between the HULL and CSQ II calculations are the much higher overpressures predicted by CSQ II for a given range, down to 20 psi. Problem #100 shows the overpressure versus range curve dropping to meet the DNA curve at about 50 psi. This, however, is an artifact of the mesh zoning. Problem #100 includes only 35 feet of air above the ground, with a transmissive boundary at this height. For Problem #200, 150 feet of air is included above ground and, as seen in Figure 4-4, the overpressure versus range curve remains more or less parallel to the DNA curve. It seems that if the mesh height above ground level is too low, material allowed to exit the calculational mesh is forever lost to the problem. It is important to retain the venting HE products in the calculation as much as possible since this material appears to ultimately influence the problem later.

There is still the problem of higher overpressures at a given range than the HULL calculation suggests. After several more attempts with different zoning the discrepancy still remained. Figure 4-5 shows the final attempt to refine the zoning. It appears that as long as enough air above the ground level is taken into account in the model, the calculation is relatively insensitive to zoning.

The break in the curve for Problem #400 at 66 psi is due to the large zone size at about the 150 foot range. At this point, the calculation was stopped and the problem was rezoned, i.e., placing finer zones near the shock front. Upon continuation of the calculation, the overpressure recovered from its drop to match the previous calculation.

A meeting was arranged with Mr. Charles Needham, who performed the full-scale rigid silo calculation at S-Cubed. After thorough discussion with Mr. Needham, it was concluded that, other than the fact that our calculations use a different hydrocode with a different HE equation-of-state, it was impossible to pinpoint the cause of the discrepancy. It was decided to continue the full-scale rigid silo calculation with the CSQ II code and proceed with the subscale predictions.

Figure 4-6 shows the final result for the full-scale rigid wall silo calculation, along with the DNA results and a 101-ton TNT tangent sphere curve. The tangent sphere data is the test data from the Prairie Flat event (Reference 4-2) scaled to 101 tons of TNT at sea-level atmosphere. Figure 4-6 suggests that a rigid silo detonation becomes similar to a surface tangent at about 20 psi. While this is not the result reported by DNA based on the S-Cubed calculation, it is not clear how the range to 1 psi was determined by DNA based on the data given in Reference 4-1 and Figure 4-6 of this report. Initially, it was

speculated that the differences between the results obtained with the two codes was attributed to differences in the respective equations-of-state for TNT. However, subsequent evaluations indicated that the equations of state were comparable. Therefore, there is no apparent resolution of this issue at the present time.

4.4 Scale Model Computations

4.4.1 Tenth-Scale Silo

The 1/10-scale silo calculation was performed to determine overpressure versus ground range for an in-silo explosion, taking into account the material properties of the silo structure and surrounding soil. This calculation also gives an insight as to how the structure responds to high pressure detonation products. Upon studying the drawings for the 1/10-scale steel test facility, it became obvious there would be difficulty in modeling the structure, given the small thickness of steel relative to the overall problem dimensions. In order to set up a reasonable model, the mesh zoning for the silo structure would be very small, leading to crude zones for areas outside the silo since the total number of zones allowed for a problem is limited by computer memory. Another problem would be cycle time steps, which would be small due to a calculational stability criterion essentially proportional to the smallest mesh zone size. This in turn would lead to long execution times on the computer. It was decided to proceed with the calculation using a 1/10-scale model of the operational concrete Minuteman silo rather than the steel test model. In this way, the preliminary job of obtaining the material properties and setting up the computer model would be complete, and the 1/4-scale calculation could proceed later simply by changing the model dimensions. Figure 4-7 shows the 1/10-scale silo model used for this calculation.

Pentolite, chosen for the test, was used in the analysis instead of TNT. Since Pentolite is more energetic than TNT, the total amount of explosive was 179 pounds. An elastoplastic model was used for the concrete and soil. The Pentolite was initiated at $t = 0$ at a point on the centerline 0.4 feet below the top surface of the charge. Only half of the 1/10-scale shown in Figure 4-7 was modeled by taking advantage of symmetric configuration with an axis of symmetry at the centerline of the 1/10-scale configurations.

Figures 4-8 through 4-13 show how the calculation proceeds out to 2.4 msec. The material boundaries shown in Figures 4-8 through 4-10 illustrate the effect of cavity formation on the silo tube and surrounding soil. The most extensive deformation occurs in

the silo tube directly opposite the original position of the HE charge. This expansion allows loading on the LER footing from below, causing the inner footing to shear upward, and the whole LER and headworks to accelerate vertically. This is clearly shown in Figure 4-18 at 2.4 msec after detonation. This figure also shows venting of the HE gases as the closure begins to lift off. For the pressure contours of Figures 4-11 through 4-13, a shock wave is clearly seen transmitting into the soil and propagating nearly spherically at a speed of about 8.0×10^4 cm/sec.

Because of a computational time constraint, the calculation for the 1/10-scale was terminated at $t = 2.4$ msec after detonation. The computer running time was such that it appeared advisable to revert to the 1/4-scale calculations prior to completion of the 1/10-scale analysis. The objective was to ensure adequate time for development of a pretest prediction of the ground range to a peak overpressure of 1 psi for the 1/4-scale test.

4.4.2 Quarter-Scale Silo

The 1/4-scale silo model is essentially the same as that used in the 1/10-scale calculation. Figure 4-14 shows the model and the dimensions. The JWL equation-of-state was used for Pentolite, and an elastoplastic constitutive model was used for the soil and concrete. A tabular equation-of-state was used for air with an initial density of 1.1×10^{-3} gm/cm³ and pressure of 8.62×10^5 dynes/cm² to simulate the atmospheric conditions of the test site at White Sands Missile Range, New Mexico with an elevation of 4900 feet above sea level. The HE charge was initiated at $t = 0$, and by 0.36 msec the detonation is completed.

In Figure 4-15 at $t = 0.4$ msec, one can see the detonation products expanding into the LER and the initial deformation of the silo tube below the LER footing. The HE products have not yet expanded downward to the silo floor nor have they reached the closure. Figure 4-16 shows the condition at about 3 msec. The LER walls are beginning to deform, the closure has started to lift off, and at the same time the whole LER is being heaved upward. The LER footing is pretty much deformed and the silo tube continues to expand outward. By this time the concrete walls of the tube have probably been rubbleized. Notice that the silo tube expansion occurs mainly opposite the initial position of the HE charge. At $t = 10.8$ msec as shown in Figure 4-17, the silo tube has expanded to about 14 times the original volume. The LER walls have fractured near the headworks which have heaved upwards about 2.5 feet above ground level. The closure is separated

from the headworks by about 2 feet. There was a strange phenomenon that happened in that the high explosive products did not vent in spite of the rather large gap between the closure and headworks. At $t = 12.9$ msec, as shown in Figure 4-18, the gases are beginning to vent, but as seen in Figure 4-19, at $t = 15.9$ msec the venting is not continuous.

The venting problem is believed to be caused by two factors. The first factor is zoning the mesh too coarsely around the closure and headworks. It is believed that the HE product gases cannot diffuse through mixed cells, i.e., zones in the mesh where gas and solids are both present. Once the closure has separated from the headworks far enough to allow at least one row of cells in which no solids are present, i.e., only gas, the HE products can vent. This could be solved by zoning more finely near the closure. The second factor is illustrated in Figures 4-16 and 4-17. As the gases expand against the closure, the closure expands radially to close the gap that initially existed between the closure and the headworks. Once this occurs, there is a very narrow region interconnecting the closure and the headworks. This happens because the code sees the closure and headworks as being of the same material and assumes they have rejoined. The gases cannot readily vent until this band of concrete has broken. This problem can probably be remedied by either defining the closure and headworks as separate materials with an interface with no strength, or give the concrete a reasonably small failure criteria which will allow this stretched band to break more easily. These remedies require, however, greater computer time than was available.

Given these difficulties with the closure and gas venting, it was decided to restart the calculation without the closure. This does not seem unreasonable since it is estimated that only 0.6% of the explosion energy is carried away by the closure as kinetic energy. The estimate of the maximum kinetic energy was obtained by taking the maximum vertical velocity of the closure from CSQ II code to be 775 ft/sec at $t = 19.8$ msec after detonation and the mass of the closure to be about 3000 pounds. The maximum kinetic energy of the closure would be then 3×10^7 ft-lb which is 0.6% of the total energy of HE.

Figure 4-20 indicates the initial configuration at $t = 0$ msec. Figure 4-21 shows the detonation gases expanding into the LER and towards the exit at $t = 0.5$ msec. At $t = 3$ msec, as shown in Figure 4-22, the condition compares well with Figure 4-16. The LER walls have started to deform and the footing has eroded away. The venting gases are clearly seen exiting the silo opening. Figure 4-23 shows the gas cloud at $t = 6$ msec extending 25 feet above ground and about 12 feet radially. The LER and headworks continue to deform while the silo cavity increases.

Figures 4-24 through 4-26 are pressure contours corresponding to Figures 4-21 through 4-23. At $t = 0.5$ msec, a shock wave begins to propagate into the soil. At $t = 3$ msec, the shock wave has spread out, noted by the larger spacing between contours. This is due to the higher sound speed for elastic waves than for the higher pressure plastic waves. Thus, the low pressure elastic waves will run out ahead as time progresses. The structure of the venting gas cloud is also shown. Most notable is the rapid decrease almost by a factor of 100 in pressure as the gases expand outside the opening. At $t = 6$ msec, the ground shock has spread out with a peak pressure of about 5×10^8 dynes/cm² located 525 cm from the silo center. Comparing this to the peak ground shock position for the 1/10-scale calculation at 2.4 msec in Figure 4-13 one sees the same peak value at 210 cm radius, thus demonstrating that shock waves due to explosive detonation will indeed scale by the cube root of the yield. The sharp decompression region is still observed in Figure 4-26 at the silo exit in the venting gases. This appears to be a standing shock indicating choked flow.

Several tracer points are located along the ground to give pressure-time histories as the shock wave in the air passes. Figures 4-27 through 4-30 show these time histories at ground ranges corresponding to 42, 78, 110, and 130 feet. The waves are about 20 msec wide with a negative phase immediately following. All the peaks have a finite rise time and are rounded at the top. This is an artifact of the computer code. All codes of this type employ an artificial viscosity to spread out a shock wave over several zone thicknesses. This is essential since these codes describe continuum physics and cannot handle discontinuities on the scale of a mean free path, such as a shock wave. In addition, the resolution of a sharp peaked waveform is limited by the size of the mesh zones; the coarser the zoning the less resolution. This accounts for the rounded peaks. This fact makes it necessary to periodically rezone the calculation. As the shock wave propagates into coarser zones, the computation is stopped, and the space mesh is rezoned such that finer zones are placed in front of the shock and coarser zones are placed behind the shock. Ten rezones were required to carry this calculation out to the 1 psi overpressure range.

It is of interest to note that detailed comparisons of the pressure contours for the 1/10- and 1/4-scale calculations for the closure-on combination indicated excellent agreement in pressure amplitude and spatial extent where the 1/10-scale time and distance parameters were scaled by a factor of 2.5 to afford a common frame of reference.

4.5 Test Predictions

The final result of this computation is shown in Figure 4-31, where peak overpressure versus ground range is plotted, with the range to 1 psi as 202 feet from the silo centerline. The figure also shows the reference tangent sphere data of the Prairie Flat event, scaled down to 3156 pounds of TNT, or 2793 pounds of Pentolite. The range to 1 psi for the tangent sphere is about 655 feet, giving a reduction in range of 69% for the silo detonation as compared to a surface tangent of equivalent yield. This is in contrast to the initial DNA estimate of a 30% reduction due to an underground in-silo explosion with non-rigid walls.

A significant reduction in the range to 1 psi is seen for the yielding silo model over the rigid-wall model, which was shown to be similar to the tangent sphere case in Figure 4-6. Several factors are responsible for this. Some of the detonation energy is directed into, and absorbed by, the concrete and soil. By 6 msec, 27% of the explosion energy released by the Pentolite is transferred to the concrete structure and 33% to the soil. This energy is not available to the shock wave propagating in the air. A second factor to consider is the volume increase of the silo interior due to cavity formation caused by the high pressure gases. At 11.8 msec the volume of the silo tube has increased by a factor of about 14, thereby reducing the pressure further.

The presence of choked flow may also contribute to the reduction in range to 1 psi. Since the gases cannot expand and propagate a shock into the air immediately, as with a surface tangent burst, some of the internal energy is instead absorbed into the concrete structure and soil, thereby cooling the gas and reducing the pressure. In contrast, with a rigid silo that also experiences choked flow, the internal energy of the gas cannot partition into the surrounding media, since the walls are perfectly reflecting. All the energy remains in the gas until it eventually vents, therefore propagating the air shock in greater strength to longer ranges.

As far as can be judged from the analytical results covering the extent of parallel calculations for the 1/10-scale and 1/4-scale cases and evaluation of the nature of the computer program, it appears reasonable to conclude that cube root scaling would be inherent in applications to any scale level.

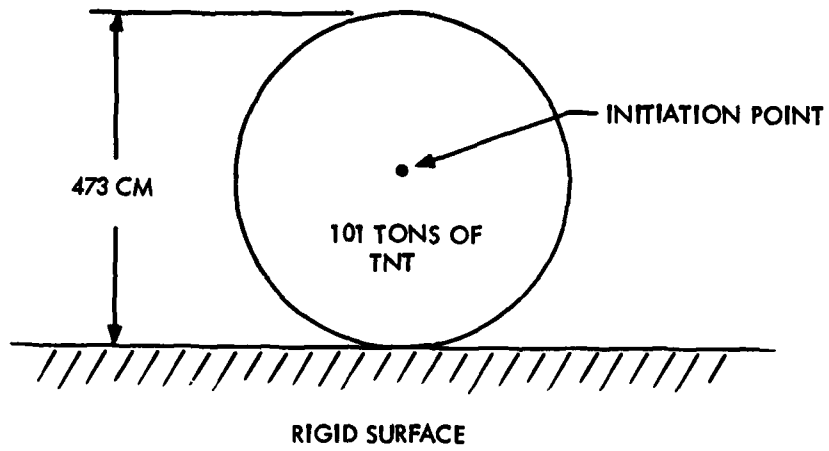


Figure 4-1. TNT Tangent Sphere Configuration

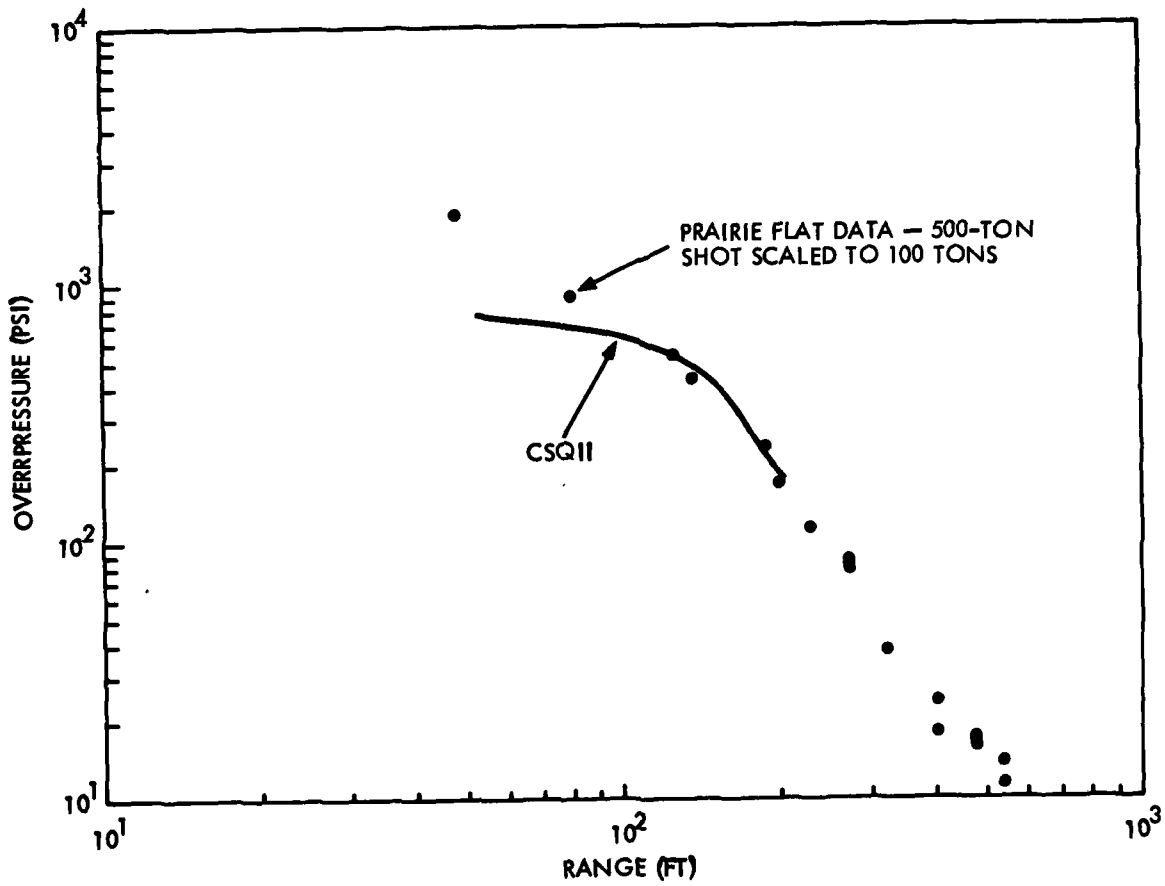


Figure 4-2. Overpressure Versus Range Curve for Tangent Sphere

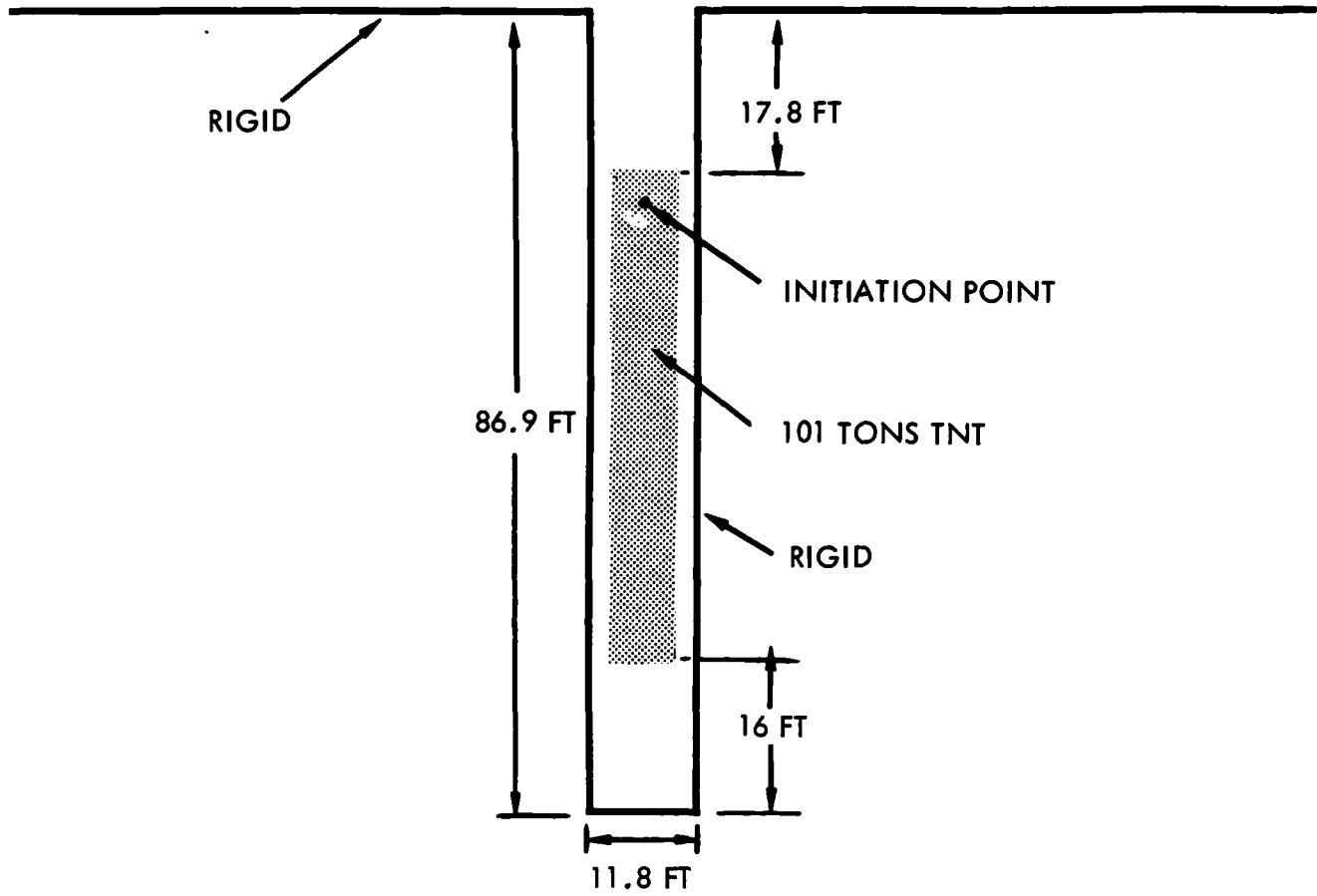


Figure 4-3. Model-Geometry for the Full-Scale Rigid Wall Silo Calculation

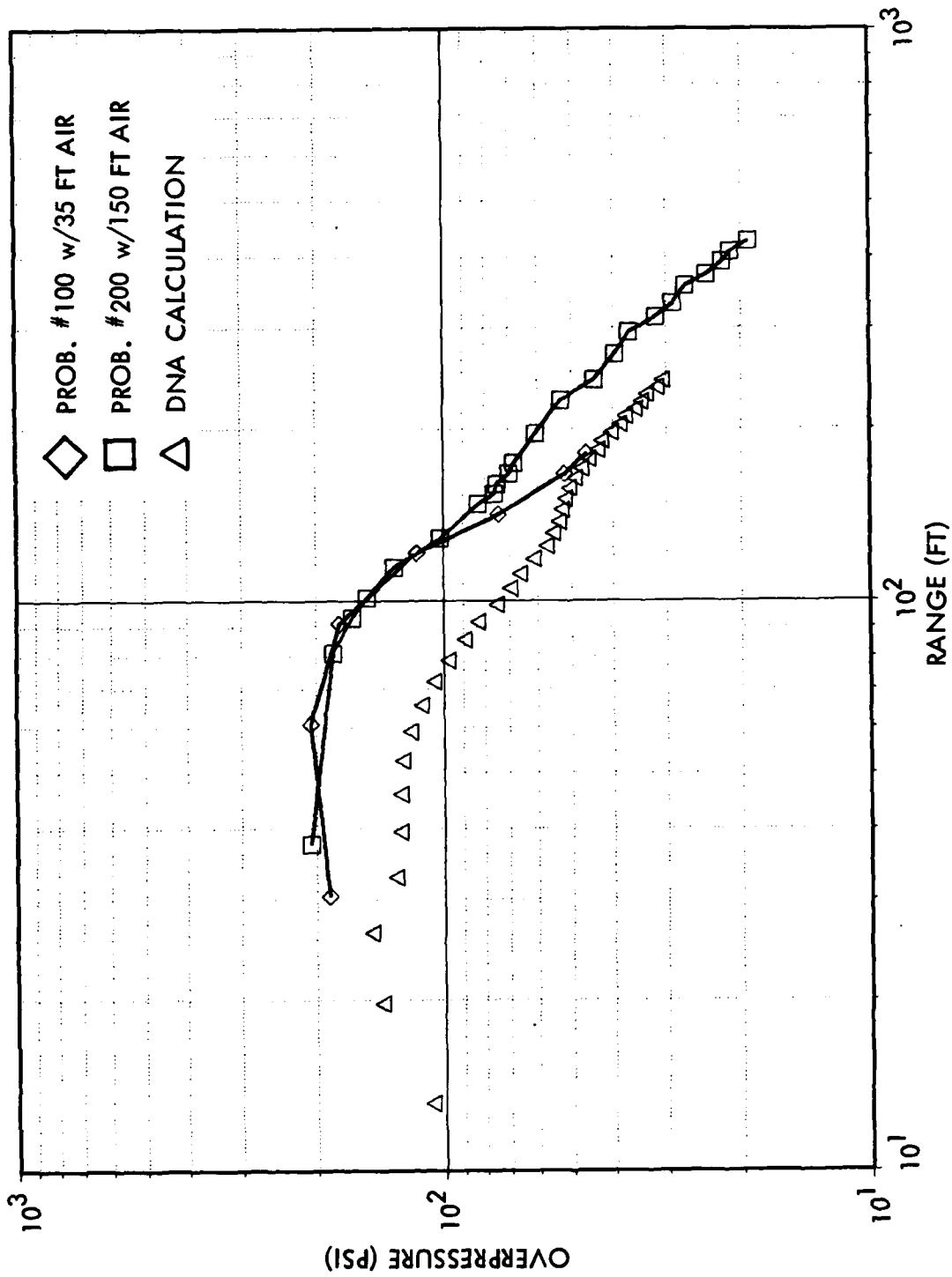


Figure 4-4. Comparison of Initial CSQ Calculations with DNA Results for Rigid Silo Detonation

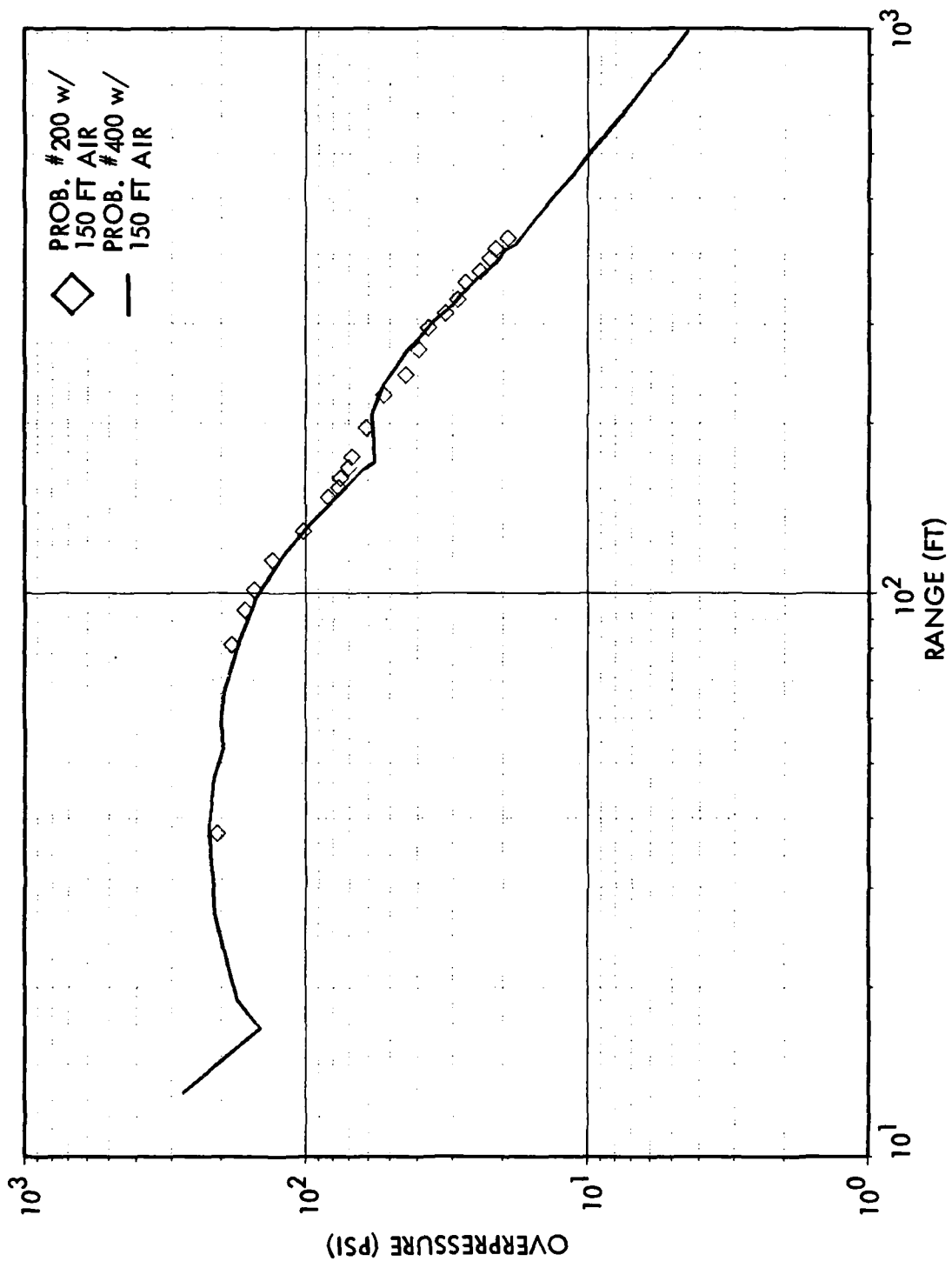


Figure 4-5. Zoning Sensitivity for Rigid Silo Calculation

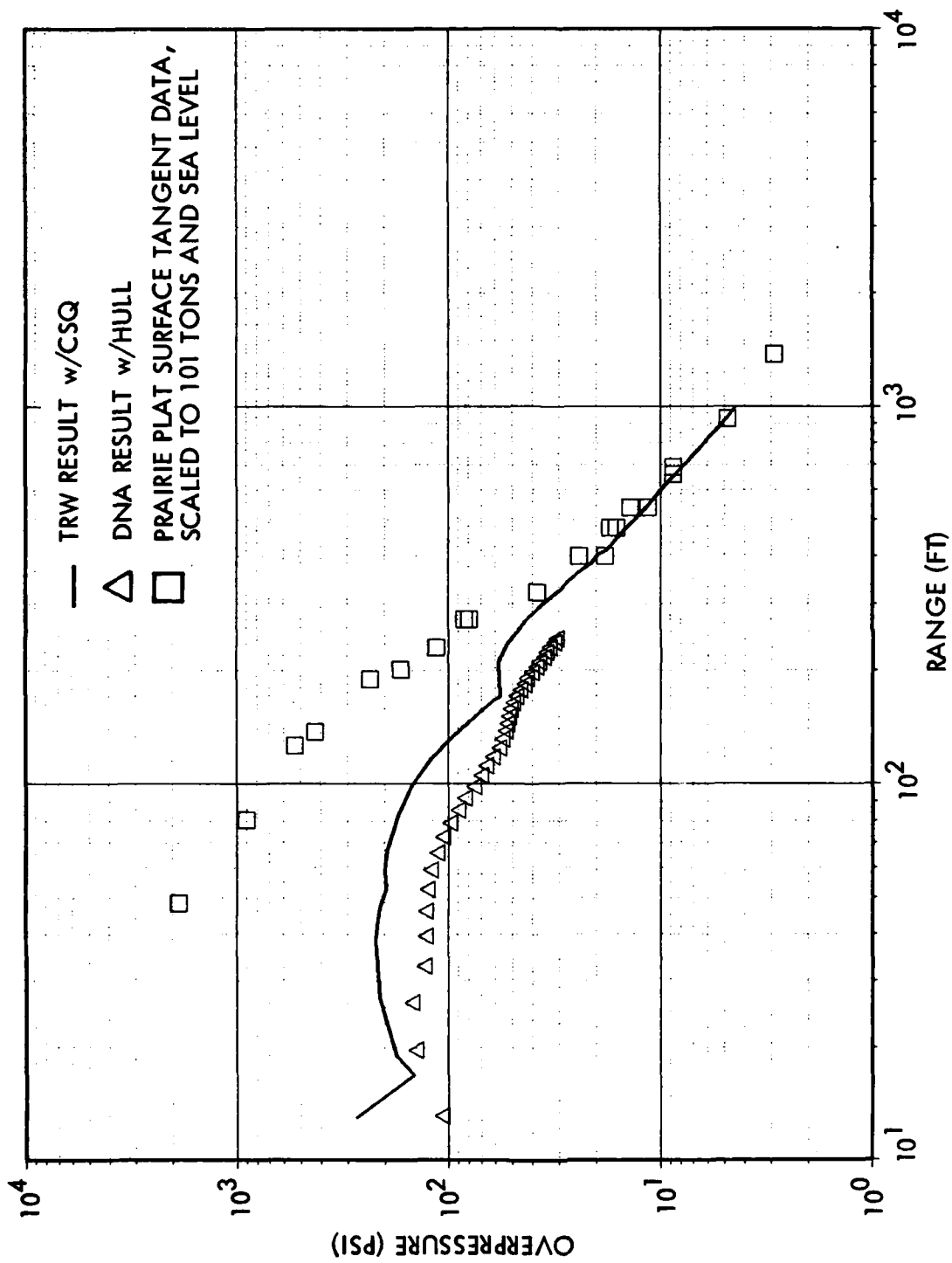


Figure 4-6. Final Result of TRW Full-Scale Rigid Silo Calculation

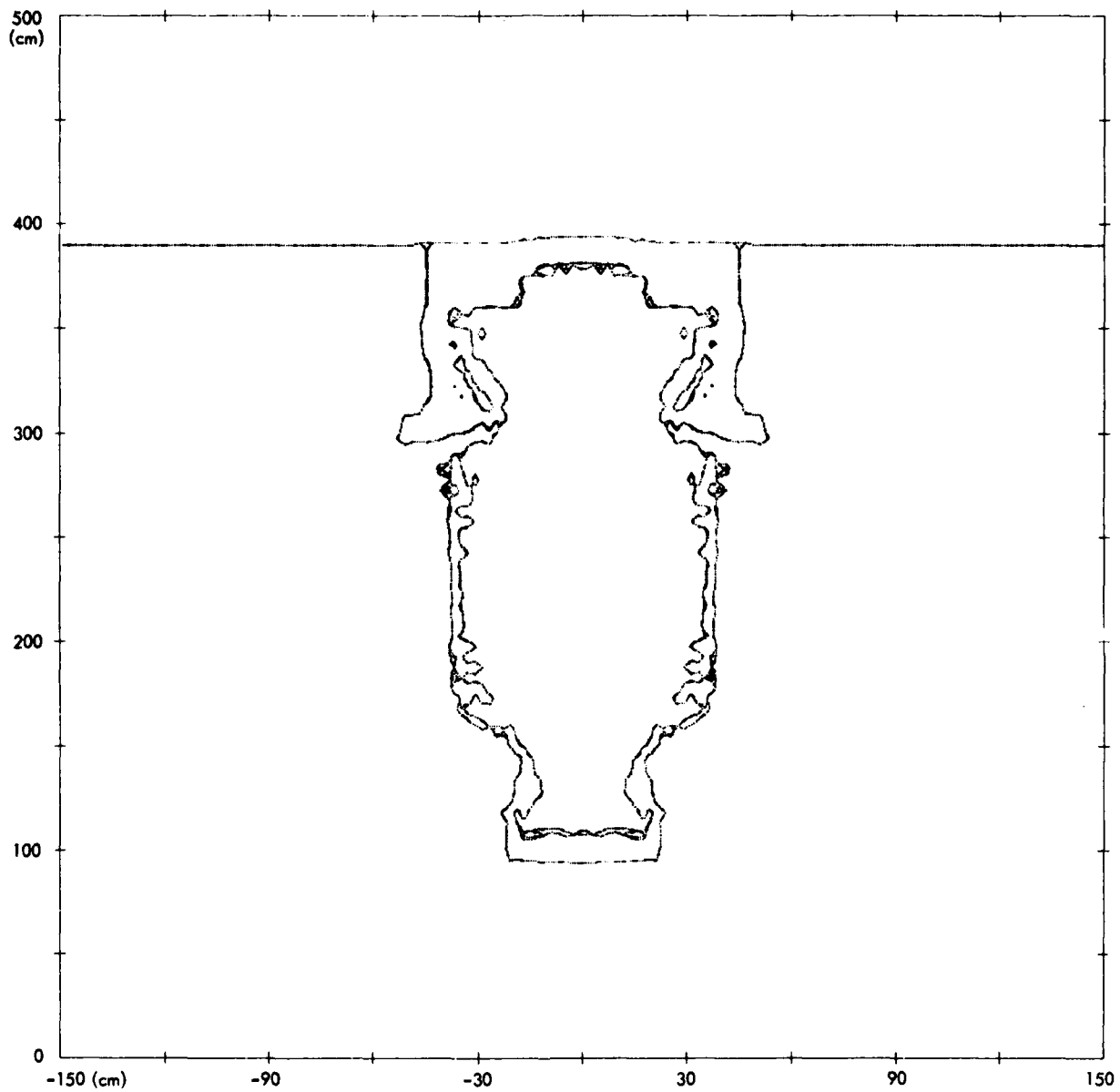


Figure 4-8. Material Boundaries for 1/10-Scale Calculation at 1.2 msec

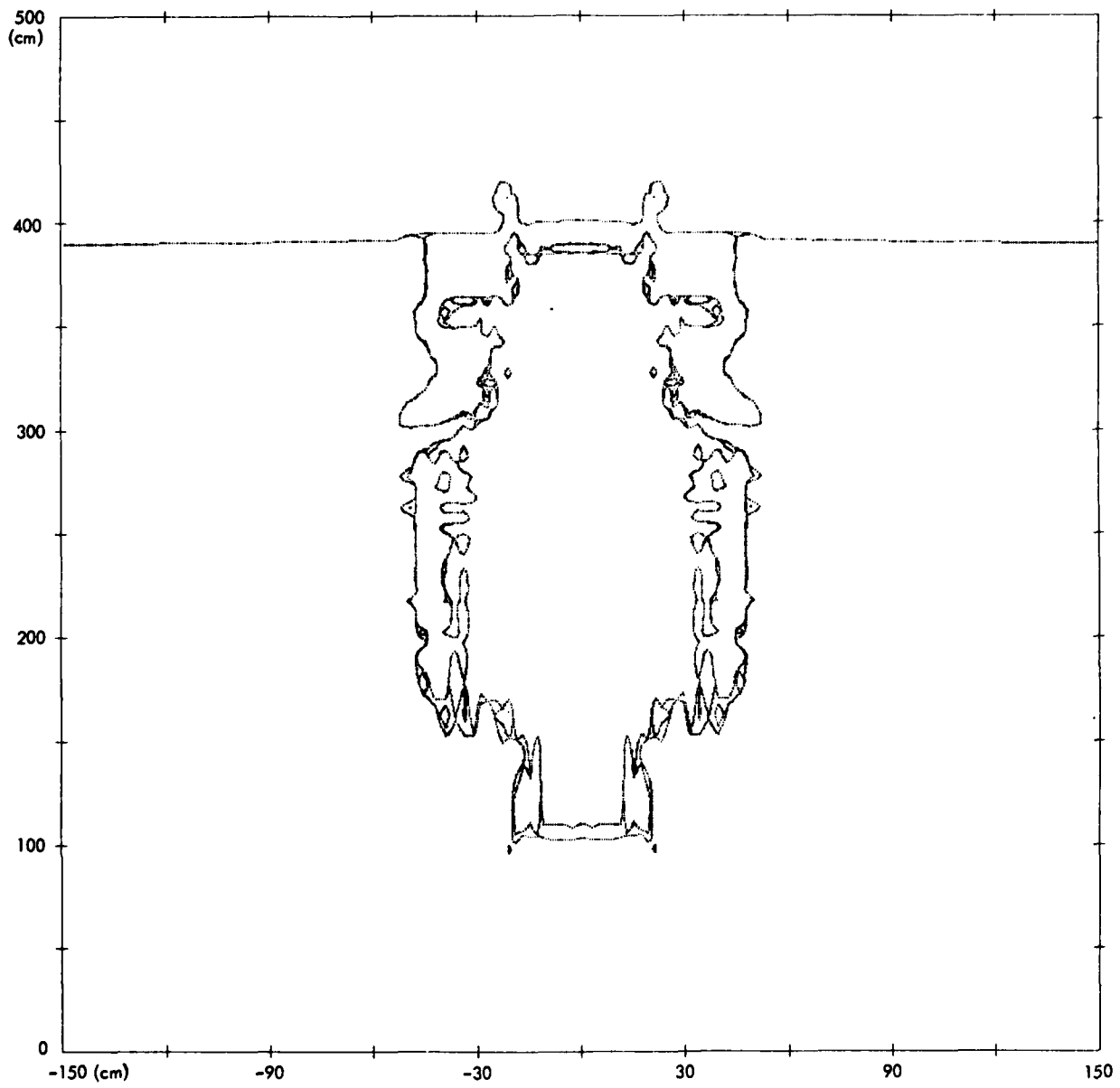


Figure 4-9. Material Boundaries for 1/10-Scale Calculation at 1.9 msec

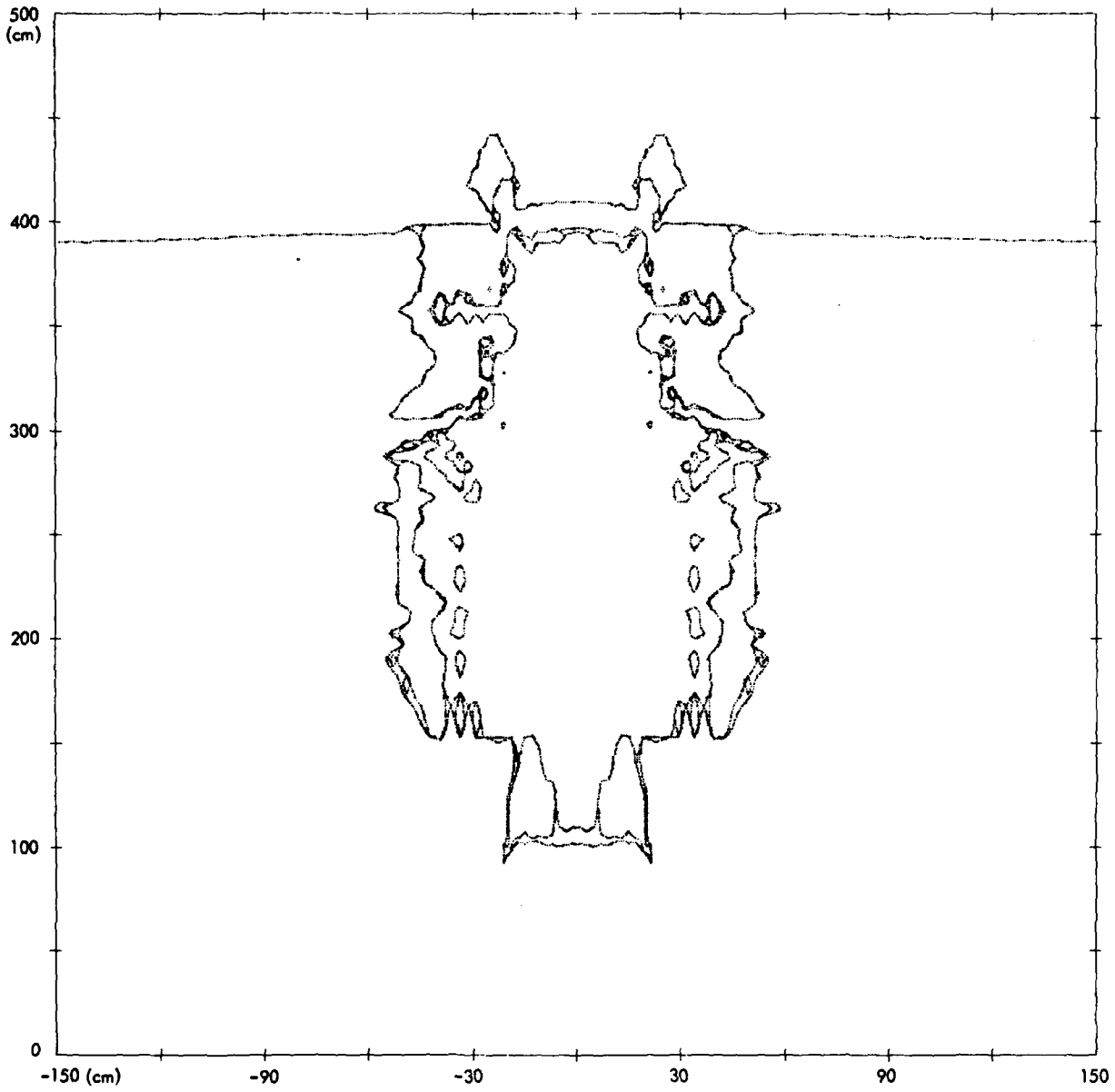


Figure 4-10. Material Boundaries for 1/10-Scale Calculation at 2.4 msec

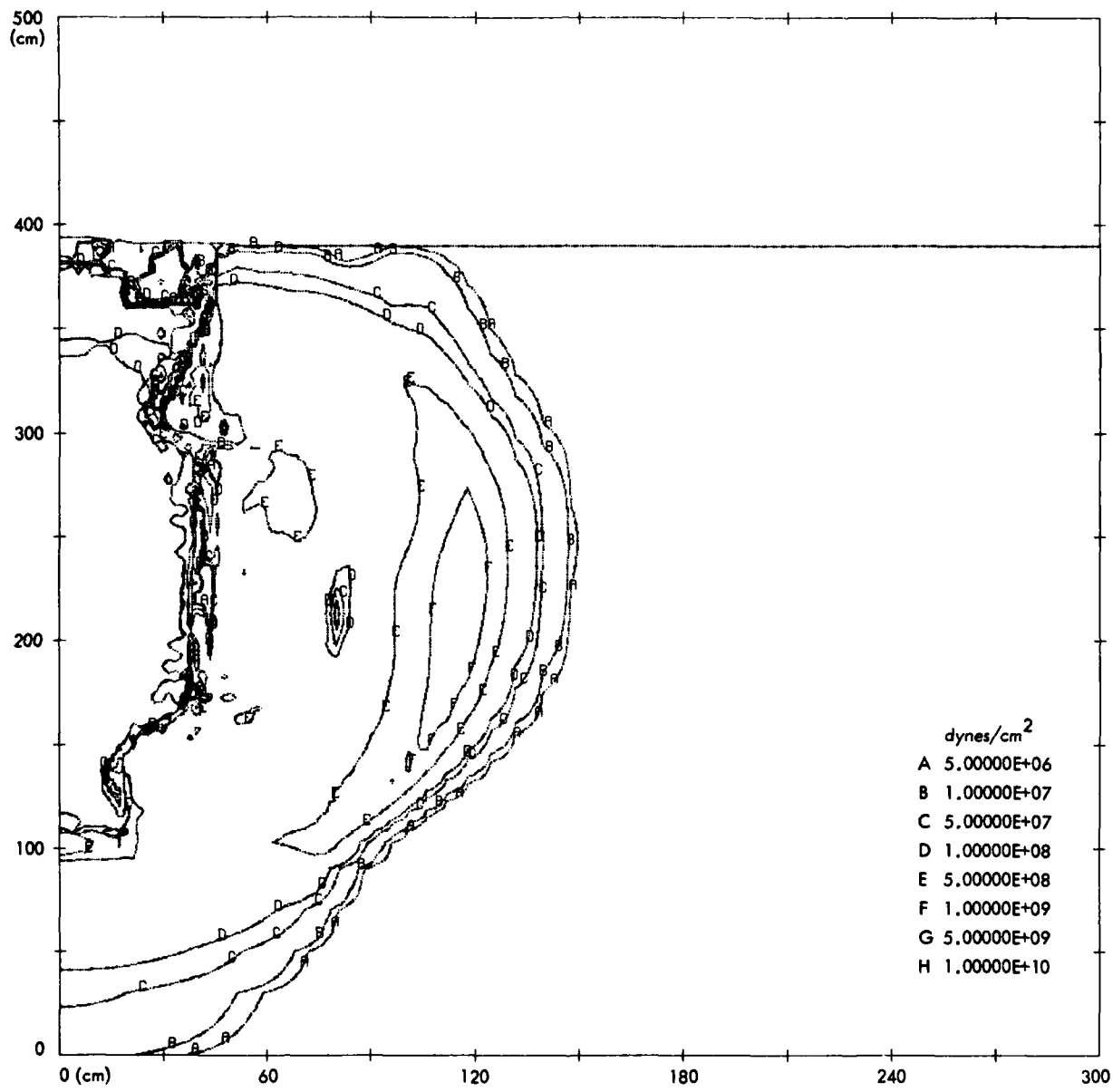


Figure 4-11. Pressure Contours for 1/10-Scale Calculation at 1.2 msec

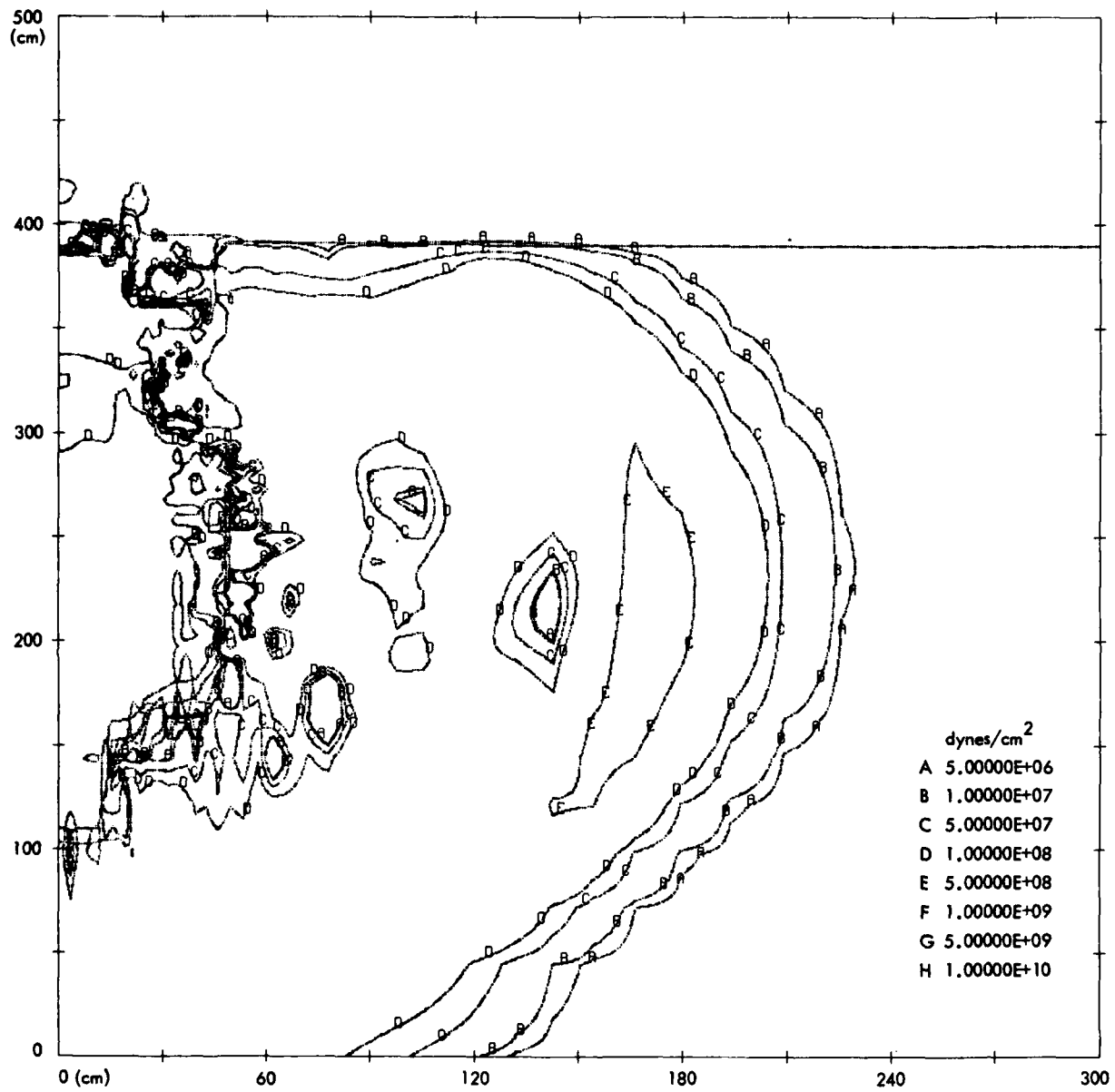


Figure 4-12. Pressure Contours for 1/10-Scale Calculation at 1.9 msec

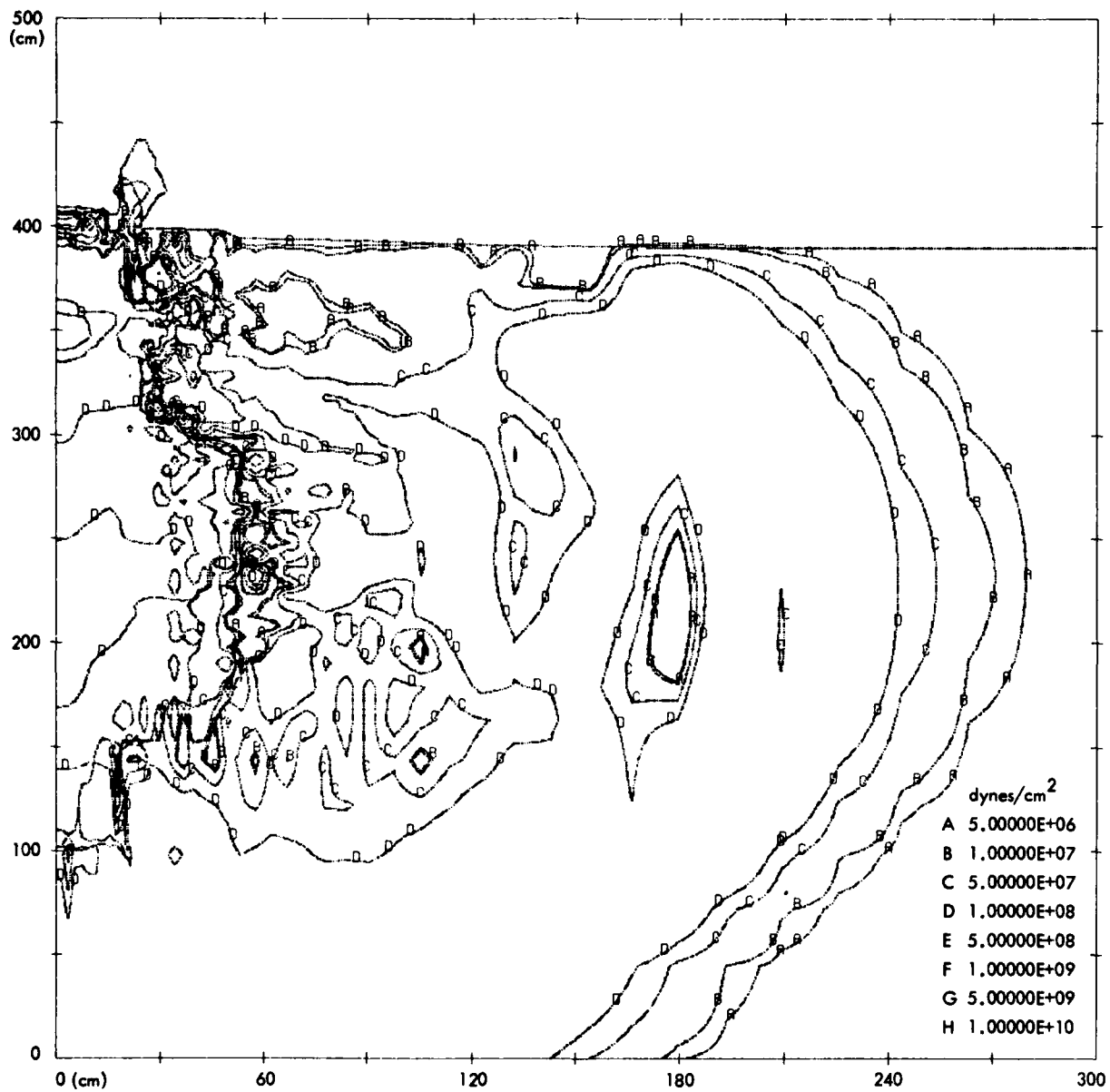


Figure 4-13. Pressure Contours for 1/10-Scale Calculation at 2.4 msec

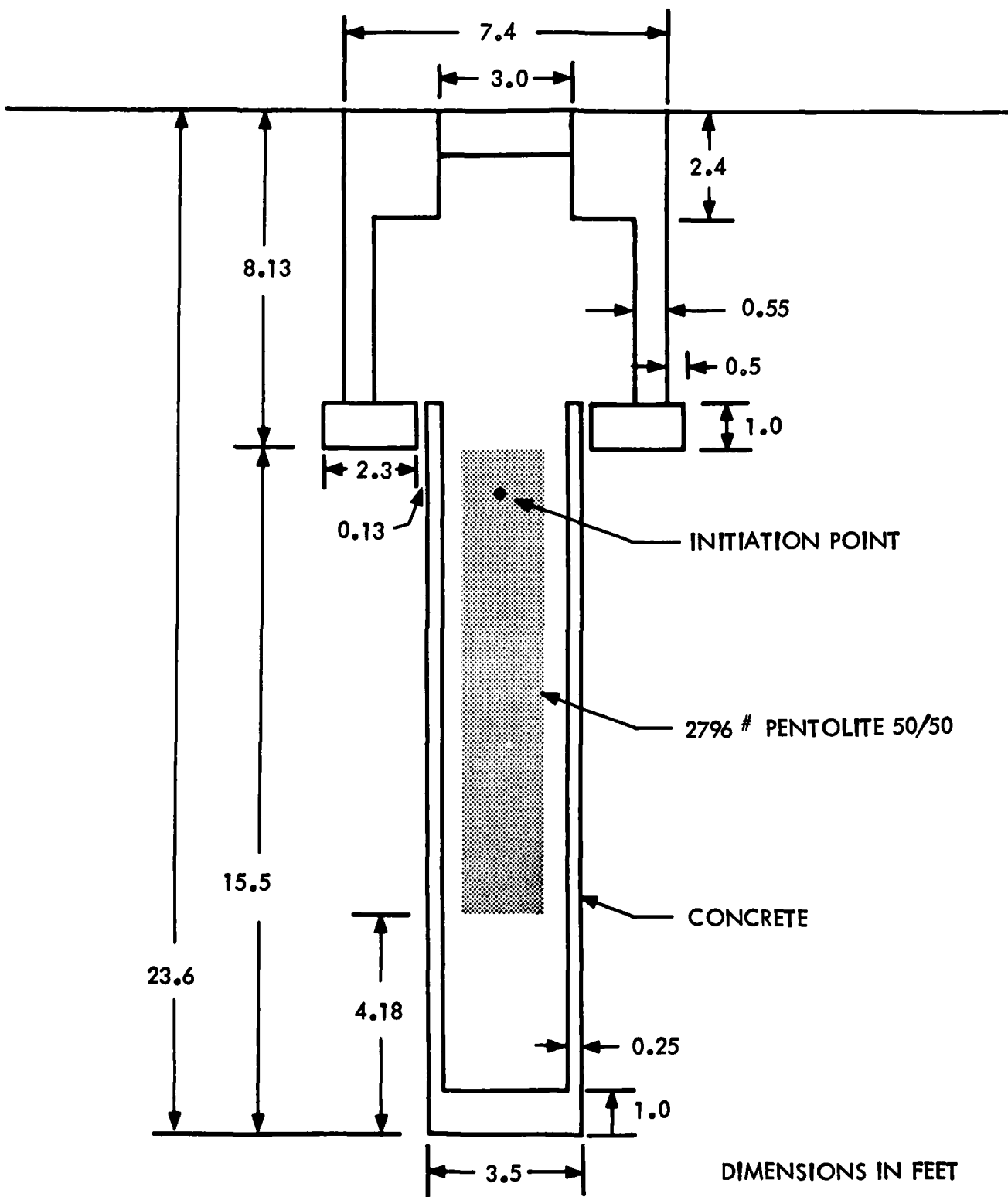


Figure 4-14. One-Quarter Scale Structure Used for Calculation

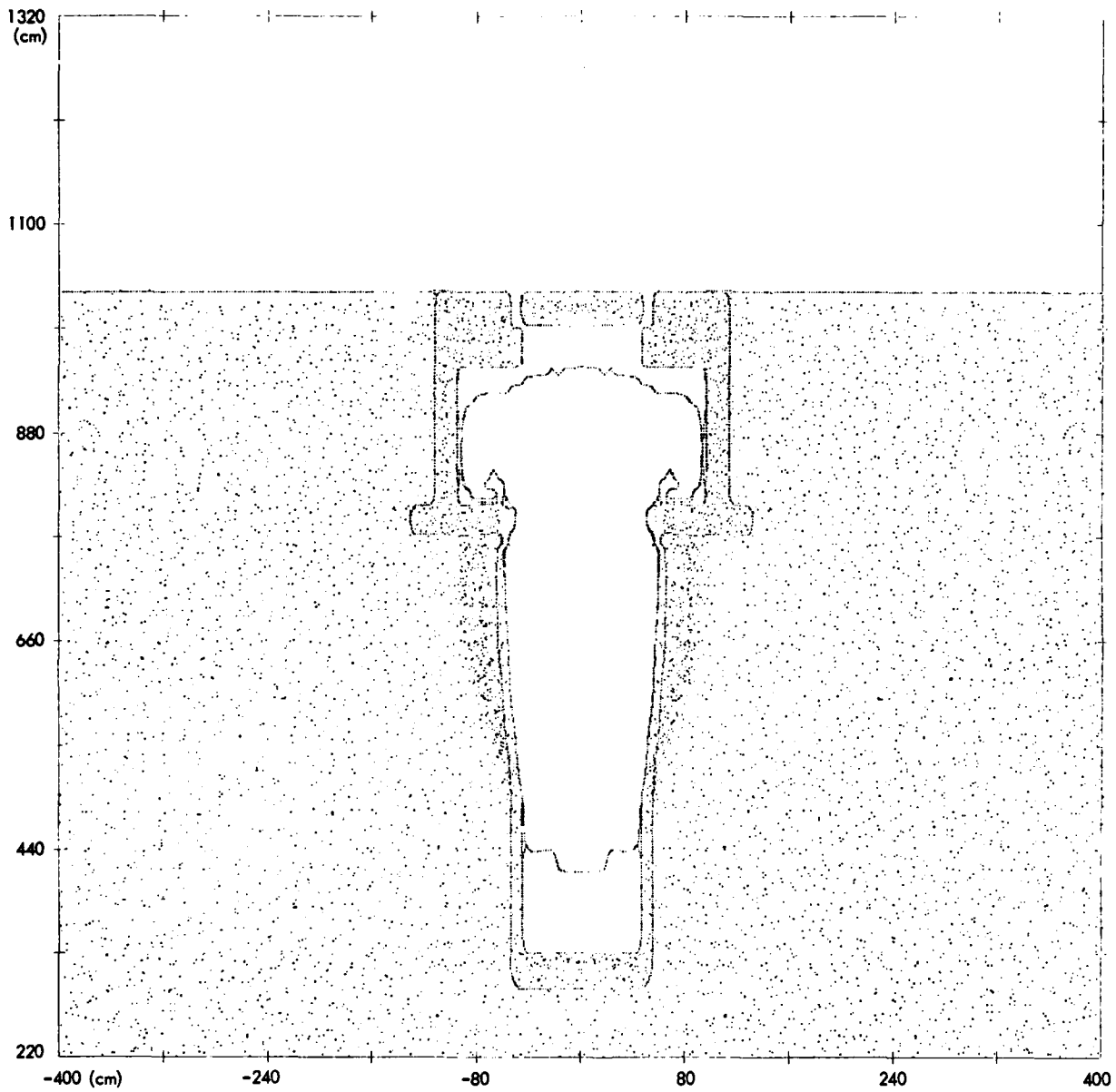


Figure 4-15. One-Quarter Scale Silo with Closure at 0.4 msec

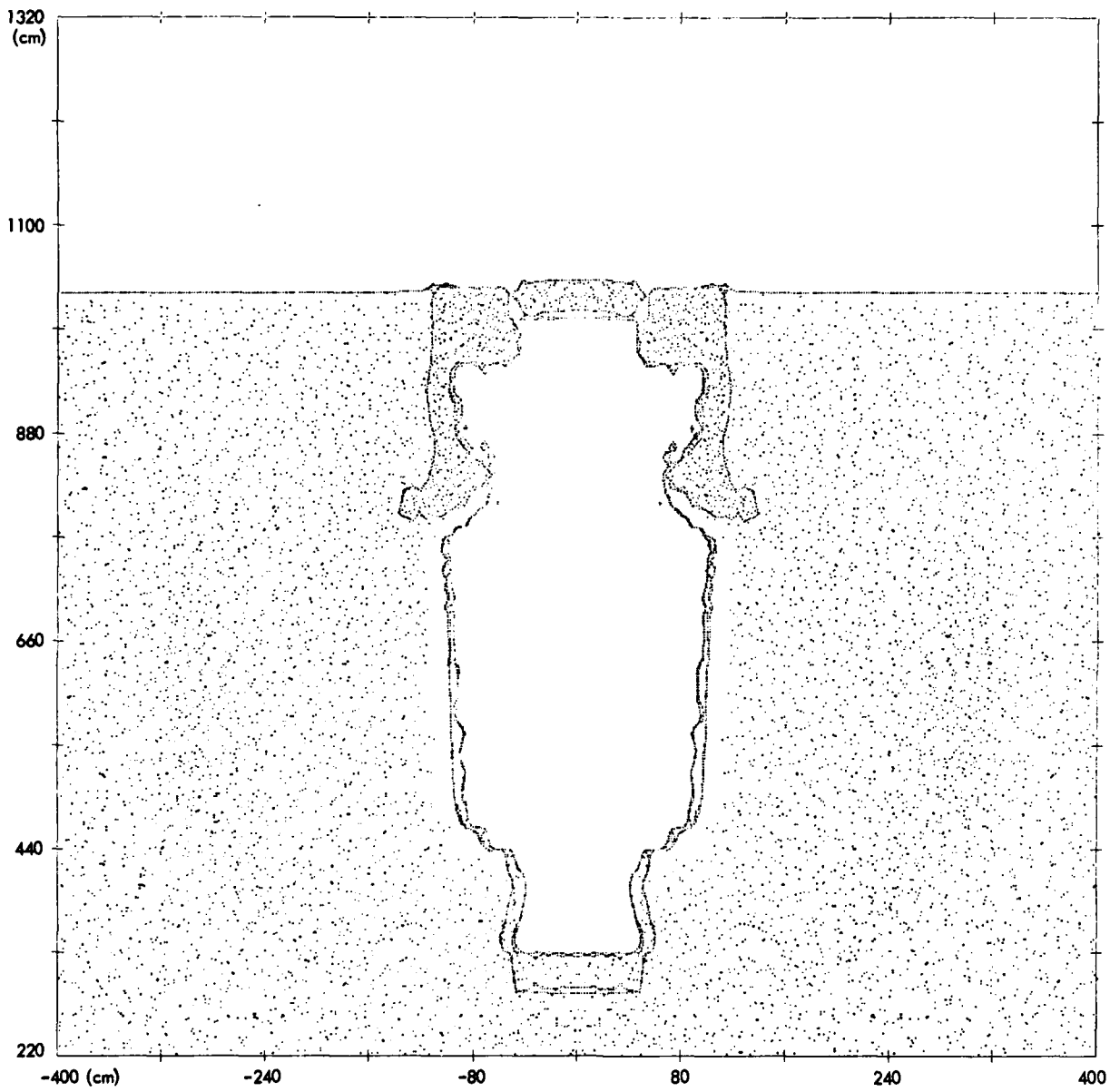


Figure 4-16. One-Quarter Scale Silo with Closure at 3 msec

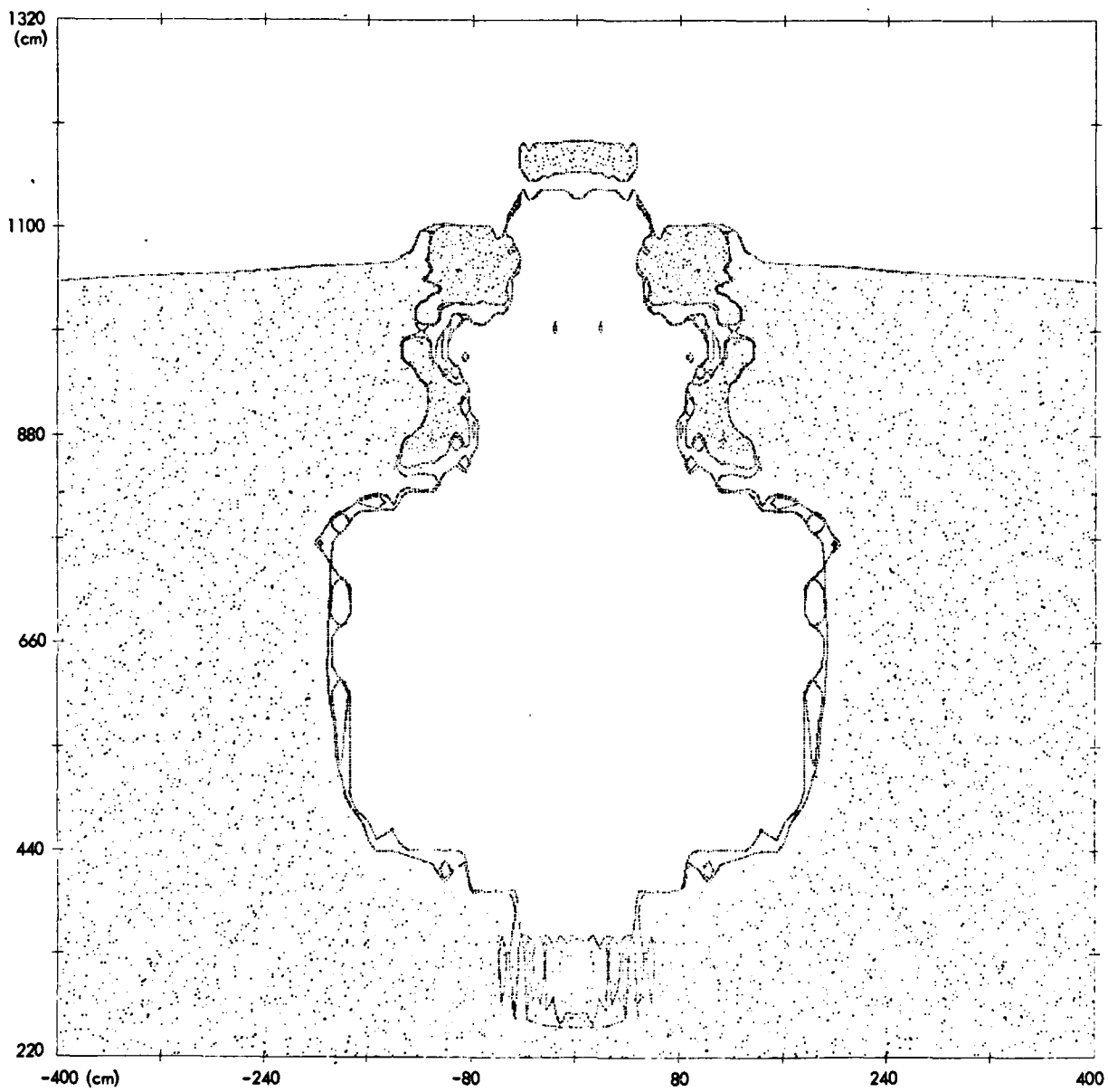


Figure 4-17. One-Quarter Scale Silo with Closure at 10.7 msec

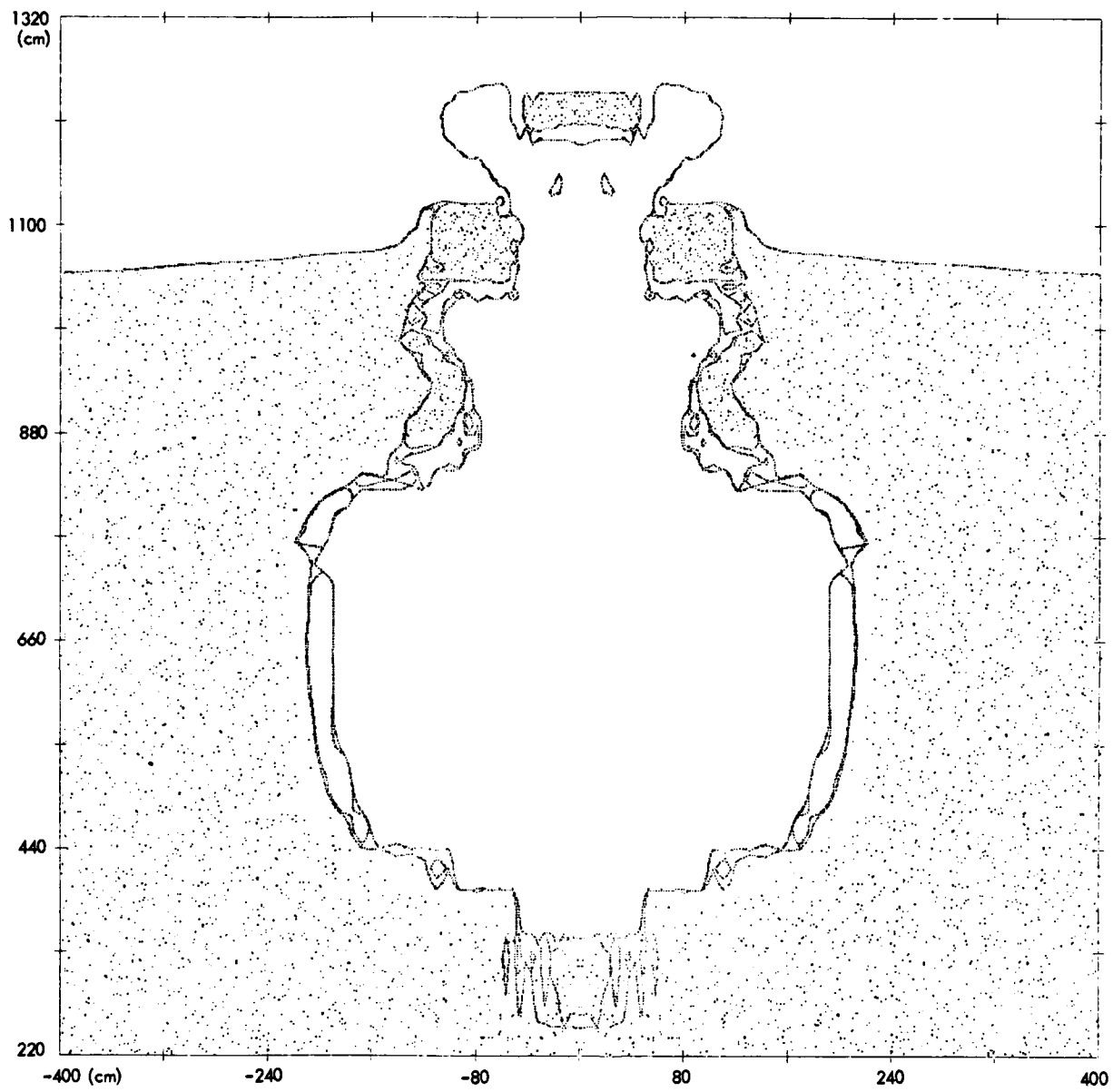


Figure 4-18. One-Quarter Scale Silo with Closure at 12.9 msec

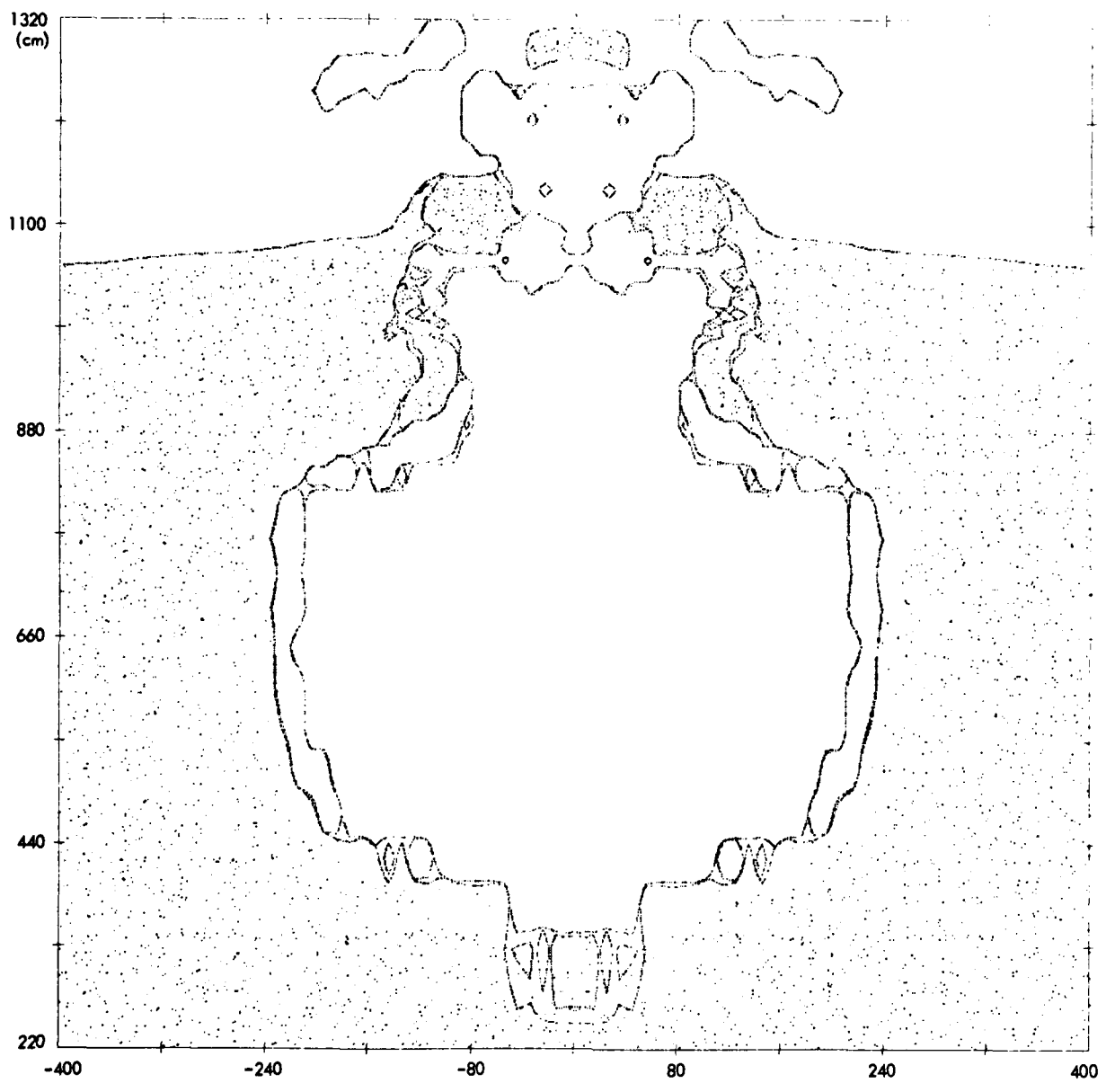


Figure 4-19. One-Quarter Scale Silo with Closure at 15.9 msec

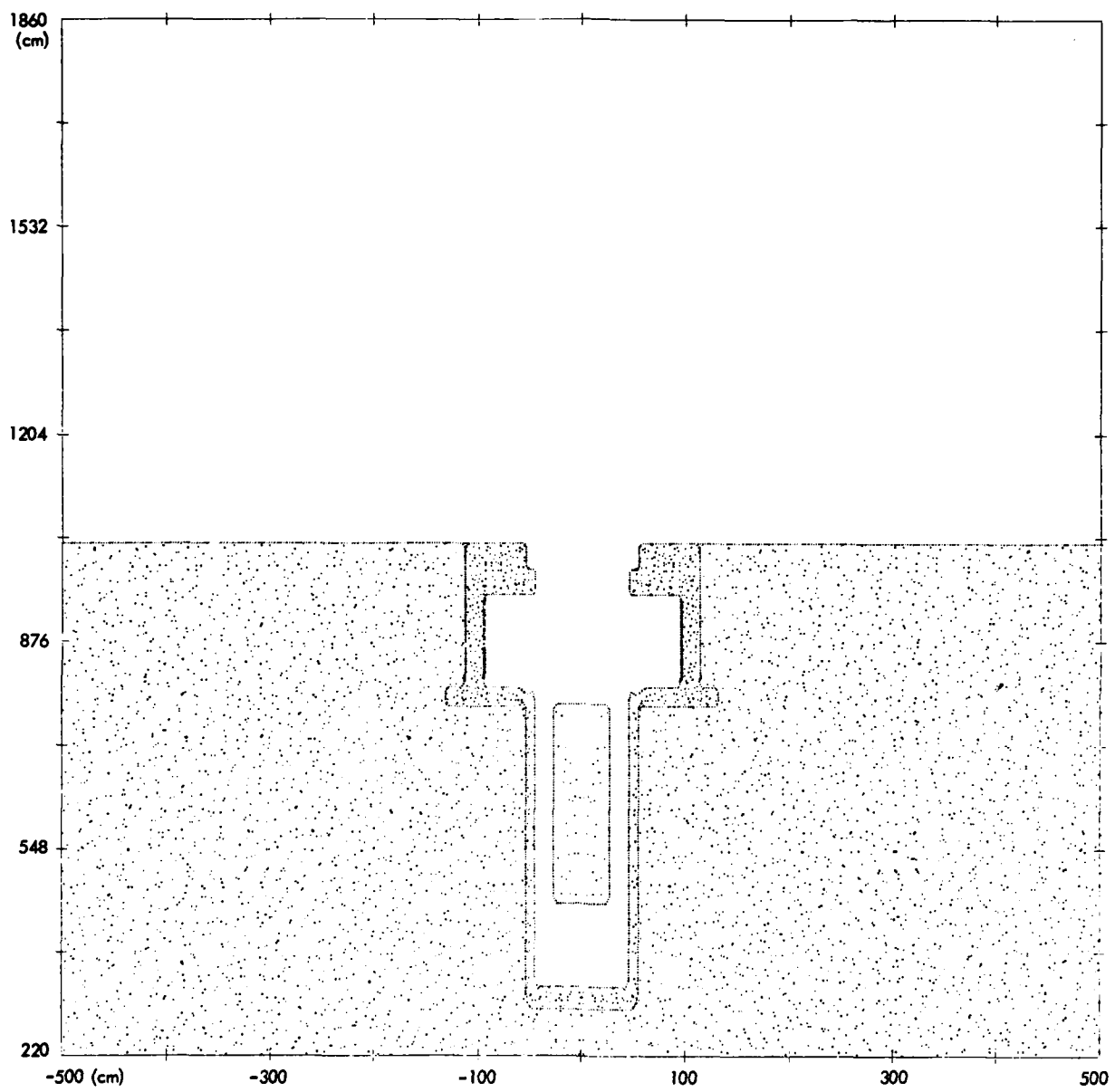


Figure 4-20. One-Quarter Scale Silo without Closure at 0 msec

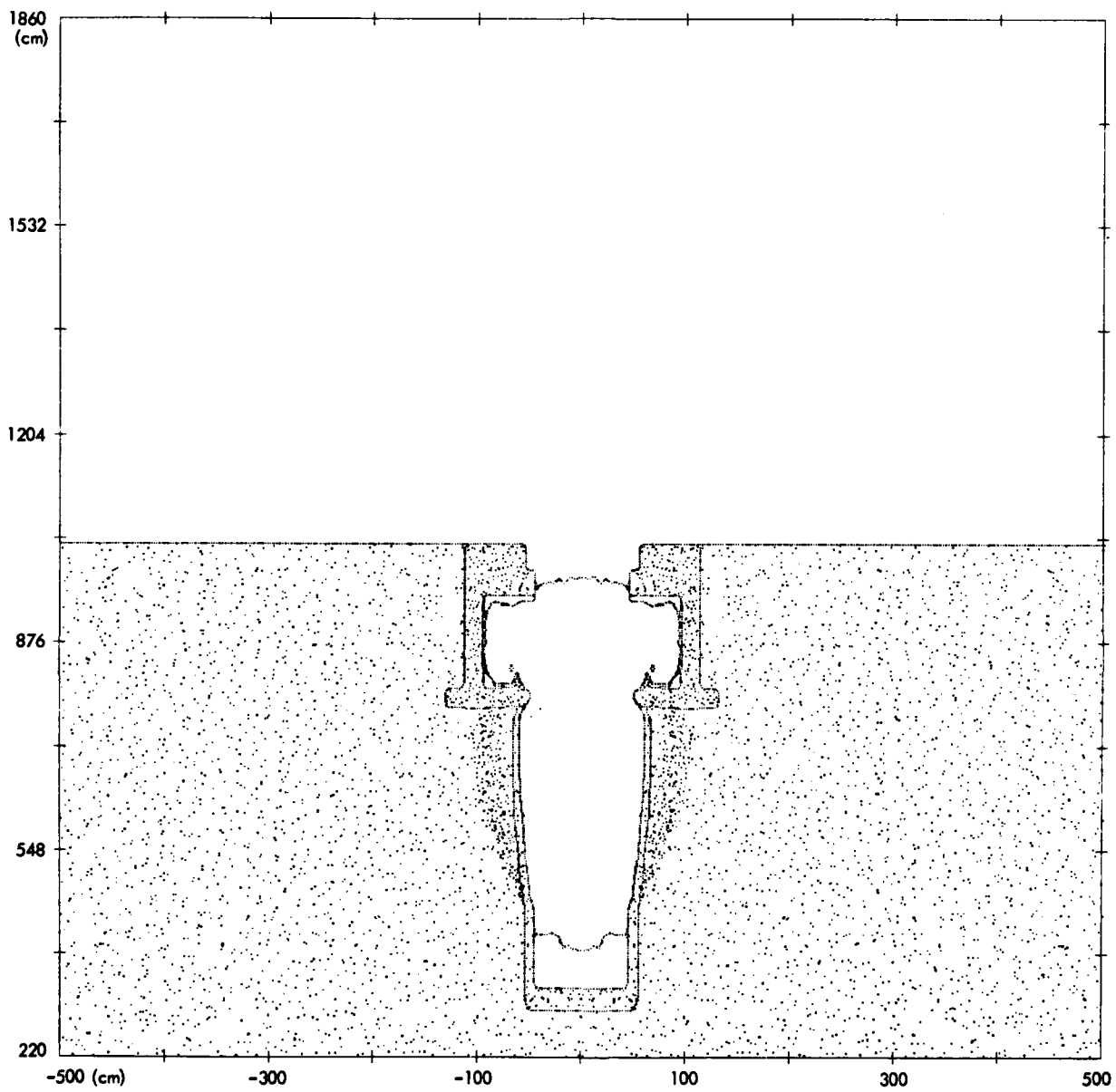


Figure 4-21. One-Quarter Scale Silo without Closure at 0.5 msec

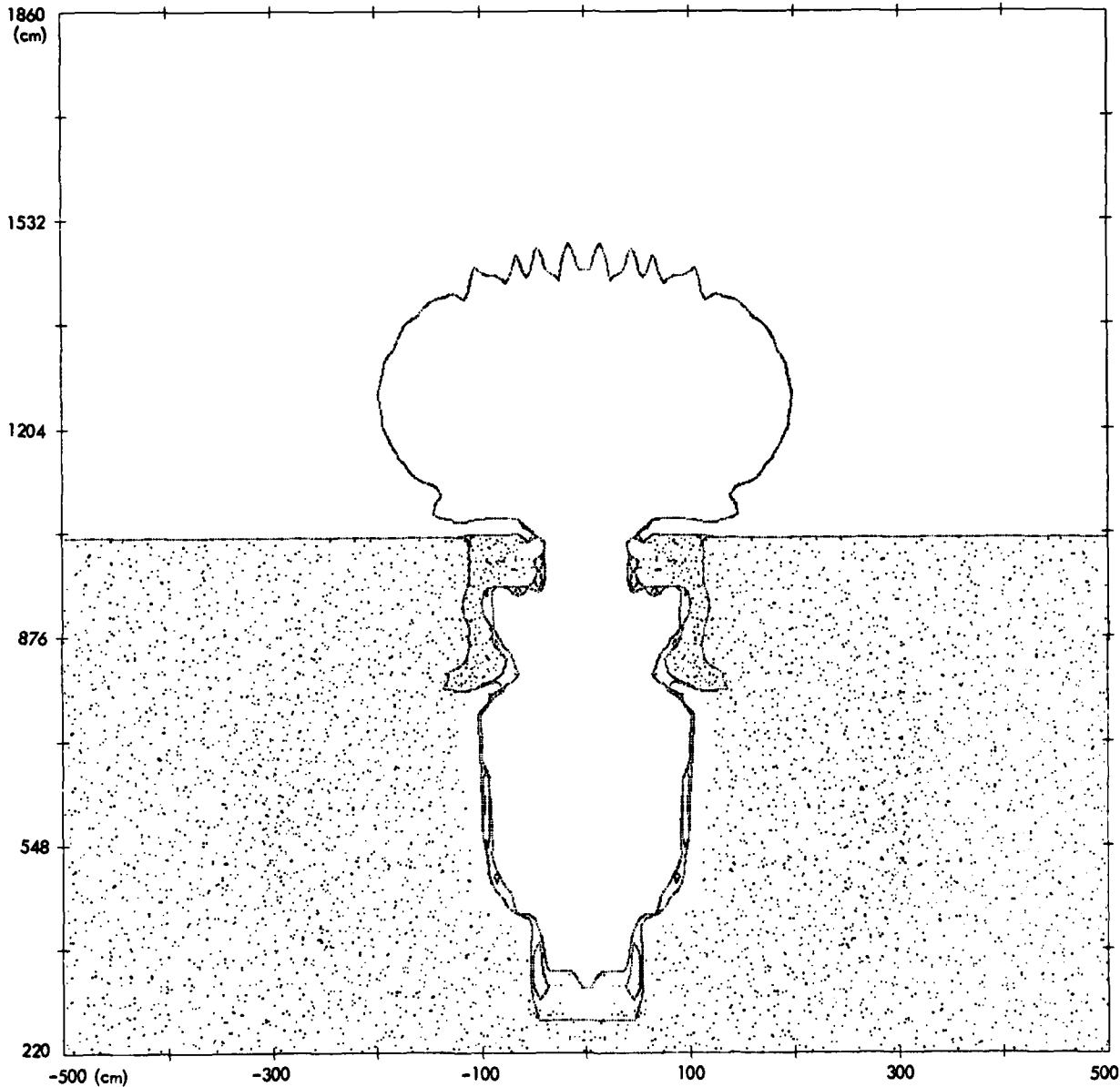


Figure 4-22. One-Quarter Scale Silo without Closure at 3 msec

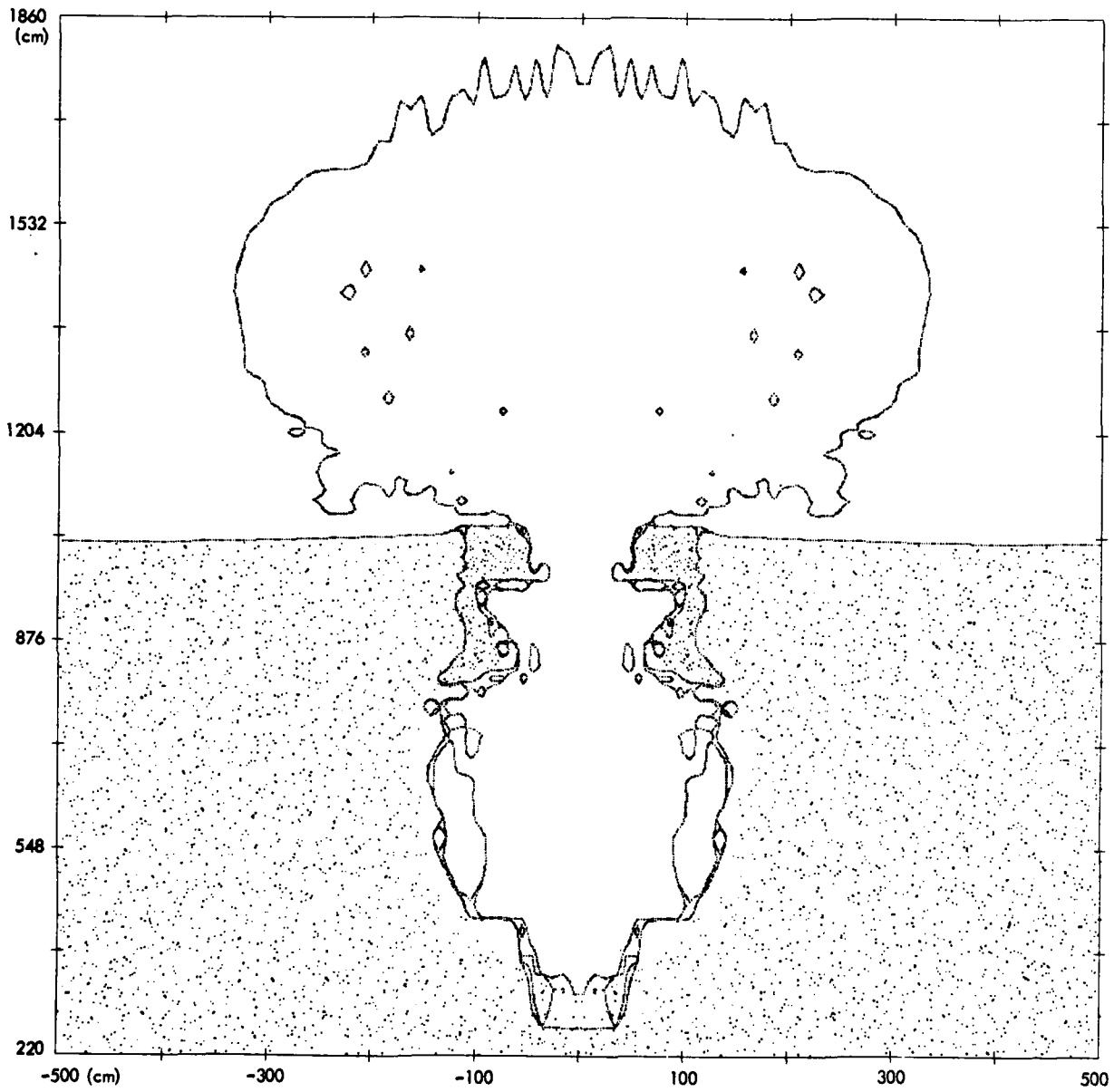


Figure 4-23. One-Quarter Scale Silo without Closure at 6 msec

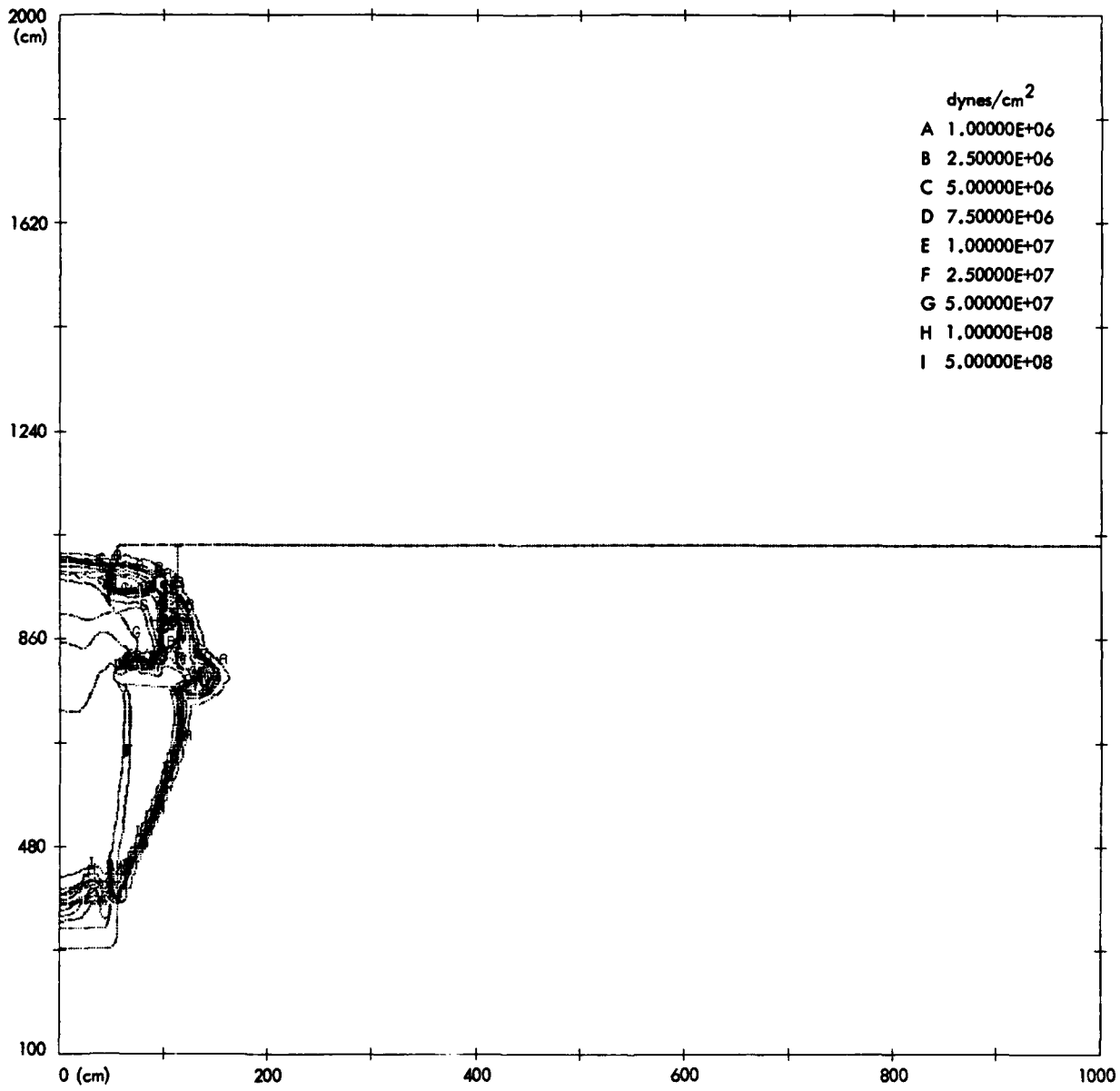


Figure 4-24. Pressure Contours for 1/4-Scale Silo without Closure at 0.5 msec

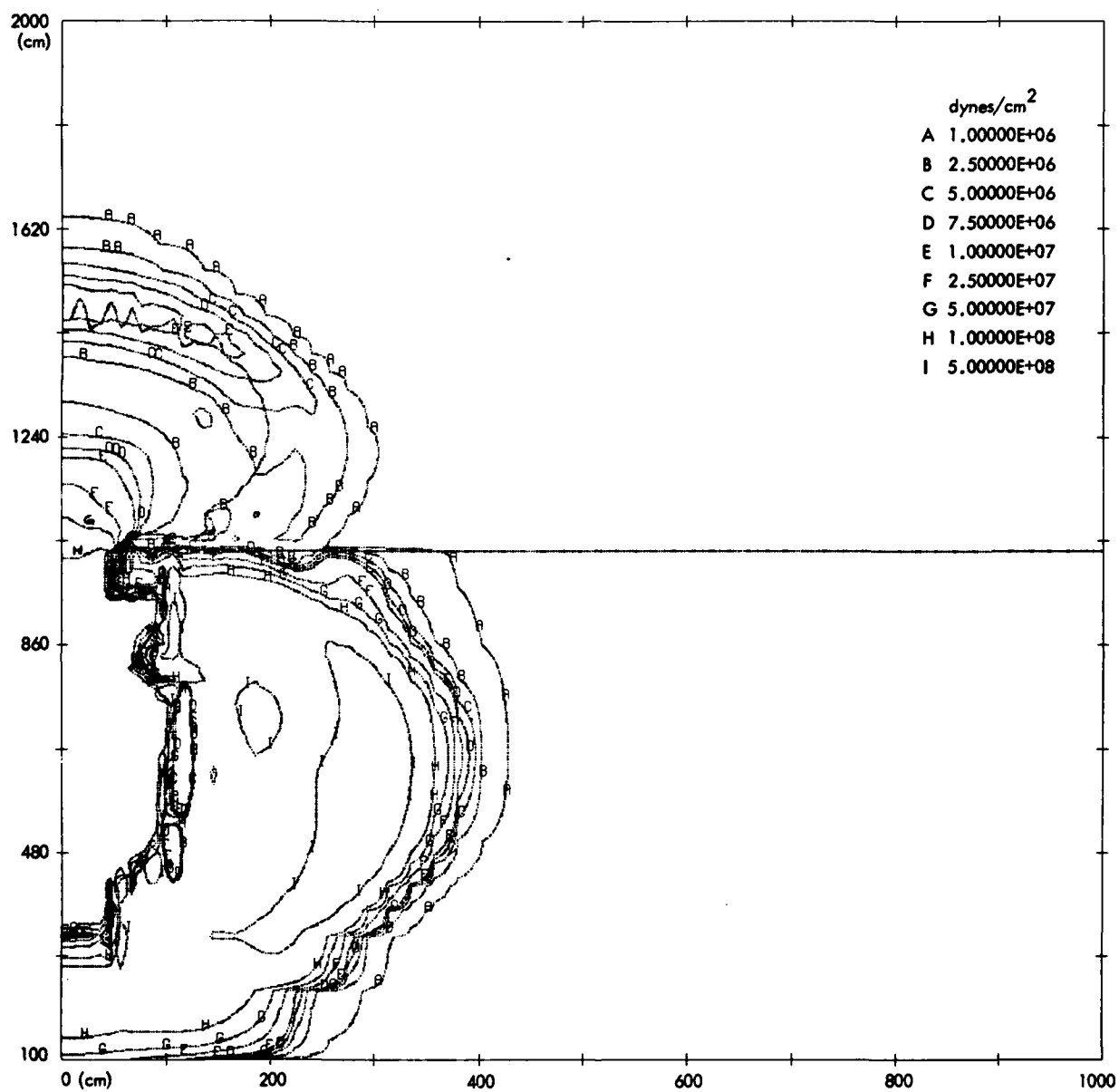


Figure 4-25. Pressure Contours for 1/4-Scale Silo without Closure at 3 msec

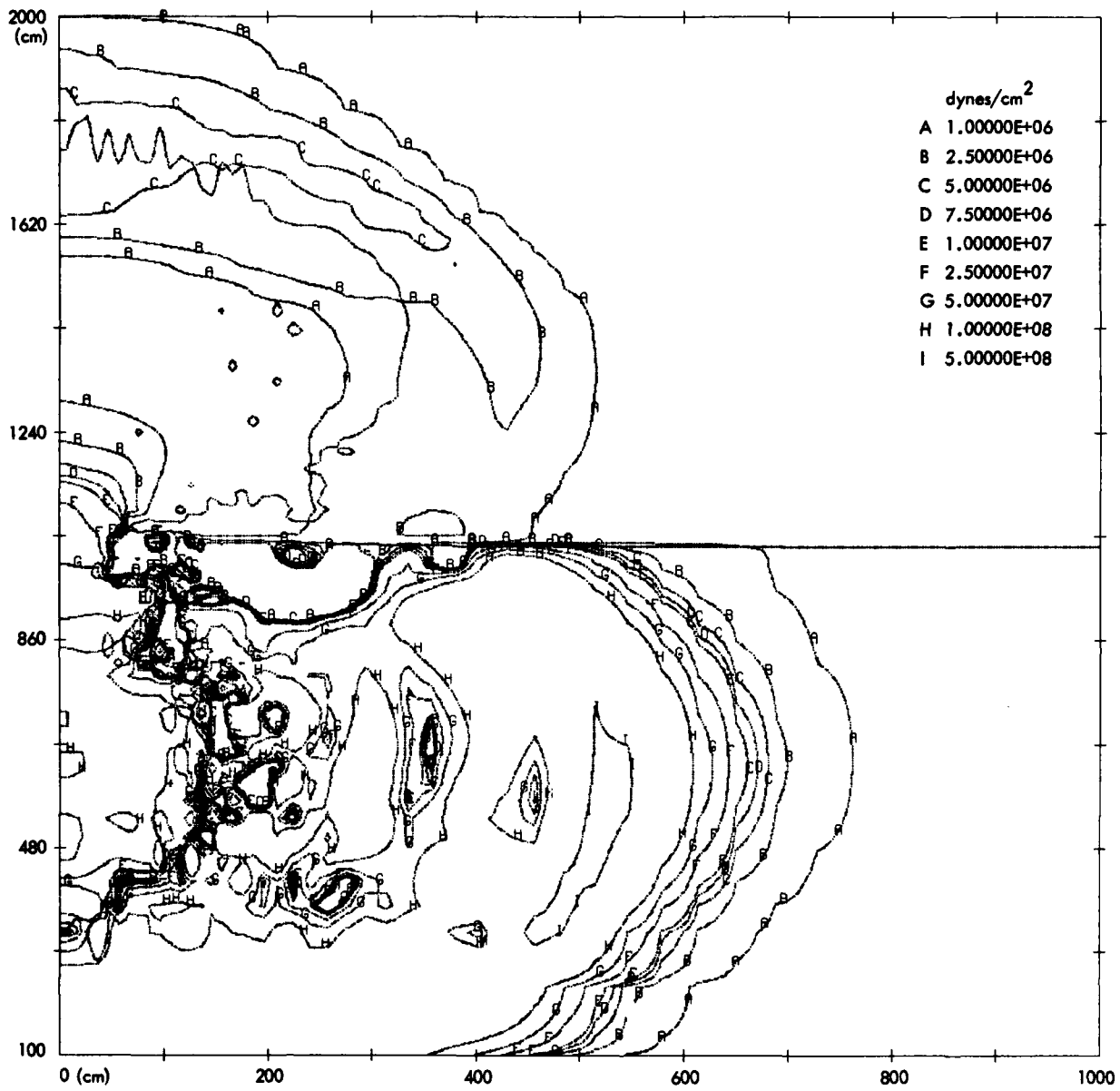


Figure 4-26. Pressure Contours for 1/4-Scale Silo without Closure at 6 msec

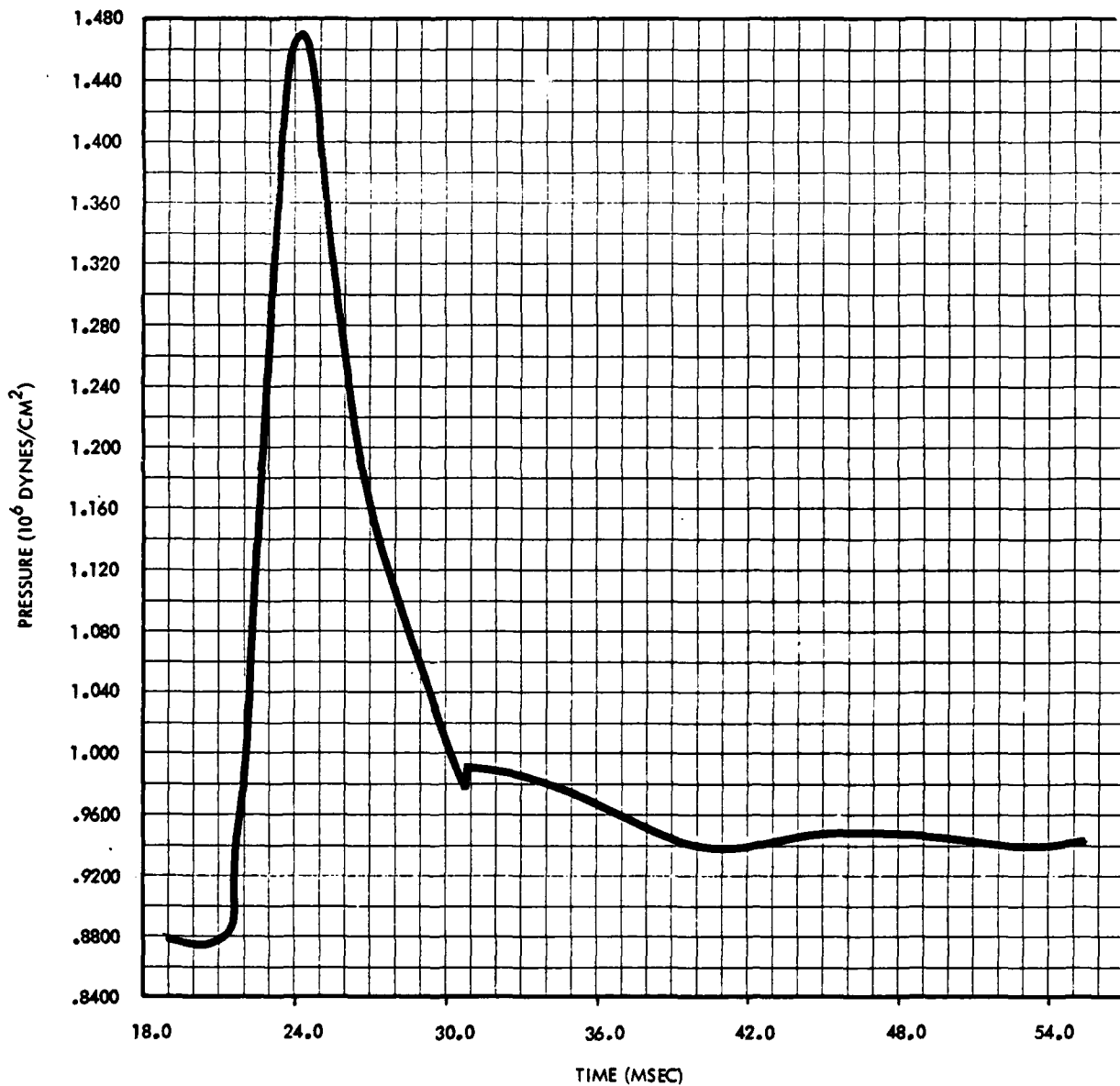


Figure 4-27. Pressure-Time History at Ground Range of 42 Feet

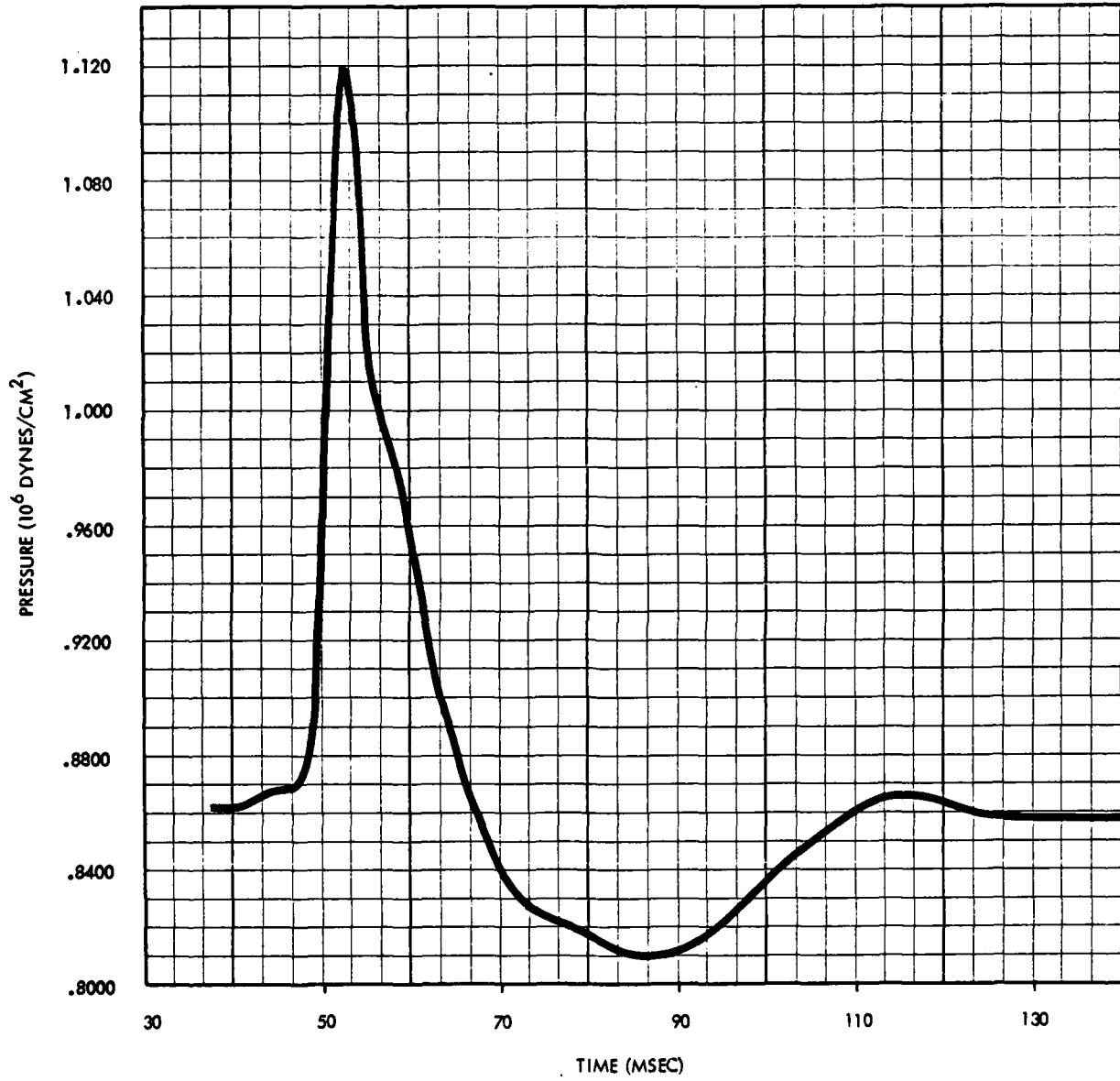


Figure 4-28. Pressure-Time History at Ground Range of 78 Feet

AD-A146 222

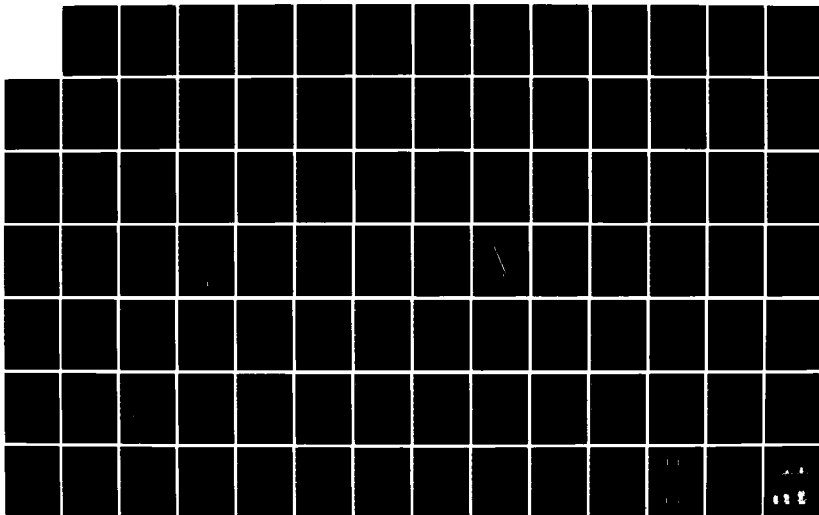
PEACEKEEPER QUANTITY-DISTANCE VERIFICATION PROGRAM AND
ADDENDUM(U) TRW DEFENSE SYSTEMS GROUP REDONDO BEACH CA
B SUSSHOLZ JUN 84 TRW-43597-6001-UT-00 BMO-TR-84-17
F04704-83-C-0045

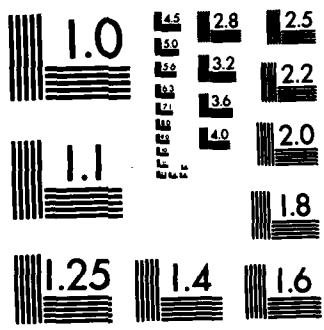
2/4

UNCLASSIFIED

F/G 16/1

NL





MICROCOPY RESOLUTION TEST CHART

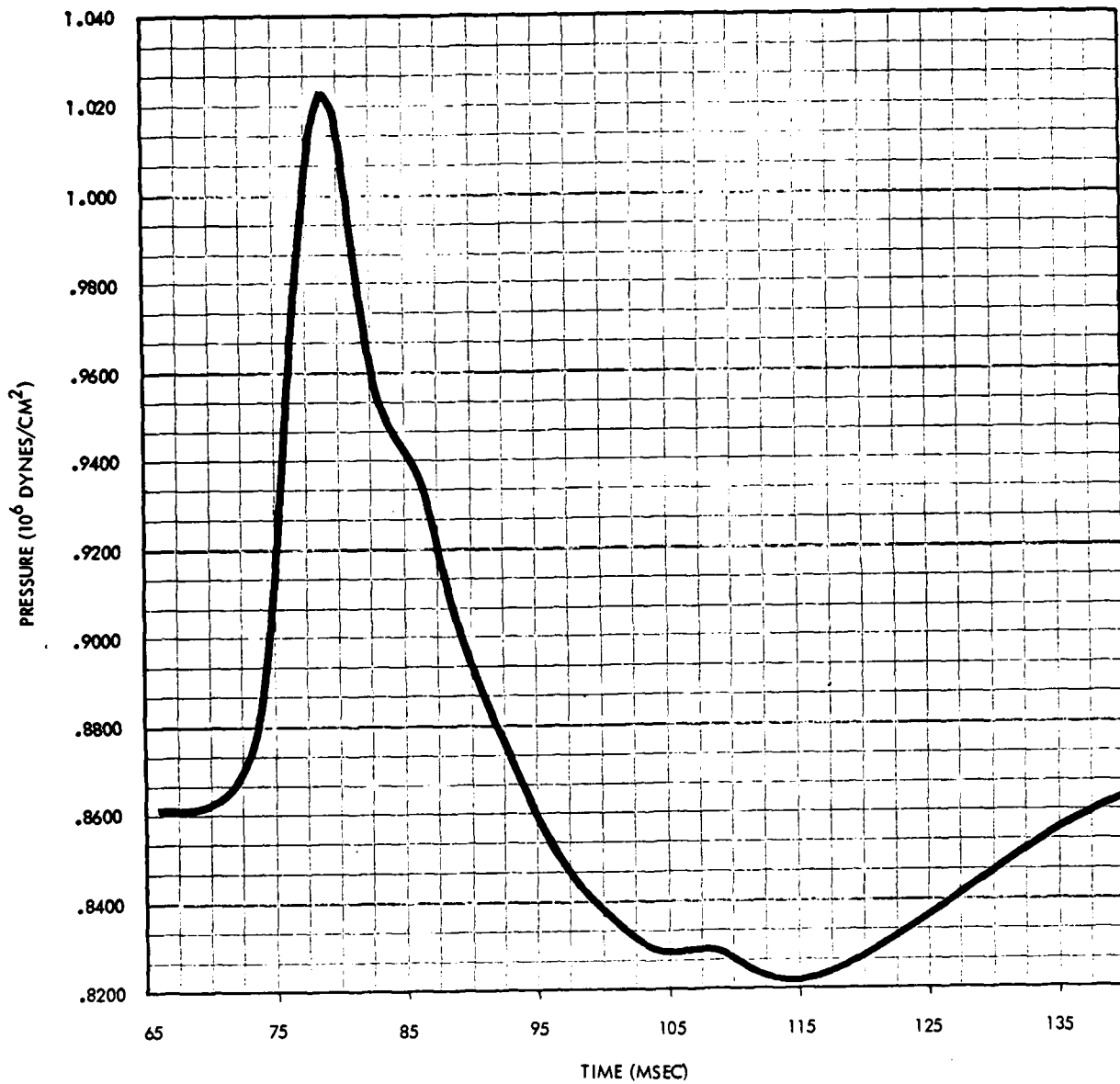


Figure 4-29. Pressure-Time History at Ground Range of 110 Feet

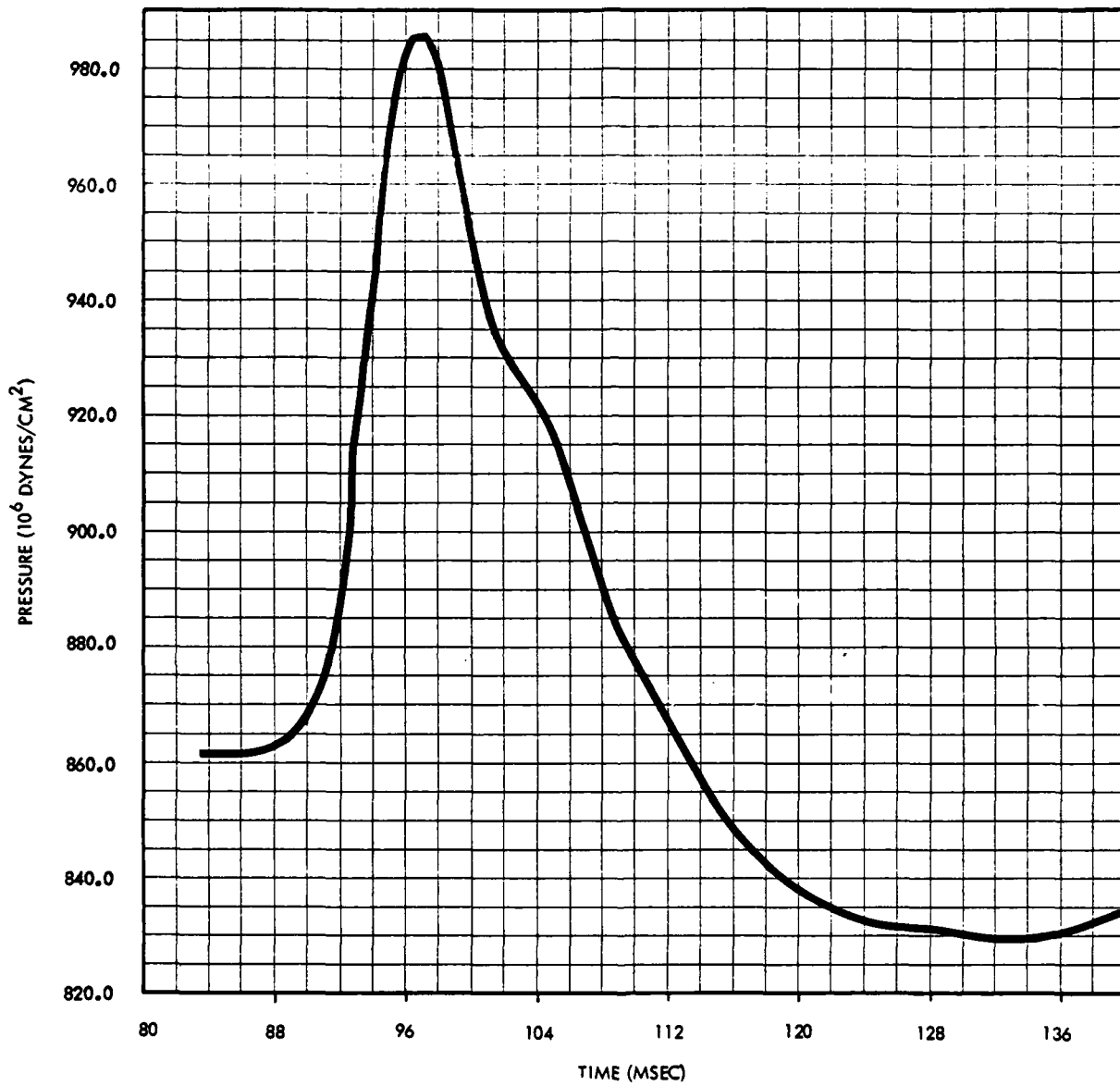


Figure 4-30. Pressure-Time History at Ground Range of 130 Feet

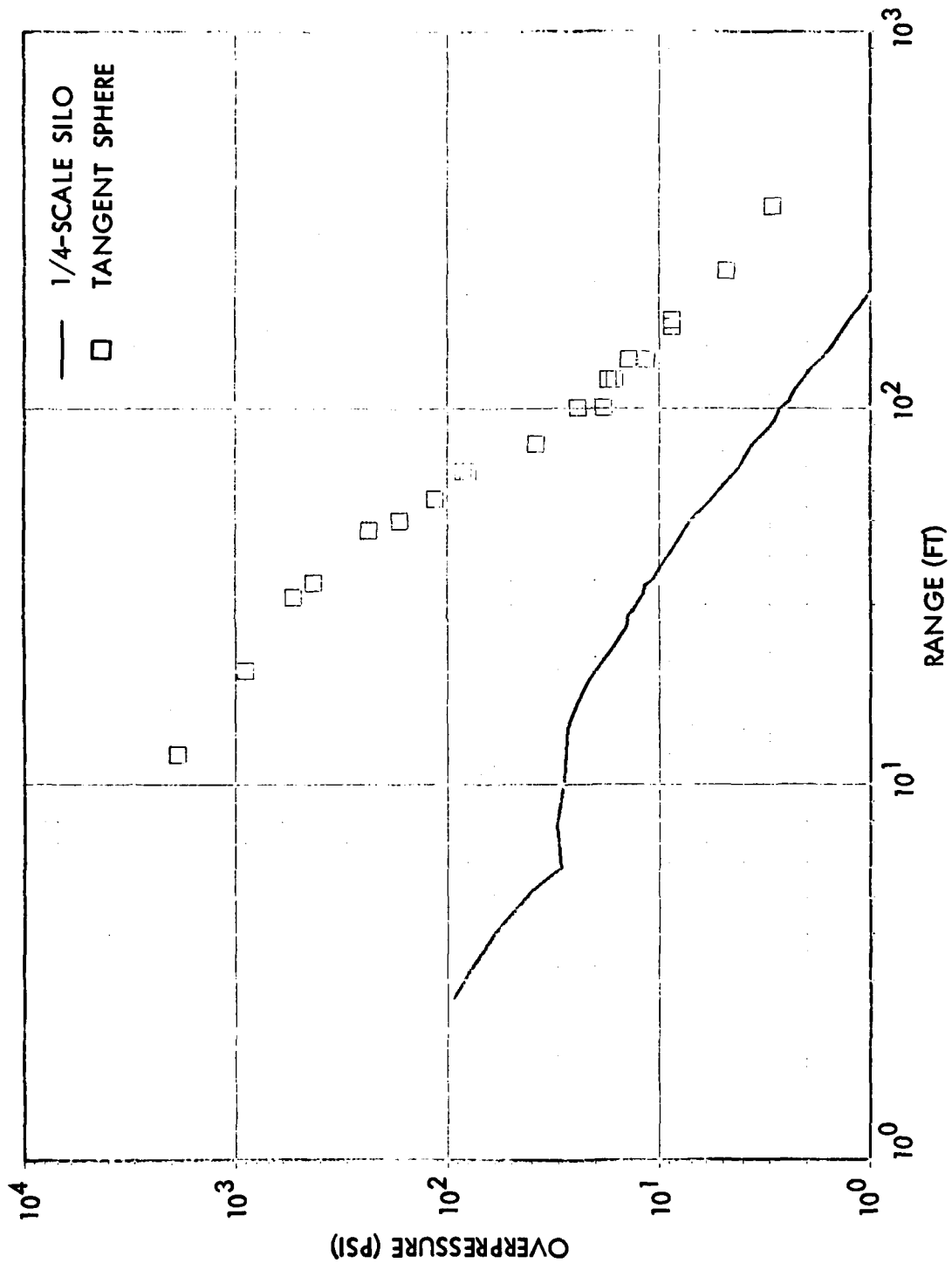


Figure 4-31. Overpressure Versus Range for 1/4-Scale Silo Calculation Without Closure

5.0 SOIL EJECTA CHARACTERISTICS

Fragments resulting from a silo explosion include structural debris and soil ejecta. Basic sources of soil ejecta are boulders, rocks, and pebbles, inherently characteristic of the Minuteman Wing V sites of interest, and large earth clumps that may evolve as a result of the natural cementation and cohesiveness of the soil particulate.

Backfill specifications for the 1/4 scale test site were based on a direct simulation of soil conditions at operational sites using gradations, density and stress-strain properties. Since the precise soil cohesivity representative of media surrounding Wing V silos could not be reproduced, estimates of size, number, and trajectories, as related to large earth clumps, were developed primarily on the basis of an analytical evaluation.

Results of a literature survey of ejecta data from buried charges are briefly summarized in the following discussion. Application of the data toward predictions of soil ejecta distributions for a full-scale event is discussed. An independent approach is described whereby specific fragment sizes are subjected to a spectrum of launch velocities and launch angles generated by the CSQ analysis of the silo explosion, and calculations are made of the ballistic trajectories to determine range and density distribution characteristics.

5.1 Ejecta Data Review

The data presented is a representative survey for the major types of soil media. No attempt was made to acquire a comprehensive collection of ejecta data.

The major types of soil media are:

- Rock (represented by basalt)
- Wet soil
- Dry soil (represented by alluvium)

This review is limited to buried bursts (explosive all below grade). An explosion of a Peacekeeper missile in a silo is more like a buried burst than a surface burst or above-ground burst.

Table 5-1 contains a summary of a data for the buried bursts considered here. Some other tests were briefly reviewed but are not included. The Essex Phase 2 tests (Reference 5-1) are not included because the results were similar to the results for Phase 1.

A number of tests in alluvium are not included because the mass loading of interest is beyond the radii where data were collected. These tests are Sedan (Reference 5-2), Scooter (Reference 5-3), and Air Vent Phase II (Reference 5-4).

The cube root of the crater volume has been used to nondimensionalize the radius from ground zero. This use is not meant to imply that this is the best scaling. The exponent $1/3.4$ is probably used more often for buried burst crater/ejecta data. Because of the large uncertainties, the two exponents do not differ significantly.

The apparent crater volume, V_a , is not always given in the referenced reports. Crater dimensions are given for Danny Boy. In this case, $V_a^{1/3}$ is calculated from

$$R \simeq 1.2 V_a^{1/3}$$

$$D \simeq 0.5 V_a^{1/3}$$

These relations for surface and near-surface bursts are taken from Reference 5-5. The average of the two values is used when both dimensions are available. For the MTCE event, only the radius is given.

Different cut-off sizes were used for counting missiles in the Wet Soil and MTCS (rock) events. No attempt was made to correct the counts for this difference. The 2-inch and 0.5-pound cutoffs are nearly the same. The cutoff used for Sprint is substantially different. After the Sprint event, the area surrounding the crater was covered with big clods of wet clay. The number of missiles might have been similar using a significantly smaller cutoff.

5.2 Safe Distance

The "safe" distance, with respect to ejecta, is defined as that distance from ground zero to missile densities of ≤ 1 per 600 sq ft with missile kinetic energy of ≥ 58 ft-lb. This kinetic energy, together with ejecta trajectory data, will define a critical particle diameter. Then the range to 1 per 600 sq ft can be estimated from the areal density on the missile counts.

5.2.1 Particle Trajectories

Ejection velocity results are available caused by the initial and final positions of artificial missiles and from following large particles photographically. The results for maximum ejection velocity for 20 tons range from 1000 ft/sec (References 5-6 and 5-7) to 300 ft/sec (Reference 5-8). The low result is caused by tracking particles photographically and is probably appropriate to the most numerous class of fragments that are visible. The higher value is only for missiles initially close to ground zero and to the surface. Ejection velocities would be higher for 101 tons buried in the same way as in Stagecoach (Reference 5-8) and Air Vent (Reference 5-6) tests. However, the silo occupies the region near ground zero and probably absorbs some of the force tending to accelerate soil ejecta.

The maximum soil particle ejection velocity for an explosion of a Peacekeeper in a Minuteman Silo is probably near 1000 ft/sec. This velocity was used for trajectory calculations with FETCH (Reference 5-9). These calculations indicate that particles smaller than 4 cm cannot reach a range of 1750 feet for still air. The size which can reach 1750 feet through the explosion flow-field will be somewhat different. The ejection velocity and the drag control the critical size since 4 cm particles launched at 1000 ft/sec will have a kinetic energy ~ 58 ft/lb on impact. Then, 4 cm is the critical particle size. Note that 4 cm is close to the 2 inches (5 cm) used as the minimum missile size in the missile counts of the more recent tests reviewed.

For those events where number densities are given, R_s is the distance where $N = 1/600$ ft². Again, no correction was made for the difference between 4 cm and the size used in the count.

5.2.2 Size Distribution Effect

If areal density is given, data concerning the size distribution of the debris are necessary to convert mass density to number density. Fits to the areal density data are reported in the test results and are collected in Table 5-2.

For the case of a rock (basalt) medium for Danny Boy, it was determined from the given size distributions that approximately one-third of the debris were particles larger than 4 cm. Also, the hard rock distribution

$$N(\sigma) = (K/\sigma^{3.5})d\sigma$$

where:

N = Number density

σ = Particle diameter

K = Constant

can be applied to these larger particles. The maximum particle size can be determined from the relation due to Gault, as quoted in Reference 5-7. This is 60 cm for the Danny Boy yield. Then the total mass required to give one particle per 600 ft² for 4 cm < σ < 60 cm is 3900 grams and the areal density at the safe distance is 6.99×10^{-2} kg/m².

Where the test medium is dry soil (alluvium), particle size distributions of ejecta from Reference 5-2 and 5-6 indicate that there is virtually no mass in particles larger than 4 cm. On the other hand, it was observed in Sedan that there were many large secondary craters but no large boulders remaining after the test. Apparently some of the mass was excavated in large clumps which broke up on impact. A model based on this observation considers some fraction of the mass breaks up like rock into large fragments with the hard rock distribution. A reasonable choice of this fraction based on the Sedan results is 10%. This assumption gives an areal density at the safe distance of 0.162 kg/m² for 20-ton events where the maximum particle size is 28.5 cm. The values of R_s for this areal density are listed in Table 5-1.

5.2.3 Data Correlation

It was desired to determine the safe distance as a function of burial depth and yield. The yield scaling implies the dependence on yield and the normalized safe distance. In Figure 5-1, $R_s/V_a^{1/3}$ is plotted against the normalized burial depth ($ft/Kt^{1/3}$).

All of the results collapse on approximately parallel straight lines. This is a reasonable correlation of the data. The slope of the lines indicate the dependence of the safe distance on burial depth.

All of the wet soil data should perhaps be shifted to the right because the critical particle size of interest (4 cm) is less than the cut-off size used to count missiles in the experiments. The slope of the line would be little affected by this correction. Also, the Peacekeeper crater would be a dry soil crater; therefore, absolute values of the rock and wet soil results are secondary.

5.2.4 Peacekeeper Application

Figure 5-1 can be used to predict the safe distance for the explosion of a Peacekeeper in a Minuteman silo given the burial depth and volume of the expected crater. The depth to the center of gravity of the Peacekeeper propellant is assumed to be the value (44 feet) used in the DNA calculations reported in Reference 5-10. The crater volume was calculated using Figure 4 of Reference 5-5. This gives $V = 150 \text{ m}^3/\text{ton}$ for an HE explosion in dry alluvium with a burial depth of $\text{HOB}/V_a^{1/3} = -0.55$. Then for 101 tons, $V_a = 5.35 \times 10^5 \text{ ft}^3$, $V_a^{1/3} = 81.2 \text{ ft}$, and $\text{HOB}/V_a^{1/3} = -0.542$.

The quantity $\text{HOB}/Kt^{1/3}$ is 94.5. Then from Figure 5-1, the predicted safe distance is approximately 1600 feet.

5.3 Test Predictions

In Section 5-2 the discussion was directed toward application of available empirical data to the question of a safe distance for large earth clumps for a full-scale silo explosion. For the purpose of establishing test predictions of the soil ejecta density variations with range for QDT-3, an independent approach involving direct calculations of small fragment trajectories was developed.

Particle size distributions and mass fraction were defined by the upper bound of the backfill gradation specifications described in Section 3-6. Ejecta diameters ranged from 0.5 to 3.0 inches and launch velocities covered a spectrum of 80 to 230 ft/sec over the region of interest as observed from results of the CSQ computations discussed in Section 4.4.2. Launch angles in all cases were taken as 45 degrees.

The velocity and angle assumptions appear reasonable when compared with the scaled data for the Stagecoach III and Scooter data shown in Figure 5-2. The Stagecoach event consisted of detonation of a 20-ton TNT charge at a depth of 34 feet, and for the Scooter event a 500-ton TNT charge was exploded at a depth of 125 feet. Both events were in alluvium and fully tamped. The respective scaled depths of burst were $1.00 \text{ ft}/\text{lb}^{1/3}$ for Stagecoach and $1.25 \text{ ft}/\text{lb}^{1/3}$ for Scooter, relatively comparable to the value of $0.90 \text{ ft}/\text{lb}^{1/3}$ for QDT-3.

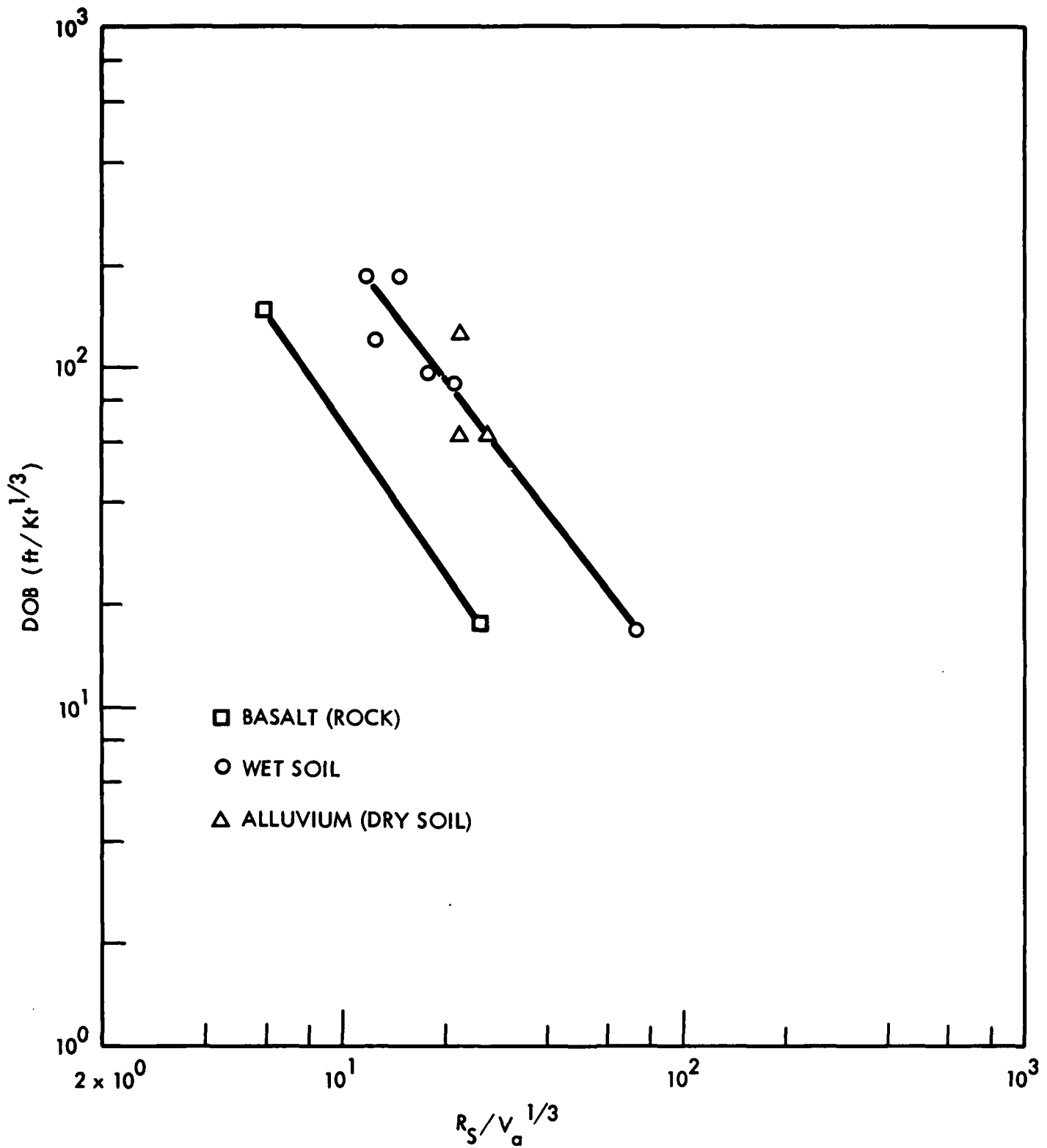
The shape for each particle was assumed spherical and trajectory calculations were performed with the FETCH code to determine fragment density distributions as a function of range. A plot of the analytical results is shown in Figure 5-3. It is estimated that a density of one fragment per 600 square feet would occur at a range of 390 feet.

Table 5-1. Summary of Ejecta Data for Selected Buried Bursts

Event	Ejecta Distribution Data	Charge Weight (tons)	Burial Depth (ft/Kt ^{1/3})	V _a (ft)	R _s (ft)	R _s /V _a ^{1/3}	Reference
BASALT (Rock)							
Danny Boy MTCS	Areal density	420 (NE)	147	1.25x10 ⁶	641	5.96	5-3
	Missiles >0.5 lb	2 (HE)	17.5	1060	259	25.4	5-12
WET SOIL							
Sprint Ft Polk (AFWL-1)	Missiles >10 lb	4 (HE)	120	4.86x10 ⁴	460	12.6	5-11
	Missiles >2 in.	0.5 (HE)	16.9	859	700	73.6	5-14
ESSEX, PHASE I							
6 MU 6 MS 12 MPS 12 MS	Missiles >2 in.	8 (HE)	90.6	1.77x10 ⁵	1000	17.7	5-13
	Missiles >2 in.	10 (HE)	89.1	2.14x10 ⁵	1280	21.4	5-13
	Missiles >2 in.	10 (HE)	183	1.89x10 ⁵	685	11.9	5-13
	Missiles >2 in.	10 (HE)	183	1.68x10 ⁵	813	14.8	5-13
DRY SOIL (ALLUVIUM)							
Stage Coach II Stage Coach III Air Vent I	Areal density	20	63.0	8.37x10 ⁴	973	22.3	5-3
	Areal density	20	126	1.45x10 ⁵	1173	22.3	5-3
	Areal density	20	63.0	5.41x10 ⁴	1047	27.0	5-6

**Table 5-2. Areal Density Functions for Danny Boy
and Dry Soil Events**

Event	Areal Density Function
Danny Boy	$\delta \text{ (kg/m}^2\text{)} = 2.69 \times 10^{18} R(m)^{-8.55}$
Stage Coach II	$\delta \text{ (kg/m}^2\text{)} = 1.95 \times 10^5 R(m)^{-2.46}$
Stage Coach III	$\delta \text{ (kg/m}^2\text{)} = 7.32 \times 10^7 R(m)^{-3.39}$
Air Vent I	$\delta \text{ (lb/ft}^2\text{)} = 2.37 \times 10^6 R(ft)^{-2.61}$



**Figure 5-1. Scaled Range to 1 Particle per 600 Square Feet
 Versus Scaled Depth of Burst**

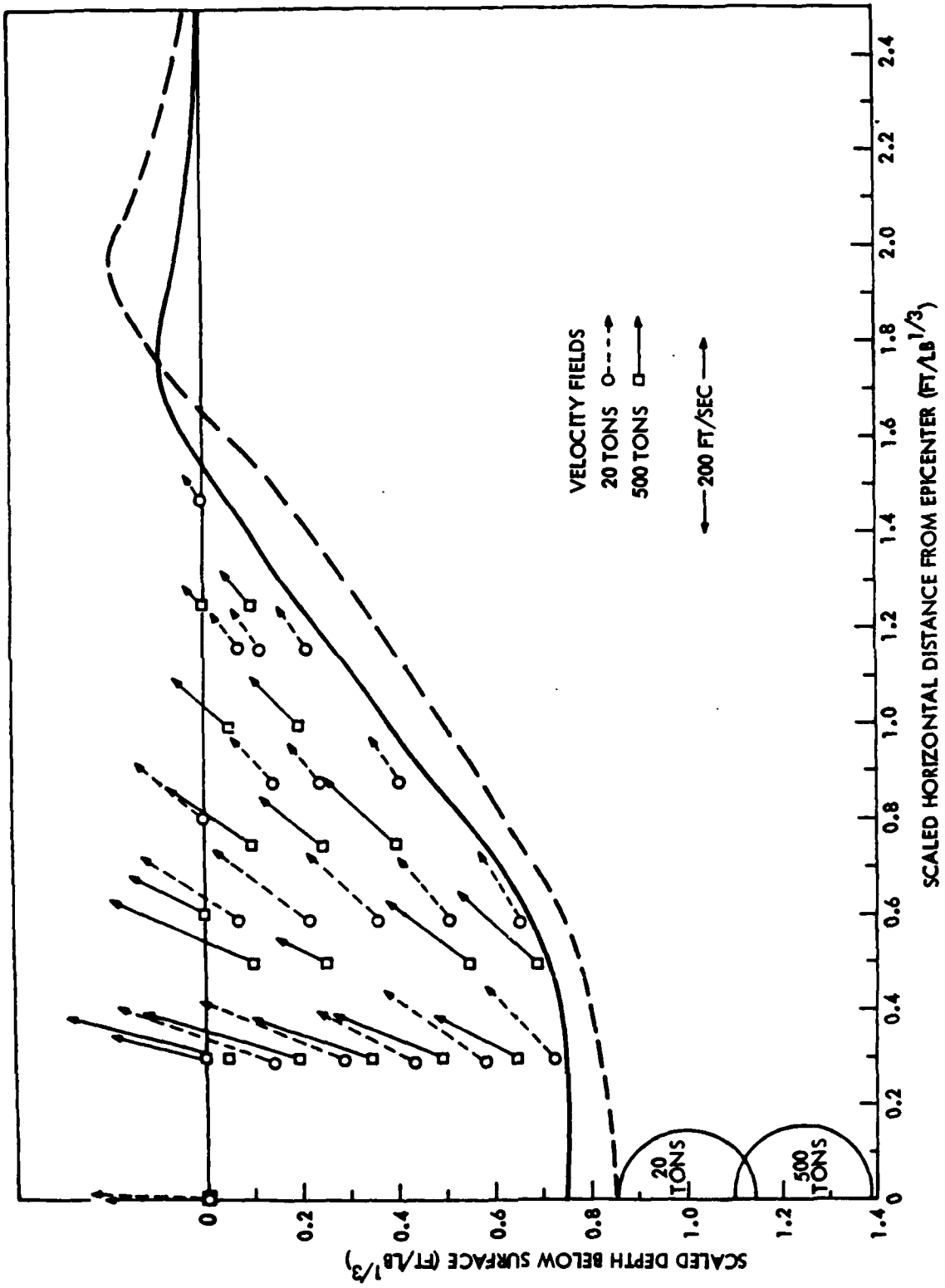


Figure 5-2. Comparison of Stagecoach and Scooter Effective Velocity Fields

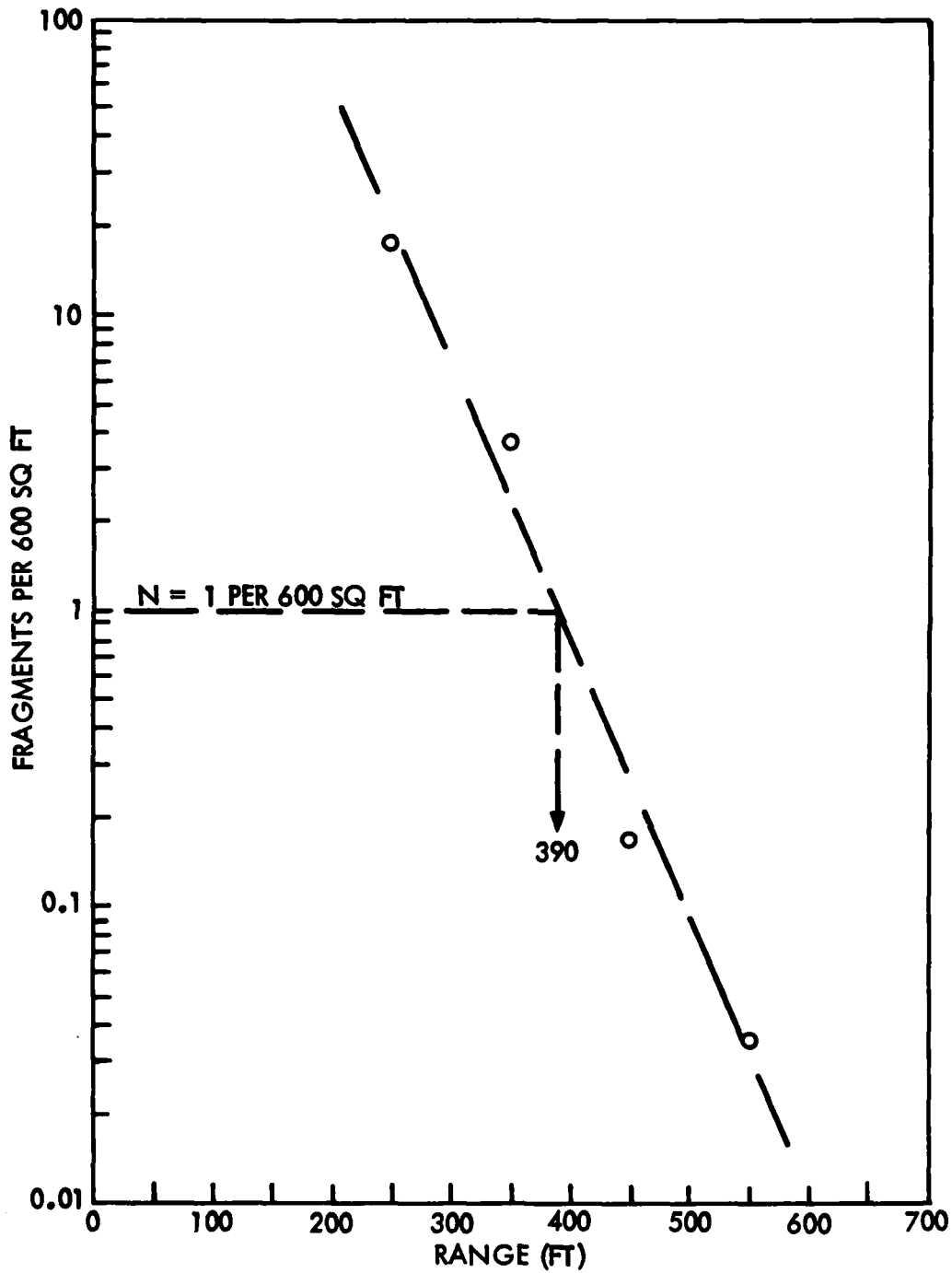


Figure 5-3. QDT-3 Soil Ejecta Density Predictions

6.0 STRUCTURAL DEBRIS

In the analysis of structural break up, attention was focused on three major areas: early time break up response, surface spallation phenomena and fragment launch parameters. Ballistic trajectories were analyzed and test predictions developed for the resulting fragment dispersion characteristics.

6.1 Early Time Break Up

A three degree-of-freedom (3DOF) model was developed to simulate the early time response of the LER headworks to internal blast pressure loading. The 3 degrees of freedom are: resistance to vertical separation of headworks from the LER wall, radial expansion of the headworks, and rotational response of the headworks as a ring beam. Equations of motion, derived assuming resistance is offered by the steel reinforcement only, were numerically integrated.

The pressure loading generated by an internal explosion loads the headworks vertically and radially. In addition, the eccentricity of the loading causes rotation of the headworks as a ring beam. To derive approximate equations of motion describing the headworks response, an axisymmetric idealization was adopted with an element of angular extent $d\psi$; see Figure 6-1. The external forces and moments acting on such an element, as shown in Figure 6-1, are: P_1 , P_2 , the resultant radial and vertical loads produced by the internal pressure; F_T , F_S , M_W , the vertical and horizontal resistance and resisting moment offered by the LER wall; and F_ψ , M_H , the hoop resisting force and moment of the headworks.

Since primarily tensile and shear stresses are produced by internal pressure loading, the contribution of concrete was neglected and only the resistance of steel reinforcement, including both rebars and the internal steel liner, was considered in this approximate analysis. An elastoplastic model was assumed for steel in both tension and shear. The elastic regime was ignored except in calculating hoop resistance. Stresses σ_y in tension and τ_U in shear were assumed constant until fracture occurs. Discrete rebars were approximated by a smeared, equivalent steel area to simplify the analysis. Vertical wall resistance included both tensile stresses in the liner and resistance to rebar pullout. Because the vertical rebars penetrate only 9 inches into the headworks, the resistance

offered by them was assumed to originate from bond resistance to rebar pull-out rather than through tensile stress in the rebars.

To obtain the hoop resistances note that hoop displacements are found by superposing the rotation on a uniform radial expansion x . The rotation produces an increase in the tensile strain of the upper hoop rebars and a decrease in the strain of the lower rebars. The hoop strains are maximum at the inner periphery and decrease toward the outside. As the strains increase, first yielding and then fracture initiate at the inner periphery and progress outward. The resulting stress variation with radius for the upper rebars is shown in Figure 6-2. The stresses in the lower rebars and in the liner on the underside of the headworks show a similar behavior.

A computer code was developed to numerically integrate the equations of motion. Appropriate terms were set to zero as rebars fractured or pulled out. The input parameter values selected for the analysis of the 1/4-scale QDT-3 test structure are shown in Table 6-1. The value of t was taken as 10.5 inches by assuming that the top 2-1/2 inch layer of concrete spalls off at an early time. The distances h_U and h_L were chosen by assuming an approximate cover for the rebars. The nonuniformity of the lower hoop bars was ignored, and t_{hU} , t_{hL} were calculated by considering the total hoop steel present. The equivalent vertical rebar thicknesses, t_{vj} and t_{v0} , were computed from the vertical rebars present, i.e., outer rebars at 3 inches on center at 43.5 inches radius and inner rebars directly across the outer bars at 38.25 inches radius. The ultimate shear stress τ_U was assumed to be 75% of the tension yield stress for which an average value of 50,000 psi was assumed, based on WES tests of the QDT-3 test structure rebar steel.

When the vertical displacement of the headworks exceeded the bonded length of 9 inches, the headworks was considered to have pulled out and the contribution of rebar bond resistance to the LER vertical resistance F_T was set equal to zero.

The maximum allowable horizontal displacement x_0 (radial expansion) before the liner ruptures or the vertical rebars shear was taken as 0.5 inches, considering that these members are not subjected to knife-edge shear loading, but undergo tensile deformation before they fail. The maximum allowable vertical displacement y_0 before the liner fails in tension was taken as 0.8 inches by assuming a fracture strain of 20% over a gage length equal to the anchor stud spacing on the liner, which is 4 inches. The yield strain of steel was taken as 0.0017, calculated from a yield stress of 50,000 psi and an elastic modulus of 3×10^7 psi. The fracture strain of steel was assumed to be 20%.

Clearly other equally reasonable choices are possible for several of the above parameters, and would influence the calculated results. Sensitivity to alternative choices of parameters was not addressed because of lack of time.

The computed results are summarized in Table 6-2 and, in particular, portray the sequence of failure of the headworks. The results show that hoop rebars and the underside of the liner start yielding at the inner periphery at very early times (0.25 msec). The upper hoop rebars show more rapid yielding than the lower rebars because of a higher tensile loading and because of less steel area. At a time of 1 msec, the liner ruptures because of the vertical tensile load and almost immediately the vertical rebars fracture in shear. Upper hoop bars begin fracturing at 2 msec followed by the initiation of fracture in the lower hoop bars and tearing of the liner at 2.5 msec. All upper hoop bars have fractured by 3 msec. All the hoop rebars and the liner on the underside of the headworks have ruptured under tensile loading by 4 msec.

The primary outcome of this analysis was that the headworks breaks up through tension failure of the hoop rebars, thereby leading to the formation of large fragments. Note that the analysis might have indicated that hoop rebars stay intact in which case the fragment size would have been limited to the rebar mesh spacing and the rebar cage would form one large fragment that would stay close to GZ.

6.2 Surface Spallation

In the following pretest analysis three spallation possibilities were investigated; spalling of the 2.5 inch thick layer of unreinforced concrete on top of the test article's closure and headworks, the 0.5 to 0.75-inch layer which covers the outer rebar of the structure, and break up of the LER due to failure of the shear steel near the back face of the closure, headworks or wall.

The analysis indicated that only the thin layer of concrete on top of the structure would spall and was predicted to break into many small pieces due to repeated impacts on an accelerating closure. Spalling of the rebar cover was not anticipated, although it was suggested that large flexural deformations could free portions of the cover. Failure of the shear steel was not expected either. However, tensile strains within the components were predicted to fracture the concrete at several depths through the thickness. These fracture planes would influence the size of debris particles should the structural response of the member to the blast loads release them.

6.2.1 Spall Phenomenology

When a compressive stress wave, traveling through concrete, contacts a free surface (or transitions to a lower impedance material such as soil), a tension wave propagates back through the structural element. The magnitude of this tension wave depends on the change in impedance and the angle of incidence. If the magnitude of the tension wave exceeds that of the compressive wave by more than the tensile capability of the concrete, then a fracture plane will form at that depth in the element and the material between the free surface and that point will spall (separate from the rest of the element with a relative velocity determined by equating the impulse of the compressive wave trapped in the layer to the momentum of the layer).

In the free surface case, the tension wave mirrors the compressive wave. If there is soil beyond the concrete, however, the magnitude of the tension wave will only be α times that of the compressive wave, where

$$\alpha = \frac{1 - \psi}{1 + \psi}$$

Here, ψ is the relative impedance of the two materials,

$$\psi = \frac{(\rho C)_{\text{concrete}}}{(\rho C)_{\text{soil}}}$$

where ρ and C are the mass density and wave speed, respectively. Assuming a typical value of 32 psi/ips for $(\rho C)_{\text{concrete}}$ and 2 psi/ips for $(\rho C)_{\text{soil}}$, the peak magnitude of the tension wave will be 88% of the compression wave. Note that attenuation of the waves due to material inelasticity is neglected and that normal incidence is assumed because it is the worst case orientation.

Five key parameters influence spalling: the slope and duration of the decay portions of the compressive wave, the double transit time (DTT) of the stress wave through the structural element, the tensile capability of the material, the ductility of the material and, finally, the impulse of the compressive wave trapped in the layer of interest. Note that with the right combination of these parameters, multiple layers can be spalled, potentially reducing a structural element to rubble.

6.2.2 Loading Functions

The loading functions used in the spalling investigation are shown in Figure 6-3. The CSQ calculation on which they were based showed many small oscillations in the pressure loading. Only the three most significant episodes of decay were considered, however. The rest were judged to have too gradual a slope or too short a duration to be important. The brief multi-kilobar spike seen near the LER wall in the CSQ calculation at about 4 msec was judged to be caused by material flowing through the Eulerian point and was not believed to represent a pressure pulse that would be seen by the headworks or wall. Figure 6-3 represents a best estimate waveform as far as the duration, slope and number of decay episodes is concerned. To account for uncertainties in these quantities (due to limitations in the CSQ model and code), the slope and duration of each decay episode was arbitrarily doubled.

6.2.3 Structural Component Failure

6.2.3.1 Top Cover

The 2.5 inch thick layer of unreinforced concrete on top of the test article (which provides radiation protection in the full-size LER) was not bonded to the rest of the structure. The question was how much break up would occur in the layer.

In the pretest analysis, the tensile stress within the layer during the first spall episode never exceeds the tensile capability of the concrete; as a result, motion only begins when the reflected tensile wave reaches the boundary between the top layer and the closure. At this time (0.035 msec into the decay episode), the total impulse in the layer (per square inch of surface) is about 0.5 lb-sec. With a mass (per square inch of surface) of $0.00056 \text{ lb-sec}^2/\text{in.}$, the peak relative velocity would be 950 ips (80 ft/sec). The acceleration of the closure at the time the first decay episode begins would be on the order of 12000 g's. Ignoring the 1 g deceleration of the spalled layer, it was estimated that the two layers would reach a maximum separation of 0.05 inches followed by the closure impacting the top layer 0.2 msec after spalling with a relative velocity of 80 ft/sec. Analyses indicate the impact velocity will always equal the initial spall velocity. After recontact, the compressive stress wave once again propagates through the layer, reflects and subsequently spalls the layer again. Since the magnitude of the compressive wave is essentially constant during the decay period, subsequent impacts would be just as severe. Dividing the cycle time by the duration of the decay period, as many as four impacts could take place during the first decay episode alone.

The effect of each impact is difficult to assess. In the time available, no references could be located describing drop tests on concrete slabs. Therefore, a series of 80 ft/sec impacts was hypothesized to shatter the top layer into many small cubes and/or powder the outer surface. Rotation of the closure and wind loads may cause peripheral portions of the layer to slide off, leading to some larger debris particles. Break up of the layer may also halt the spalling process.

Two other factors were considered significant as far as the particle size distribution prediction was concerned. First, test results, reported in Reference 6-1, suggest that the layer would break up as it spalled with aspect ratios possibly as high as 15 to 1. Second, the dynamic tensile strength for 7000 psi concrete, though highly uncertain, lies somewhere between 700 psi (Reference 6-2) and 2000 psi (Reference 6-3). Assuming a midpoint value of 1350 psi, the 2100 psi tensile stress anticipated during decay episode 3 would split the layer roughly in two.

Table 6-3 is the pretest estimate of the debris size distribution resulting from spalling of the top layer. Based on the observations in the previous paragraph, it assumed there will be no particles with an aspect ratio greater than 10 to 1 (10 inch by 10 inch by 2 inch). It also assumed that the slope of the cumulative probability distribution of fragment weight would be the same as that reported for test data in Reference 6-2. Note that a volume of 0.13 in.³ corresponds to the critical Q-D hazard size (a cube with 0.5 inch sides).

6.2.3.2 Rebar Cover

A comparison of the expected tensile stress (200 to 600 psi) versus the tensile strength indicated above, suggested that spalling of the rebar cover was unlikely. Scabbing and the impact of the top layer on the closure, however, might flake the rebar cover off portions of the outer surface. There were reports in the literature that scabbing occurs at bending strains as small as 0.4% (which would surely be exceeded in most regions of the test article).

6.2.3.3 Stirrups

Finally, the possibility that spalling will induce a tensile failure in the shear steel (stirrups) was investigated. For this to occur, the tensile stress must first exceed the combined tensile capability of the steel and the concrete, fracturing the concrete and

yielding the steel. Then, there must be sufficient velocity imparted to the spalled mass to exceed the ductility of the steel and break the rebars.

With an assumed dynamic tensile strength of 80,000 psi (based on the 55,000 psi yield strength reported by WES and an assumed dynamic strength enhancement factor of 1.5), the tensile strength in various parts of the test article averaged over the cross section are summarized as follows:

	Closure	Headworks		LER Wall
		Top	Bottom	
Stirrup size	3/16" wire	#2 bars	#4 bars	#2 bars
Stirrup spacing	1.5" each way	2.5" each way	2.5" each way	3" each way
Avg tensile strength	1000 psi	600 psi	1200 psi	700 psi

A combined concrete and steel tensile strength of 2000 psi was assumed as a lower bound. The failure strain of the stirrups were taken to be 15%, at which time only the steel will contribute to the resistance.

Consider the prediction for the third decay episode, the one thought most likely to cause rupture of the steel. With a peak tensile stress of 8400 psi possible at the back face, the concrete and steel would yield at a depth of 2.4 inches. Assuming that the gage length for the steel is 7.6 inches (the remainder of the section), at 15% strain, 1.14 inches of deformation would be necessary to break the stirrups. The maximum deformation of a mass supported on an elastoplastic spring is given by the equation (Reference 6-4),

$$X_m = \frac{Q}{2k} \left[\left(\frac{k x_0}{Q \omega} \right)^2 + 1 \right]$$

where Q is the yield stress of the spring, k is its initial modulus, $\omega = \sqrt{k/m}$ and m is the spalled mass. x_0 , the initial velocity of the spalled mass, is found by equating the momentum of the mass and the impulse of the compressive wave trapped in the layer:

$$x_0 = \int_0^{0.14 \text{ msec}} \frac{F(t)}{m} dt$$

Calculations indicated that a maximum deformation of 0.24 inches could be expected, much less than the 1.14 inches corresponding to 15% strain.

One might have reasonably assumed a smaller gage length for the strains in the rebar. With a gage length of one-half the previous value, 0.57 inches of deformation over a length of 3.8 inches of rebar would result in 15% strain. The maximum expected deformation, given this assumption, is 0.14 inches, roughly the same percentage of the failure deformation as before. Thus, the conclusion that spalling would not break the rebars appeared to be insensitive to the assumption of the gage length.

Note also that it takes a finite amount of time for the spring to reach its maximum deformation. The equation (Reference 6-4)

$$t_m = \frac{1}{\omega} \left[\sin^{-1} \left(\frac{Q \omega}{k \dot{x}_0} \right) + \sqrt{\left(\frac{k \dot{x}_0}{Q \omega} \right)^2 - 1} \right]$$

which is the closed form solution for this time, indicates it would take at least 1 msec to reach the maximum displacements calculated above. During this time, the closure accelerates and quickly places the stirrups back in compression. This is another reason why rupture of the rebar due to spall induced tension was thought to be unlikely. It also makes the fact that there are multiple episodes less significant.

The only major uncertainty in the closure response was that the impact of the lower portion of the section into the upper portion might jar loose some of the concrete; especially if it happened repeatedly. Steel stirrups, however, are likely to mitigate the severity of the impact because as the two layers near recontact, the compression in the stirrups will gradually accelerate the upper section.

The last remaining issue was whether tensile stirrup failures were possible in the headworks or wall. Since these components were predicted to experience roughly the same environments and have the same or greater tensile capacity, they were not predicted to fail. Spalling was not even expected to break the top portion of the headworks (Figure 6-4). Note, however, that the deformation is very sensitive to the velocity. Increasing the velocity by a factor of only 1.4 resulted in tensile failure of the bar. On the other hand, the upward acceleration of the headworks, which reduces the strain, was neglected. Note also that the gap which opens between the two sections of the headworks would allow kilobar pressures to enter, possibly splitting the two components completely.

6.2.3.4 LER Footing and Launch Tube Wall

Spalling of the LER footing and launch tube wall was not investigated because the pressures in these regions of the structure were predicted to be so high (on the order of 10 Kbar) that deformations of the reinforcing cage would probably reduce the wall to fragments no larger than the spacing between the reinforcing. In addition, microcracking might literally pulverize the concrete. In any case, the material in the LT was confined by the soil around it and, therefore, was expected to behave like ejecta.

6.3 Fragment Launch Characteristics

In the following pretest evaluation, only the portion of the test article above the LER footing was addressed because the extremely high pressures adjacent to the explosive charge were expected to pulverize the concrete in the launch tube.

6.3.1 Analytical Approach

To aid the identification of fragments, the test article was divided into the regions shown in Figure 6-5 and 6-6. The top layer (level A) is a concrete slab added to the closure and most of the headworks to provide additional radiation protection in the actual silo. Although this layer contains a small amount of temperature steel, it was treated as unreinforced in this analysis as the steel was not shown on the drawings. Areas B0 and B1 comprise the closure, a steel pan filled with heavily reinforced concrete that has a frame made from steel angles and channels embedded in it. The closure opens by sliding on three steel tracks that project towards the south on a separate reinforced concrete foundation. The rest of the structure is reinforced concrete with a steel liner on the inner surface. There are construction (cold) joints between each change in color in the test article concrete.

This effort utilized the results from a variety of single-degree-of-freedom (SDOF), multi-degree of freedom (MDOF) and finite element (FE) models as the basis for velocity and launch angle predictions. Fragment size estimates relied primarily on the use of engineering judgment in the interpretation of the analytical results. The small amount of data that exists for problems of this type was also utilized.

SDOF models were used to analyze the following failure modes: shearing of the closure, flexure of the closure, shearing of the headworks overhang around the closure, liftoff of the level B headworks (due to pressurization of the construction joint) and, finally, radial expansion and fragmentation of headwork levels B and C. The model shown

in Figure 6-7 was coded into a general purpose integration routine (YOUINT) for these investigations.

NONSAFE, a two dimensional, large deformation, beam finite element code, developed by TRW to evaluate the response and fragility of reinforced concrete structures, was also used. The code accounts for the dynamic, structure-media-interaction (SMI) and nonlinear material modeling aspects encountered in this type of problem. It was modified to allow simultaneous SMI and airblast loads on elements. Specific details of the NONSAFE models are given later.

The loading functions used in this investigation were of two types: pressure histories derived from the CSQ calculations and velocity histories derived from intermediate structural response calculations. The pressure time histories used to load the surfaces of the structure are shown in Figure 6-8. The figure also gives the closure motions used as input in some of the SDOF calculations.

6.3.2 Closure Shear

Figure 6-9 shows the internal structure of the closure. Of particular interest is the frame, made of steel angles with channels embedded in it. Shearing, along the outer edge of the southernmost channel, was expected to occur because venting along the periphery of area B1 would reduce the pressure on the portion of the closure which overhangs the headworks compared to that of the rest of the closure. The critical inputs to the SDOF model for this case (see Figure 6-10) were the motion of the main body of the closure, the load on the overhang, the mass of the overhang and the shear force/deformation characteristics.

Provided the assumption that the load in region B1 is half that in region B0 is correct, uncertainties in the dynamic shear resistance dominate the response. The details of the resistance curve used in this effort were taken from References 6-5 through 6-7, several recent surveys of the literature. Hawkin's direct shear criteria was used to define the overall shape of the resistance curve. It would predict fracture of the rebars at very small displacements (on the order of 0.1 inches), however. Since diagonal tension probably controls, two to five inches of relative displacement was assumed at failure. This is consistent with the amount of deformation reported in the literature. Note, also, that the peak resistance used in these calculations (about $17\sqrt{f'_c}$) is near the upper bound of the

data. The dynamic strength enhancement factor 1.5, suggested in Reference 6-6, was used. It could be much higher.

It should be mentioned that a preliminary calculation showed an inconsistency in the pressure and velocity histories for the closure. When the full pressure was applied to a SDOF model of region B1, the velocity of the region was not the same as that in Figure 6-8, the input for region B0. To insure that this condition was satisfied in all calculations, a multiplier (0.88) was applied to the pressure pulse before dividing it by half to reflect venting.

The sensitivity of the SDOF results to assumptions about the parameters defining the shear resistance curve was investigated over a range of input parameters corresponding to K factors of about 1.5. In almost all cases, the closure split between 1 and 3 msec after arrival of the airblast. Therefore, a shear time of 2 msec was recommended as a reasonable mean for the analysis. Checks were also made for the portion of the closure which overhangs to the east and west. Neither of these was found to shear.

6.3.3 Closure Flexure

The possibility of flexure breaking off region B1 of the closure was also checked using a SDOF model. The results indicated that if the pressure waveform beneath the overhang is half the magnitude of that loading the rest of the closure, this should not occur. In any case, flexure is a lower frequency response mode than shear so that the failure in shear predicted earlier should preclude a failure in flexure.

6.3.4 Headworks Shear

Based on the results from another SDOF model, it was considered unlikely that movement of the closure or venting along the periphery of the closure would shear off the portion of the headworks which overhangs the closure on the east and west sides. Movement of the headworks (assumed, based on CSQ results, to be 2/3 that of the closure) was a primary reason for there being no shear failure.

6.3.5 Level B Headworks Fragmentation

Figure 6-11 lists the assumptions made in modeling the postulated break up of the level B headworks. The major assumption is that the spalling phenomena discussed in Reference 1, although insufficient to break the vertical steel rebars connecting levels B and C, would be enough to allow the pressure pulse to enter the construction joint. If this

occurs, then the SDOF analysis (Figure 6-12A) showed that the rebars will quickly break in tension with the level B headworks reaching a peak vertical velocity over 670 ft/sec.

To determine how the layer behaves in the radial direction, both SDOF and FE models were utilized. First, level B was postulated to fail in hoop tension at discontinuities in the direction in which the internal pressure is applied. The SDOF result described in Figure 6-12B supported this assumption. Next, to estimate the horizontal component of the motion in each of the load directions, this SDOF model was employed (with appropriate masses and loaded areas). In each case, the resistance provided by the soil was assumed to prevent any horizontal motion for 1 msec after arrival of the blast.

Later, two NONSAFE calculations were made using the mesh of the level B headworks shown in Figure 6-13. No SMI loads were applied. Instead, one calculation was performed with a t_{initial} equal to zero (QD3Z) while the other used a t_{initial} of 4 msec (QD3Y). Since the CSQ calculation indicated the relative displacement between the soil and the structure should be about half of the thickness of Level B at a time of 4 msec, the QD3Y case was judged to be a reasonable approximation of the effect of soil confinement on the radial response.

Figure 6-13 shows the results of the NONSAFE calculations. Note that if the soil provided no constraint, horizontal velocities were much higher, with correspondingly shallower launch angles. The strains in the QD3Z case exceeded 20% in most elements, indicating broken steel. Even though the QD3Y case showed considerably less deformation at 10 msec, the strains calculated by the code (see figure) still substantiated the conclusion that flexure and radial expansion would fail the structure in many places. Although shear failure criteria were not part of the NONSAFE code, it was considered likely that shearing due to the non-uniform mass would also lead to some break up. Overall, it appeared likely that the number of large fragments would roughly correspond to the number of load directions. Smaller debris (roughly the size of the rebar spacing) would be produced as these large pieces separated. This debris would tend to scatter at azimuths between the large pieces. The liner would remain attached to the inner surface of the large pieces. Scabbing on the outer surface and break up of a 2-inch layer of concrete at the bottom (separating level B and C) was also postulated.

6.3.6 Level C Headworks Fragmentation

Break up of the level C headworks was quantified using the NONSAFE code to model the entire LER (below level B) and, again, by applying considerable judgment. Figure 6-14 shows the NONSAFE model. The soil was modeled with an SMI transfer function relating the interface stresses to the relative velocity of the structure and the free-field. The axisymmetric aspect of the problem was approximated through the use of force/displacement springs whose characteristics were derived using the formulas in the figure.

Figure 6-15 shows the results in terms of displacements, velocities and steel strains at 10 msec (the end of the pressure load). It definitely appeared that the headworks would separate from the wall and experience sufficient radial motion to fail in hoop (assuming, conservatively, 20% strain in the circumferential bars at failure). Also, note that the indicated NONSAFE model did not take into account the fact that the headworks loses some of its soil confinement during the loaded phase. This would tend to decrease the launch angle. In fact, earlier NONSAFE runs, made with and without soil confinement, showed a decrease of 5 degrees due to relative structure/soil motion. Therefore, for the prediction, the average launch angle of level C in Figure 6-15 (83 degrees) was reduced to 78 degrees.

Unfortunately, the NONSAFE analysis gave few clues as to the size of the fragments that would be produced. To obtain this distribution, an assumption about the maximum particle size was made; namely, that the larger fragments would have an aspect ratio of roughly 1 or 2 to 1. Figure 6-16 shows actual weight distributions of debris reported in Reference 6-2 for tests simulating internal explosions in various types of above ground ammunition storage facilities. All the distributions have the same slope. Therefore, this slope was used to define the fragments produced in the zones between the large pieces in the QDT-3 test, noting that their size should be a function of the rebar spacing. The velocity and launch angles assigned to each of the fragments in this layer came from the NONSAFE calculation at 10 msec. Note that given the assumptions behind the large fragment description, the azimuths for this layer could be off by as much as 25 degrees.

6.3.7 LER Wall and Footing Fragmentation

The results of both the NONSAFE and CSQ calculations indicated that the LER walls and footings would separate from the headworks. The NONSAFE results suggested that the center portion of the LER wall would remain intact vertically. The horizontal displacements, calculated in Figure 6-15, corresponded to hoop failure. In calculations

for a cylinder, the hoop strain and hoop resistance are equal around the circumference. In the real world, however, some area is weakest and fails first. Once this happens, a pure hoop condition would no longer exist, but the presence of the soil should keep flexure from dominating radial response. Therefore, expansion would continue and progressively smaller and smaller arc segments would be created until differences in the direction of the load on adjacent segments were not enough to cause further hoop failure. SDOF results indicated this minimum arc length to be on the order of 20 to 45 degrees. Therefore 12 segments of 30 degrees each were predicted.

It was assumed that about 30% of the mass in element 3 (Figure 6-13) travels with the velocity vector of the level C headworks. In defining the particle sizes in this region, rebar spacing was used as the guide. A considerable portion of the volume (more than 30%) was assumed to reduce to dust. The rest of the element was assumed to follow the LER wall which is driven into the soil and, hence, has the velocity vector of the ejecta. Since this material is deep, it probably would not affect the Q-D criteria.

According to the NONSAFE calculation, the footing would separate from the LER wall. None of the analytical tools had sufficient fidelity to show the details of footing response. The pressures near the explosives were predicted to be so high, however, that large portions of the footing could conceivably be reduced to dust. In any case, debris from the footing would have no impact on the Q-D criteria.

6.4 Test Predictions

The debris prediction is summarized in Table 6-4 for all fragments greater than the critical Q-D particle size (1/2 inch diameter at 1/4 scale). Considering the many uncertainties inherent in these results, it was suggested that the fragments in any given zone/layer combination be distributed over velocities of plus or minus 25%, launch angles of plus or minus 10 degrees and azimuths of plus or minus 20 degrees about the values indicated.

As explained in Section 6.2, the fragments spalled from level A would have the same initial velocity vector as the underlying material in level B. SDOF analyses indicated that inertial effects would shear the closure into two large pieces. Both were expected to travel in a southerly direction; however, the smaller one would have a larger horizontal component because of the venting along the shear failure plane (there would be venting on all sides of the large piece, balancing its horizontal load).

The analysis in Section 6.2 suggested that spalling phenomena would allow pressurization of the construction joint between levels B and C. SDOF results indicated that if such pressurization occurred, the rebar connecting the two portions of the headworks would quickly break, allowing the level B headworks to reach a high vertical velocity. Furthermore, SDOF and finite element analyses indicated that once level B becomes a free body, shear and flexure stresses caused by the radial pressure loads would break it into several pieces with large horizontal velocity components. In general, the liner was expected to remain attached to the large concrete fragments.

Finite element (FE) calculations performed on the portion of the LER below level B showed that the level C headworks would fail in hoop. The distribution of fragment sizes predicted for this layer, however, was a matter of considerable conjecture. The FE calculations also suggested that the LER wall and footing would suffer a hoop failure with the possibility that some portions would be reduced to very small fragments. Most of the LER wall and footing would be driven into and travel with the soil ejecta and therefore would not be of concern to Q-D.

Analyses indicate that the PAS B plug would impact the A plug at a relative velocity exceeding 250 ft/sec. This would separate both from the headworks, probably shattering the concrete in plug A in the process. The pins in both plugs would shear but ductile deformations could prevent them from becoming independent projectiles.

The small tensile strength of the track anchors means that the tracks would not affect headwork motion although they might, possibly, be pulled loose from both the headworks and the foundation. The anchors themselves might become free as a result. Variations in surface ejecta motions and inertia differences in the track foundations would break the foundation into several large pieces. On the whole, however, it was expected to remain intact, traveling with the ejecta and, therefore, not a concern for Q-D.

Assuming ballistic trajectories for the fragment characteristics shown in Table 6-4 and taking into account the sensitivity of drag to fragment dimensions, a prediction of debris density for the 1/4 scale test was developed as plotted in Figure 6-17. It was estimated that a density of one fragment per 600 square feet would occur at a range of 721 feet.

Table 6-1. Input Parameter Values Used in Headworks 3DOF Analysis

Parameter	Value	Parameter	Value	Parameter	Value
R ₁ in.	18.0	t _{vi} in.	0.042	E _s psi	3 x 10 ⁷
R ₂ in.	37.5	t _{vo} in.	0.037	σ _y psi	50000
R ₃ in.	44.25	h ₁ in.	9.0	τ _u psi	37500
R ₄ in.	24.0	h ₂ in.	12.0	F _{pi} lb	38435
R _{vi} in.	38.25	h _u in.	6.75	F _{po} lb	38435
R _{vo} in.	43.5	h _L in.	6.75	x ₀ in.	0.5
t ₁ in.	10.5	t _{hu} in.	0.033	y ₀ in.	0.8
t ₂ in.	28.5	t _{hL} in.	0.161	y ₁ in.	9.0
t _L in.	0.09	ρ lb sec ² /in. ⁴	0.000225		

Table 6-2. Calculated Sequence of Headworks Failure

Time (msec)	Position of Headworks			Failure Event
	Radial Displacement x, in.	Vertical Displacement z, in.	Rotation ϕ , deg	
0.26	0.03	0.05	0.13	Initial yield in lower hoop rebars and headworks underside liner. Most of upper hoop rebars yielded prior to this time.
0.95	0.46	0.80	1.9	Vertical liner breaks in tension.
1.0	0.50	0.89	2.1	Vertical rebars break in shear. Headworks has now separated from LER wall.
2.0	2.03	3.58	8.3	First breakage of upper hoop rebars.
2.5	3.11	5.49	12.7	First breakage of lower hoop rebars.
2.8	3.71	6.56	15.2	All upper hoop rebars broken.
2.8	3.71	6.56	15.2	Headworks underside liner starts to tear.
4.0	7.28	12.87	29.7	All lower hoop rebars and underside liner fractured. Headworks is now completely shattered.

Table 6-3. Particle Size Distribution for Debris from Spalling of Top Layer

Debris Particle Volume, V (in. ³)	% of Total Volume	No. of Particles (Average Size)
V < 0.13	10	----
0.13 ≤ V < 0.5	15	7693
0.5 ≤ V < 1.0	15	3231
1.0 ≤ V < 5	30	1615
5 ≤ V < 10	13	236
10 ≤ V < 20	9	97
20 ≤ V < 50	6	28
50 ≤ V < 100	3	6
100 ≤ V ≤ 200	2	3
>200	1	0

Table 6-4. Structure Fragmentation Summary

Zone	Dimensions (in.)	Remarks	Number of Fragments	Velocity (fps)	Azimuth (deg)*	Elevation (deg)**	Total Volume (in. ³)
A0	½ x ½ x ½	See Section 6.2	5,840	540	345	86	730
	1 x ¾ x ¾		1,356				763
	1½ x 1½ x 1½		500				1,406
	2½ x 2½ x 1½		70				547
	3½ x 3½ x 1½		27				601
	3½ x 3½ x 2½		8				167
	5½ x 5½ x 2½		2				151
	7½ x 7½ x 2½		2				281
						4,646	
B0	54 x 36 x 10	Between B0/B1	1	540	345	87	20,520
	2 x 2 x 2		135				
A1	½ x ½ x ½	See Section 6.2	1,845	613	345	61	231
	1 x ¾ x ¾		429				241
	1½ x 1½ x 1½		167				470
	2½ x 2½ x 1½		23				180
	3½ x 3½ x 1½ or 2½		12				251
	5½ x 5½ x 2½		1				76
	7½ x 7½ x 2½		1				141
B1	(54+10)/2 x 18 x 10	Between B0/B1	1	613	345	61	6,400
	2 x 2 x 2		80				
A2	½ x ½ x ½	See Section 6.2	1,766	710	252	71	220
	1 x ¾ x ¾		409				230
	1½ x 1½ x 1½		145				408
	2½ x 2½ x 1½		20				156
	3½ x 3½ x 1½ or 2½		10				209
	5½ x 5½ x 2½		1				76
B2	2 x 2 x 2	Bottom surface	150	710	252	71	1,200
	4 x 2½ x ¾	Outer surface	34				255
	4 x 2½ x 1½	Between zones	24				300
	4 x 2½ x 2½	Remaining	24				600
	28 x 18 x 8		1				4,032
						6,357	
A3	½ x ½ x ½	See Section 6.2	1,595	700	190	73	199
	1 x ¾ x ¾		370				207
	1½ x 1½ x 1½		145				406
	2½ x 2½ x 1½		20				156
	3½ x 3½ x 1½ or 2½		10				209
	5½ x 5½ x 2½		1				76
B3	2 x 2 x 2	Bottom surface	140	700	190	73	1,120
	4 x 2½ x ¾	Outer surface	25				188
	4 x 2½ x 1½	Between zones	34				425
	4 x 2½ x 2½	Remaining	34				850
	30 x 10 x 8		1				2,400
						4,983	
A4	½ x ½ x ½	See Section 6.2	1,517	684-700	165	77-78	190
	1 x ¾ x ¾		352				198
	1½ x 1½ x 1½		130				364
	2½ x 2½ x 1½		18				140
	3½ x 3½ x 1½ or 2½		9				188
	5½ x 5½ x 2½		1				76
			1,156				

*Counterclockwise from magnetic south
 **Measured from horizontal

Table 6-4. Structure Fragmentation Summary (Continued)

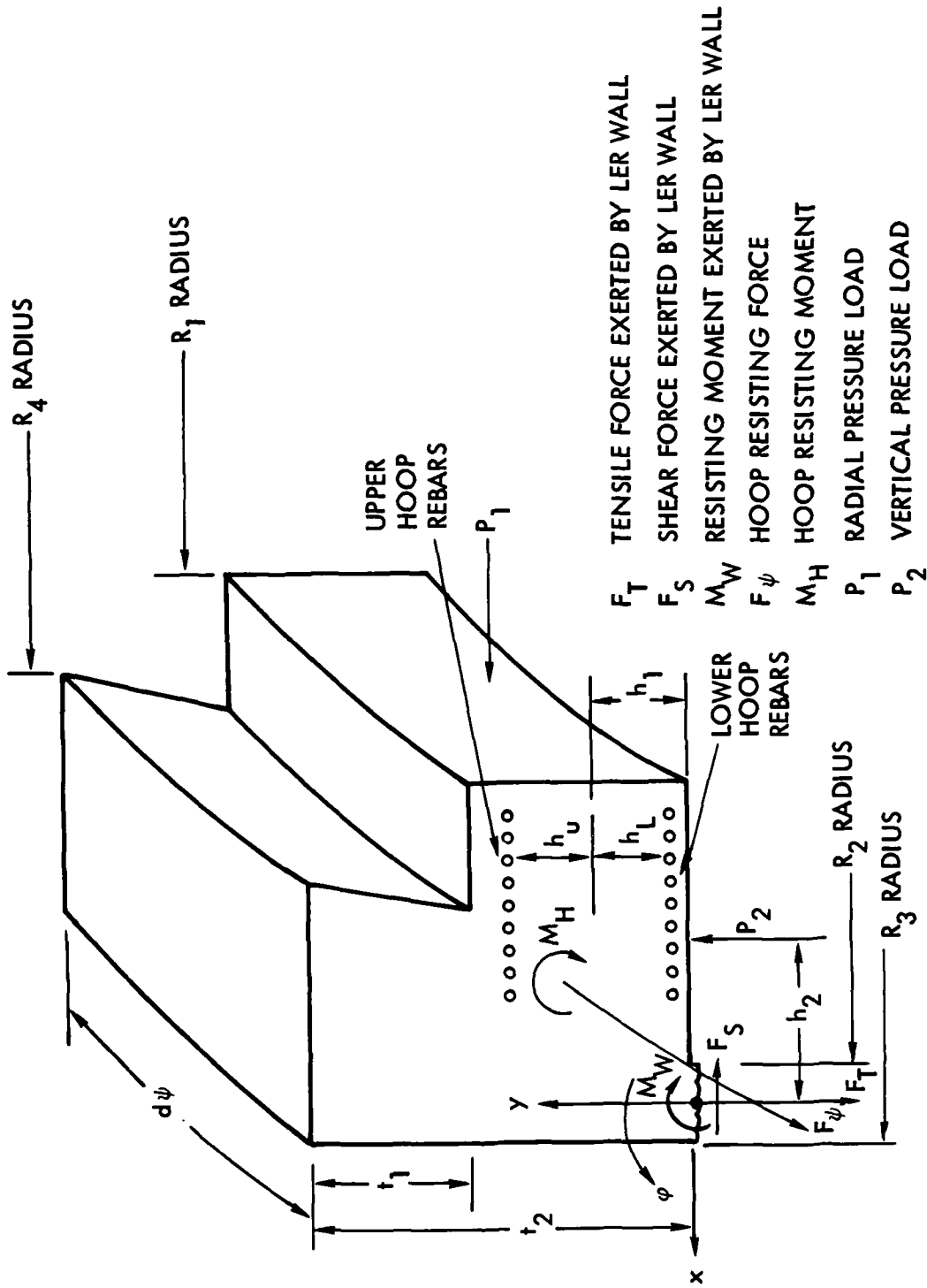
Zone	Dimensions (in.)	Remarks	Number of Fragments	Velocity (fps)	Azimuth (deg)*	Elevation (deg)**	Total Volume (in. ³)
B4	2 x 2 x 2	Bottom surface	140	684	165	78	1,120
	4 x 2½ x ¾	Outer surface	25				188
	4 x 2½ x 1½		34				425
	4 x 2½ x 2½	Between zones	34				850
	30 x 10 x 8	Remaining	1				2,400
						4,983	
A5	½ x ½ x ½	See Section 6.2	4,283	675	135	83	535
	1 x ¾ x ¾		994				559
	1½ x 1½ x 1½		371				1,043
	2½ x 2½ x 1½		52				406
	3½ x 3½ x 1½ or 2½		26				543
	5½ x 5½ x 2½		1				76
			3,162				
B5	2 x 2 x 2	Bottom surface	372	675	135	83	2,976
	4 x 2½ x ¾	Outer surface	58				435
	4 x 2½ x 1½		43				538
	4 x 2½ x 2½	Between zones	43				1,075
	36 x 31 x 8	Remaining	1				8,928
						13,952	
A6	½ x ½ x ½	See Section 6.2	1,756	698-720	77	70-74	220
	1 x ¾ x ¾		409				230
	1½ x 1½ x 1½		145				408
	2½ x 2½ x 1½		20				156
	3½ x 3½ x 1½ or 2½		10				209
	5½ x 5½ x 2½		1				76
			1,299				
B6	2 x 2 x 2	Bottom surface	150	698-720	77	70-74	1,200
	4 x 2½ x ¾	Outer surface	34				225
	4 x 2½ x 1½		24				300
	4 x 2½ x 2½	Between zones	24				600
	28 x 18 x 8	Remaining	1				4,032
						6,357	
C017	½ x ½ x ½		1,182	400	315,20	78	148
	1 x 1 x 1		295				295
	2 x 2 x 2		73				584
	2½ x 2½ x 2½		47				735
	9 x 2½ x 2½		26				1,463
	20 x 18 x 15		2				10,800
			14,025				
C2	½ x ½ x ½		1,182	400	255	78	148
	1 x 1 x 1		295				295
	2 x 2 x 2		73				584
	2½ x 2½ x 2½		47				735
	9 x 2½ x 2½		26				1,463
	20 x 18 x 15		1				5,400
			8,625				
C3	½ x ½ x ½		1,182	400	205	78	148
	1 x 1 x 1		295				295
	2 x 2 x 2		73				584
	2½ x 2½ x 2½		47				735
	9 x 2½ x 2½		26				1,463
	25 x 24 x 18		1				10,800
			14,025				

*Counterclockwise from magnetic south
 **Measured from horizontal

Table 6-4. Structure Fragmentation Summary (Continued)

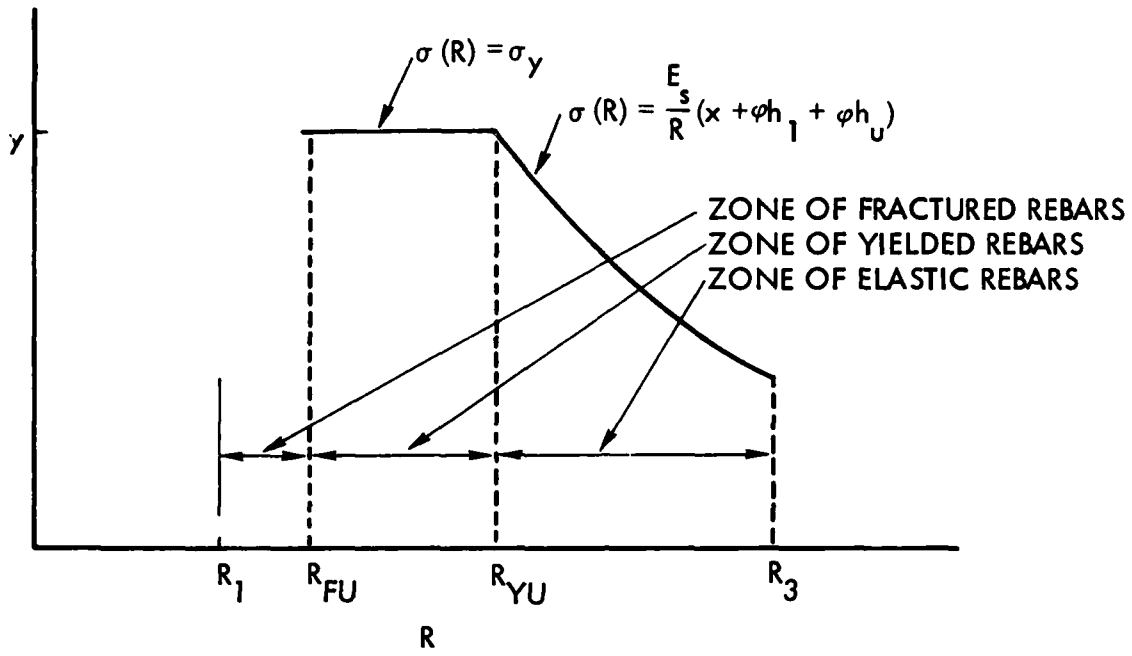
Zone	Dimensions (in.)	Remarks	Number of Fragments	Velocity (fps)	Azimuth (deg)*	Elevation (deg)**	Total Volume (in. ³)
C4	½ x ½ x ½		1,182	400	165	78	148
	1 x 1 x 1		295				295
	2 x 2 x 2		73				584
	2½ x 2½ x 2½		47				735
	9 x 2½ x 2½		26				1,463
	25 x 24 x 18		1				10,800
						14,025	
C5	½ x ½ x ½		1,182	400	130	78	148
	1 x 1 x 1		295				295
	2 x 2 x 2		73				584
	2½ x 2½ x 2½		47				735
	9 x 2½ x 2½		26				1,463
	40 x 30 x 18		1				21,600
						24,824	
C6	½ x ½ x ½		1,182	400	75	78	148
	1 x 1 x 1		295				295
	2 x 2 x 2		73				584
	2½ x 2½ x 2½		47				735
	9 x 2½ x 2½		26				1,463
	20 x 18 x 15		1				5,400
						8,625	
D	½ x ½ x ½	Travels with Level C	13,800	400	Uniform Around Circumference	78	1,725
	1 x 1 x 1		660				660
	2 x 2 x 2		60				480
						2,865	
E	½ x ½ x ½	Travels with Ejecta	12,000	Ejecta	Uniform Around Circumference	Ejecta	1,500
	1 x 1 x 1		816				816
	2 x 2 x 2		54				432
	21 x 21 x 7		12				37,044
						39,792	
F	Shattered			Ejecta	Uniform	Ejecta	
G	Mostly shattered			Ejecta	Uniform	Ejecta	
Plug A	10½ diam x 5 2½ x 2½ x 2½	Steel Concrete filler	1 16	500	130	78	250
Plug B	10½ diam x 10½	Steel	1	500	130	78	
Shear pins		None separate					
Actuator Housing	18 x 12 x 1½	Steel	1	400	345	78	
Tracks:							
Center	6 x 5½ x 3/8	Steel	1	300	345	50	
Side	7½ x 5½ x 3/8	Steel	2	350	315,30	62	
Track Foundation	Mostly large pieces			300	315 to 30	45	

*Counterclockwise from magnetic south
**Measured from horizontal



- F_T TENSILE FORCE EXERTED BY LER WALL
- F_S SHEAR FORCE EXERTED BY LER WALL
- M_W RESISTING MOMENT EXERTED BY LER WALL
- F_ψ HOOP RESISTING FORCE
- M_H HOOP RESISTING MOMENT
- P_1 RADIAL PRESSURE LOAD
- P_2 VERTICAL PRESSURE LOAD

Figure 6-1. Freebody Diagram of Headworks Element



NOTE: THE STRESS DISTRIBUTION IN THE UPPER REBARS IS SHOWN. THE STRESS DISTRIBUTION IN THE LOWER REBARS IS SIMILAR.

Figure 6-2. Hoop Stress Distribution in Headworks

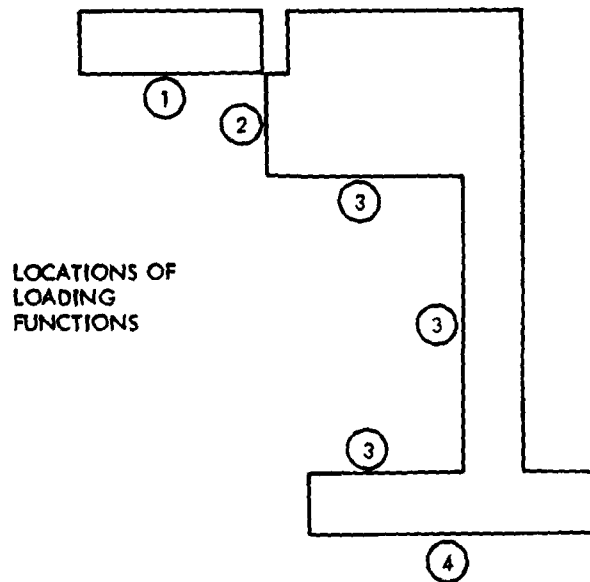
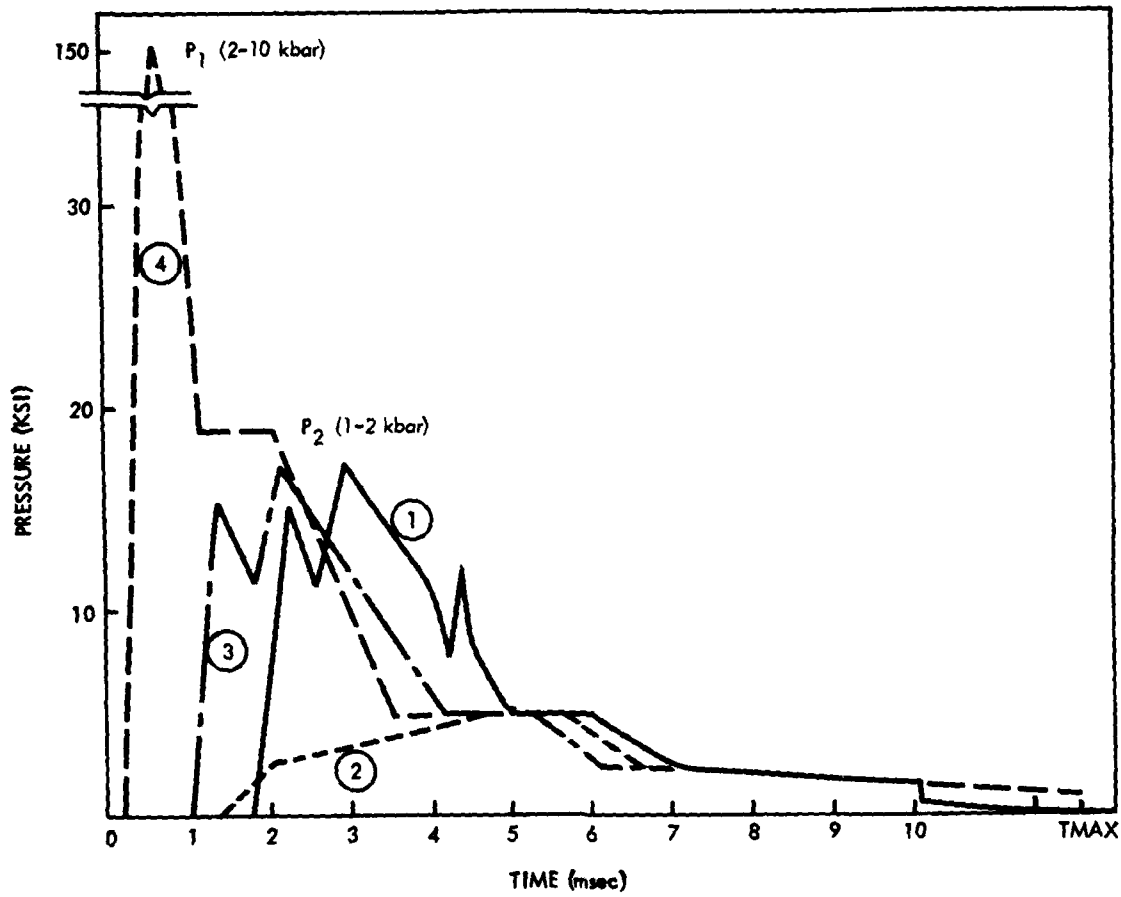
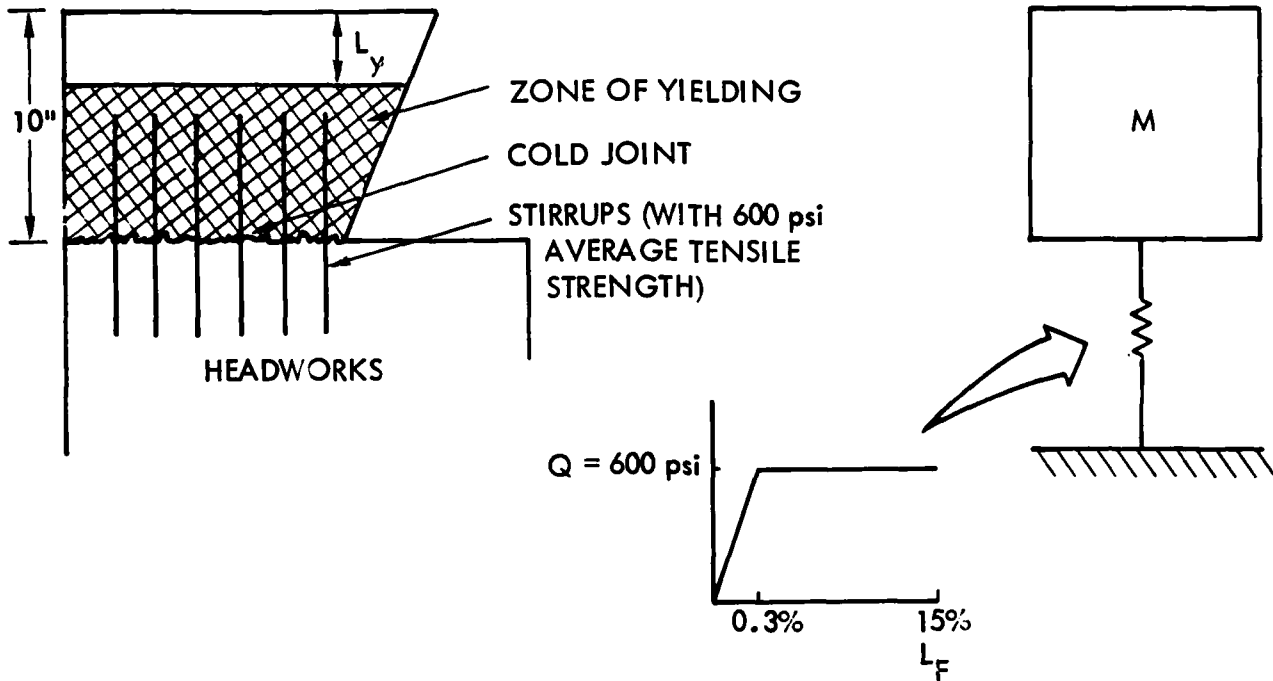


Figure 6-3. Recommended Blast Loadings for Spalling Analysis of 1/4-Scale Test



EXAMPLE: $L_G = 10'' - L_y = 7.6''$ $L_F = 1.1''$ (SAME AS WITH CLOSURE)

$$K = \frac{600}{0.003 (7.6)} = 26000 \text{ psi/in}$$

$$M = 2.2 \times 10^{-3} \frac{\text{lb sec}^2}{\text{in}}$$

$$\omega = \sqrt{K/M} = 3440$$

$$\dot{X}_0 = \int_0^{0.14 \text{ msec}} \frac{F(t)}{M} dt \approx \frac{10,000 (0.00014) (1)}{2.2 \times 10^{-3}} = 636 \text{ in/sec}$$

$$X_M = \frac{Q}{2K} \left[\left(\frac{K \dot{X}_0}{Q \omega} \right)^2 + 1 \right] = \frac{500}{2(26000)} \left[\left(\frac{26000 \times 636}{600 \times 3440} \right)^2 + 1 \right] = 0.75 \text{ in}$$

Figure 6-4. Spring-Mass Check of Top Headworks Stirrup Failure Due to Spalling Phenomenon

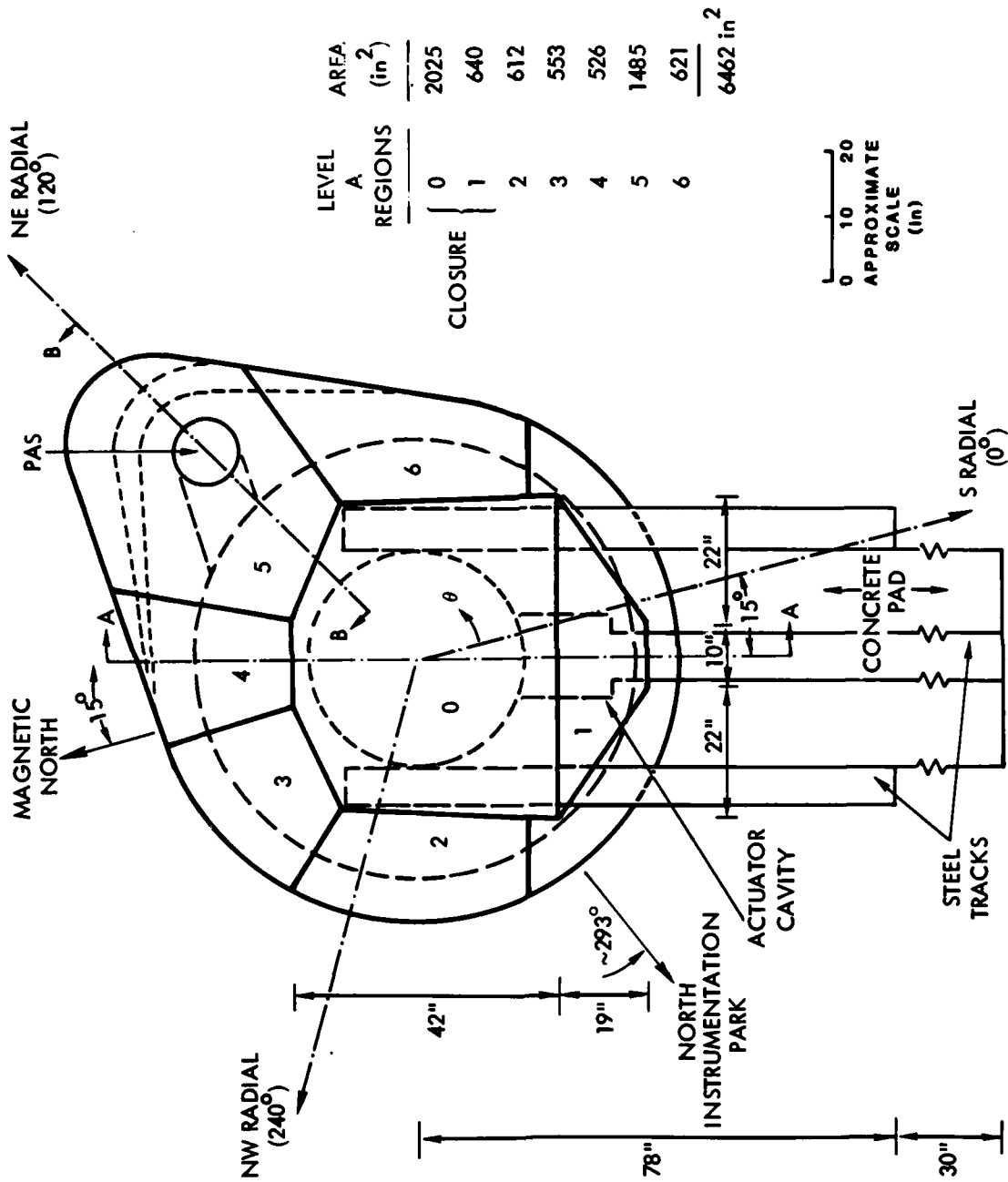


Figure 6-5. ODT-3 LER Plan View

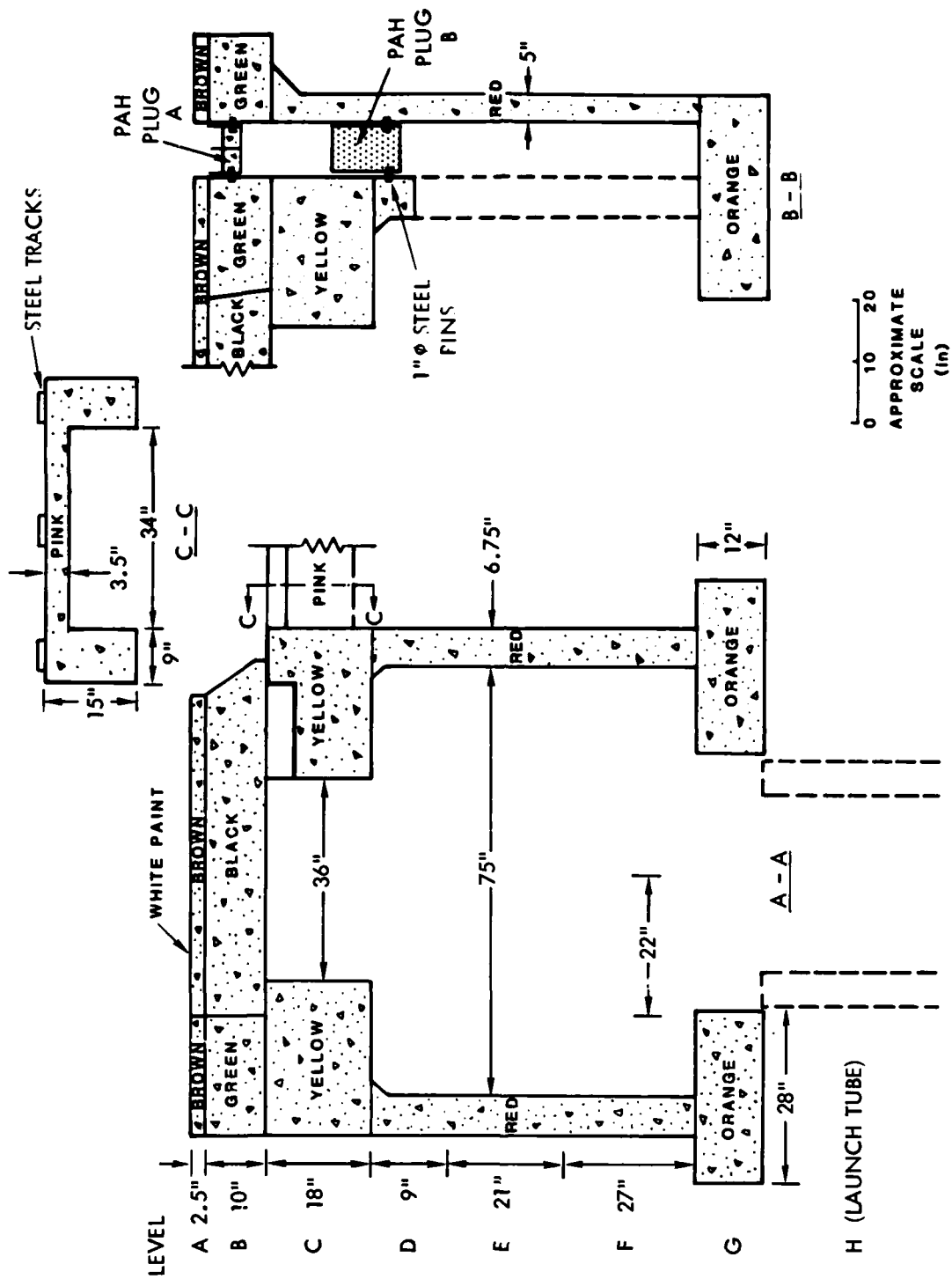


Figure 6-6. QDT-3 LER Cross-sections

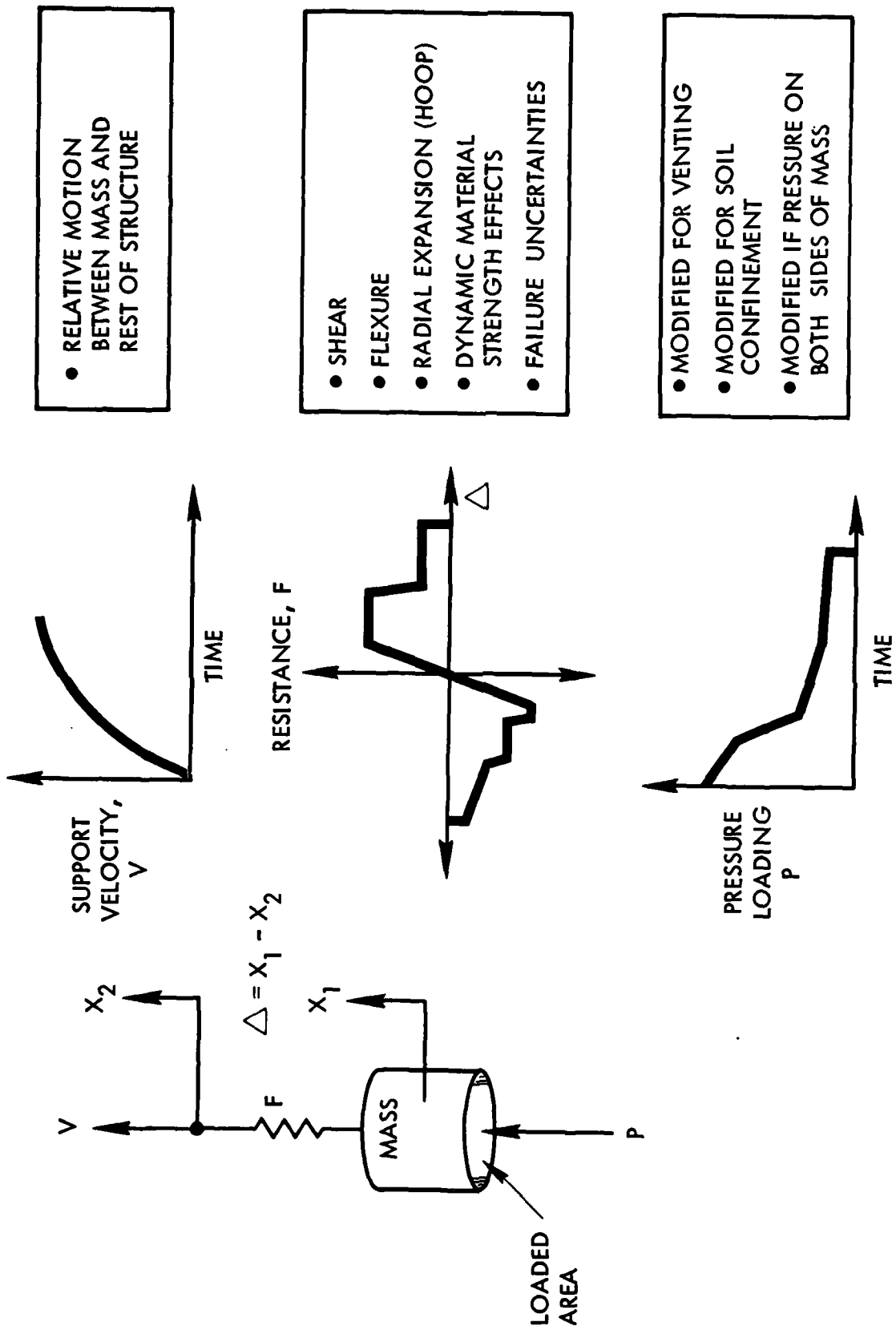
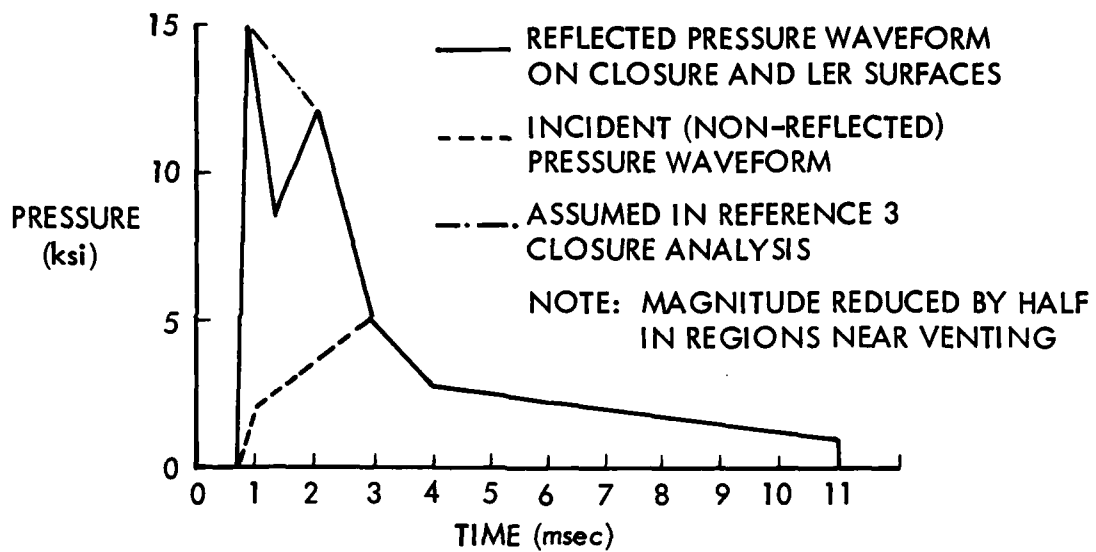
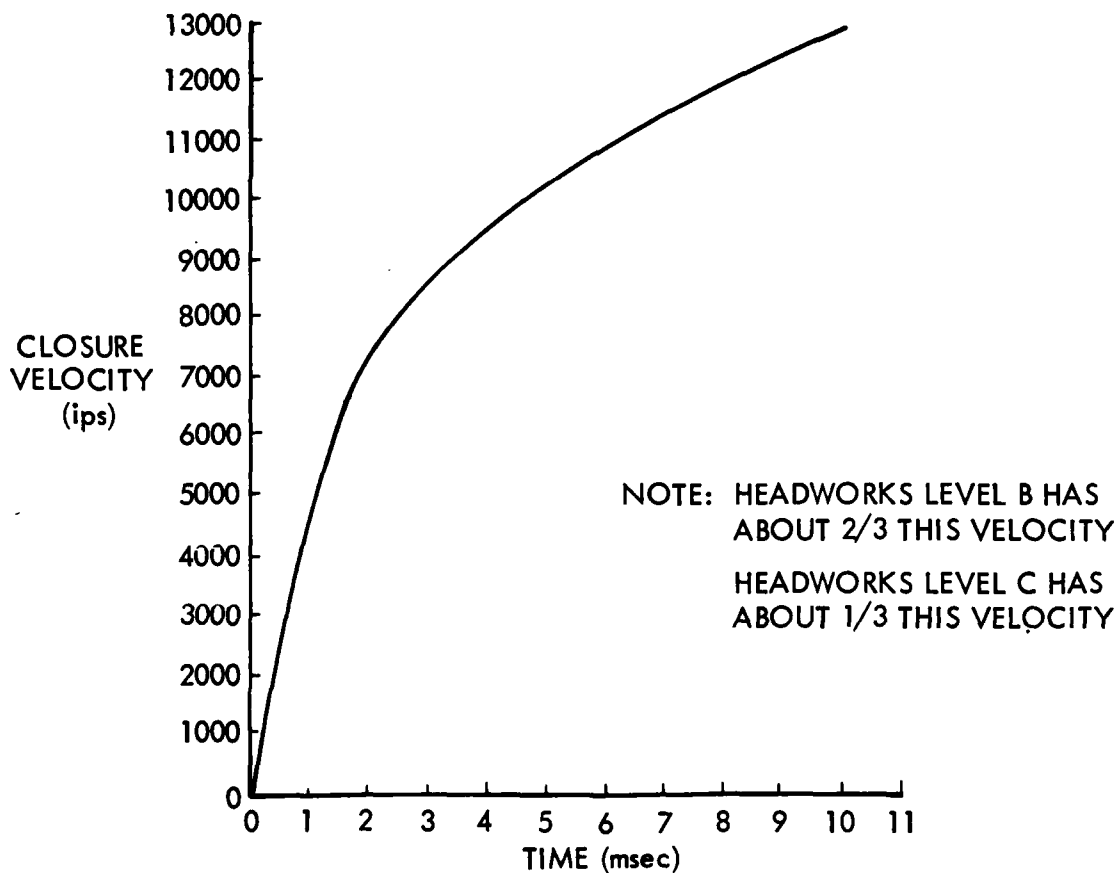


Figure 6-7. General SDOF Model for Fragmentation Analyses



(a) Pressure History for Structural Response Calculations



(b) Closure Velocity for INPUT to SDOF Models

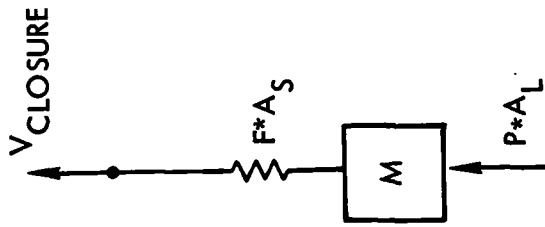
Figure 6-8. Loading Functions for QDT-3 Fragmentation Studies

- A_L , LOADED AREA = $(\frac{60'' + 24''}{2}) * 18'' = 756 \text{ in}^2$

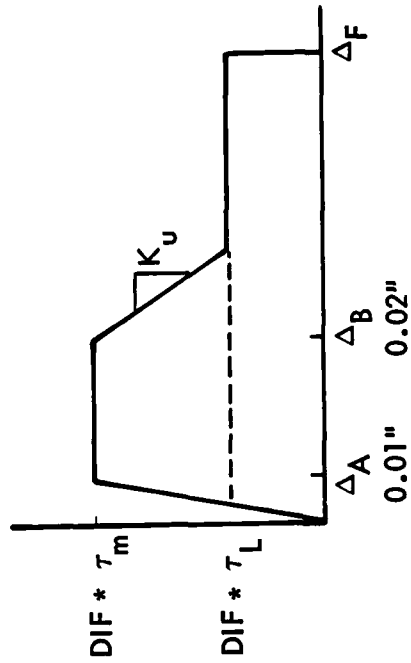
- A_S , SHEAR AREA = $60'' * 10'' = 600 \text{ in}^2$

- M , OVERHANGING MASS = $\frac{10'' * 756 * 150}{386.4(1728)} = 1.7 \frac{\text{lb sec}^2}{\text{in}}$

- P , V_{CLOSURE} FIGURE 4



- F , SHEAR RESISTANCE CURVE



- HAWKINS DIRECT SHEAR CRITERIA

$$\tau_m = 8 \sqrt{f'_c} + 0.8 \rho_f y = 1470 \text{ psi}$$

$$\tau_L = 0.85 (\rho_{\text{bottom rebar}}) f'_s = 510 \text{ psi}$$

$$K_u = 2000 + 0.75 f'_c = 7250 \text{ psi/in}$$

DIF (DYNAMIC INCREASE FACTOR) = 1.5

$$\Delta_F = 1''$$

- DIAGONAL TENSION

$$\Delta_F = 2 - 5''$$

Figure 6-10. SDOF Modeling of Closure Shear

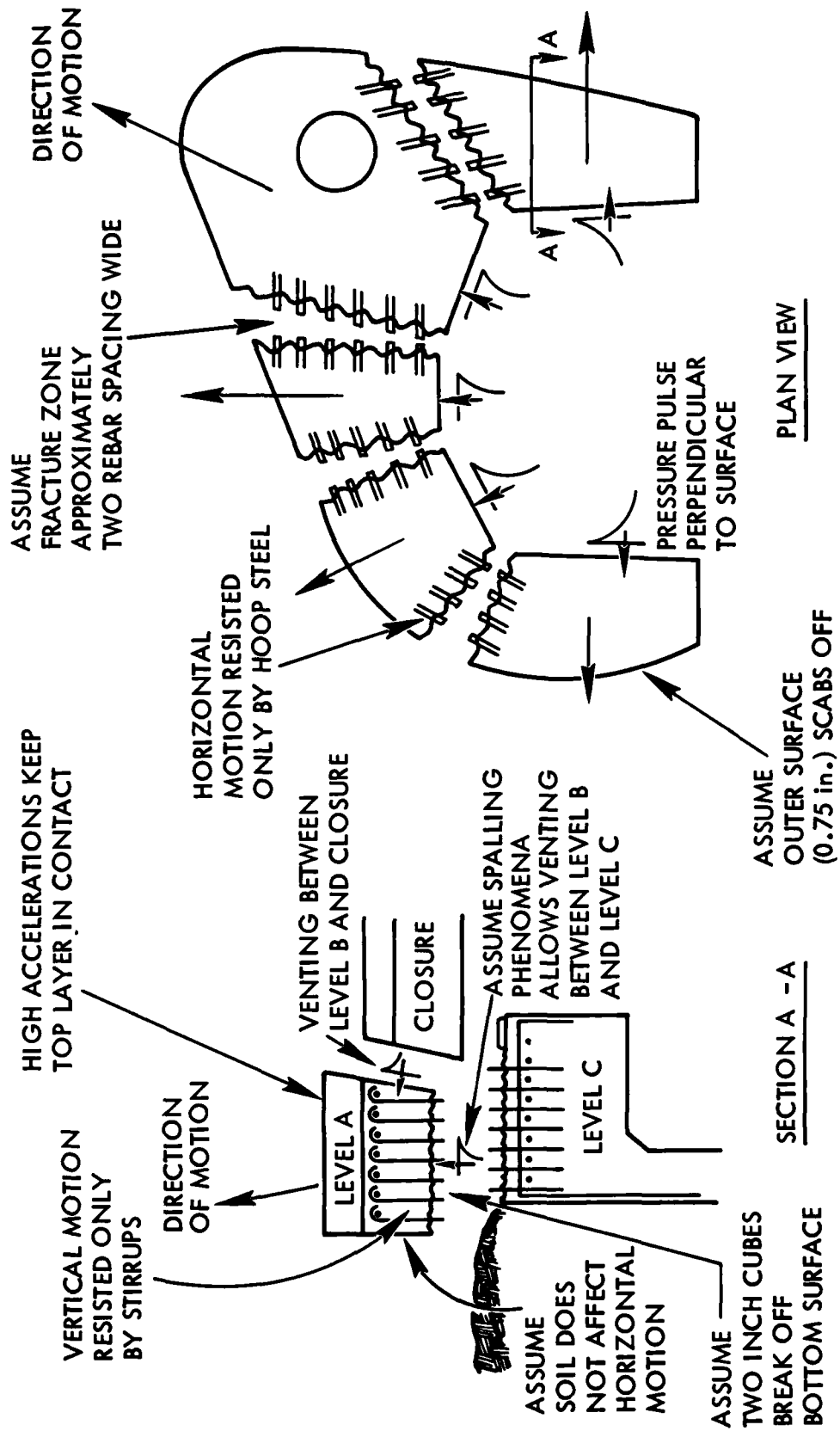
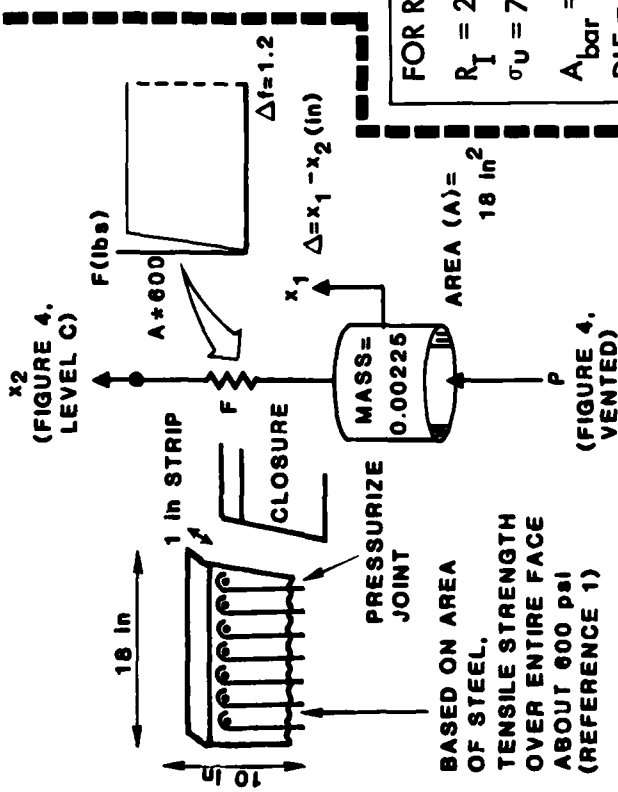
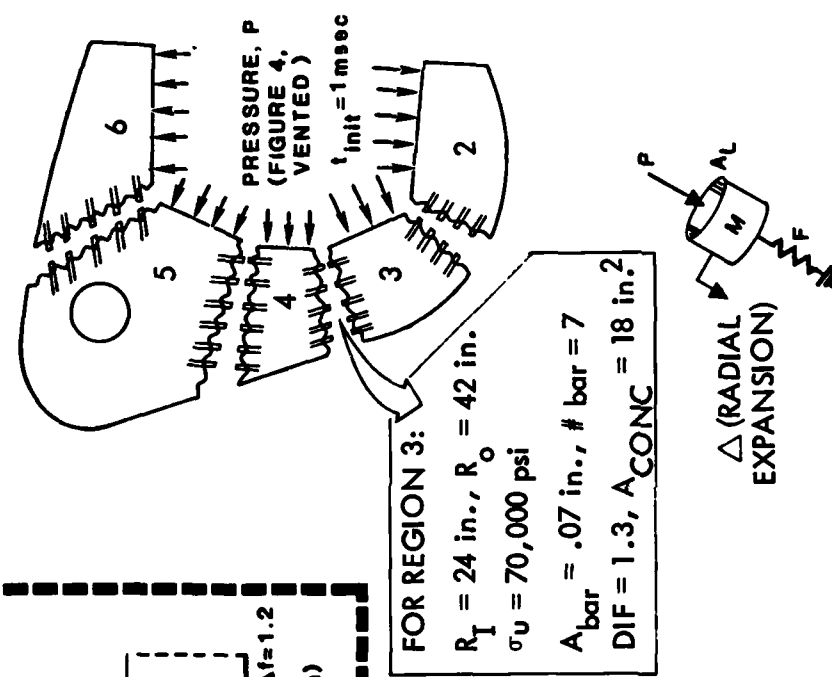


Figure 6-11. Failure Mode of Level B Headworks

A) VERTICAL CASE



B) HORIZONTAL CASE



HOOP STEEL RESISTS EXPANSION

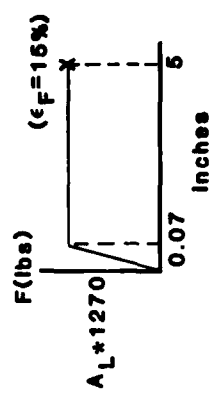
AVERAGE STRESS CAPABILITY:

$$\sigma_T = \frac{DIF * \# \text{ bars} * A_{\text{bar}} * \sigma_u}{A_{\text{CONC}}} = 2500 \text{ psi (REGION 3)}$$

PRESSURE VS HOOP STRESS

$$P = \sigma_T \frac{R_o^2 - R_i^2}{R_o^2 + R_i^2}$$

$$P = 2500 \frac{42^2 - 24^2}{42^2 + 24^2} = 1270 \text{ psi}$$



REGION	LOADED AREA (in ²)	MASS (lb.sec ² /in.)	MAX HORIZONTAL VELOCITY (fps)
2, 6	360	1.5	250
3	240	1.1	225
4	120	.8	155
5	210	3.4	65

Figure 6-12. Results of SDOF Analyses of Level B Headworks

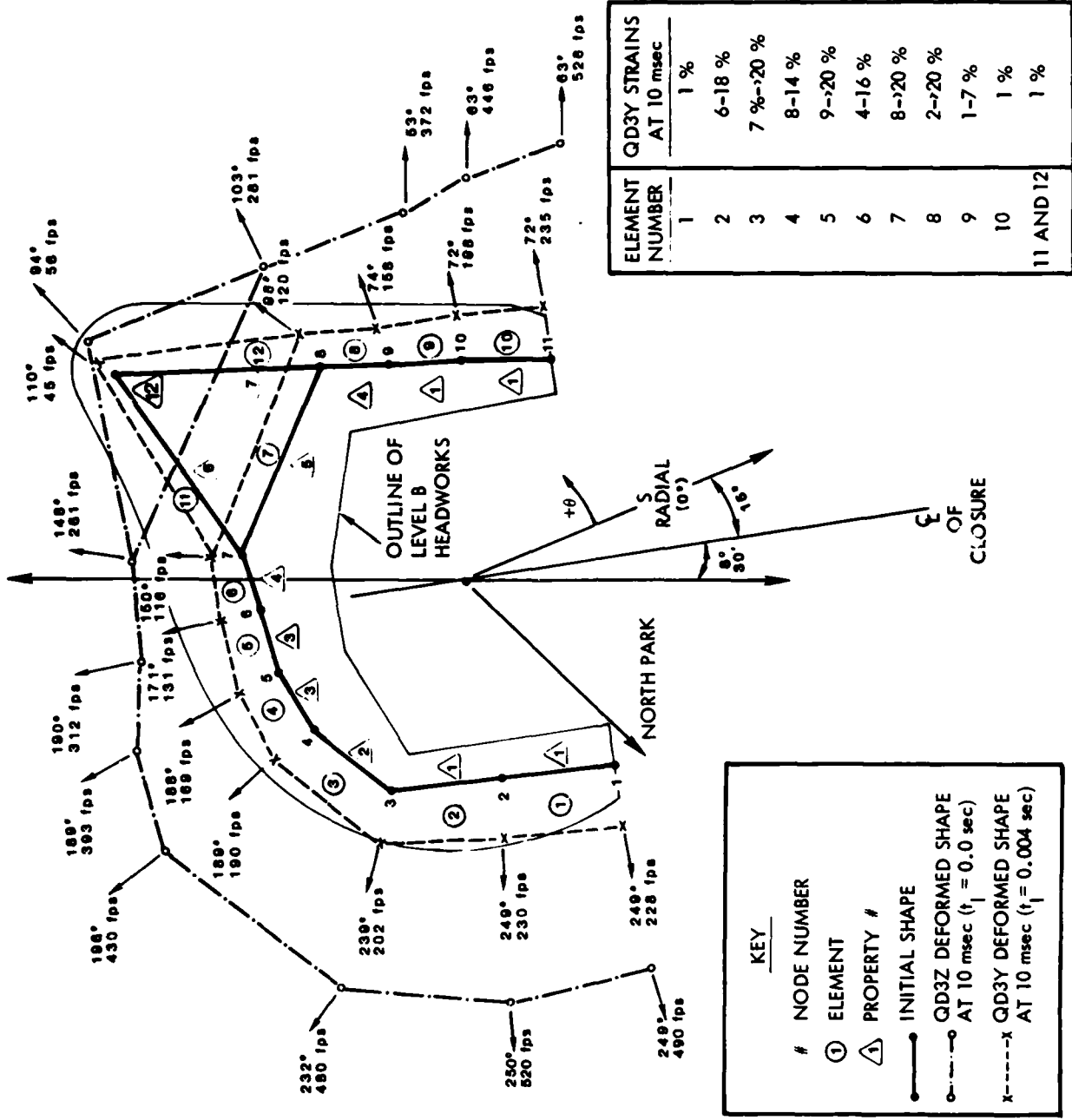
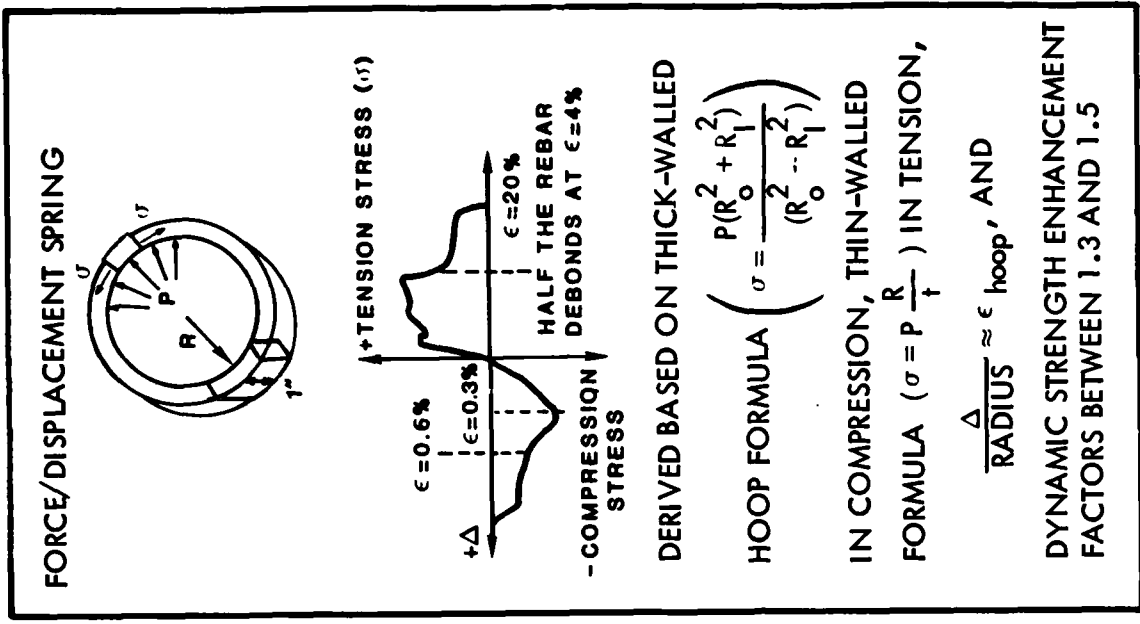
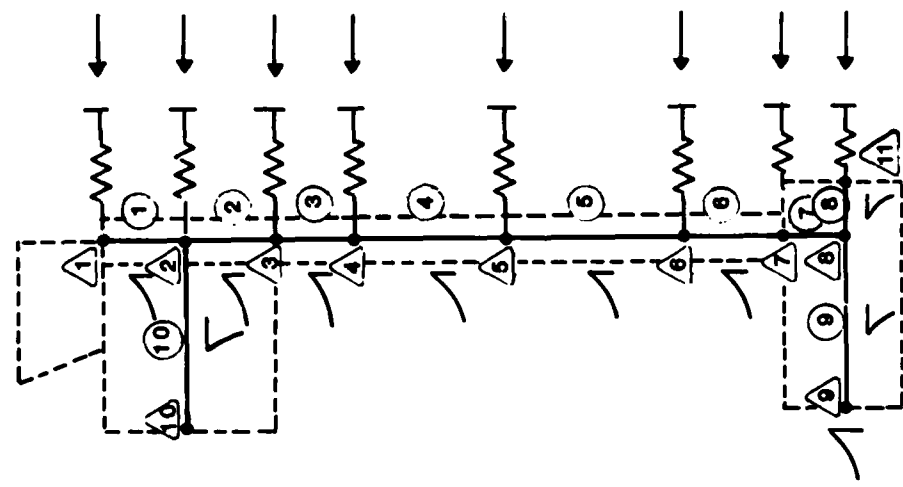


Figure 6-13. Nonsafe Model and Results for Level B Headworks in the Horizontal Plane



ASSUME LEVEL B REMOVED BY PRESSURIZATION OF CONSTRUCTION JOINT



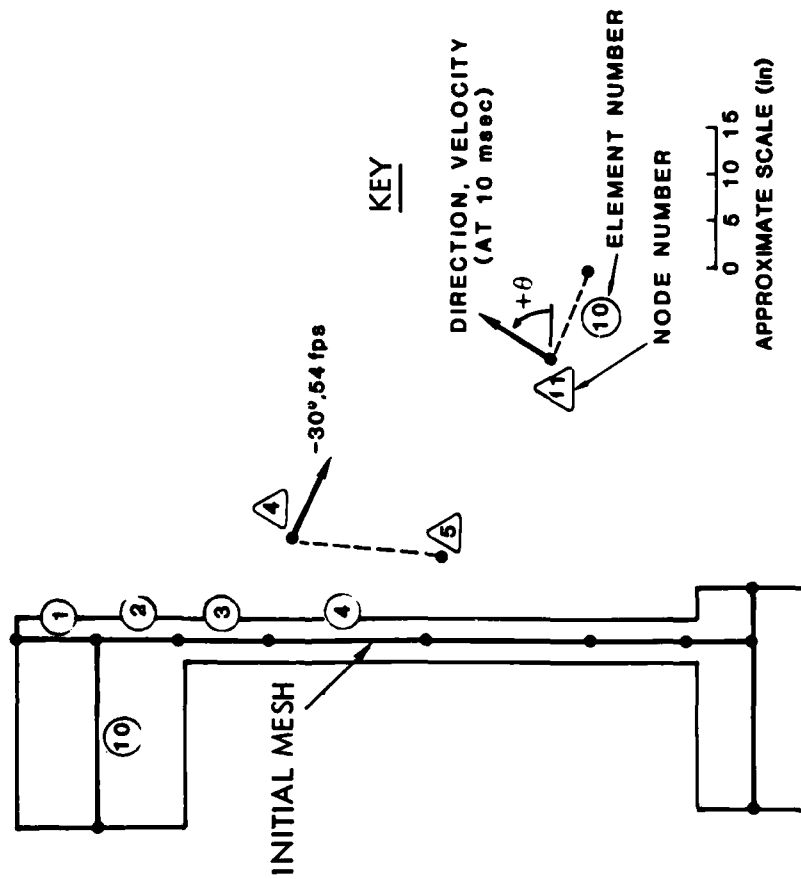
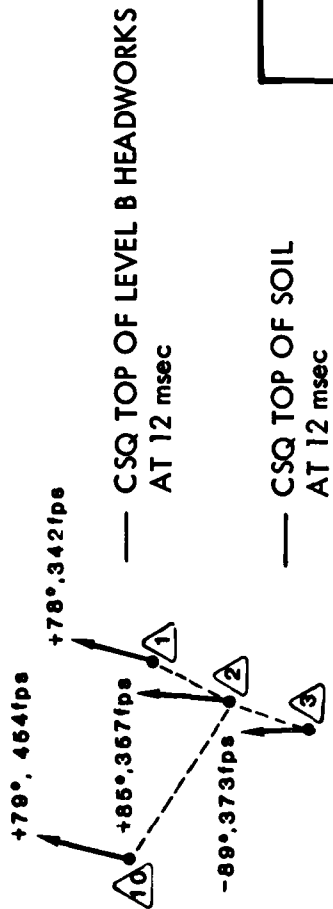
KEY

- INITIAL ELEMENT GEOMETRY
- - - OUTLINE OF TEST ARTICLE
- ↙ PRESCRIBED STRESS OR NODAL LOAD APPLIED HERE (REPRESENTS BLAST)
- ← PCV SMI TRANSFER FUNCTION AT THIS NODE
- DISTRIBUTED FORCE/DISPLACEMENT SPRING AT THIS NODE
- △ NODE NUMBER
- ① ELEMENT NUMBER

0 6 10 15 20
APPROXIMATE SCALE (in)

FOR MORE DETAILS ON MATERIAL PROPERTIES, GEOMETRY, AND LOAD FUNCTIONS, SEE APPENDIX 2

Figure 6-14. Nonsafe Model for Response of QDT-3 LER Below Level B Headworks



STRAINS AT 10 msec					
LOCATION IN ELEM	ELEMENT NUMBER				
	1	2	3	4	5
BOTTOM LINER	<1%	10%	>20%	10%	<10%
TOP LINER	<1%	<1%	>20%	<3%	<2%
HOOP (BASED ON F/D SPRING)	>20%	>20%	>20%	>20%	-

Figure 6-15. Nonsafe Results at 10 msec

— TEST DATA (REFERENCE 8)
 AT VARIOUS ENERGY LEVELS
 - - - LEVEL C FRAGMENTATION
 LEVEL D FRAGMENTATION

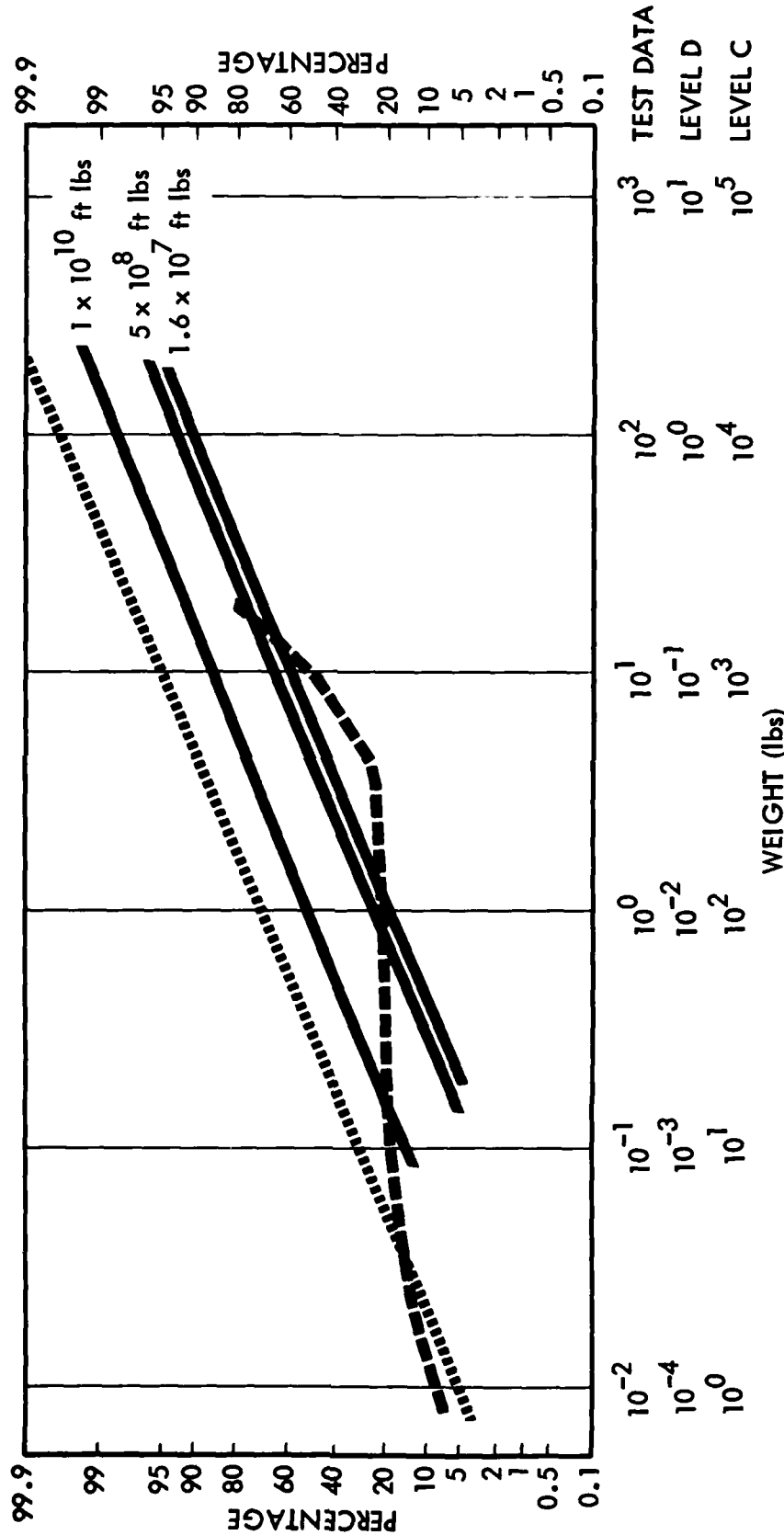


Figure 6-16. Cumulative Probability Distribution of Fragment Weight

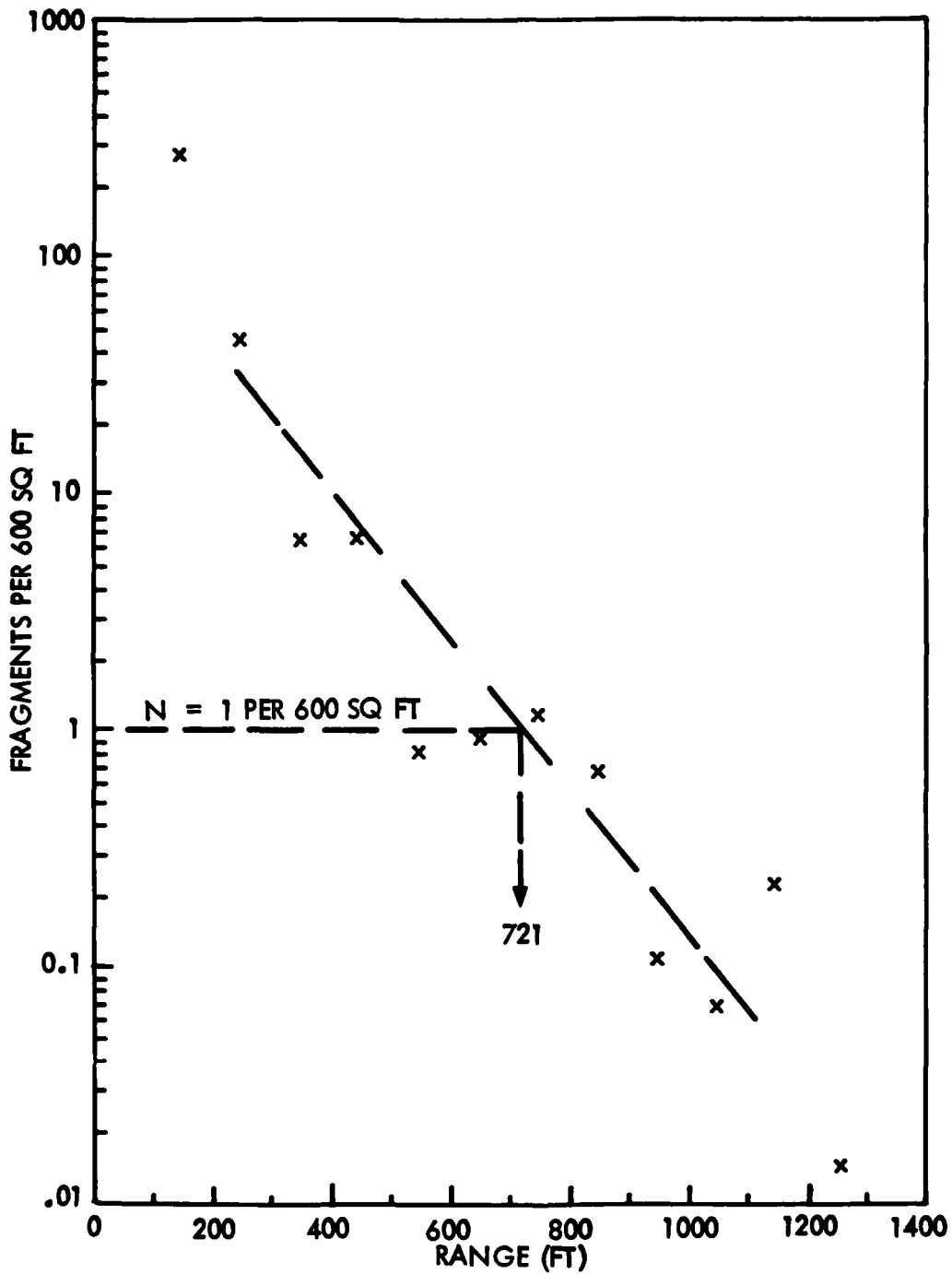


Figure 6-17. QDT-3 Debris Density Predictions

7.0 FRAGMENT SCALING METHODOLOGY

As noted in Section 2.2, one aspect of the analytical program was to explore the possibility of development of a theoretical debris scaling model which would permit the evolution of a bridge directly from the one-quarter scale QDT-3 data to the required full-scale debris distribution estimates. Two approaches were developed, one governed by statistical simulation, and the other by trajectory limitation. These methods appeared to offer independent techniques toward establishing reasonable bounds for full-scale debris criteria. A description of the two methods follows.

7.1 Impact Energy Criterion

For the full-scale quantity-distance criteria, it is required that the fragment density not exceed one per 600 sq ft and that the fragment impact energies be equal to or greater than 58 ft-lb.

Assuming ballistic trajectories, calculations were made for fragments of various sizes in order to determine a lower bound in fragment dimension whereby the impact energy would be 58 ft-lb or greater for a broad spectrum of launch velocities and launch angles.

The equations of motion were as follows:

$$\ddot{y} = -g - \frac{1}{2} \frac{C_D \rho_a A}{\rho_c V} \sqrt{\dot{x}^2 + \dot{y}^2} \dot{y}$$

$$\ddot{x} = -\frac{1}{2} \frac{C_D \rho_a A}{\rho_c V} \sqrt{\dot{x}^2 + \dot{y}^2} \dot{x}$$

- where
- y = vertical component of motion
 - x = horizontal component of motion
 - g = acceleration due to gravity
 - C_D = fragment drag coefficient
 - ρ_a = density of air
 - ρ_c = density of concrete
 - A = fragment cross-sectional area during flight
 - V = fragment volume

As a frame of reference for fragment parameters, the results of the Distant Runner Test Program (Reference 7-1) were assumed as applicable. Event 5 of the program involved the simultaneous detonation of 48 Mark 82 bombs (explosive weight of 9168 pounds TRITONAL) inside a full scale, reinforced, concrete-hardened aircraft shelter of approximately 185,000 cu ft volume. The concrete debris data were evaluated as to shape and number/size/weight distributions. The shape factor relating the debris weight with a length dimension (or an area) was found to be $B = 0.44$ for the function:

$$M = B\rho_c L^3 = B\rho_c A^{3/2}$$

where the drag area is assumed equal to L^2 . The ratio of area to volume is therefore given by:

$$\frac{A}{V} = \frac{1}{BL} = \frac{1}{0.44L}$$

This value for A/V was substituted into the equations of motion such that ballistic trajectories were dependent on only two variables, namely, principal fragment dimension L and drag coefficient C_D .

The debris analysis for Distant Runner was limited to fragments with weights equal to or greater than 0.3 pound, which corresponds to a value for L of 2 inches. It was of interest to determine whether this size limitation for full-scale debris distributions would also be applicable for the range of velocities and angles under consideration in the present study.

Figure 7-1 shows a comparative plot of impact energy versus maximum range for fragment sizes of 1.75 inches, 2.00 inches, and 2.25 inches subjected to launch velocities ranging from 100 to 900 ft/sec and launch angles from 5 to 85 degrees. These curves correspond to a drag coefficient of 0.5. A similar set of contours for lengths of 2.00 inches, 2.25 inches, and 2.50 inches and drag coefficient of 1.0 is plotted in Figure 7-2.

It is estimated that the drag coefficients for the broad spectrum of fragment shapes and tumbling characteristics would generally fall between the values of 0.5 and 1.0. Therefore, it appears reasonable to conclude that limiting the full-scale fragment sizes to 2 inches and greater would assure that the impact energy criterion of 58 ft-lb would automatically be satisfied and would not require any further consideration.

Based on a lower limit of 2 inches for full-scale debris, the effective 1/4-scale fragment size was taken as 0.5 inch; although, it was recognized that the impact energy criterion would not be applicable for the predominance of the QDT-3 debris data corresponding to fragment lengths less than 2 inches. It is noted that analysis of debris data for the 1/4-scale test was limited to fragment weights of (0.3 pound)/64 or essentially about 2 grams.

7.2 Statistical Simulation Model

The basic steps associated with the statistical simulation method for debris scaling are briefly summarized as follows:

- Determine fragment size distribution relative to fragment dimension.
- Compute ballistic trajectories for large number of fragments of respective lengths L .
- Establish a band of launch velocities and launch angles of interest and identify appropriate probability factors for various combinations of velocity and angle.
- Amortize the total number of fragments in each length category by the summation of weight factors associated with the effective velocity and angle combinations.
- Tabulate the maximum ranges for each individual length category within progressive range segments of equal increments.
- Assess the total number of fragments in each range segment by application of the designated weight factors.
- Calculate the fragment density distribution as a function of range.
- Repeat set of calculations for each length category for a fragment dimension of $4L$.
- Evaluate the ratio of ranges for a debris density of one fragment per 600 sq ft for the L and $4L$ cases.

7.2.1 Fragment Size Distribution

A plot is shown in Figure 7-3 of the debris number distribution for Distant Runner Event 5 covering a 5-degree sector from about 600 to 1100 feet for the concrete fragments from the front wall. The explosive charges were located in relatively close proximity to the front wall of the shelter as compared to the side and rear walls. It is noted that the rebar spacing was 7 inches such that a predominant fraction of the total debris occurred with principal dimensions less than the rebar spacing. The slope of the

line in Figure 7-3 is -0.697 which signifies that for each incremental increase of 1 inch in length there is a decrease by a factor of 2 in the number of fragments.

In the following calculations the debris number gradient of 1/2, similar to the Distant Runner result, was assumed for each 1/4-inch increment in fragment length for the 1/4-scale analysis, and similarly for each 1-inch increment in fragment length for the full-scale case. A value of 300,000 was assumed for the total number of fragments associated with an in-silo explosion.

7.2.2 Launch Parameter Spectra

Trajectory calculations were based on initial velocities of 100 to 1000 ft/sec in increments of 100 ft/sec, and initial angles of 45 to 85 degrees (due to the narrow conical angle of vertical throwout) in increments of 5 degrees. Two types of distributions for combinations of launch velocity and launch angle were applied as indicated in Figure 7-4. The uniform distribution consisted of equal probability of occurrence of a combination of any of the 10 values of velocity with any of the 9 angles. The total number of possibilities is 90, and therefore, the fragment number for each combination of V_0 and θ_0 is given by $N(L)/90$, where $N(L)$ is the fragment total for each length category L .

In the case of the skewed distribution, a step function was assumed for variation in probability of occurrence for individual values of velocity and angle, with weight a factor assessment for each respective launch parameter. For example, for a combination of 600 ft/sec and 65 degrees, the associated weight factor is 3 x 2. Integration of the weight factors in the 90 possible combinations of velocity and angle leads to a sum of 324. Therefore, the fragment number for each individual combination of V_0 and θ_0 would be given by $N(L)/324$ multiplied by the associated weight factor.

7.2.3 Analytical Results

The statistical simulation method was applied to nine different cases in order to evaluate the sensitivity of the debris scaling criteria to variations in various parameters. Assumptions for the respective cases and associated analytical results are shown in Table 7-1.

As an illustrative example of the analytical procedures, a brief review is presented of the quantitative calculations related to Case 4. For this case, the launch parameter spectrum corresponds to the skewed distribution, the drag coefficient is 1/2 and the

fragment number gradient is 1/2. The total number of fragments in each length category is given in Table 7-2. Also noted in Table 7-2 are the amortized values of $N(L)/324$ required for the detailed calculations.

A tabulation of maximum ranges for ballistic trajectories of 0.5 inch fragments is shown in Table 7-3 for each of the 90 possible combinations of launch velocity and launch angle. A similar tabulation for 2-inch fragments is presented in Table 7-4. For example, in Table 7-3, the maximum ranges were all within a band of 125 to 150 feet for initial velocities of 400, 500, and 600 ft/sec and initial angle of 75 degrees.

In Table 7-5, the number of fragments given in each range increment was determined from the distribution of Table 7-3, the weight factor spectrum identified in Figure 7-4, and the amortized value of 231 shown in Table 7-2 for 0.5-inch fragments. A similar representation for 2-inch fragments is shown in Table 7-6 where a value of 231 was also applied. This set of tables constitutes an evaluation of the distribution of 0.5-inch fragments for the 1/4-scale analysis and correspondingly for 2-inch fragments for the full-scale analysis.

For the 1/4-scale analysis, the same procedure is followed for fragments of length 0.50, 0.75, 1.00, 1.25, 1.50, 1.75, and 2.00 inches. The number of fragments in each case for the respective range increments are tabulated and summed as shown in Table 7-7. For each range increment, an estimate is made of the total number of fragments per 600 sq ft by means of the following relations:

$$\begin{aligned}
 \text{Area Increment:} \quad A &= \pi (R_2^2 - R_1^2) \\
 &= \pi (R_2 + R_1) (R_2 - R_1) \\
 &= 50 \pi \bar{R}
 \end{aligned}$$

$$\begin{aligned}
 \text{Fragment Density:} \quad N/600 \text{ sq ft} &= \frac{\sum N}{\Delta A/600} \\
 &= \frac{12 \sum N}{\pi \bar{R}}
 \end{aligned}$$

The fragment densities for the 1/4-scale analysis of Case 4 are listed as a function of range in the last column of Table 7-7. A least squares analysis was performed to determine a suitable analytic function for debris density distribution. Of a number of options, it appeared that an exponential function yielded the minimum standard deviation.

A plot is shown in Figure 7-5 of the data and curve fit for the 1/4-scale analysis. A similar representation for the full-scale analysis is plotted in Figure 7-6.

Three scaling approaches were applied as denoted by A, B, and C in Table 7-1. For scaling approach A, a ratio was taken of the ranges in each case corresponding to a debris density of one per 600 sq ft. The respective ranges were 773 and 1572 feet, and therefore the ratio was 2.03.

For scaling approach B, the procedure was as follows: determine by trial and error a debris density for the 1/4-scale case designated by λ^2 , such that if the associated range is multiplied by λ the result would be the same as the full-scale range for a density of one per 600 sq ft. A representative case for $\lambda^2 = 4$ is shown in Figure 7-7.

Considering the analytical results for Case 4 shown in Figures 7-5 and 7-6, the value of λ^2 is found to be 8.3 with an associated range of 546 feet for the 1/4-scale case, such that the range determined by $\sqrt{8.3} \times 546 = 1570$ feet is essentially equal to the value of 1572 feet obtained for the full-scale case.

In principle, scaling approach B constitutes a modification of the analytical function representing the 1/4-scale data into a function which will have the same range for a density of one per 600 sq ft as determined by the independent full-scale analysis. Essentially, the analytical procedure is as follows:

- a) By trial and error, determine λ^2
- b) Modify the 1/4-scale analytical function

$$N_{1/4} = 1340 e^{-0.00932 R}$$

by dividing the coefficient 1340 by λ^2 and dividing the coefficient 0.00932 by λ .

- c) As noted above, $\lambda^2 = 8.3$ and $\lambda = 2.88$ such that the modified full-scale function is therefore:

$$\begin{aligned} \text{Modified } N_{FS} &= \frac{1340}{(2.88)^2} e^{-\frac{0.00932}{2.88} R} \\ &= 162 e^{-0.00324 R} \end{aligned}$$

For this relation

$$N = 1 \text{ per } 600 \text{ sq ft at } R = 1570 \text{ feet}$$

d) The full-scale function determined analytically is:

$$N_{FS} = 121 e^{-0.00305 R}$$

In this case

$$N = 1 \text{ per } 600 \text{ sq ft at } R = 1572 \text{ feet}$$

A comparative plot of the respective analytical functions is presented in Figure 7-8 indicating a relatively small difference between the modified full-scale density distribution and results of the original full-scale analysis.

The third technique, designated as scaling approach C, consists essentially of determining the range for the 1/4-scale analysis where the fragment density is 16, and multiplying this range by $\sqrt{16}$ or 4 to determine a full-scale range corresponding to a density of one per 600 sq ft. This approach is related to standard procedures of geometric scaling, which is readily recognized as conservative since the drag effects are non-linear as the fragment sizes are scaled by a factor of 4. For Case 4, the 1/4-scale range for a density of 16 per 600 sq ft is 475 feet, such that one obtains, for the full-scale case, a range of 4×475 or 1900 feet for a density of one per 600 sq ft. As a first order measure of the degree of conservatism, it is noted that the value of 1900 feet is 21% greater than the calculated full-scale range of 1572 feet.

A similar set of calculations of 1/4-scale and full-scale density distributions were performed for nine cases where an evaluation was made of sensitivity to variation of various parameters. A summary of comparative results is presented in Table 7-1 with an identification of the assumption for the respective cases.

With reference to Case 7, the analysis was based on the assumption that the debris scaling was 2 to 1 for each fragment dimension rather than 4 to 1 as associated with the geometric scaling approach applied for all of the other cases. For the 4-to-1 scaling the mass of each fragment increases by a factor of 64, similar to the total mass increase from the 1/4-scale model to the full-scale structure, and therefore the number of fragments from the 1/4-scale and full-scale events are the same. However, for the 2-to-1 scaling, the mass increase per fragment is a factor of 8, and therefore it is necessary to increase the total number of fragments by a factor of 8 in order to conserve mass.

The 2-to-1 scaling analysis was performed in order to explore the sensitivity of the scaling evaluation to the possibility of other scale factors contributing to the structural break up phenomena. The results for Case 7 in Table 7-1 indicate that the associated parameters for scaling approaches A, B and C are quite similar to the values obtained for the other cases corresponding to geometric scaling.

The purpose of evaluating the relative merits of scaling approaches A and B was to determine whether either method reflected a parameter that was relatively insensitive to the broad variations in analytical assumptions. The standard deviation of the values for approach A was about 6% from the mean, whereas, for approach B, the standard deviation was approximately 12%. It appears that approach A is somewhat more favorable and, therefore, was selected as one of the methods for scaling the QDT-3 results. In essence, the QDT-3 range for a debris density of one per 600 sq ft was to be multiplied by the factor 2.02 in order to determine an estimate of the corresponding full-scale range for the same debris density.

7.3 Trajectory Limitation Technique

The trajectory limitation technique for debris scaling is governed by an evaluation of the ratio of the maximum ranges of fragments of various 1/4-scale dimensions and corresponding full-scale dimensions for similar launch parameters.

A family of contours is shown in Figure 7-9 representing the results of ballistic trajectory calculations for launch velocities of 200 to 1000 ft/sec and launch angles of 5 to 85 degrees associated with several fragment lengths. In Figure 7-9(a) the abscissa scale indicates the maximum range R for a 1-inch fragment, and the ordinate scale represents the ratio R_4/R_1 of maximum ranges of 4-inch and 1-inch fragments when subjected to the same set of launch parameters. A similar family of contours is depicted in Figure 7-9(b) for comparison of the response characteristics of 2-inch and 8-inch fragments. For these calculations, the drag coefficient was assumed to be 0.5.

With reference to Figure 7-9(a), it appears that encompassing all launch parameters an upper bound in scaling from ranges for 1-inch fragments to ranges for 4-inch fragments would be to multiply the 1/4-scale ranges by a factor of about 3.30. In essence, application to QDT-3 would mean multiplying the range observed for each 1-inch fragment by this factor in order to establish the appropriate range for a corresponding 4-inch fragment from a full-scale event.

For the case of scaling from 2-inch to 8-inch fragments, the associated range multiplication factor corresponding to an upper bound criterion is 3.15 as determined from the curves presented in Figure 7-9(b). This approach would be applicable for each fragment length where an associated multiplication factor would be applied in the scaling process. After converting all of the QDT-3 debris data in this manner, an analysis would be performed to determine the full scale range of fragment density of one per 600 sq ft regardless of the fragment dimension.

A similar evaluation shown in Figure 7-10 was performed for the case of a drag coefficient of 1.0 in order to establish some measure of the sensitivity of the range multiplication factors to drag coefficient. A list of values for the multiplication factors covering the domain of the scaling analysis is given in Table 7-8. It appears that a single value of about 3.5 would encompass all cases of interest and establish an upper bound for a spectrum of launch velocities up to 1000 ft/sec. As may be noted by the convergence of the higher velocity curves in Figures 7-9 and 7-10, it is estimated that the increment in the range multiplication factor for higher velocities would not differ significantly from a value of 3.5.

For the application of a single range multiplication factor covering all fragment dimensions of interest, a considerable simplification occurs in the scaling of QDT-3 data to full scale. The procedure in this event is to consider 3.5 as equal to $\sqrt{3.5}$, as defined for the statistical simulation method. Determine the range for the QDT-3 debris density distribution corresponding to a density of $(3.5)^2$ fragments for 600 sq ft, and multiply this range by 3.5 to obtain the required full scale range for a density of one per 600 square ft.

Table 7-1. Debris Scaling Analyses by Statistical Simulation Method

Case	Launch V_0 and θ_0 Spectrum	Drag Coefficient	Number Gradient	Scaling Approach A			Scaling Approach B			Scaling Approach C					
				$R_{1/4}$ for $1/600 \text{ ft}^2$ (ft)	$(RFS)_1$ for $1/600 \text{ ft}^2$ (ft)	$(RFS)_1 / R_{1/4}$	Scale Factor λ	λ^2	$R_{1/4}$ for $\lambda^2/600 \text{ ft}^2$ (ft)	$(RFS)_1$ for $1/600 \text{ ft}^2$ (ft)	Scale Factor λ	$(R_{1/4})^4$ for $16/600 \text{ ft}^2$ (ft)	$(RFS)_4$ for $1/600 \text{ ft}^2$ (ft)	$(RFS)_4 / (RFS)_1$	
				$1/600 \text{ ft}^2$ (ft)	$1/600 \text{ ft}^2$ (ft)	$R_{1/4}$	Scale Factor λ	λ^2	$\lambda^2/600 \text{ ft}^2$ (ft)	$1/600 \text{ ft}^2$ (ft)	Scale Factor λ	$16/600 \text{ ft}^2$ (ft)	$1/600 \text{ ft}^2$ (ft)		
1	Uniform	1/2	1/2	848	1644	1.93	2.72	7.4	604	1644	4	16	512	2048	1.24
2	Uniform	1/2	2/3	1020	1999	1.96	2.88	8.3	694	1999	4	16	593	2322	1.19
3	Uniform	1/2	3/8	732	1446	1.98	2.74	7.5	528	1446	4	16	453	1812	1.25
4	Skewed	1/2	1/2	773	1572	2.03	2.88	8.3	546	1572	4	16	367	1468	1.18
5	Uniform	1	1/2	553	1249	2.26	3.11	9.7	402	1249	4	16	336	1340	1.16
6	Skewed	1	1/2	516	1150	2.23	3.11	9.7	370	1150	4	16	512	2048	1.20
7	Uniform; Scaling 2:1	1/2	1/2	848	1704	2.01	2.88	8.3	591	1704	4	16	596	2348	1.26
8	Uniform; 2No	1/2	1/2	932	1889	2.03	2.76	7.6	684	1889	4	16	427	1708	1.22
9	Uniform; 1/2No	1/2	1/2	764	1398	1.83	2.64	7.0	530	1398	4	16	16	1708	1.21
	Average					2.03	2.86	8.2							

Table 7-2. Number of Fragments Per Length Category

Fragment Length (in)		Number of Fragments N(L)	$\frac{N(L)}{324}$
1/4 Scale Analysis	Full Scale Analysis		
0.50	2.00	75,000	231
0.75	3.00	37,500	116
1.00	4.00	18,750	58
1.25	5.00	9,375	29
1.50	6.00	4,688	14
1.75	7.00	2,344	7
2.00	8.00	1,172	4
	Total	148,829	

Table 7-3 Case 4 - Maximum Range Distribution for 0.5-Inch Fragments

Range ΔR (ft)	LAUNCH VELOCITIES (FT/SEC) FOR SPECIFIC LAUNCH ANGLES									
	45°	50°	55°	60°	65°	70°	75°	80°	85°	
0 - 25								100	200, 300, 400, 500	
25 - 50							100	200	600, 700, 800, 900, 1000	
50 - 75										
75 - 100					100	100	200	300, 400, 500		
100 - 125		100	100	100			300	600, 700, 800, 900, 1000		
125 - 150	100					200	400, 500, 600			
150 - 175				200	200	300, 400	700, 800, 900, 1000			
175 - 200			200		300	500, 600, 700				
200 - 225	200	200		300	400, 500	800, 900, 1000				
225 - 250		300	300	400, 500	600, 700, 800					
250 - 275	300		400	600	900, 1000					
275 - 300	400	400	500, 600	700, 800 900						
300 - 325	500	500, 600	700, 800	1000						
325 - 350	600	700, 800	900, 1000							
350 - 375	700, 800	900, 1000								
375 - 400	900, 1000									

Table 7-4 Case 4 - Maximum Range Distribution for 2-Inch Fragments

Range ΔR (ft)	LAUNCH VELOCITIES (FT/SEC) FOR SPECIFIC LAUNCH ANGLES									
	45°	50°	55°	60°	65°	70°	75°	80°	85°	
0 - 25										100
25 - 50										200
50 - 75									100	300
75 - 100									200	400
100 - 125						100	100			500, 600
125 - 150										700, 800, 900, 1000
150 - 175				100	100				200	
175 - 200										
200 - 225	100	100	100							
225 - 250									300	
250 - 275									400	
275 - 300										
300 - 325						200			500	
325 - 350									600, 700	
350 - 375					200				800	
375 - 400									900, 1000	
400 - 425										
425 - 450				200						
450 - 475		200								
475 - 500						300				

Table 7-4 Case 4 - Maximum Range Distribution for 2-Inch Fragments (Continued)

Range ΔR (ft)	LAUNCH VELOCITIES (FT/SEC) FOR SPECIFIC LAUNCH ANGLES									
	45°	50°	55°	60°	65°	70°	75°	80°	85°	
500 - 525	200				300	400	700			
525 - 550							800, 900			
550 - 575						500	1000			
575 - 600			300							
600 - 625					400	600				
625 - 650			300			700				
650 - 675					500					
675 - 700		300		400		800				
700 - 725	300					900				
725 - 750						1000				
750 - 775			400	500						
775 - 800										
800 - 825		400			800					
825 - 850				600	900					
850 - 875			500		1000					
875 - 900				700						
900 - 925		500								
925 - 950			600	800						
950 - 975			700	900						
975 - 1000										
1000 - 1025				1000						
1025 - 1050		600								

Table 7-4 Case 4 - Maximum Range Distribution for 2-Inch Fragments (Continued)

Range ΔR (ft)	LAUNCH VELOCITIES (FT/SEC) FOR SPECIFIC LAUNCH ANGLES									
	45°	50°	55°	60°	65°	70°	75°	80°	85°	
1050 - 1075	600	700	900							
1075 - 1100			1000							
1100 - 1125										
1125 - 1150	700	800								
1150 - 1175										
1175 - 1200	800	900								
1200 - 1225		1000								
1225 - 1250										
1250 - 1275	900									
1275 - 1300										
1300 - 1325	1000									

Table 7-5. Case 4 - Number Density for 0.5-Inch Fragments

Range (ft)	V_0 and θ_0 Combinations	Total Weight Factors	Number of Fragments
0 - 25	1	3	693
25 - 50	5	27	6,237
50 - 75	7	33	7,623
75 - 100	6	28	6,468
100 - 125	9	37	8,547
125 - 150	5	27	6,237
150 - 175	8	30	6,930
175 - 200	5	21	4,851
200 - 225	8	24	5,544
225 - 250	7	28	6,468
250 - 275	5	14	3,234
275 - 300	7	20	4,620
300 - 325	6	15	3,465
325 - 350	5	9	2,079
350 - 375	4	6	1,386
375 - 400	2	2	462
Total	90	324	74,844

Table 7-6. Case 4 - Number Density for 2-Inch Fragments

Range (ft)	V_0 and θ_0 Combinations	Total Weight Factors	Number of Fragments
0 - 25	--	---	----
25 - 50	1	3	693
50 - 75	--	---	----
75 - 100	2	6	1,386
100 - 125	2	9	2,079
125 - 150	2	8	1,848
150 - 175	4	23	5,313
175 - 200	5	20	4,620
200 - 225	3	3	693
225 - 250	2	9	2,079
250 - 275	1	6	1,386
275 - 300	--	---	----
300 - 325	2	11	2,541
325 - 350	3	21	4,851
350 - 375	2	8	1,848
375 - 400	3	12	2,772
400 - 425	1	2	462
425 - 450	2	13	3,003
450 - 475	2	10	2,310
475 - 500	1	1	231
500 - 525	4	15	3,465
525 - 550	2	9	2,079
550 - 575	2	9	2,079
575 - 600	1	4	924
600 - 625	2	10	2,310
625 - 650	2	6	1,386
650 - 675	1	6	1,386
675 - 700	3	10	2,310

Table 7-6. Case 4 - Number Density for 2-Inch Fragments (Continued)

Range (ft)	V_0 and θ_0 Combinations	Total Weight Factors	Number of Fragments
700 - 725	2	4	924
725 - 750	2	8	1,848
750 - 775	3	12	2,772
775 - 800	--	---	----
800 - 825	2	6	1,386
825 - 850	2	8	1,848
850 - 875	3	7	1,617
875 - 900	1	4	924
900 - 925	1	3	693
925 - 950	2	7	1,617
950 - 975	2	5	1,155
975 - 1000	1	2	462
1000 - 1025	2	5	1,155
1025 - 1050	1	2	462
1050 - 1075	2	5	1,155
1075 - 1100	1	1	231
1100 - 1125	1	1	231
1125 - 1150	2	4	924
1150 - 1175	--	---	----
1175 - 1200	2	3	693
1200 - 1225	1	1	231
1225 - 1250	--	---	----
1250 - 1275	1	1	231
1275 - 1300	--	---	----
1300 - 1325	1	1	231
Total	90	324	74,844

Table 7-7. Case 4 - 1/4-Scale Debris Density Distribution

Range (ft)	Number of Fragments								Σ N	Average Range R̄ (ft)	$\frac{12 \Sigma N}{\pi \bar{R}}$
	1/2"	3/4"	1"	1-1/4"	1-1/2"	1-3/4"	2"				
0 - 25	693	---	---	---	---	---	---	---	693	12.5	212
25 - 50	6237	696	174	87	42	21	12	12	7,269	37.5	740
50 - 75	7632	3828	696	174	84	21	---	---	11,040	62.5	675
75 - 100	6468	3016	1914	435	84	21	24	24	11,962	87.5	522
100 - 125	8547	928	986	928	252	63	36	36	11,740	112.5	399
125 - 150	6237	3480	580	319	364	119	32	32	11,131	137.5	309
150 - 175	6930	3248	1160	232	140	203	92	92	12,005	162.5	282
175 - 200	4851	1740	928	348	112	42	80	80	8,332	187.5	170
200 - 225	5544	2436	1160	522	140	56	12	12	11,256	212.5	202
225 - 250	6468	2552	464	580	126	63	36	36	10,289	237.5	165
250 - 275	3234	1624	1276	174	322	63	24	24	6,717	262.5	97.7
275 - 300	4620	1972	1044	232	126	77	---	---	8,071	287.5	107
300 - 325	3465	2552	986	696	154	126	44	44	8,023	312.5	98.1
325 - 350	2079	696	464	174	---	56	84	84	3,553	337.5	40.2
350 - 375	1386	2784	696	522	210	42	32	32	5,672	362.5	59.8
375 - 400	462	1044	928	319	224	105	48	48	3,130	387.5	30.8
400 - 425		1624	696	406	210	---	8	8	2,944	412.5	50.9
425 - 450		464	696	116	182	112	52	52	1,622	437.5	14.2
450 - 475		1044	812	406	---	105	40	40	2,407	462.5	19.9
475 - 500		928	638	406	196	28	4	4	2,200	487.5	20.4
500 - 525		348	348	174	84	63	60	60	1,077	512.5	8.03
525 - 550		464	464	348	140	98	36	36	1,550	537.5	11.0
550 - 575		116	580	232	140	---	36	36	1,104	562.5	7.50
575 - 600			116	203	112	42	16	16	489	587.5	3.18
600 - 625			406	174	168	98	40	40	886	612.5	5.52
625 - 650			232	290	56	42	24	24	644	637.5	3.86
650 - 675			58	174	140	56	24	24	452	662.5	2.61
675 - 700			174	174	70	84	40	40	542	687.5	3.01

Table 7-7. Case 4 - 1/4-Scale Debris Density Distribution (Continued)

Range (ft)	Number of Fragments								Σ N	Average Range \bar{R} (ft)	$\frac{12 \Sigma N}{\pi \bar{R}}$
	1/2"	3/4"	1"	1-1/4"	1-1/2"	1-3/4"	2"	2"			
700 - 725			58	58	84	---	16		216	712.5	1.16
725 - 750			58	174	140	42	32		446	737.5	2.31
750 - 775				87	28	77	48		240	762.5	1.20
775 - 800				87	140	56	--		283	787.5	1.37
800 - 825				87	28	---	24		139	812.5	0.65
825 - 850				29	70	70	32		201	837.5	0.058
850 - 875				---	42	14	28		84	862.5	0.37
875 - 900				29	14	49	16		108	887.5	0.46
900 - 925					28	21	12		61	912.5	0.26
925 - 950					42	14	28		84	937.5	0.34
950 - 975					14	42	20		76	962.5	0.30
975 - 1000					14	---	8		22	987.5	0.085
1000 - 1025					14	35	20		69	1012.5	0.26
1025 - 1050						---	8		8	1037.5	0.029
1050 - 1075						7	20		27	1062.5	0.097
1075 - 1100						21	4		25	1087.5	0.088
1100 - 1125						7	4		11	1112.5	0.038
1125 - 1150						---	16		16	1137.5	0.054
1150 - 1175						7	---		7	1162.5	0.023
1175 - 1200							12		12	1187.5	0.038
1200 - 1225							4		4	1212.5	0.013
1225 - 1250							---		--	1237.5	---
1250 - 1275							4		4	1262.5	0.012
1275 - 1300							---		--	1287.5	---
1300 - 1325							4		4	1312.5	0.012

Table 7-8. Upper Bound Range Multiplication Factors

Fragment Length (in.)		R_{4L}/R_L	
1/4 Scale	Full Scale	$C_D = 0.5$	$C_D = 1.0$
0.50	2	3.41	3.48
0.75	3	3.33	3.44
1.00	4	3.30	3.41
1.50	6	3.22	3.33
2.00	8	3.15	3.30

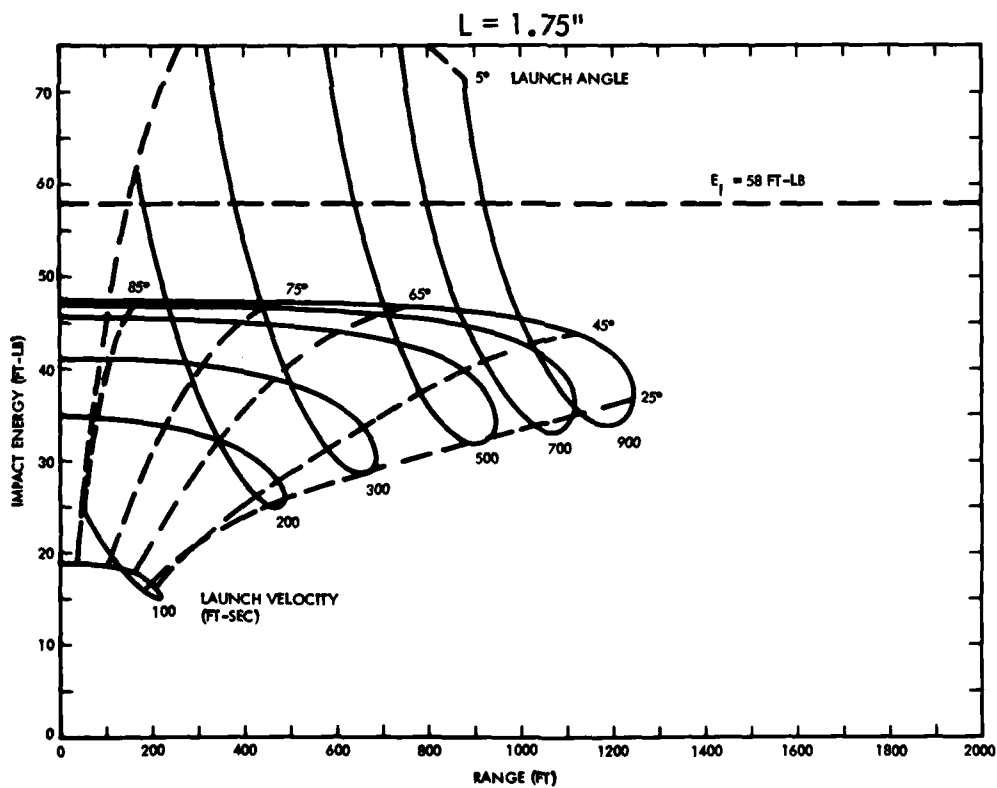
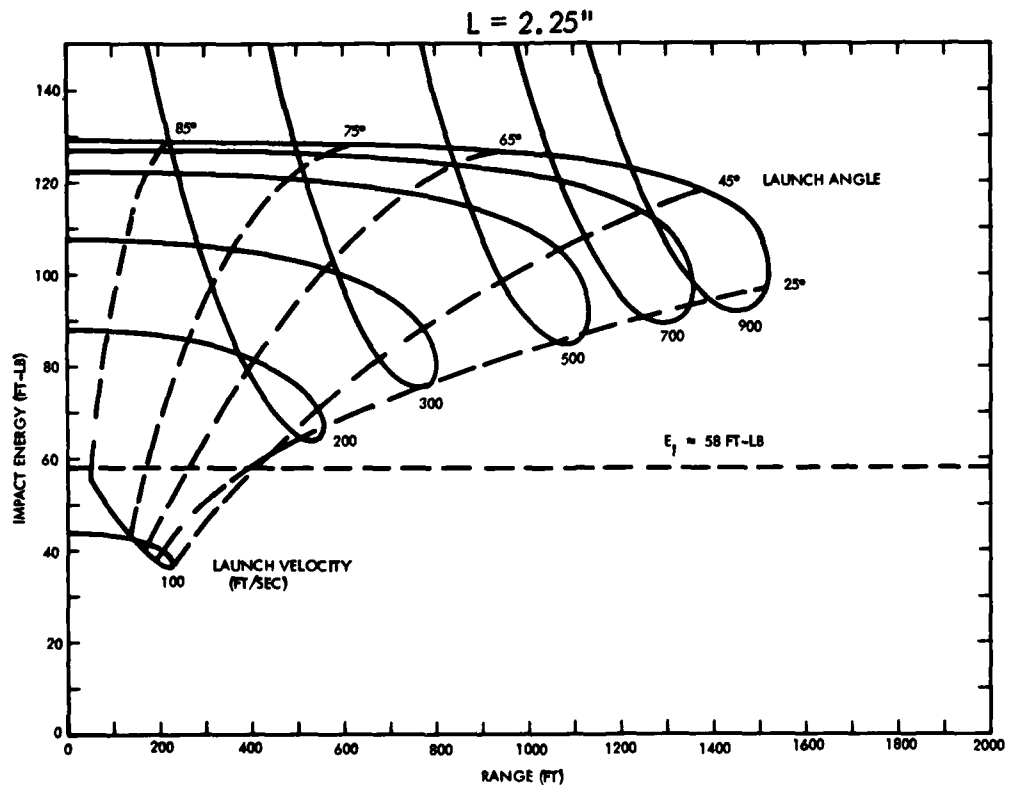
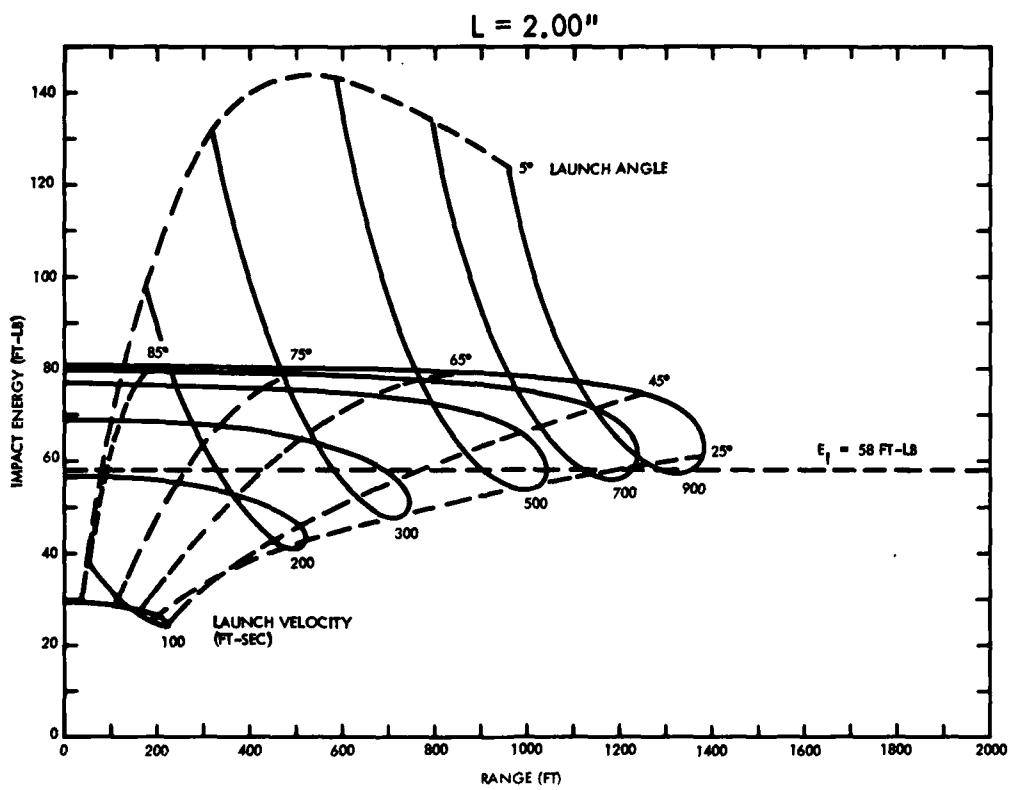


Figure 7-1. Fragment Size Limitation for Impact Energy Criterion of 58 ft-lb and Drag Coefficient of 0.5



**Figure 7-1. Fragment Size Limitation for Impact Energy
Criterion of 58 ft-lb and Drag Coefficient of 0.5 (Continued)**

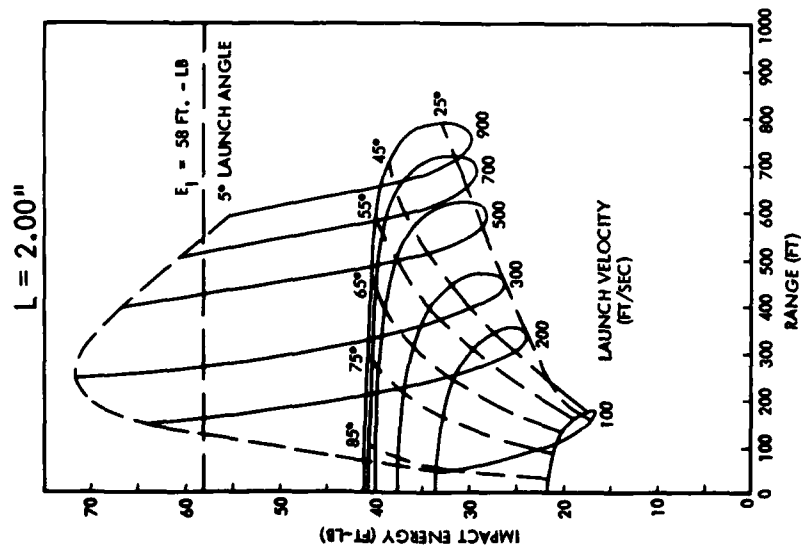
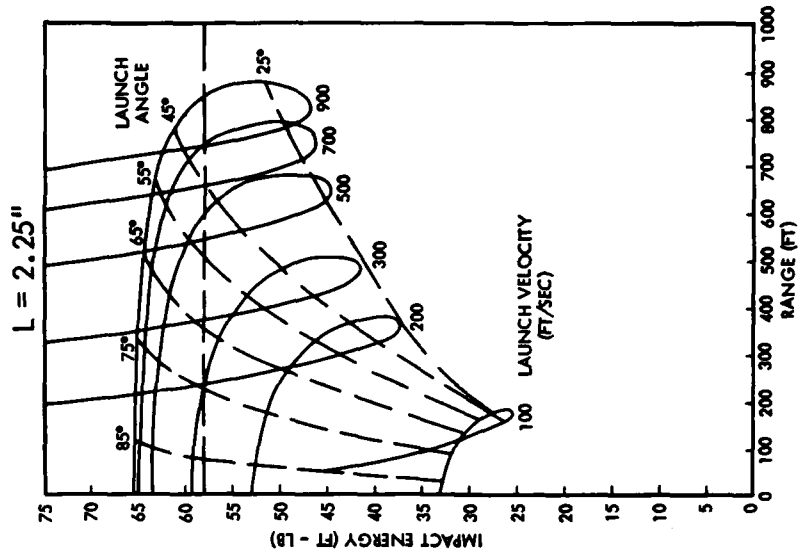
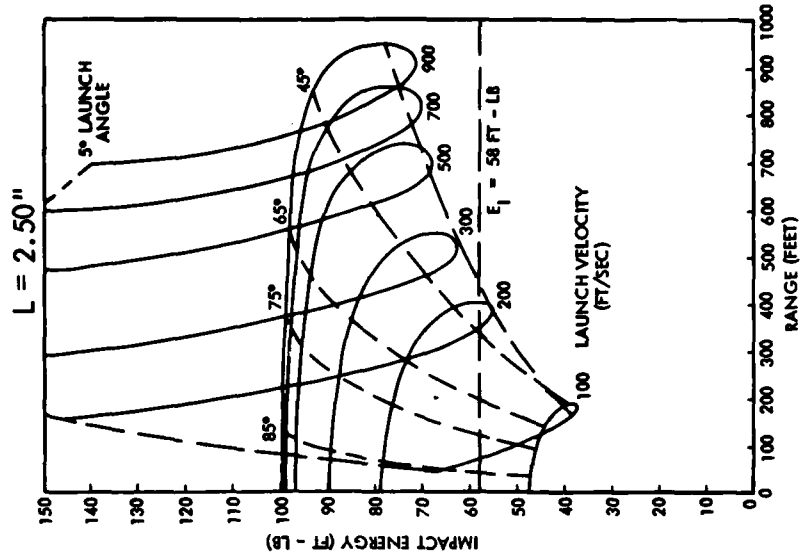


Figure 7-2. Fragment Size Limitation for Impact Energy Criterion of 58 ft-lb and Drag Coefficient of 1.0

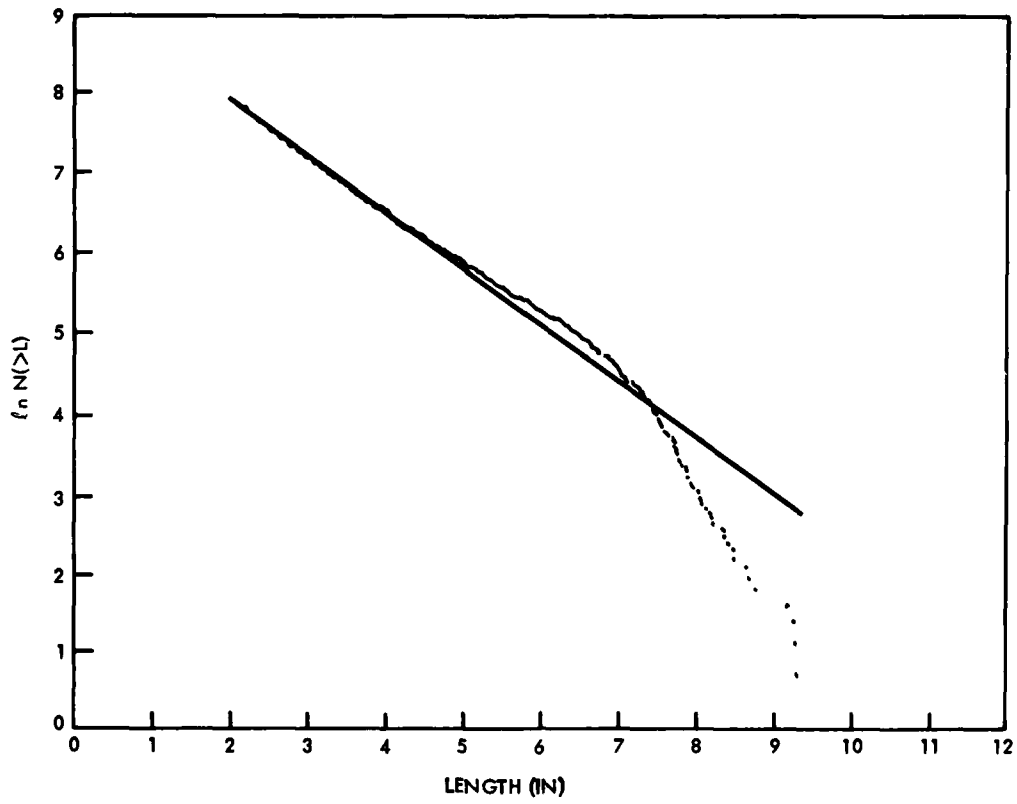


Figure 7-3. Debris Number Distribution for Distant Runner Event 5 Front Wall

LAUNCH PARAMETERS	
<ul style="list-style-type: none"> ● 10 VELOCITIES: 100, 200, 300, 400, 500, 600, 700, 800, 900, 1000 FT/SEC ● 9 ANGLES: 45, 50, 55, 60, 65, 70, 75, 80, AND 85 DEGREES 	
UNIFORM DISTRIBUTION	
<ul style="list-style-type: none"> ● FRAGMENT NUMBER OF $\frac{N(L)}{90}$ FOR EACH V_0 AND θ_0 COMBINATION ● OCCURRENCE FREQUENCY $N(L)$ SPECIFIED PER FRAGMENT SIZE 	
SKewed DISTRIBUTION	
LAUNCH VELOCITY (FT/SEC)	LAUNCH ANGLE (DEG)
WEIGHT FACTOR 	
<ul style="list-style-type: none"> ● FRAGMENT NUMBER OF $\frac{N(L)}{324}$ X ASSOCIATED WEIGHT FACTORS FOR EACH V_0 AND θ_0 COMBINATION ● OCCURRENCE FREQUENCY, $N(L)$, SPECIFIED PER FRAGMENT SIZE 	

Figure 7-4. Velocity and Angle Distribution for Scaling Analyses

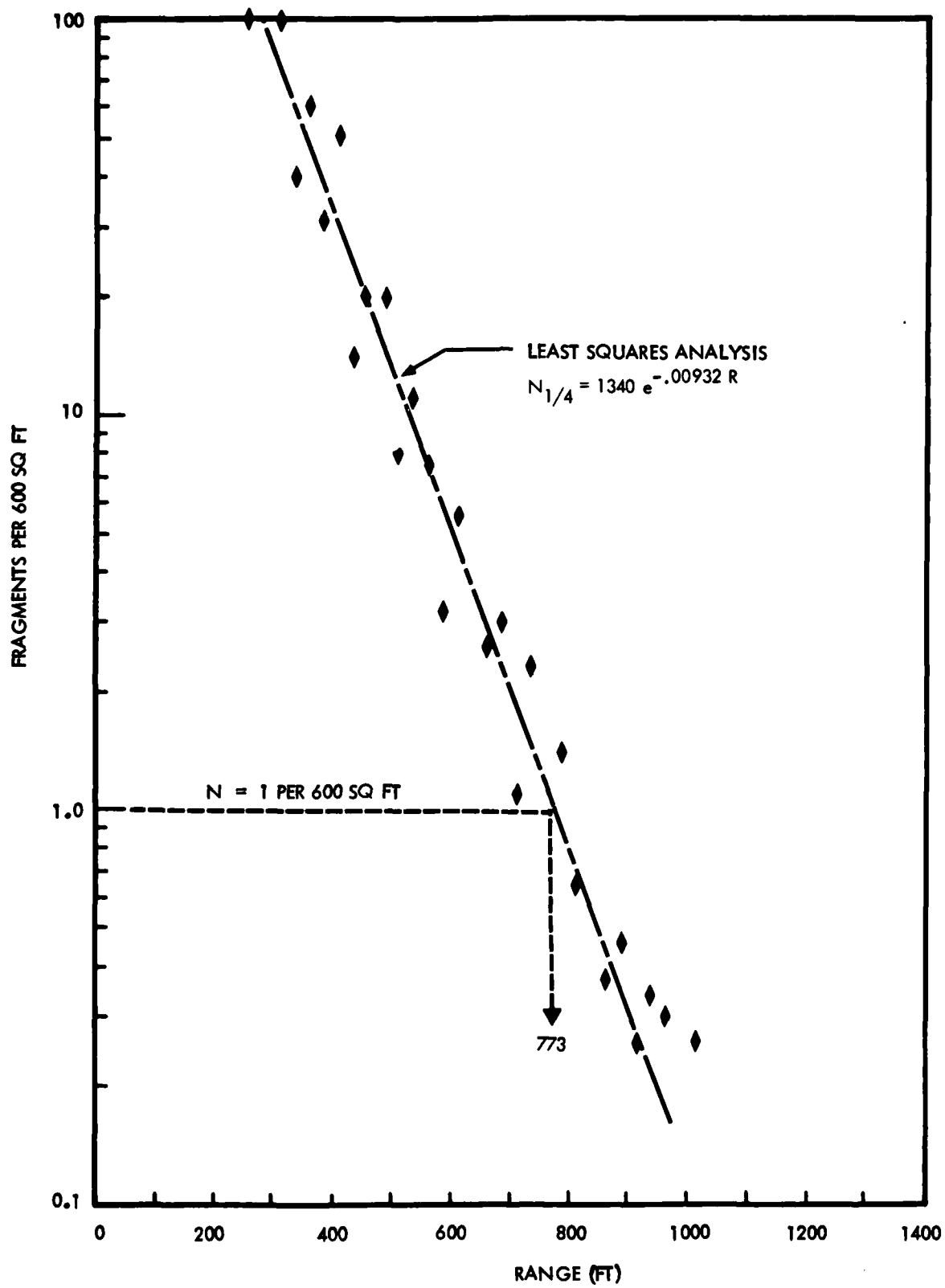


Figure 7-5. Case 4A - 1/4-Scale Debris Density Variation with Range

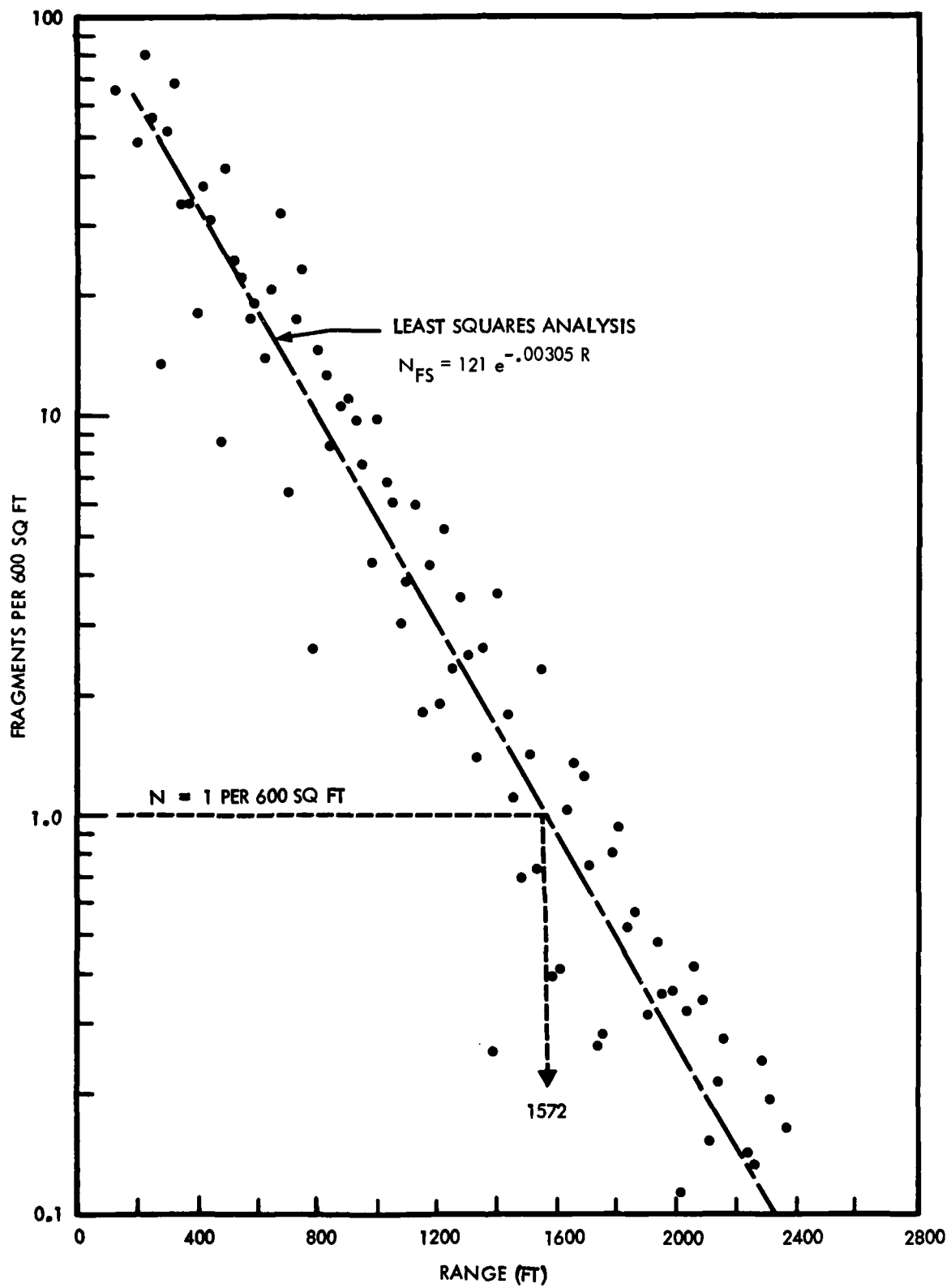
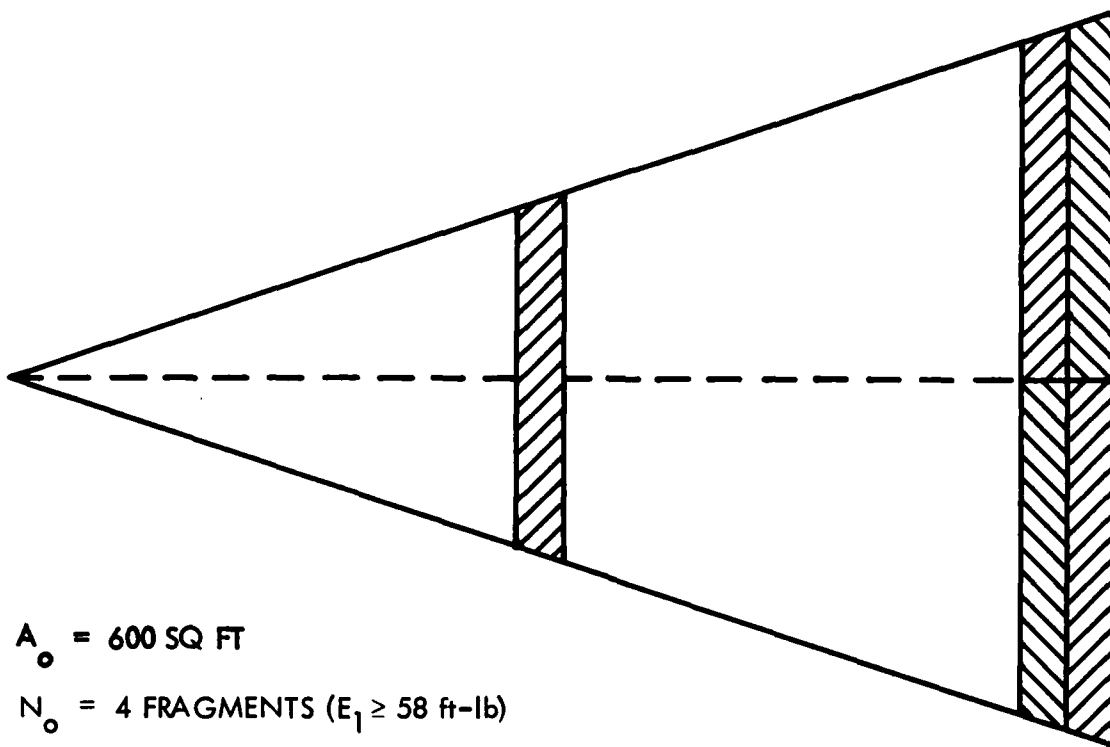


Figure 7-6. Case 4B - Full-Scale Debris Density Variation with Range



$A_o = 600 \text{ SQ FT}$

$N_o = 4 \text{ FRAGMENTS } (E_f \geq 58 \text{ ft-lb})$

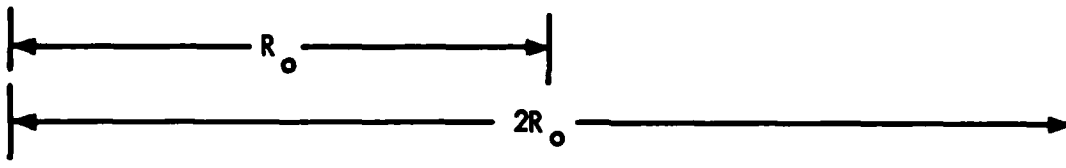


Figure 7-7. Representative Fragment Density Scaling Procedure

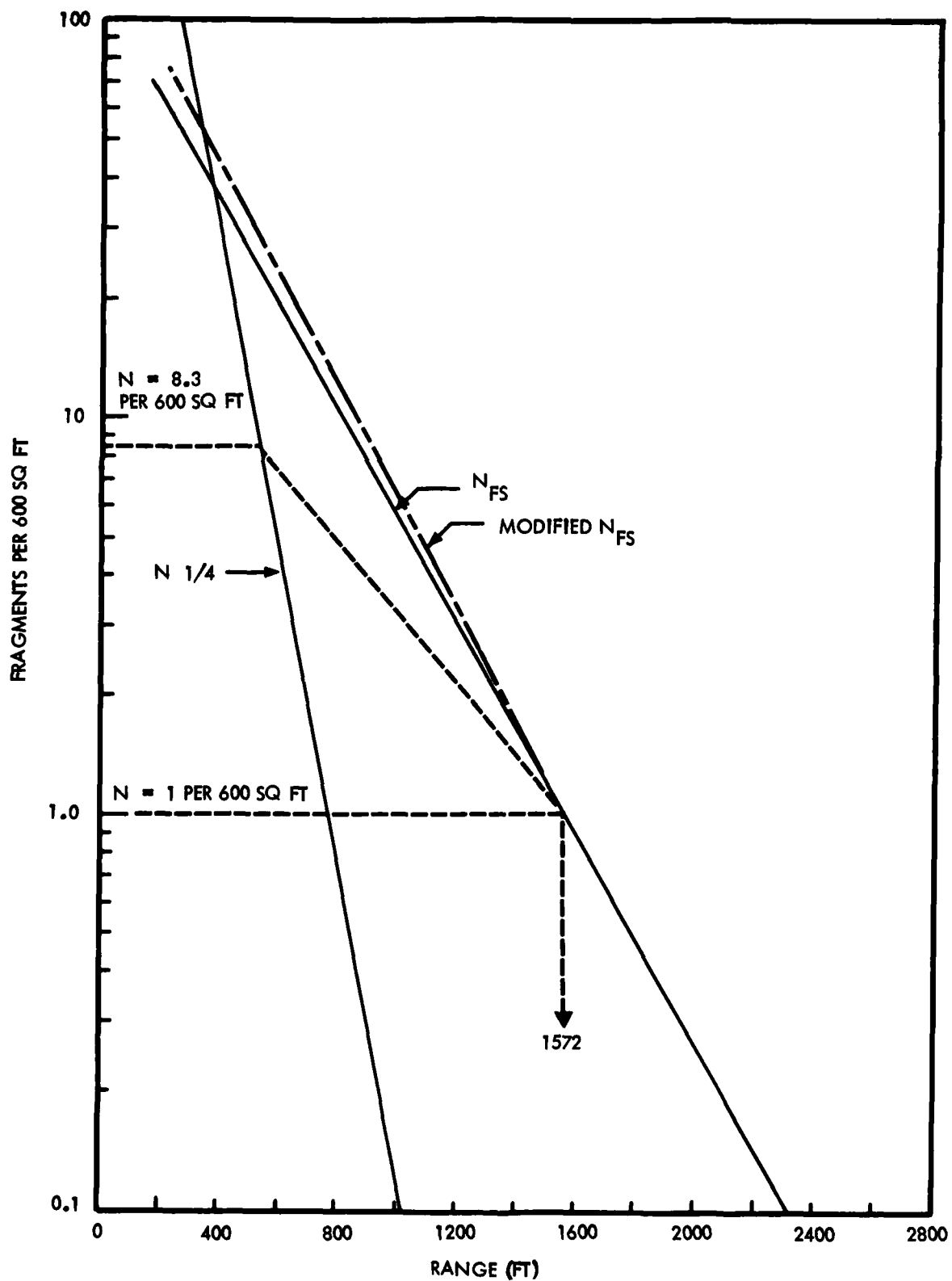


Figure 7-8. Case 4 - Analytical Function Modification for Scaling Approach B

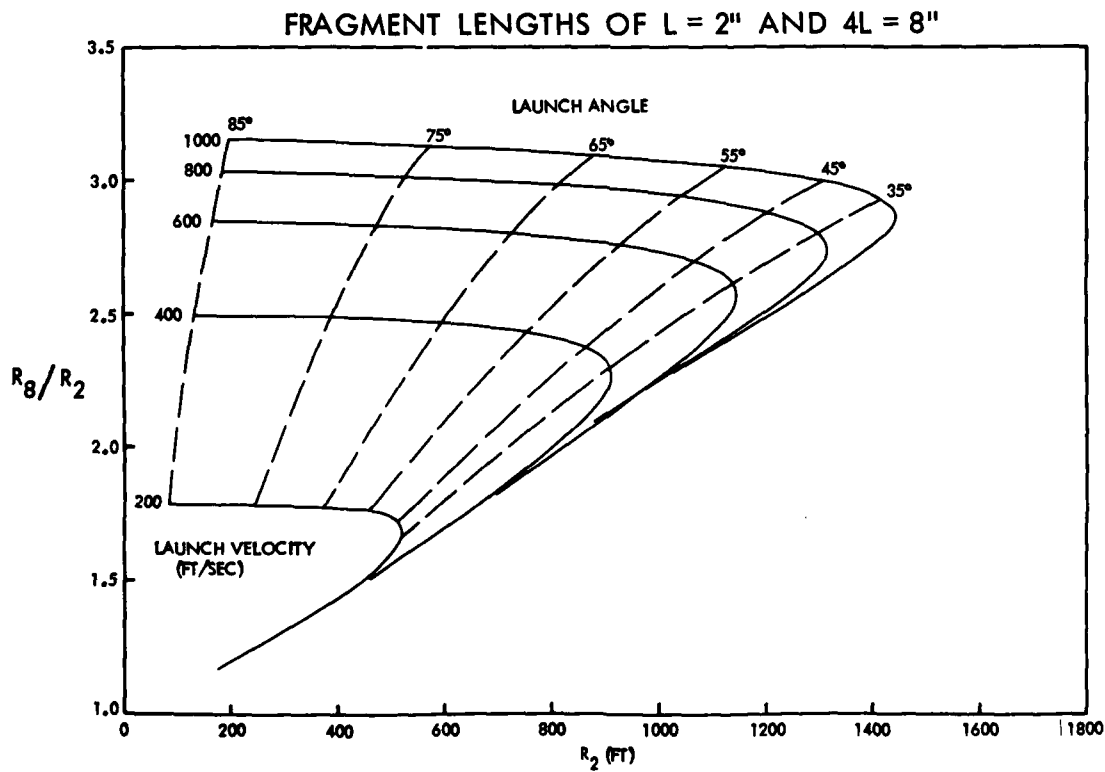
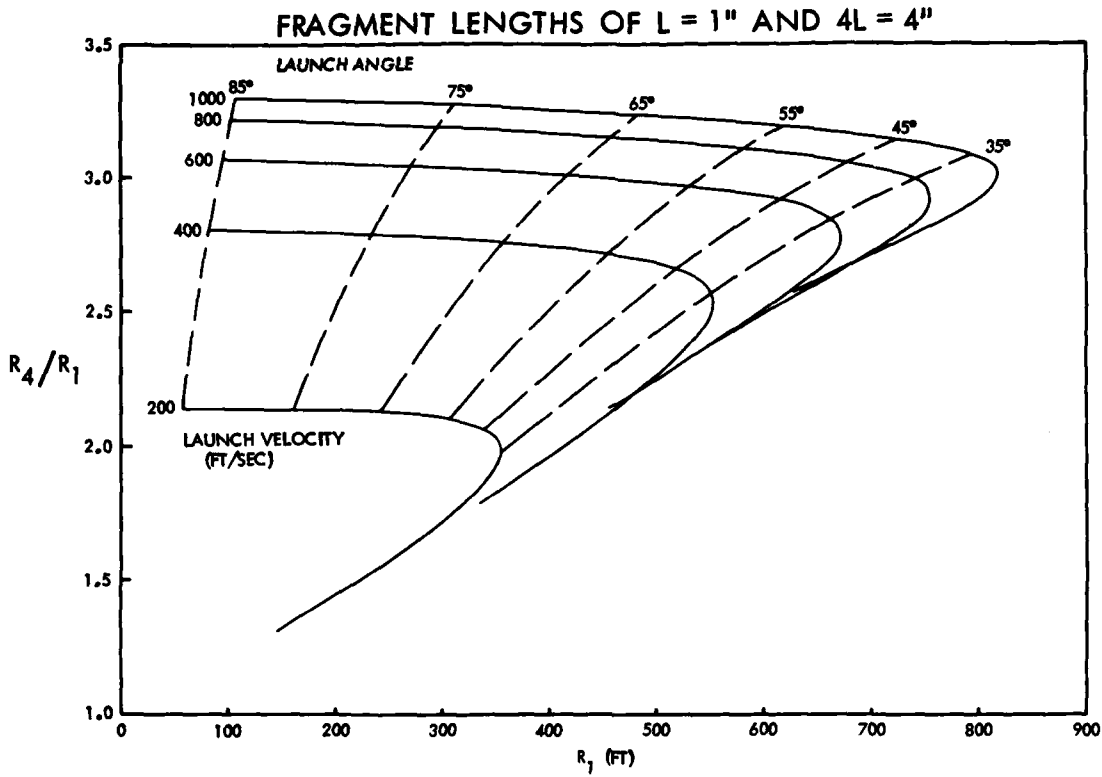
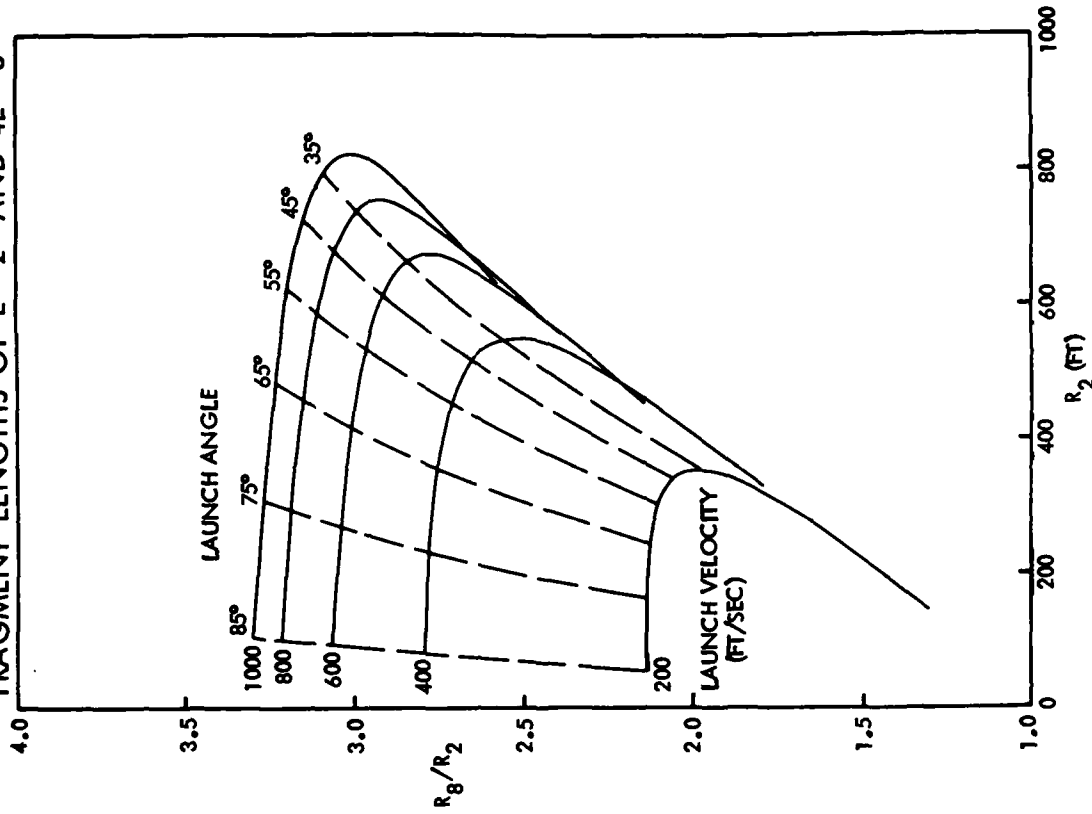


Figure 7-9. Comparison of Maximum Range Ratios for Fragment Lengths L and 4L for Drag Coefficient of 0.5

FRAGMENT LENGTHS OF L = 2" AND 4L = 8"



FRAGMENT LENGTHS OF L = 1" AND 4L = 4"

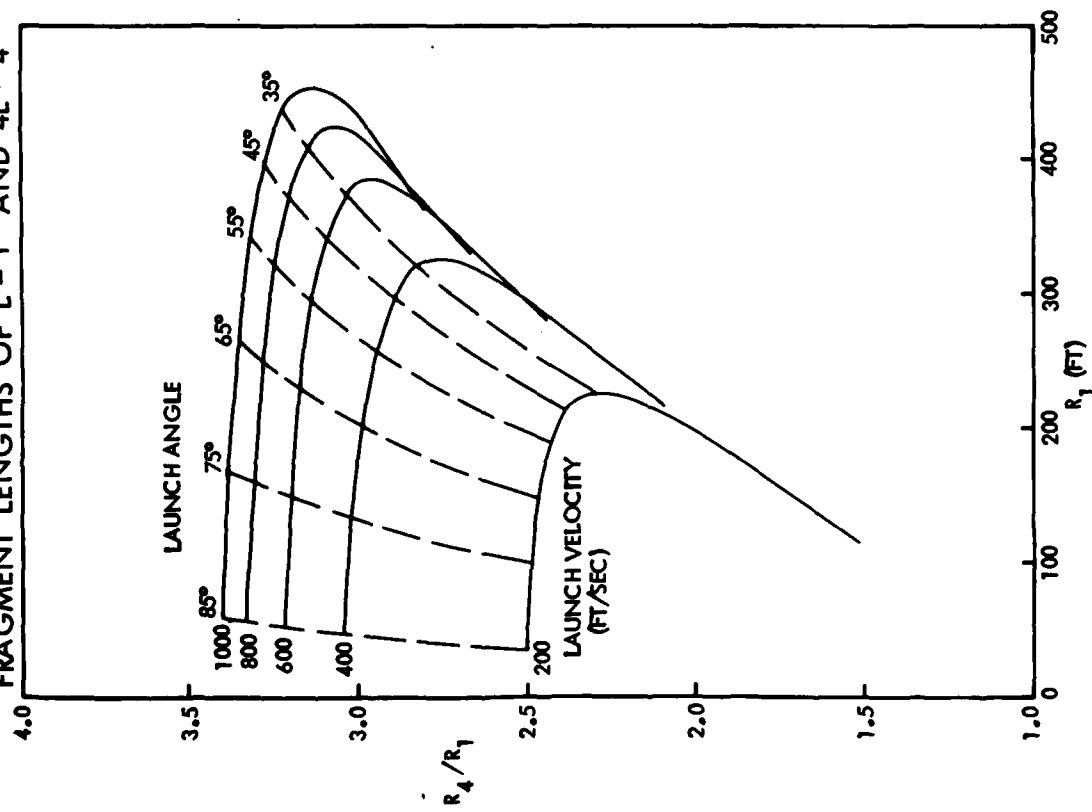


Figure 7-10. Comparison of Maximum Range Ratios for Fragment Lengths L and 4L for Drag Coefficient of 1.0

8.0 TEST RESULTS

8.1 Airblast

The airblast measurements were highly successful. All of the 150 pressure channels recorded and provided good data. The original test program incorporated only two 1/10-scale tests and the 1/4-scale test. During the course of the test events, it became apparent that the resulting peak overpressure levels were considerably lower than had originally been anticipated. Therefore, it was considered advisable to conduct a calibration shot in order to evaluate the reliability of the sensors and recording equipment as a total integrated system.

8.1.1 Tenth Scale Tests

The 1/10-scale QDT-1 and QDT-2 tests were conducted on 26 January and 01 February 1984, respectively. The explosive charges consisted of 172 pounds of Pentolite 50/50. A set of the QDT-1 airblast records (Reference 8-1) is presented in Appendix B with the QDT-2 airblast records (Reference 8-2) shown in Appendix C. The heavy curves of the airblast records in the Appendices represent the pressure-time histories, and the light curves are the time-integrals of the pressure contours and, therefore, correspond to the variation of impulse with time. A brief summary is given in Table 8-1 of the peak pressure, positive duration, and arrival time data as a function of range for QDT-1 and QDT-2.

The surface wind velocities as measured in close proximity to the Instrumentation Trailer were essentially zero at shot time for both tests, with measurements of meteorological conditions indicating wind velocities increasing with altitude up to the order of several miles per hour at heights of about 200 feet for QDT-1 and 1000 feet for QDT-2.

The average crater dimensions for QDT-1 were 12.9 feet radius and 8.3 feet deep, whereas the corresponding dimensions for QDT-2 were 12.3 feet radius and 7.6 feet deep. None of the QDT-1 test structure was observed within the apparent crater. However, a piece of the QDT-2 launch tube remained in the crater after the explosion.

8.1.2 Quarter Scale Test

The 1/4-scale QDT-3 test was conducted on 29 February 1984. The explosive charge consisted of 2685 pounds of Pentolite 50/50. A set of the QDT-3 airblast records (Reference 8-3) is presented in Appendix D. A summary of the peak pressure, positive duration, and arrival time as a function of range is shown in Table 8-2.

Surface wind velocity as measured near the Instrumentation Trailer at shot time was 10 mph in a direction of 110 degrees azimuth relative to True North. The data for wind velocities at various altitudes is shown in Table 8-3.

The average crater dimensions were 23.7 foot radius and 10.0 foot depth. Upon inspecting the crater, it was apparent that none of the structure remained in the test bed. It appeared that complete detonation of the explosive charge had occurred. Profiles of the QDT-3 apparent crater are shown in Figure 8-1.

8.1.3 Calibration Shot

The QDT-3 calibration shot was conducted on 7 March 1984. A tangent sphere of 1017 pounds of TNT was located at the ground zero of the QDT-3 test bed which had been reconstituted prior to the calibration test. Figure 8-2 indicates the charge characteristics. Airblast measurements were taken with 15 gages located along the centerline of each of the three radials at distances starting at 42 feet and extending out to 1320 feet. A set of the 45 records is shown in Appendix E. A summary of peak overpressure, positive duration, and arrival time data is presented in Table 8-4. Wind velocity at ground surface was approximately one mph at zero time.

8.2 Debris/Ejecta

8.2.1 Structural Debris

Table 8-5 presents a summary of the number of concrete fragments located within the S, NE, and NW radials from ranges of 125 to 1000 feet. No fragments were observed within the respective radials from ranges of 1000 to 1750 feet.

Summarized in Table 8-6 are the debris data acquired circumferentially at a range of 400 feet in order to evaluate the symmetry of the debris distribution. The ring sample areas for the ground survey were approximately 33 feet long by 24 feet wide (area of 792 sq ft).

It was originally assumed that the proposed distribution of debris collector pads of 10 by 10 foot dimension would yield sufficient data for analysis of the QDT-3 results and scaling to a full-scale event. However, immediately following collection of the witness sheet data, it became apparent that the observed total of 853 fragments would be entirely inadequate to afford a reasonable data base for a statistical analysis. It was estimated that this number of fragments represented perhaps less than 1% of the total number expected for an event of this nature. It would appear that application of small sample statistics would have been required which was considered unsatisfactory for the purpose intended.

A second debris collection effort was initiated covering specific regions of 50 by 57.5 foot dimension (area of 2875 sq ft) located on the right of the centerline of the cleared areas of the three radials. An additional group of 424 fragments were recorded by this means. At this stage, the total of 1277 fragments was still considered inadequate. As a third collection effort, the entire left segments of the three radials were covered, whenever possible, which yielded another increment of 3455 fragments for a total of 4732, which was considered to be a reasonable statistical sample.

The total collection area covered in the process was about 190,000 sq ft, which represented 6.2% of the circumferential area between radii of 125 and 1000 feet. To a first order extent, assuming azimuthal symmetry, it is estimated that a total of $4732/0.062$, or 76,300 fragments, were projected within the ranges covered by the debris collection.

A considerable data reduction effort was instituted toward determining a set of debris characteristics in relation to dimensions, weight, color, and location for each of the fragments collected. Results of this effort and associated analyses are summarized in Section 9.4.

8.2.2 Artificial Missiles

Table 8-7 (Reference 8-3) provides post-shot survey data for the artificial missiles emplaced in the silo backfill material. The data are grouped by missile cluster numbers, along with their original depth and range from the GZ axis, and the number of missiles in each size class recovered (compared with the number emplaced) and the maximum, minimum, and mean deposition ranges of missiles in each size class.

The longest-range missile was an 8-inch cube originally in a cluster buried 0.5 feet, at a range of 6 feet from GZ, which traveled to a range of 340 feet from GZ. While many of

the longer-range missiles may have rolled a short distance after impact, the cubic shape of the missiles was selected (in part) to minimize roll, so the surveyed positions of the missiles should not be much more than their ballistic travel distances.

The influence of missile size on mean deposition range is evident for those missiles originally located near the surface or close to the silo (e.g., clusters R, T, V, H, and O). The smaller cubes tend to have shorter mean ranges than larger cubes in the same cluster due to air drag effects.

8.2.3 Soil Ejecta

As may be noted from Table 8-8, the soil ejecta attributed to the backfill gradations were limited principally to ranges of the order of 200 to 300 feet. Results of this nature appear reasonable based on the relatively low launch velocities and launch angles associated with the explosion configuration.

8.3 Strain Gage

Fifteen of the sixteen strain gages were recored in QDT-3. Because strain gages cannot accurately record strains of more than about 5%, the only information gleaned from the resulting records was the times at which certain events might have occurred. The failure times of the entire set of strain gages were found to be within a range of 0.7 to 2.1 milliseconds.

8.4 Technical Photography

Twelve of the thirteen motion picture cameras installed to photograph debris ejection or impact operated successfully. The camera which failed to operate was the one installed to obtain high-speed closeup IR photography of the initial venting of the explosion. Unfortunately, the initial silo breakup designed to be captured by a camera with frame speed of about 6000 frames/sec, using normal film, was largely obscured by the emerging fireball. Other cameras provided excellent coverage of the ejection of large pieces of the closure.

Since the impact ranges of silo debris along the radial survey areas could not be predicted exactly, camera coverage was extended to a range of 510 feet along the NE radial and 680 feet on the south radial. Excellent photographs were obtained of the terminal ballistics of debris impacting out to a range of about 600 feet.

A sequence of photographs of the QDT-3 explosion is shown in Figure 8-3 with a designation of the respective times.

Table 8-1. QDT-1 and QDT-2 Airblast Test Results

Range (feet)	QDT-1 Data						QDT-2 Data					
	S Radial			W Radial			S Radial			W Radial		
	Peak Pressure (psi)	Positive Duration (msec)	Arrival Time (msec)									
17	11.4	3.88	10.1	11.9	4.65	9.3	11.2	3.61	9.20	8.39	6.49	10.7
30	5.37	6.20	19.2	4.96	7.75	20.1	5.70	7.76	18.6	5.24	7.36	19.6
44	3.00	7.75	30.1	3.10	8.53	27.0	3.39	8.44	30.6	3.28	8.50	31.2
52	2.33	9.30	36.7	2.48	9.30	37.0	2.60	9.10	37.4	2.88	8.96	37.9
65	1.49	9.80	48.4	1.88	10.1	47.8	1.83	9.40	47.2	2.27	9.44	48.9
82	1.04	10.4	62.6	1.04	10.4	61.6	1.22	9.70	61.5	1.15	10.0	63.4
100	1.12	10.8	77.0	0.88	10.8	77.8	1.33	10.4	76.8	0.86	10.6	79.1
130	0.59	11.6	103	0.61	11.6	104	0.62	11.2	103	0.65	11.5	106
160	0.49	12.4	129	0.48	12.4	131	0.52	11.7	129	0.51	12.2	132
200	0.39	13.2	165	0.40	13.2	166	0.38	12.6	164	0.57	13.0	169
245	0.29	13.6	205	0.30	14.0	206	0.33	12.8	203	0.35	13.5	210
295	0.26	14.0	249	0.20	14.7	251	0.25	13.6	248	0.22	14.8	255
350	0.20	14.3	299	0.15	14.0	301	0.21	14.3	296	0.17	14.5	305
430	0.20	14.7	371	0.12	15.5	373	0.17	14.7	366	0.13	14.4	379
530	0.13	15.5	460	0.09	16.3	463	0.12	15.5	455	0.09	16.0	470

Table 8-2. QDT-3 Airblast Test Results

Range (feet)	S Radial			NE Radial			NW Radial		
	Peak Pressure (psi)	Positive Duration (msec)	Arrival Time (msec)	Peak Pressure (psi)	Positive Duration (msec)	Arrival Time (msec)	Peak Pressure (psi)	Positive Duration (msec)	Arrival Time (msec)
42	13.8	11.8	20	13.1	13.8	22	11.4	11.8	24
78	6.68	15.7	45	5.17	15.7	49	6.25	15.7	49
110	3.53	19.7	70	3.32	21.6	74	4.07	20.7	66
130	3.06	21.6	85	2.78	23.6	91	2.82	21.6	93
160	2.02	23.6	112	1.83	24.6	116	1.96	22.6	116
200	1.14	25.6	145	1.16	25.6	149	1.71	23.6	149
250	1.21	27.8	189	0.94	27.6	193	1.09	24.6	191
325	0.87	31.5	258	0.66	29.5	260	0.64	25.6	258
400	0.57	33.5	324	0.46	31.5	324	0.60	27.6	324
500	0.41	35.4	414	0.45	33.5	416	0.50	29.5	416
610	0.28	37.4	514	0.27	35.4	514	0.28	31.5	510
740	0.23	39.4	631	0.20	36.4	630	0.33	32.5	626
880	0.17	41.3	758	0.16	37.4	756	0.26	34.4	741
1080	0.12	43.3	941	0.12	38.4	935	0.21	36.4	918
1320	0.08	45.3	1158	0.11	39.4	1141	0.19	37.4	1143

Table 8-3. QDT-3 Meteorological Data

SOTIN 3 Station - 2.7 Miles from QDT-3 Ground Zero		
Geometric Altitude (MSL Feet)	Wind Direction (Degrees TN)	Wind Speed (mph)
4848	180.0	4.5
5000	182.5	4.4
5500	191.6	4.1
6000	201.3	4.0
6500	211.2	4.0
7000	221.2	4.8
7500	227.7	6.7
8000	232.1	8.2
Instrument Trailer - 2000 Ft from QDT-3 Ground Zero		
Wind velocity: 10 mph		
Wind direction: 110 degrees azimuth relative to True North		

Table 8-4. Calibration Shot Airblast Test Results

Range (feet)	S Radial			NE Radial			NW Radial		
	Peak Pressure (psi)	Positive Duration (msec)	Arrival Time (msec)	Peak Pressure (psi)	Positive Duration (msec)	Arrival Time (msec)	Peak Pressure (psi)	Positive Duration (msec)	Arrival Time (msec)
42	89.0	16.7	5.9	91	----	----	78	15.7	7.9
78	17.3	18.7	25.9	16	18.7	25.9	16.5	18.7	25.9
110	8.5	23.6	47.9	8	25.6	47.9	8.8	23.6	47.9
130	6.4	27.6	62	6.3	29.5	62	6.2	28.5	63.9
160	4.3	30.5	85.9	3.7	31.5	85.9	3.8	30.5	85.9
200	2.5	32.5	120	2.7	33.5	120	3.6	33.5	120
250	2.8	36.4	162	2.1	36.4	162	2.14	36.4	160
325	1.8	41.3	226	1.34	40.4	226	1.05	40.4	224
400	1.09	44.3	294	0.93	43.3	290	1.05	42.3	290
500	0.78	47.2	382	0.75	45.3	380	0.71	44.3	378
610	0.62	49.2	480	0.54	48.2	476	0.55	48.2	476
740	0.46	51.2	598	0.40	50.2	592	0.47	51.2	592
880	0.38	53.1	724	0.33	52.2	718	0.37	53.1	718
1080	0.285	55.1	904	0.26	55.1	898	0.26	56.1	898
1320	0.195	57.1	1122	0.27	57.1	1114	0.21	58.1	1114

Table 8-5. QDT-3 Debris Data Summary

Range (ft)	Radial			Range (ft)	S Radial		NE Radial		NW Radial	
	Area 3 (10 ft x 10 ft)				Area 57.5 ft x 50 ft		Area 57.5 ft x 50 ft		Area 57.5 ft x 50 ft	
	S	NE	NW		Left Segment	Right Segment	Left Segment	Right Segment	Left Segment	Right Segment
125	135	122	126*	130-187	143	---	273	---	---	---
250	67	49	188	187-245	395	---	179	---	---	---
375	18	15	60	255-312	179	---	130	---	410	---
500	1.1	2	42	312-370	90	---	91	---	721	---
625	0	1	7	380-437	70	54	39	37	271	---
750	0	0	4	437-495	68	20	32	8	227	---
875	0	0	2	505-562	43	15	16	11	---	103
1000	2	0	2	562-620	13	12	4	10	---	52
Total	233	189	431	630-687	15	9	2	5	---	33
Number of Fragments 4732				687-745	4	5	2	2	---	12
Area $A_0 = 190,900 \text{ ft}^2$				755-812	6	4	0	2	8	9
Total Area				812-870	1	5	4	2	13	5
$A_T = \pi (1000^2 - 125^2)$				880-938	1	1	0	2	3	2
$A_T = 3,090,000 \text{ ft}^2$				938-995	0	0	0	1	2	3
$\frac{A_0}{A_T} = 6.2\%$				Total	1028	125	772	80	1655	219
Total Number of Fragments										
$N_T = \frac{4732}{0.062} = 76,300$										
*Data for two witness sheets										

Table 8-6. QDT-3 Debris Data Acquisition at 400 ft Range

Radial	Azimuth Relative To Magnetic South (deg)	Number of Fragments (Unit Area 33 x 24 ft)
S	330	21
	345	16
	015	11
	030	15
NE	090	18
	105	14
	135	30
	150	75
NW	210	46
	225	63
	255	30
	270	38
W (QDT-1, 2)	290	33
	300	23
Total		433

Table 8-7. Artificial Missile Data

Cluster No.	Origin (ft)		Missile Size (in.)	Number Recovered/Emplaced	Deposition Range (ft)		
	Depth	Range			Max	Min	Mean
R	0.5	6.0	1/2	15/32	130	40	71
			1	12/16	216	44	89
			2	8/8	234	78	134
			4	3/4	271	166	213
			8	2/2	340	186	263
			14	1/1	---	---	197
T	0.5	8.7	1/2	10/32	104	41	68
			1	11/16	153	57	88
			2	6/8	96	49	77
			4	4/4	152	103	121
			8	2/2	168	116	142
			14	1/1	---	---	89
V	0.5	12.7	1/2	5/32	103	83	90
			1	5/16	82	72	78
			2	8/8	113	80	89
			4	3/4	95	83	91
			8	2/2	86	86	86
			14	1/1	---	---	321
Z	0.5	17.0	1/2	1/32	---	---	72
			1	0/16	---	---	---
			2	3/8	82	76	79
			4	4/4	85	68	75
			8	2/2	77	63	70
			14	1/1	---	---	99
H	3.0	6.0	1/2	7/32	177	83	122
			1	6/16	162	36	92
			2	4/8	128	101	117
			4	2/4	170	160	165
			8	2/2	167	131	149
			14	1/1	---	---	78
K	3.0	9.0	1/2	5/32	111	84	92
			1	3/16	174	78	113
			2	7/8	87	78	84
			4	3/4	92	78	85
			8	2/2	110	100	105
			14	1/1	---	---	65

Table 8-7. Artificial Missile Data (Continued)

Cluster No.	Origin (ft)		Missile Size (in.)	Number Recovered/Emplaced	Deposition Range (ft)		
	Depth	Range			Max	Min	Mean
L	3.0	13.0	1/2	5/32	87	47	75
			1	5/16	86	50	72
			2	6/8	87	72	78
			4	4/4	82	63	74
			8	2/2	74	70	72
			14	1/1	---	---	78
N	3.0	17.0	1/2	0.32	---	---	---
			1	6/16	162	80	122
			2	3/8	43	32	37
			4	3/4	43	34	37
			8	2/2	53	35	44
			14	1/1	---	---	60
D	5.5	6.0	1/2	1/32	---	---	56
			1	12/16	119	74	98
			2	7/8	119	78	96
			4	4/4	114	83	105
			8	2/2	113	95	104
F	5.5	9.0	1/2	3/32	83	57	71
			1	3/16	66	55	59
			2	2/8	57	56	57
			4	4/4	68	57	63
			8	2/2	68	61	65
J	5.5	13.0	1/2	9/32	116	81	109
			1	4/16	68	54	56
			2	3/8	54	42	46
			4	4/4	65	36	53
			8	2/2	53	44	49
B	8.5	6.0	1/2	4/32	131	64	92
			1	6/16	83	41	64
			2	4/8	80	40	60
			4	2/4	73	37	55
			8	1/2	---	---	72
C	8.5	9.0	No data recovered				
A	11.5	6.8	1/2	1/32	---	---	41
			1	1/16	---	---	41
			2	2/8	43	43	43
			4	0/4	---	---	---
			8	0/2	---	---	---

Table 8-8. Soil Ejecta Test Data

Range (ft)	Number of Fragments		
	S Radial	NE Radial	NW Radial
DATA SOURCE: WITNESS SHEETS			
125	684	407	700
250	15	3	137
375	2	0	19
500	0	0	3
625	0	0	0
759	0	0	0
875	0	0	0
1000	0	0	0
DATA SOURCE: GROUND SURVEY*			
375 - 437	17	0	0
437 - 500	6	0	0
500 - 562	3	0	0
562 - 625	1	0	0
625 - 687	1	0	0
687 - 750	0	0	0
750 - 812	1	0	0
812 - 875	0	0	0
875 - 977	0	0	0
937 - 1000	0	0	0

*Right segment of cleared radial areas

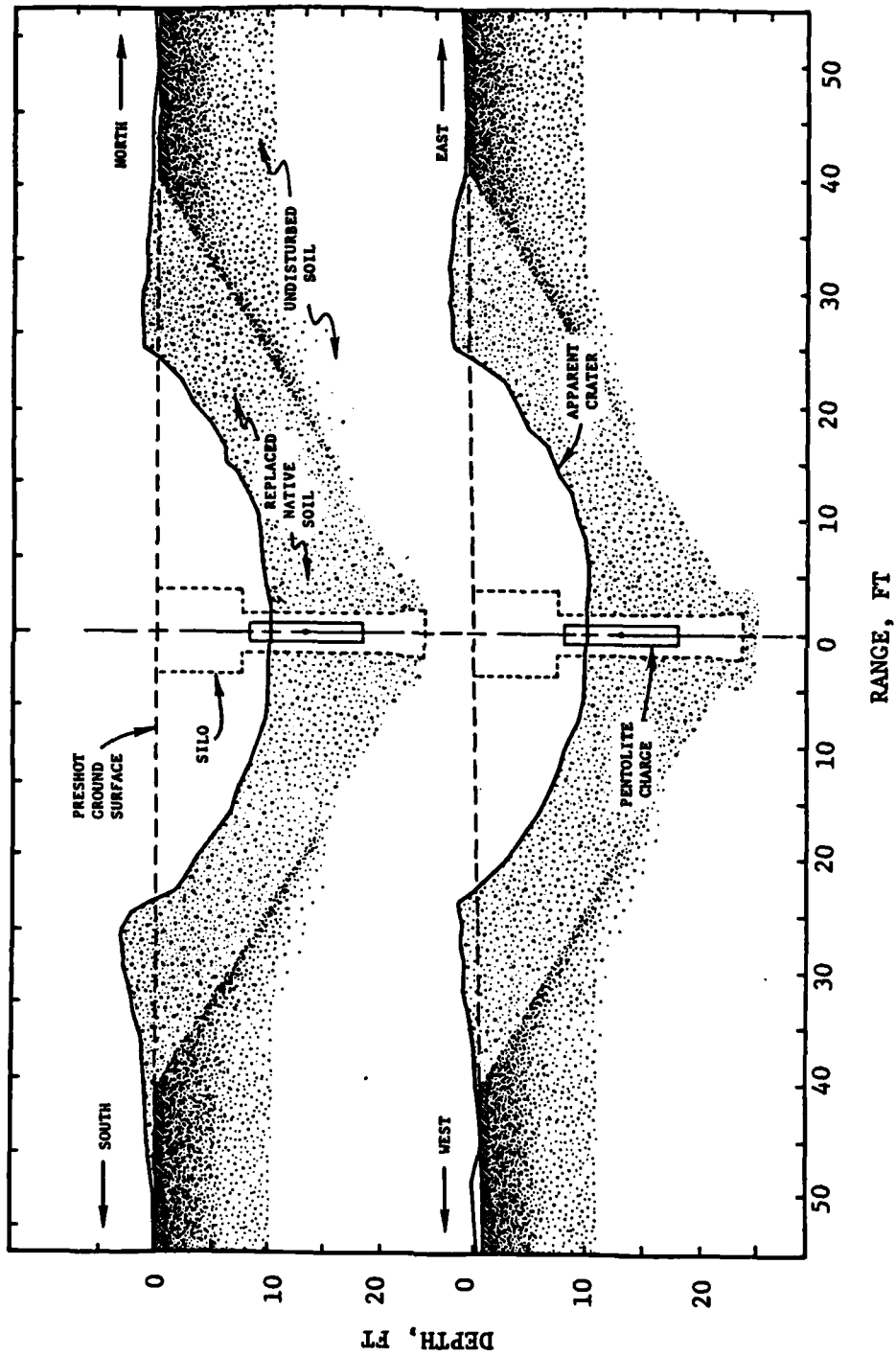


Figure 8-1. Profiles of QDT-3 Apparent Crater

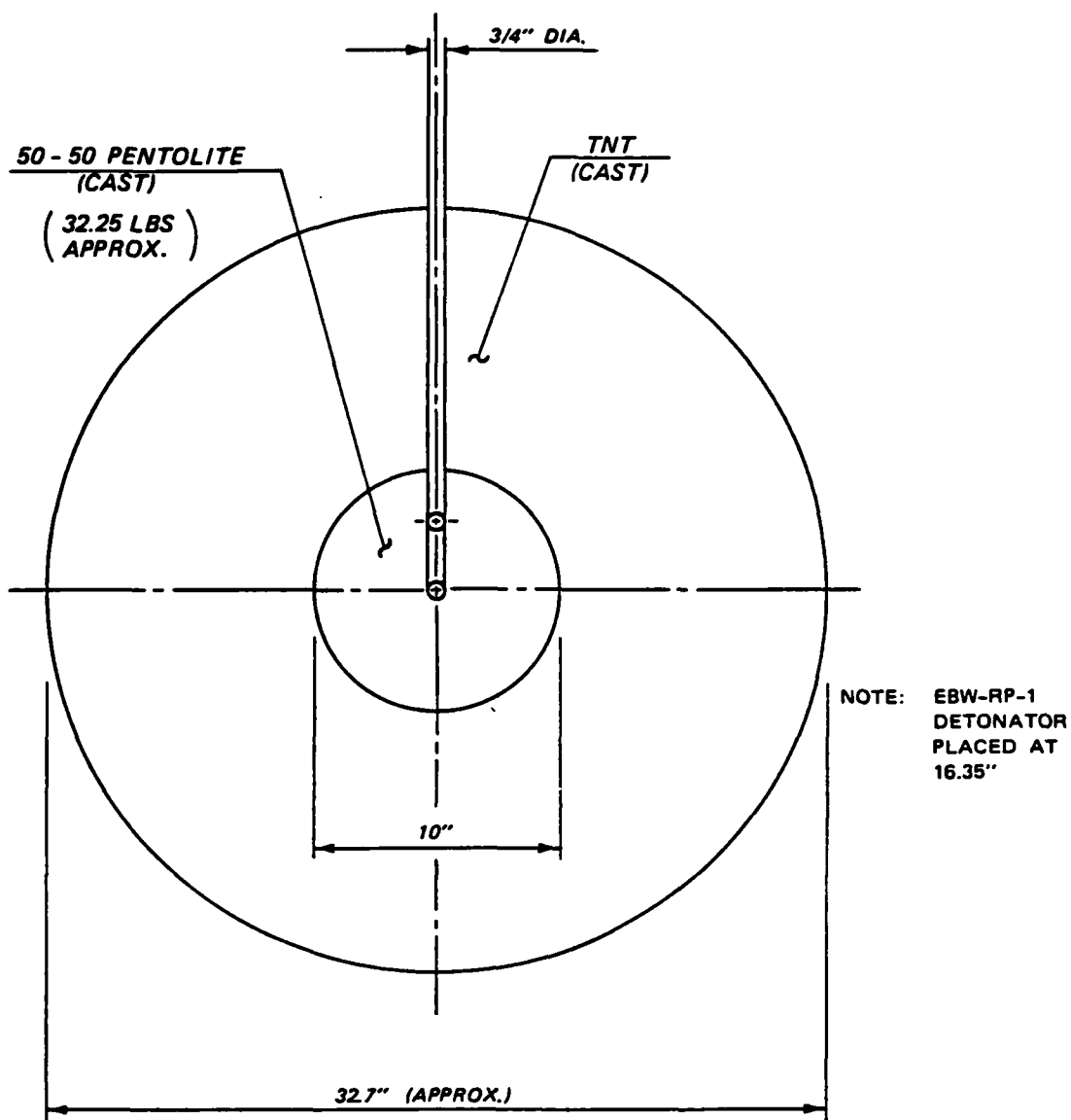


Figure 8-2. As-Built Charge for Calibration Shot

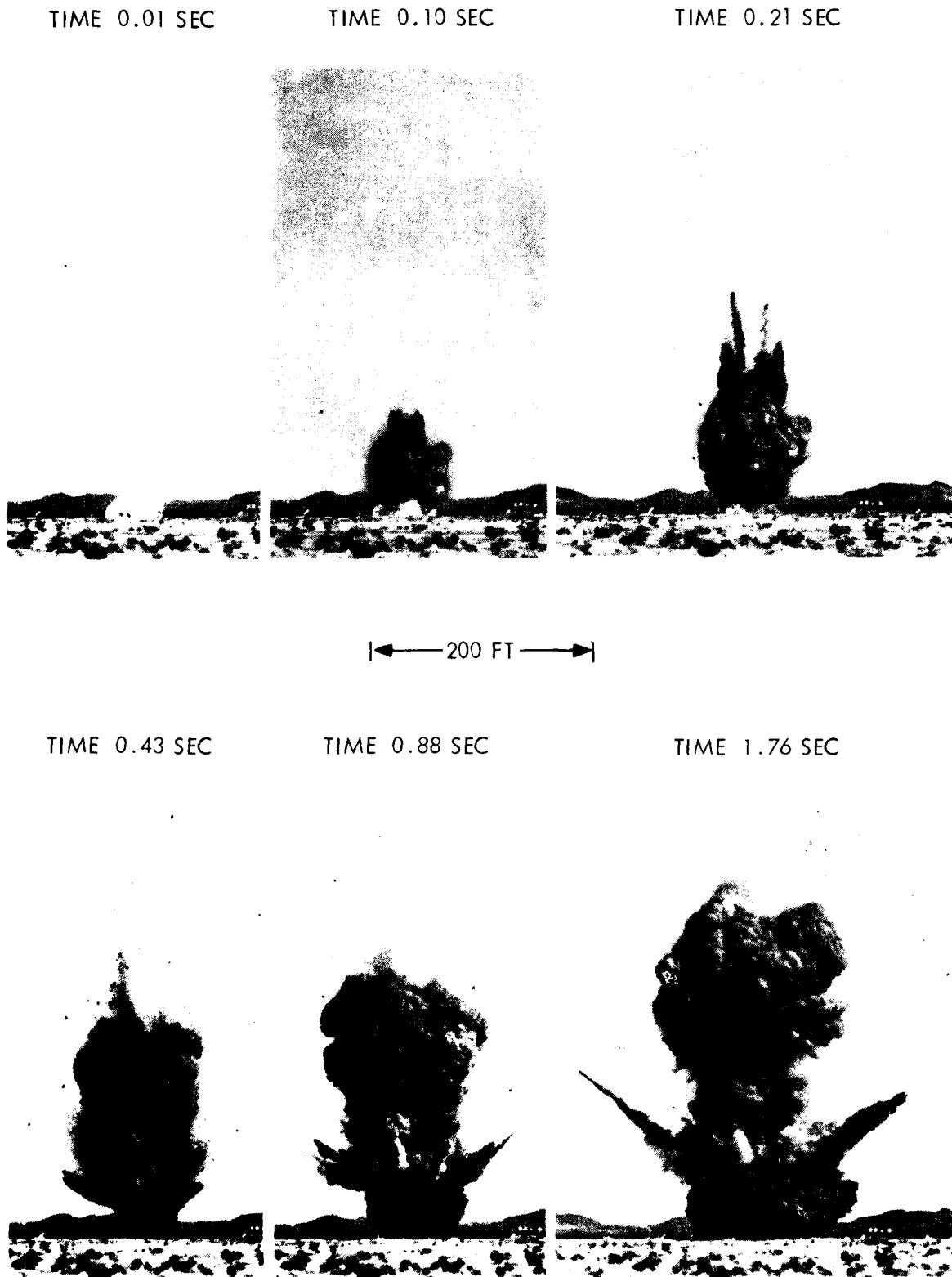
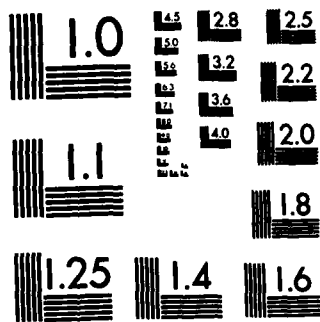


Figure 8-3. Photographic Sequence of QDT-3 Explosion



MICROCOPY RESOLUTION TEST CHART

9.0 TEST DATA ANALYSIS

9.1 Airblast Scaling

A comparative plot of peak pressures versus range is presented in Figure 9-1 for the following data:

- Average values of QDT-1 and QDT-2 peak pressures with associated ranges scaled to QDT-3 ranges by multiplication by the scale factor of 2.5.
- QDT-3 test results.
- QDT-3 analytical prediction.

It is evident that cube root scaling of peak airblast overpressure is readily applicable between the 1/10-scale and 1/4-scale events. This conclusion is substantiated for other airblast parameters such as positive duration and arrival time by the data comparison presented in Table 9-1. Comparison of airblast waveforms on a scaled time and range basis, as indicated by the representative case for BP-22 gage stations for QDT-2 and QDT-3 shown in Figure 9-2, again indicates good agreement. Only minor differences for the QDT-1 records occurred and were related to the advent of the delayed compression wave originating as a result of gas venting because of the ground eruption.

The second pulse of smaller amplitude occurs on all test records, including those of the calibration shot, at about 10 milliseconds following onset of the negative phase of the primary pulse regardless of the range or time scale. These secondary shocks have been observed on almost all tests involving the detonation of high explosive charges. The cause of this type of secondary shock is attributed to the implosion of rarefaction waves from the contact surface between explosion products and air.

The prediction curve shown in Figure 9-1 falls somewhat lower than the test data. However, as noted in Section 4.4, it was anticipated that, due to the computer zoning technique, some reduction in the peak pressure predictions would result. A representative waveform comparison for the prediction at 110 feet range and the QDT-3 test record is shown in Figure 9-3. The difference between the two pulses at early times is due to a rounding effect caused by computer zoning. It appears that an enhancement in the analytical results of the order of 30 to 40% may be warranted. Under these circumstances, the agreement between analytical and experimental results in Figure 9-1 would be more favorable.

The blast pressure data for QDT-3, plotted in Figure 9-4, indicates a divergence at the lower pressure levels among the data from the NW radial as compared to the results for the S and NE radials. This effect is attributable to the wind bias at surface level. In essence, the wind velocity was 10 mph downwind as the airblast wave propagated along the NW radial, and thereby enhancing the pressure amplitude, whereas for the S and NE radial, the wind velocity was about 5 mph upwind causing a pressure reduction. No effort was made to eliminate the wind bias from the respective records by means of analytical corrections.

At shot time, the ambient pressures at the test sites were generally about 12.5 psi. Figure 9-5 indicates the elevation histogram for the 100 Wing V Peacekeeper sites of interest. The average elevation is about 5100 ft and the corresponding ambient pressure approximately 12.2 psi. Therefore, it appears that the test data would be directly applicable to an operational event without requiring a correction factor for ambient pressure differences.

For the case of a peak overpressure level of 1 psi in conjunction with the quantity-distance scaling analysis, the QDT-3 data indicates a ground range of 270 feet.

In Figure 9-6, the peak pressure data for the calibration shot are compared with a curve established using References 9-1 and 9-2 for the surface burst of a 1000-pound TNT tangent sphere, where only small differences from a tangent hemisphere occur above a pressure level of 20 psi. As a result of the good agreement between test data and predictions, there does not appear to be any question regarding the reliability of the QDT airblast measurements.

In Figure 9-6, a comparison is shown of the curve for a 1000 pound TNT surface burst and the contour obtained from the QDT-3 test results. The two curves are parallel for pressure levels of 10 psi and less, indicating that one can approximate the QDT-3 contour by means of a surface burst of an equivalent TNT charge. Based on cube root scaling, the equivalent charge is estimated to be given by $1000 (270/422)^3 = 262$ pounds. The test charge was 2685 pounds of Pentolite with a TNT equivalence of 3034 pounds. Therefore, the relative blast efficiency of the QDT-3 explosion as compared to a surface burst was $262/3034$, or 8.6%.

9.2 Soil Ejecta Considerations

9.2.1 Backfill Properties

An evaluation was conducted by the Waterways Experiment Station (Reference 8-3) of the properties of the soil backfill added to the QDT-3 site excavation. The fill had been placed out to a radius of 7 feet from the reinforced concrete structure at the depth of the center of gravity of the charge, and increasing in radial extent out to a distance of 20 feet at ground surface.

The soil actually used for the fill was delivered to the test site in seven lots between 1 and 7 February 1984. A sieve analysis was performed independently for each lot. The mean gradation curve for the entire lot, along with its standard deviation, is shown in Figure 9-7 where it is compared with the criterion gradation band of the original backfill specifications. The observed data fall within the required band.

Prior experience with granular materials native to the Peacekeeper siting area suggested that the QD soil be placed at a uniform dry density equal to or in excess of 100 lb/ft³. Field density data collected during construction of the fill indicate that a fairly uniform placement was achieved and that the average dry unit weight was 110 lb/ft³.

Mechanical property tests were conducted to determine stress-strain and strength characteristics of the QD soil in a stress range of 0-10,000 psi. The principal objective of these experiments was to establish a data base for comparison with similar dynamic properties of the soil characteristics of operational sites. A total of eleven laboratory uniaxial strain compressibility tests were conducted, as well as eight constant confining pressure triaxial compression shear tests and two comparisons by hydrostatic compression tests. Results of this test program are discussed in detail in Reference 8-3. Recommendations are made of stress-strain and strength relations to be applied in the modeling of the QD soil for comparisons of interest.

9.2.2 Cratering Effects

Table 9-2 presents a comparison of the QDT crater radii with data from a number of buried bursts in alluvium and wet clay. It is of interest to note that the crater radii for QDT-1 and QDT-2 are approximately equal even though the crater from the QDT-1 event was refilled with native soil and compactness reconstituted by tamping, such that the ground zero locations for the two tests were the same.

The scaled crater radius for QDT-3 is about 30% smaller than scaled results for QDT-1 and QDT-2, for which no explanation is available. However, comparison of the QDT-3 value with the scaled Stagecoach test data indicates reasonable agreement. In an overall sense, there does not appear to be any major anomaly in the QDT cratering results.

9.2.3 Ejecta Scaling

As stated in Section 5.0, the gradations of the QD soil were intended to be similar to the operational site characteristics and, therefore, the ejecta sizes would be the same for the full-scale event as compared to the QDT-3 distribution, with the number of ejecta in each size category being enhanced by a factor of 64. Since the maximum QDT-3 range for the ejecta was about 300 feet, approximately the same range would be anticipated for the full-scale in-silo explosion with higher fragment densities at closer ranges. This conclusion is predicated on the assumption that the launch velocities and launch angles are similar between the 1/4-scale and full-scale events. It appears, therefore, that soil ejecta will not be of major significance toward quantity-distance considerations.

With reference to the possible occurrence of large earth clumps due to the natural cohesiveness of the soil particulate, the discussion in Section 5.2.4 indicates that, for a full-scale explosion, the range to a fragment density of one per 600 sq ft, is estimated to be approximately 1600 feet. The analysis associated with this result was based on the assumption that 10% of the soil fractured like rock. The value of 10% is considered to be highly conservative, perhaps by an order of magnitude, and was applied for the purpose of determining an upper bound estimate of safe distance for earth clumps for comparison with the ground range of 1750 feet of interest. It appears reasonable to conclude that the impact of earth clumps in the evaluation of quantity-distance for a full-scale event is negligible.

9.3 Structural Break-Up Characteristics

9.3.1 Large Fragment Survey

Much of the pre-test analysis in Section 6.0 concentrated on understanding the response mechanisms involved in structural break up and predicting the size and behavior of the resulting large fragments. While the large fragments may not be of direct concern in quantity-distance (Q-D) calculations (i.e., their number has little effect on the one fragment per 600 sq ft criterion), the fractures between them are the source of the smaller fragments which are of direct Q-D concern. Therefore, by understanding the

break up and behavior of these large fragments, it was felt that a better understanding of how to scale the number and size of small fragments could be achieved.

Figure 9-8 is a comparison between the predicted and actual, far-field, large fragment locations and sizes. In general, the observed data agreed quite well with the predicted response. With only a few notable exceptions, the structure broke in the expected manner with the resulting fragments having the expected initial velocities and launch angles.

The closure failed in shear, as expected, although it broke into three, instead of two, large pieces. The lateral load that was postulated for the portion of the closure overhanging the headworks seems to have been correct because the trajectory of the piece corresponded unbelievably well with the prediction. The data suggests that this unbalanced lateral load also acts on the other two pieces. Such an unbalanced load would have caused them to travel in an easterly and westerly direction (consistent with the photos). They were not found within the 2500 feet from ground zero that was surveyed in those directions. Note, also, that the disproportionate number of small black (closure) fragments that were found in the south, east, and west directions is consistent with this conclusion.

As predicted, spalling did not cause mid-plane failures of any structural element, but it did contribute to separation of the headworks cap and the headworks at the construction joint between them. Once they separated, they independently failed in flexure and hoop tension with fractures in roughly the locations predicted before the test. As Figure 9-9 indicates, approximately 60% of the headworks cap (green, level B) and 30% of the headworks (yellow, level C) concrete was recovered in the form of large fragments. Because the rebar projecting from the large pieces was stripped of concrete, another 30 and 20% of these layers, respectively, is believed to have been reduced to small fragments. All in all, the behavior of about 10% of level B and 50% of level C could be indirectly deduced after the test. In general, the headworks regions fractured circumferentially, as predicted, although there appears to be a tendency for failure planes about midway through the width of the headworks cap. These are probably due to radial strains or torsion which the analytical tools used in the prediction could not model.

Another important response that was not foreseen (but should have been) was splitting of the headworks in the personnel access system (PAS) region. PAS plug A and the upper part of the PAS cavity pipe was located near the expected point of impact. The

solid steel PAS plug B and the lower portion of the cavity pipe, however, was not found (although an extensive search was made). It is postulated that the blast drove plug B through the lower cavity pipe wall, breaking up the headworks and headworks cap concrete in the process. Also, pressurization of the gyro alignment system cavity in the headworks would have created tensile stresses that the structure was not reinforced to resist. This would explain the apparently severe fracture of the headworks in this region. In any case, rupture of the concrete surrounding the PAS may have released a significant number of Q-D criteria type fragments.

The LER wall and footing broke into the 30-degree arc segments that were expected and did not contribute many fragments of importance to Q-D. The footings did not separate from the wall, which suggests that the load beneath them was greater than that assumed in the calculations of Section 6.0. As predicted, the footing sheared along the inside surface of the LER wall due to the very high unbalanced pressures in this region. The orange pieces of footing that were found at the larger distances most likely came from this area.

It is worth noting, however, that while the steel liner was stripped from every large fragment that was found, no pieces of liner were found at ranges of concern to the Q-D issue. The overwhelming drag forces on these fragments must prevent them from traveling very far.

Finally, the ranges that fragments traveled compares reasonably well with the analytical prediction, suggesting that the combination of velocities and launch angles was correctly predicted. The agreement is good considering the uncertainties inherent in this type of problem. One aspect of significance is that analysis of the photography showed that most of the fragments radiated from a single point, indicating that separation of the large fragments occurred early and within a short span of time.

9.3.2 Small Fragment Survey

In order to use the QDT-3 test results in predicting the full-scale Q-D criteria, the behavior of the concrete between each of the large fragments must be understood. It appears that the postulated $2/3$ rebar spacing width of these interstitial zones, as they are termed, is correct. The maximum concrete fragment size within these zones was assumed to be governed by the rebar spacing. Figure 9-10 shows the size distributions measured in the test for fragments from various regions of the structure. They are based on data from samples collected on the radials. The maximum size in distributions appears to

correspond to the maximum rebar spacing in the indicated region. The median size fragment appears to be about half the average rebar spacing in a region. This also checks with cracks that were seen in some of the large fragments midway between the rebar. It is also worth noting that a sizable number of the small Q-D criteria fragments were comprised mostly of aggregate.

9.3.3 Large Fragment Scaling

The determination of full-scale response from the 1/4-scale results is an exceedingly difficult problem. In the event material properties were unaffected by the scale factor, fragment size would scale linearly and the velocity/launch angles would remain the same.

Unfortunately, the literature indicates a strong relationship between scale, strain rate, element size, and material strength. The left side of Figure 9-11 is typical of data relating strain rate to yield strength for rebar like that used in the QDT-3 test article. Based on the NONSAFE results of Section 6.0, a strain rate of about 20 is reasonable in the QDT-3 test. Since strain rate is inversely proportional to the scale factor, this suggests a full-scale strain rate of about 5. As one can see, the data clearly indicates the yield strength of the rebar is sensitive to such a change in strain rate. Note that although (limited) data indicates less sensitivity of ultimate strength and failure strain, there is still a definite reduction in these parameters with increased scale.

Two other factors are worth mentioning in the context of strength reduction. First, if there is more material in a full-scale fragment, it will contain more microcracks and, therefore, have a greater probability of breaking up. Second, the steels used in the QDT-3 test article were generally higher strength than those believed to exist in the actual silos.

While one can definitely say that an operational silo would be weaker in the event of an explosion than the QDT-3 structure, neither the existing data base or the available analytical tools are sufficient to precisely define this strain-rate/size sensitivity or how it affects the fracture pattern of a structure like the one in question. Considerable engineering judgment is, therefore, necessary to estimate the number and size of fragments at full scale. As indicated in the lower left corner of Figure 9-11, a bounding conjecture was used to determine the scaling of the large fragments. The net effect of the assumptions is to double the number of interstices in the full-scale structure. Such an assumption could correspond to the fracture pattern postulated in the right of Figure 9-11. This fracture pattern does not seem unreasonable considering the reductions in strength previously discussed.

9.3.4 Small Fragment Scaling

Figure 9-12 summarizes the source of most small fragments in the QDT-3 test. First, surface spalling, scabbing and peeling of the liner off the large fragments appears to have contributed few Q-D criteria type fragments. In-flight breakup of large fragments may be a factor, but most small fragments appear to come from the interstices between the large fragments at the time they initially separate.

The fact the data indicates the size of the small fragments (in the QDT-3 test) is related to the rebar spacing and aggregate size, geometric scaling of the small fragment distributions between the interstices is believed to be reasonable. There are some uncertainties associated with this assumption that need to be discussed, however.

First, strain rate and size effects may result in smaller fragments. Because small fragments contain no rebar, have less severe aspect ratios, and see more uniform loads, these effects should be less significant than with large fragments. Another possibility is that full-scale large fragments (which are postulated to be at least twice the size of the 1/4-scale large fragments) will have a greater tendency to break up in-flight. Finally, the flow field effects on small particles may scale differently, affecting not only the size of the small fragments but the way they behave once released.

As an upper bound for the scaling of small fragments it is estimated that the number of fragments observed for QDT-3 may be doubled with geometric scaling of size.

9.3.5 Strain Data Evaluation

The QDT-3 model was instrumented with strain gages at 16 locations with 15 of the sensors yielding data. All of the gages exceeded their strain limits and failed within about the first two milliseconds after charge initiation. Figure 9-13 indicates the results of a preliminary analysis of the QDT-3 strain gage data. The inconsistency between the postulated behavior in this figure and the post-test speculations regarding structural failure mechanisms based on features of the large fragments suggests that the strain data cannot be used for evaluating the failure modes. Progressive events during the explosion may have caused major perturbations in the fragment evolution history.

9.4 Debris Density Distribution

9.4.1 Symmetry Evaluation

Table 9-3 indicates the variation of the QDT-3 debris data with azimuth at a range of 400 feet with Figure 9-14 presenting a polar coordinate plot of the results. It is quite evident that the density distribution is skew symmetric in the direction of the NW radial due to the effect of wind velocities at shot time.

Table 9-4 indicates the potential impact of a 10 mph wind on the debris distribution associated with an in-silo explosion. It appears that over the spectrum of fragment sizes and initial conditions of interest, the enhancement of maximum range would not exceed an increment of the order of 300 feet.

9.4.2 Size Distribution

The debris size distribution for a group of 3400 fragments is shown in Figure 9-15. This group of fragments was collected at the test site and shipped to TRW/Space Park for detailed laboratory analysis. The remainder of the debris data was analyzed only to a limited extent at the test site. The slope of the curve in Figure 9-15 indicates that the number of fragments having a principal dimension of $L + 1/4$ inch is 0.66 times the fragment number for length L for each successive length category. Results of an evaluation of the variation of dispersion range with fragment size are shown in Table 9-5 for the entire set of QDT-3 data.

9.4.3 Shape Factor

A question of particular significance is how the shape factor for the QDT-3 fragments compared with the characteristics of the Distant Runner debris that were assumed as part of the pre-test trajectory analysis. As a representative example, the mass distribution for 796 one-inch fragments is plotted in Figure 9-16. The average shape factor, α , based purely on weight considerations turned out to be 0.17 rather than the 0.44 value for the Distant Runner Test. The average QDT-3 weight for a 1-inch fragment was 6.5 gm, whereas an average value of 16.7 gm was estimated for Distant Runner.

As discussed in Section 7.1, it is necessary to take into account the cross-sectional area of a fragment during the course of its trajectory, which coupled with its volume would yield the value of A/V required for the drag factor in the equations of motion. Figure 9-17 indicates the relative frequency of intermediate and minimum dimensions of

fragments with maximum dimension of one inch. Similar evaluations were performed for fragments of other lengths.

Since photographic data indicated that tumbling was quite typical of most fragments, an average cross-sectional area was assumed to be given by the following relation:

$$A = \frac{1}{3} (L_1L_2 + L_1L_3 + L_2L_3)$$

where L_1 is the principal dimension and L_2 and L_3 are the other two dimensions measured orthogonally. The area shape factor was designated as β and defined by:

$$\beta = \frac{A}{L^2}$$

An evaluation was made of the ratio α/β as applicable to the equations of motion. Figure 9-18 presents the variation of the parameters α and α/β as a function of principal fragment dimension L . Over the range of fragment lengths of 1/2 inch to 7 inches the value of α/β decreased from 0.44 to 0.18.

9.4.4 Fragment Density Estimates

Calculations were made of debris density per 600 sq ft as a function of range from 250 to 1000 feet, with results shown in Table 9-6 for the composite set of data covering the S, NE, and NW radials and for the NW radial separately. The estimate for only the NW radial data constitutes an assumption that this extreme distribution is representative of the total area in all directions and, therefore, corresponds essentially to a conservative upper bound value. For the results presented in Table 9-6, the data from the witness sheets were assumed as representative of uniform distributions over bands of 10-foot lengths across the 100-foot widths of the respective radials, and that the total quantity for each band was amortized equally between the adjacent segments.

A plot of the density data is shown in Figure 9-19 as a function of range. A least squares analysis covering various analytical functions was performed for the data, with the minimum standard deviation obtained for the following exponential functions:

$$\text{S, NE, and NW Radials: } N_{1/4} = 544 e^{-0.00776 R}$$

$$\text{NW Radial Only : } N_{1/4} = 2023 e^{-0.00850 R}$$

where $N_{1/4}$ is the number of fragments per 600 square feet and R is the range in feet.

For the first relation the range corresponding to a density of one per 600 sq ft is 812 feet, and for the second relation the range is 896 feet. There appears to be reasonably good correlation with the test prediction of 721 feet.

Equivalent exponential functions as indicated in Figure 9-19 are as follows:

$$\text{S, NE, and NW radials: } N_{1/4} = e^{6.3 \left(1 - \frac{R}{812}\right)}$$

$$\text{NW radial only: } N_{1/4} = e^{7.6 \left(1 - \frac{R}{896}\right)}$$

For the soil ejecta distribution, the test data indicated a range of about 300 feet for a density of 1 per 600 square feet as compared to the prediction of 390 feet.

9.5 Dust Cloud Considerations

9.5.1 Photographic Results

Figure 9-20 indicates the variation with time of the velocities and angles of fragments ranging in size from 3 to 40 inches as observed immediately after exiting from the expanding dust cloud. Since the evaluation is based on the projection of the fragment path in the focal plane normal to the line of sight, the velocities are essentially lower bounds whereas the angles are upper bounds.

The test data plotted in Figure 9-20 and 9-21 indicate the characteristics of relatively large fragments of limited number as compared to the extensive distribution of 1/2- to 2-inch fragments. Similar information for the smaller size fragments was unavailable due to a limitation in resolution.

A set of contours are shown in Figure 9-20 for velocities in free air of 3-inch and 10-inch fragments with launch velocities of 500 and 1000 ft/sec. Similar curves for fragments of greater lengths would lie at higher values. In Figure 9-20, a curve is also plotted for the vertical velocity of the top of the dust cloud.

Comparison of the data in Figure 9-20 appears to indicate that the dust cloud tends to accelerate fragments moving with lower relative velocities and decelerate fragments with higher relative velocities. This effect is attributable to the high densities within the dust-laden cloud causing large drag forces. Since drag effects increase with decreasing

fragment size, it is anticipated that the convergence of fragment velocities to that of the dust cloud would occur more rapidly for the fragments smaller than the sizes indicated in Figure 9-20.

9.5.2 Impact Analysis

An evaluation was performed of the dust cloud impact on the debris sizes and scaling aspects of interest. The analysis was based on a one dimensional model limited to fragment propagation only in the vertical direction. Characteristics of the dust cloud growth are shown in Table 9-7.

Results of the analysis are presented in Table 9-8. As a figure of merit of the dust cloud impact, a comparison is made of the fragment velocity, V_E , as it exits the cloud with the velocity of the fragment, V_A , based on propagation in free air. Both velocities correspond to a range equal to the cloud height at exit time. A value of $V_E/V_A = 1$ would signify zero dust cloud impact relative to the subsequent ballistic trajectories.

The analytical results in Table 9-8 were developed for fragment launch times, or time delay following charge initiation, of 10 and 50 milliseconds. The lower bound value of 10 ms was selected on the basis of the duration of the structural loading history shown in Figure 6-8(a), and the associated data constitute upper limits.

For the case of a fragment launch velocity of 250 ft/sec, the values of V_E/V_A are significantly lower for a time delay of 50 ms as compared to 10 ms. For higher launch velocities, the corresponding values of V_E/V_A would be progressively lower, and less than unity in some cases.

It appears, therefore, that the impact of the dust cloud, to a first order extent, is relatively negligible within the bounds of uncertainty of launch time within a few tens of milliseconds. It is highly probable that the structural fragmentation phenomena would result in some spectral distribution of launch times.

It can be shown that similar considerations are applicable to the case of a full-scale event where times and dimensions for the cloud growth and fragment motion scale as the cube root law, with velocities and angles invariant. It appears reasonable to conclude that the dust cloud impact may be considered negligible in the development of quantity-distance estimates for the structural debris.

Table 9-1. Scaling Comparison of Positive Duration and Arrival Time

Range* (ft)	Positive Duration (msec)		Arrival Time (msec)	
	Average Value QDT-1 and -2*	QDT-3	Average Value QDT-1 and -2*	QDT-3
42	11.6	12.5	25	22
78	18.2	15.7	48	48
110	20.8	20.7	74	70
130	22.9	22.3	93	90
160	24.2	23.6	120	115
200	25.4	24.9	156	148
250	26.6	26.7	194	191
325	28.7	28.9	260	259
400	30.5	30.9	326	324
500	32.5	32.8	415	415
610	33.7	34.8	515	513
740	35.0	36.1	627	629
880	36.0	37.7	750	752
1080	37.1	39.4	931	931
1320	39.0	40.7	1155	1147

*QDT-1 and QDT-2 values scaled to QDT-3 by multiplication by factor of 2.5.

Table 9-2. Comparison of Cratering Effects

Test	TNT Charge (lb)	Burst Depth (ft)	DOB/W ^{1/3} (ft/lb ^{1/3})	Crater Radius (ft)	R/W ^{1/3} (ft/lb ^{1/3})	R/W ^{1/3.4} (ft/lb ^{1/3.4})
ALLUVIUM SOIL						
QDT-1	194	4.8	0.83	12.9	2.23	2.74
QDT-2	194	4.8	0.83	12.3	2.12	2.61
QDT-3	3,034	13.2	0.92	23.7	1.64	2.24
Sprint	5,000	----	----	38.0	2.22	3.10
Stagecoach I	40,000	80.0	2.34	57.0	1.67	2.52
Stagecoach II	40,000	17.1	0.50	50.5	1.48	2.24
Stagecoach III	40,000	34.2	1.00	58.6	1.71	2.60
Scooter	10 ⁶	125	1.25	154	1.54	2.65
WET CLAY SOIL						
Essex 3MU	18,000	9.8	0.38	69.6	2.66	3.90
Essex 3MS	23,000	9.8	0.35	71.2	2.50	3.72
Essex 6MU	16,000	19.7	0.78	77.4	3.07	4.50
Essex 6MS	20,000	19.7	0.72	85.9	3.16	4.67
Essex 12MU	16,000	39.4	1.56	49.2	1.95	2.86
Essex 12MS	20,000	39.4	1.45	61.6	2.27	3.35

Table 9-3. Debris Distribution Symmetry Evaluation at 400-Foot Range

Radial	Azimuth Relative to Magnetic South (deg)	Number of Fragments	Fragments per 600 sq ft
400 FT RANGE (Unit Area 33 x 24 ft)			
S	330	21	15.9
	345	16	12.1
	15	11	8.3
	30	15	11.4
NE	90	18	13.6
	105	14	10.6
	135	30	22.7
	150	75	56.8
NW	210	46	34.8
	225	63	47.7
	255	30	22.7
	270	38	28.8
W (QDT-1,2)	290	33	25.0
	300	23	17.4
		433 Total	23.4 Average
380-437 FT RANGE (Unit Area 57.5 x 50 ft)			
S	0	54	11.3
NE	120	32	6.7
S	0	70	14.7
NE	120	39	8.1
NW	240	271	56.6
		466 Total	19.5 Average

Table 9-4. Enhancement of Maximum Ranges Due to Downwind Velocity of 10 mph

Launch Velocity (fps)	Launch Angle (deg)	Maximum Range (ft)				
		0.5"	1"	2"	4"	8"
200	45	58	64	63	55	42
	65	66	69	68	58	44
	85	64	65	59	48	33
400	45	82	99	115	126	125
	65	95	115	131	140	137
	85	99	116	128	130	120
600	45	93	118	144	169	187
	65	111	139	167	193	210
	85	117	144	170	190	196
800	45	101	129	162	197	229
	65	121	154	191	229	262
	85	128	163	198	232	257
1000	45	107	138	176	218	261
	65	128	166	209	256	302
	85	138	176	219	264	303

Table 9-5. Variation of Fragment Distribution with Size

Range (ft)	No. of Fragments per Respective Lengths (in.)								Total
	0.50-0.75	0.75-1.00	1.00-1.25	1.25-1.50	1.50-1.75	1.75-2.00	2.00-7.00		
125-187	269	259	132	71	30	11	27	799	
187-250	209	200	122	72	48	26	49	726	
250-312	224	205	230	84	59	25	44	871	
312-375	197	228	249	108	87	29	50	948	
375-437	53	77	132	69	85	25	77	518	
437-500	19	32	75	55	60	33	108	382	
500-562	20	16	37	25	31	21	66	216	
562-625	5	4	11	5	9	12	49	95	
625-687	0	7	4	8	7	9	33	68	
687-750	1	0	2	1	1	0	22	27	
750-812	0	0	3	1	2	1	24	31	
812-875	1	1	1	2	1	2	23	31	
875-937	0	0	0	0	2	0	8	10	
937-1000	1	0	0	0	0	0	9	10	
Total	999	1029	998	501	422	194	589	4,732	

Table 9-6. QDT-3 Debris Density Variation With Range

Range (ft)	Average Range (ft)	S, NE, and NW Radials			NW Radial Only		
		Area (sq ft)	Total No. of Fragments	Fragments per 600 sq ft	Area (sq ft)	Total No. of Fragments	Fragments per 600 sq ft
250 - 312	281	9,375	973	62.3	3,125	567	109
312 - 375	344	9,375	979	62.3	3,125	771	148
375 - 437	406	15,625	575	22.1	3,125	321	61.6
437 - 500	469	15,625	412	9.41	3,125	262	50.3
500 - 562	531	15,625	245	9.41	3,125	138	26.5
562 - 625	594	15,625	99	3.80	3,125	58	11.1
625 - 687	656	15,625	72	2.76	3,125	39	7.49
687 - 750	719	15,625	28	1.08	3,125	15	2.88
750 - 812	781	18,750	33	1.06	6,250	23	2.21
812 - 875	844	18,750	34	1.09	6,250	22	2.11
875 - 937	906	18,750	16	0.512	6,250	9	0.864
937 - 1000	969	18,750	14	0.448	6,250	9	0.864

Table 9-7. Dust Cloud Growth Characteristics

Time (msec)	Height (ft)	Width (ft)	Vertical Velocity* (ft/sec)	Horizontal Velocity* (ft/sec)	Cloud Volume** (ft ³)	Cloud Density (lb/ft ³)
4	16	32	4000	4000	1.29 x 10 ⁴	15
67	68	79	825	373	3.08 x 10 ⁵	2.5
145	108	95	430	86	7.66 x 10 ⁵	1.0
223	137	105	367	63	1.19 x 10 ⁶	0.64
457	210	105	269	0	1.82 x 10 ⁶	0.42
613	215	105	32	0	1.86 x 10 ⁶	0.41

* Average values for time increments
 ** Assuming cylindrical column shape

Table 9-8. Evaluation of Dust Cloud Impact

Fragment Length (in.)	Fragment Launch Time (msec)	Fragment Launch Velocity (ft/sec)	Fragment Exit Time (msec)	Dust Cloud Height (ft)	Dust Cloud Velocity (ft/sec)	Fragment Exit Velocity (ft/sec)	Fragment Velocity in Free Air (ft/sec)	$\frac{V_E}{V_A}$
0.5	10	1000	130	100	419	564	490	1.15
		750	180	119	361	488	321	1.52
	50	500	210	130	336	456	198	2.30
		250	220	132	329	447	98	4.58
2	10	250	738	208	0	81	57	1.43
		1000	93	84	488	753	798	0.94
	50	750	145	106	398	613	563	1.09
		500	200	127	344	539	355	1.52
8	10	250	250	143	310	488	170	2.87
		250	698	208	0	170	142	1.20
	50	1000	80	77	522	883	920	0.96
		750	140	105	404	691	670	1.03
50	500	232	137	321	550	431	1.28	
	250	371	177	259	445	206	2.16	
	50	250	751	208	0	218	199	1.10

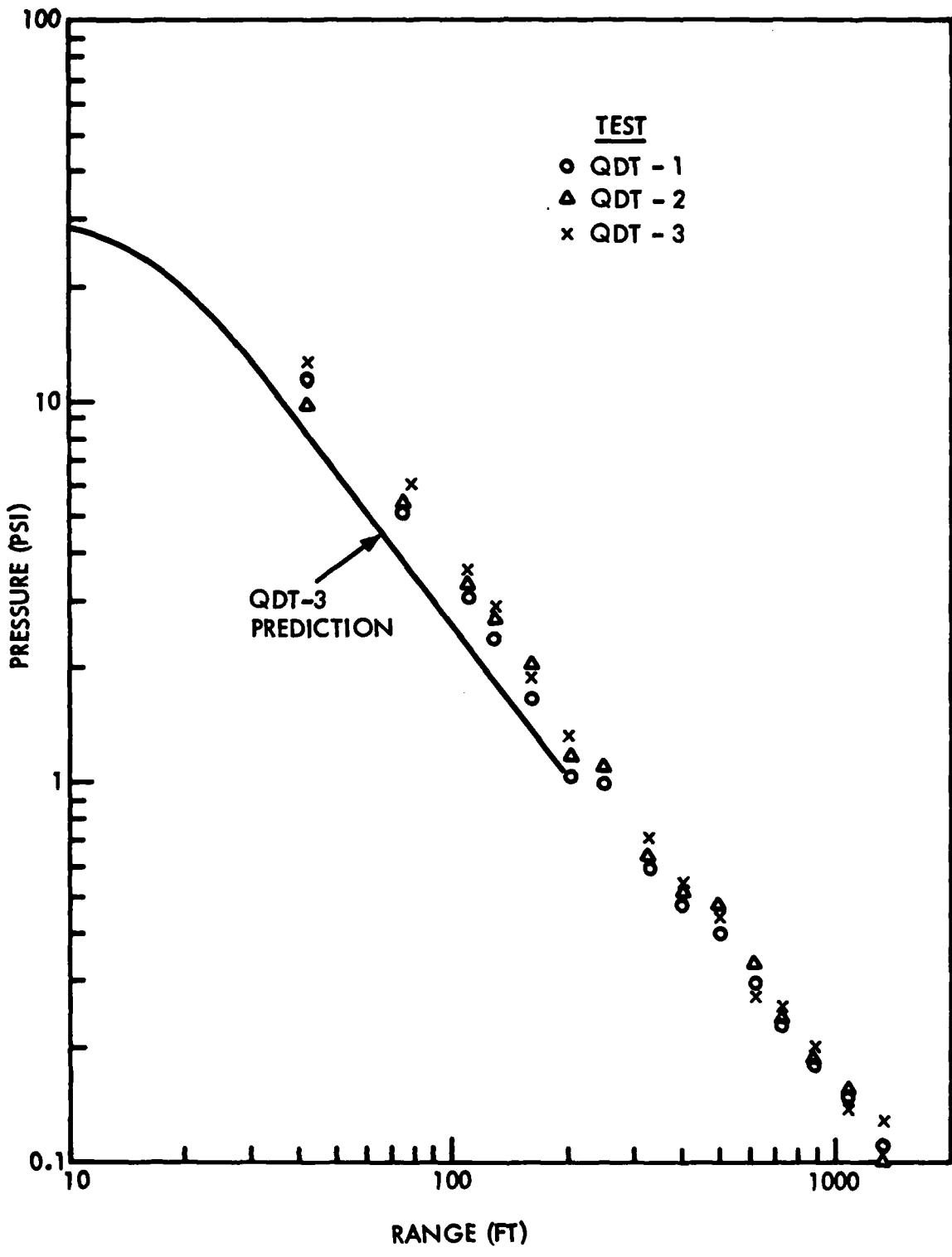


Figure 9-1. Comparison of QDT Airblast Data

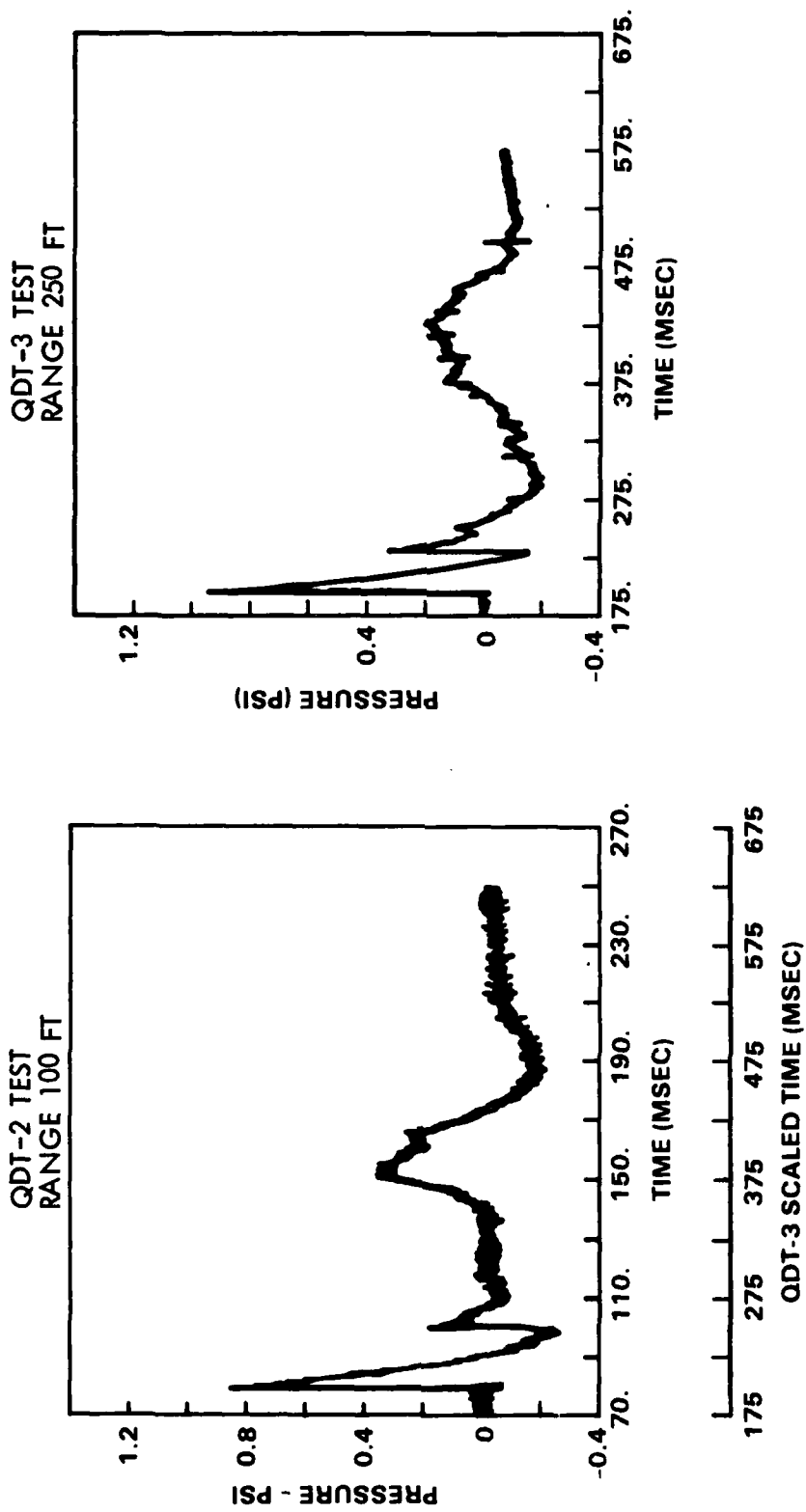


Figure 9-2. Airblast Waveform Comparison

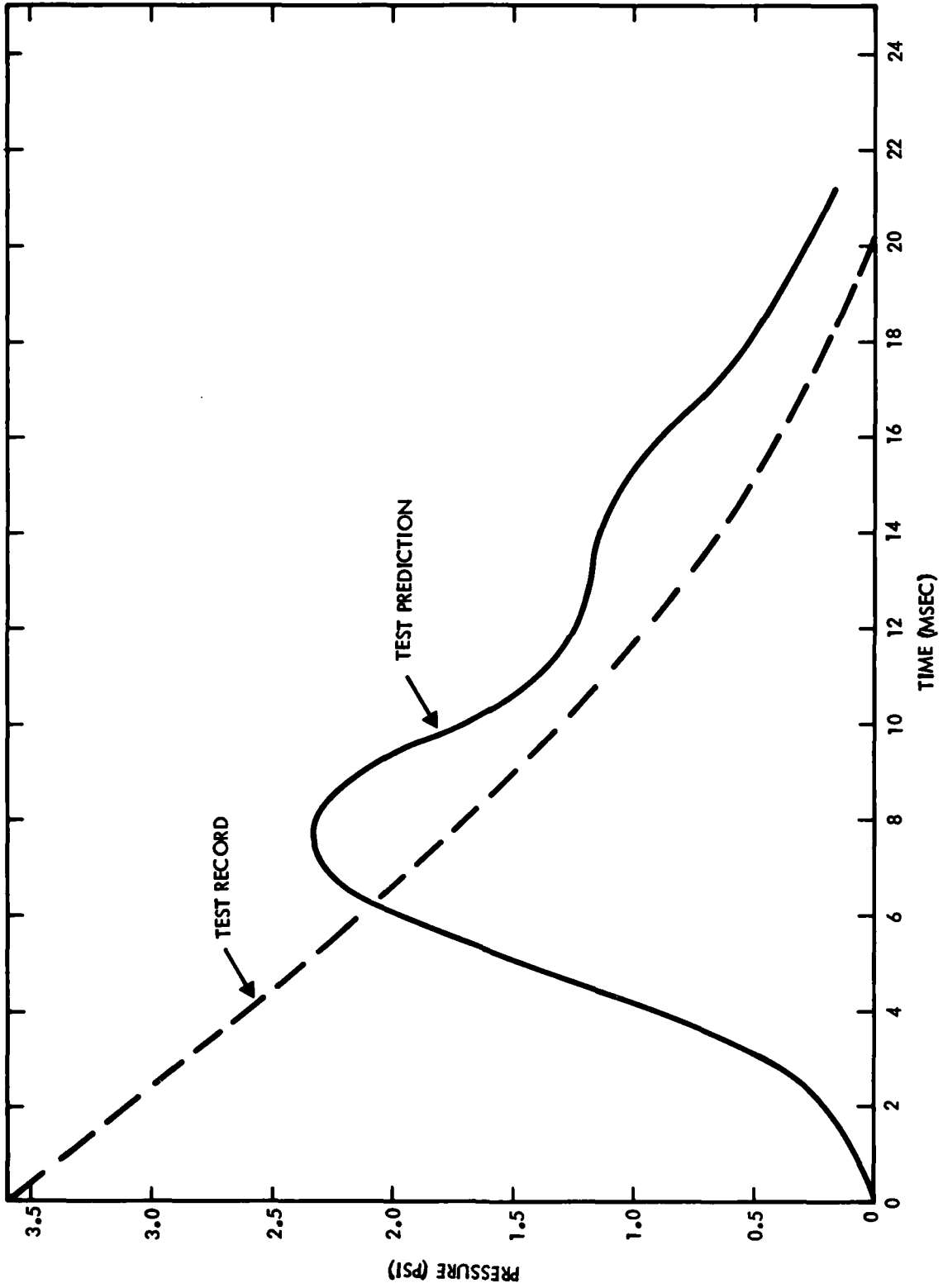


Figure 9-3. QDT-3 Pressure-Time History Prediction at 110-Foot Range

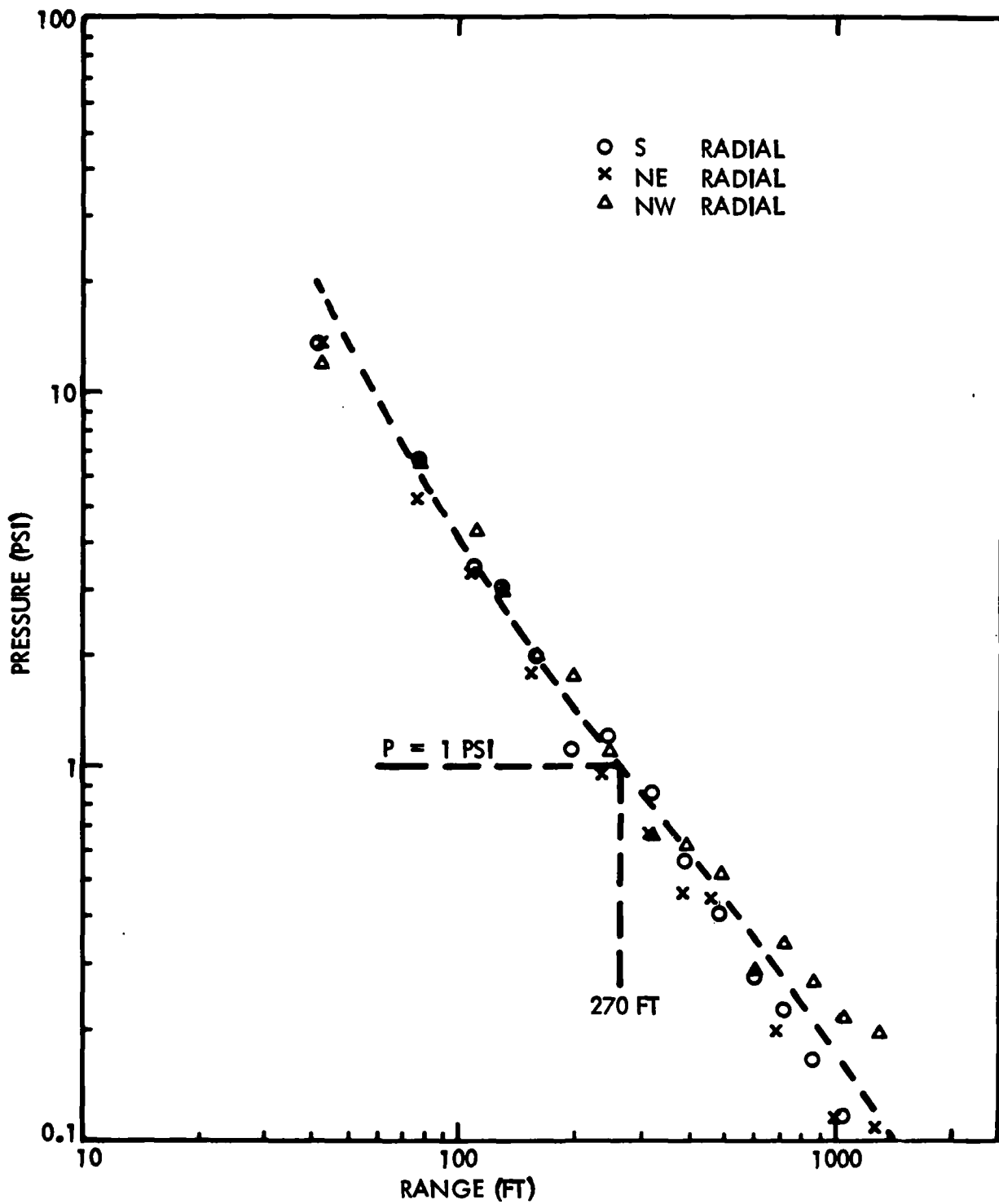


Figure 9-4. QDT-3 Blast Pressure Data

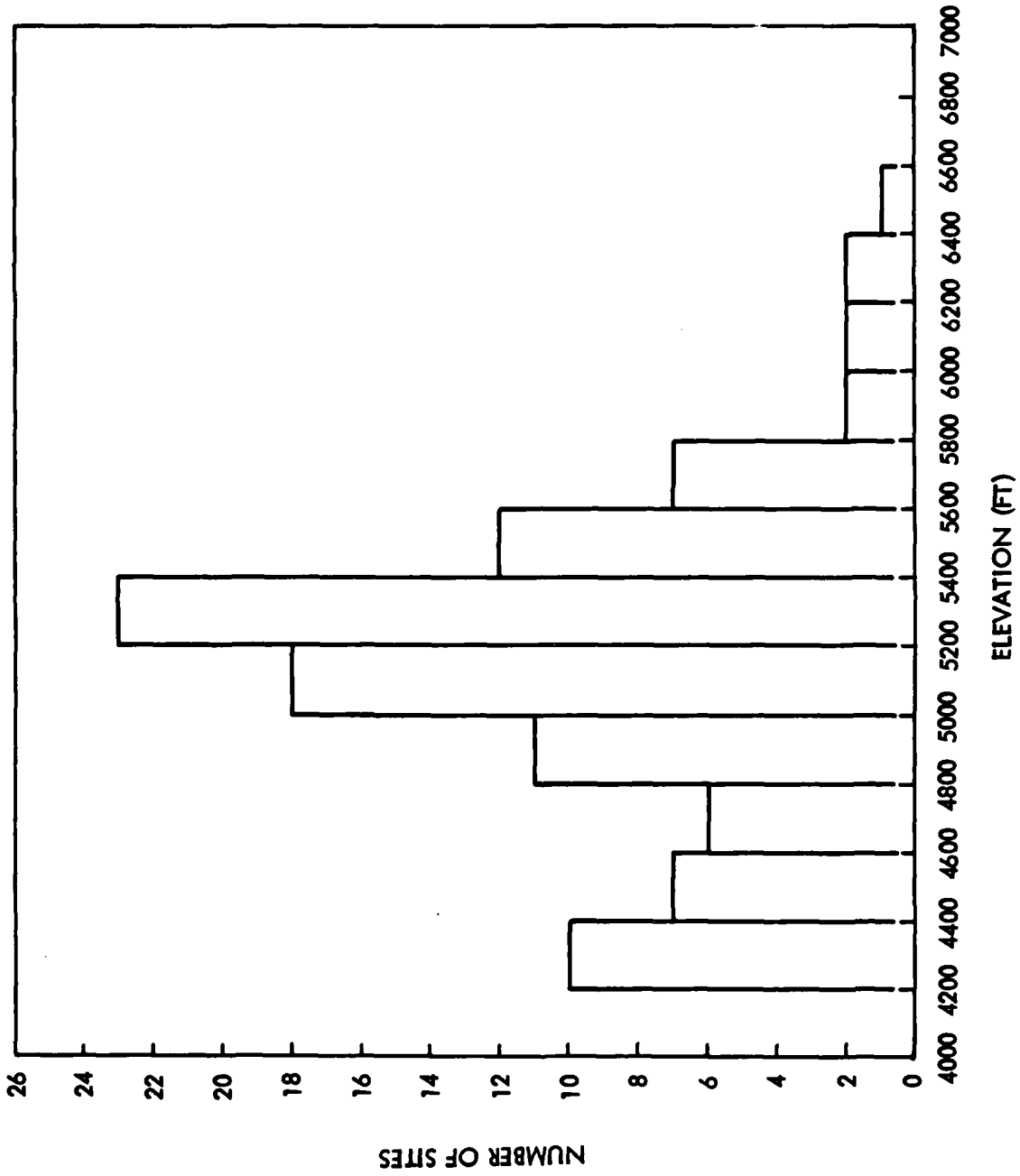


Figure 9-5. Elevation Histogram at Wing V Sites

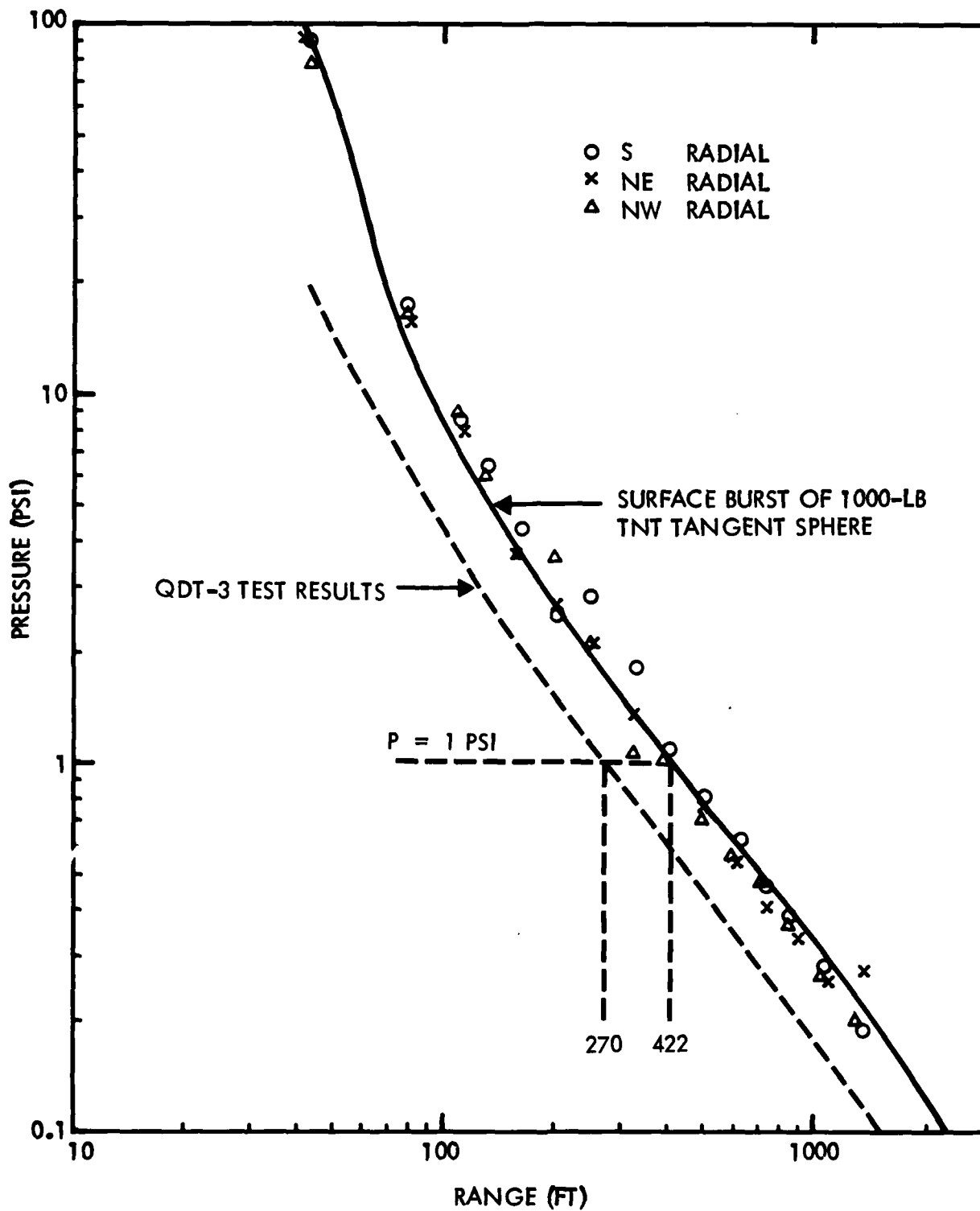


Figure 9-6. Calibration Shot Airblast Data

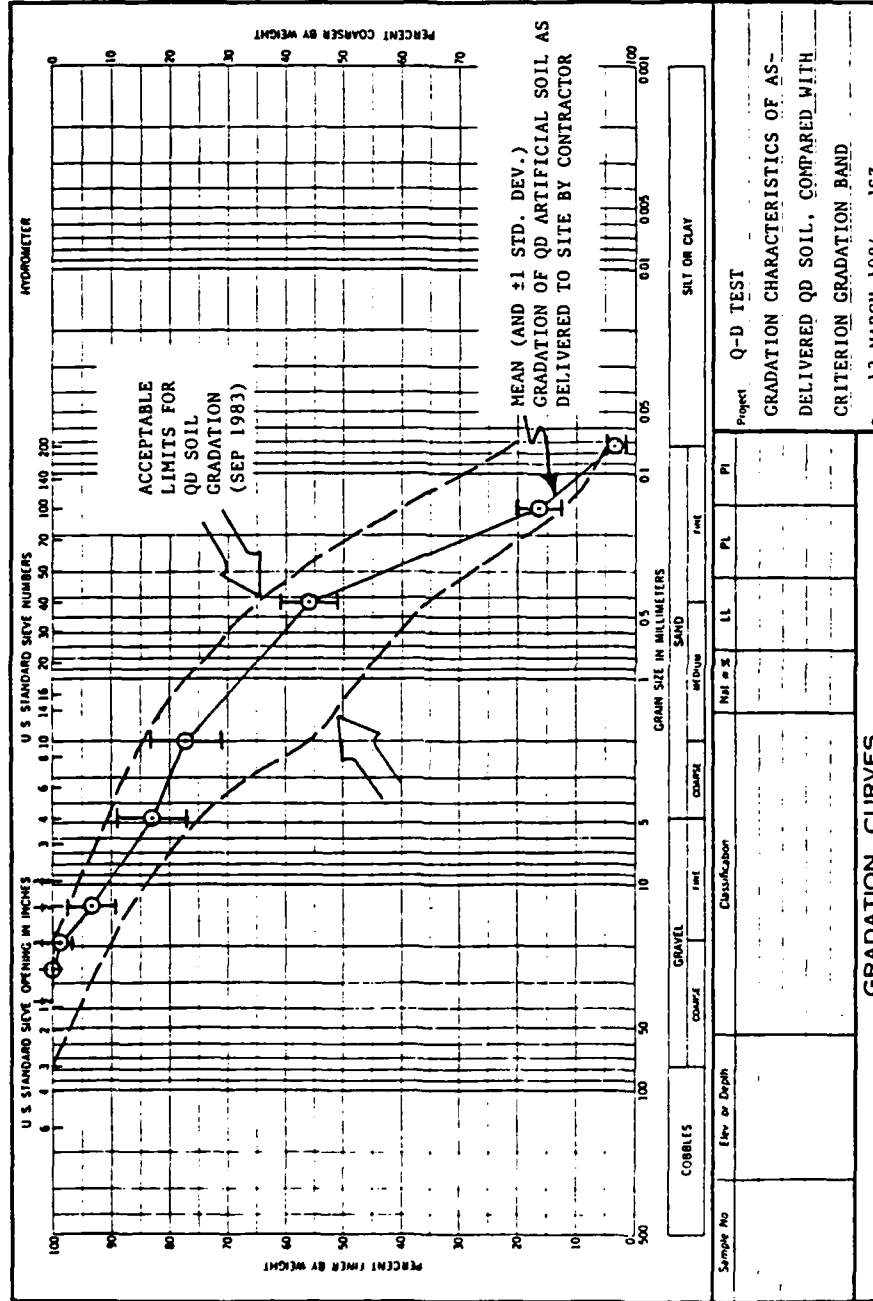
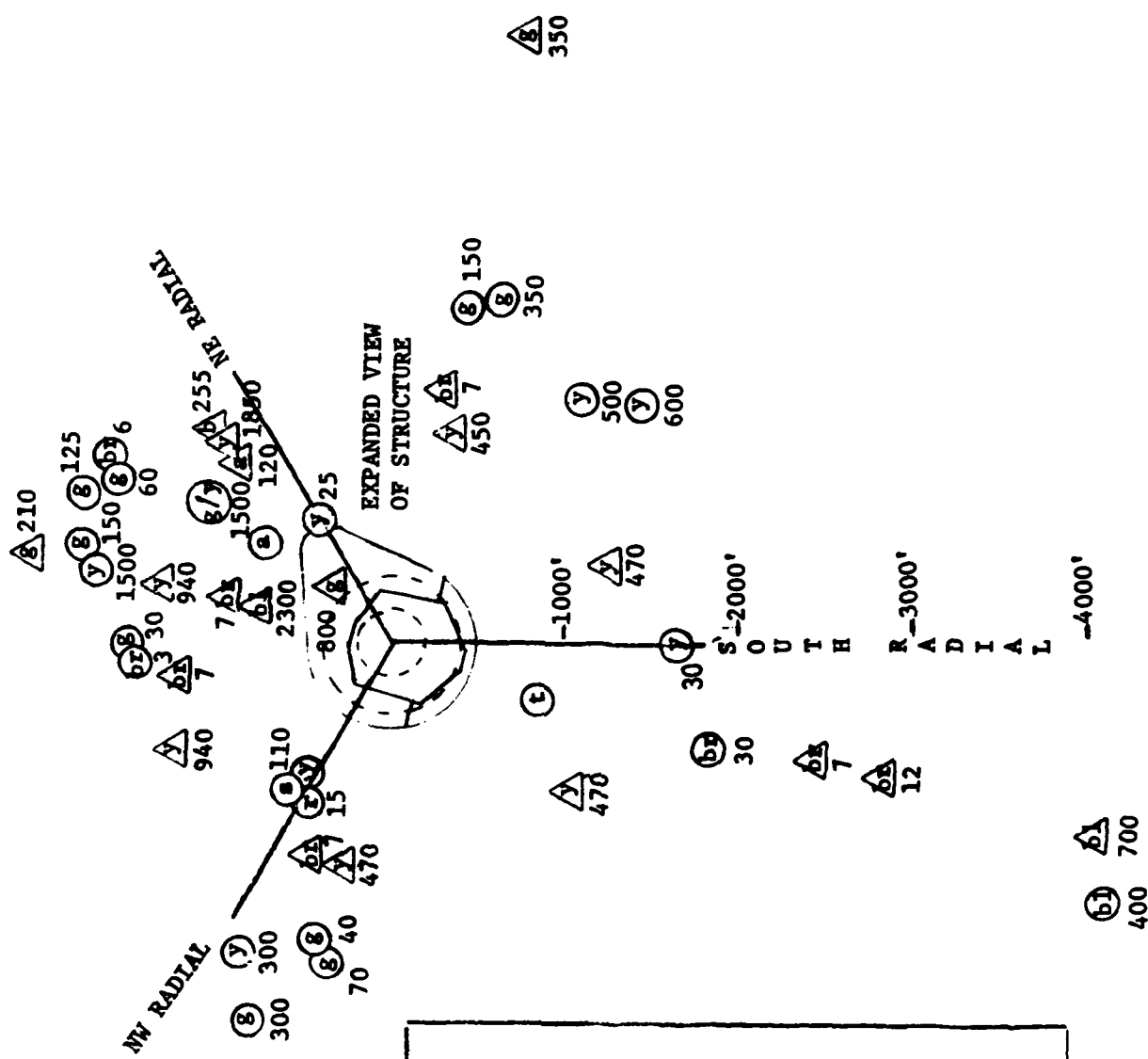


Figure 9-7. Gradation Characteristics of QD Soil Delivered to Test Site



KEY

APPROX. FRAGMENT WEIGHT (lbs) QDT3 DATA PREDICTION

○ 50 △ 12

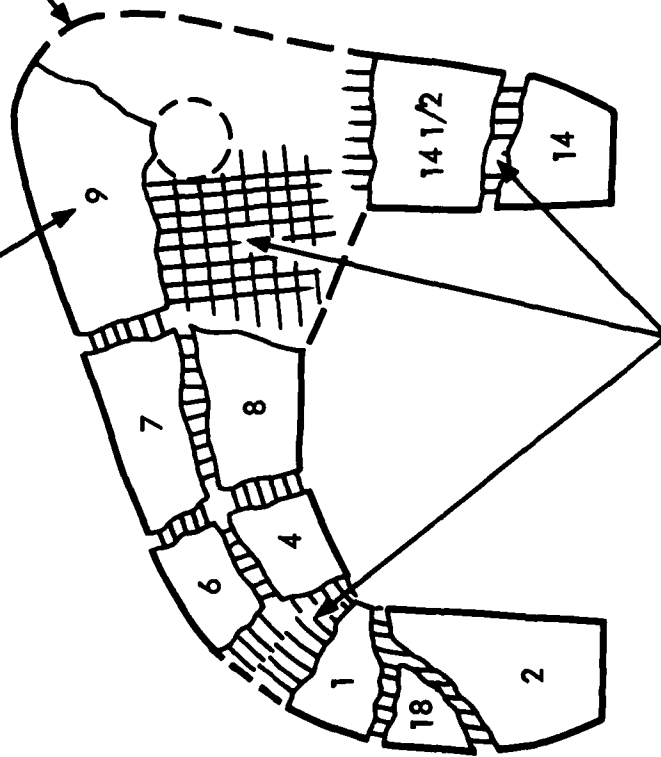
br - Brown (Level A)
 bl - Black (Closure)
 g - Green (Level B)
 y - Yellow (Level C)
 a - PAS PLUG A
 b - PAS PLUG B
 t - CLOSURE TRACK
 s - SIS FLOOR SECTION
 r - PORTION OF LEVEL C BEARING RING

Figure 9-8. Comparison of QDT-3 Far Field Large Fragment Survey with Pretest Predictions

CONCRETE STRIPPED OFF
REBAR IN THESE REGIONS

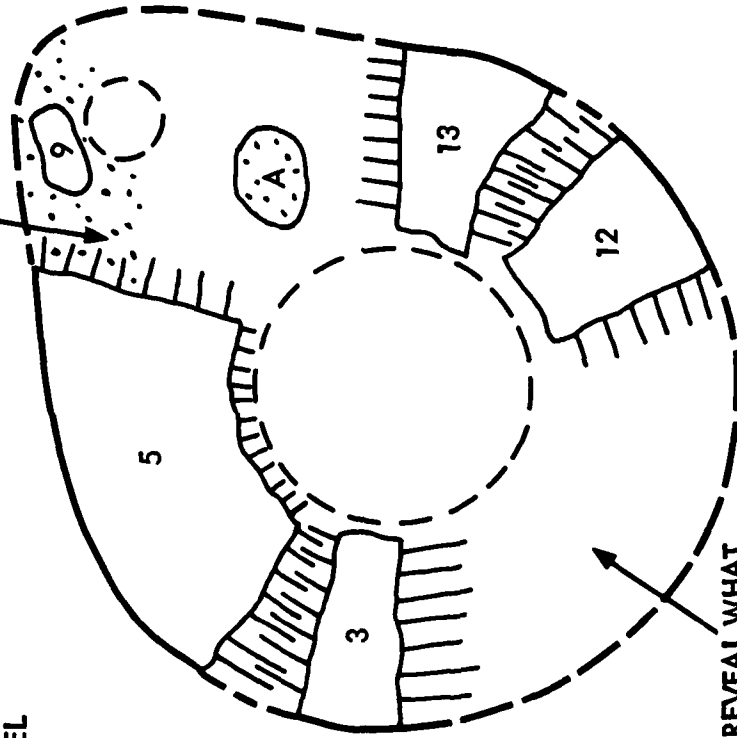
ORIGINAL
OUTLINE
AT THIS
LEVEL

OFF-RADIAL NEAR AND FAR-FIELD
LARGE FRAGMENT IDENTIFIERS



CONCRETE STRIPPED OFF
REBAR IN THESE REGIONS
(TYPICAL)

TEST DATA DID NOT REVEAL WHAT
HAPPENED TO CONCRETE IN THESE
REGIONS



LEVEL C (YELLOW)

LEVEL B (GREEN)

Figure 9-9. QDT-3 Headworks Level B and Level C Fragment Recovery

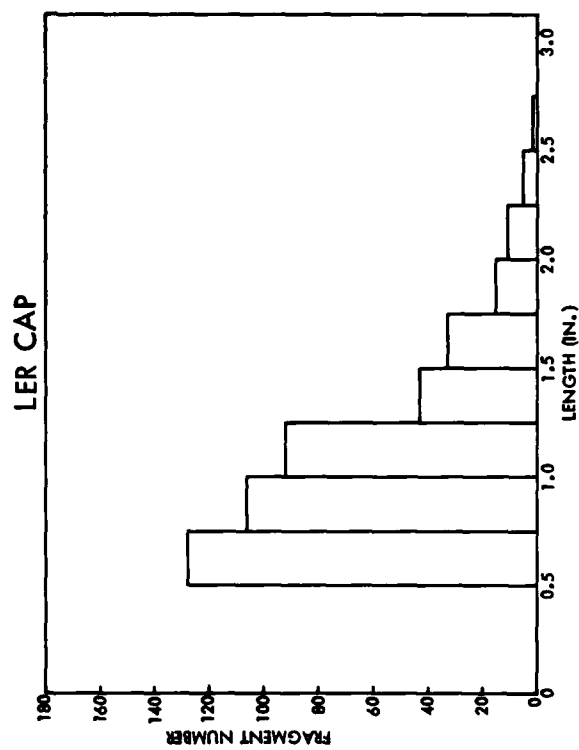
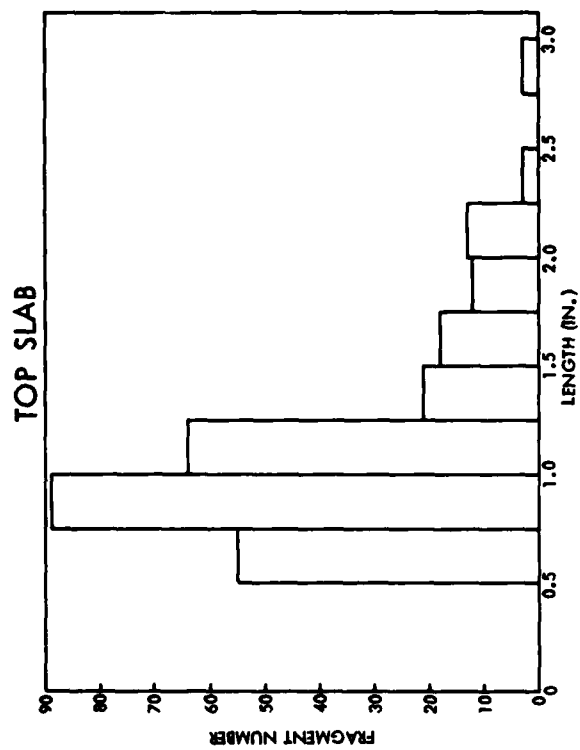
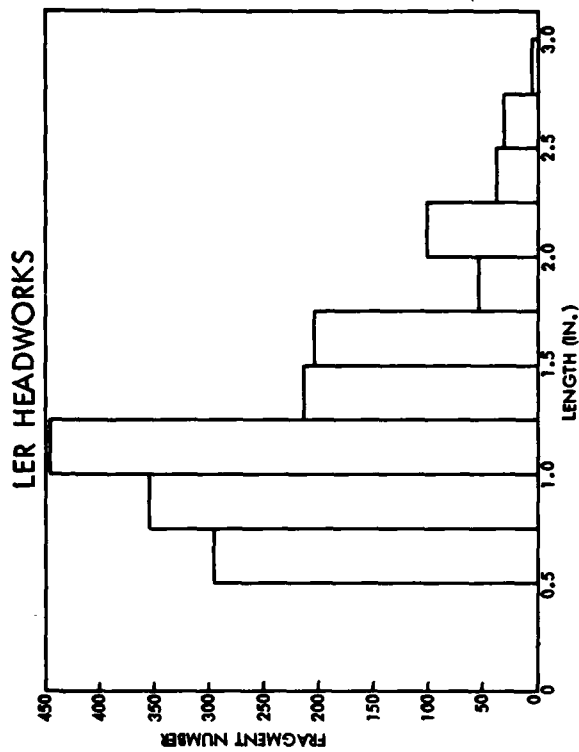
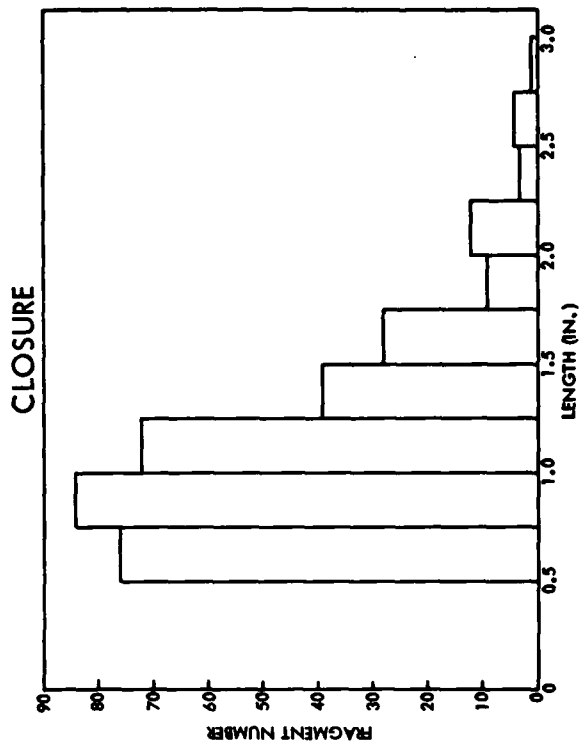
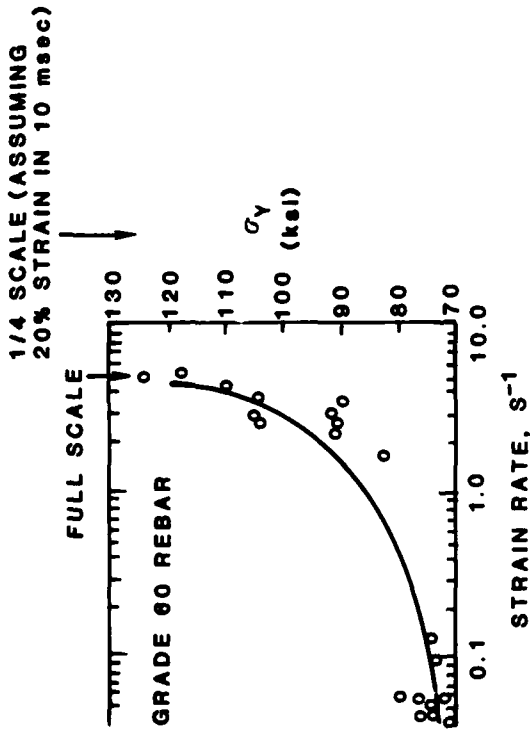


Figure 9-10. Fragment Occurrence Frequencies for Various Structural Elements

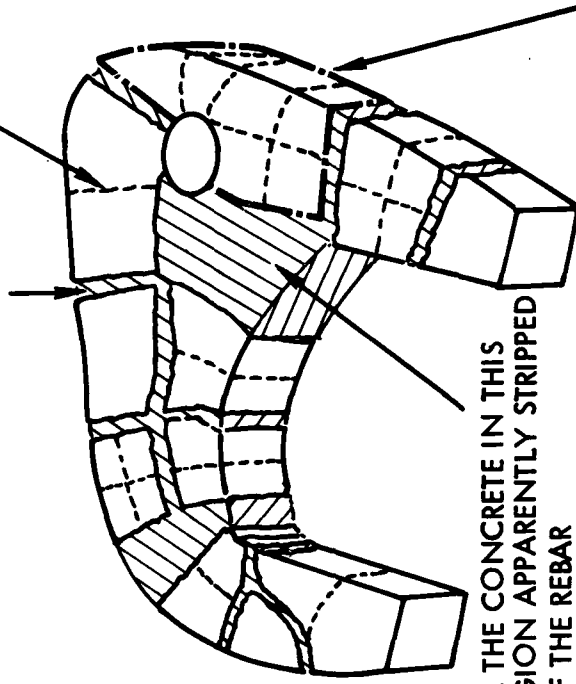
- AT FULL SCALE THERE WILL BE MORE LARGE FRAGMENTS BECAUSE:
- STRAIN RATES DECREASE WHICH REDUCE MATERIAL STRENGTHS



- LARGE FRAGMENTS CONTAIN MORE MICROCRACKS (SIZE EFFECT)
- STEEL STRENGTH IN QDT-3 WAS GENERALLY HIGHER THAN IN ACTUAL SILOS
- BOUNDING CONJECTURE FOR LARGE FRAGMENTS
 - 1/2 OF THEM SCALE GEOMETRICALLY
 - 1/2 BREAK INTO 2 FRAGMENTS
 - 1/4 BREAK INTO 4 FRAGMENTS
 - THIS DOUBLES THE NUMBER OF INTERSTICES

POSTULATED ADDITIONAL FULL SIZE FRACTURE ZONES

INTERSTITIAL ZONES WERE TYPICALLY 2-3 REBAR SPACING WIDE



ALL THE CONCRETE IN THIS REGION APPARENTLY STRIPPED OFF THE REBAR

TEST DATA DID NOT REVEAL WHAT HAPPENED TO THE CONCRETE IN --- REGION

QDT-3 HEADWORKS CAP (LEVEL B) FRACTURE PATTERN

Figure 9-11. Scaling of Large Fragment Distribution

- QDT-3 OBSERVATIONS
 - SOURCES
 - SURFACE SPALLING, SCABBING AND PEELING (OF THE LINER) CONTRIBUTE FEW Q-D CRITERIA TYPE FRAGMENTS
 - INTERSTITIAL ZONES (CREATED BY STRUCTURE BREAK UP ARE THE SOURCE OF MOST SMALL FRAGMENTS
 - IN-FLIGHT BREAK UP OF LARGE FRAGMENTS (DUE TO ROTATIONS) MAY BE IMPORTANT SOURCE
 - SIZE DISTRIBUTION
 - LOG-NORMAL DISTRIBUTION WITH MEAN OF ONE-HALF THE REBAR SPACING
 - MAXIMUM FRAGMENT SIZE EQUAL TO REBAR SPACING
 - AGGREGATE COMPRISES SIZABLE FRACTION OF SMALLER FRAGMENTS
- SCALING APPROACH
 - ASSUME GEOMETRIC SCALING BASED ON OBSERVED RELATIONSHIP OF SIZE DISTRIBUTIONS TO SCALABLE QUANTITIES (REBAR SPACING, AGGREGATE SIZE)
- SCALING UNCERTAINTIES
 - STRAIN RATE AND SIZE EFFECTS MAY RESULT IN SMALLER FRAGMENTS
 - AT FULL SCALE, LARGE FRAGMENTS MAY HAVE A GREATER TENDENCY TO BREAK UP IN-FLIGHT
 - FLOW FIELD EFFECTS ON SMALL PARTICLES AT DIFFERENT SCALES MAY AFFECT INTERSTITIAL BREAK UP

Figure 9-12. Scaling of Small Fragment Distribution



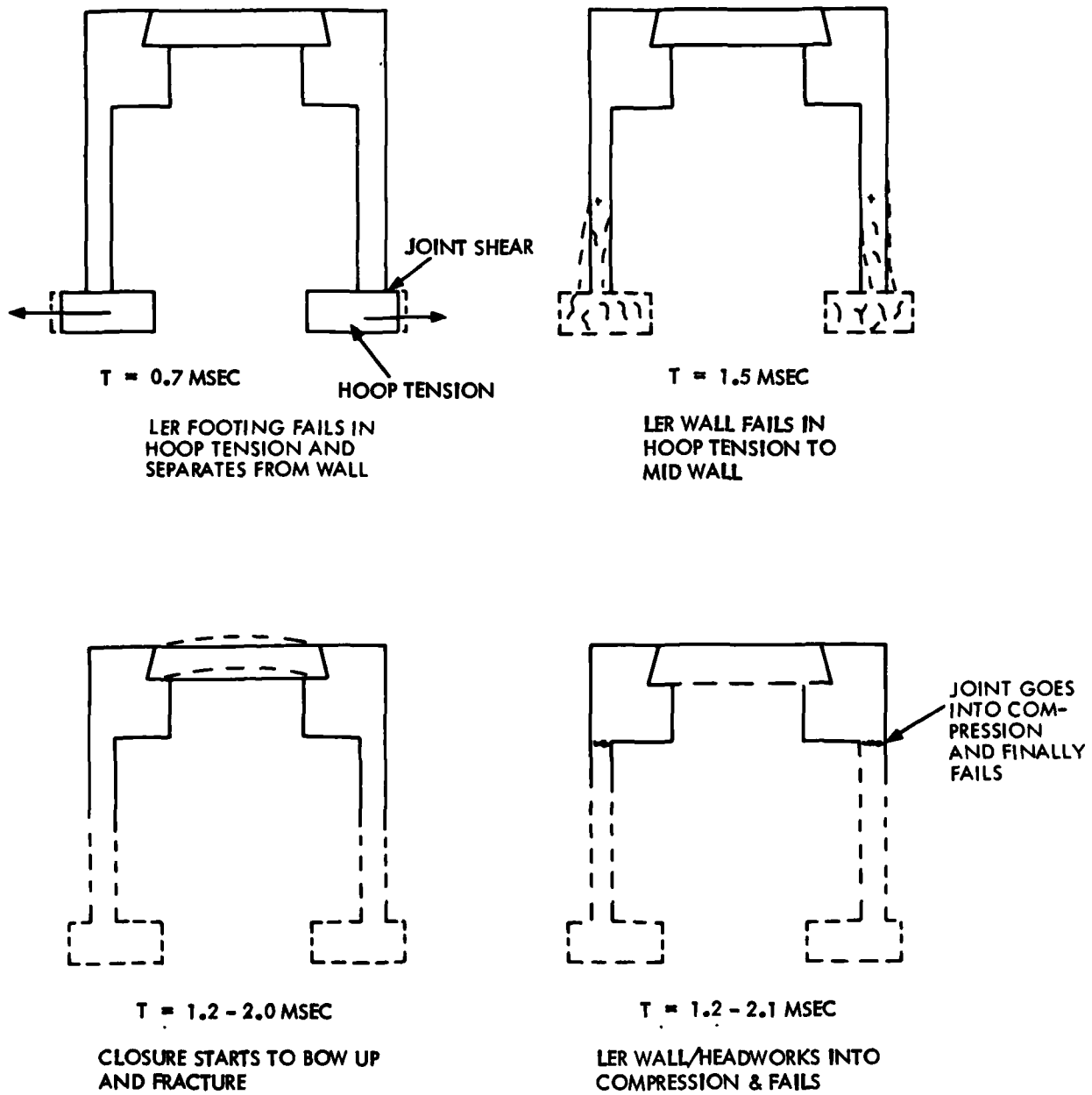


Figure 9-13. Analysis of QDT-3 Strain Gage Data

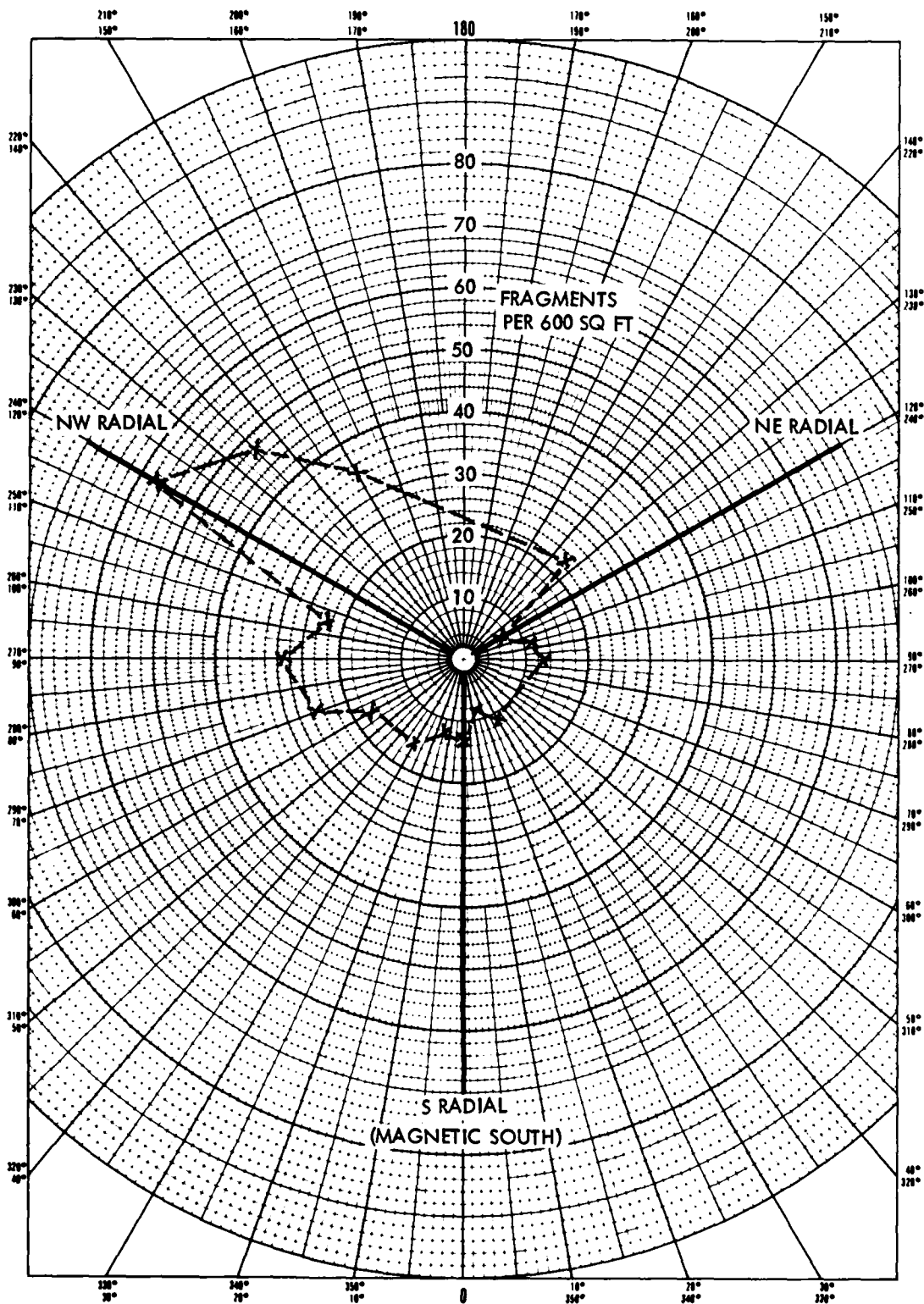


Figure 9-14. Fragment Density Variation with Azimuth at 400-Foot Range

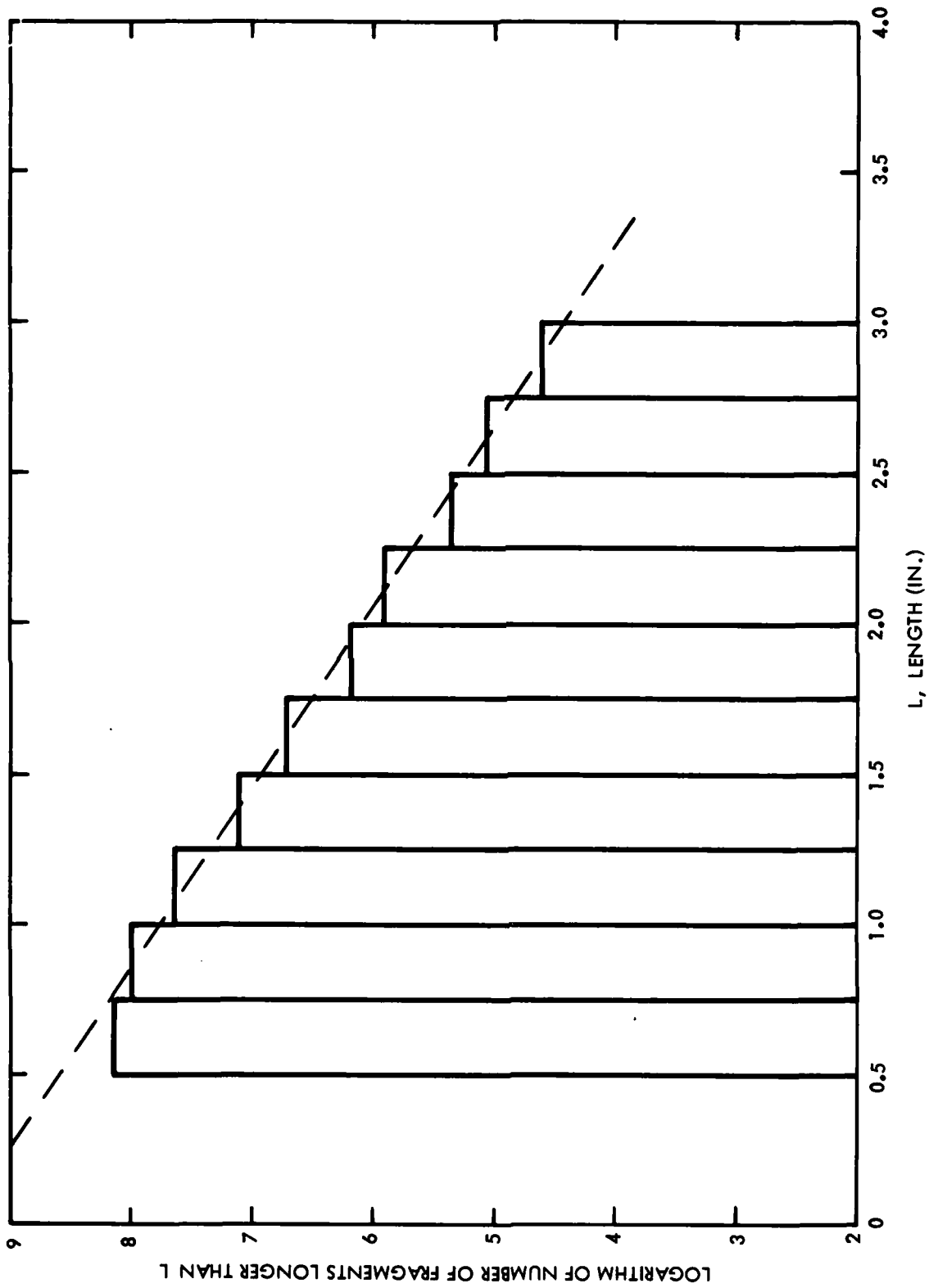


Figure 9-15. QDT-3 Debris Size Distribution

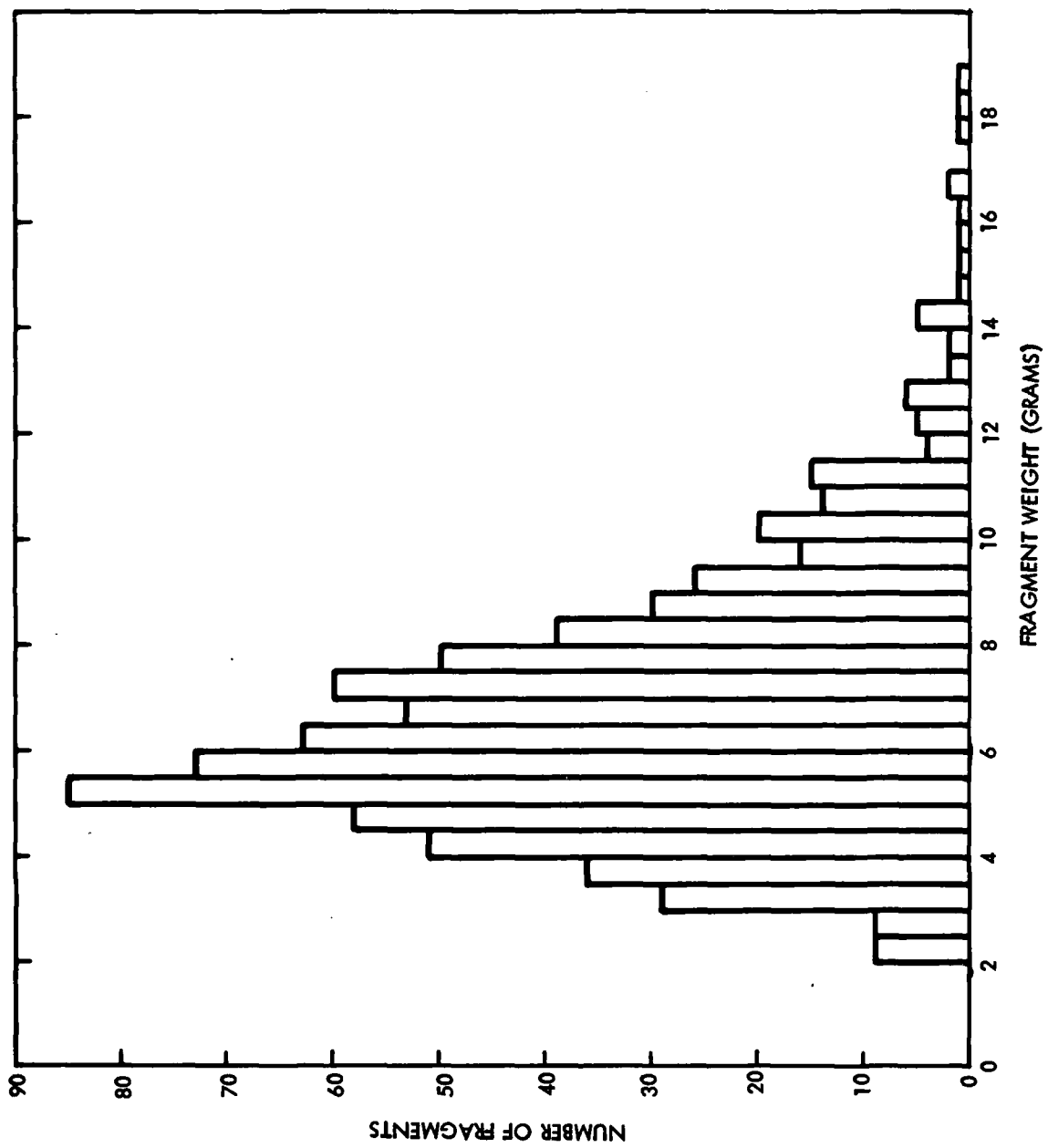


Figure 9-16. QDT-3 Mass Distribution for 1-Inch Structural Fragments

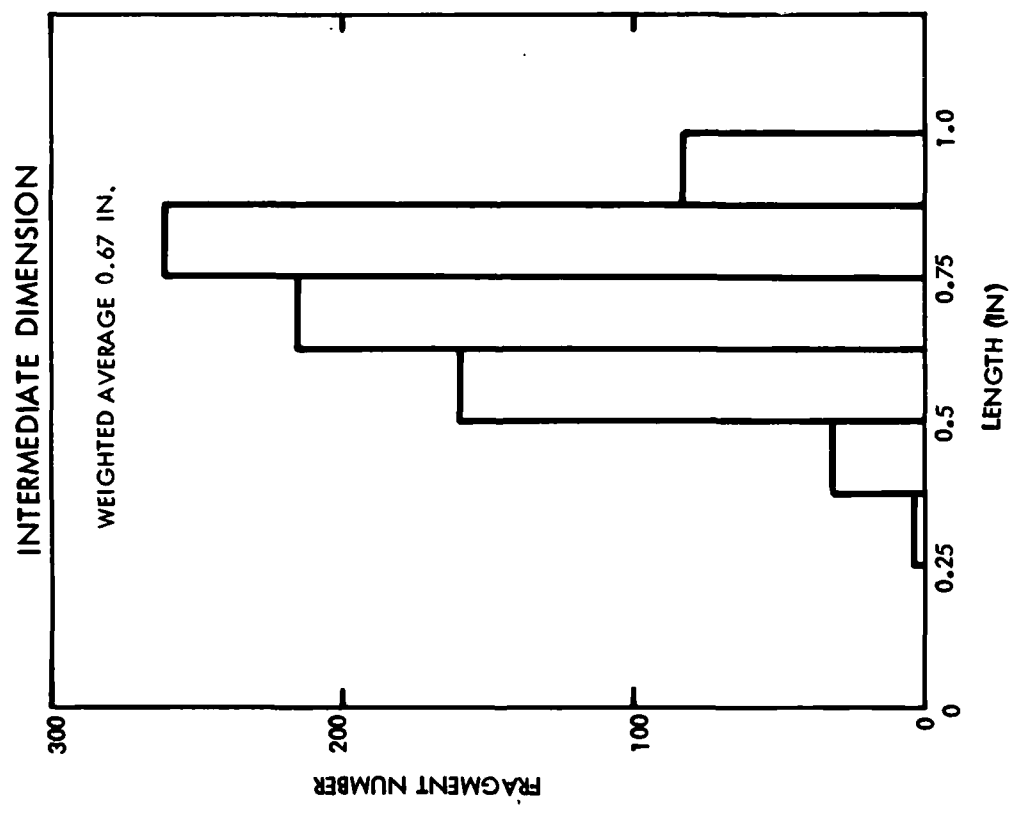
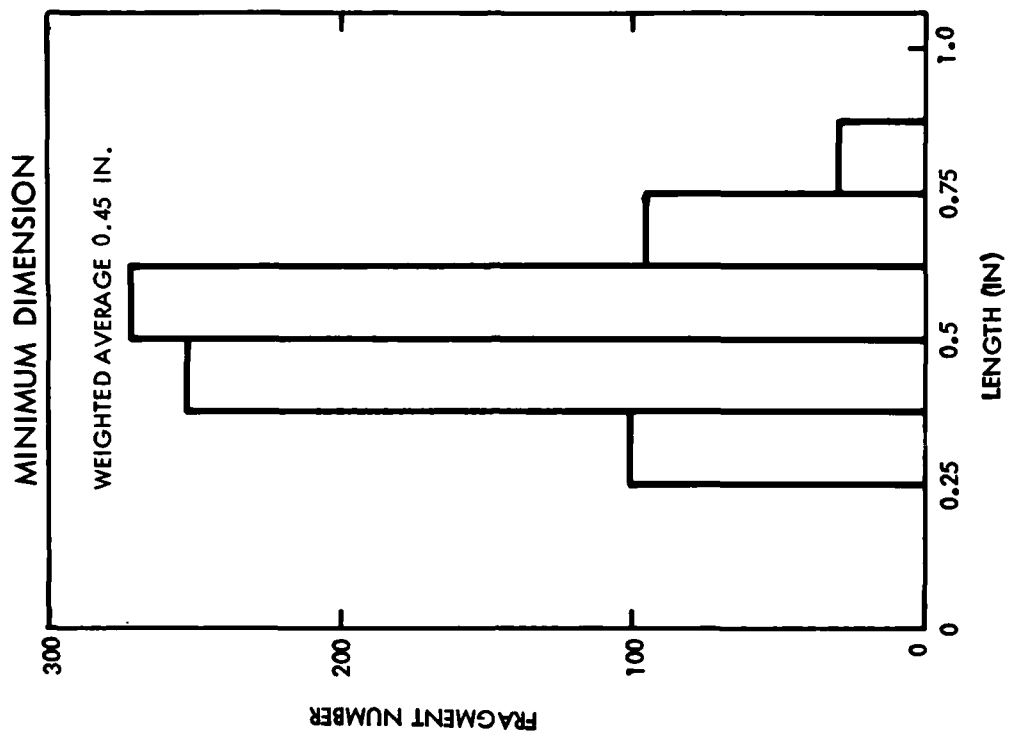
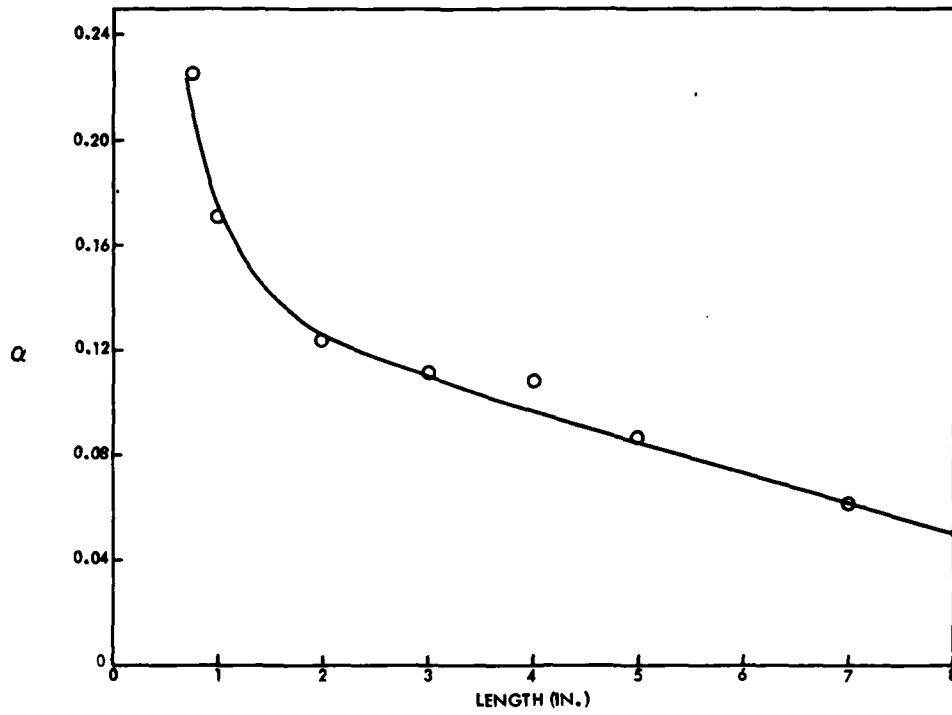


Figure 9-17. Occurrence Frequency of Other Dimensions of 1-Inch Fragments

VOLUME DEPENDENCE



AREA VOLUME DEPENDENCE

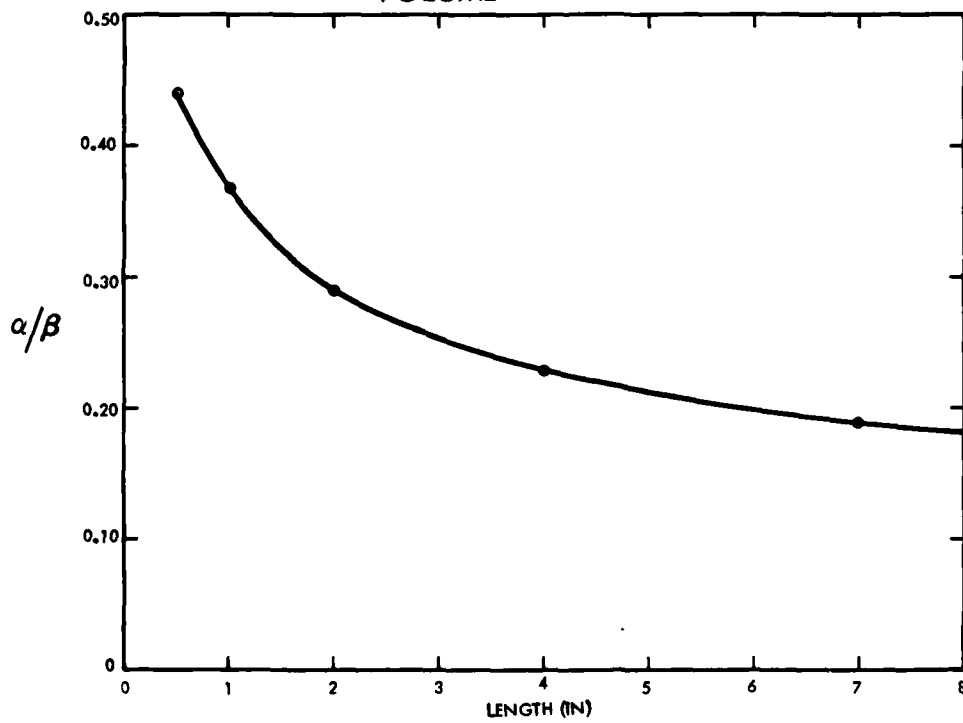


Figure 9-18. QDT-3 Fragment Shape Factor Variation with Length

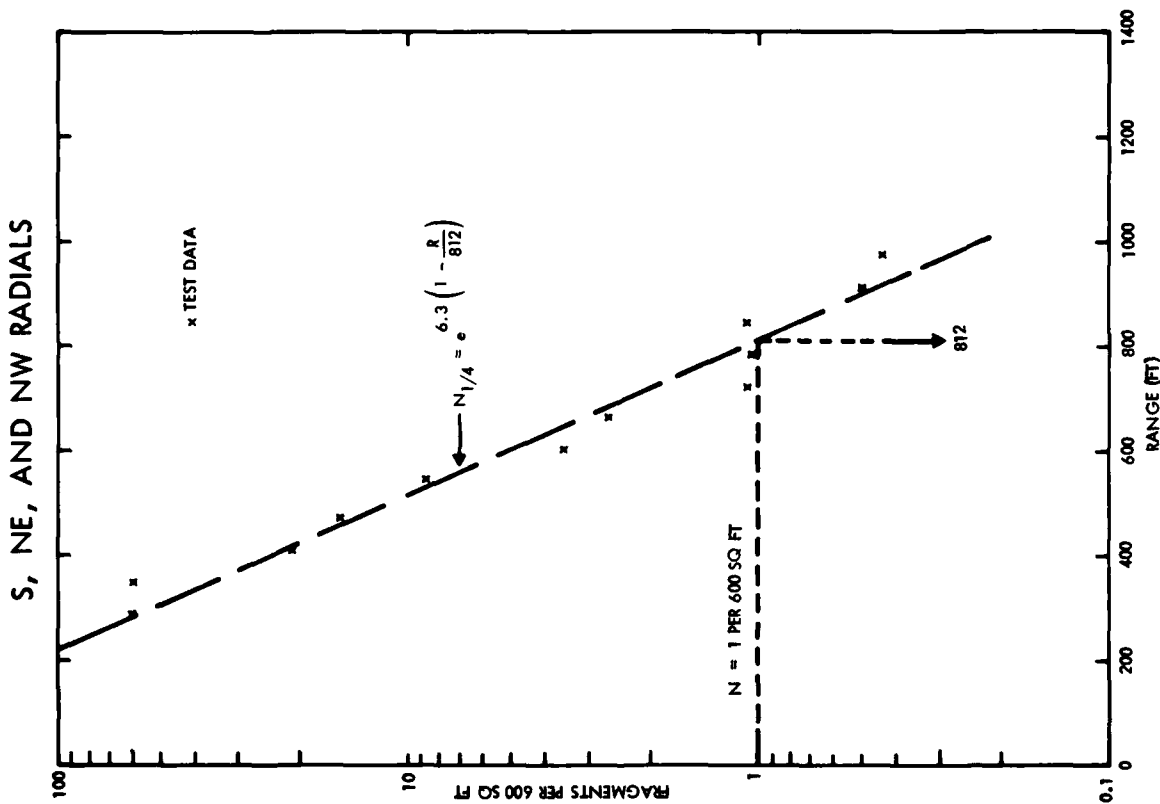
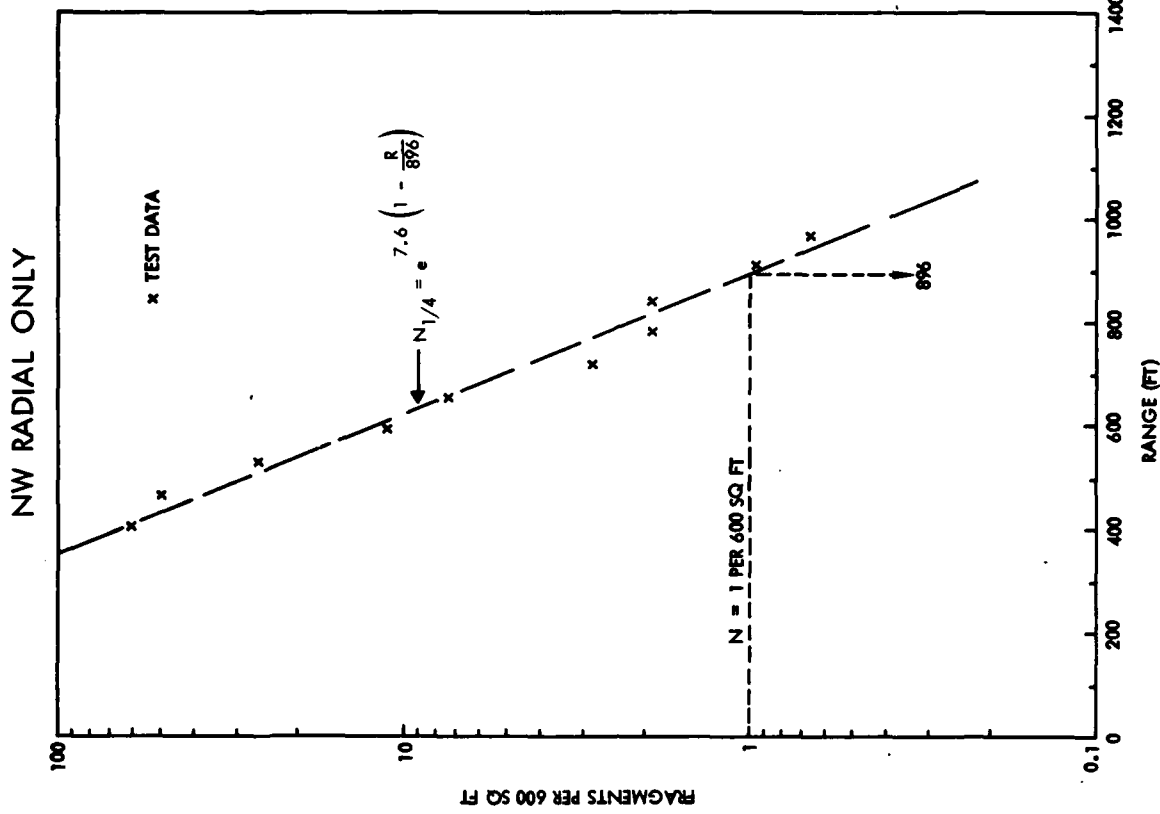


Figure 9-19. QDT-3 Debris Density Distribution

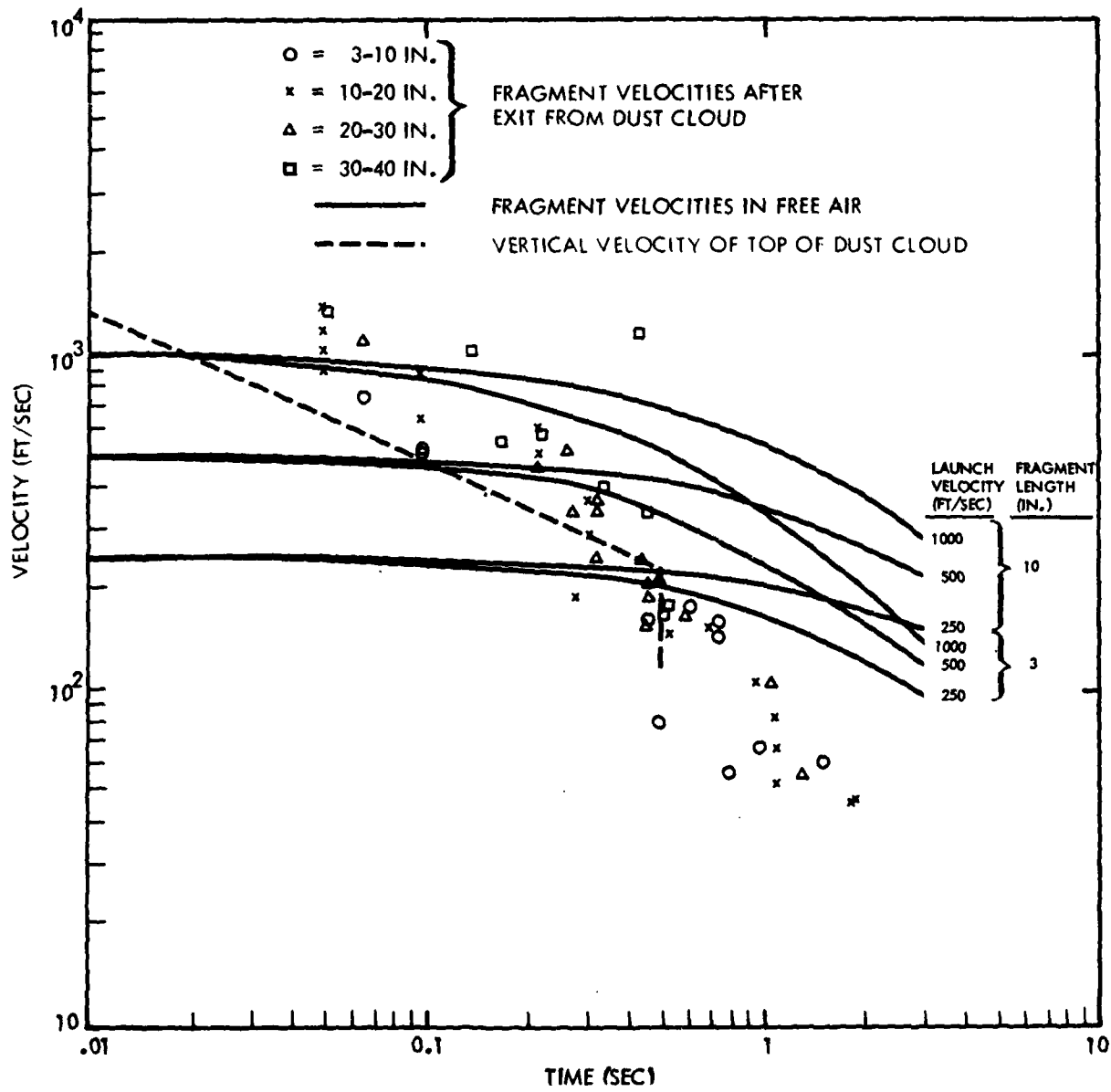


Figure 9-20. Comparison of Fragment and Dust Cloud Velocities

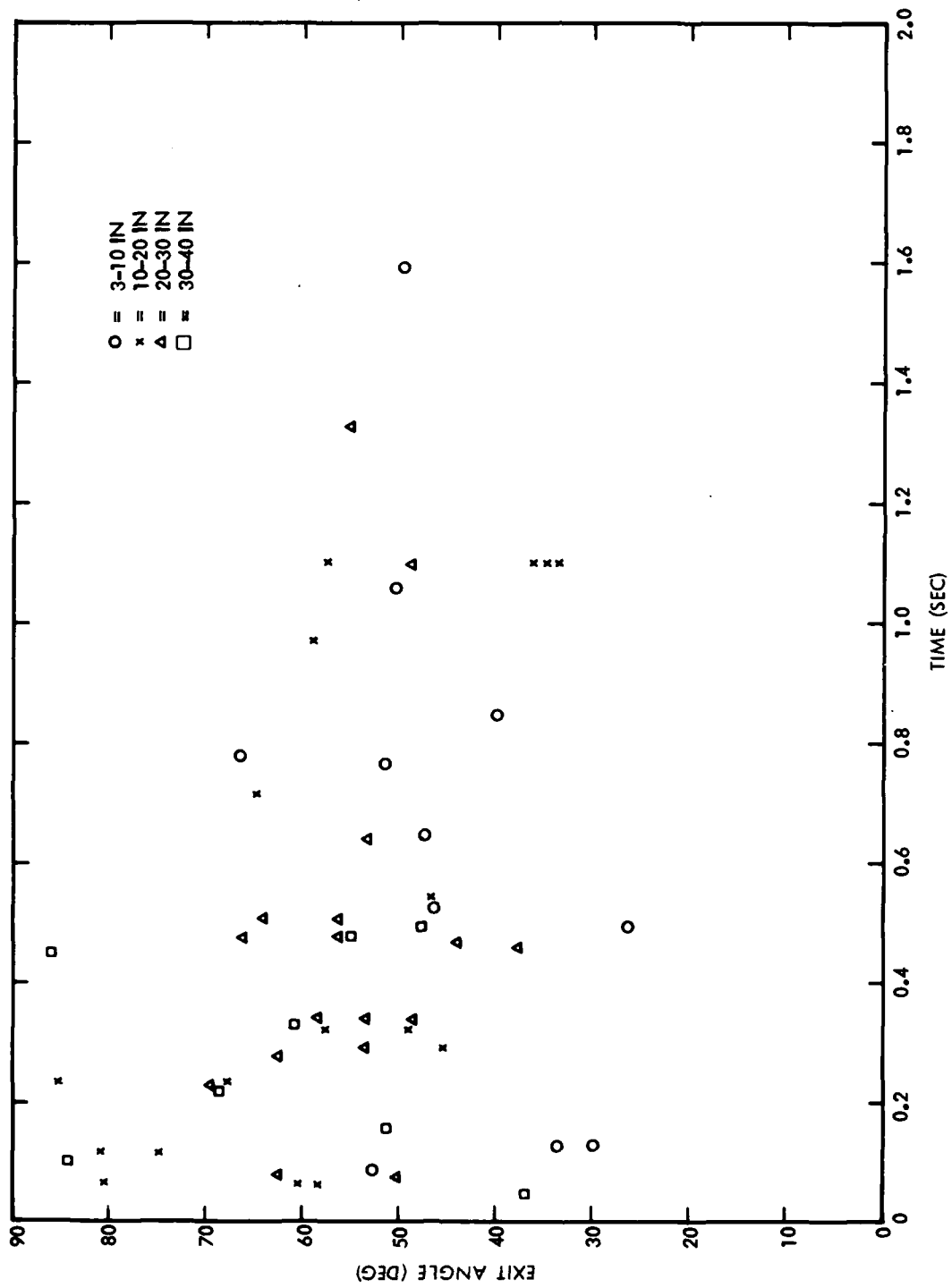


Figure 9-21. Fragment Angles After Exit from Dust Cloud

10.0 QUANTITY-DISTANCE VERIFICATION

10.1 Airblast

Results of the data analyses presented in Section 9.1 indicate that cube root scaling for airblast effects is readily applicable over the domain of the 1/10-scale and 1/4-scale experiments. The analytical predictions for the QDT-3 test were in agreement with the experimental results, with the associated computer model inherently reflecting cube root scaling for events of any scale magnitude. As far as can be judged from analytical and experimental results of the present study, it appears reasonable to conclude that the cube root law would be applicable for scaling of the data from the small scale tests to a full-scale event. The ground range to 1 psi for QDT-3 was 270 feet. It is, therefore, estimated that the quantity-distance for airblast overpressure would be 4 x 270 feet or 1080 feet for a full-scale explosion.

Figure 10-1 shows a comparative plot of peak overpressure versus scaled ground range for a TNT surface burst, the S-Cubed results for a rigid silo analysis and the QDT-3 test results. In planning for the scale model tests, the full-scale Net Equivalent Weight of the Peacekeeper missile was assumed to be 202,000 pounds TNT. The quantity-distance of 1750 feet specified for planning purposes, therefore, corresponded to a scaled ground range of $29.8 \text{ ft/lb}^{1/3}$. On the basis of the foregoing estimate of 1080 feet, the scaled ground range to 1 psi becomes $18.4 \text{ ft/lb}^{1/3}$.

The early DNA calculations were based on a rigid silo model, with an estimated reduction of about 5% in ground range to account for the flexible silo walls, the LER configuration, and the presence of a closure. In essence, a reduction of 5% in range would correspond to a reduction of 15% in energy on the basis of cube root scaling. The results of the CSQ computations described in Section 4.4 indicated that for both of the 1/10-scale and the 1/4-scale events, the total energy loss to the concrete and soil was approximately 65%. The energy transfer in each case occurred within the first few milliseconds of the explosion. A plot of the data is presented in Figure 10-2. The same result was obtained for both the door-on and door-off calculations, indicating that the presence of the closure caused a relatively insignificant effect on this phenomena.

The predicted airblast pressure distribution was based on a door-off analysis whereas QDT-3 was a door-on experiment. The good agreement between analytical and test data appears to indicate a high probability that the presence or lack of the closure would yield

similar airblast results for a full-scale event. It appears reasonable to conclude that the major causes for the lower ground ranges of the present study may be attributed to the energy loss to the flexible walls and surrounding medium, and to the reduction in early gas pressures by expansion into the LER cavity at the top of the silo launch tube.

10.2 Soil Ejecta

The QDT-3 soil ejecta distribution was not significant beyond ranges of about 300 feet. Since the soil gradations were similar to the operational site conditions, it is anticipated that, for a full-scale event, the soil ejecta ranges would be quite similar.

Regarding the possibility of large earth clumps, it appears reasonable to estimate that the number of earth clumps would be small, and therefore, would not contribute significantly toward determining quantity-distance criteria for debris and ejecta.

10.3 Structural Debris

10.3.1 Shape Factor Impact

A number of post-test calculations was performed by the statistical simulation and trajectory limitation techniques in order to evaluate the sensitivity of results to the variation of shape factors for the QDT-3 fragments as compared to the Distant Runner characteristics assumed in the pretest analyses.

In Section 7.2, results of the calculations for nine cases, based on the Distant Runner shape factors, were presented in Table 7-1. Three additional cases were evaluated on the basis of the QDT-3 debris data. Two calculations were for the skewed velocity/angle distribution and one calculation corresponded to the uniform distribution. In all three cases, application was made of the revised shape factor dependence on length. The number gradient was assumed as one-half for Case 10 and two-thirds for Cases 11 and 12. The tabulation in Table 7-1 has been reproduced in Table 10-1 with the addition of the results for Cases 10 to 12 for comparison. The scaling parameters determined by Approaches A and B are quite similar among Cases 10, 11 and 12, but differ significantly with the corresponding results for Cases 1 to 9.

For the results of Case 11 shown in Figure 10-3, the ratio of 1/4-scale and full-scale ranges corresponding to a density of one per 600 sq ft is 1.75 for Approach A with the full-scale range determined to be 1310 feet. For Approach B, the required density was found to be 4.5 per 600 sq ft with associated range of 616 feet, in order that scaling to the

full-scale range for a density of 1 per 600 sq ft also yields a value of 1310 feet. Applying the parameter $\lambda^2 = 4.5$ to the exponential function for the 1/4-scale distribution resulted in the modified full-scale density function denoted by the dashed curve.

Approach A was selected for application toward scaling of the QDT-3 debris data since the values of the scaling factor for Cases 1 to 9 in Table 10-1 were less sensitive to variations in the parameters associated with the respective cases.

The parameters corresponding to Case 11 in Table 10-1 appeared to be a reasonable representation of the conditions associated with the QDT-3 test and therefore a scaling factor of 1.75 was assumed for the following quantity-distance scaling evaluation.

A similar evaluation regarding shape factor impact was performed by the trajectory limitation scaling technique. Figure 10-4 presents a set of contours which were based on the same analytical procedure applied in development of the curves of Figure 7-9. For the results of Figure 7-9, an upper bound in ratios of maximum ranges was estimated to be about 3.4, whereas for the data shown in Figure 10-4, a value of 2.24 for λ appeared reasonable. The corresponding value of λ^2 is 5. It is of interest to note that a λ^2 value of 4.5 was the result of scaling Approach B for Case 11.

10.3.2 Full-Scale Criteria

Scaling of the QDT-3 data for the S, NE, and NW radials by the statistical simulation method is represented by the plot of Figure 10-5(a). For a constant value of N_0 , the full-scale range to a density of one per 600 sq ft is estimated as 812 feet (1/4-scale range) multiplied by 1.75 resulting in a value of 1421 feet. As an upper bound, the full-scale range corresponding to a total fragment number of $2 N_0$ is 901 feet multiplied by 1.75 or 1577 feet.

A similar evaluation based on the trajectory limitation method is shown by the plot of Figure 10-5(b). For a fragment total of N_0 , the 1/4-scale range for a density of 5 per 600 sq ft is 604, such that the full-scale range to a density of 1 per 600 sq ft is, therefore, $604 \times 2.24 = 1353$ sq ft. For the case of $2 N_0$, the full-scale range is $694 \times 2.24 = 1554$ feet.

The preceding results correspond to scaling of the QDT-3 data on the basis of the debris distribution for the S, NE, and NW radials. The same set of calculations was performed for the data based only on the debris distribution for the NW radial as a means of establishing upper limits to the full-scale ranges. The results are shown in Figure 10-6.

A summary of the scaling evaluations is presented in Table 10-2. It is recognized that there are various uncertainties associated with each full-scale range in addition to relative degrees of conservatism. It appears reasonable to recommend that the average of all of the values, including the highly conservative, be considered as the required quantity-distance criterion. This average value, as given in Table 10-2, is 1567 feet.

Table 10-1. Comparison of Debris Scaling Evaluations by Statistical Simulation Method

Case	Launch V_0 and θ_0 Spectrum	Drag Coefficient	Number Gradient	Scaling Approach A			Scaling Approach B			Scaling Approach C					
				$R_{1/4}$ for $1/600 \text{ ft}^2$ (ft)	$(RFS)_{1/4}$ for $1/600 \text{ ft}^2$ (ft)	Scale Factor λ	λ^2	$R_{1/4}$ for $1/600 \text{ ft}^2$ (ft)	$(RFS)_{1/4}$ for $1/600 \text{ ft}^2$ (ft)	Scale Factor λ	λ^2	$(R_{1/4})_{1/4}$ for $1/600 \text{ ft}^2$ (ft)	$(RFS)_{1/4}$ for $1/600 \text{ ft}^2$ (ft)	$\frac{(RFS)_{1/4}}{(RFS)_{1/4}}$	
1*	Uniform	1/2	1/2	848	1644	1.93	2.72	7.4	604	1644	4	16	512	2048	1.24
2	Uniform	1/2	2/3	1020	1999	1.96	2.88	8.3	694	1999	4	16	593	2322	1.19
3	Uniform	1/2	3/8	732	1446	1.98	2.74	7.5	528	1446	4	16	453	1812	1.25
4	Skewed	1/2	1/2	773	1572	2.03	2.88	8.3	546	1572	4	16	475	1900	1.21
5	Uniform	1	1/2	553	1249	2.26	3.11	9.7	402	1249	4	16	367	1468	1.18
6	Skewed	1	1/2	516	1150	2.23	3.11	9.7	370	1150	4	16	336	1340	1.16
7	Uniform; Scaling 2:1	1/2	1/2	848	1704	2.01	2.88	8.3	591	1704	4	16	512	2048	1.20
8	Uniform; $2N_0$	1/2	1/2	932	1889	2.03	2.76	7.6	684	1889	4	16	596	2348	1.26
9	Uniform; $1/2N_0$	1/2	1/2	764	1398	1.83	2.64	7.0	530	1398	4	16	427	1708	1.22
Average						2.03	2.86	8.2							1.21
10**	Skewed	1/2	1/2	670	1159	1.73	2.10	4.4	552	1159	4	16	450	1800	1.55
11	Skewed	1/2	2/3	750	1310	1.75	2.12	4.5	616	1310	4	16	504	2016	1.54
12	Uniform	1/2	2/3	712	1140	1.60	2.14	4.6	531	1140	4	16	384	1536	1.35

* Cases 1-9: Distant Runner shape factors - pretest calculations

** Cases 10-12: QDT-3 shape factors - post-test calculations

Table 10-2. Full Scale Quantity-Distance Estimates for Structural Debris

Debris Scaling Method	QDT-3 Radials	Total Fragment Number	Fragments per 600 ft ²	QDT-3 Range (ft)	Scale Factor	Full Scale Range (ft)
Statistical Simulation	S, NE, NW	N ₀	1	812	1.75	1421
		2N ₀	1	901	1.75	1577
	NW	N ₀	1	896	1.75	1568
		2N ₀	1	977	1.75	1710
Trajectory Limitation	S, NE, NW	N ₀	5	604	2.24	1353
		2N ₀	5	694	2.24	1554
	NW	N ₀	5	706	2.24	1581
		2N ₀	5	790	2.24	1770
Average						1567

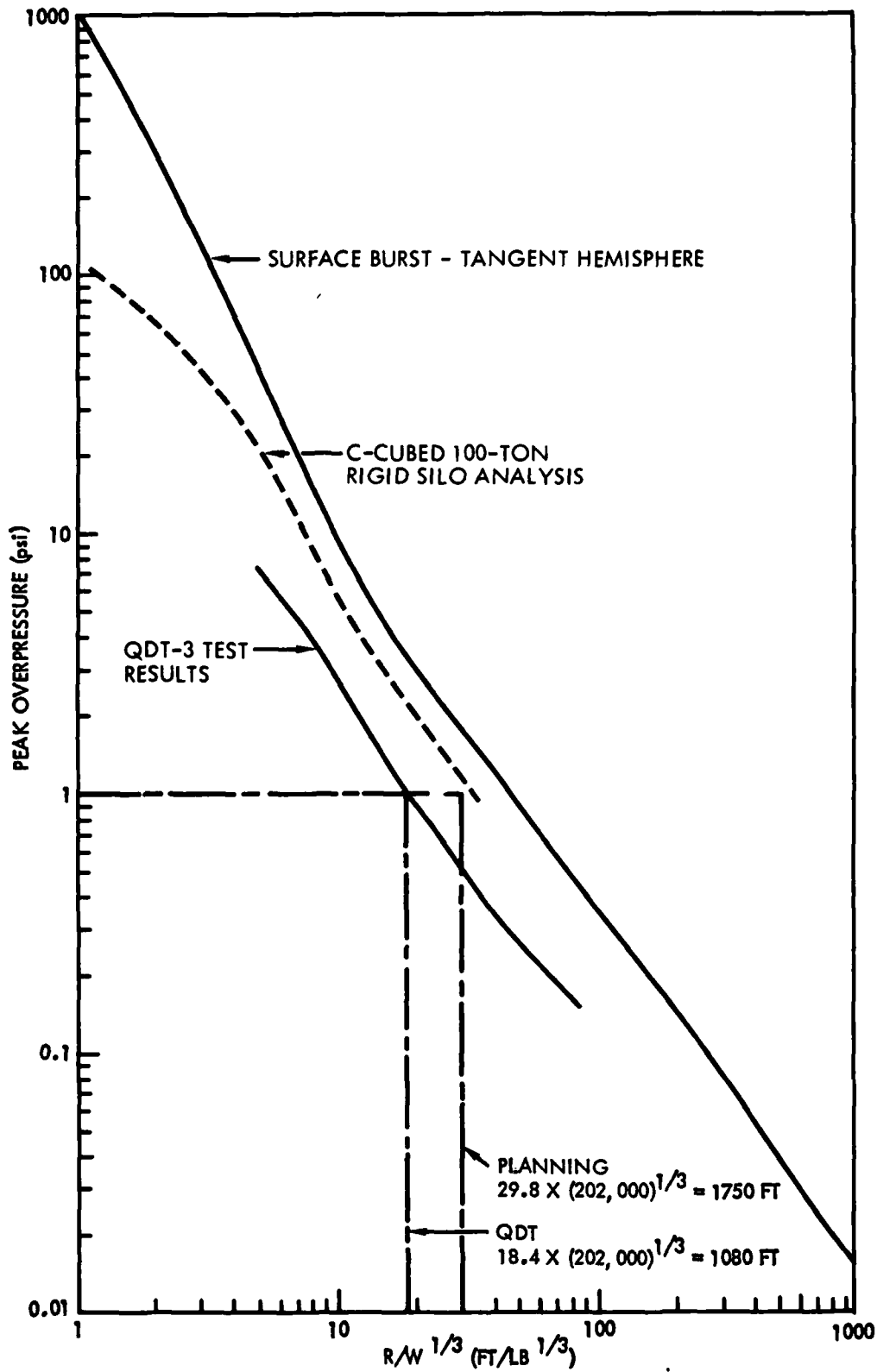


Figure 10-1. Peak Overpressure versus Scaled Range

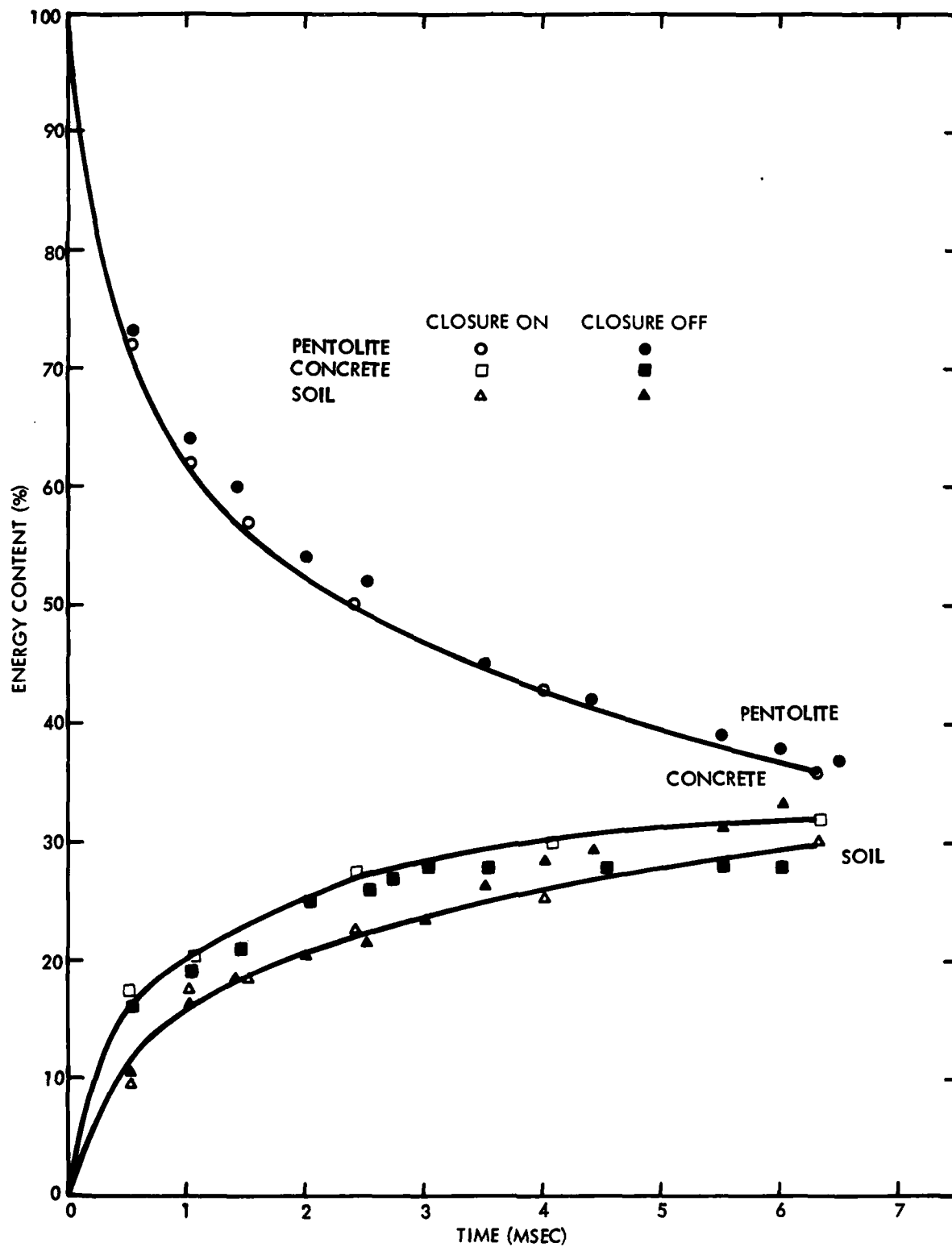
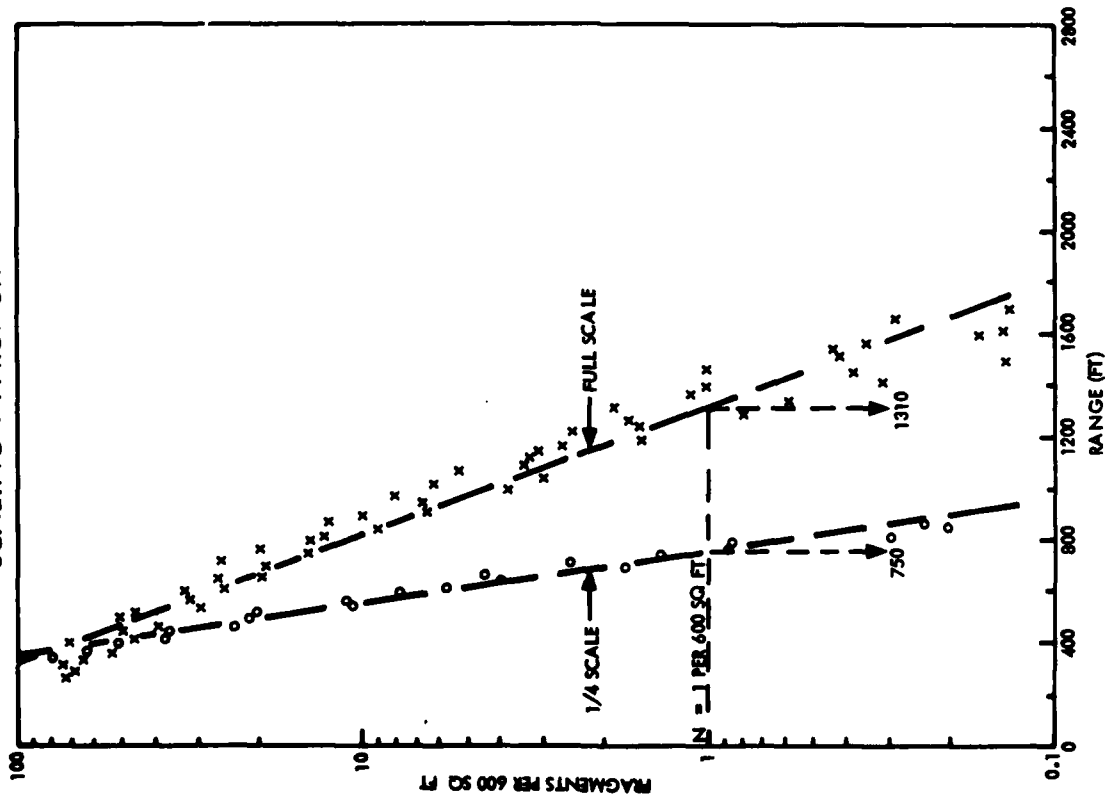


Figure 10-2. Energy Distribution versus Time

SCALING APPROACH A



SCALING APPROACH B

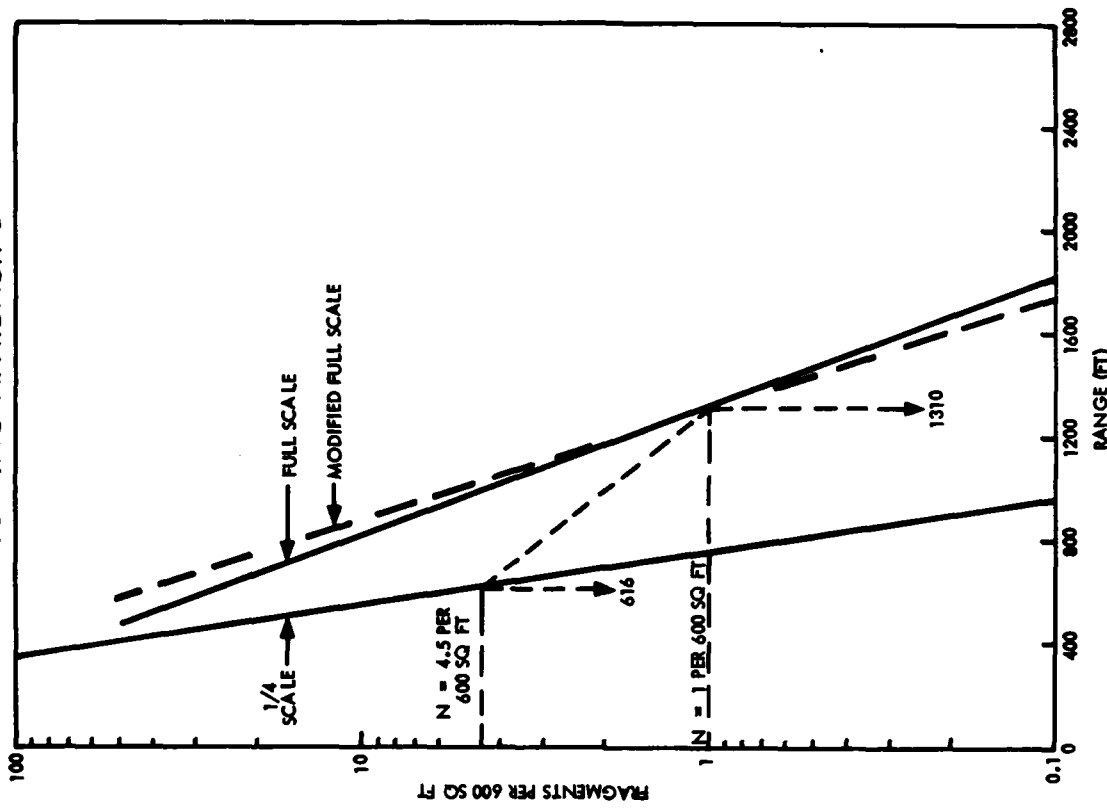
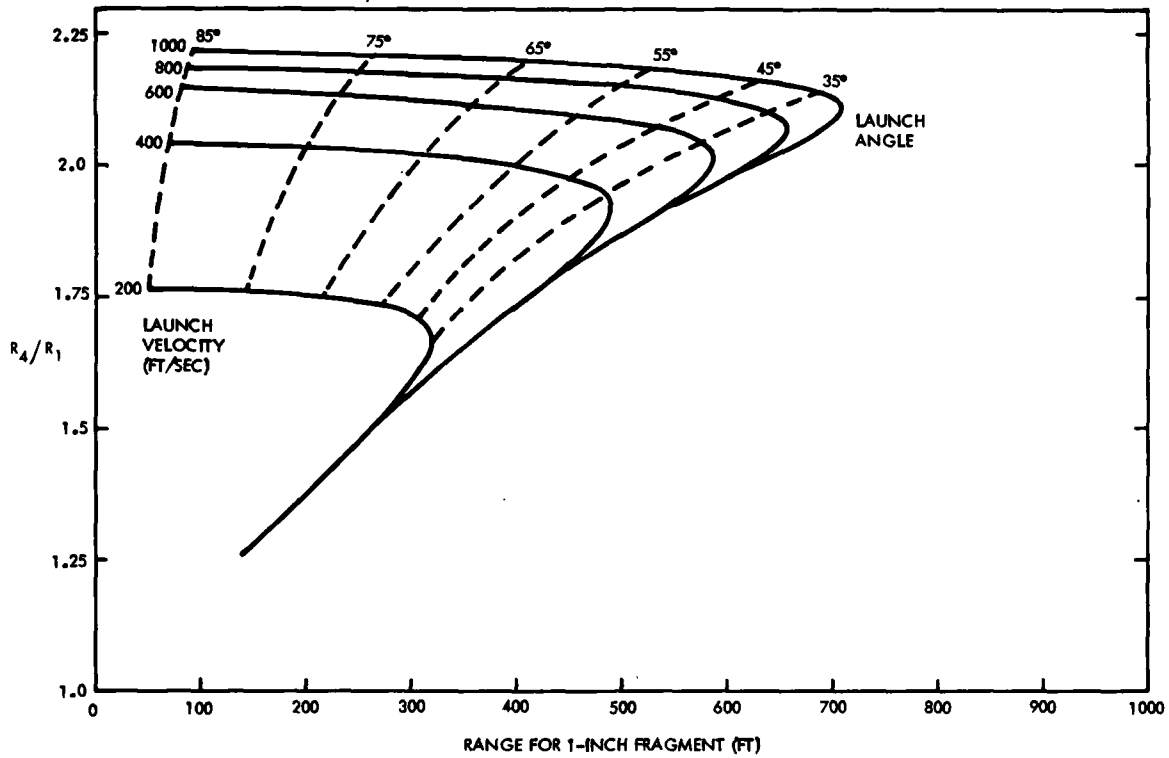


Figure 10-3. Case 11 - Debris Density Scaling by Statistical Simulation Method

(a) FRAGMENT LENGTHS OF $L = 1''$, $4L = 4''$



(b) FRAGMENT LENGTHS OF $L = 2''$, $4L = 8''$

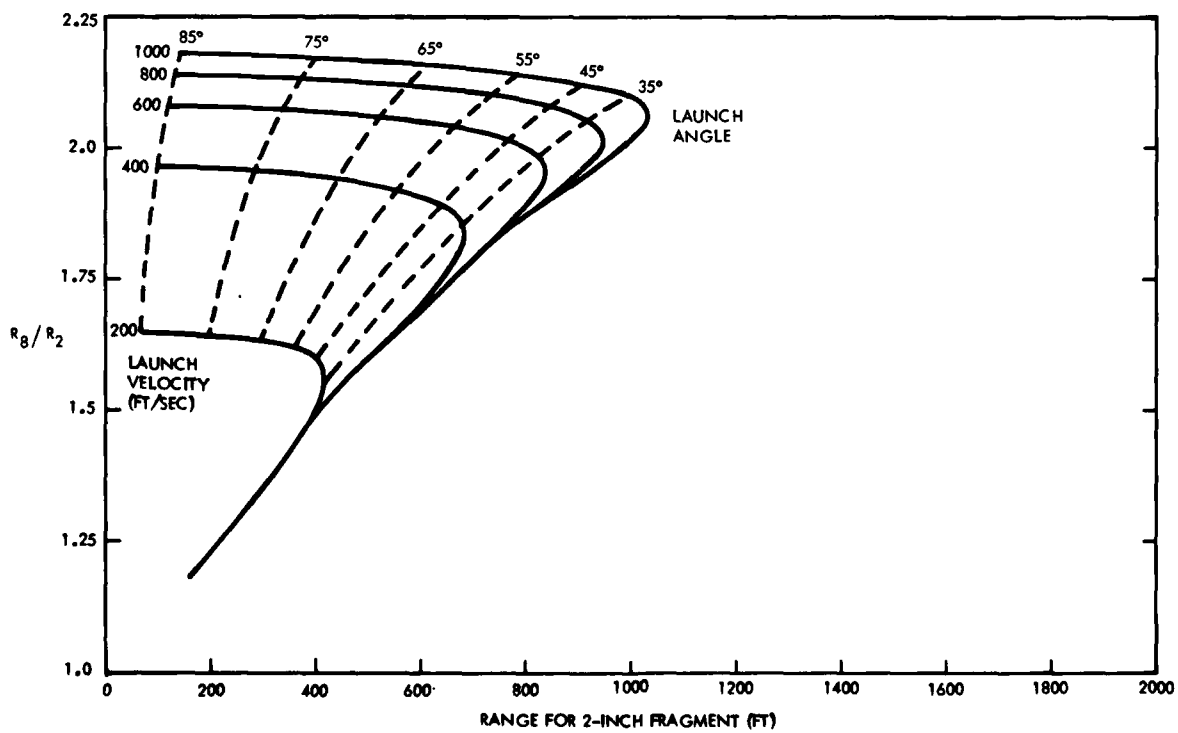
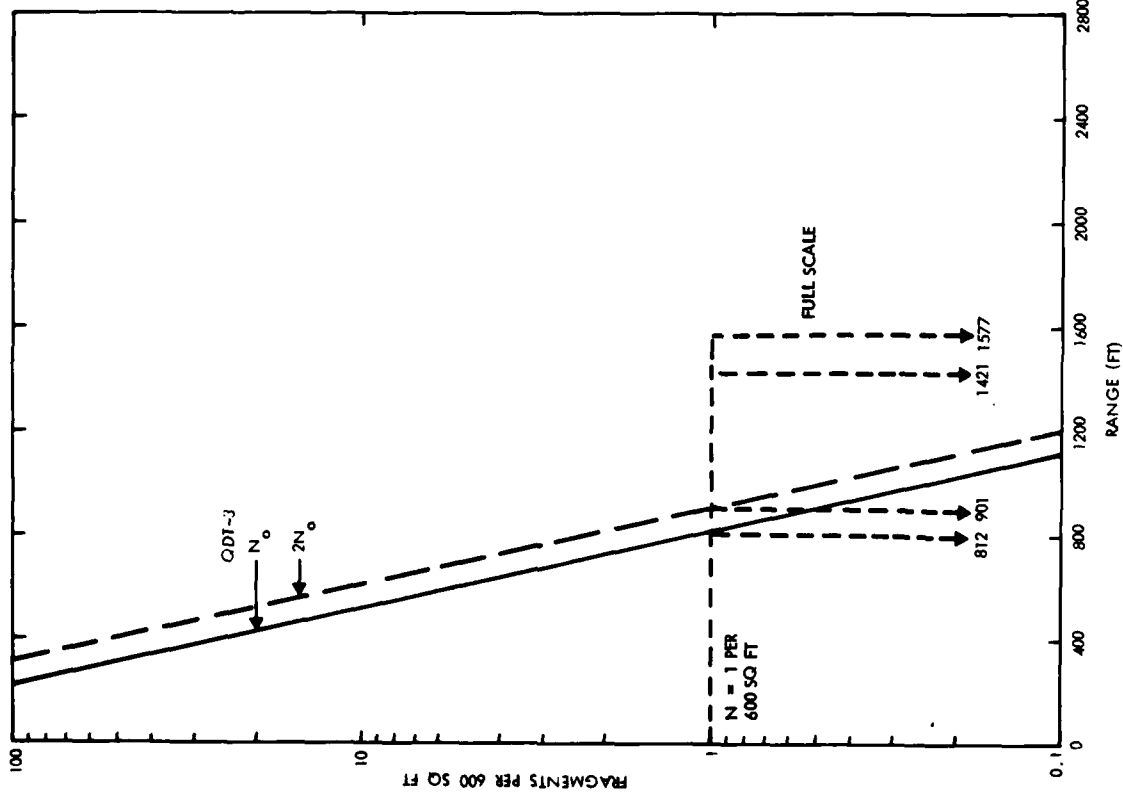


Figure 10-4. Comparison of Maximum Range Ratios Corresponding to QDT-3 Fragment Shape Factors and Drag Coefficient of 0.5

(a) STATISTICAL SIMULATION METHOD



(b) TRAJECTORY LIMITATION METHOD

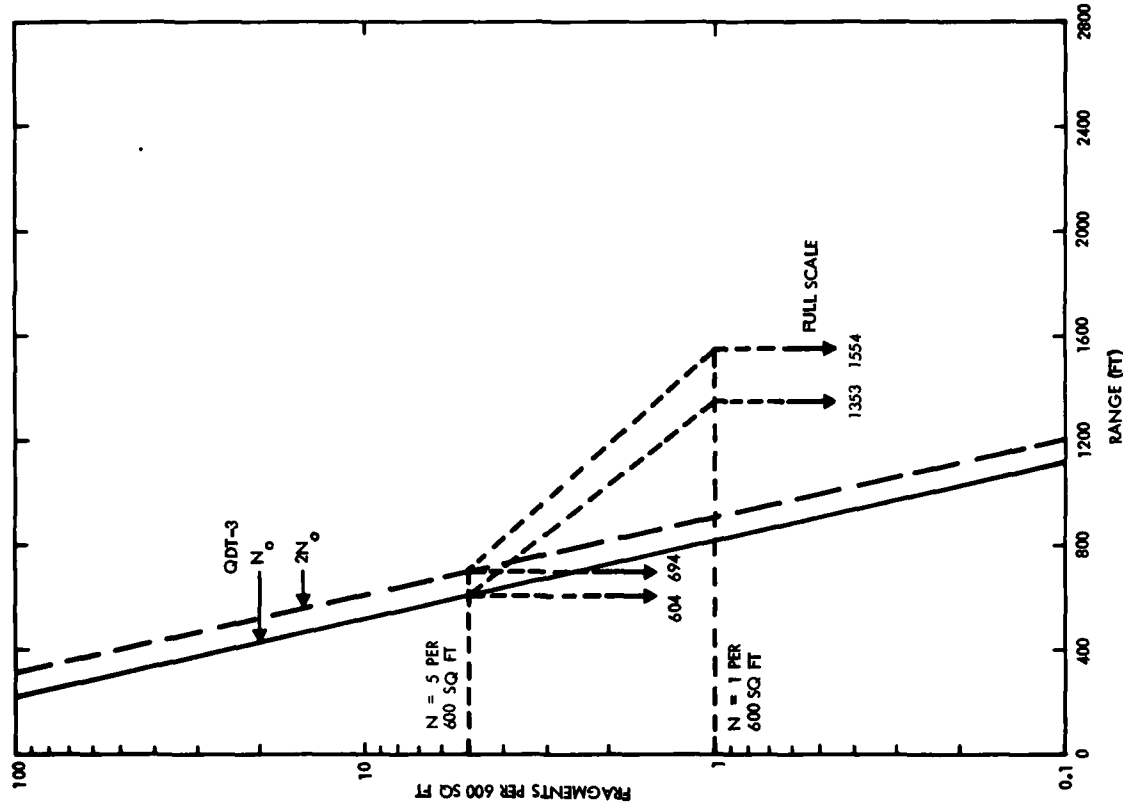
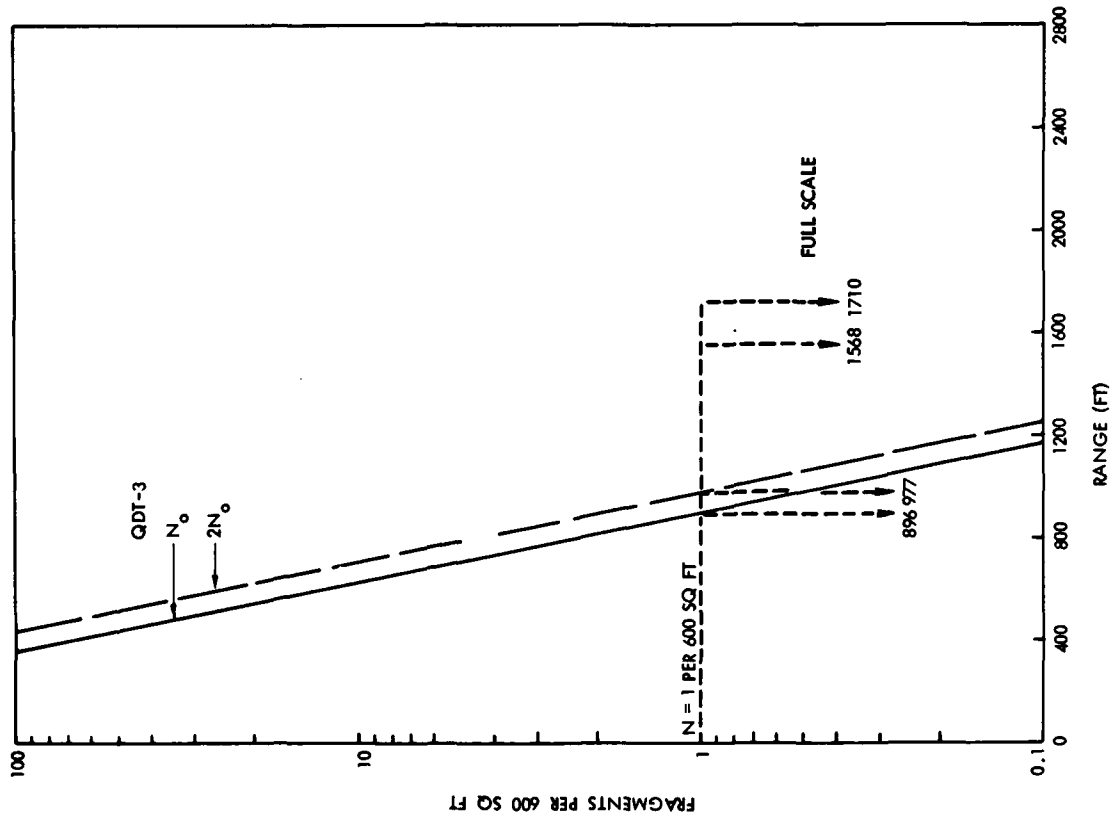


Figure 10-5. Debris Density Scaling for Data on S, NE, and NW Radials

(a) STATISTICAL SIMULATION METHOD



(b) TRAJECTORY LIMITATION METHOD

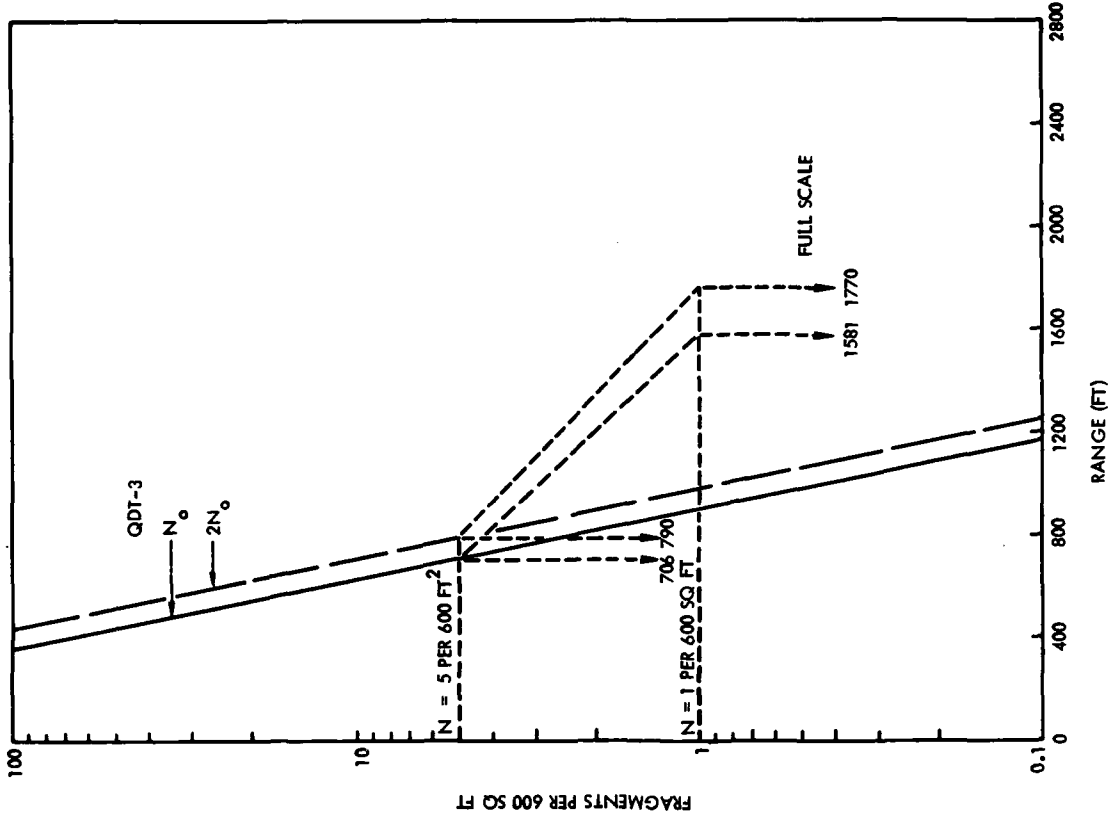


Figure 10-6. Debris Density Scaling for Data on NW Radial Only

11.0 SUMMARY AND CONCLUSIONS

Results of the study are briefly summarized as follows:

- Airblast
 - 1) The airblast data for the 1/10-scale and 1/4-scale tests verified applicability of cube root scaling.
 - 2) Excellent agreement between test data and predictions for the calibration shot validated the reliability of the airblast measurements.
 - 3) Analytical predictions for the 1/4-scale test were in agreement with the empirical data.
 - 4) The ground range to a peak pressure level of 1 psi for the 1/4-scale test was determined to be 270 feet with a corresponding full-scale value estimated as 1080 feet.
- Soil Ejecta
 - 1) The eject distribution for the 1/4-scale test extended out to relatively limited ranges.
 - 2) The impact of ejecta on quantity-distance considerations was considered to be negligible.
- Structural Debris
 - 1) There was good correlation between predictions of structural fragmentation and test results.
 - 2) Geometric scaling of fragment dimensions was considered applicable for a full-scale event.
 - 3) An increase in total fragment number by a factor of two was established as an upper limit for a full-scale explosion.
 - 4) An upper bound of the required quantity-distance was determined to be 1567 feet.

It is readily apparent that structural debris is the governing hazard as related to determining quantity-distance criteria. Based on the analytical and experimental results of the present study, it is concluded that the adequacy of 1750 feet for the quantity-distance for the Peacekeeper system has been verified.

12.0 REFERENCES

- 3-1 Albritton, G.E., Davis, L.K., and Jones, P.S., "Test Plan for Peacekeeper Quantity Distance Verification Program: Quantity Distance Tests (QDT)," Structures Laboratory, U.S. Army Engineer Waterways Experiment Station, Vicksburg, Miss., November 1983.
- 3-2 Zelasko, J.S., Memo Pertaining to Acceptable Gradation Range for QDT Backfill, prepared by U.S. Army Engineer Waterways Experiment Station, Vicksburg, Miss., 27 September 1983.
- 3-3 Jones, P.S., Tilson, D.L., Albritton, G.E., Davis, L.K., and Zelasko, J.S., "Final Report for Peacekeeper Quantity Distance Verification Program: Quantity Distance Test-3 (QDT-3)," Structures Laboratory, U.S. Army Engineer Waterways Experiment Station, Vicksburg, Miss., April 1984.
- 4-1 Ullrich, G.W., "Transmittal of Airblast Predictions in Support of MX Safety Study," letter to Lt. Col. J. Greening, AF/IGF, Defense Nuclear Agency (SPSS), 8 March 1982.
- 4-2 Needham, C.E., "Prairie Flat Airblast Calculations," AFWL-TR-69-4, Air Force Weapons Laboratory, Kirtland Air Force Base, N. Mex., January 1969.
- 5-1 Dishon, J. F., "ESSEX-DIAMOND ORE Research Program: Ejecta Measurements Report, ESSEX I, Phase 2," WES-TR-SL-79-9, U.S. Army Engineer Waterways Experiment Station, Vicksburg, Miss., October 1979.
- 5-2 Carlson, R.H. and Roberts, W.A., "Mass Distribution and Throwout Studies (Project SEDAN)," PNE-217F, U.S. Atomic Energy Commission, 6 August 1963.
- 5-3 Rooke, A.D. and Davis, L.K., "Mass Distribution Measurements of Crater Ejecta and Dust (Project DANNY BOY)," PDR 1815, U.S. Atomic Energy Commission, 13 February 1964.
- 5-4 Carlson, R.H. and Jones, C.D., "Ejecta Distribution Studies (Project Air Vent)," D2-90575, The Boeing Company, November 1964.
- 5-5 Cooper, H.F., "A Summary of Explosion Cratering Phenomena Relevant to Meteor Crater Events," Impact and Explosion Cratering, Proceedings of the Symposium on Planetary Cratering Mechanics, September 1976, Pergamon Press, New York, 1977.
- 5-6 Ahlers, E.B., "Crater Ejecta Studies - Air Vent Phase I," IIT Research Institute, Project M6072, May 1965.
- 5-7 Vortman, L.J., et al., "Project Stagecoach, 20-Ton HE Cratering Experiments in Desert Alluvium," SC-4596 (RR), Sandia Corporation, May 1962.
- 5-8 Seebaugh, W.R., "A Dynamic Crater Ejecta Model," Impact and Explosion Cratering, Proceedings of the Symposium on Planetary Cratering Mechanics, September 1976, Pergamon Press, New York, 1977.

- 5-9 Yu, P.H.C., and Mazzola, T.A., "A Summary of Debris and Fetching Studies," 74.4735.9-69, TRW Systems, September 1974.
- 5-10 Ullrich, G.W., "Transmittal of Airblast Predictions in Support of MX Safety Study," letter to Lt. Col. J. Greening, AF/IGF, Defense Nuclear Agency (SPSS), 8 March 1982.
- 5-11 Rooke, A.D., and Chew, T.D., "Crater and Ejecta Measurements for a Full-Scale Missile in an Underground Cell (SPRINT)," Misc Paper No. 1-853, U.S. Army Engineer Waterways Experiment Station, Vicksburg, Miss., November 1966.
- 5-12 Henney, R.W., and Carlson, R.H., "Distribution of Natural Missiles Resulting from Cratering Explosions in Hard Rock," Annals of the New York Academy of Sciences, Vol. 152, pp. 404-431, 28 October 1968.
- 5-13 Dishon, J.F., "ESSEX-DIAMOND ORE Research Program: Ejecta Measurements Report, ESSEX I, Phase 1," DNA PR 0009, Defense Nuclear Agency, February 1975.
- 5-14 Harvey, W.T., Dishon, J.F., and Tami, T.M., "Near Surface Cratering Experiments, Fort Polk, Louisiana," AFWL-TR-74-351, Air Force Weapons Laboratory, Kirtland Air Force Base, N. Mex., November 1975.
- 6-1 Coltharp, D.R., "Symposium Proceedings: The Interaction of Non-Nuclear Munitions with Structures: Blast Response Tests of Reinforced Concrete Box Structures," U.S. Army Engineer Waterways Experiment Station, U.S. Air Force Academy, Colorado, 10-13 May 1983.
- 6-2 "A Manual for the Prediction of Blast and Fragment Loadings on Structures," DOE/TIC-11268, U.S. Department of Energy, November 1980.
- 6-3 Kot, C.A., et al., "Effects of Air Blast on Power Plant Structures and Components," MUREG/CR-0442, Argonne National Laboratory, October 1978.
- 6-4 Timoshenko, S., et al., Vibration Problems in Engineering, John Wiley and Sons, New York, 1974.
- 6-5 Murtha, R., and Crawford, J., "Dynamic Shear Failure Predictions of Shallow-Buried Reinforced Concrete Slabs," NCEL TM M-51-81-04, May 1981.
- 6-6 Ross, T.J., "Direct Shear Failure in Reinforced Concrete Beams under Impulsive Loading," AFWL-TR-83-84, Air Force Weapons Laboratory, Kirtland Air Force Base, N. Mex., September 1983.
- 6-7 Albritton, G.E., "Response of Deep Reinforced and Unreinforced Concrete Slabs to Static and Dynamic Loading," N-68-5, U.S. Army Engineer Waterways Experiment Station, Vicksburg, Miss.
- 7-1 Ward, J.M., "Distant Runner - Debris Recovery and Analysis Program for Events 4 and 5," Naval Surface Weapons Center, White Oak Laboratory, Silver Spring, Maryland, April 1982.

- 8-1 Jones, P.S., and Albritton, G.E., "Final Report for Peacekeeper Quantity Distance Verification Program: Quantity Distance Test-1 (QDT-1)," Structures Laboratory, U.S. Army Engineer Waterways Experiment Station, Vicksburg, Miss., February 1984.
- 8-2 Jones, P.S., and Albritton, G.E., "Final Report for Peacekeeper Quantity Distance Verification Program: Quantity Distance Test-2 (QDT-2)," Structures Laboratory, U.S. Army Engineer Waterways Experiment Station, Vicksburg, Miss., March 1984.
- 8-3 Jones, P.S., Tilson, D.L., Albritton, G.E., Davis, L.K., and Zelasko, J.S., "Final Report for Peacekeeper Quantity Distance Verification Program: Quantity Distance Test-3 (QDT-3)," Structures Laboratory, U.S. Army Engineer Waterways Experiment Station, Vicksburg, Miss., April 1984.
- 8-4 Tilson, D.L., "Data Report for Peacekeeper Quantity Distance Verification Program: Quantity Distance Test-3 Calibration Shot," Structures Laboratory, U.S. Army Engineer Waterways Experiment Station, Vicksburg, Miss., March 1984.
- 9-1 Kingery, C.N., "Air Blast Parameters Versus Distance for Hemispherical TNT Surface Bursts," BRL Report 1344, U.S. Army Material Command, Ballistic Research Laboratories, Aberdeen Proving Ground, Maryland, September 1966.
- 9-2 "Nuclear Weapon Blast Phenomena," Volume IV, NASA 1200-IV, Defense Nuclear Agency, July 1973.

APPENDIX A
PHOTOGRAPHIC SEQUENCE OF 1/4-SCALE SILO CONSTRUCTION
AND
QDT-3 TEST SITE PREPARATION

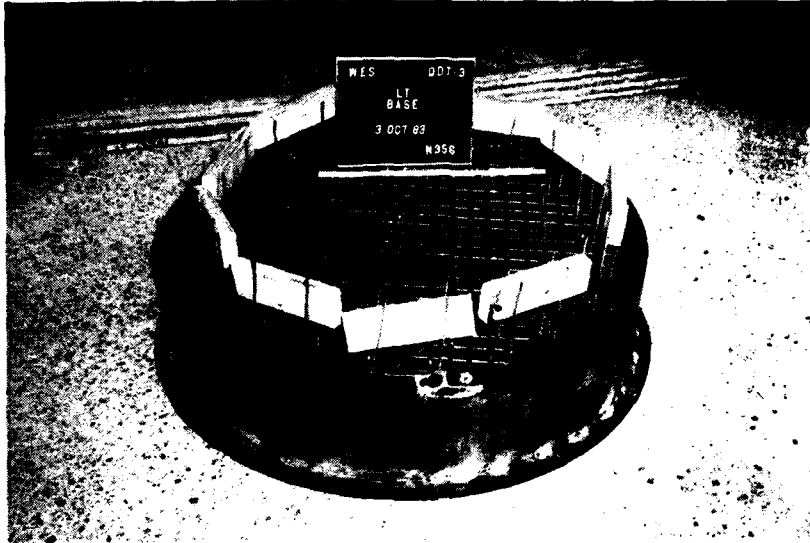


Figure A-1. LT Base Reinforcement



Figure A-2. LT Without Core Liner Extension

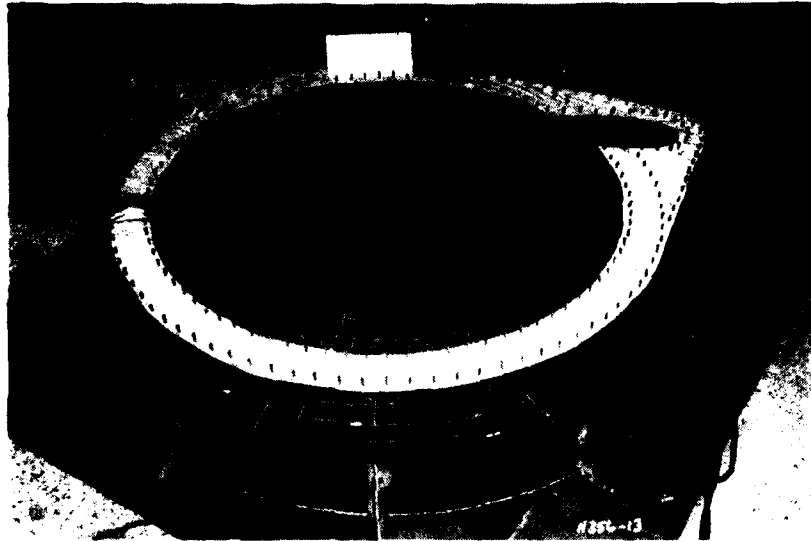


Figure A-3. LER Footing Reinforcement



Figure A-4. LER Core Liner

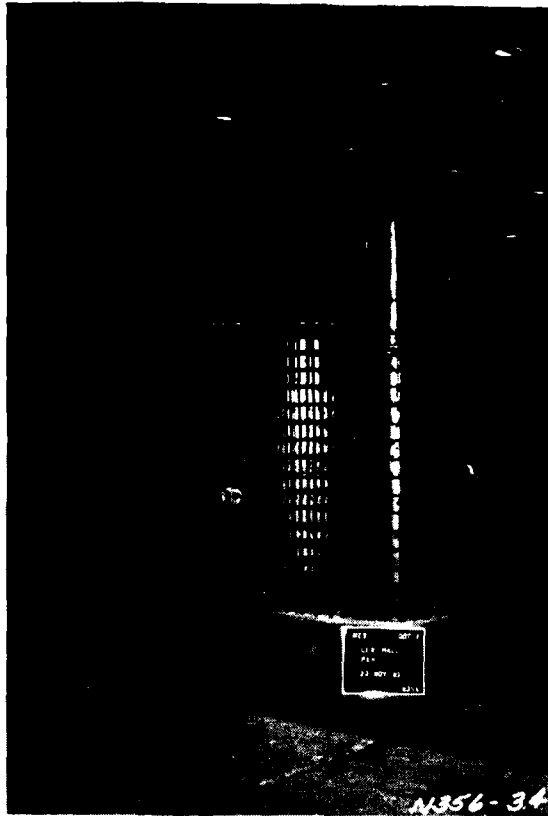


Figure A-5. Completed LER Wall Reinforcement

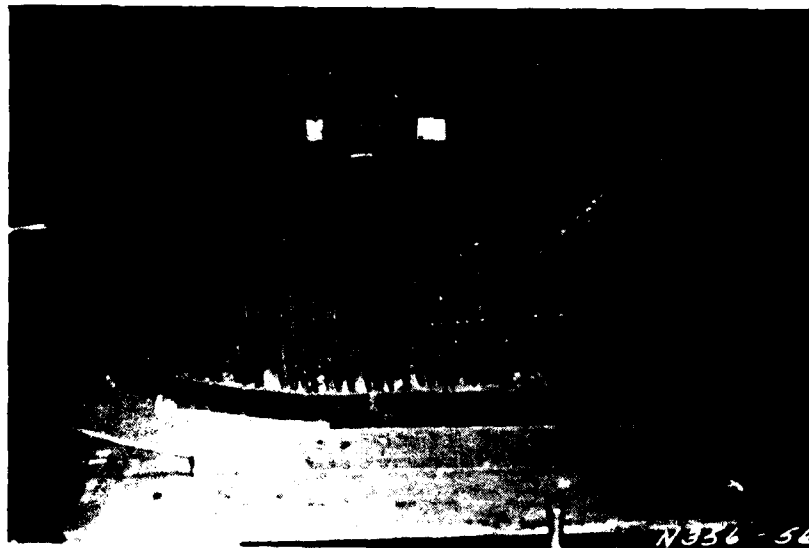


Figure A-6. LER Lower Ceiling Reinforcement

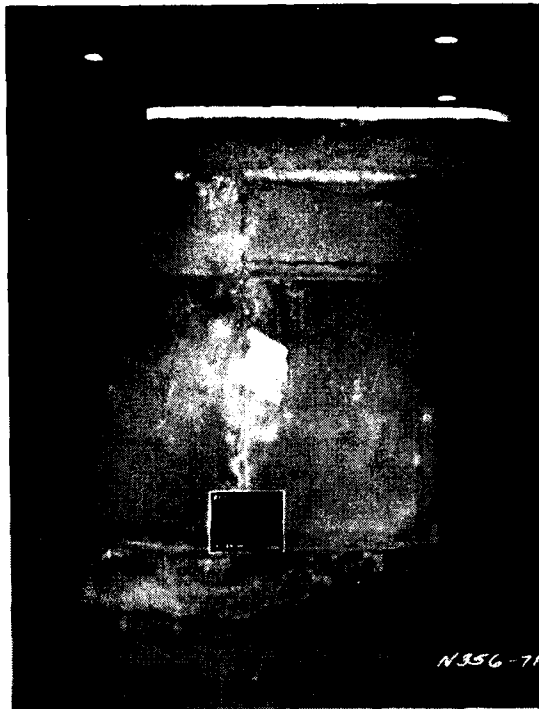


Figure A-7. Side View of Completed LER

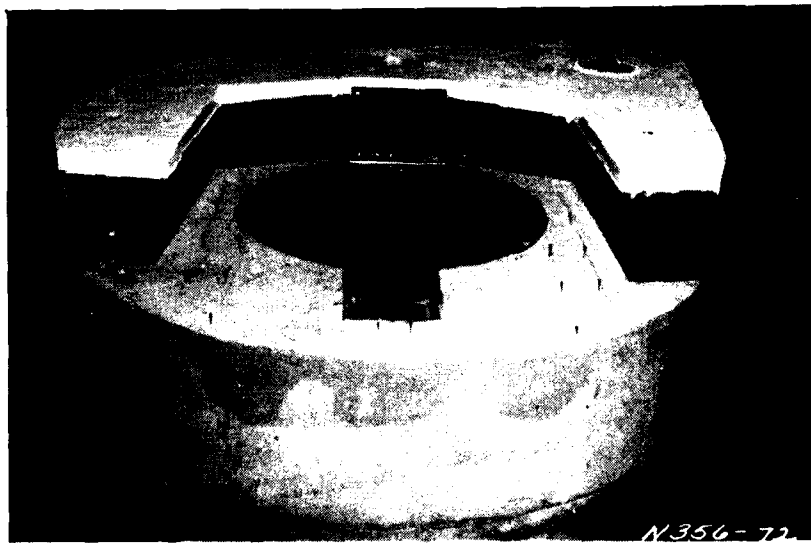


Figure A-8. Top View of Completed LER

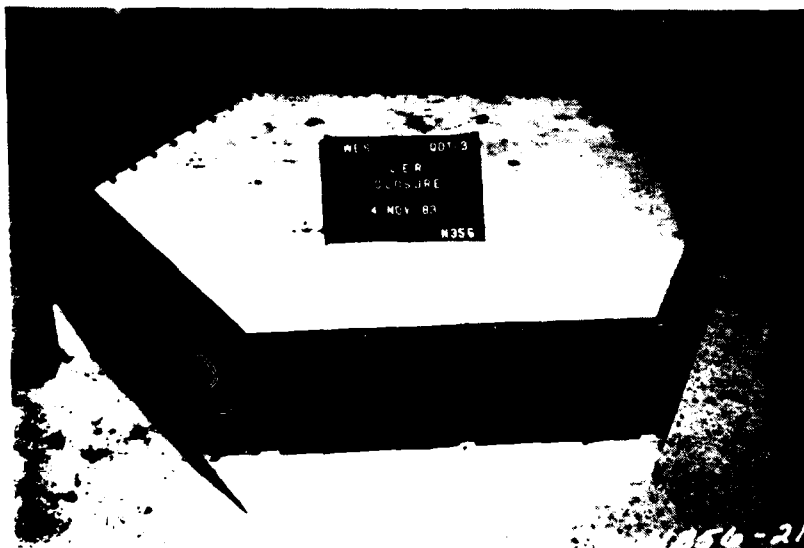


Figure A-9. Side Panels for Closure

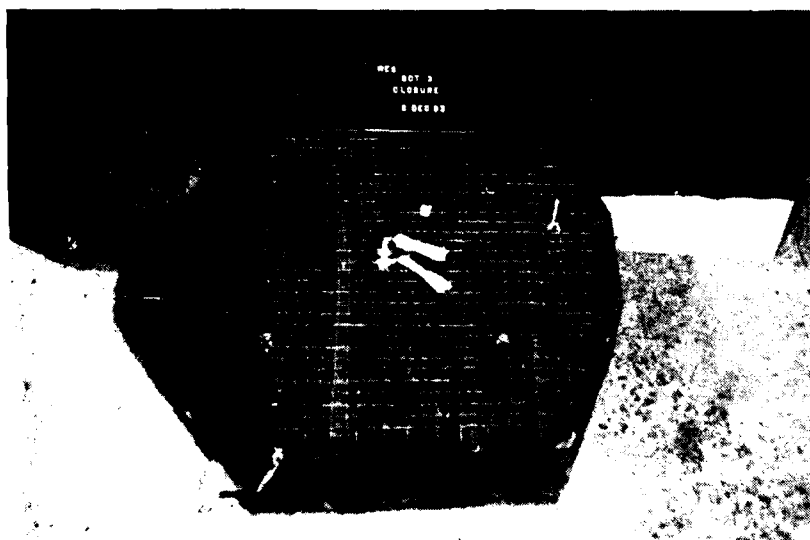


Figure A-10. Reinforcement Spacing in Closure

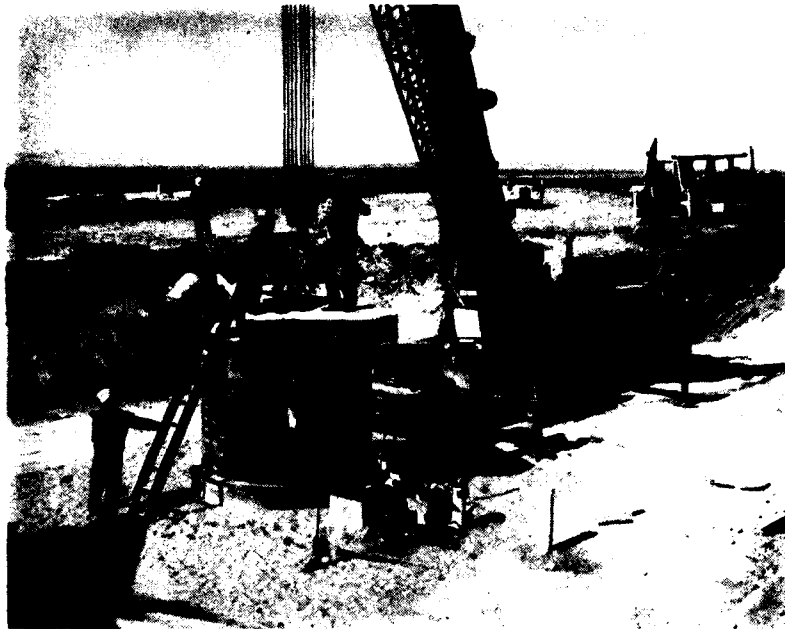


Figure A-13. LER Lowered into Position

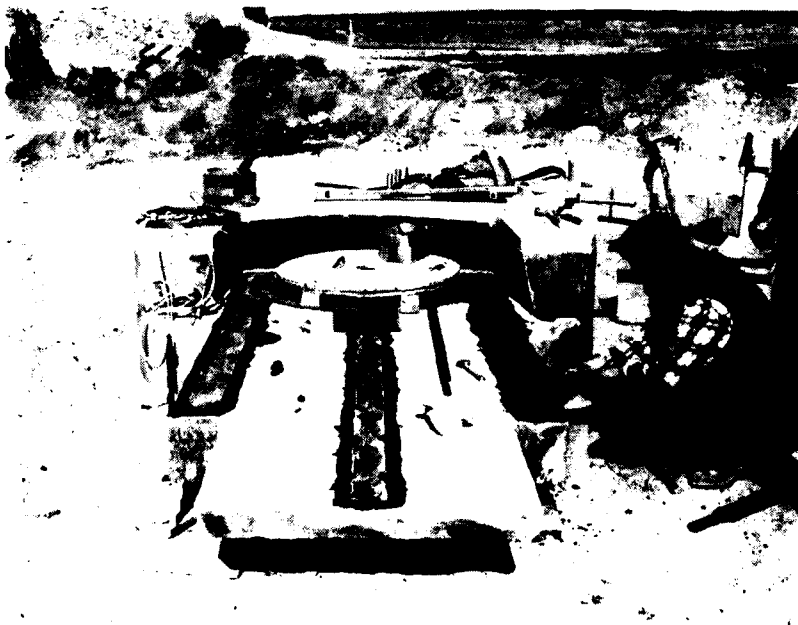


Figure A-14. Closure Tracks Being Installed on Track Footing



Figure A-15. Completed Structure Buried in Test Bed

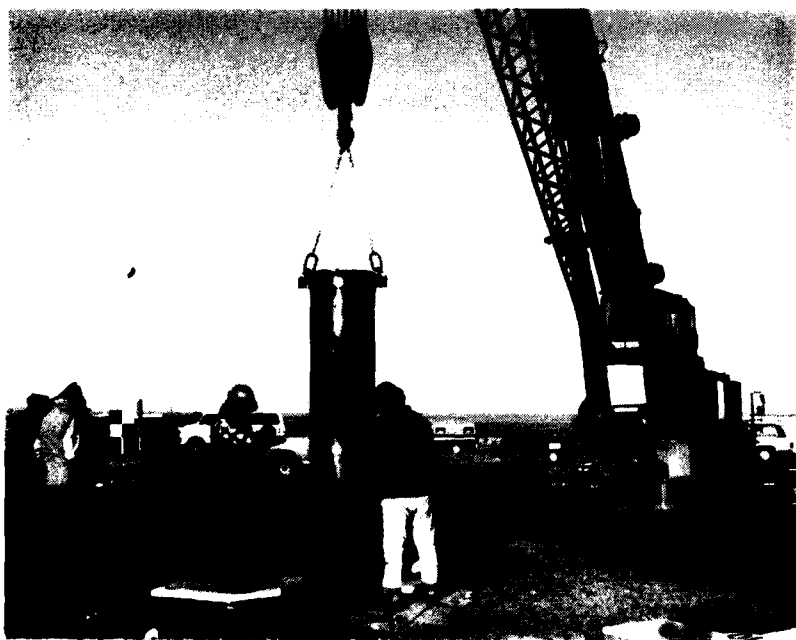


Figure A-16. Completed Charge Being Lowered into Structure

APPENDIX B
QDT-1 AIR BLAST RECORDS

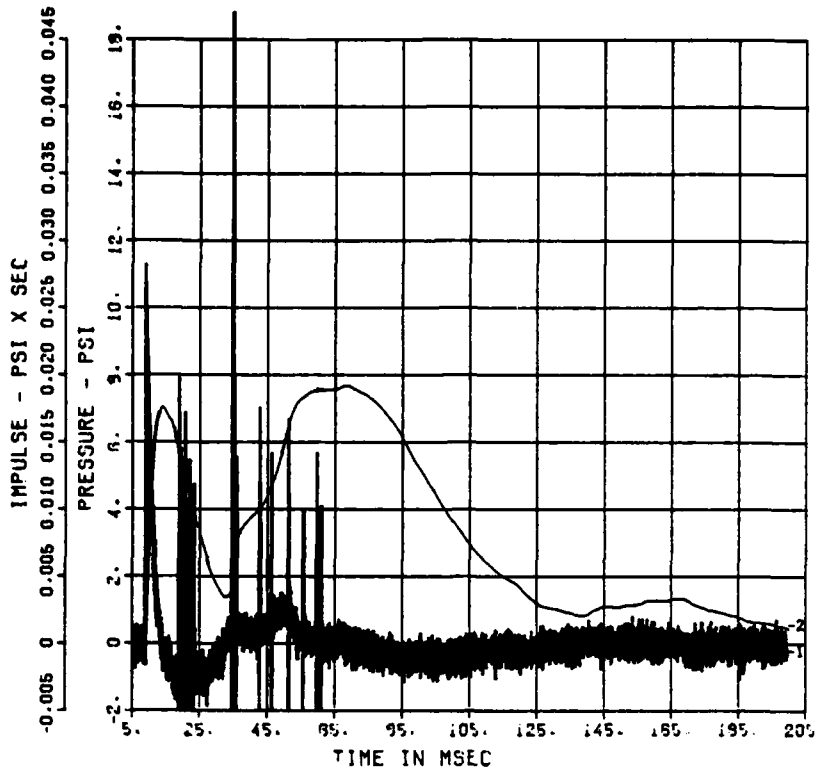


Chart B-1. QDT-1 Air Blast Record at 17 Feet on South Radial

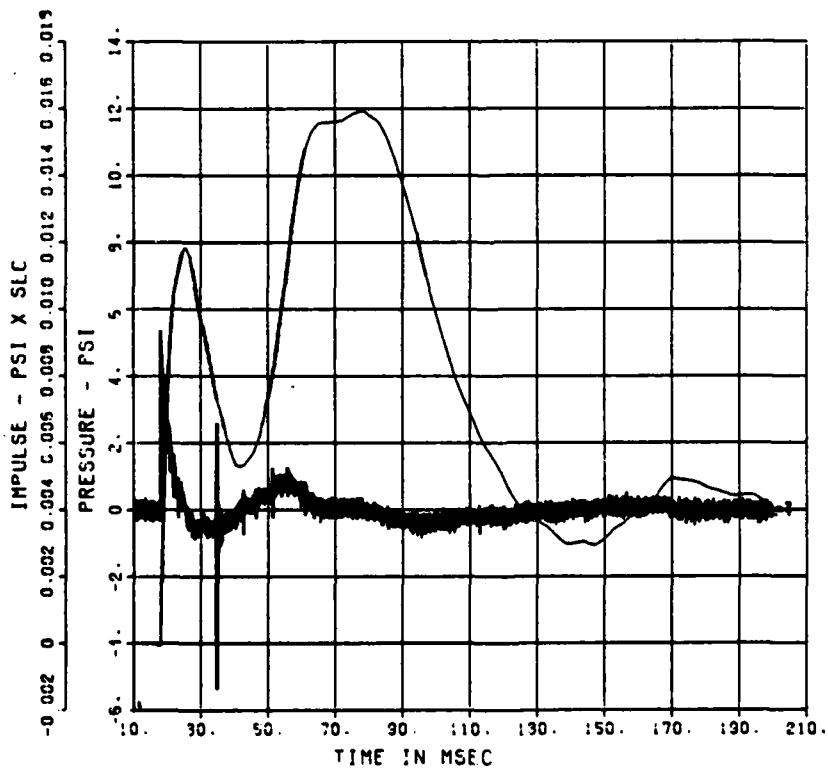


Chart B-2. QDT-1 Air Blast Record at 30 Feet on South Radial

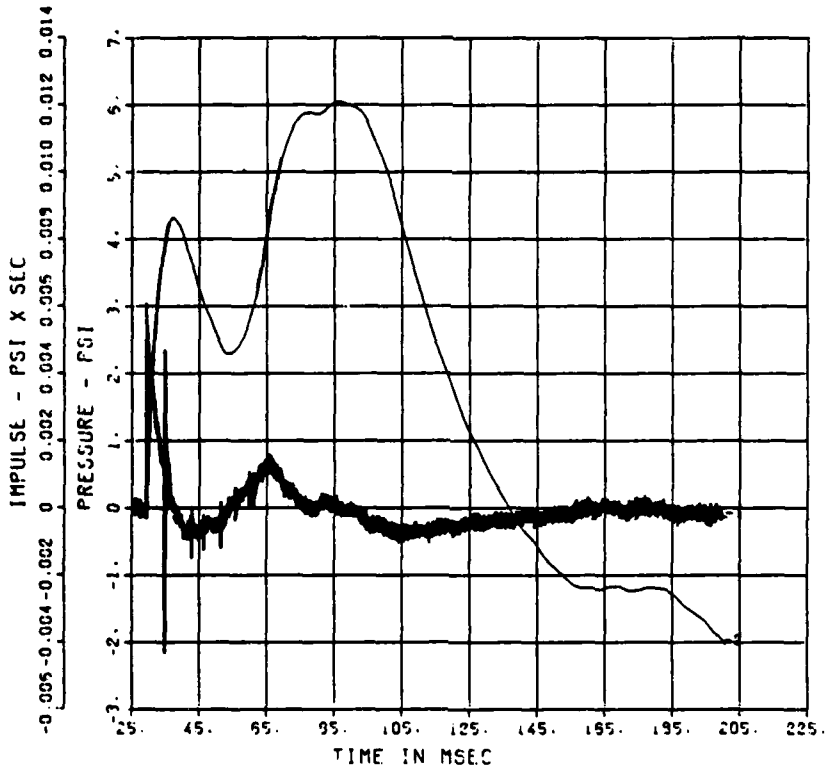


Chart B-3. QDT-1 Air Blast Record at 44 Feet on South Radial

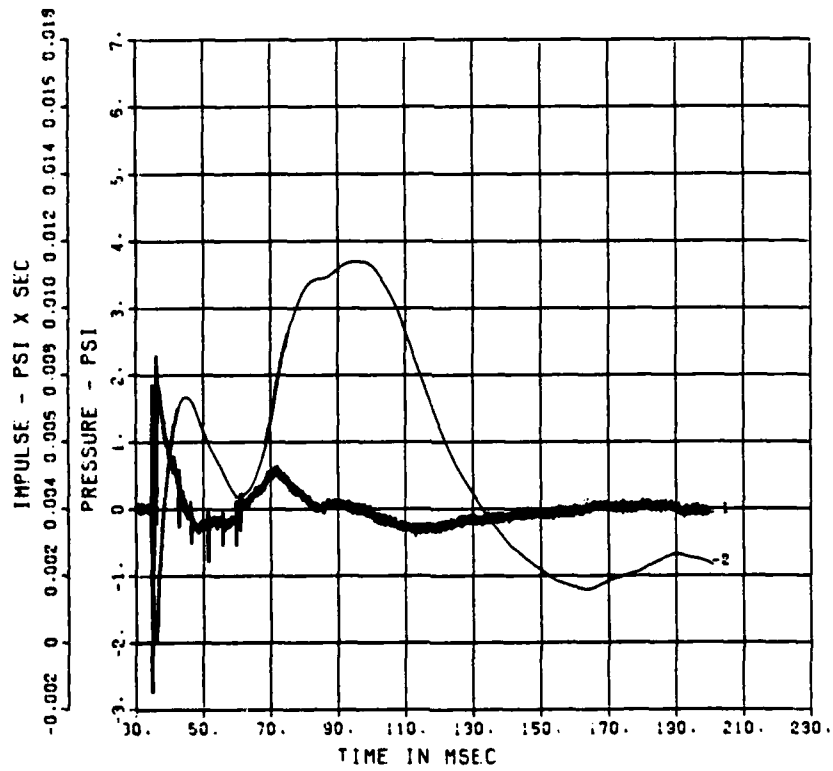


Chart B-4. QDT-1 Air Blast Record at 52 Feet on South Radial

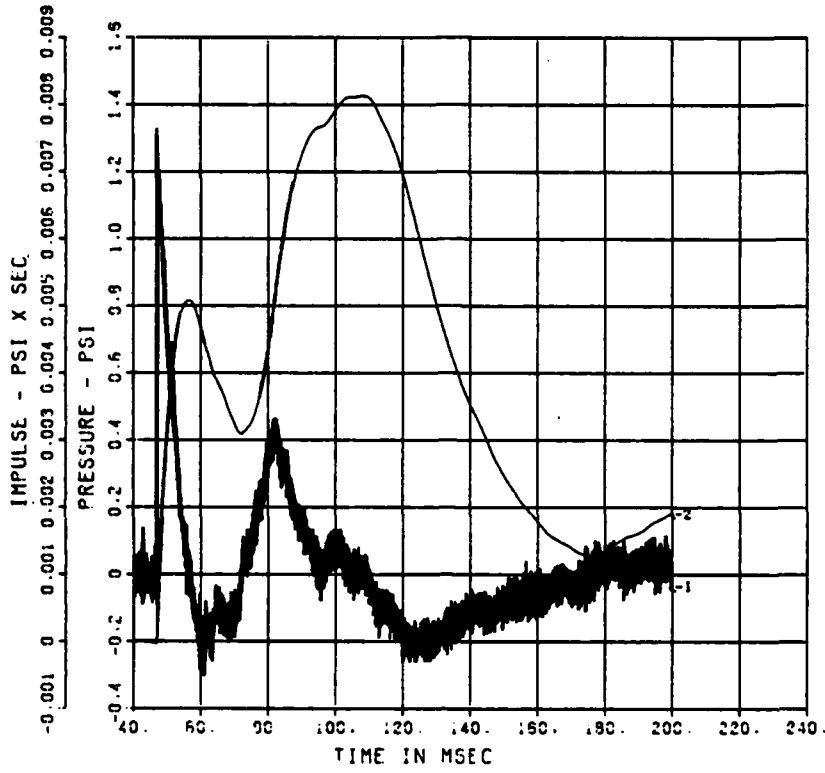


Chart B-5. QDT-1 Air Blast Record at 65 Feet on South Radial

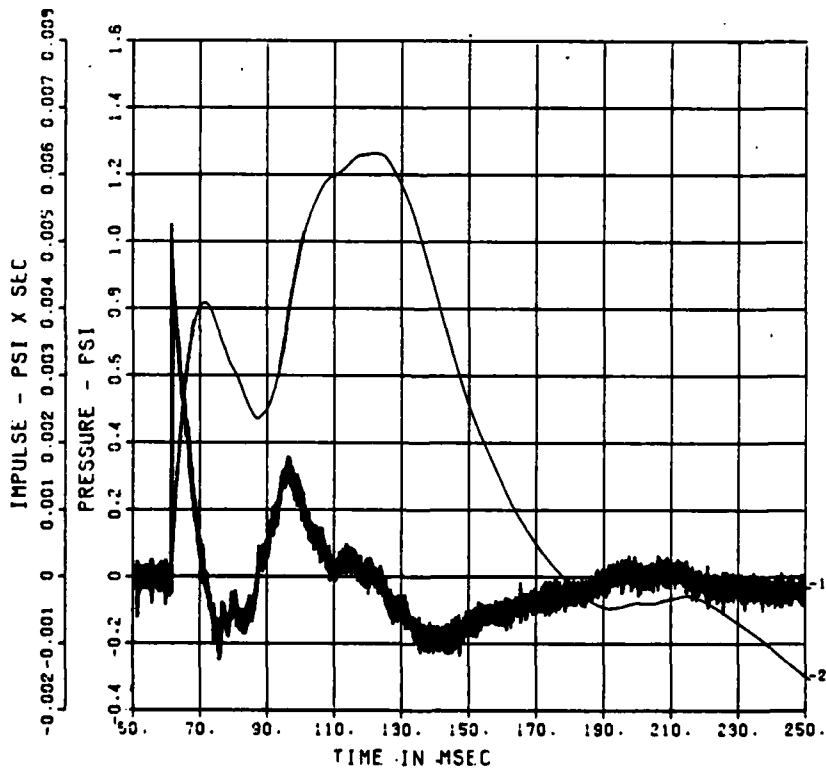


Chart B-6. QDT-1 Air Blast Record at 82 Feet on South Radial

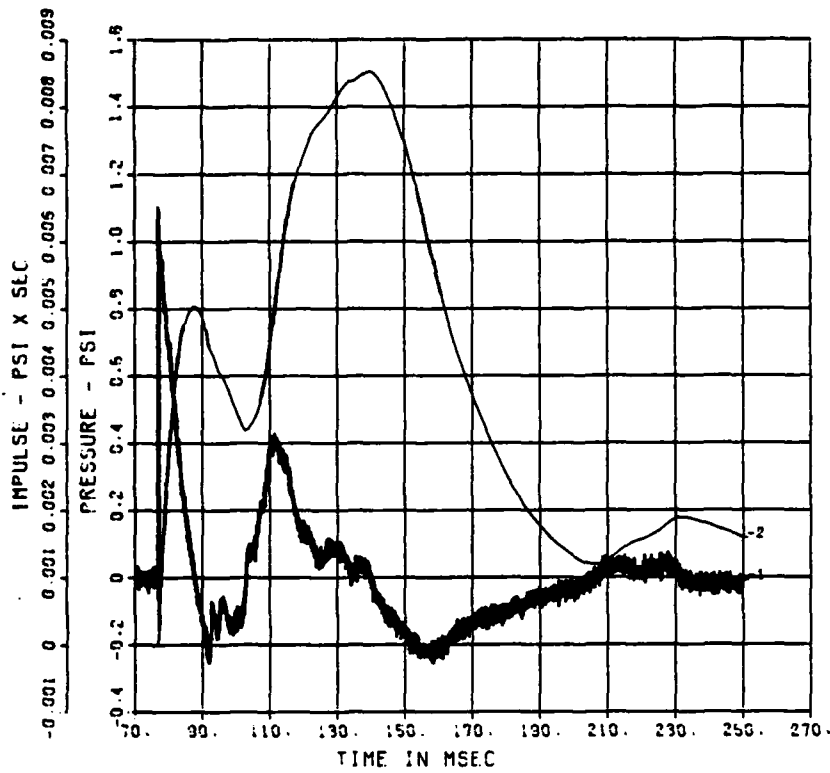


Chart B-7. QDT-1 Air Blast Record at 100 Feet on South Radial

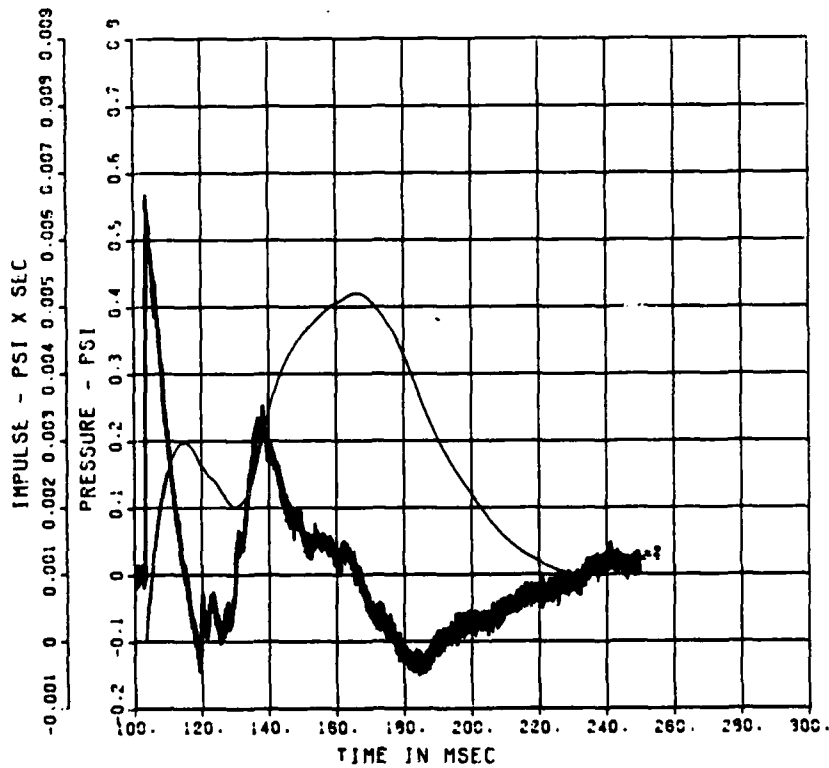


Chart B-8. QDT-1 Air Blast Record at 130 Feet on South Radial

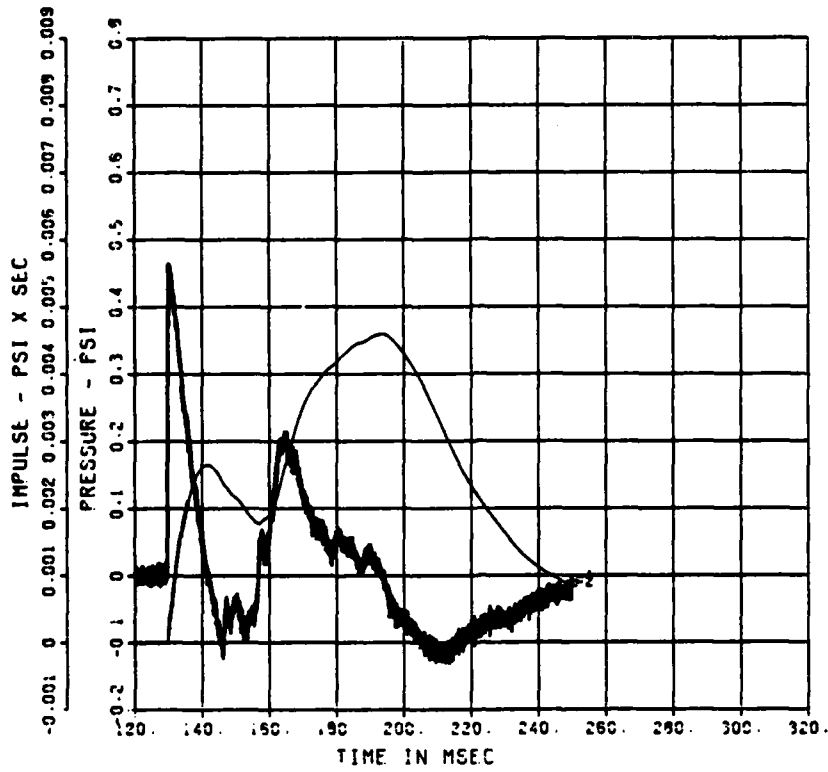


Chart B-9. QDT-1 Air Blast Record at 160 Feet on South Radial

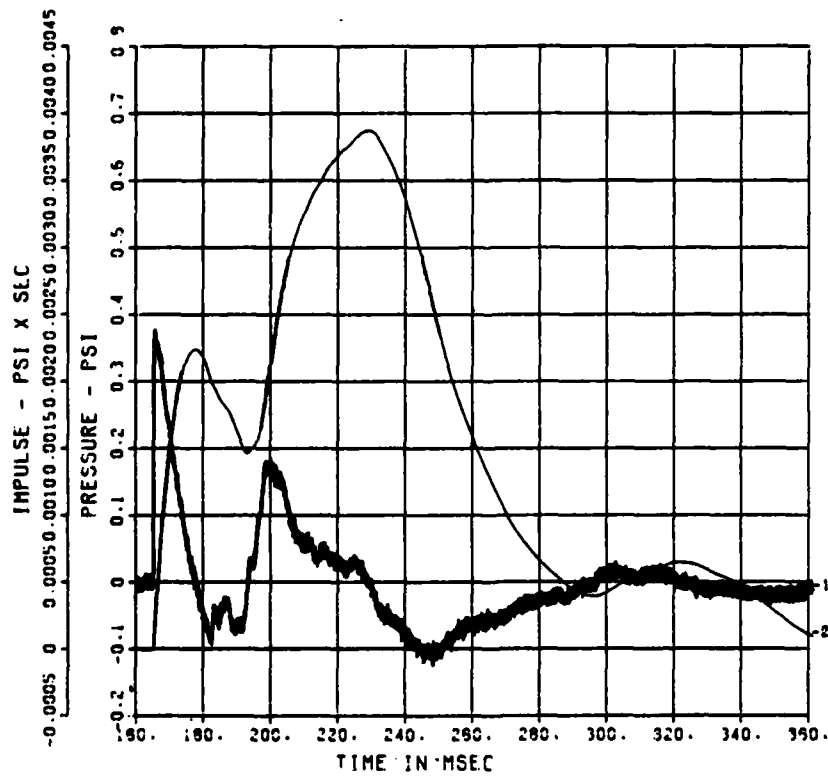


Chart B-10. QDT-1 Air Blast Record at 200 Feet on South Radial

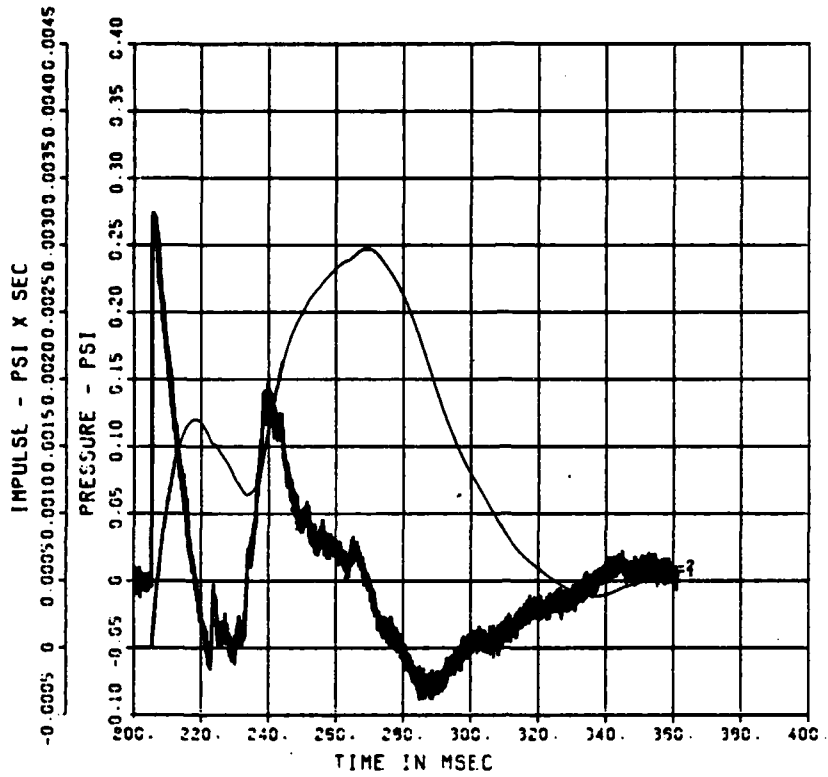


Chart B-11. QDT-1 Air Blast Record at 245 Feet on South Radial

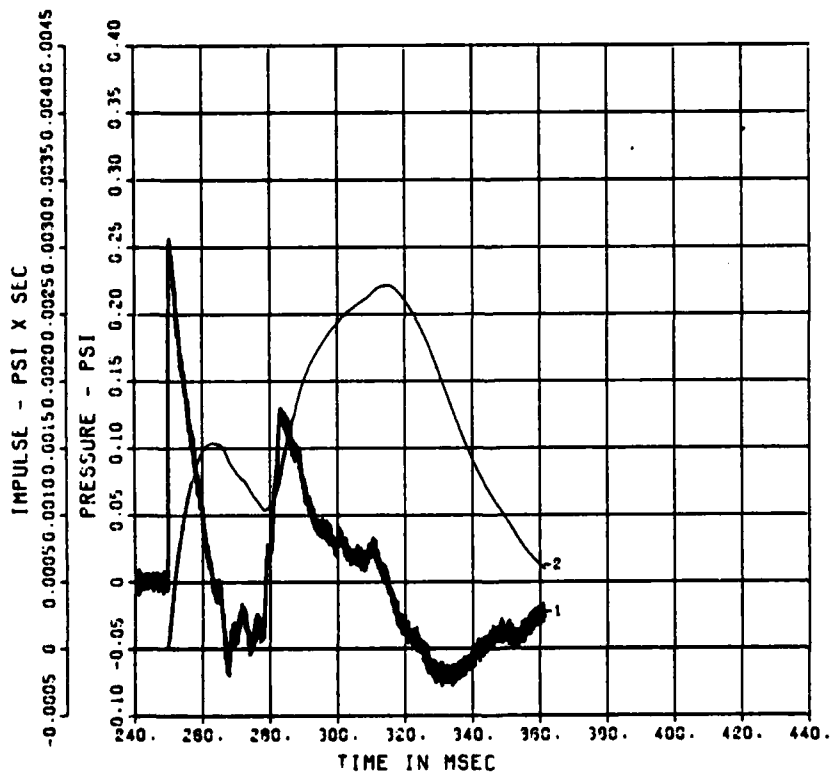


Chart B-12. QDT-1 Air Blast Record at 295 Feet on South Radial

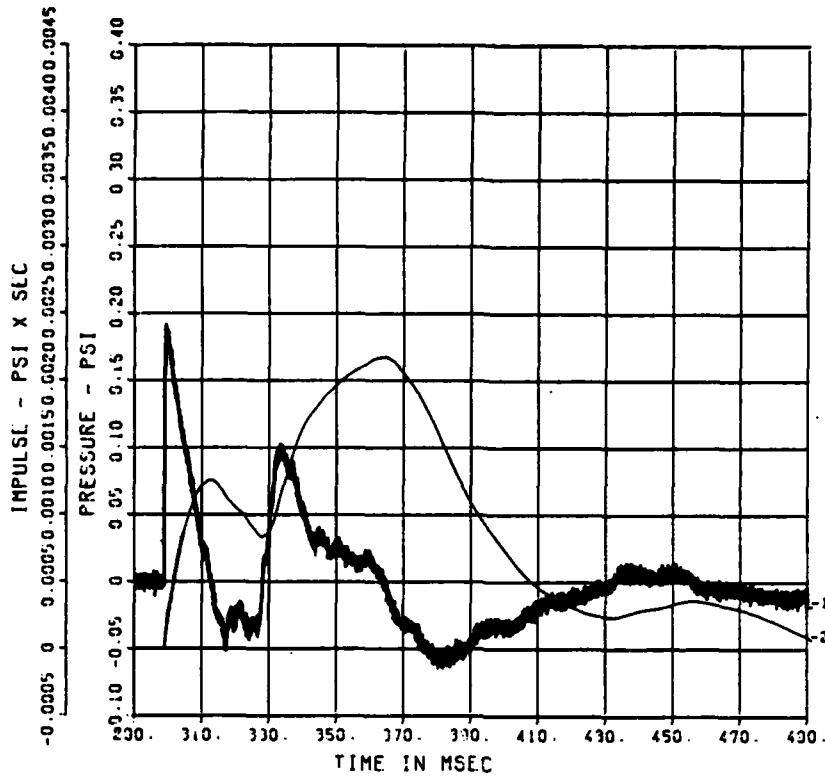


Chart B-13. QDT-1 Air Blast Record at 350 Feet on South Radial

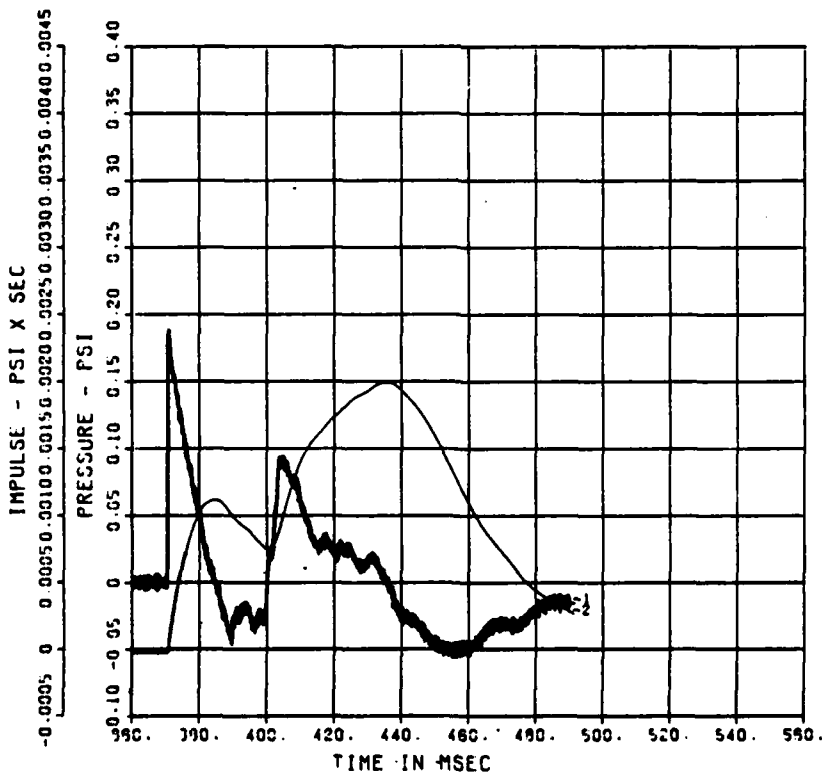


Chart B-14. QDT-1 Air Blast Record at 430 Feet on South Radial

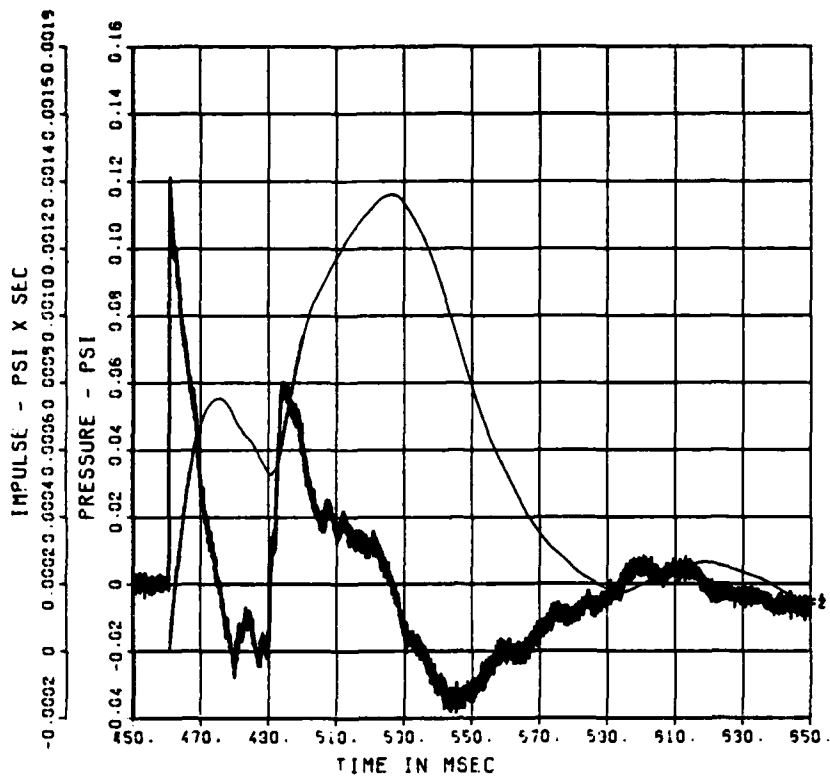


Chart B-15. QDT-1 Air Blast Record at 530 Feet on South Radial

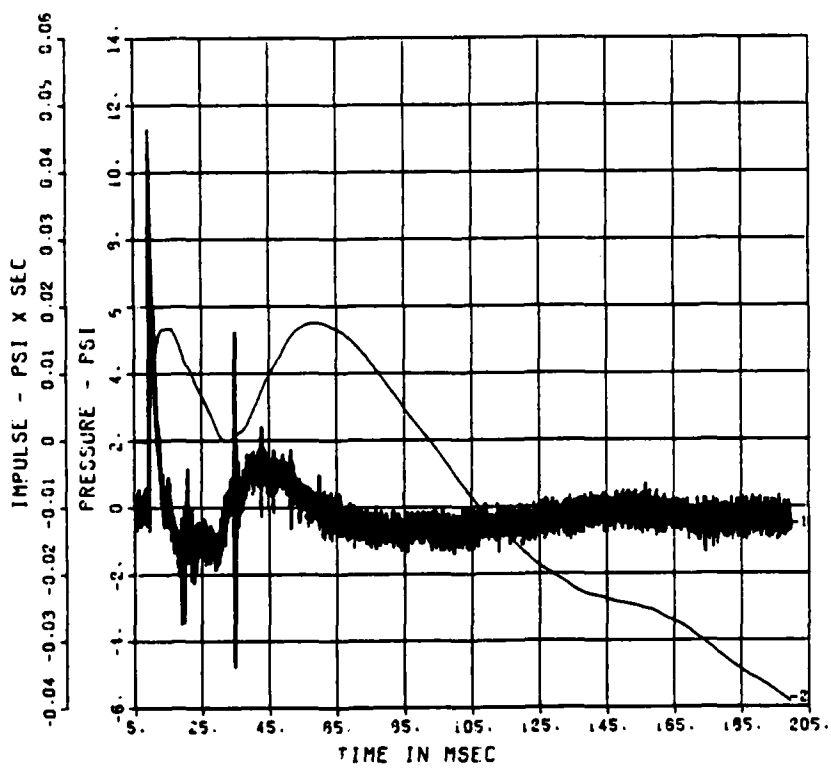


Chart B-16. QDT-1 Air Blast Record at 17 Feet on West Radial

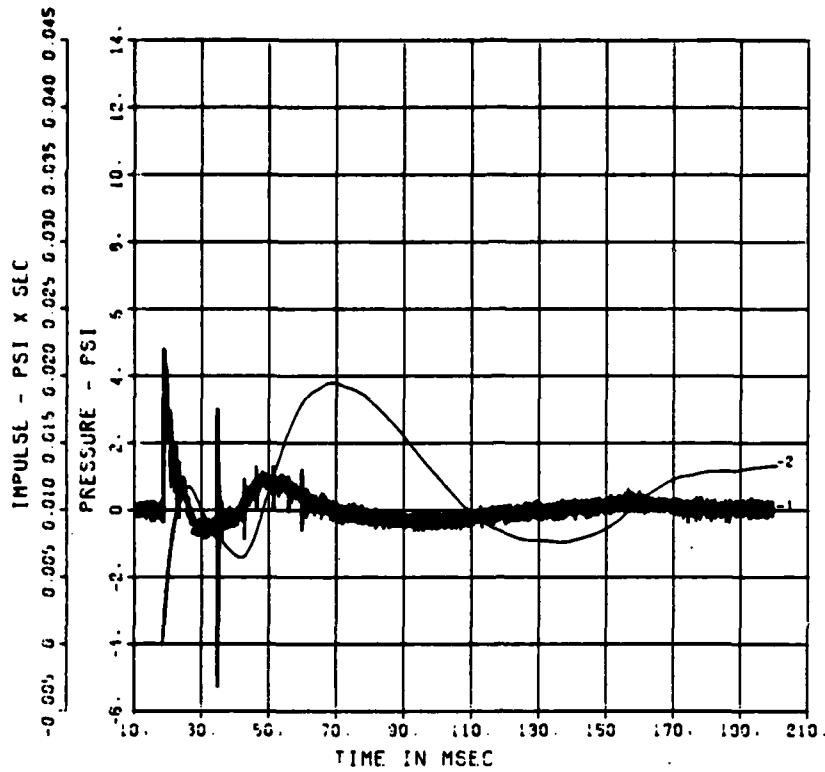


Chart B-17. QDT-1 Air Blast Record at 30 Feet on West Radial

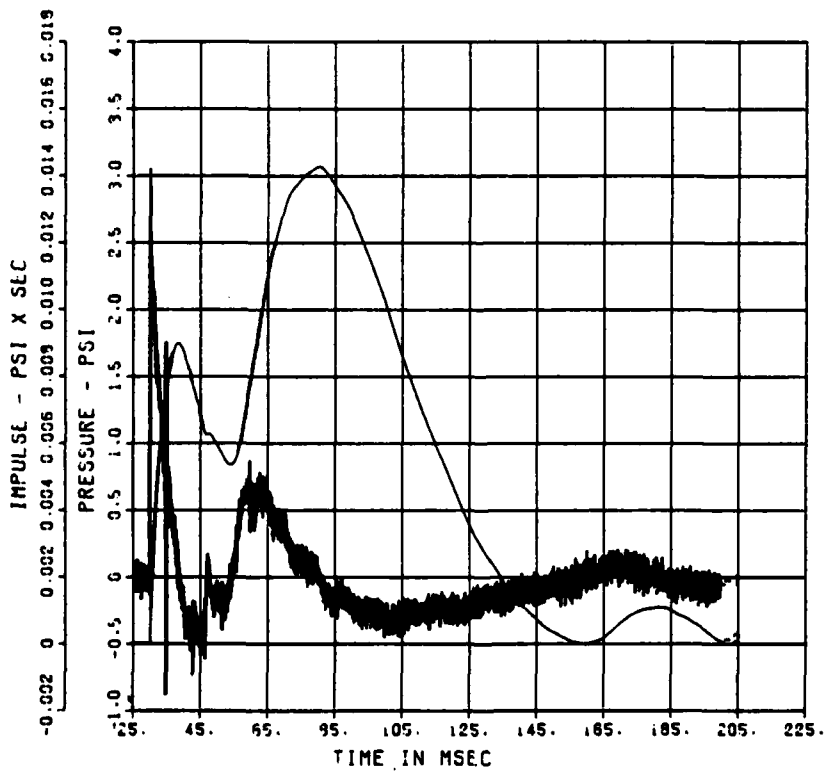


Chart B-18. QDT-1 Air Blast Record at 44 Feet on West Radial

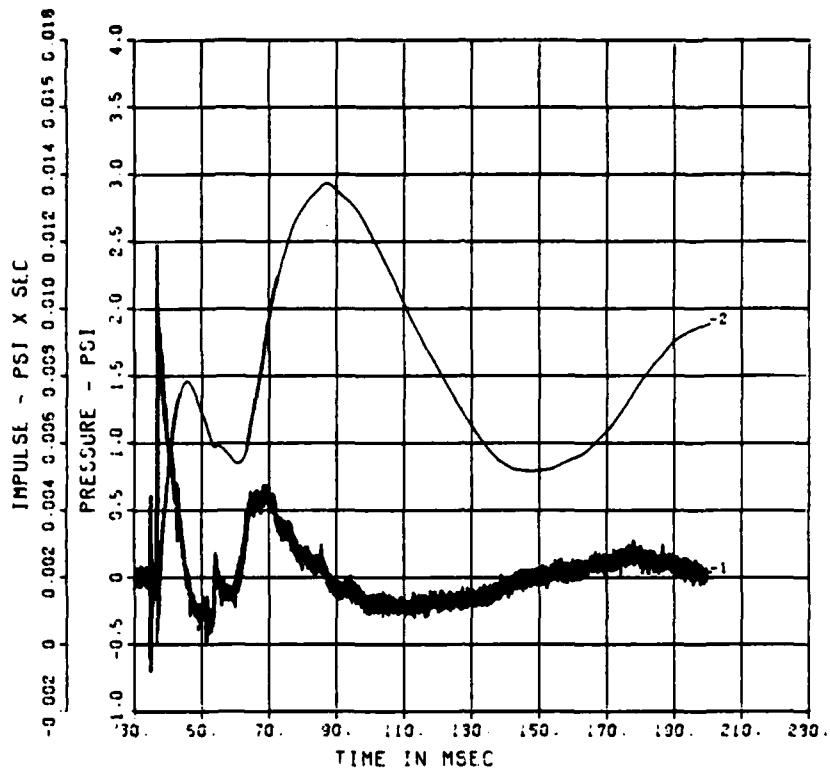


Chart B-19. QDT-1 Air Blast Record at 52 Feet on West Radial

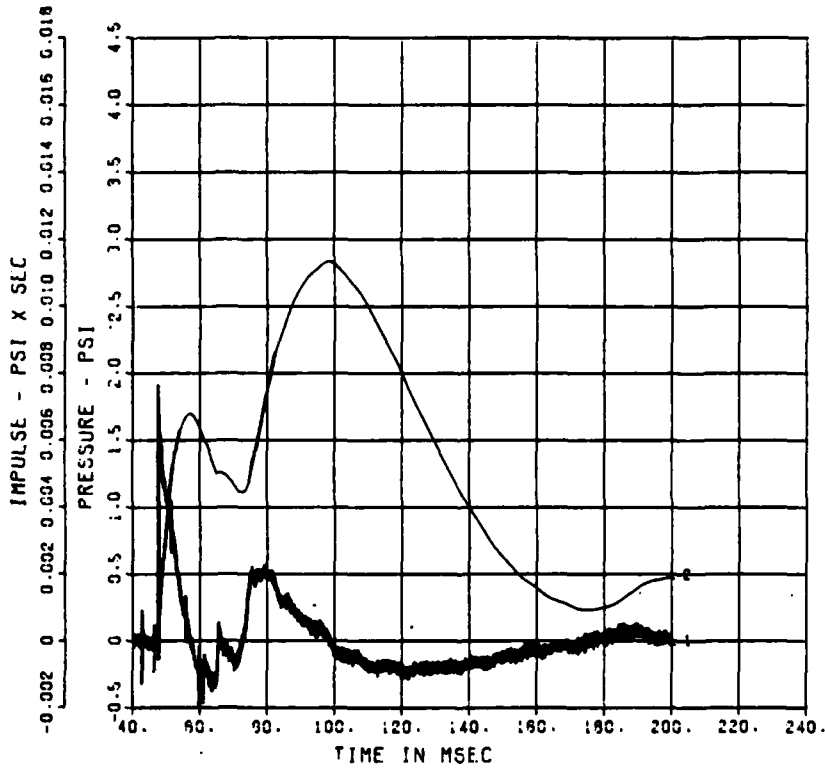


Chart B-20. QDT-1 Air Blast Record at 65 Feet on West Radial

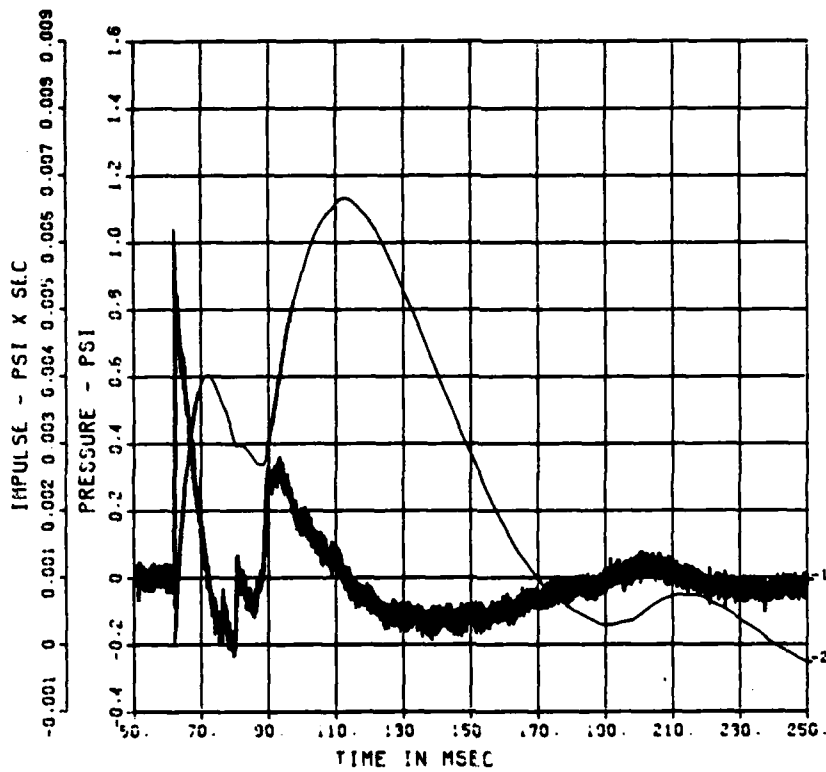


Chart B-21. QDT-1 Air Blast Record at 82 Feet on West Radial

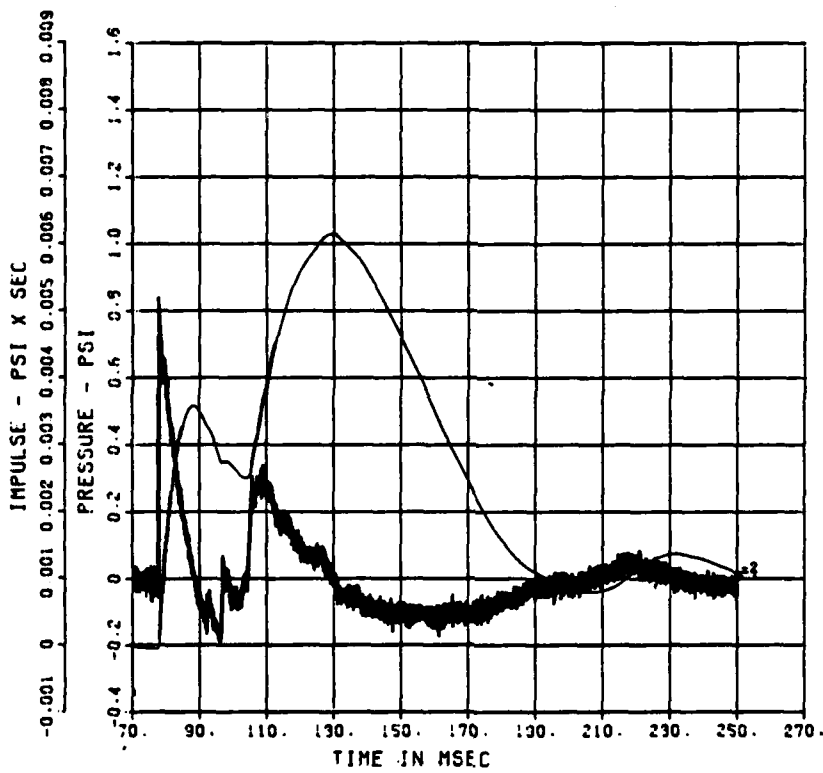


Chart B-22. QDT-1 Air Blast Record at 100 Feet on West Radial

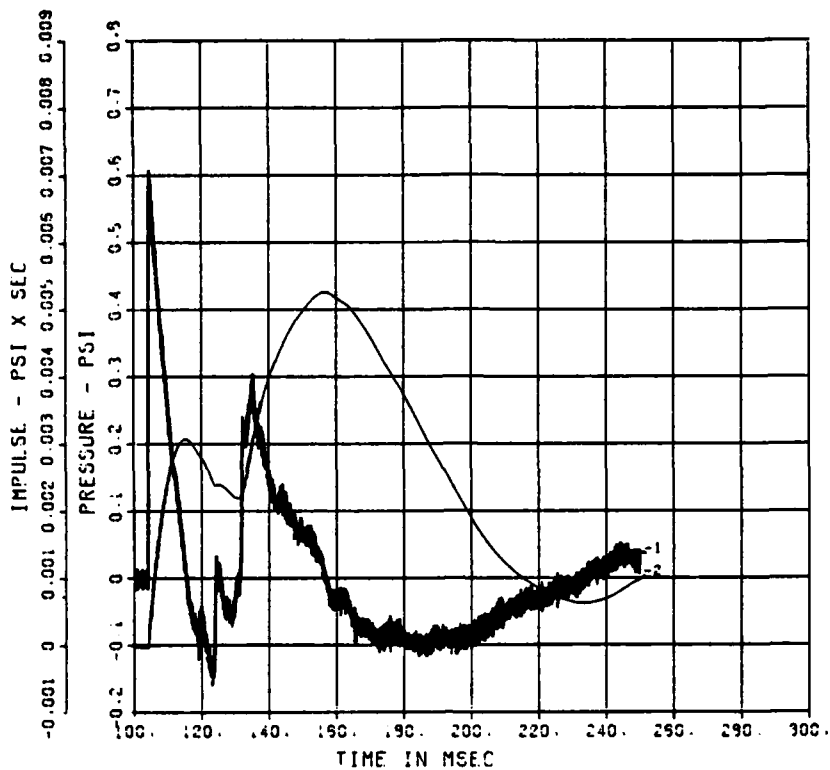


Chart B-23. QDT-1 Air Blast Record at 130 Feet on West Radial

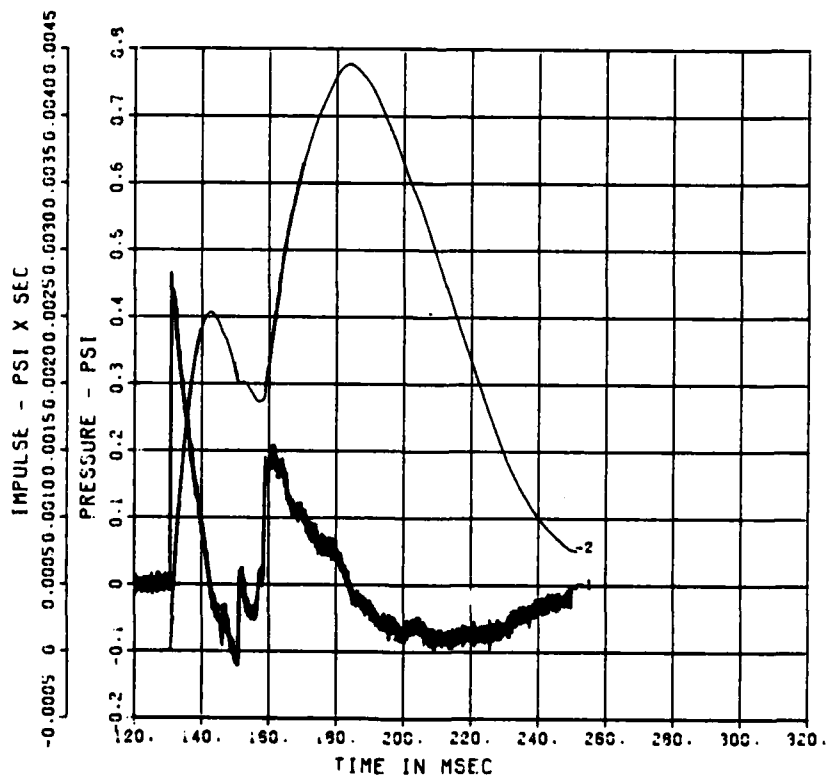


Chart B-24. QDT-1 Air Blast Record at 160 Feet on West Radial

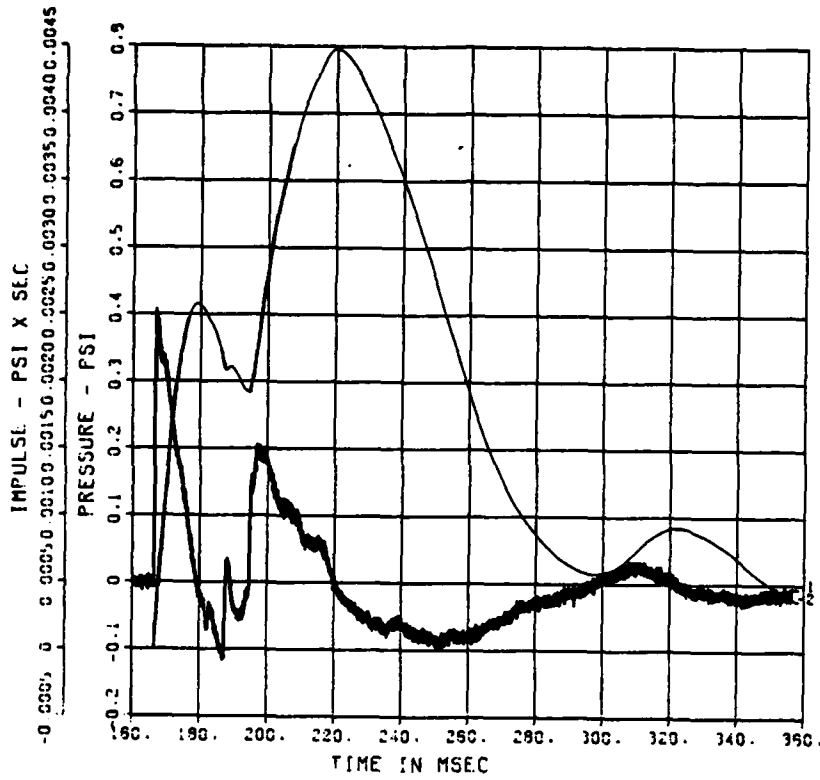


Chart B-25. QDT-1 Air Blast Record at 200 Feet on West Radial

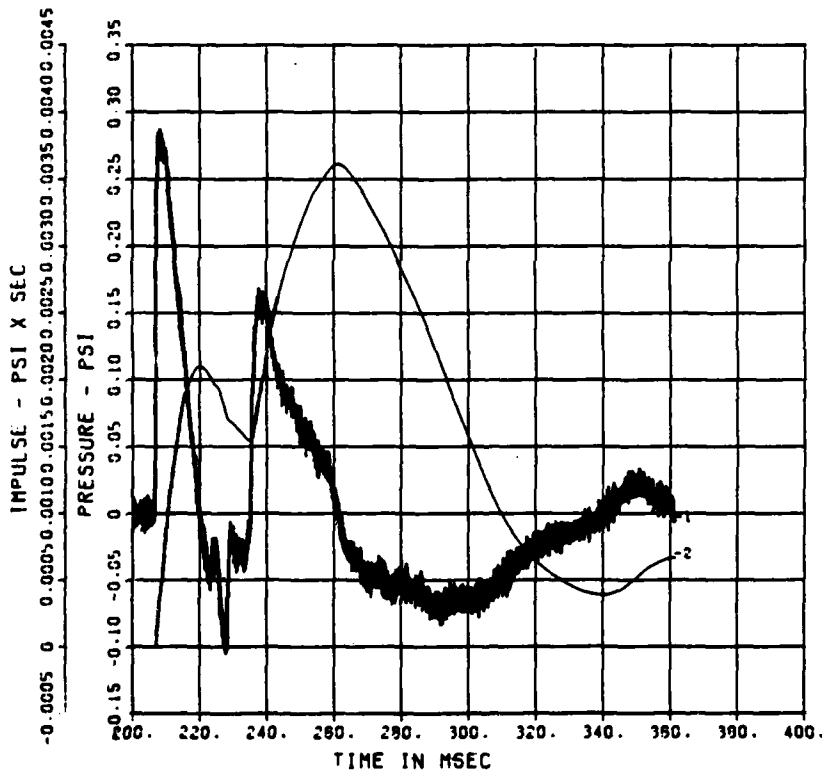


Chart B-26. QDT-1 Air Blast Record at 245 Feet on West Radial

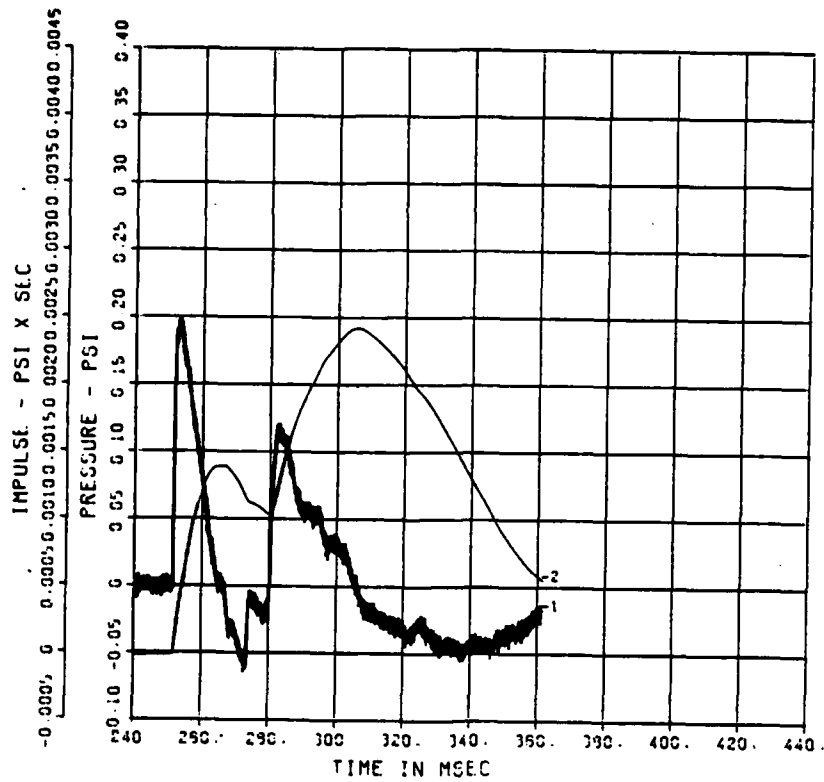


Chart B-27. QDT-1 Air Blast Record at 295 Feet on West Radial

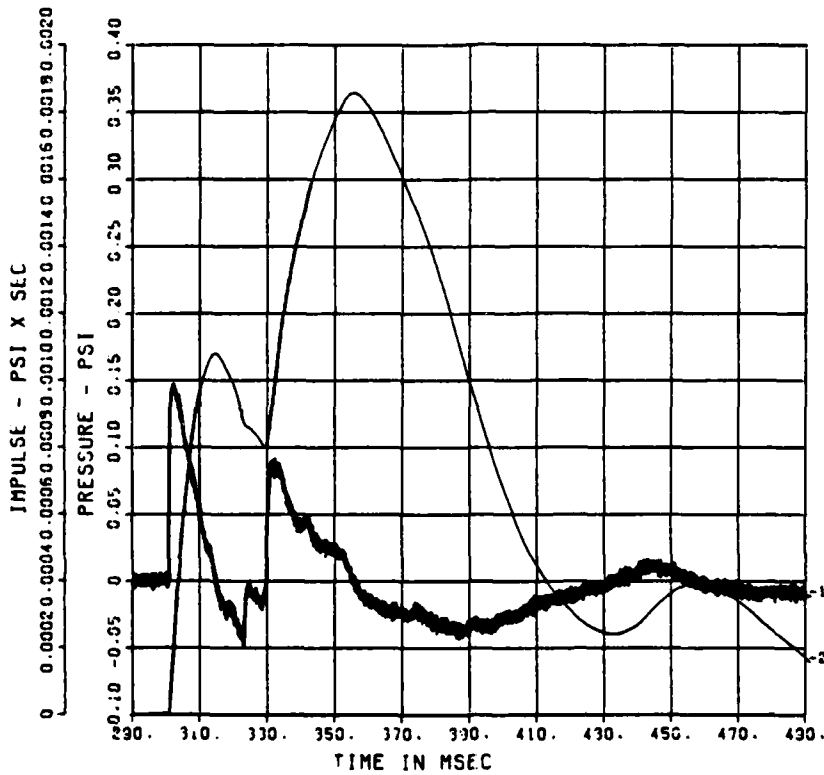


Chart B-28. QDT-1 Air Blast Record at 350 Feet on West Radial

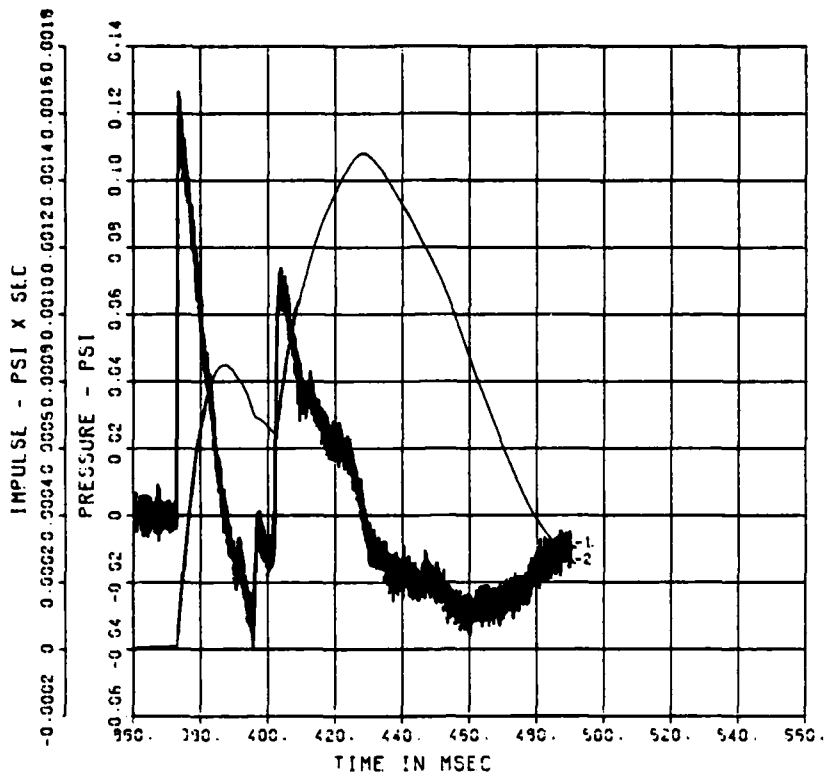


Chart B-29. QDT-1 Air Blast Record at 430 Feet on West Radial

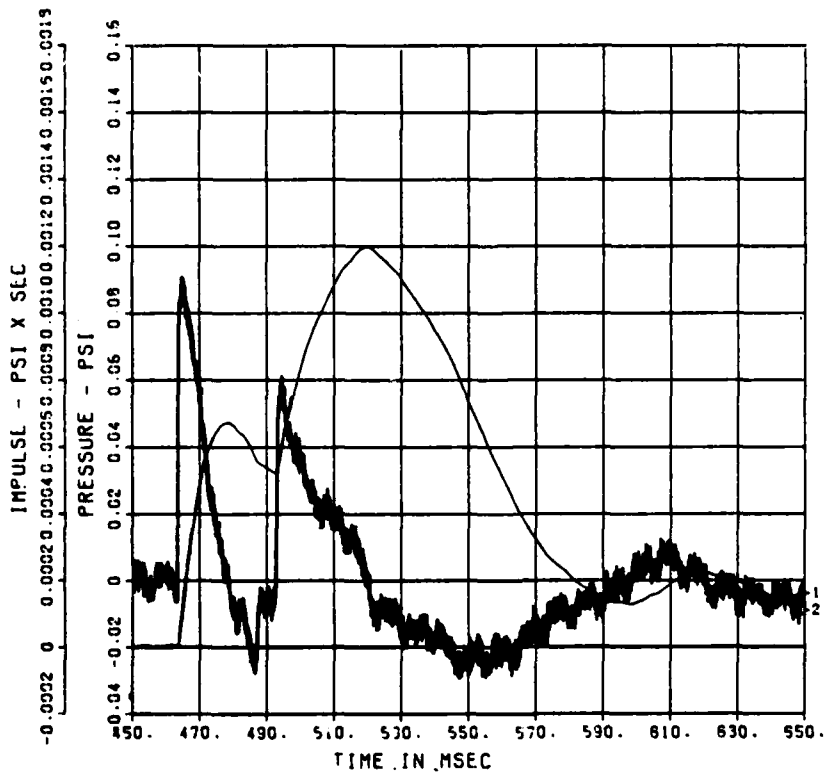


Chart B-30. QDT-1 Air Blast Record at 530 Feet on West Radial

APPENDIX C
QDT-2 AIR BLAST RECORDS

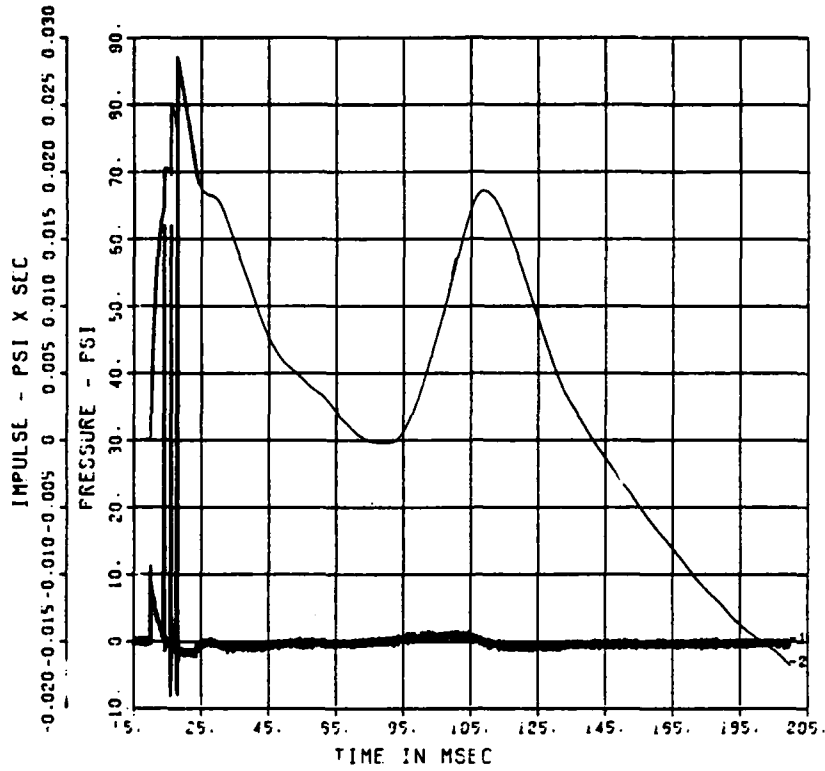


Chart C-1. QDT-2 Air Blast Record at 17 Feet on South Radial

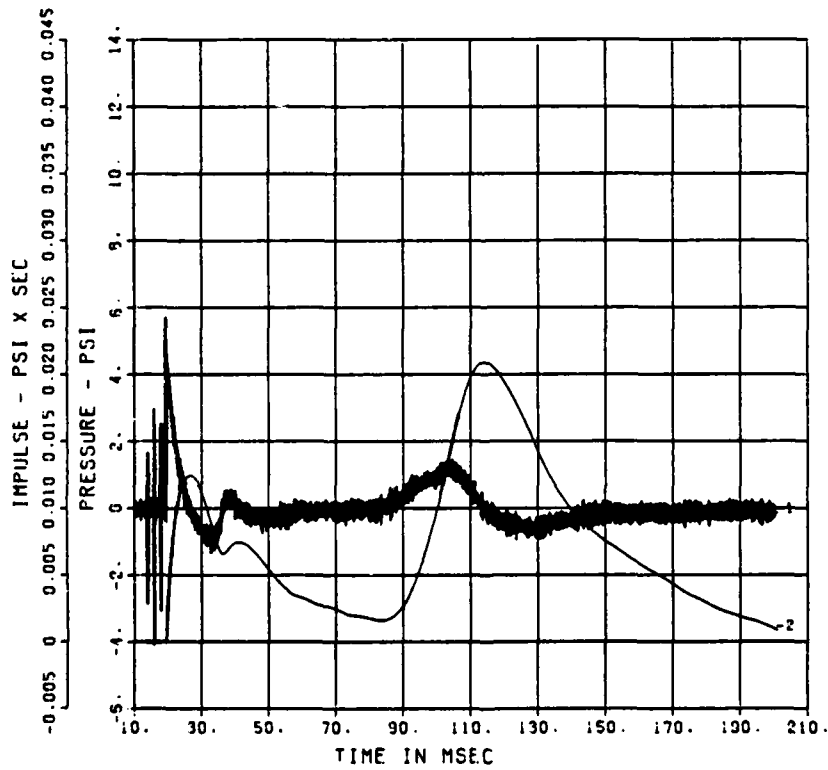


Chart C-2. QDT-2 Air Blast Record at 30 Feet on South Radial

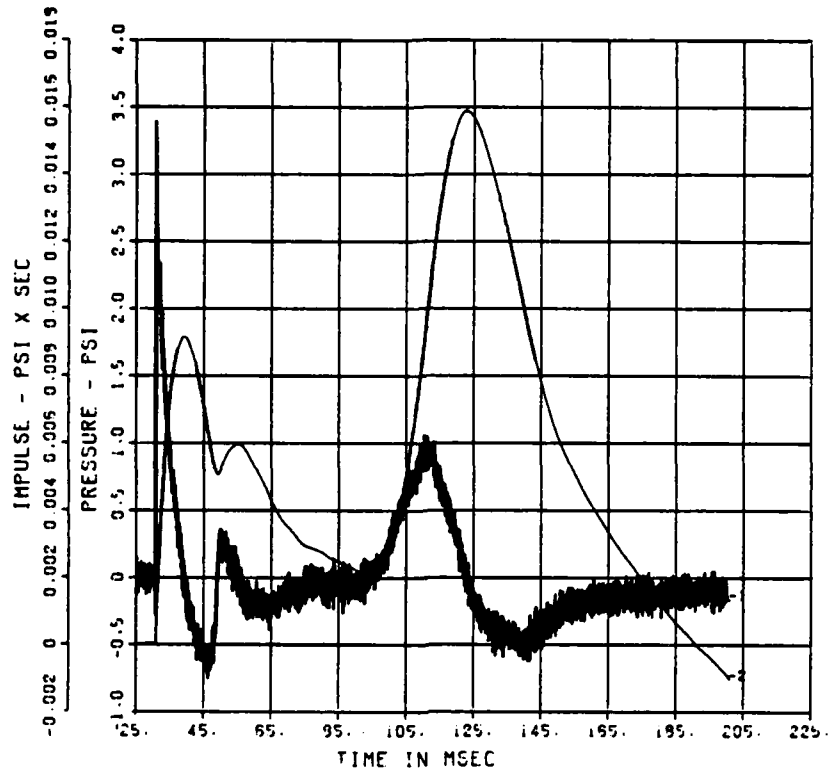


Chart C-3. QDT-2 Air Blast Record at 44 Feet on South Radial

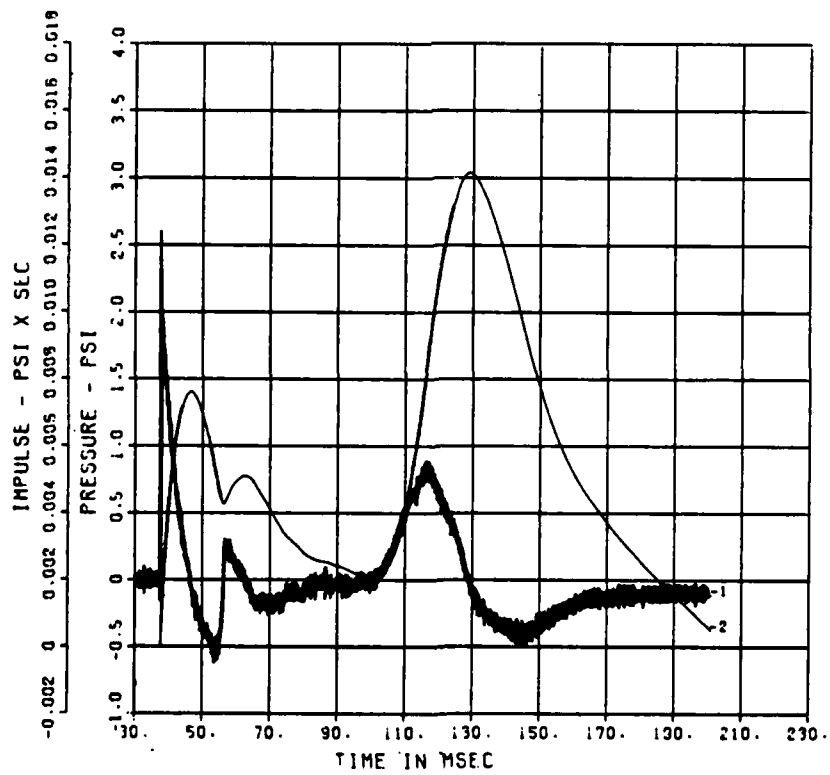


Chart C-4. QDT-2 Air Blast Record at 52 Feet on South Radial

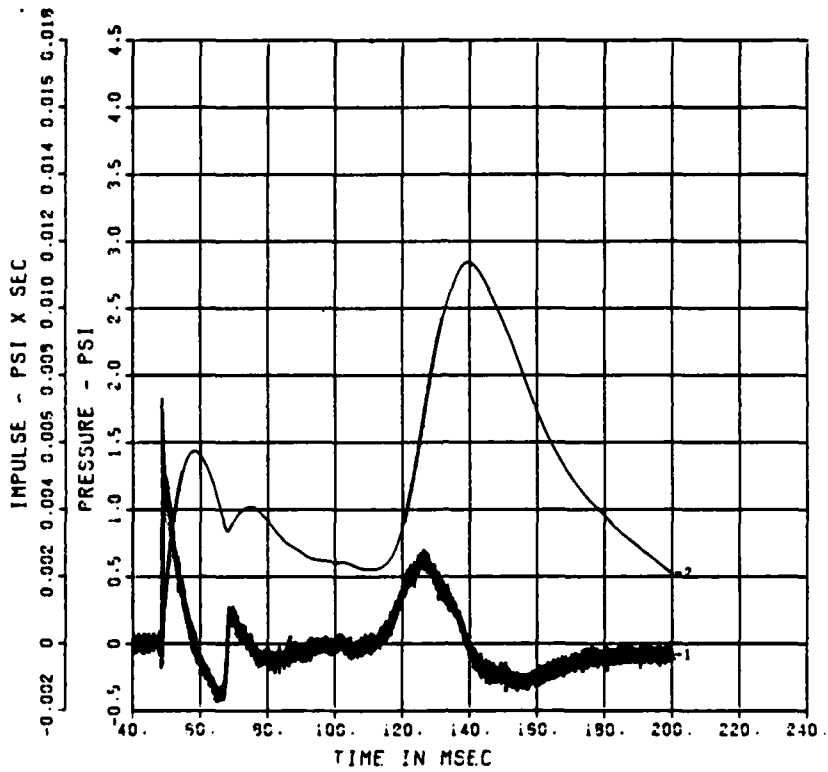


Chart C-5. QDT-2 Air Blast Record at 65 Feet on South Radial

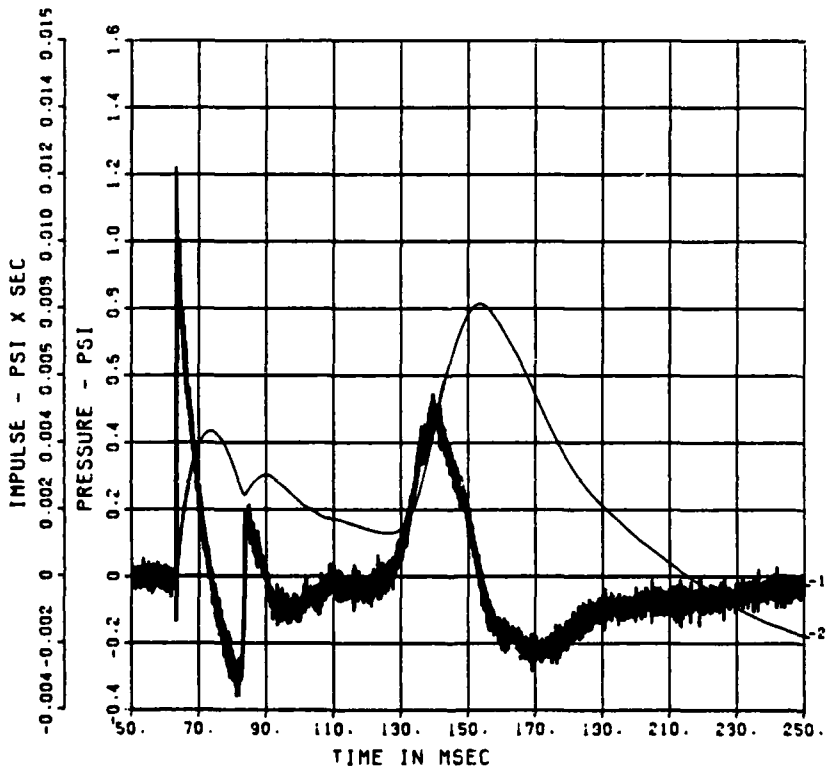


Chart C-6. QDT-2 Air Blast Record at 82 Feet on South Radial

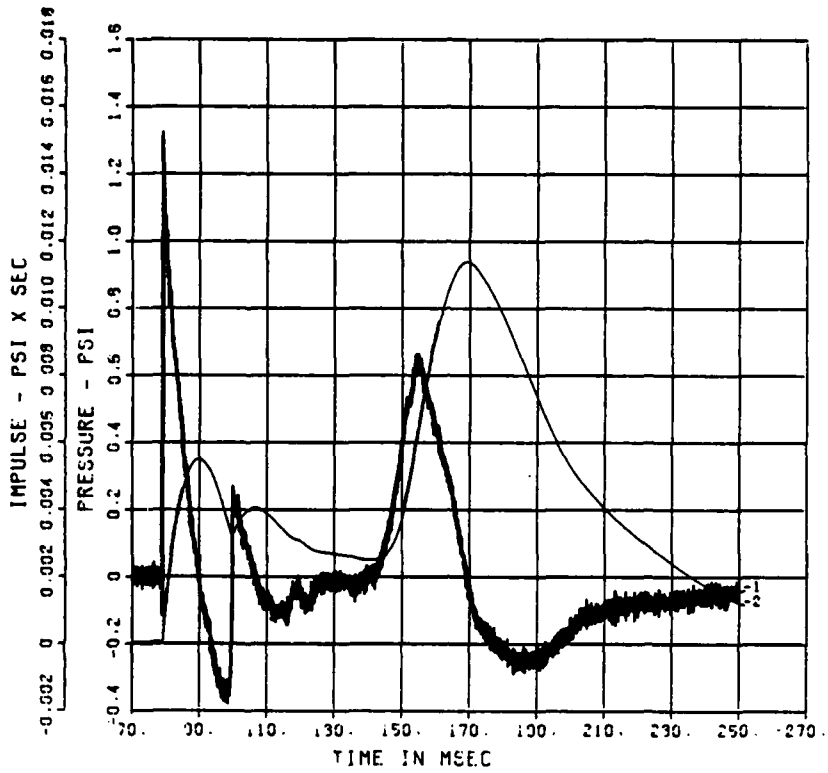


Chart C-7. QDT-2 Air Blast Record at 100 Feet on South Radial

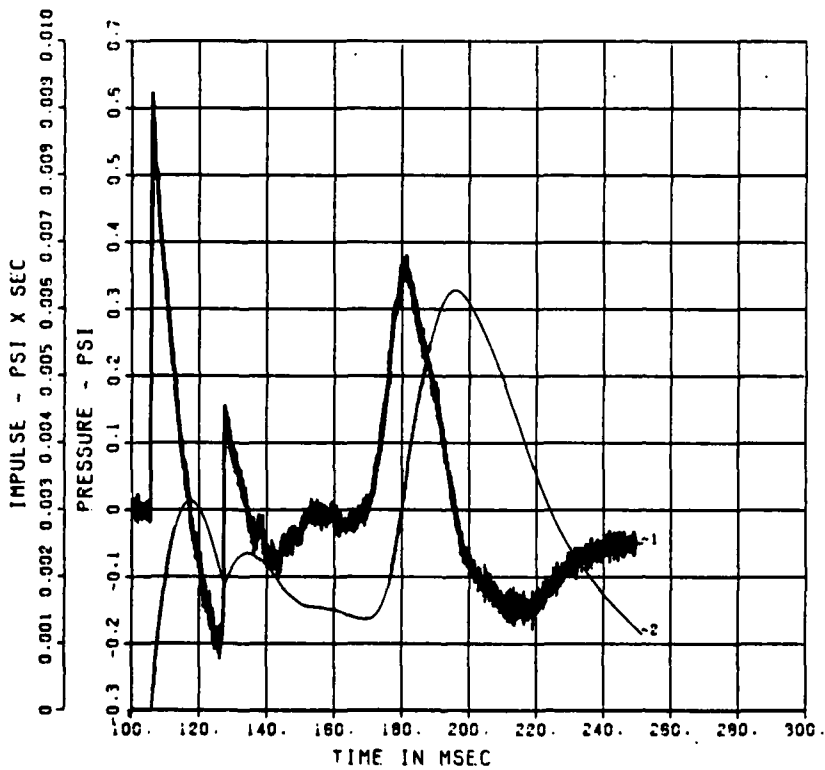


Chart C-8. QDT-2 Air Blast Record at 130 Feet on South Radial

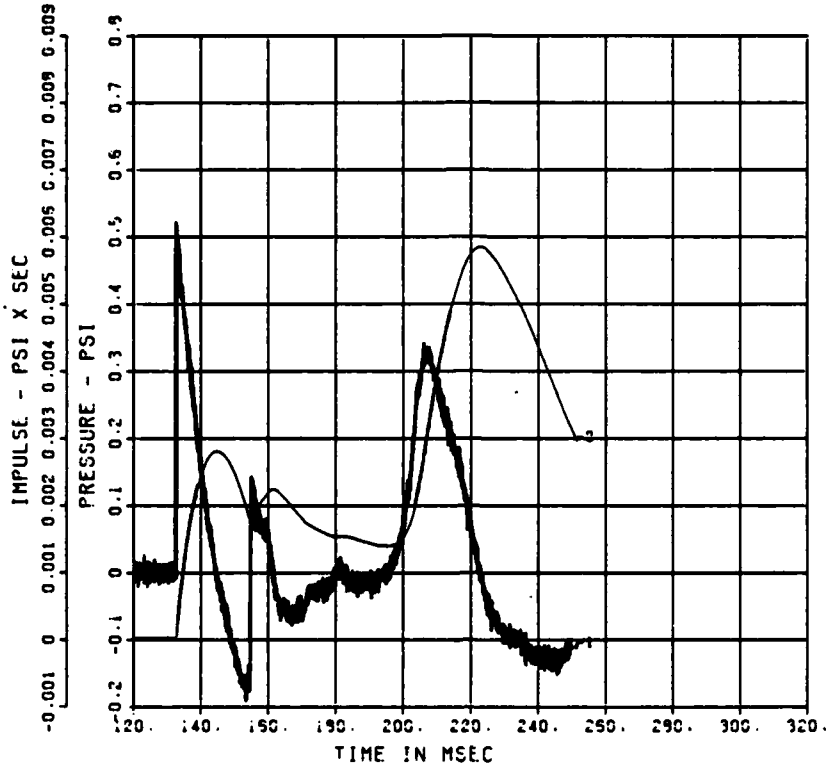


Chart C-9. QDT-2 Air Blast Record at 160 Feet on South Radial

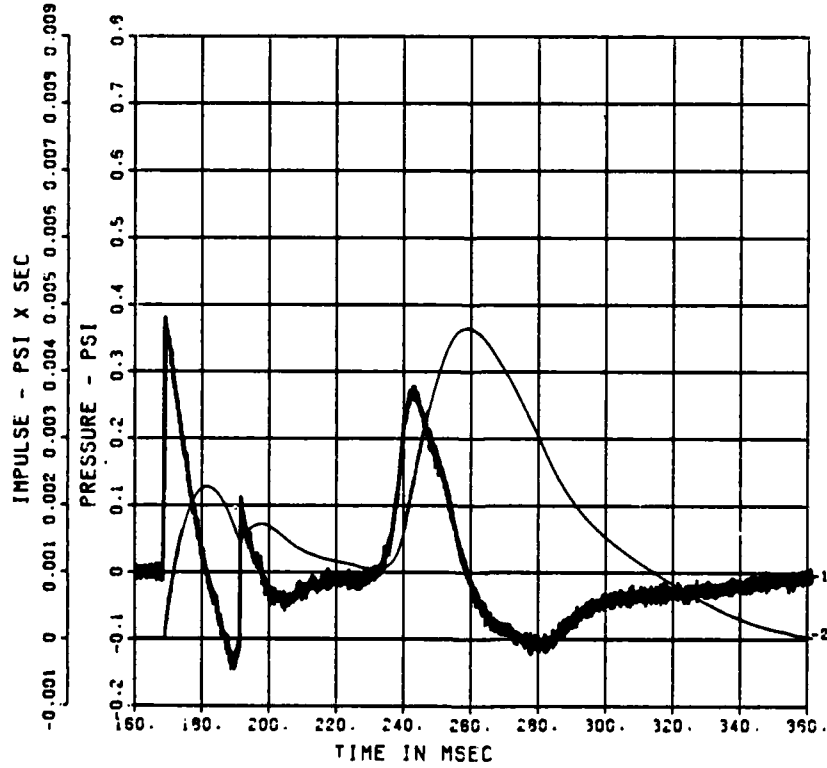


Chart C-10. QDT-2 Air Blast Record at 200 Feet on South Radial

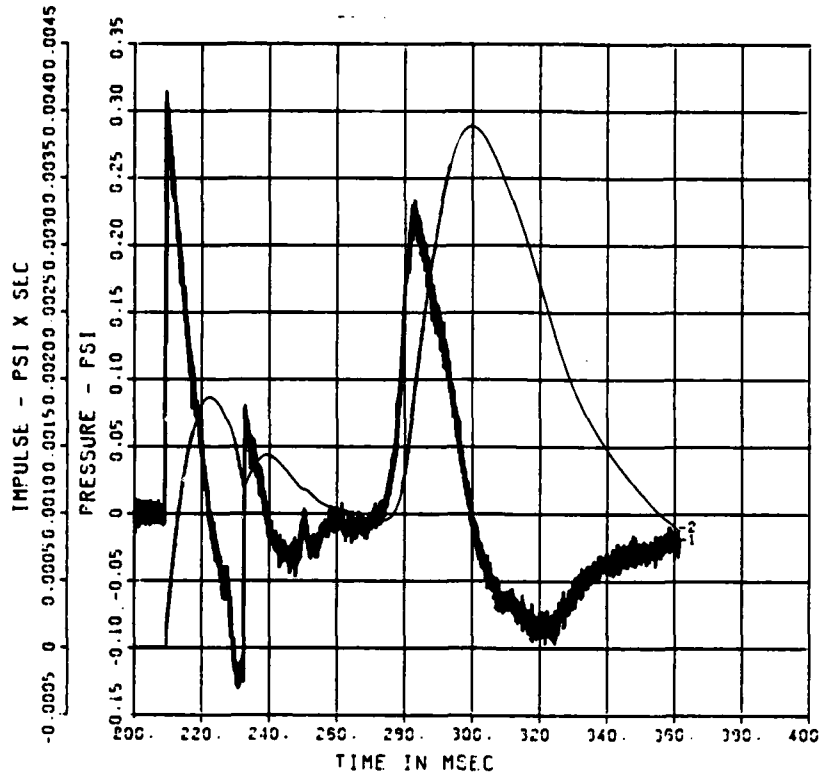


Chart C-11. QDT-2 Air Blast Record at 245 Feet on South Radial

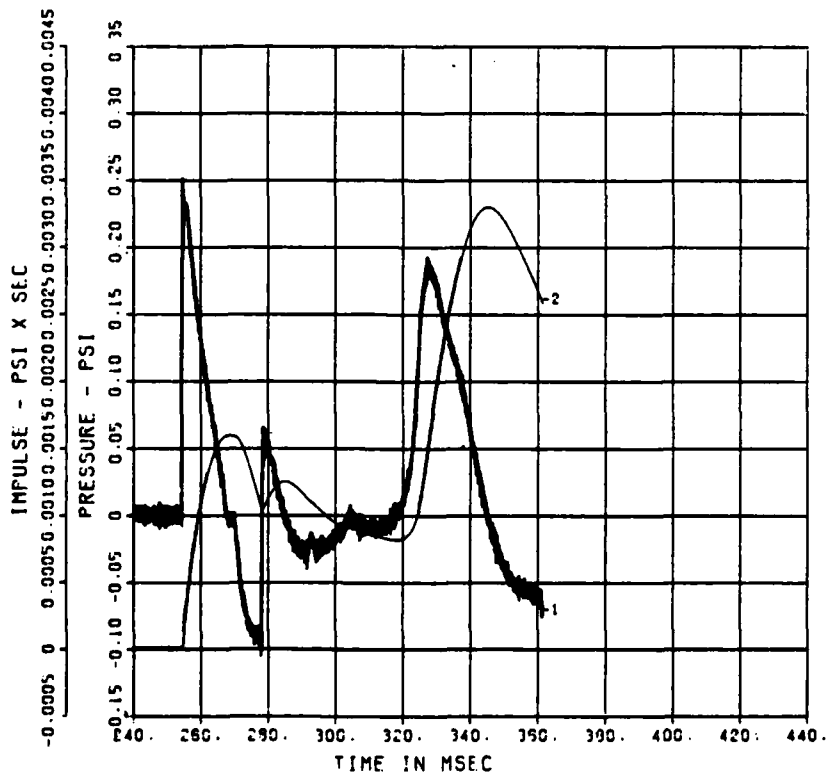


Chart C-12. QDT-2 Air Blast Record at 295 Feet on South Radial

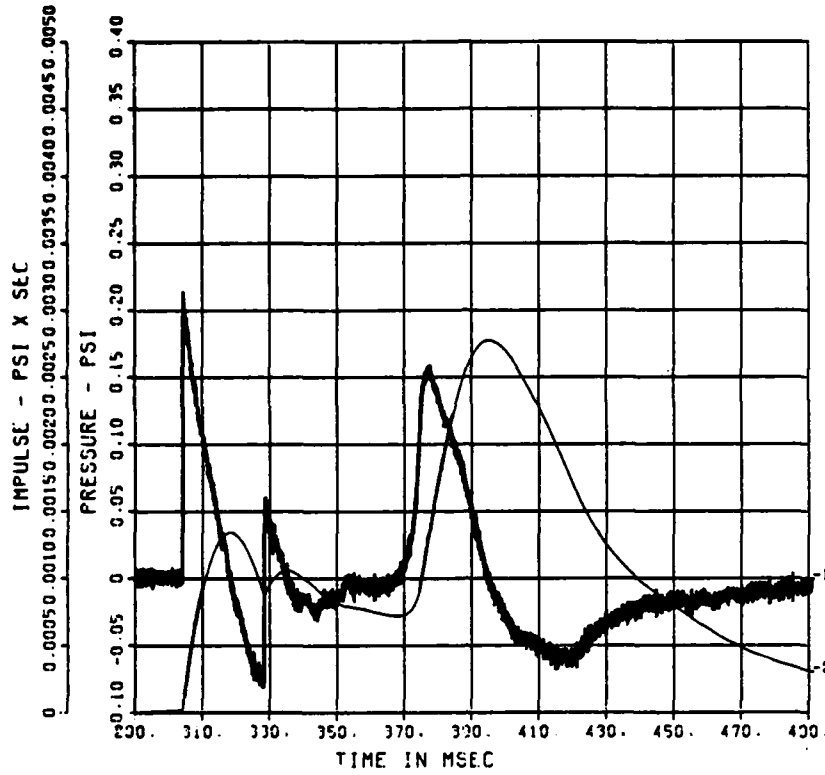


Chart C-13. QDT-2 Air Blast Record at 350 Feet on South Radial

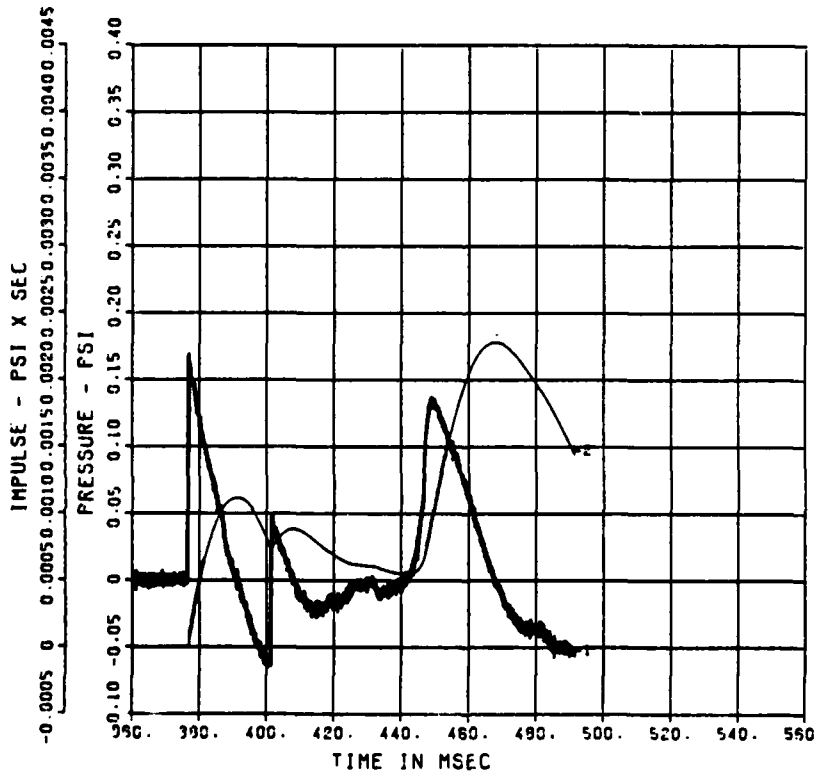


Chart C-14. QDT-2 Air Blast Record at 430 Feet on South Radial

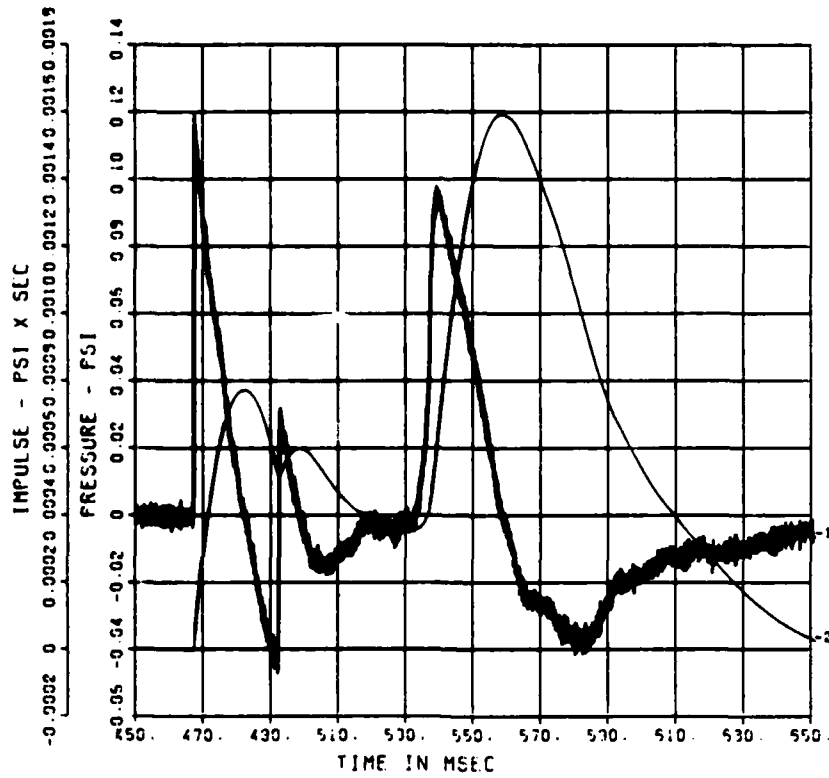


Chart C-15. QDT-2 Air Blast Record at 530 Feet on South Radial

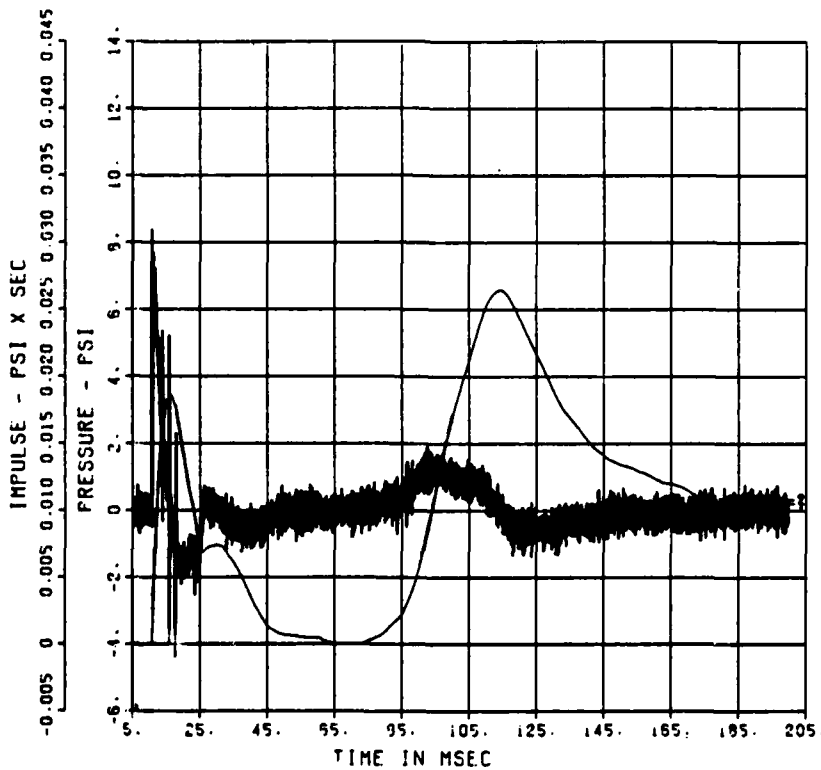


Chart C-16. QDT-2 Air Blast Record at 17 Feet on West Radial

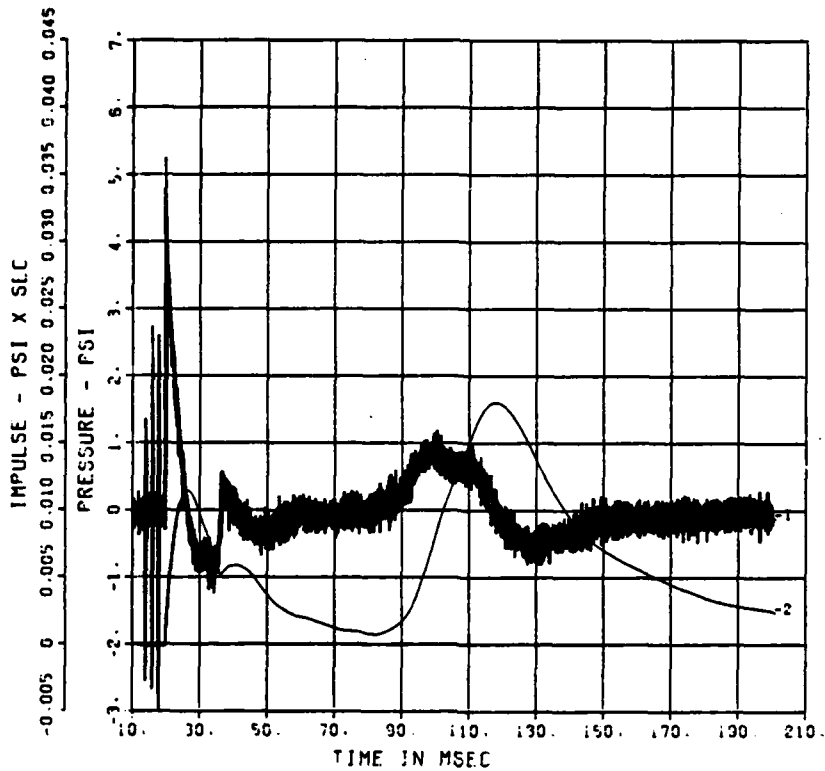


Chart C-17. QDT-2 Air Blast Record at 30 Feet on West Radial

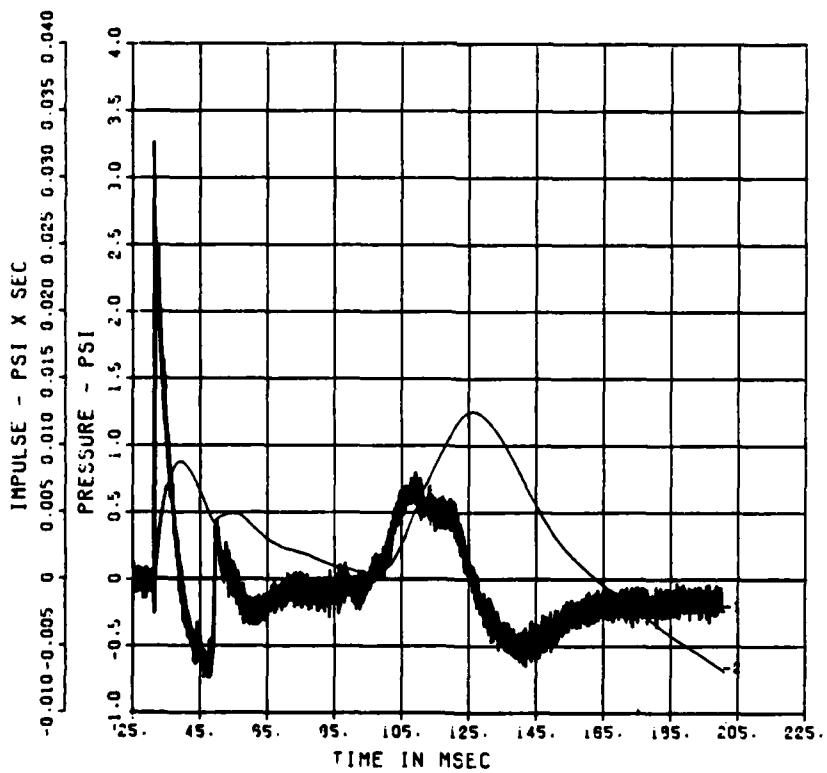


Chart C-18. QDT-2 Air Blast Record at 44 Feet on West Radial

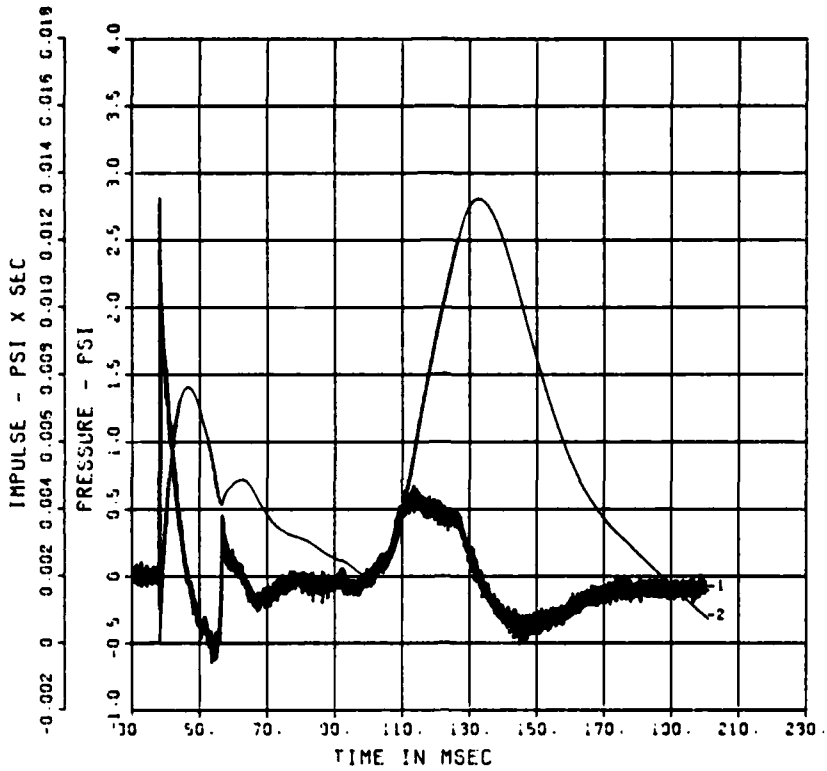


Chart C-19. QDT-2 Air Blast Record at 52 Feet on West Radial

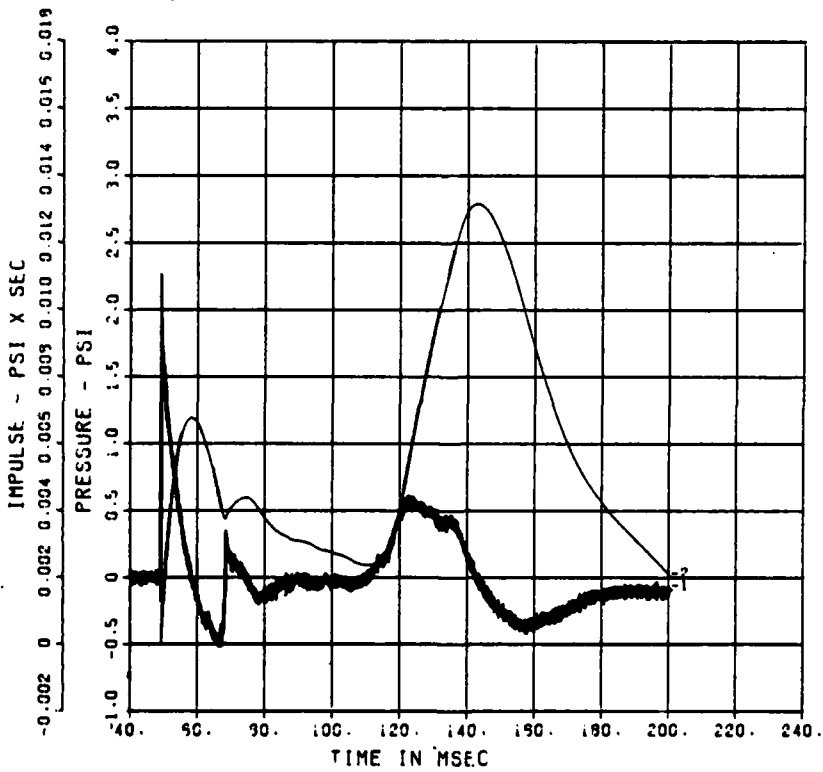


Chart C-20. QDT-2 Air Blast Record at 65 Feet on West Radial

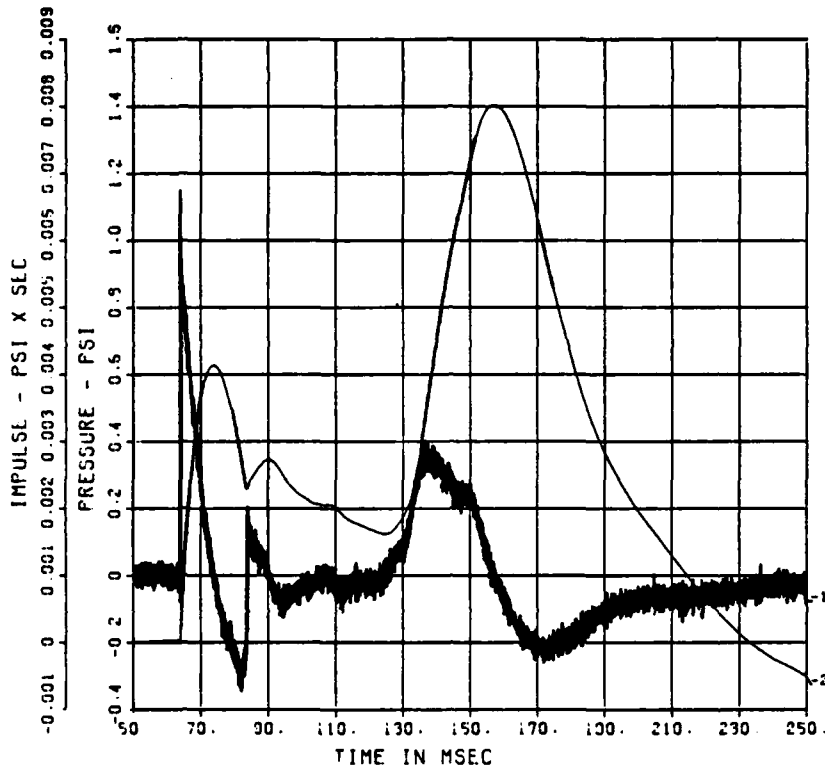


Chart C-21. QDT-2 Air Blast Record at 82 Feet on West Radial

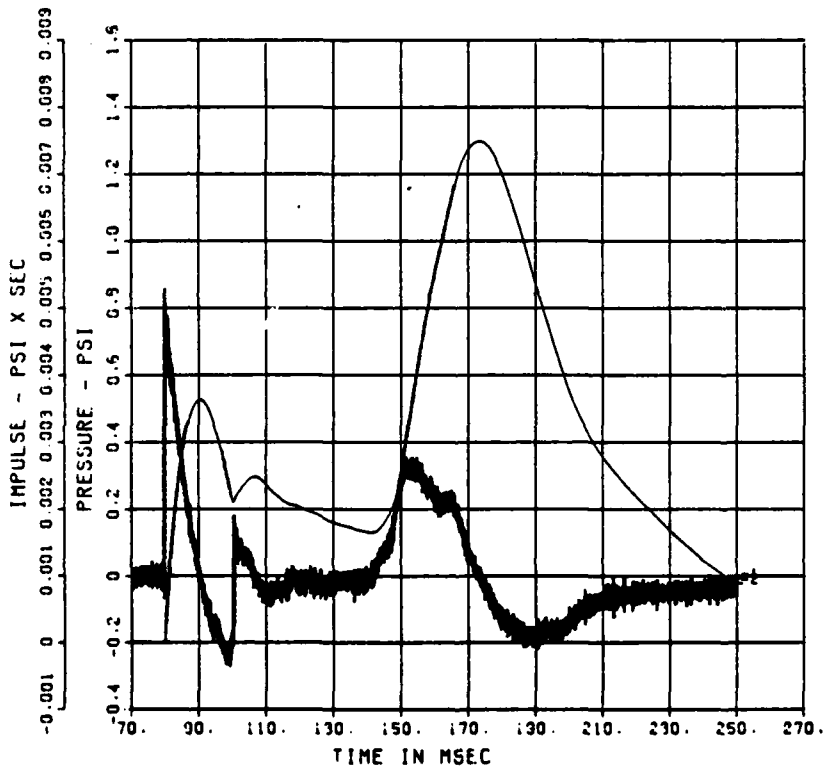


Chart C-22. QDT-2 Air Blast Record at 100 Feet on West Radial

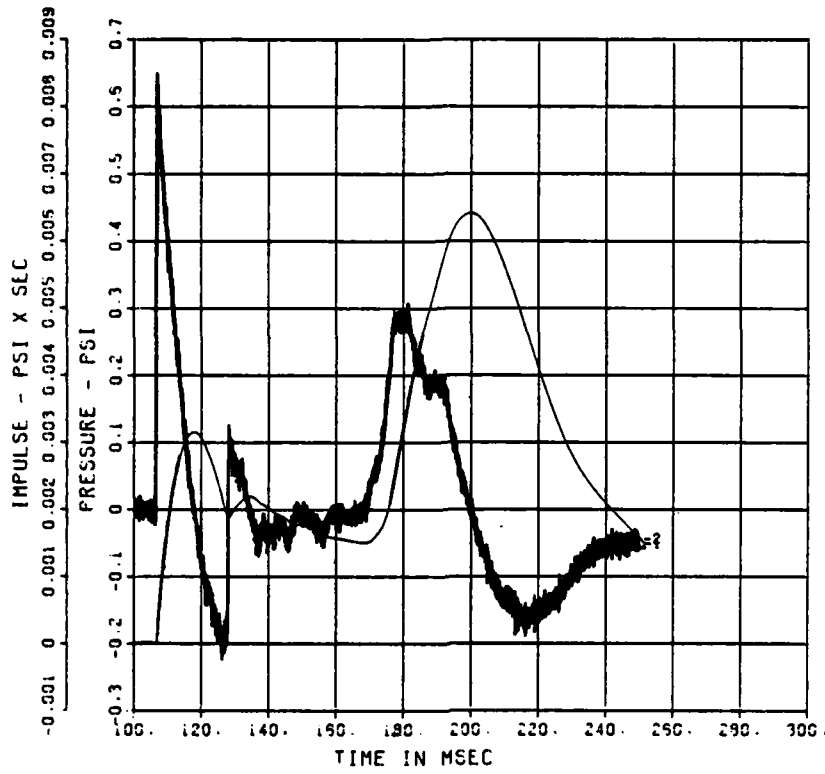


Chart C-23. QDT-2 Air Blast Record at 130 Feet on West Radial

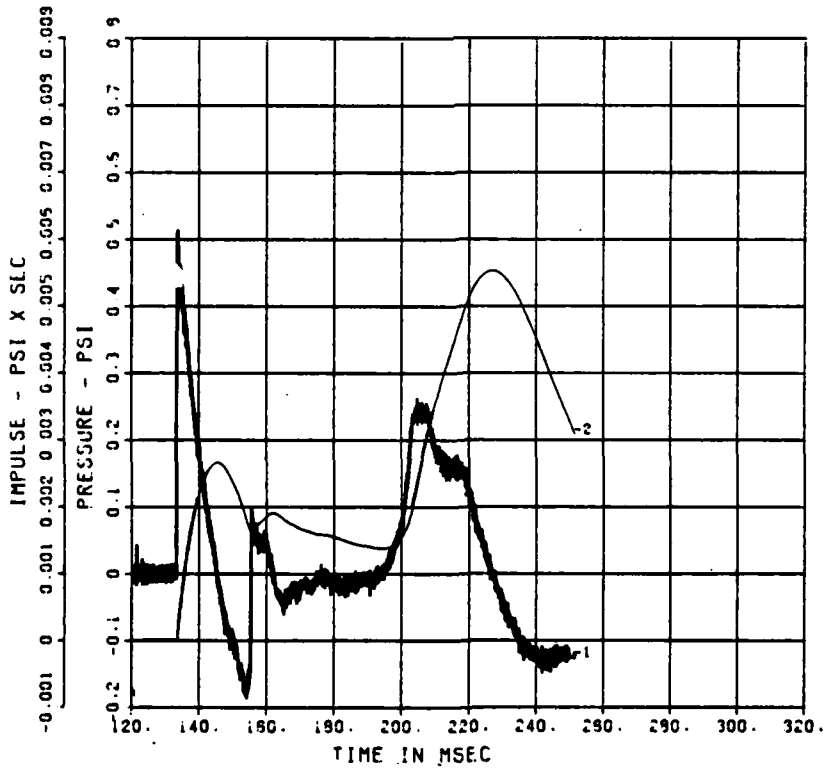


Chart C-24. QDT-2 Air Blast Record at 160 Feet on West Radial

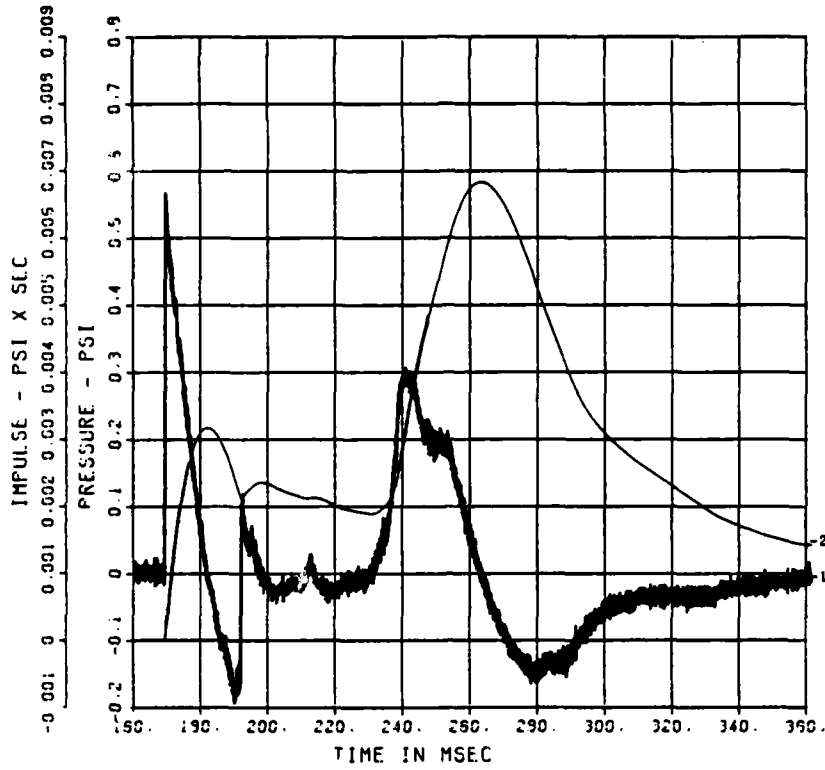


Chart C-25. QDT-2 Air Blast Record at 200 Feet on West Radial

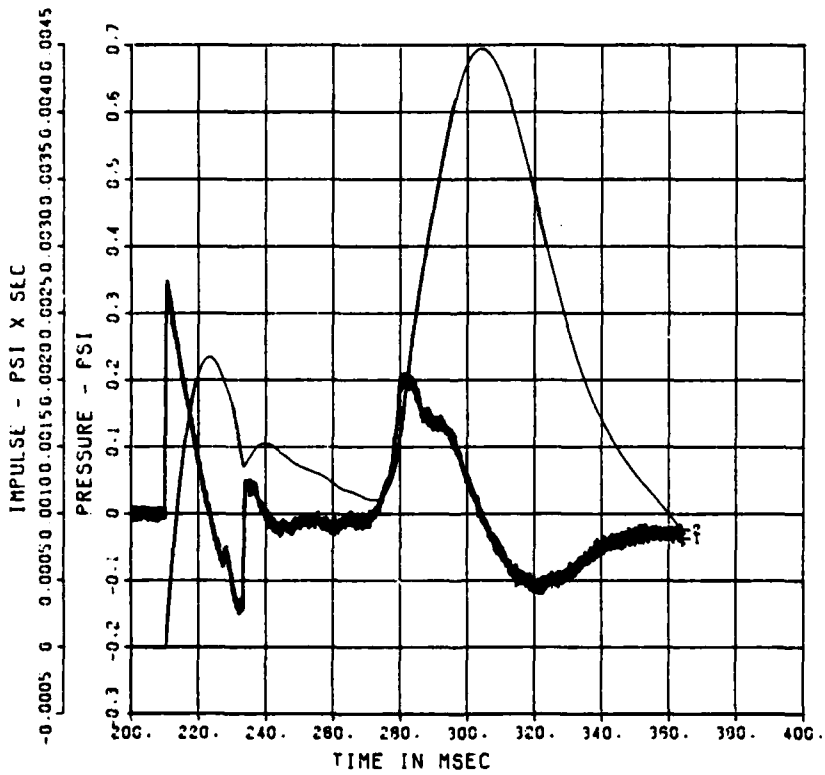


Chart C-26. QDT-2 Air Blast Record at 245 Feet on West Radial

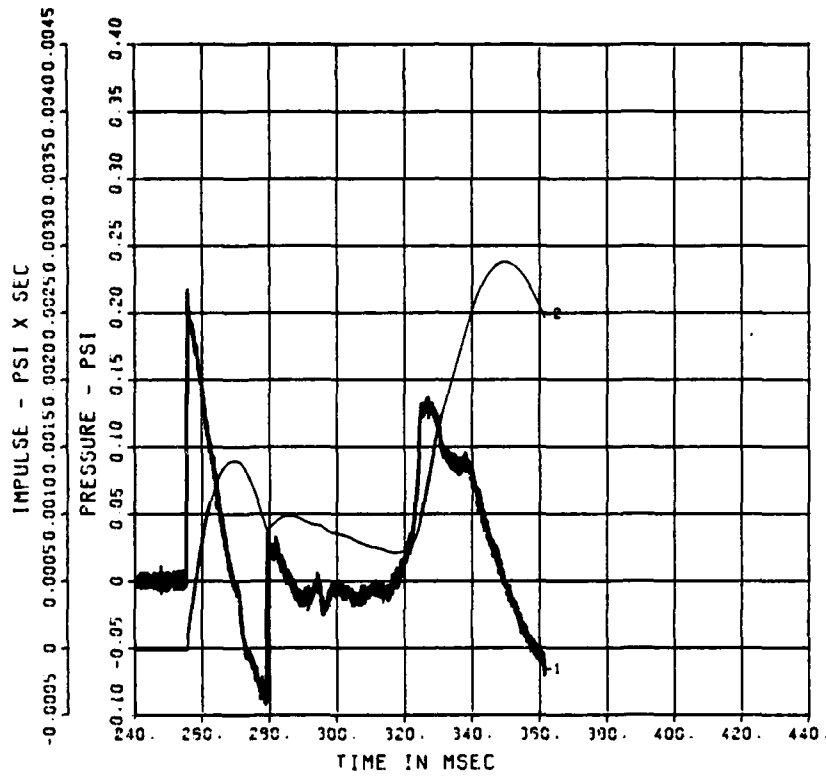


Chart C-27. QDT-2 Air Blast Record at 295 Feet on West Radial

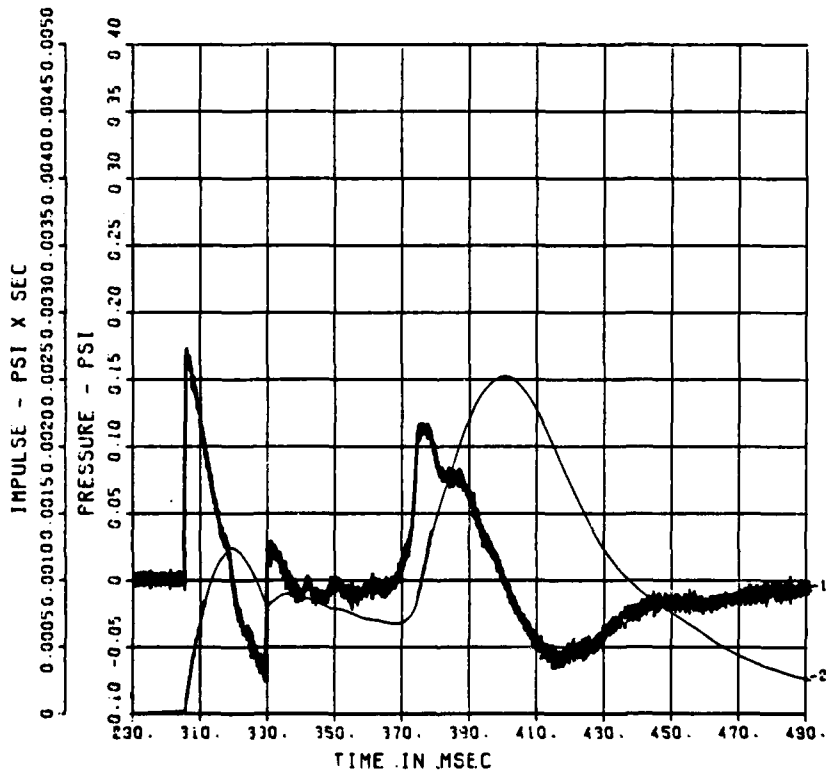
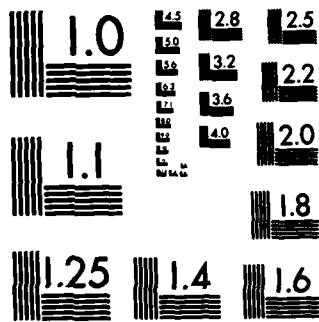


Chart C-28. QDT-2 Air Blast Record at 350 Feet on West Radial



MICROCOPY RESOLUTION TEST CHART

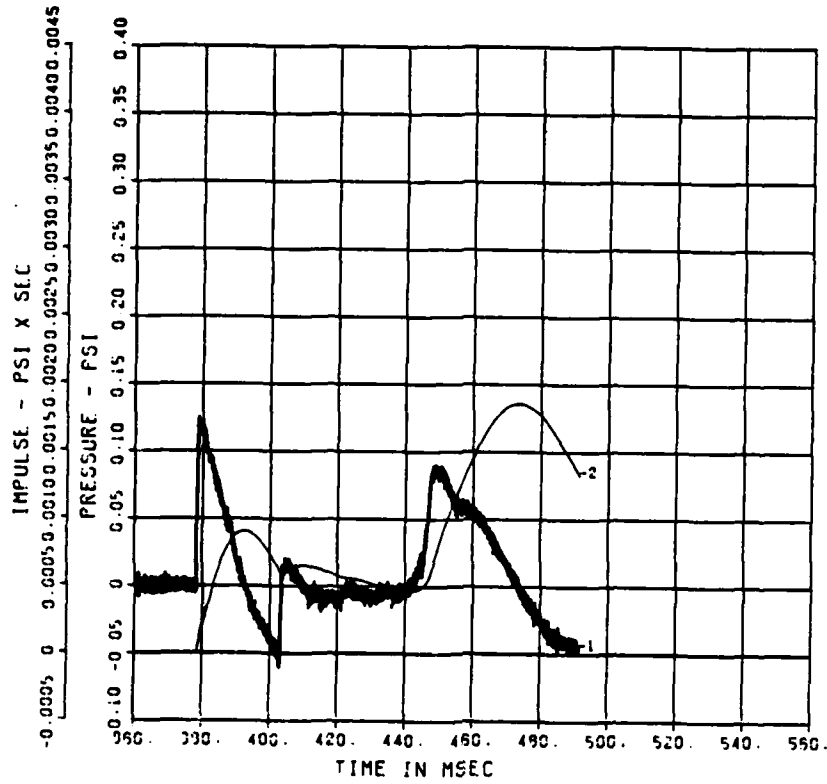


Chart C-29. QDT-2 Air Blast Record at 430 Feet on West Radial

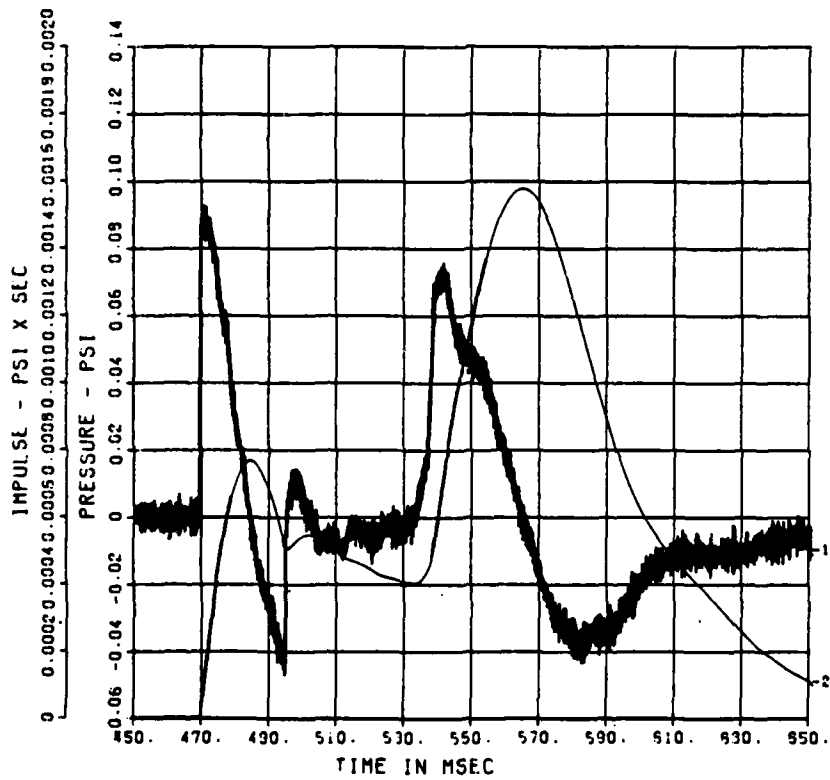


Chart C-30. QDT-2 Air Blast Record at 530 Feet on West Radial

APPENDIX D
QDT-3 AIR BLAST RECORDS

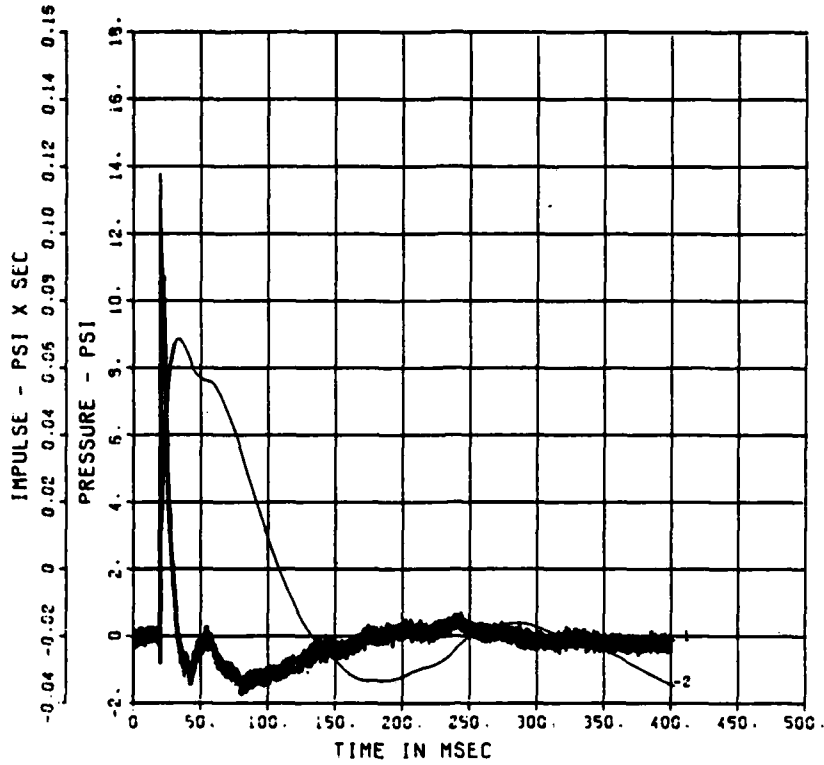


Chart D-1. QDT-3 Air Blast Record at 42 Feet on South Radial

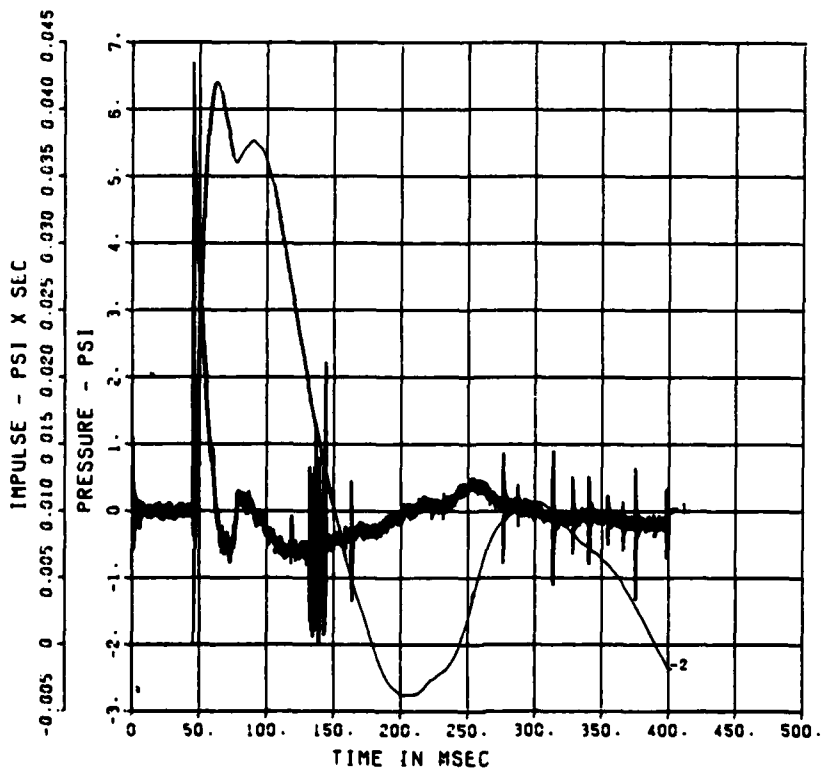


Chart D-2. QDT-3 Air Blast Record at 78 Feet on South Radial

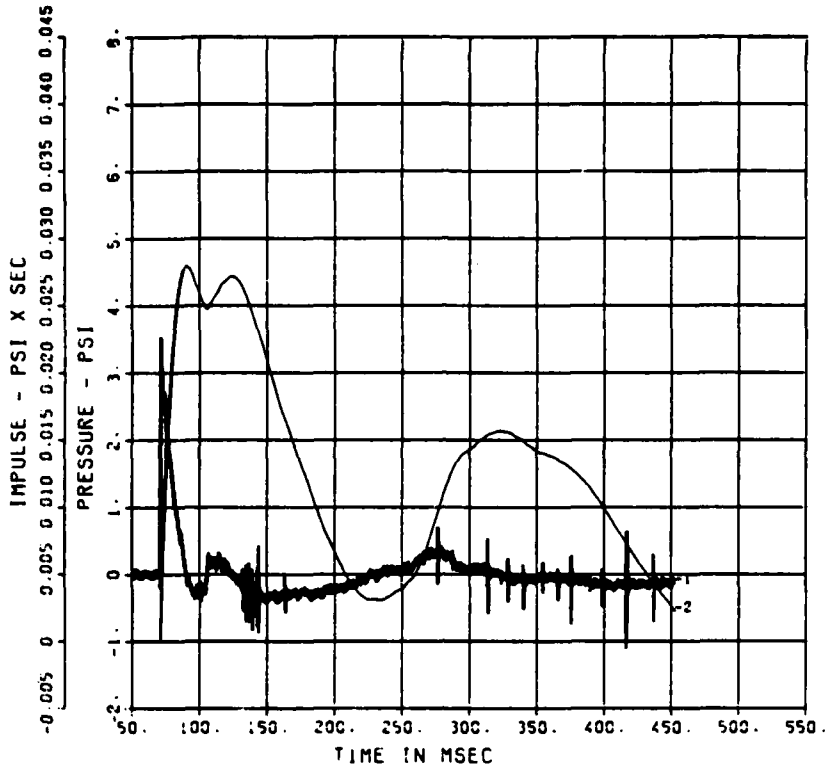


Chart D-3. QDT-3 Air Blast Record at 110 Feet on South Radial

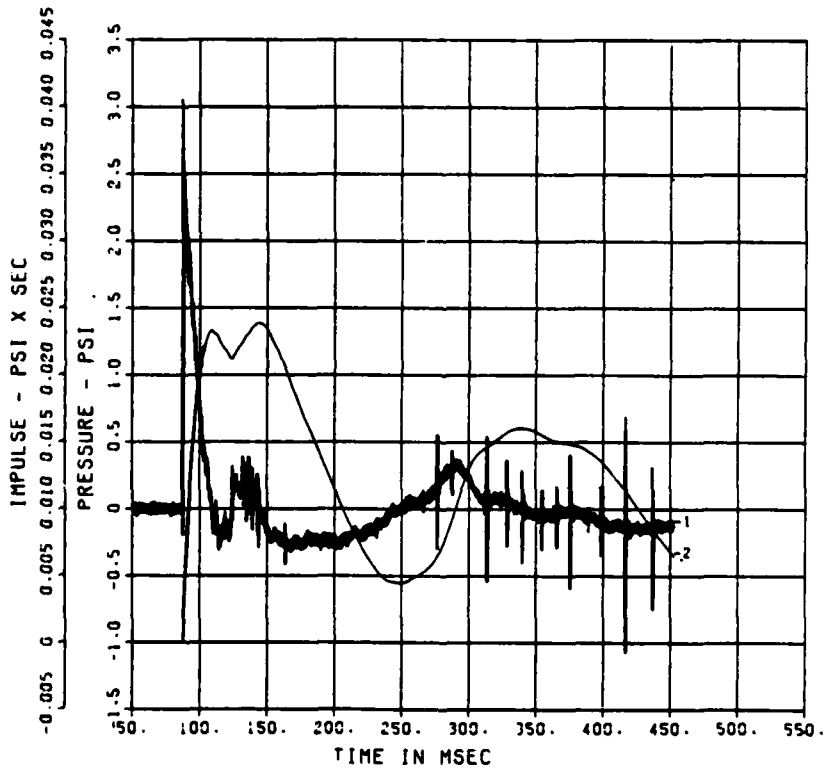


Chart D-4. QDT-3 Air Blast Record at 130 Feet on South Radial

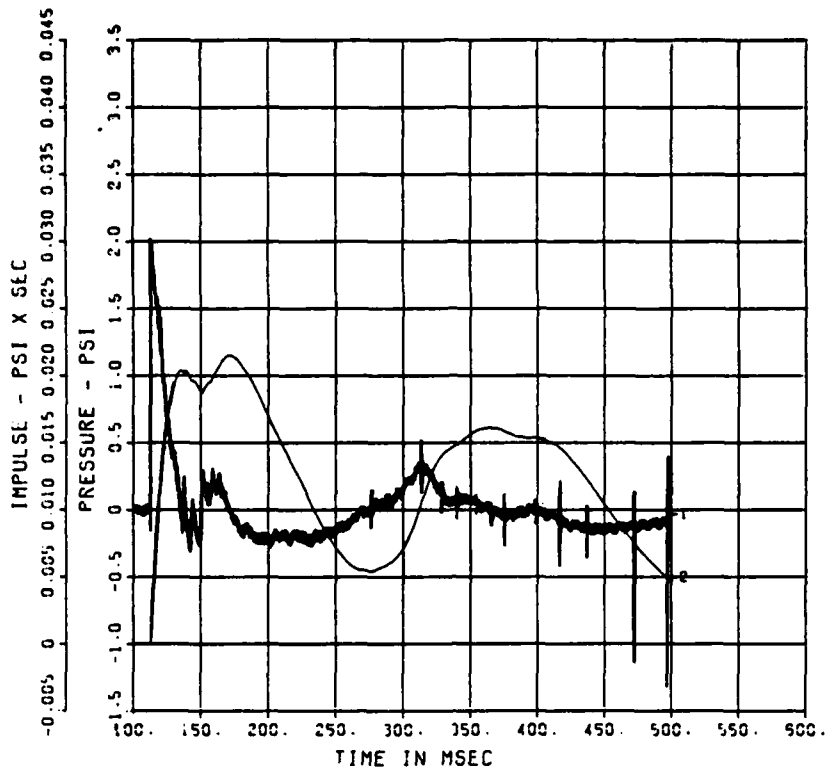


Chart D-5. QDT-3 Air Blast Record at 160 Feet on South Radial

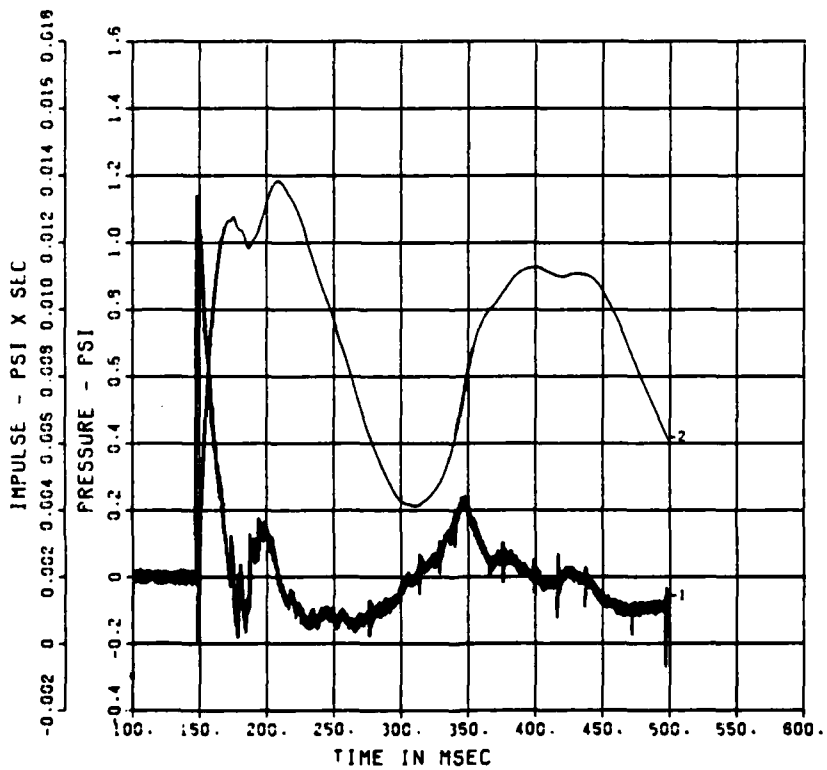


Chart D-6. QDT-3 Air Blast Record at 200 Feet on South Radial

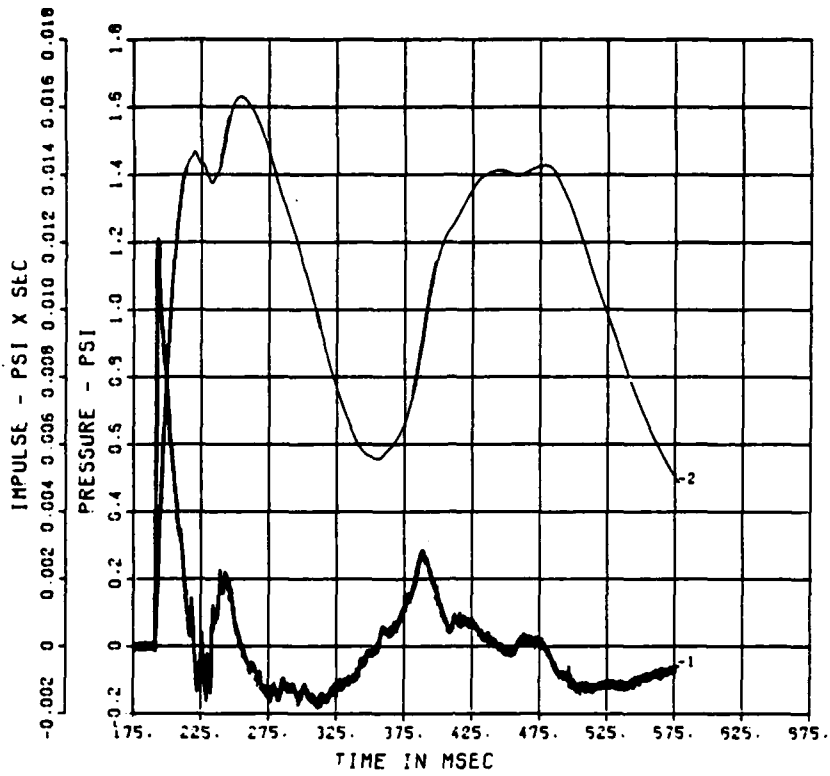


Chart D-7. QDT-3 Air Blast Record at 250 Feet on South Radial

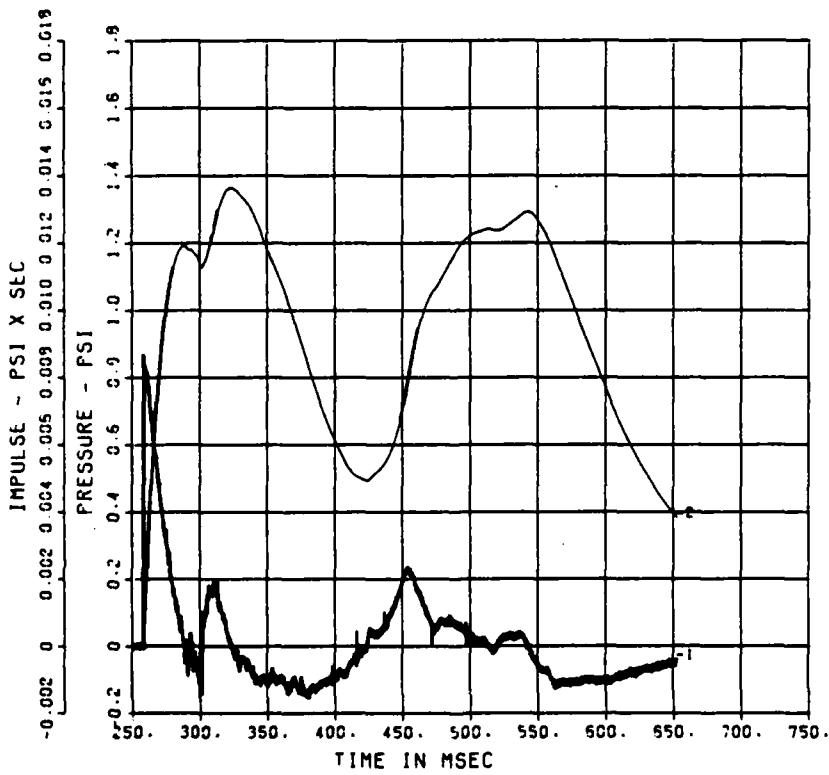


Chart D-8. QDT-3 Air Blast Record at 325 Feet on South Radial

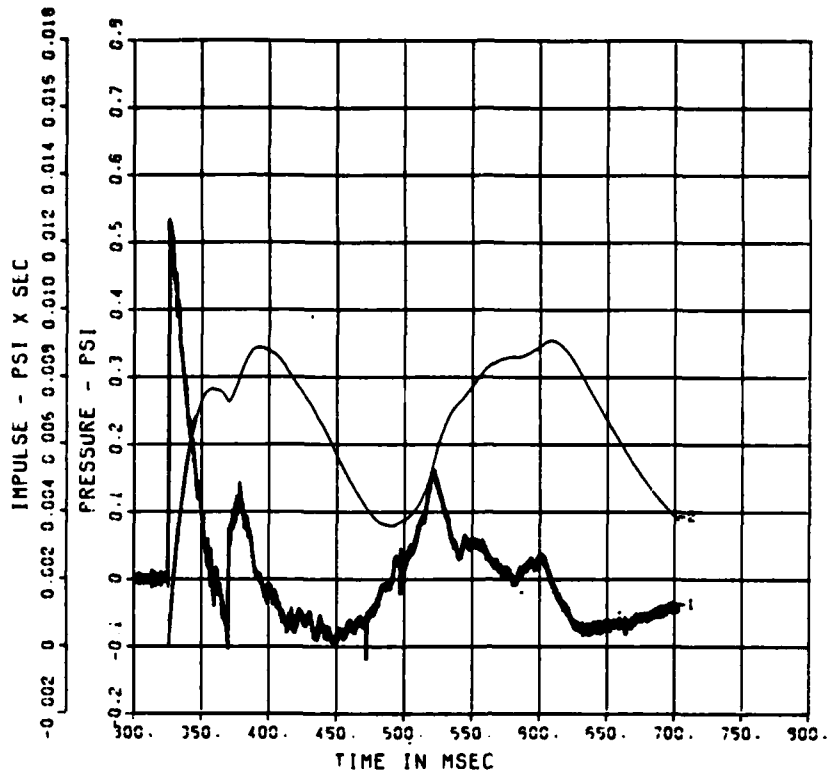


Chart D-9. QDT-3 Air Blast Record at 400 Feet on South Radial

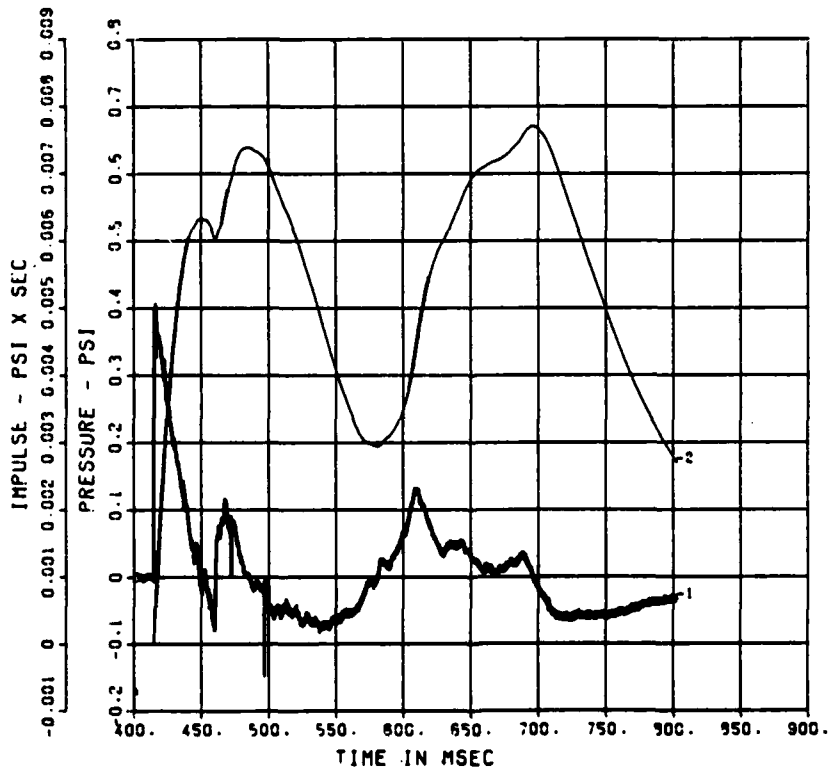


Chart D-10. QDT-3 Air Blast Record at 500 Feet on South Radial

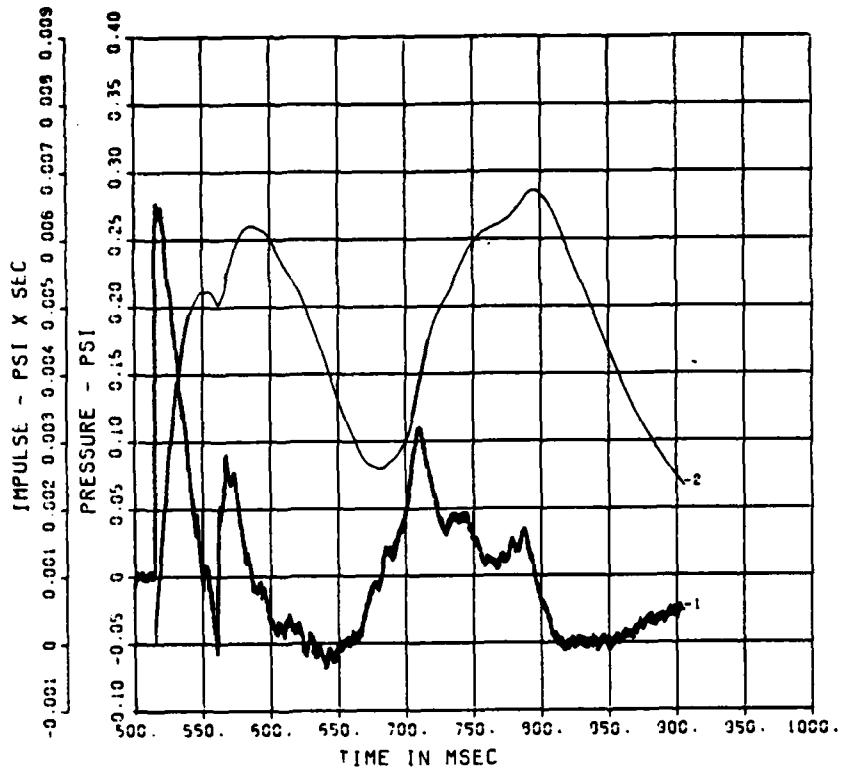


Chart D-11. QDT-3 Air Blast Record at 610 Feet on South Radial

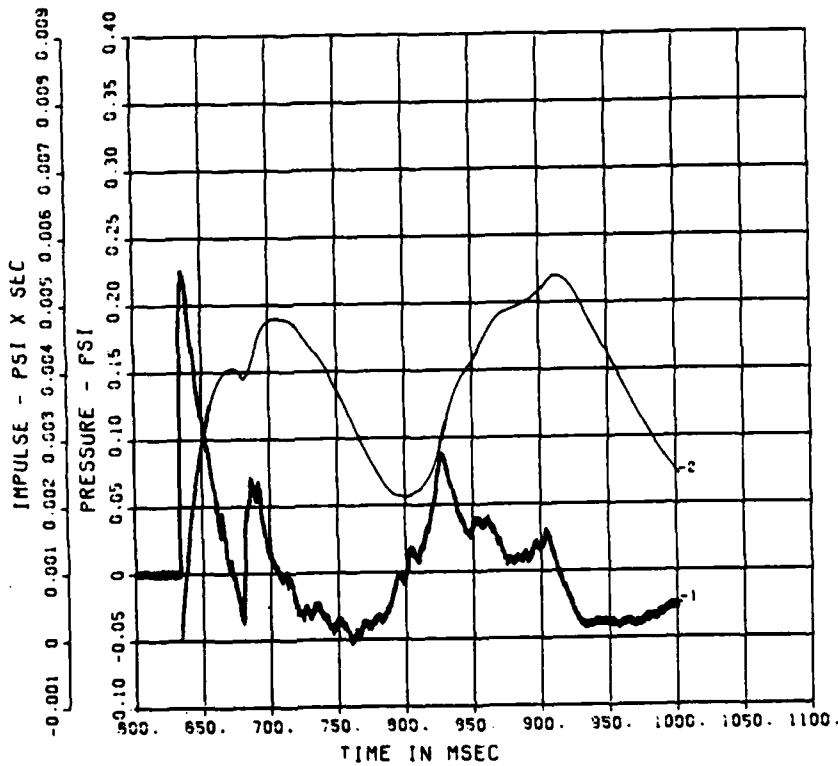


Chart D-12. QDT-3 Air Blast Record at 740 Feet on South Radial

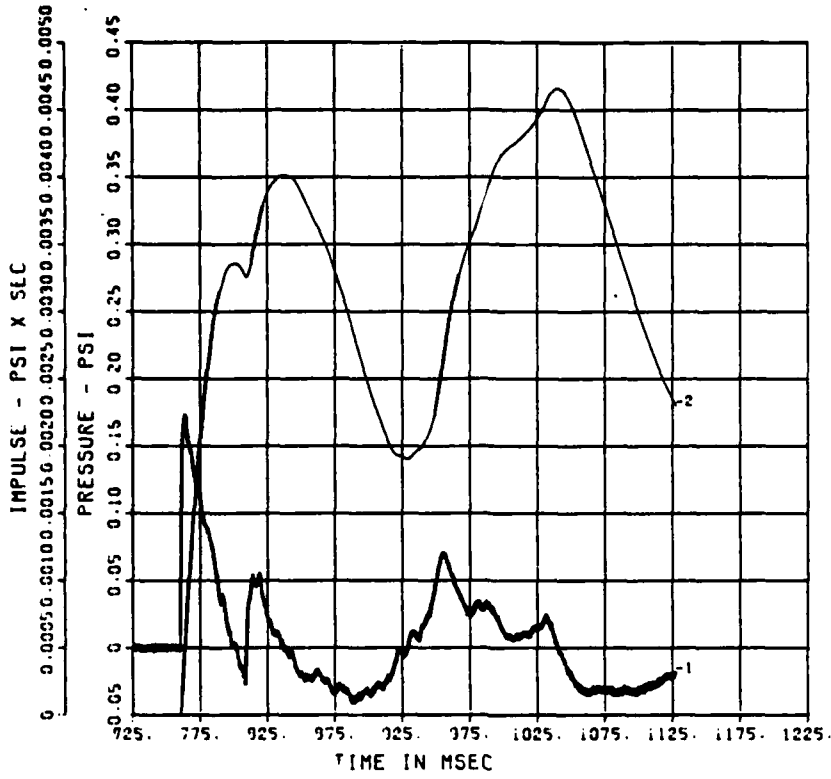


Chart D-13. QDT-3 Air Blast Record at 880 Feet on South Radial

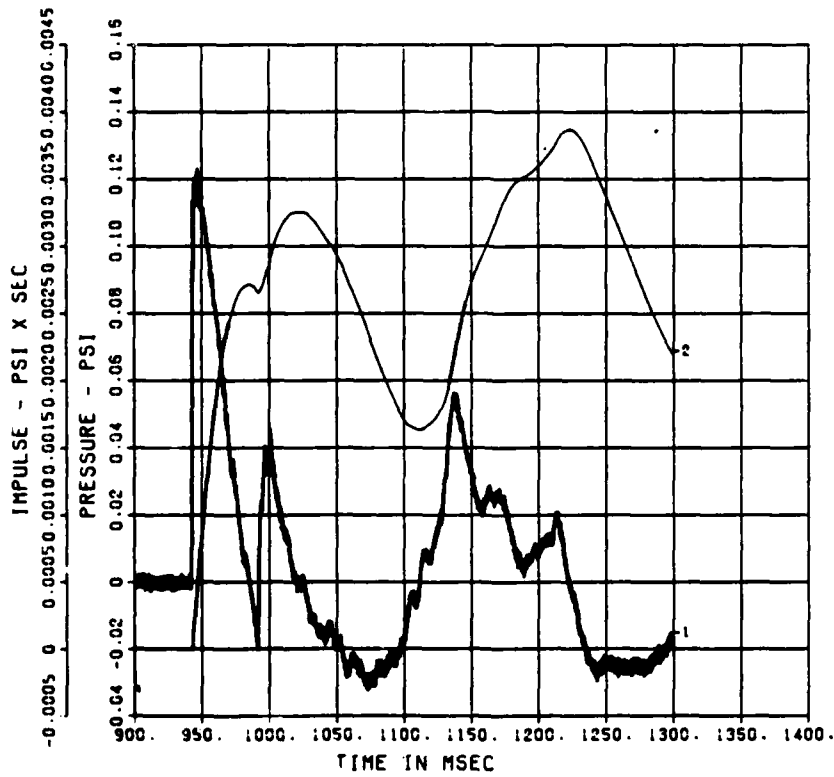


Chart D-14. QDT-3 Air Blast Record at 1080 Feet on South Radial

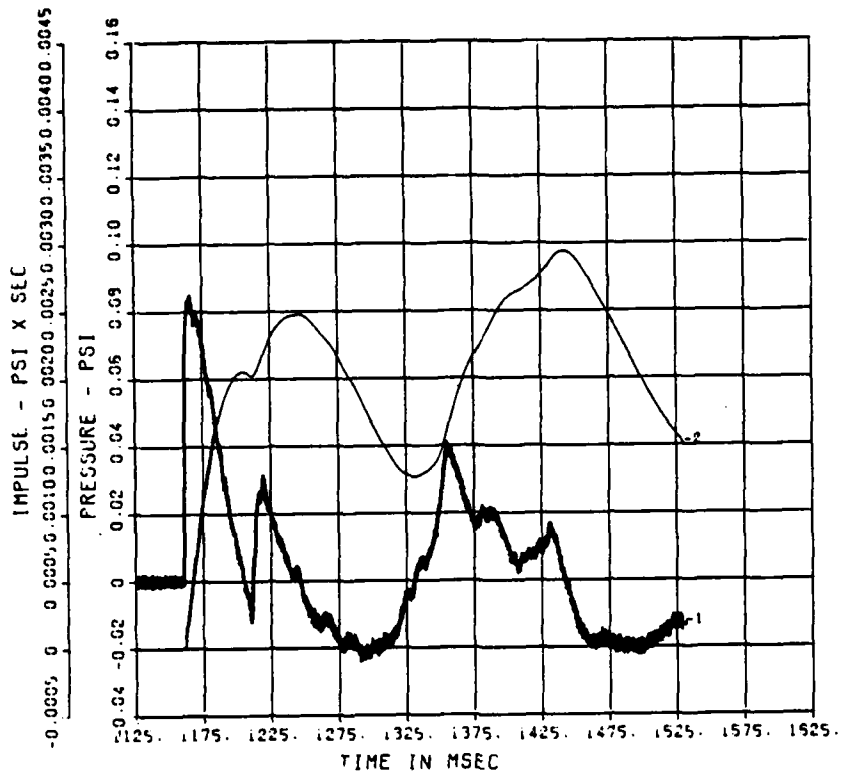


Chart D-15. QDT-3 Air Blast Record at 1320 Feet on South Radial

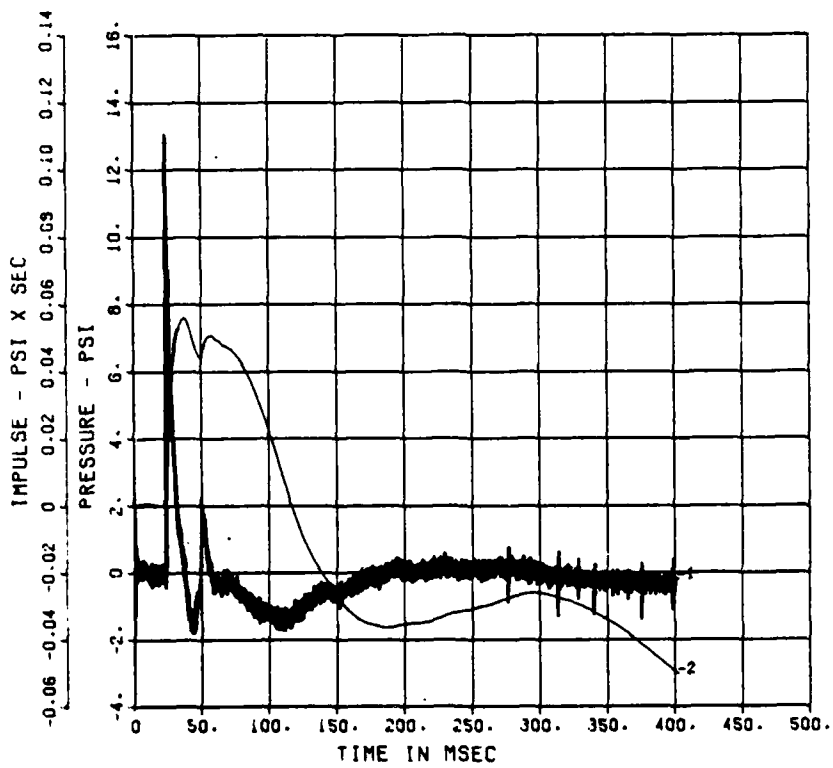


Chart D-16. QDT-3 Air Blast Record at 42 Feet on Northeast Radial

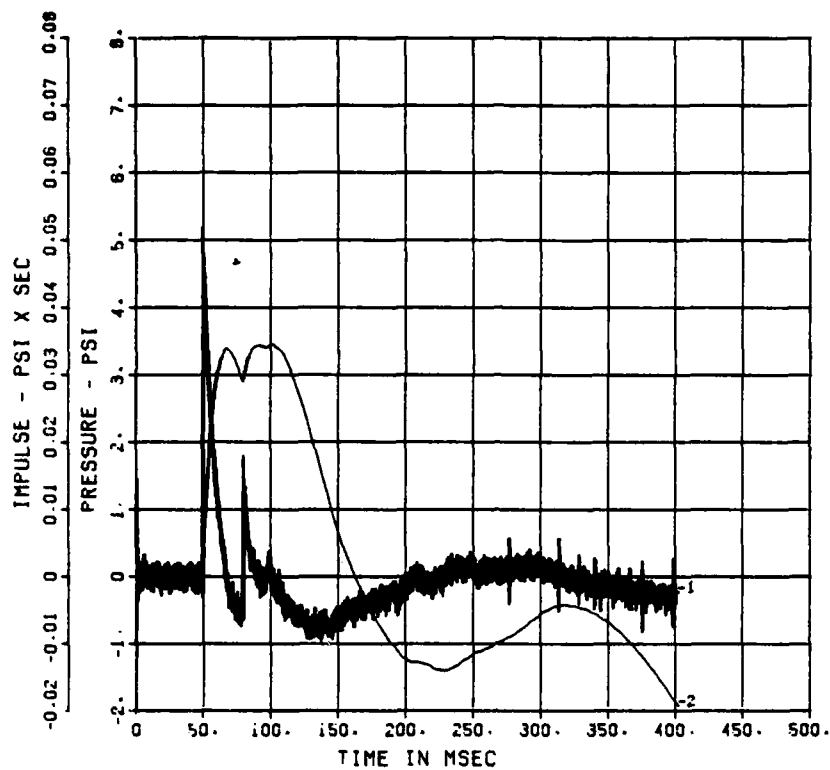


Chart D-17. QDT-3 Air Blast Record at 78 Feet on Northeast Radial

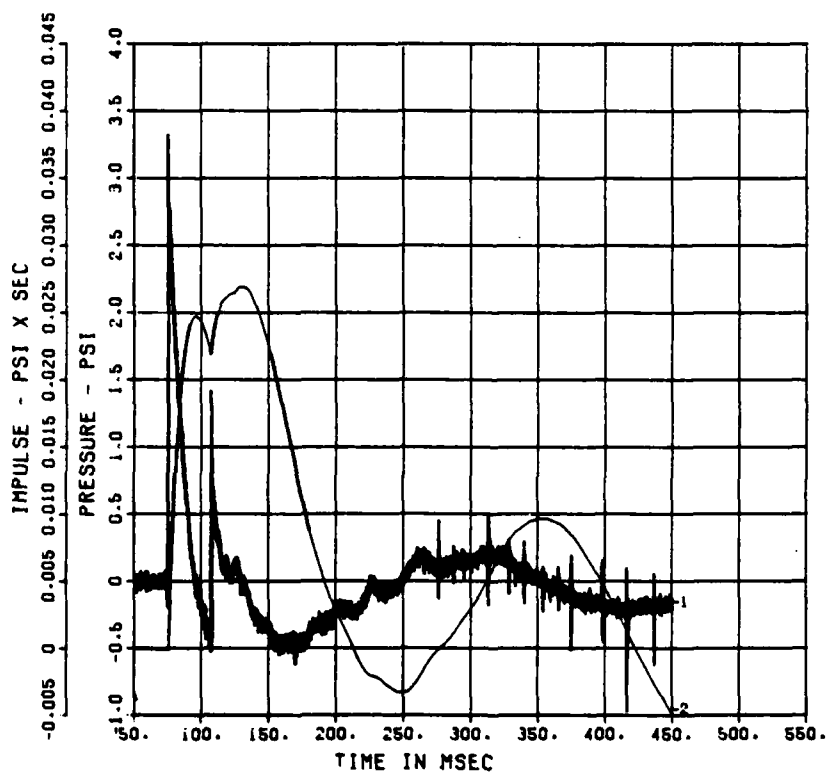


Chart D-18. QDT-3 Air Blast Record at 110 Feet on Northeast Radial

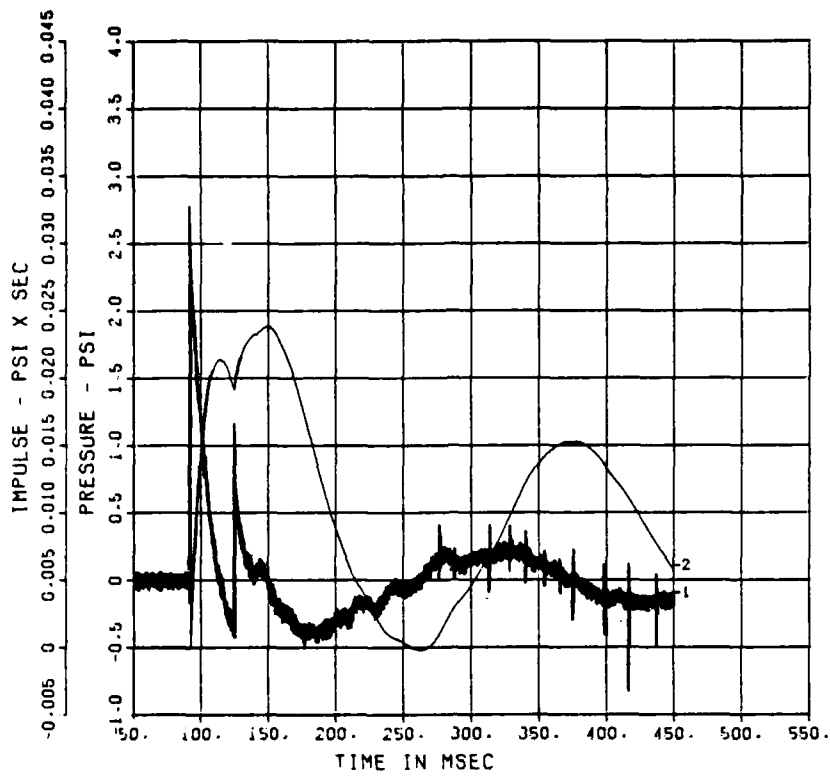


Chart D-19. QDT-3 Air Blast Record at 130 Feet on Northeast Radial

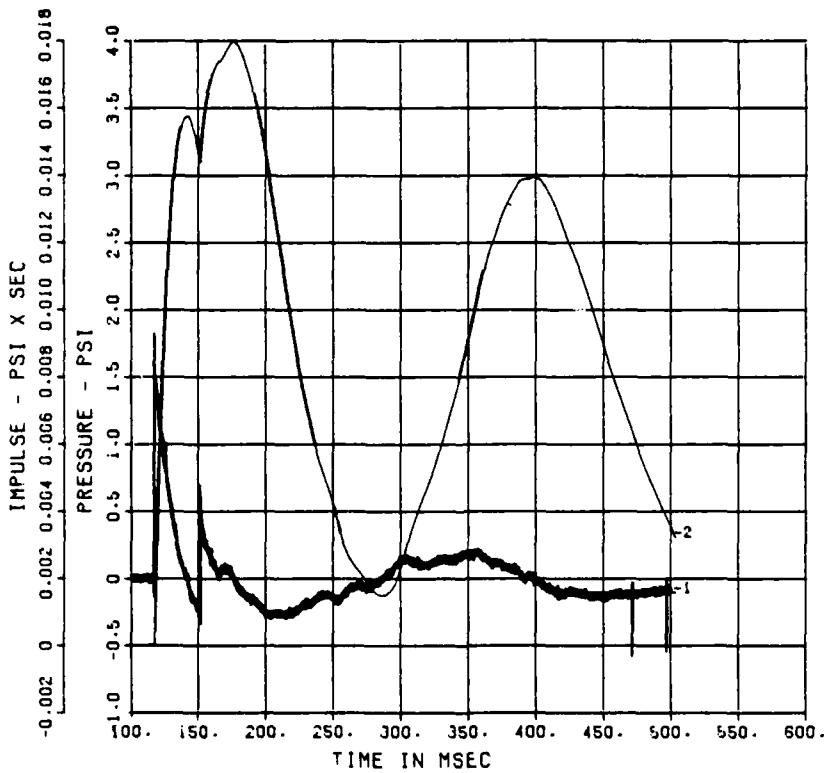


Chart D-20. QDT-3 Air Blast Record at 160 Feet on Northeast Radial

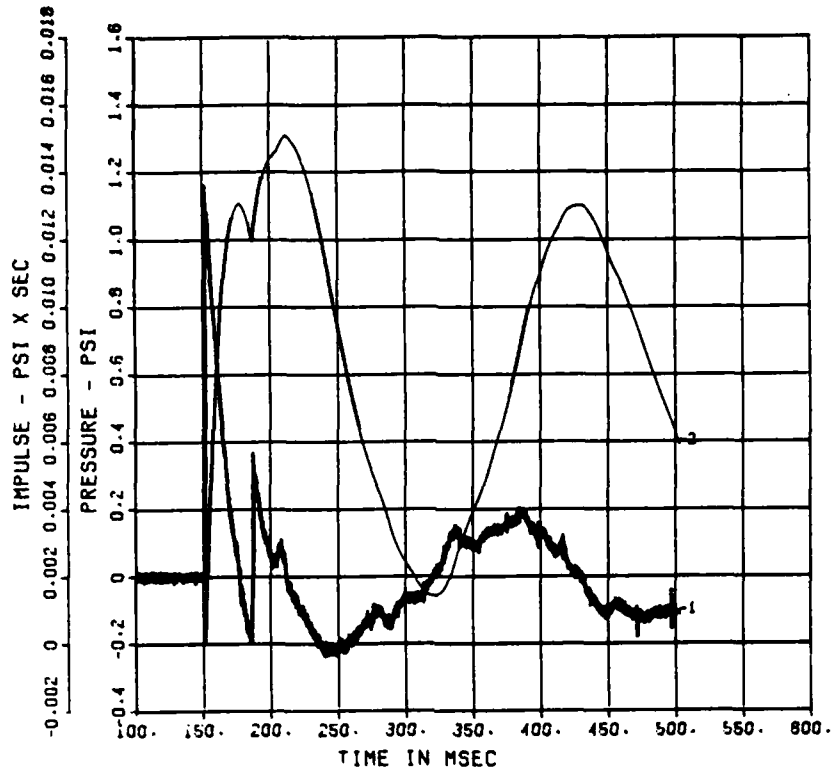


Chart D-21. QDT-3 Air Blast Record at 200 Feet on Northeast Radial

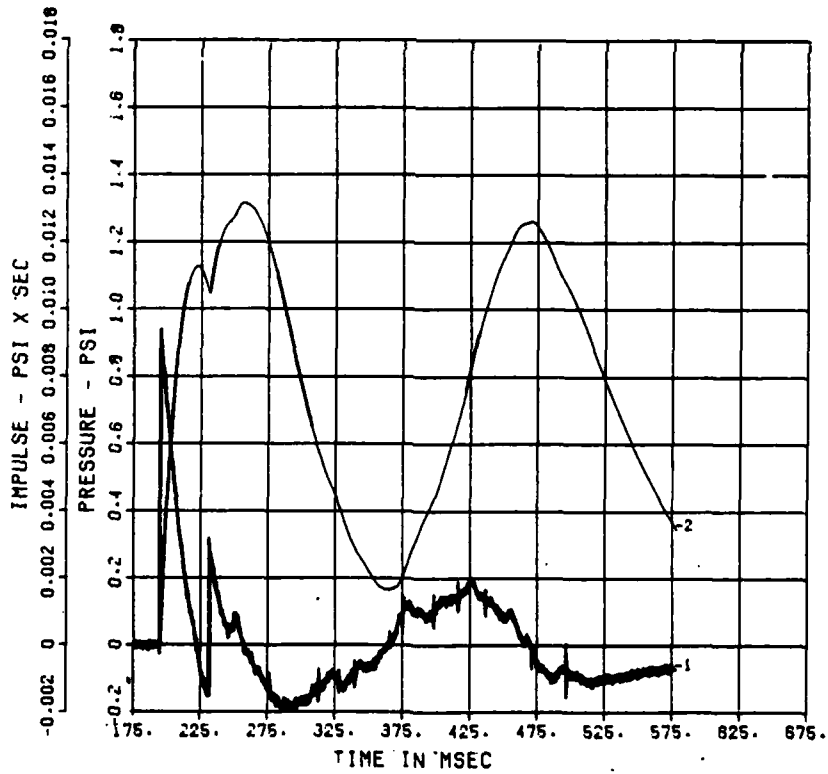


Chart D-22. QDT-3 Air Blast Record at 250 Feet on Northeast Radial

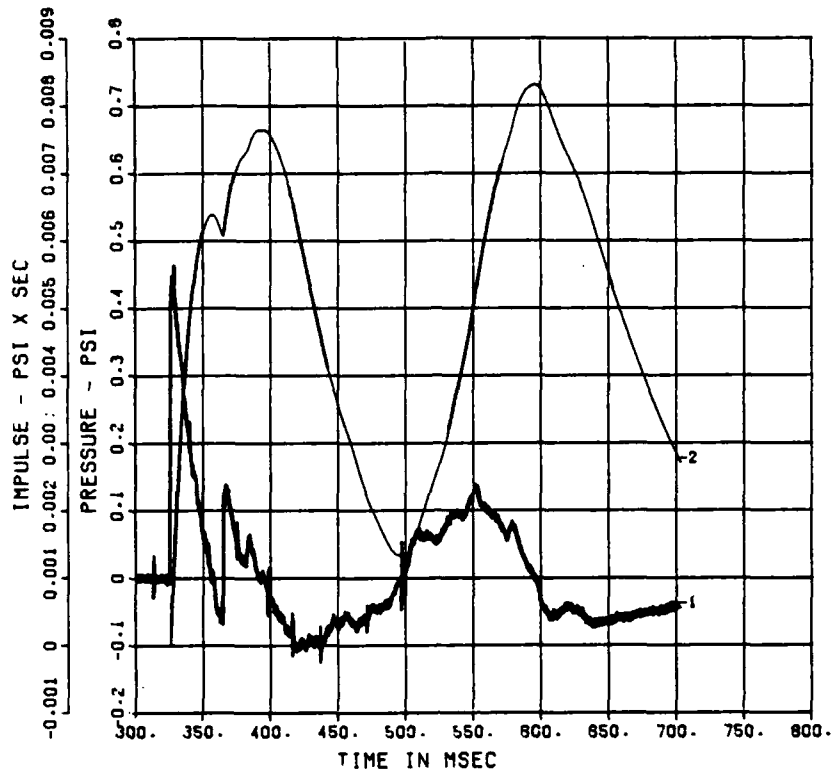


Chart D-23. QDT-3 Air Blast Record at 325 Feet on Northeast Radial

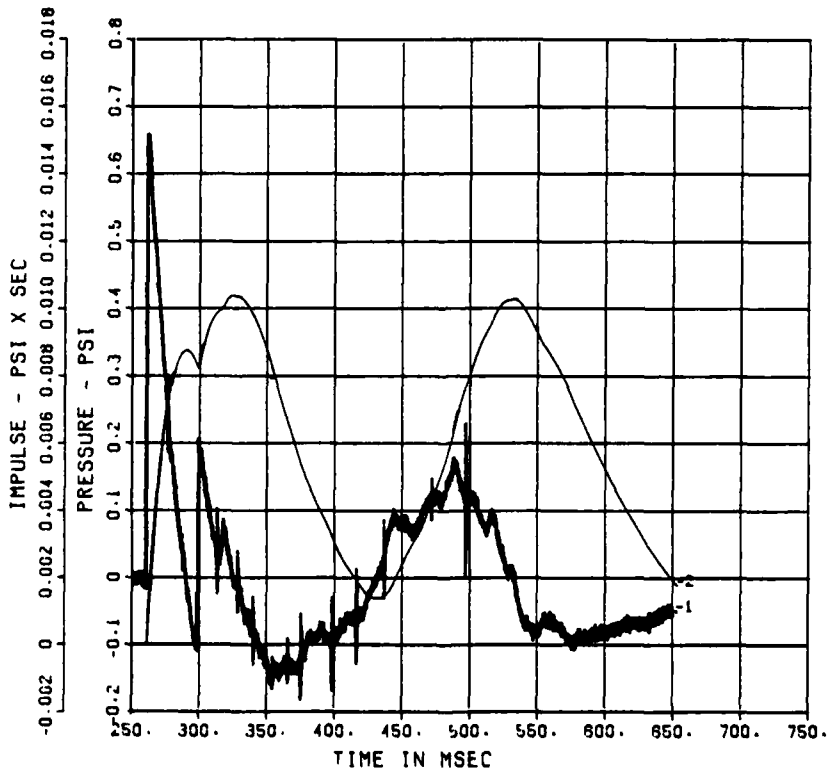


Chart D-24. QDT-3 Air Blast Record at 400 Feet on Northeast Radial

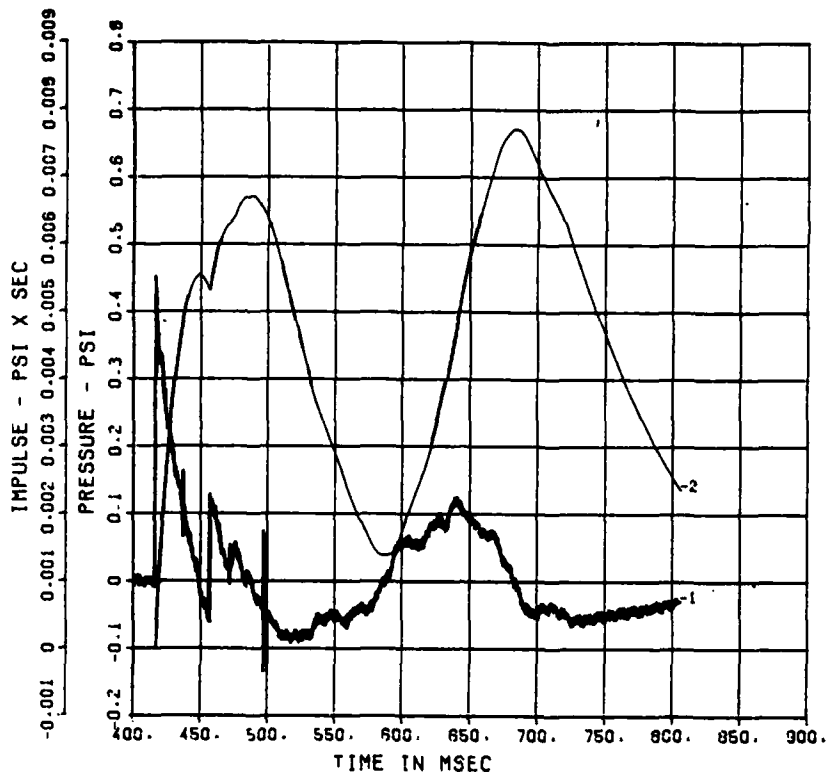


Chart D-25. QDT-3 Air Blast Record at 500 Feet on Northeast Radial

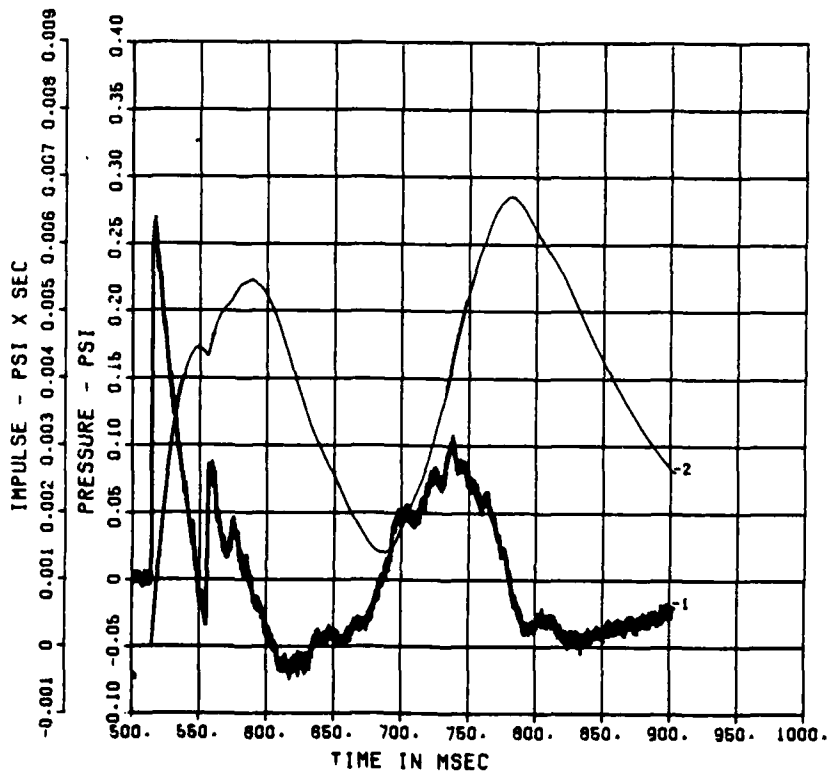


Chart D-26. QDT-3 Air Blast Record at 610 Feet on Northeast Radial

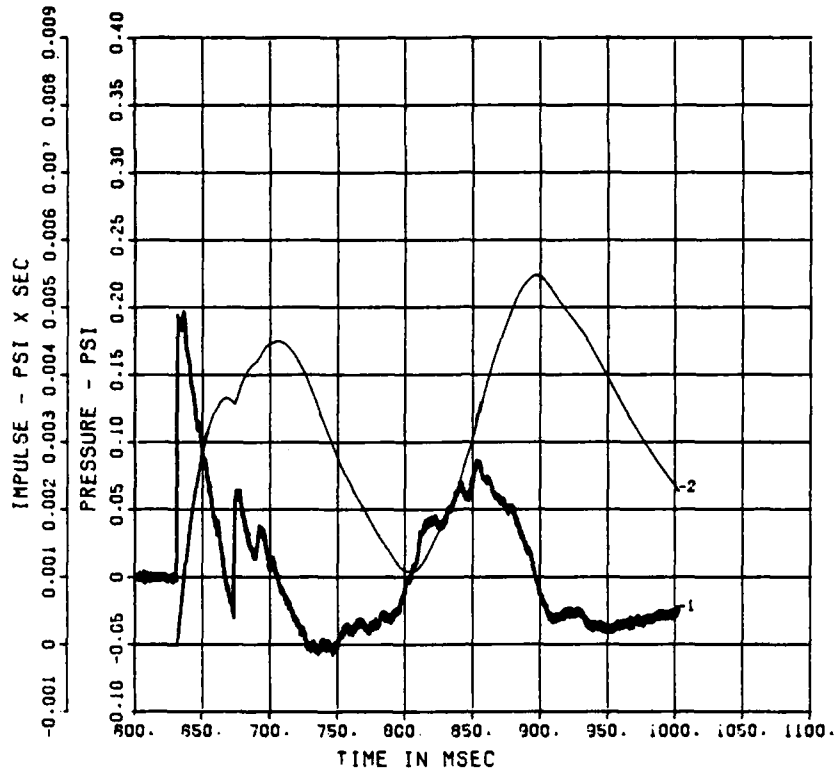


Chart D-27. QDT-3 Air Blast Record at 740 Feet on Northeast Radial

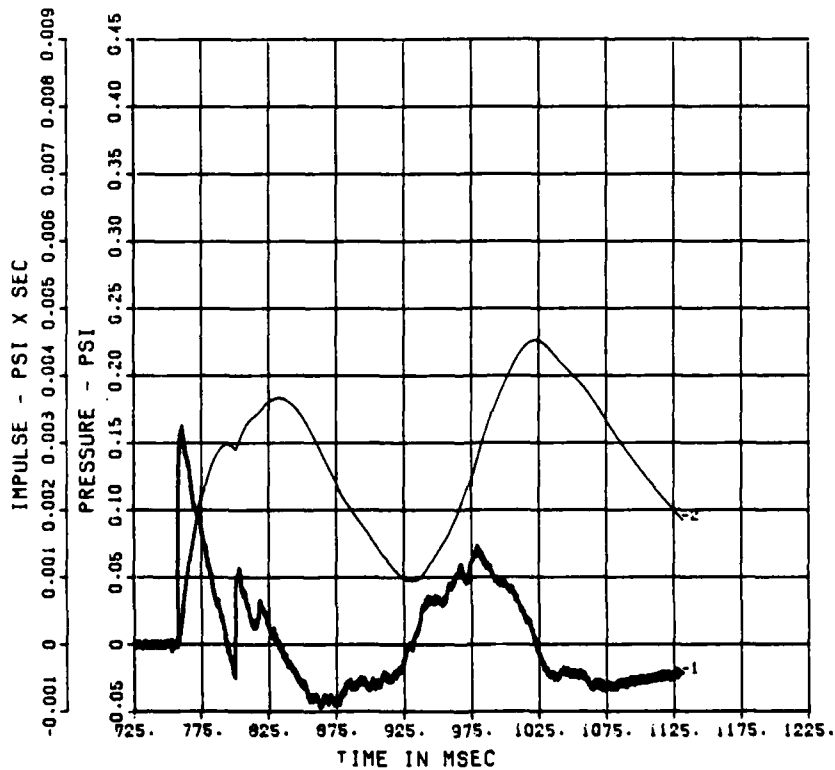


Chart D-28. QDT-3 Air Blast Record at 880 Feet on Northeast Radial

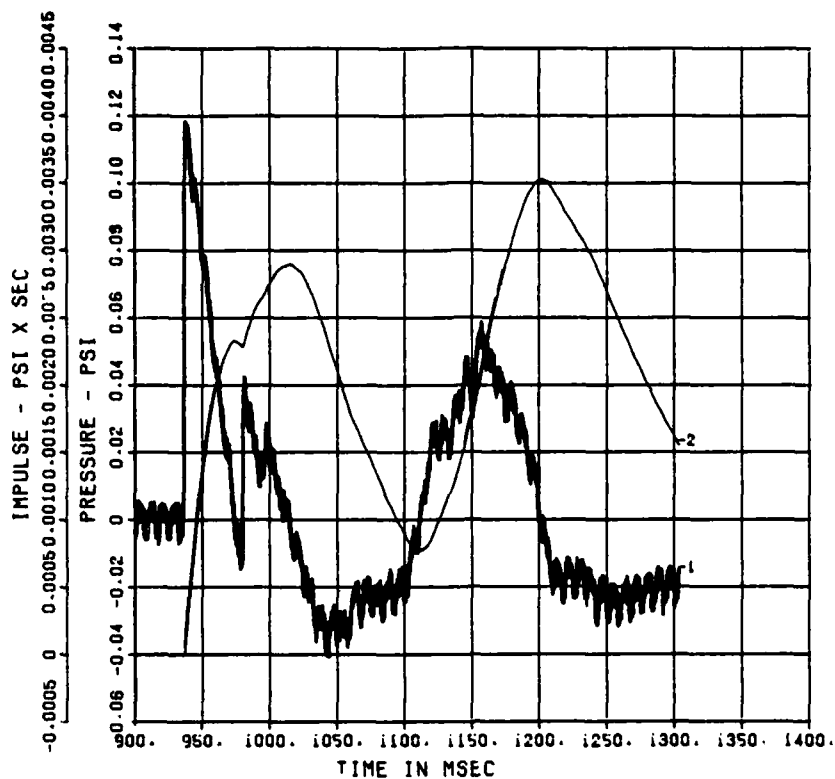


Chart D-29. QDT-3 Air Blast Record at 1080 Feet on Northeast Radial

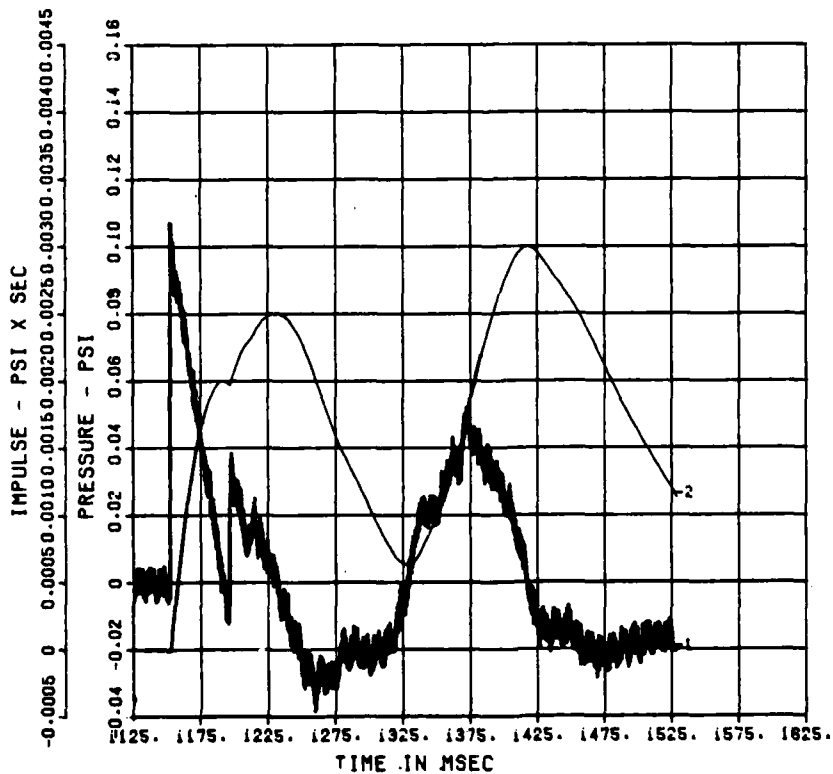


Chart D-30. QDT-3 Air Blast Record at 1320 Feet on Northeast Radial

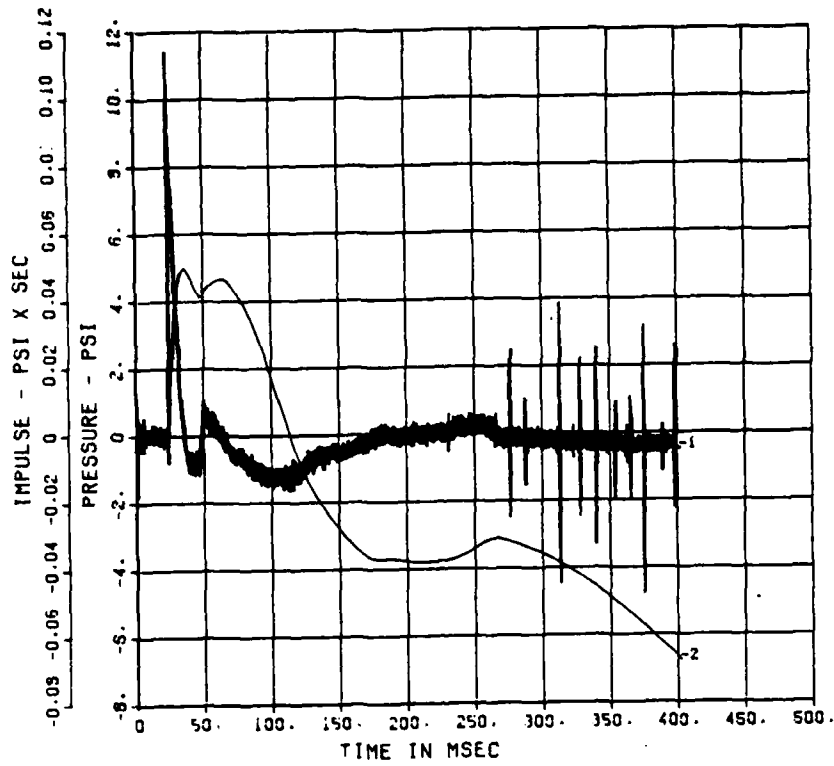


Chart D-31. QDT-3 Air Blast Record at 42 Feet on Northeast Radial

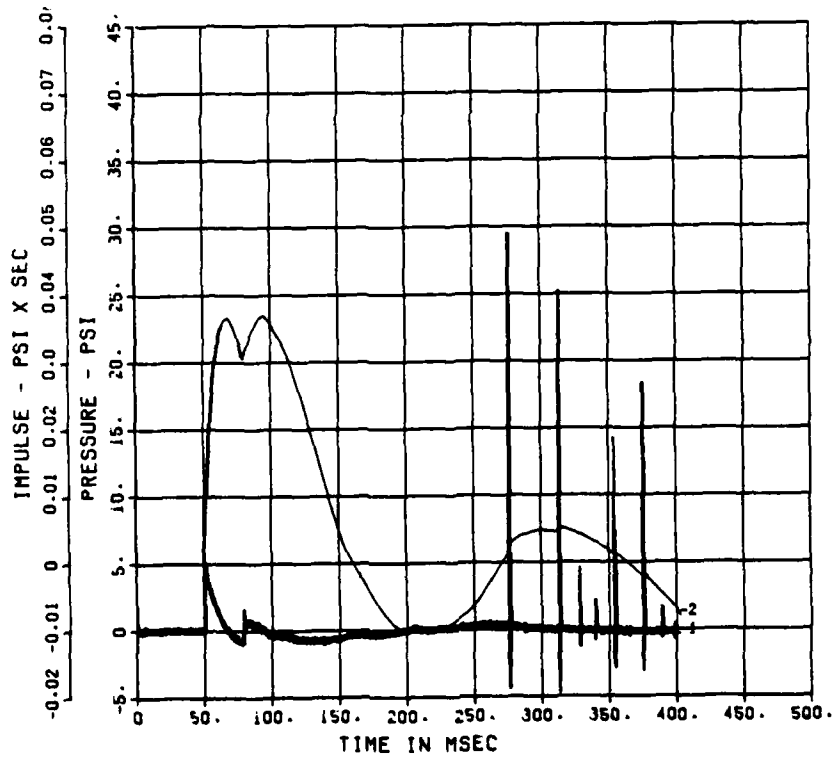


Chart D-32. QDT-3 Air Blast Record at 78 Feet on Northwest Radial

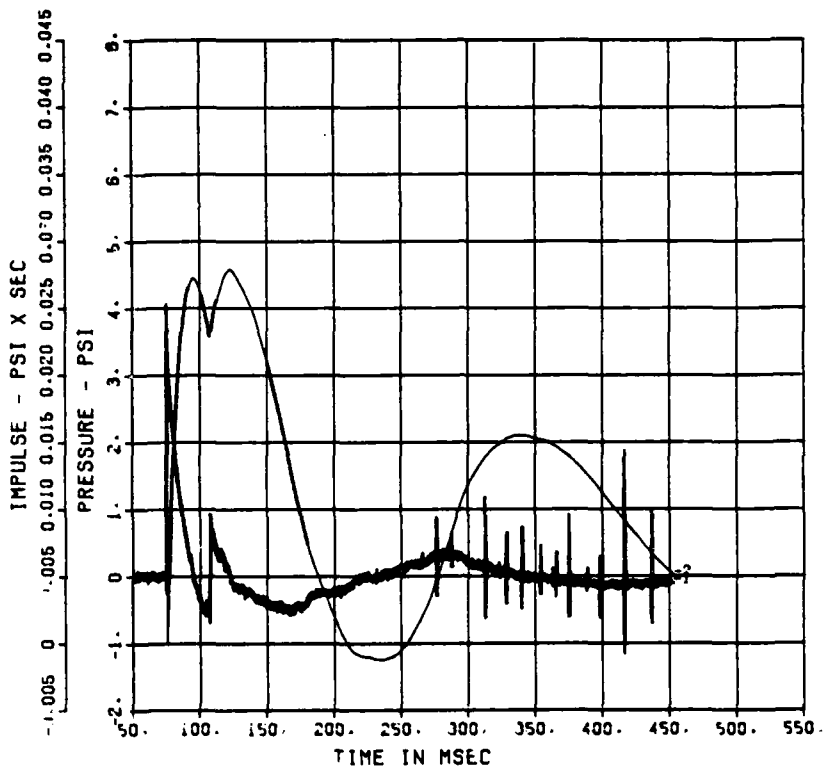


Chart D-33. QDT-3 Air Blast Record at 110 Feet on Northwest Radial

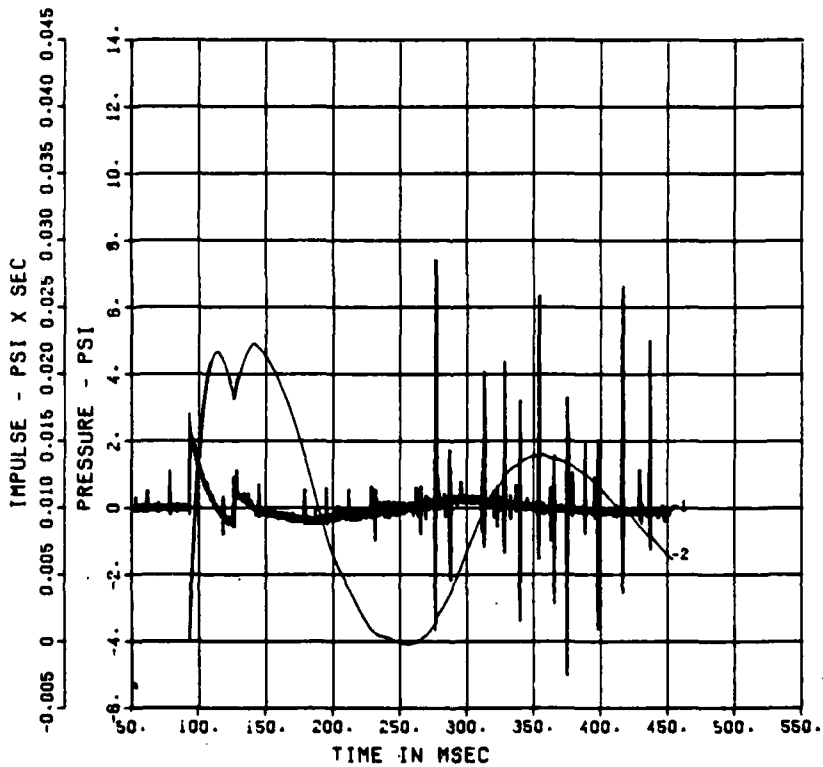


Chart D-34. QDT-3 Air Blast Record at 130 Feet on Northwest Radial

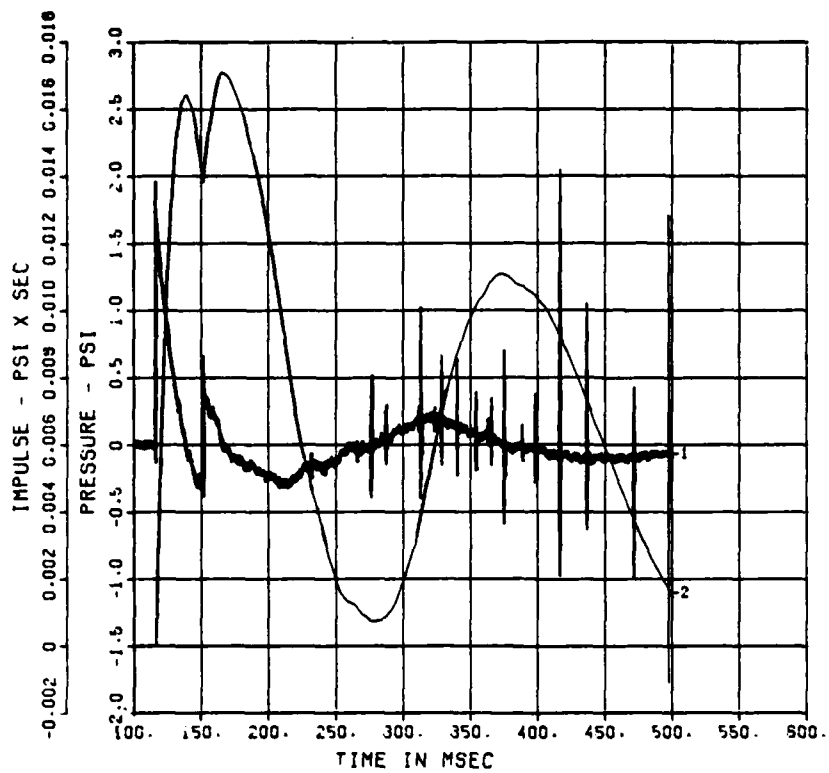


Chart D-35. QDT-3 Air Blast Record at 160 Feet on Northwest Radial

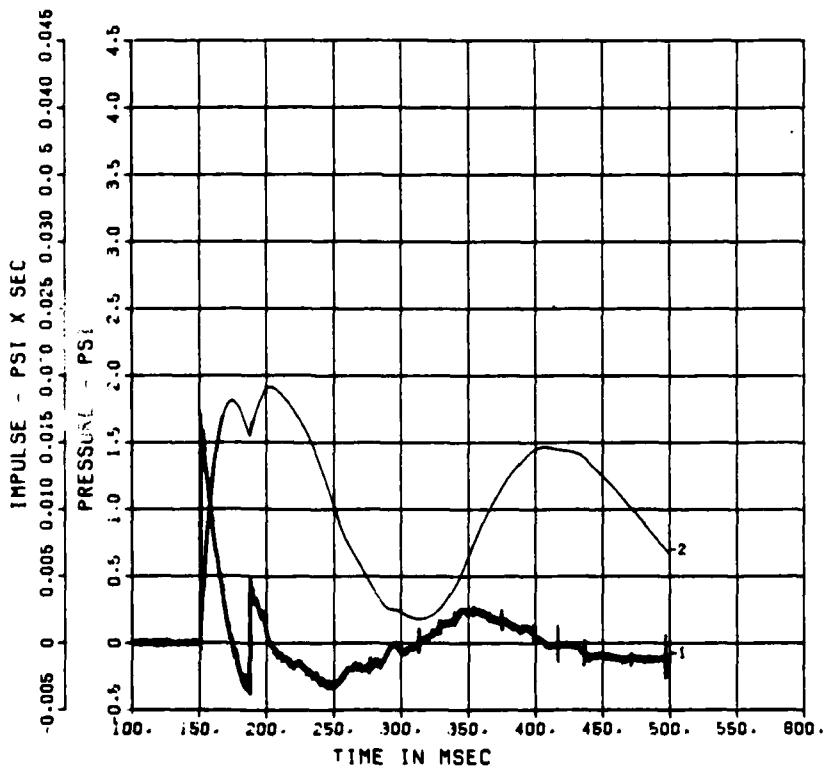


Chart D-36. QDT-3 Air Blast Record at 200 Feet on Northwest Radial

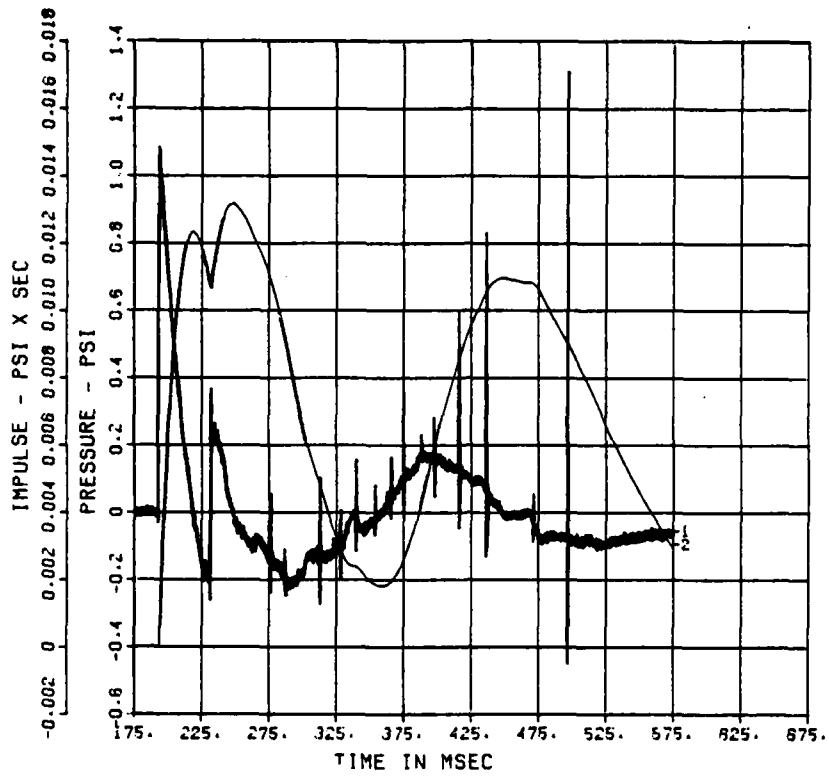


Chart D-37. QDT-3 Air Blast Record at 250 Feet on Northwest Radial

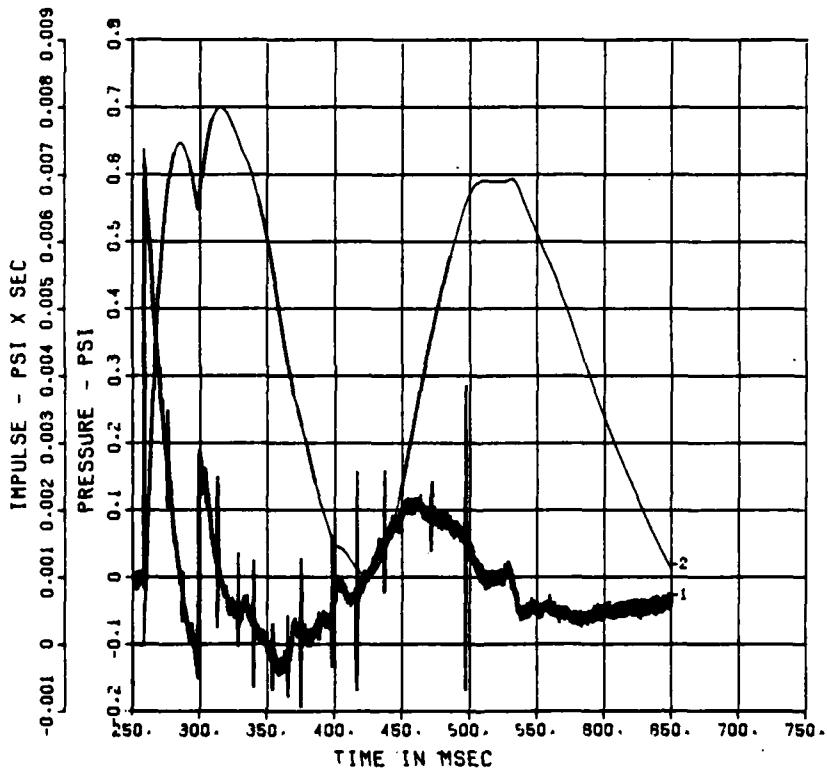


Chart D-38. QDT-3 Air Blast Record at 325 Feet on Northwest Radial

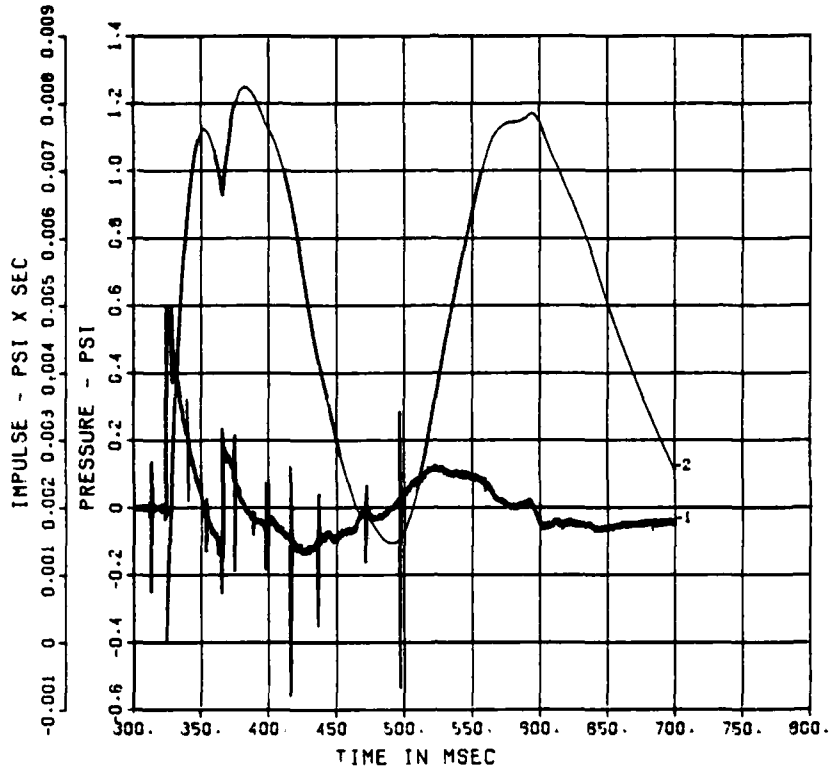


Chart D-39. QDT-3 Air Blast Record at 400 Feet on Northwest Radial

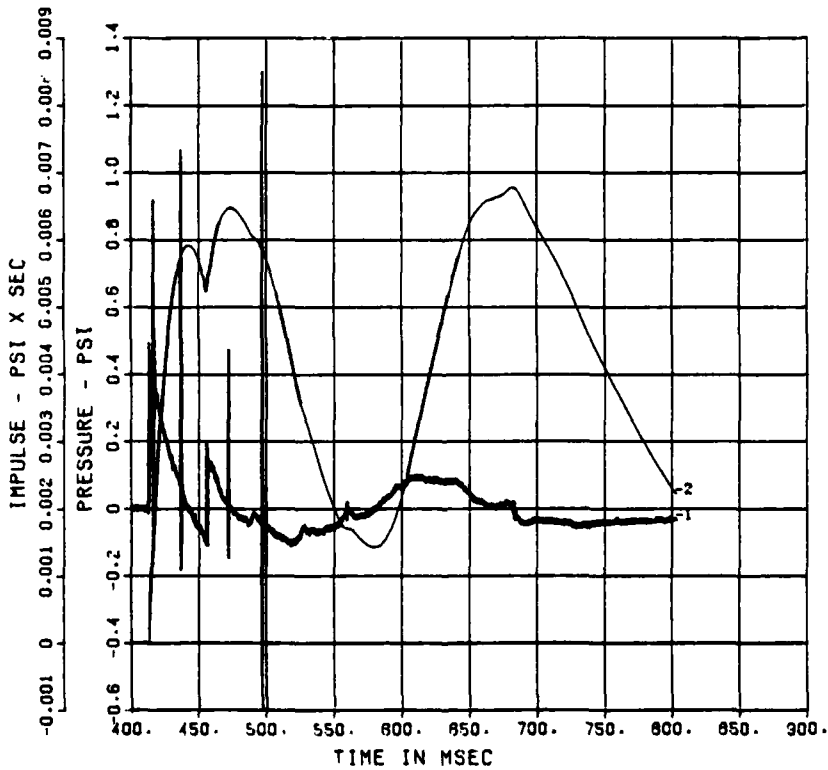


Chart D-40. QDT-3 Air Blast Record at 500 Feet on Northwest Radial

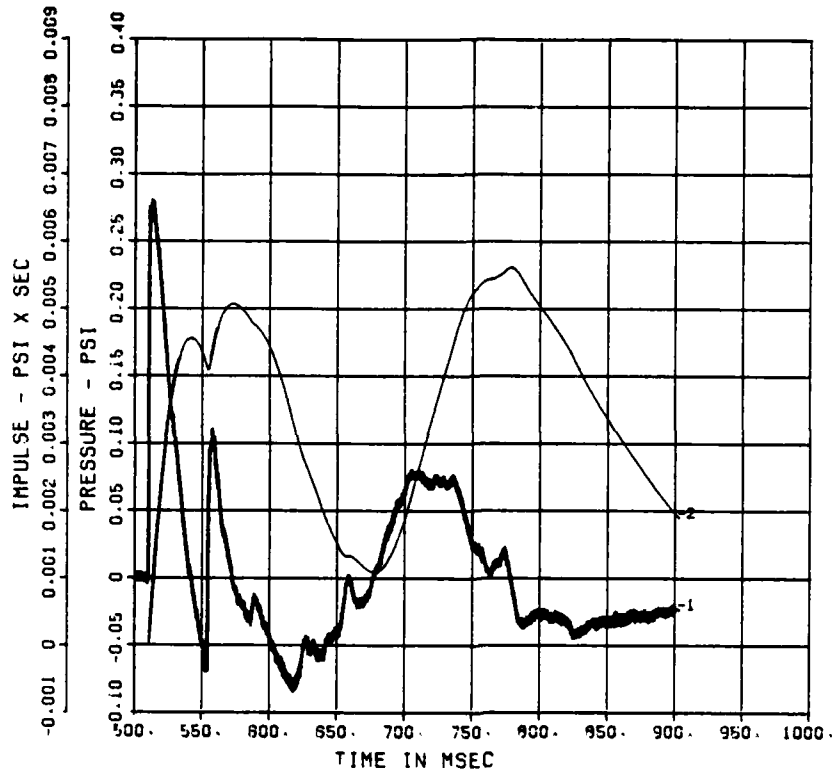


Chart D-41. QDT-3 Air Blast Record at 610 Feet on Northwest Radial

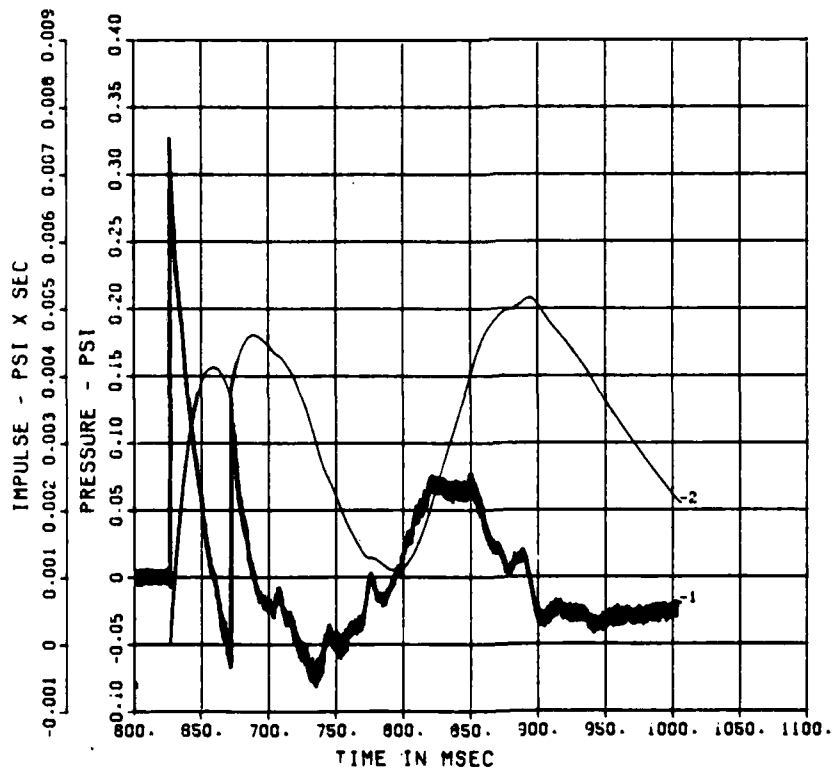


Chart D-42. QDT-3 Air Blast Record at 740 Feet on Northwest Radial

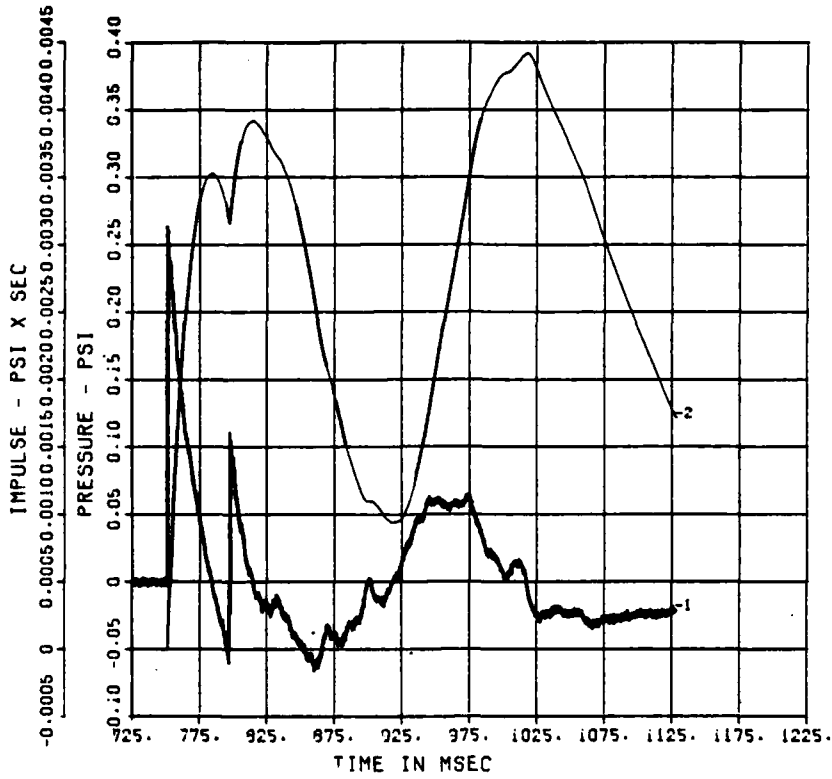


Chart D-43. QDT-3 Air Blast Record at 880 Feet on Northwest Radial

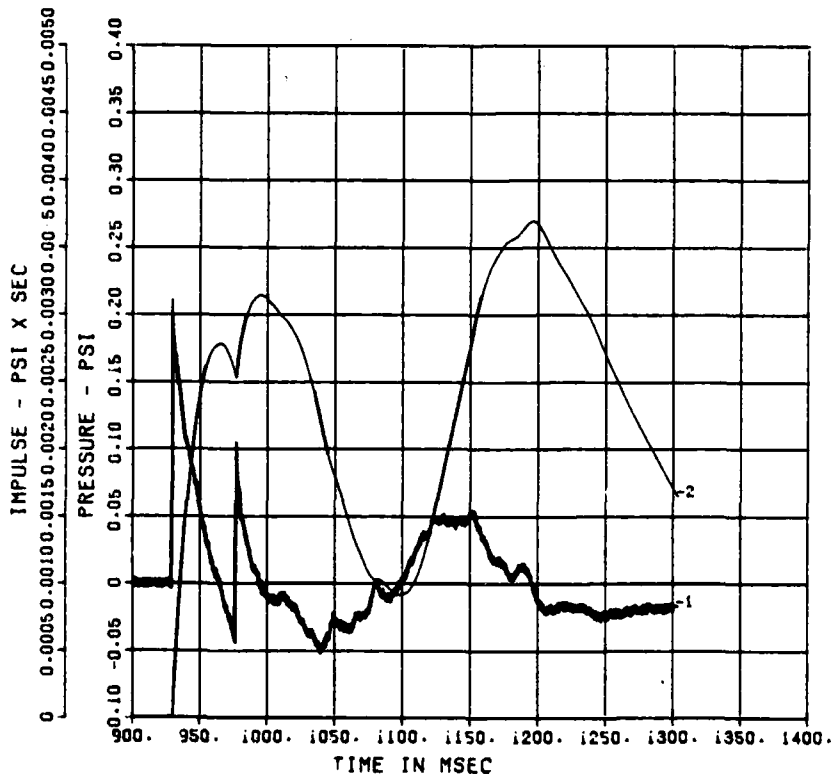


Chart D-44. QDT-3 Air Blast Record at 1080 Feet on Northwest Radial

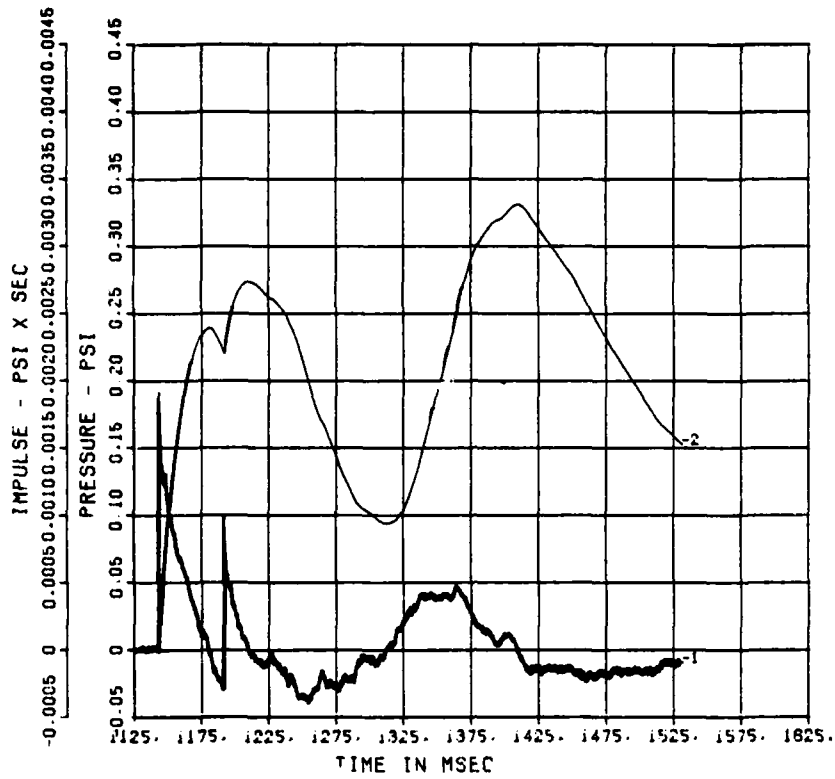


Chart D-45. QDT-3 Air Blast Record at 1320 Feet on Northwest Radial

APPENDIX E
CALIBRATION SHOT AIR BLAST RECORDS

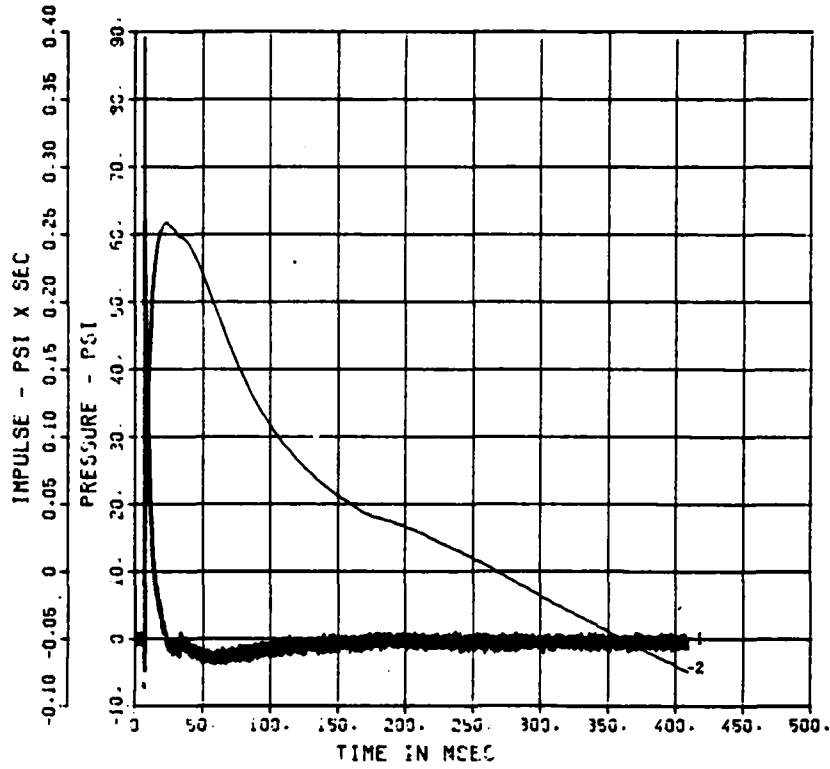


Chart E-1. Calibration Shot Air Blast Record at 42 Feet on South Radial

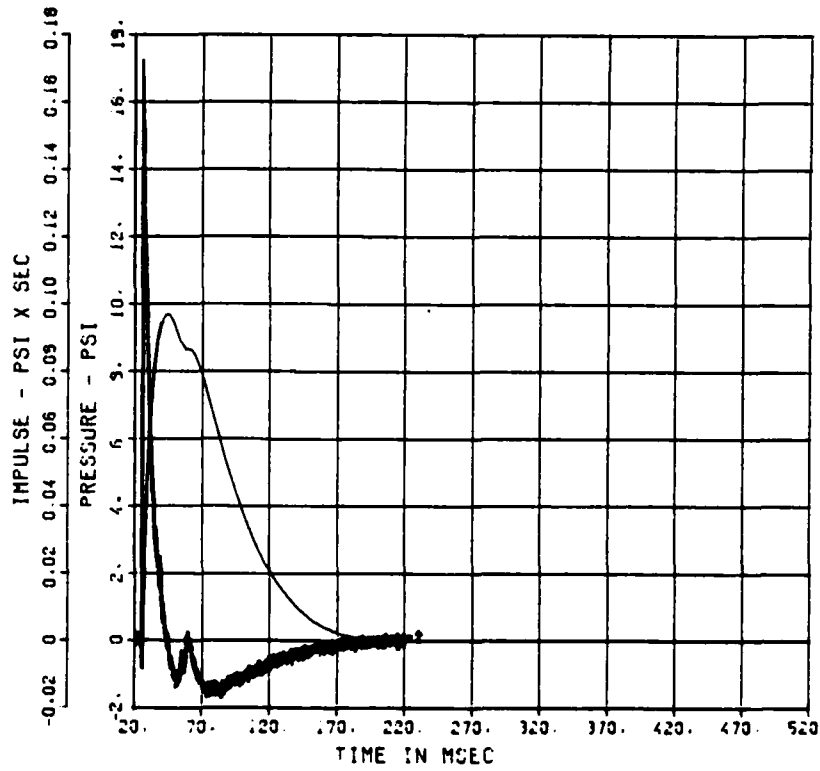


Chart E-2. Calibration Shot Air Blast Record at 78 Feet on South Radial

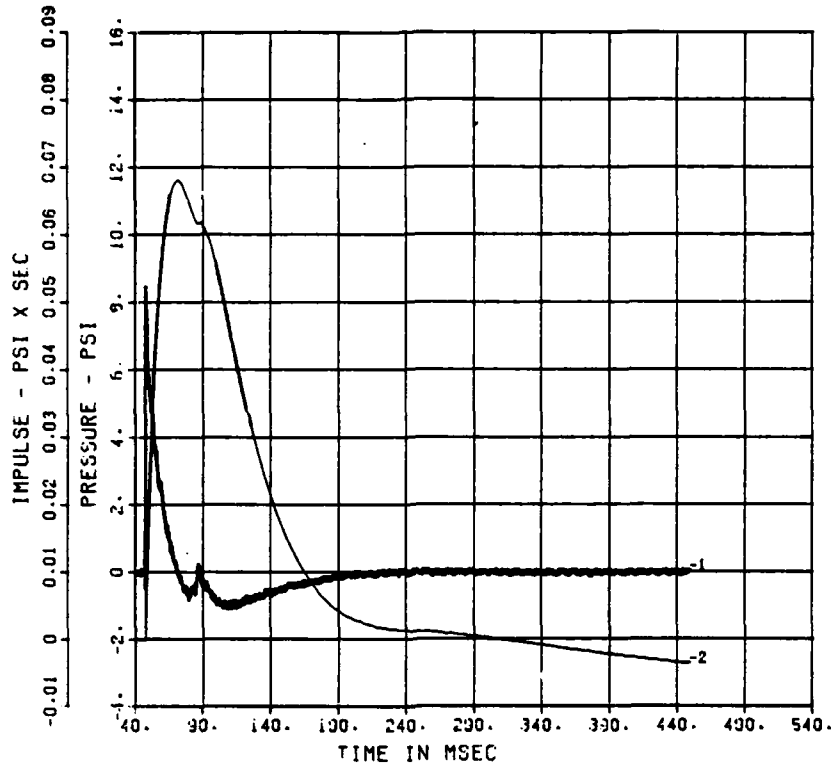


Chart E-3. Calibration Shot Air Blast Record at 110 Feet on South Radial

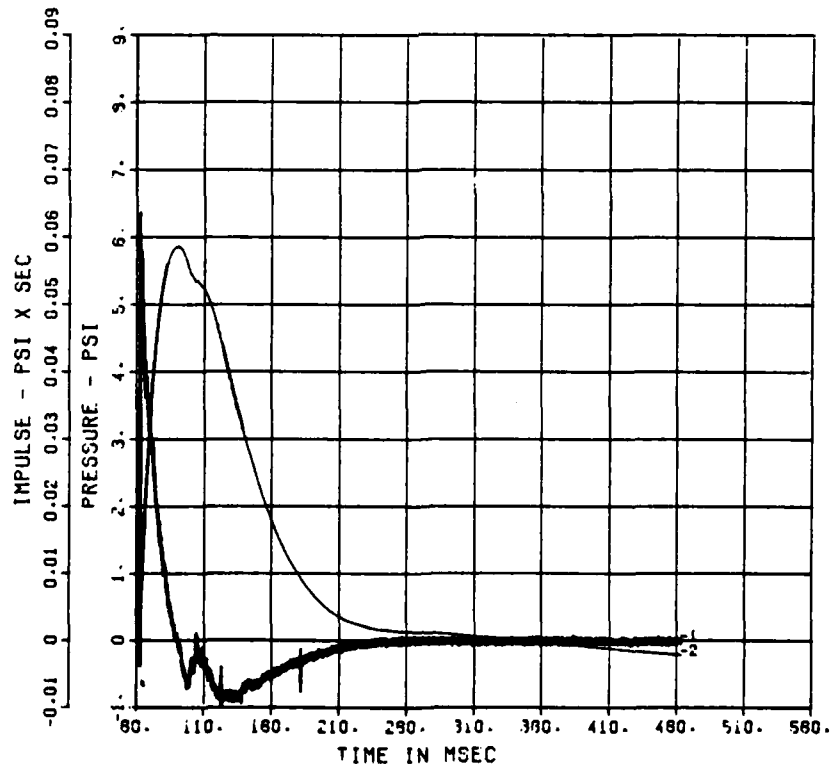


Chart E-4. Calibration Shot Air Blast Record at 130 Feet on South Radial

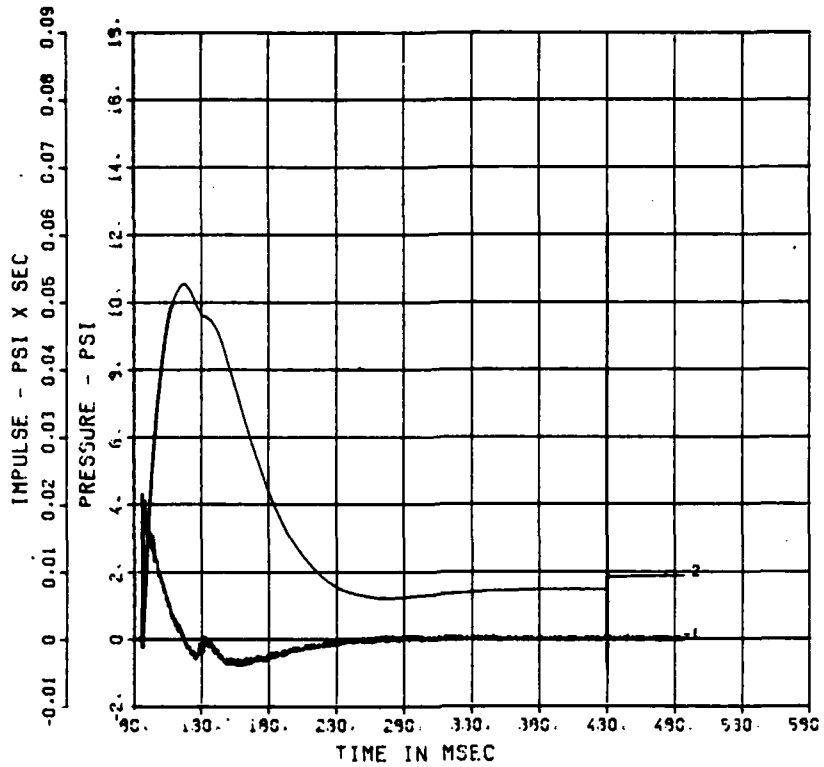


Chart E-5. Calibration Shot Air Blast Record at 160 Feet on South Radial

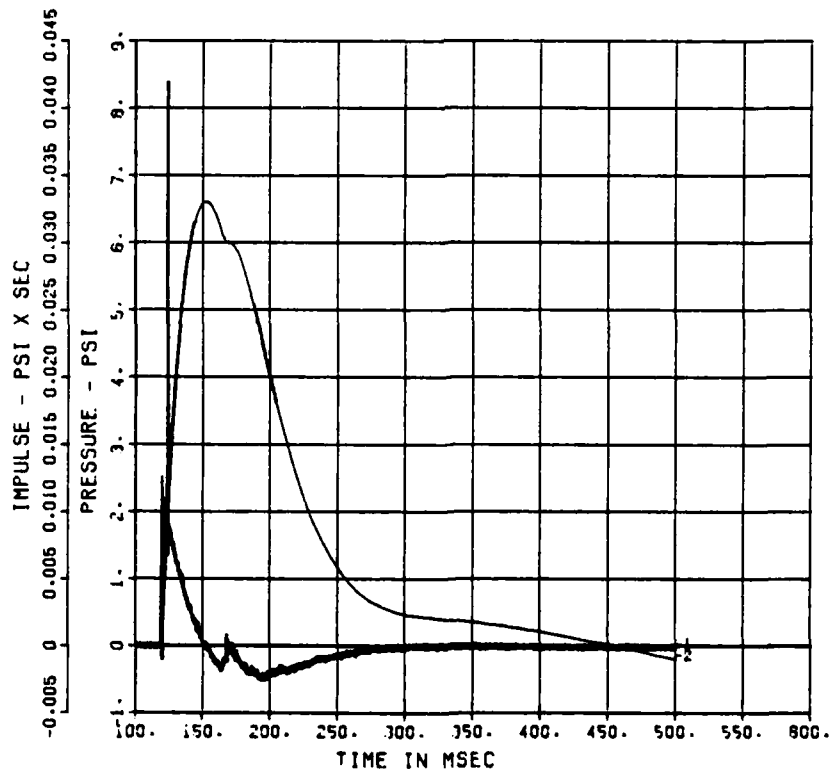


Chart E-6. Calibration Shot Air Blast Record at 200 Feet on South Radial

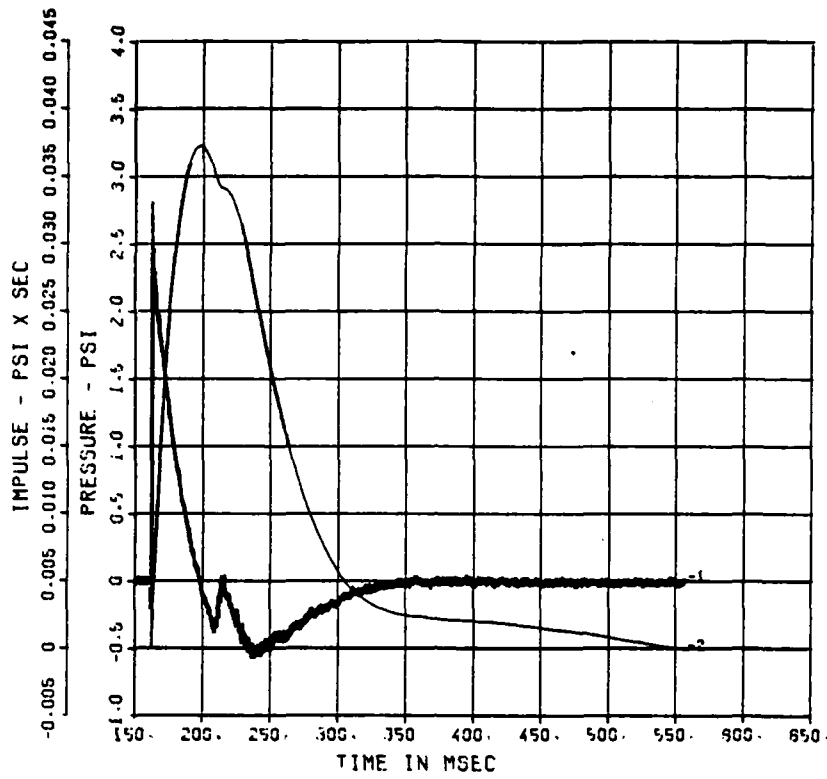


Chart E-7. Calibration Shot Air Blast Record at 250 Feet on South Radial

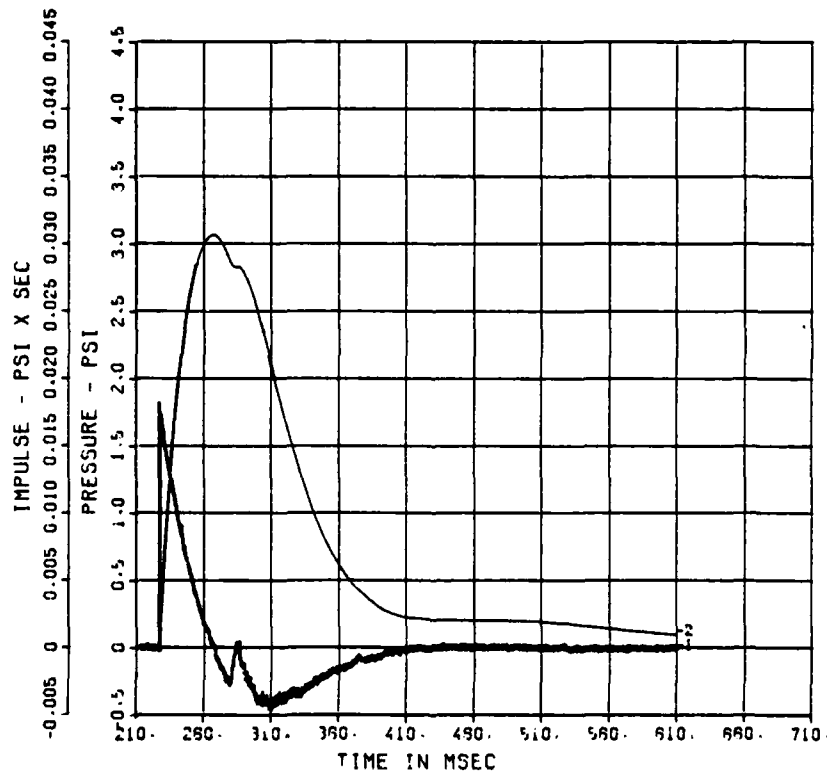


Chart E-8. Calibration Shot Air Blast Record at 325 Feet on South Radial

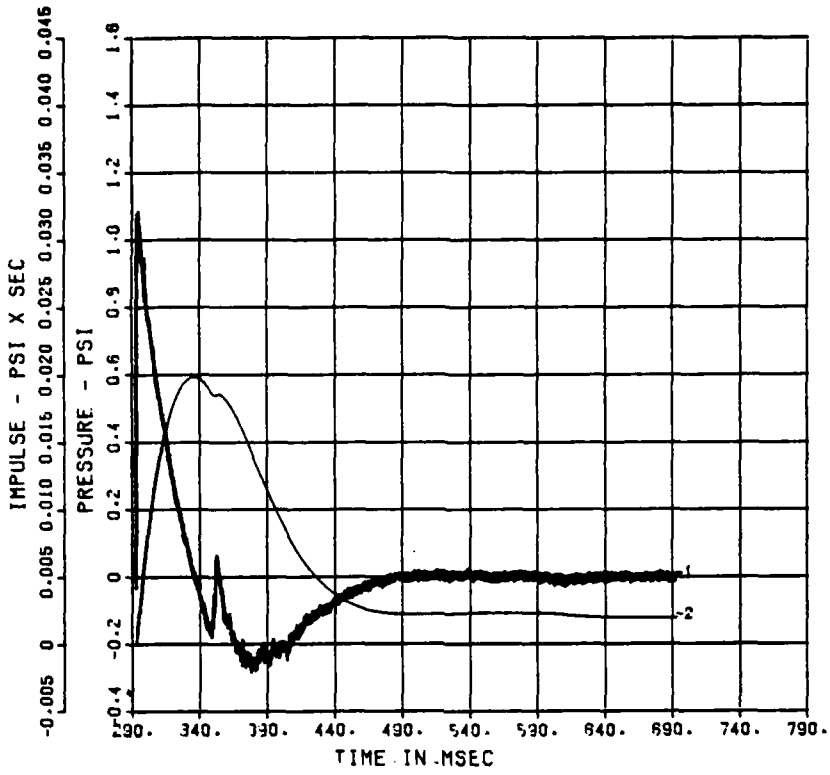


Chart E-9. Calibration Shot Air Blast Record at 400 Feet on South Radial

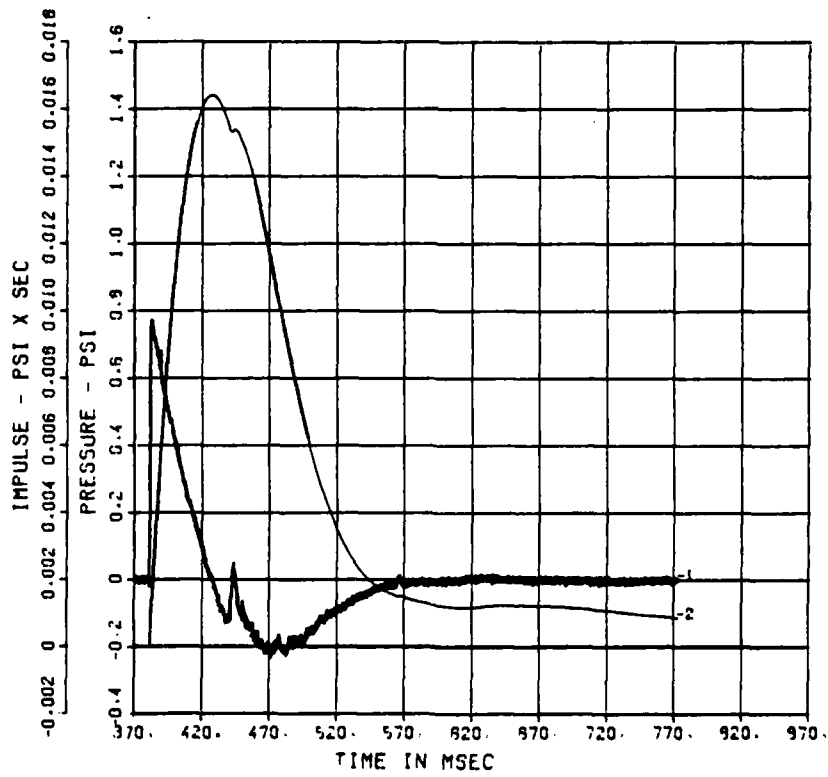


Chart E-10. Calibration Shot Air Blast Record at 500 Feet on South Radial

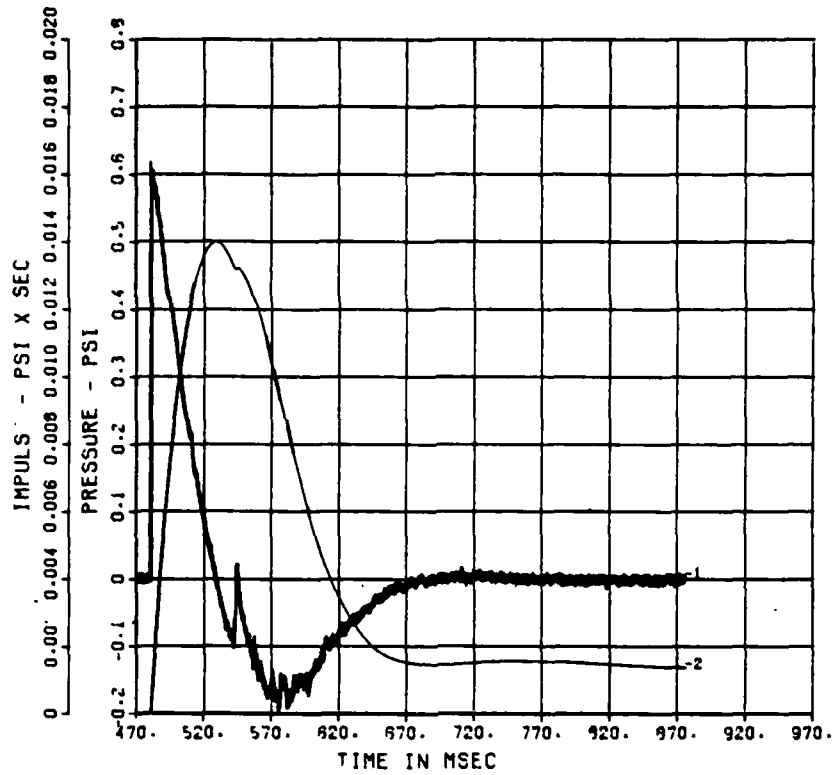


Chart E-11. Calibration Shot Air Blast Record at 610 Feet on South Radial

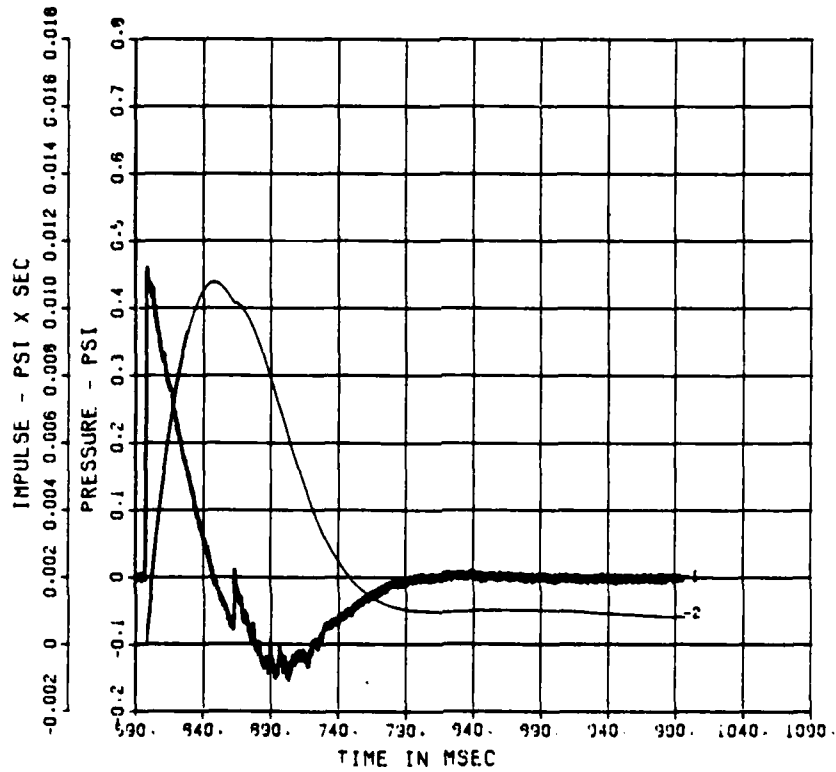


Chart E-12. Calibration Shot Air Blast Record at 740 Feet on South Radial

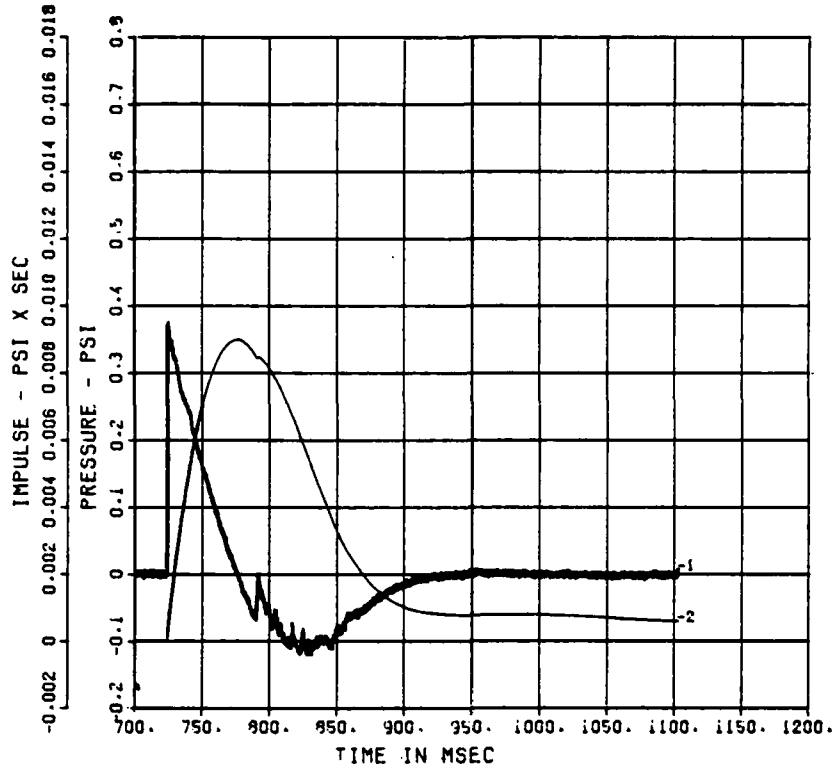


Chart E-13. Calibration Shot Air Blast Record at 880 Feet on South Radial

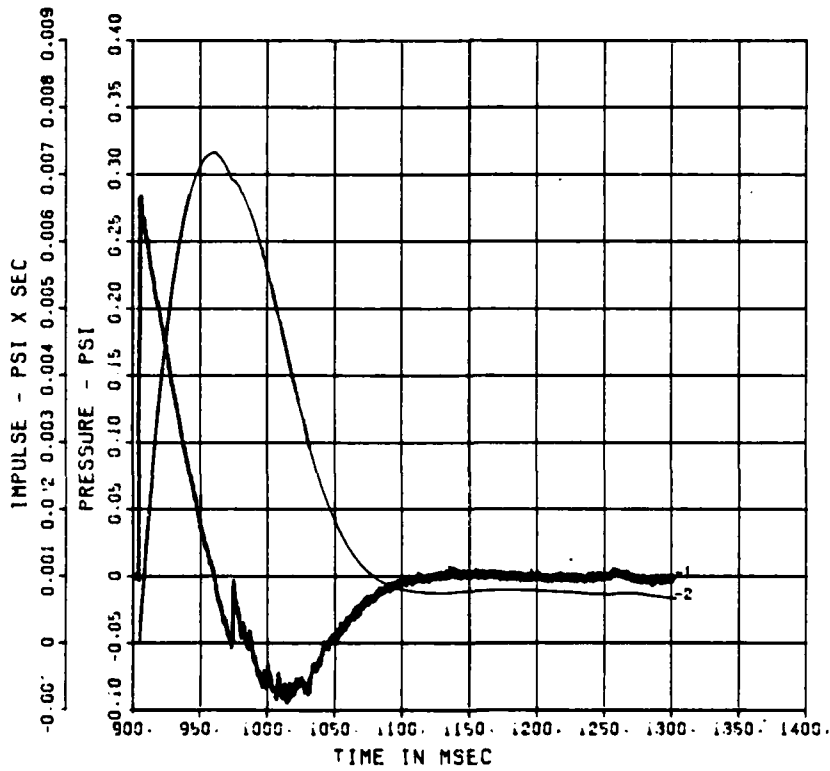


Chart E-14. Calibration Shot Air Blast Record at 1080 Feet on South Radial

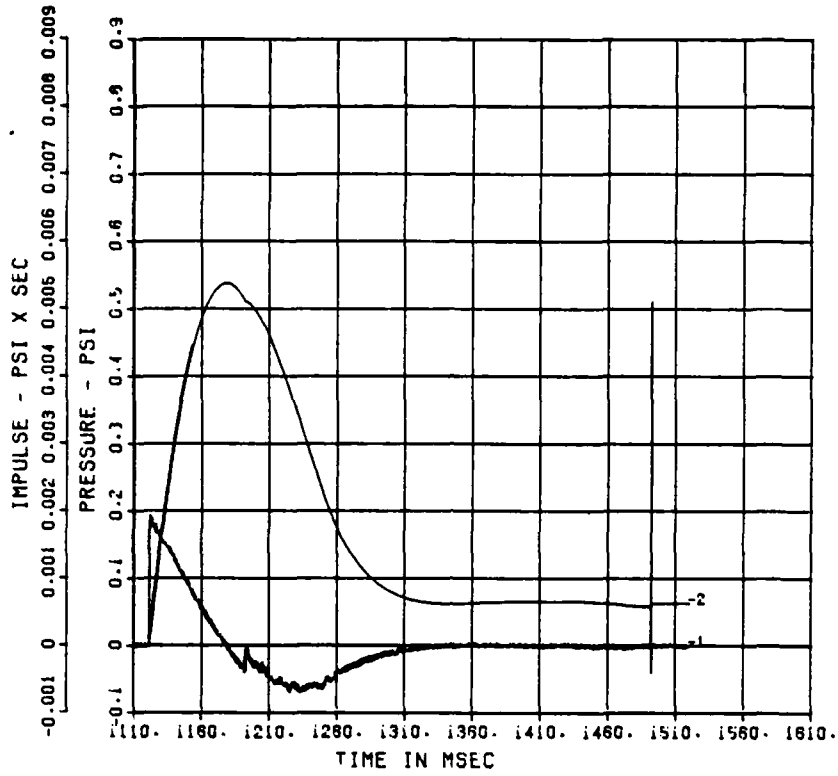


Chart E-15. Calibration Shot Air Blast Record at 1320 Feet on South Radial

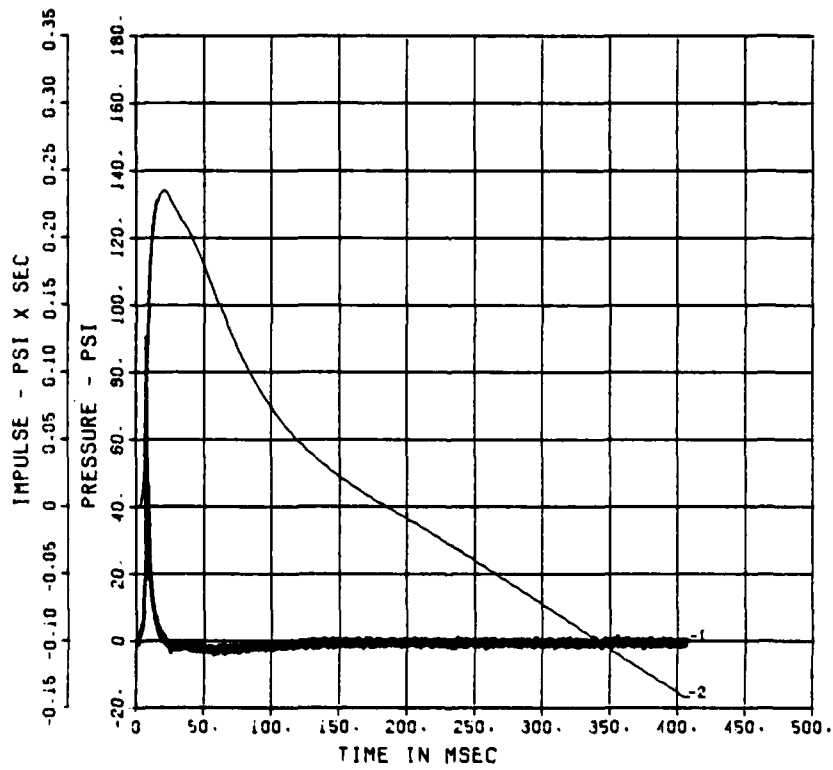


Chart E-16. Calibration Shot Air Blast Record at 42 Feet on Northeast Radial

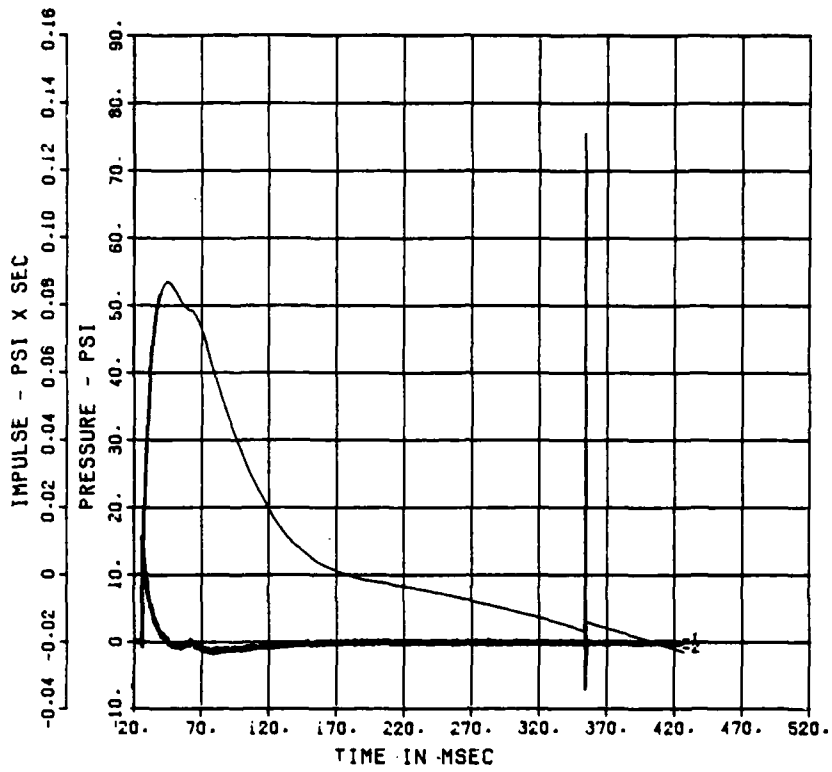


Chart E-17. Calibration Shot Air Blast Record at 78 Feet on Northeast Radial

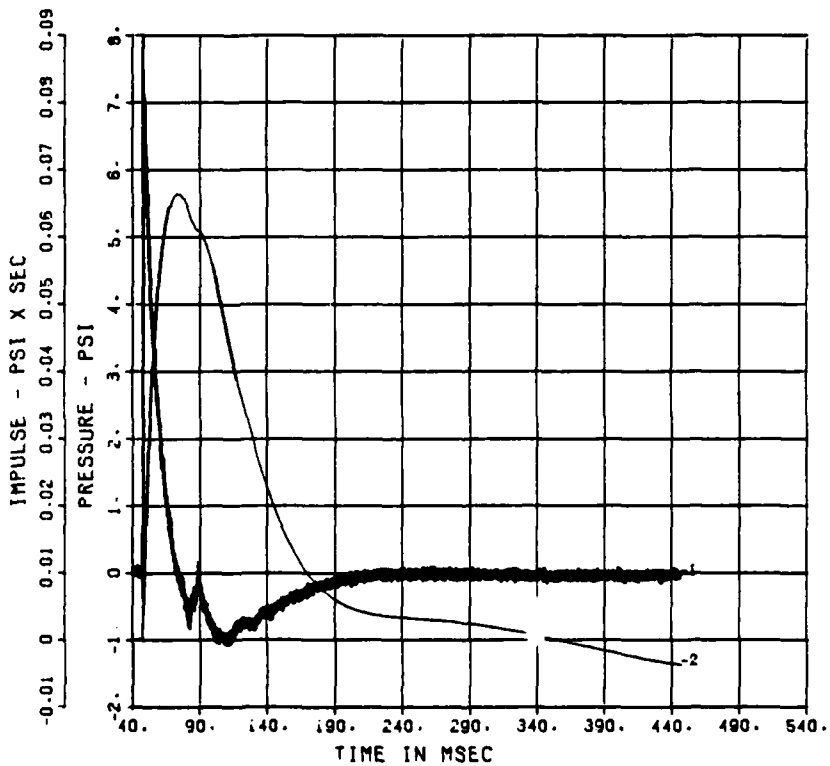


Chart E-18. Calibration Shot Air Blast Record at 110 Feet on Northeast Radial

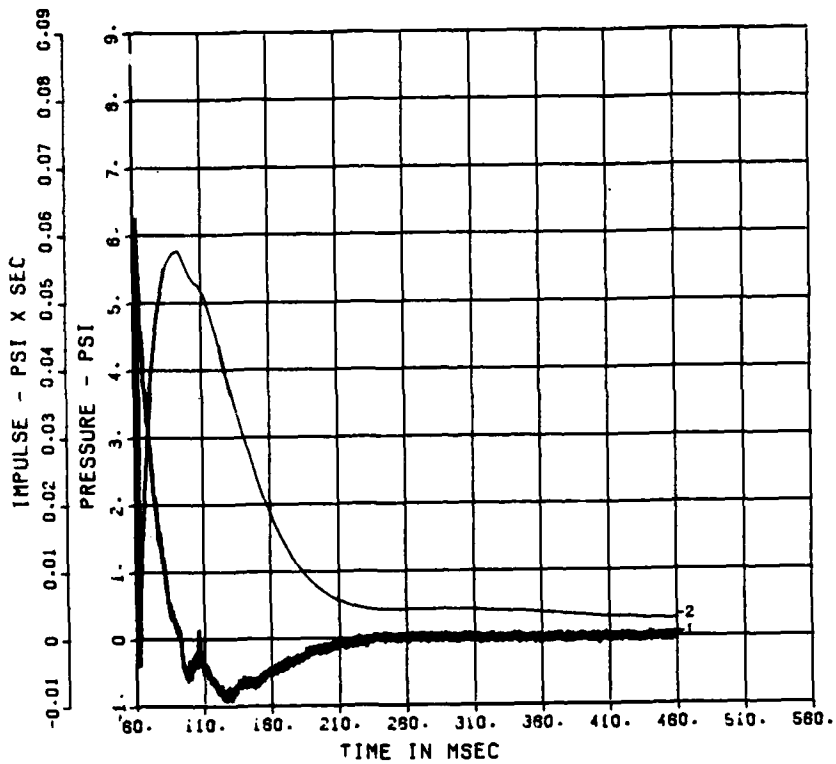


Chart E-19. Calibration Shot Air Blast Record at 130 Feet on Northeast Radial

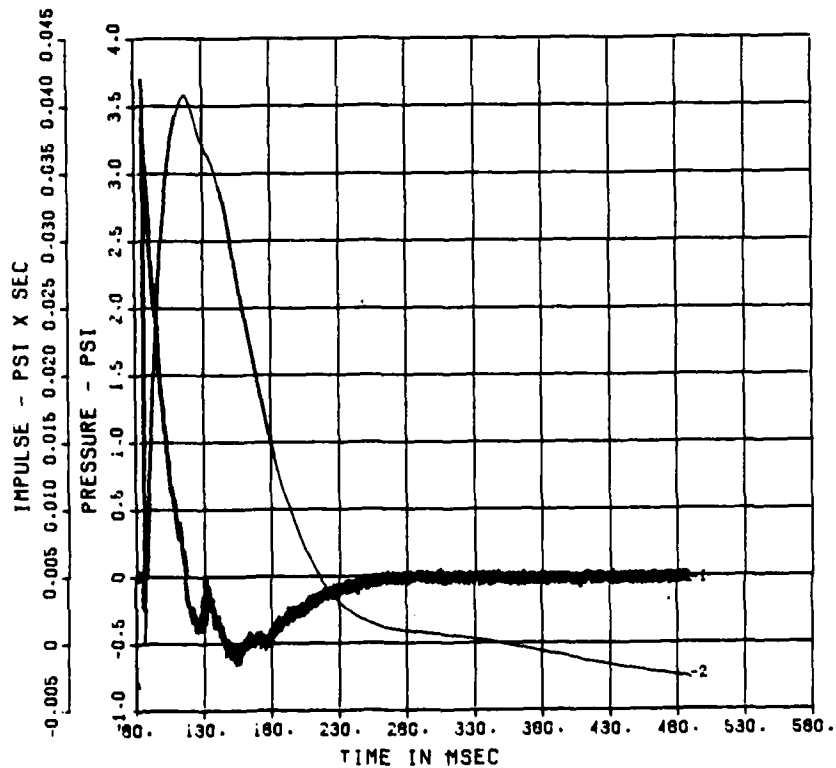


Chart E-20. Calibration Shot Air Blast Record at 160 Feet on Northeast Radial

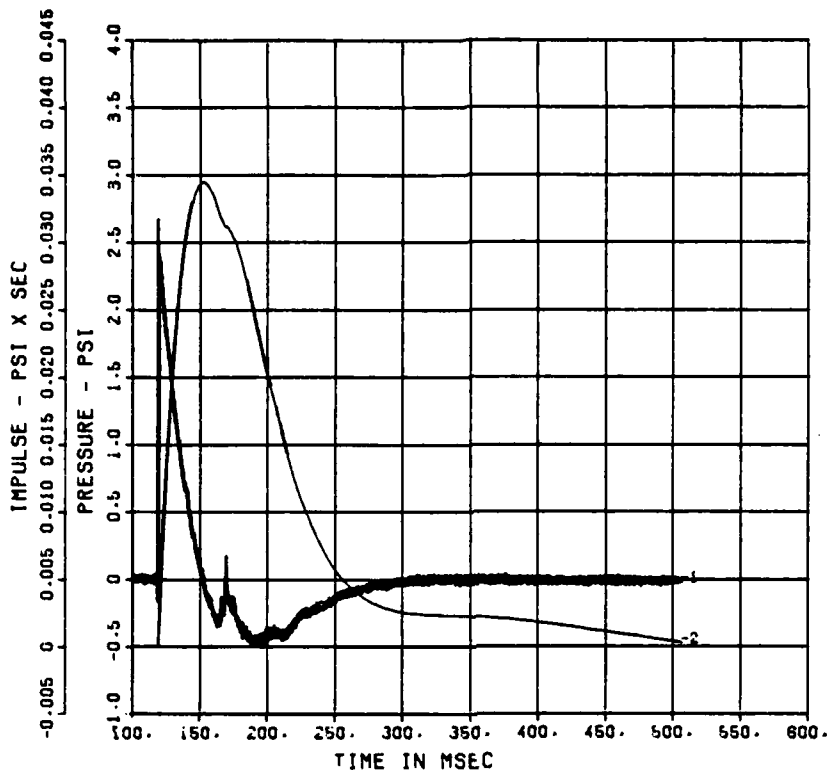


Chart E-21. Calibration Shot Air Blast Record at 200 Feet on Northeast Radial

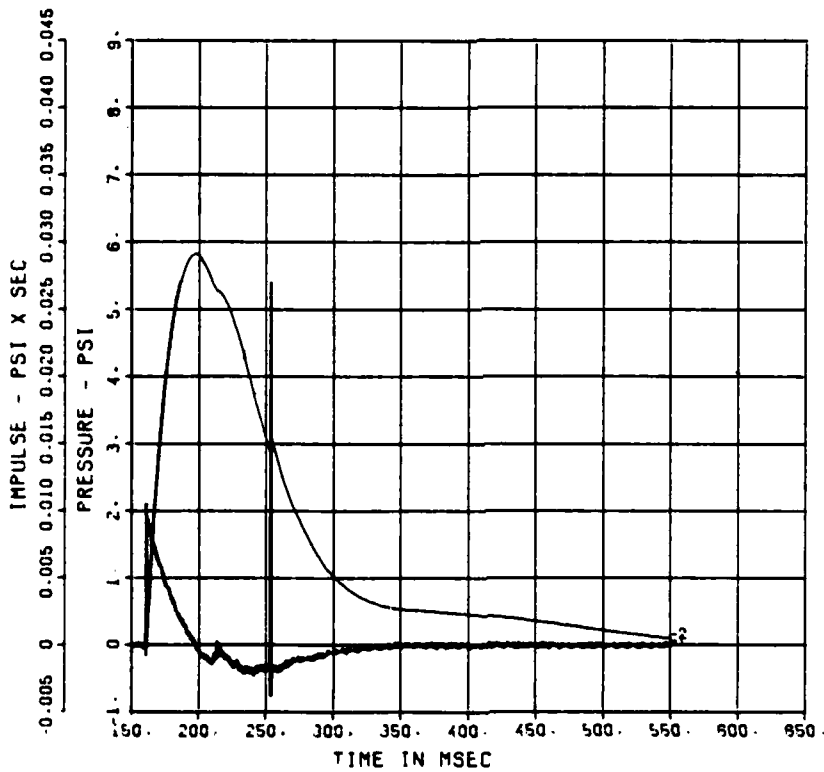


Chart E-22. Calibration Shot Air Blast Record at 250 Feet on Northeast Radial

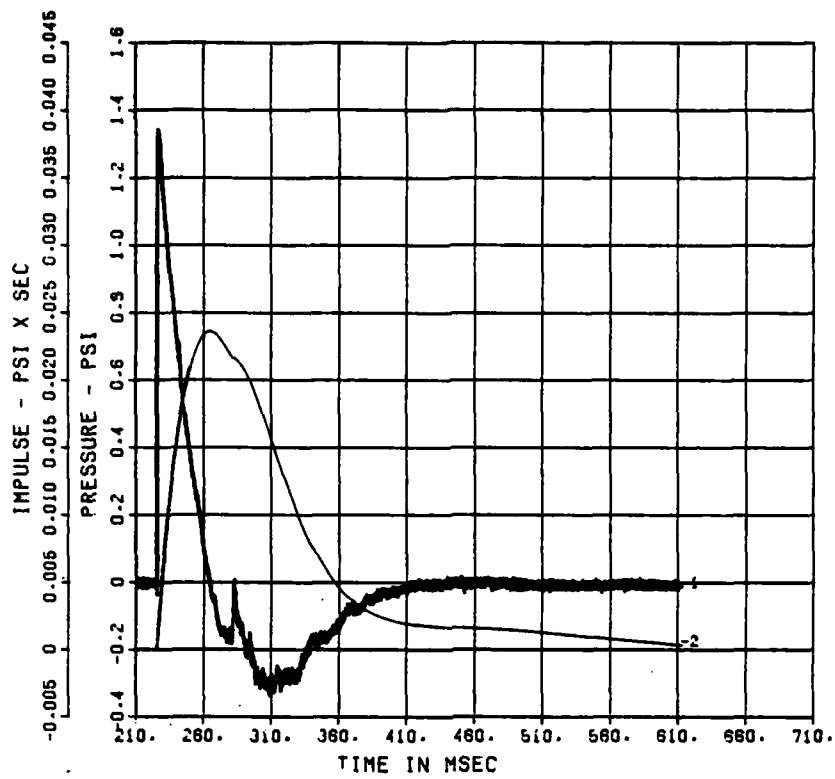


Chart E-23. Calibration Shot Air Blast Record at 325 Feet on Northeast Radial

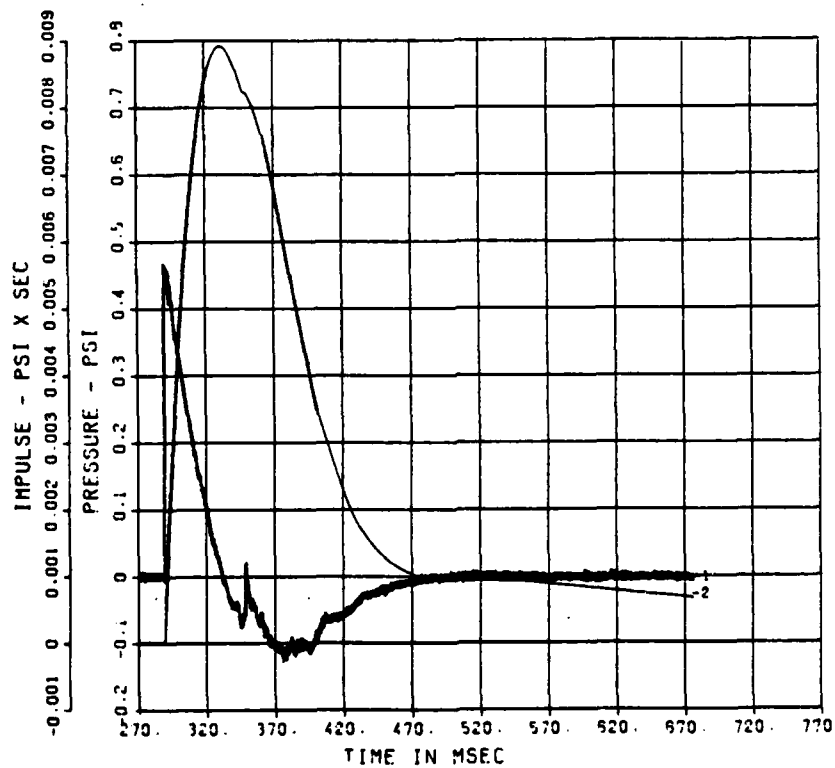


Chart E-24. Calibration Shot Air Blast Record at 400 Feet on Northeast Radial

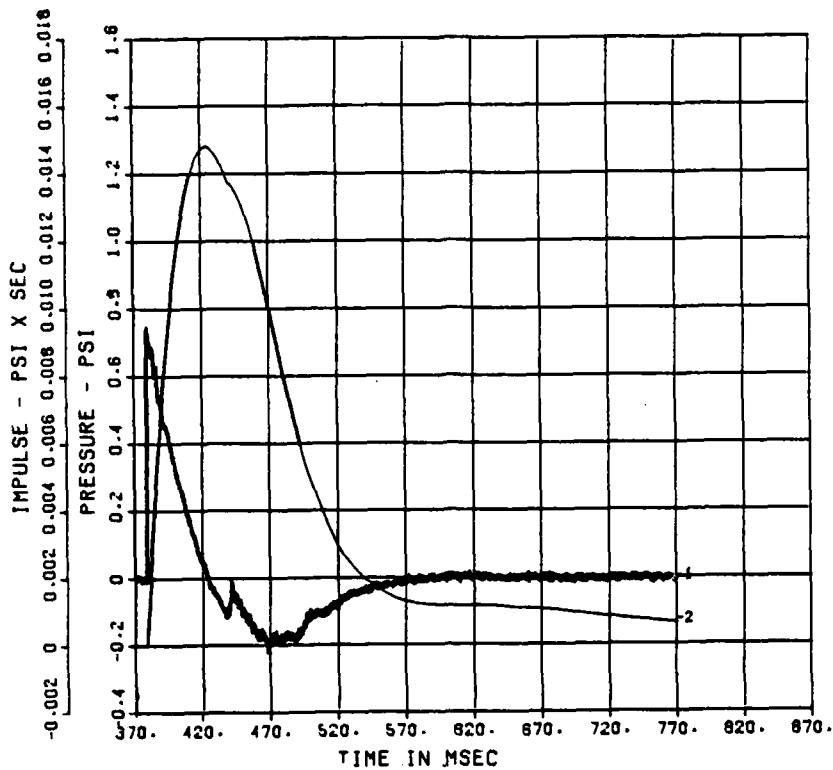


Chart E-25. Calibration Shot Air Blast Record at 500 Feet on Northeast Radial

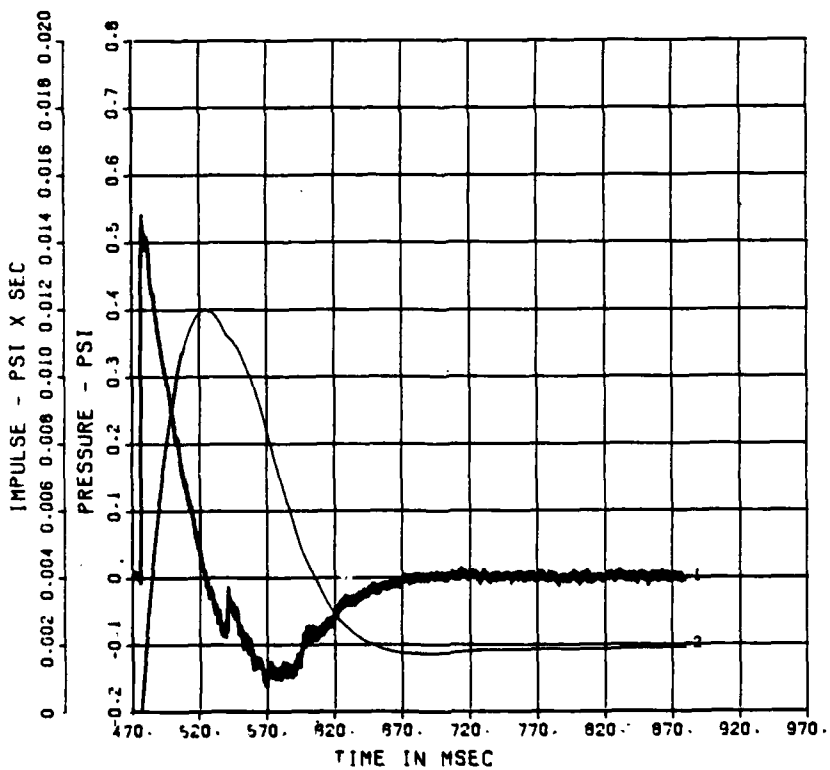


Chart E-26. Calibration Shot Air Blast Record at 610 Feet on Northeast Radial

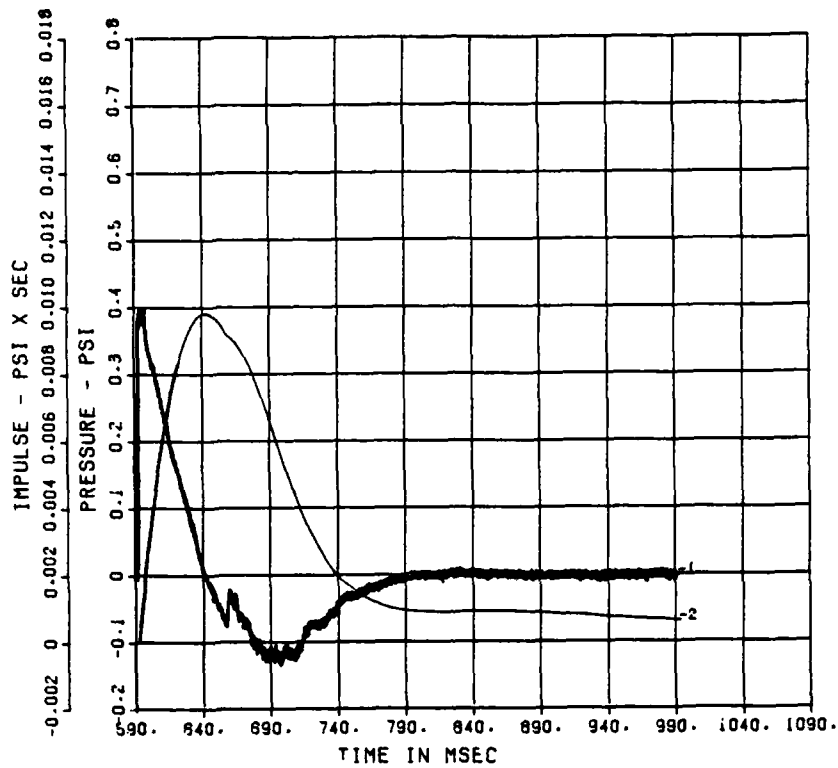


Chart E-27. Calibration Shot Air Blast Record at 740 Feet on Northeast Radial

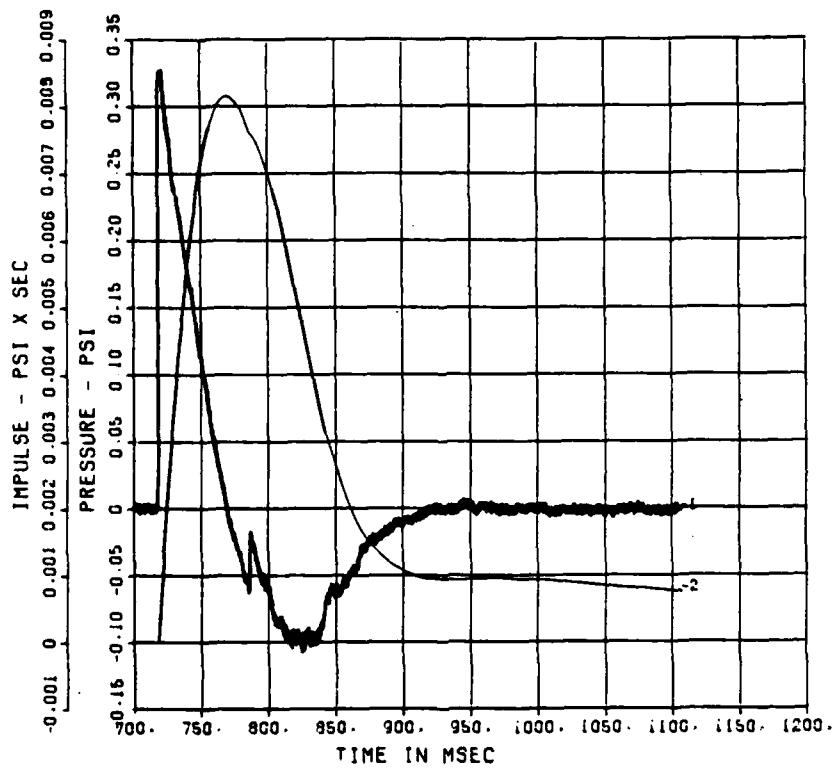


Chart E-28. Calibration Shot Air Blast Record at 880 Feet on Northeast Radial

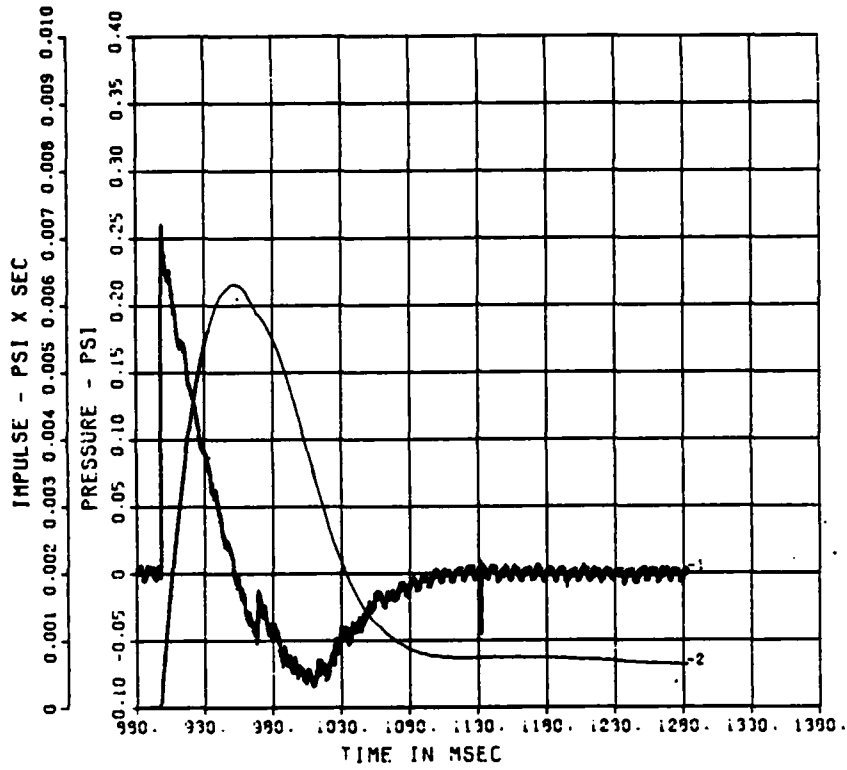


Chart E-29. Calibration Shot Air Blast Record at 1080 Feet on Northeast Radial

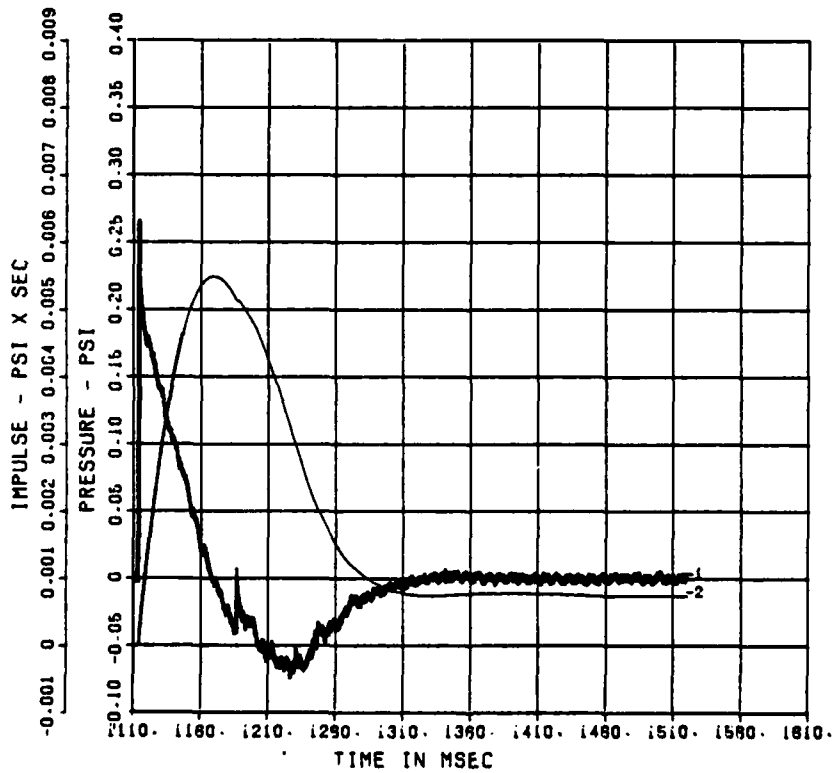


Chart E-30. Calibration Shot Air Blast Record at 1320 Feet on Northeast Radial

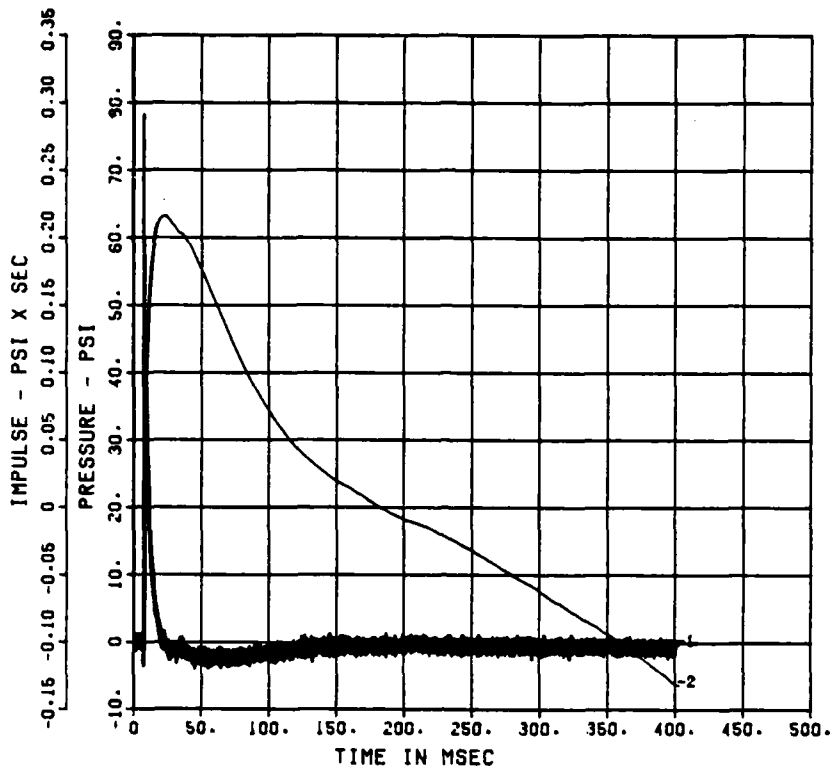


Chart E-31. Calibration Shot Air Blast Record at 42 Feet on Northwest Radial

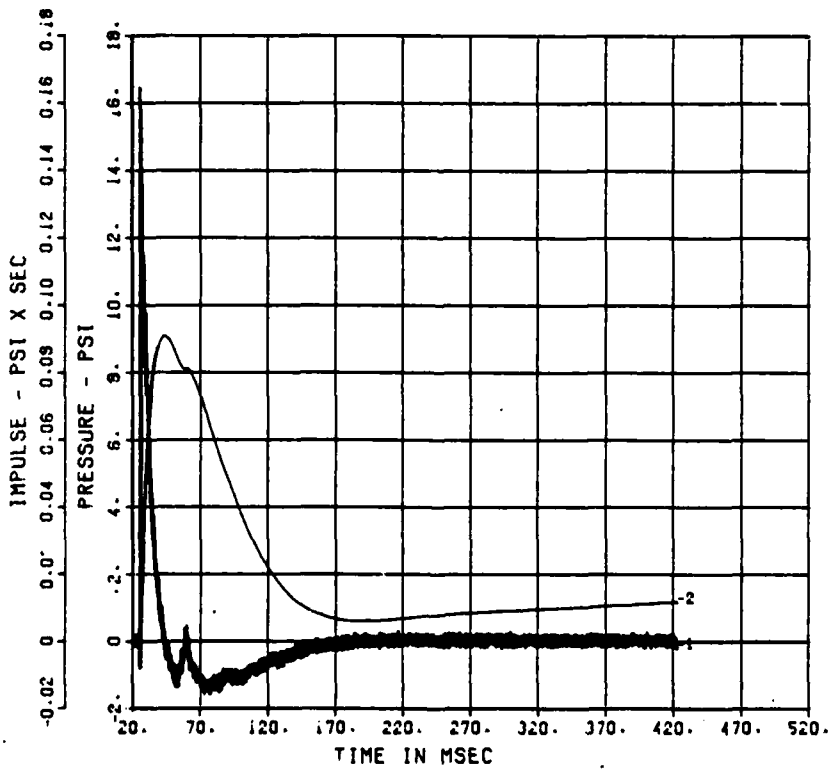


Chart E-32. Calibration Shot Air Blast Record at 78 Feet on Northwest Radial

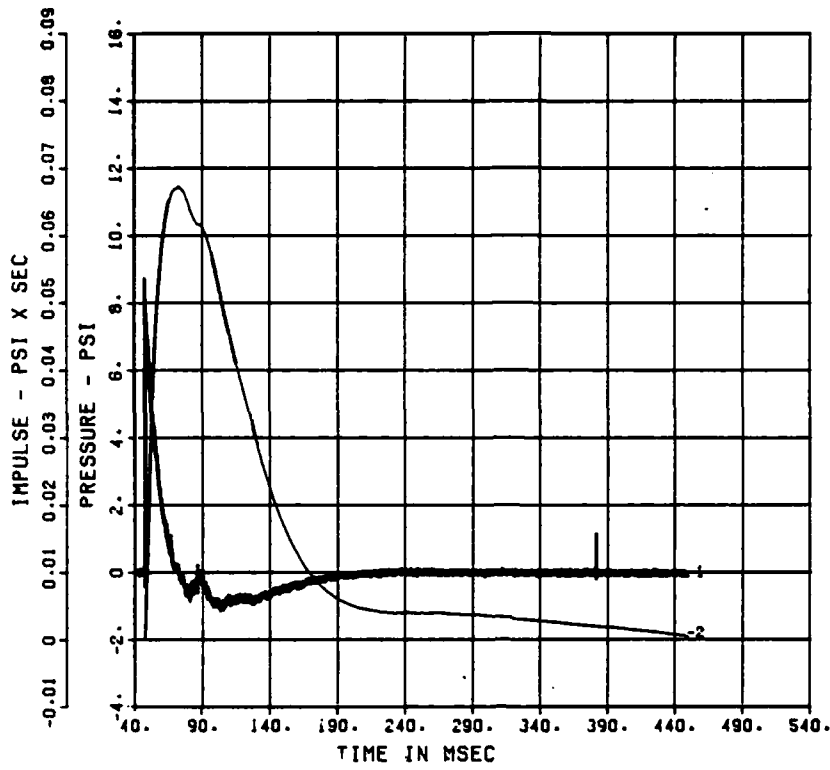


Chart E-33. Calibration Shot Air Blast Record at 110 Feet on Northwest Radial

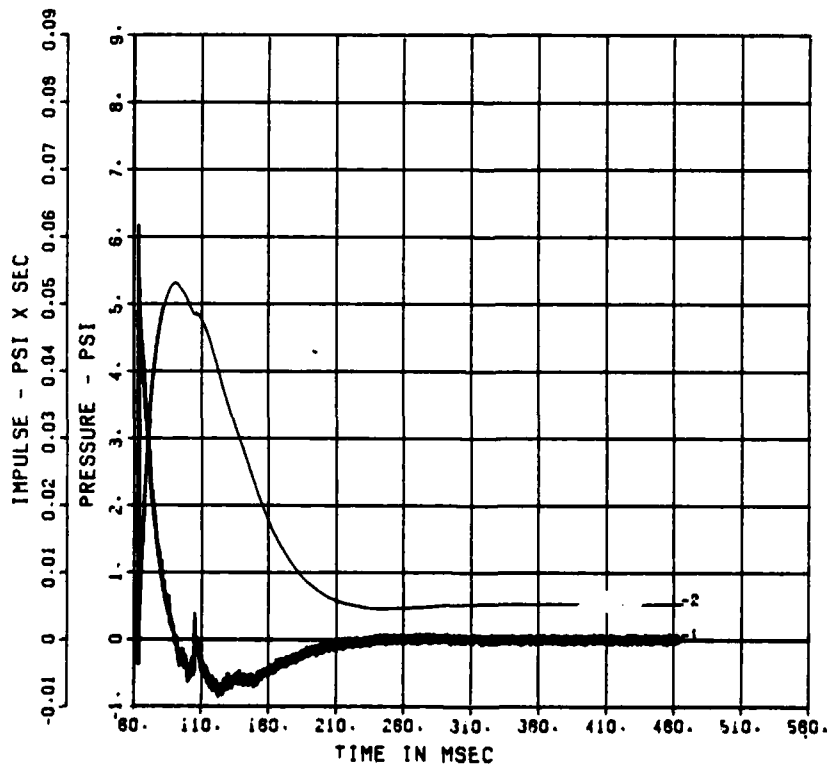


Chart E-34. Calibration Shot Air Blast Record at 130 Feet on Northwest Radial

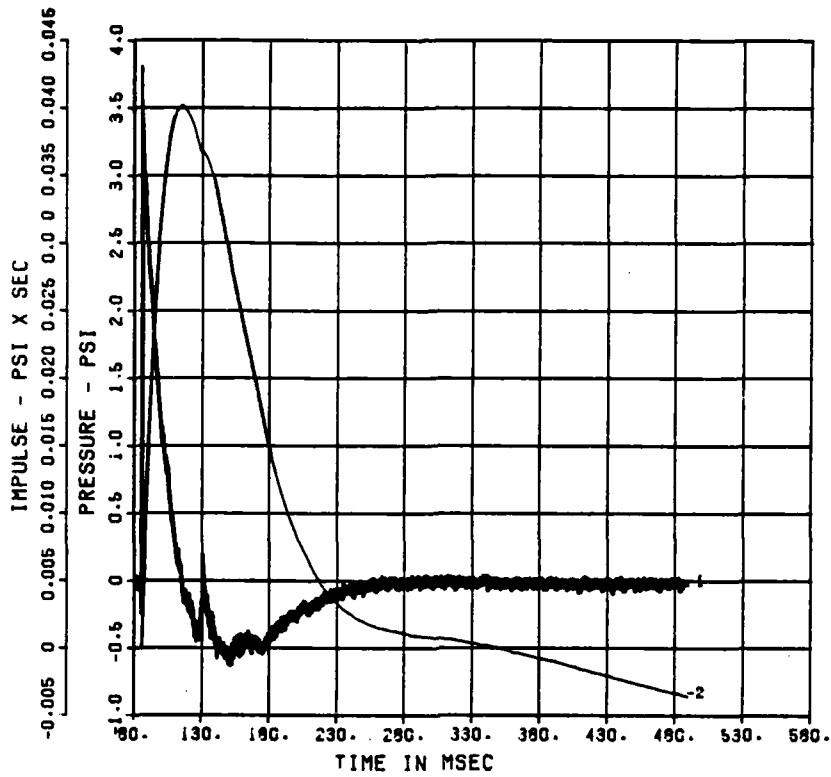


Chart E-35. Calibration Shot Air Blast Record at 160 Feet on Northwest Radial

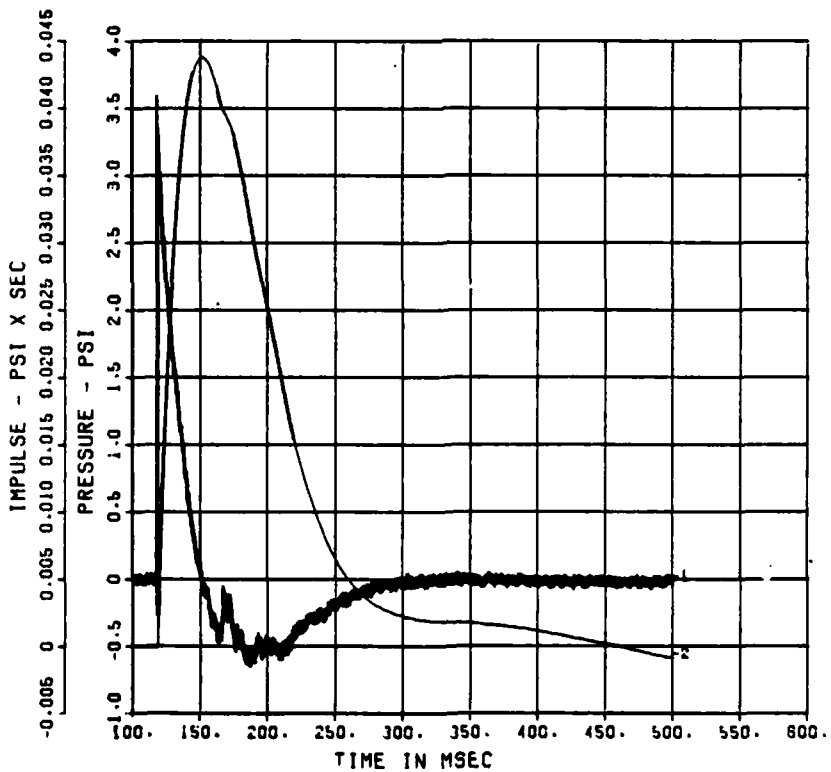


Chart E-36. Calibration Shot Air Blast Record at 200 Feet on Northwest Radial

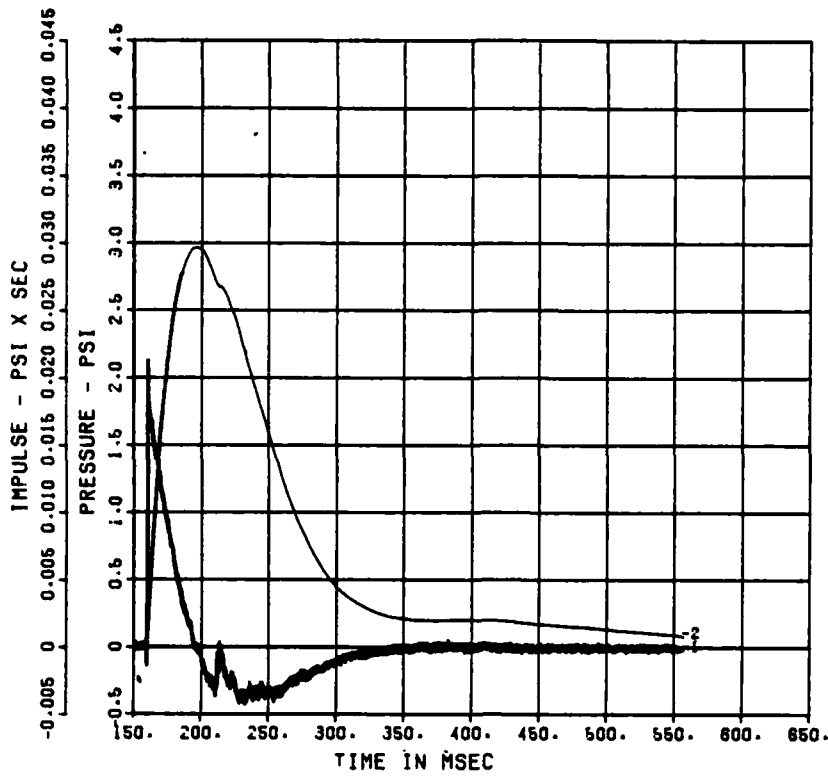


Chart E-37. Calibration Shot Air Blast Record at 250 Feet on Northwest Radial

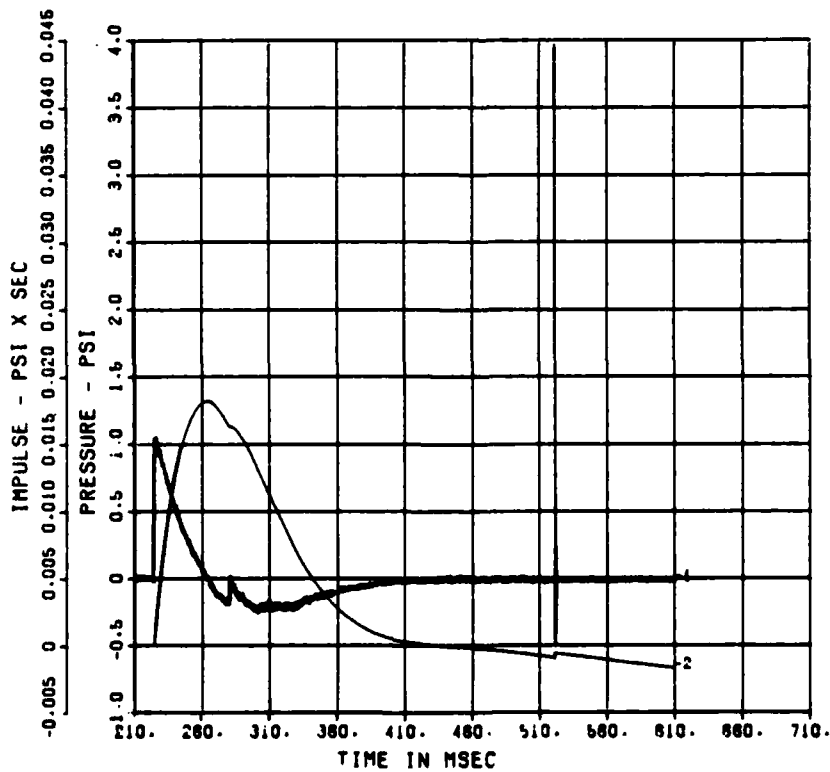


Chart E-38. Calibration Shot Air Blast Record at 325 Feet on Northwest Radial

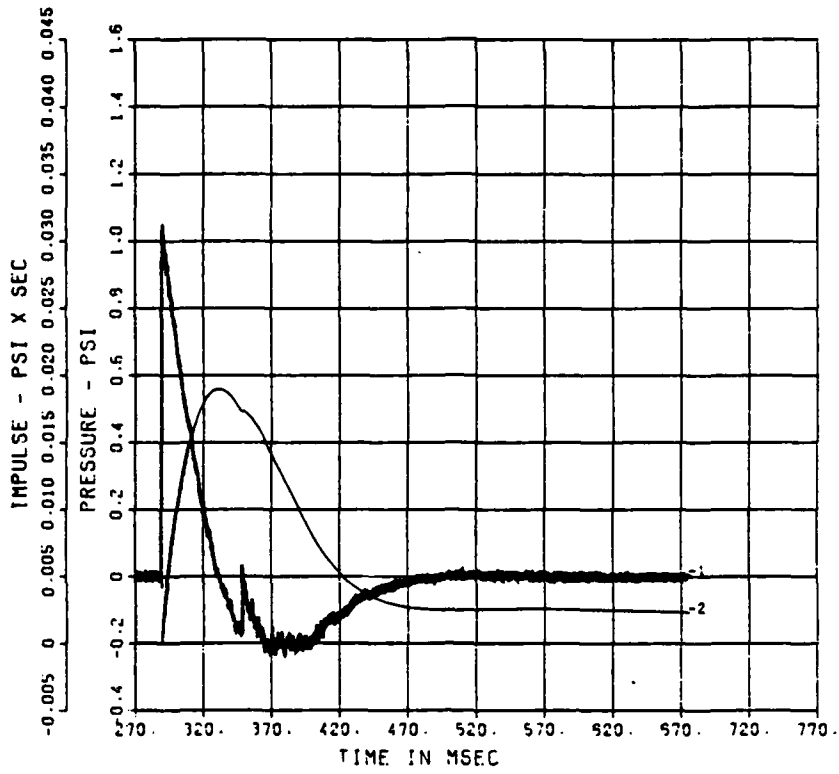


Chart E-39. Calibration Shot Air Blast Record at 400 Feet on Northwest Radial

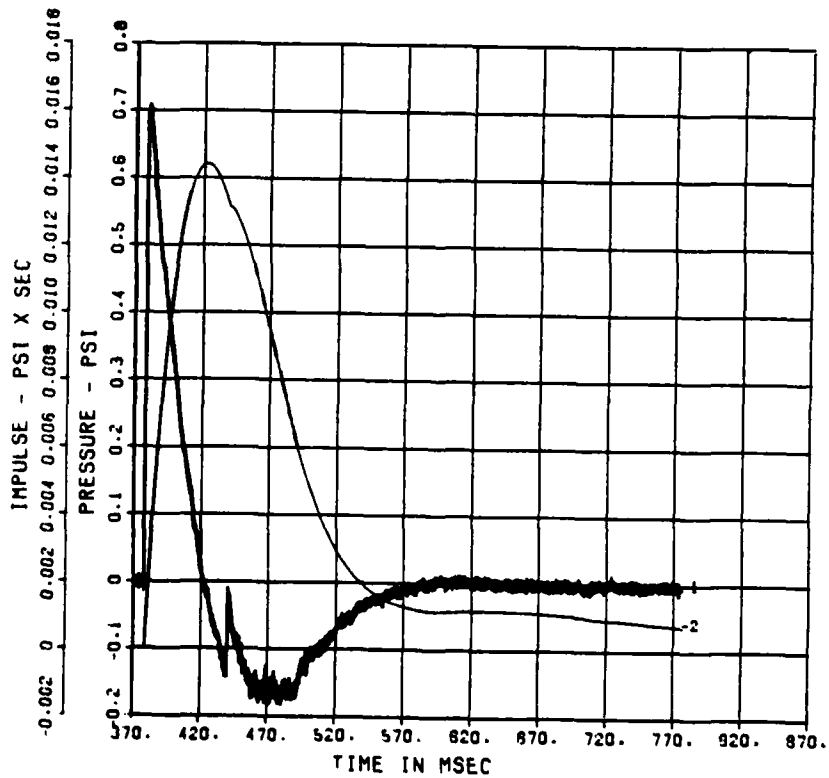


Chart E-40. Calibration Shot Air Blast Record at 500 Feet on Northwest Radial

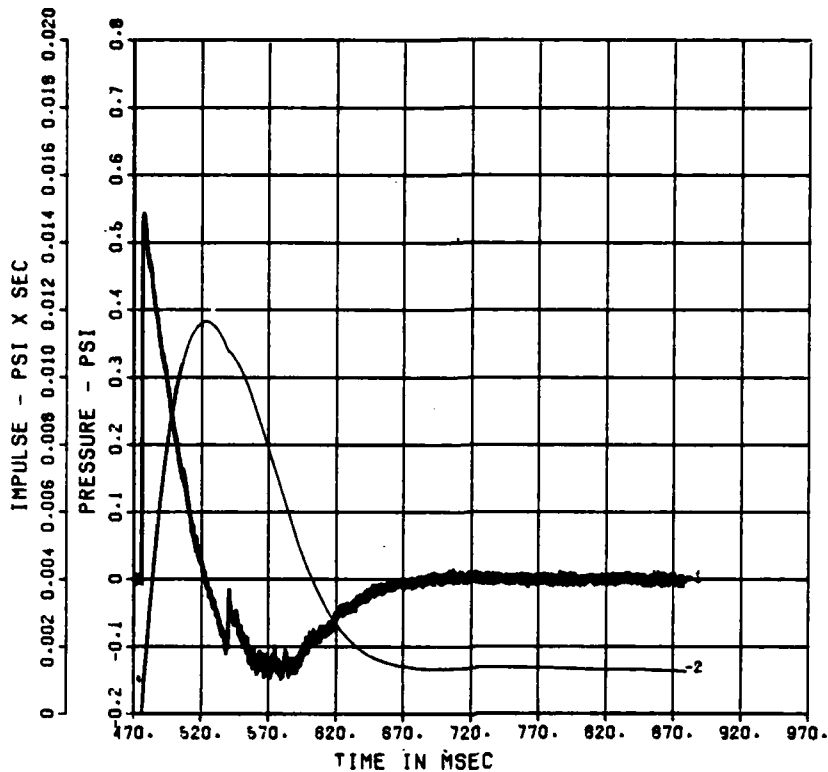


Chart E-41. Calibration Shot Air Blast Record at 610 Feet on Northwest Radial

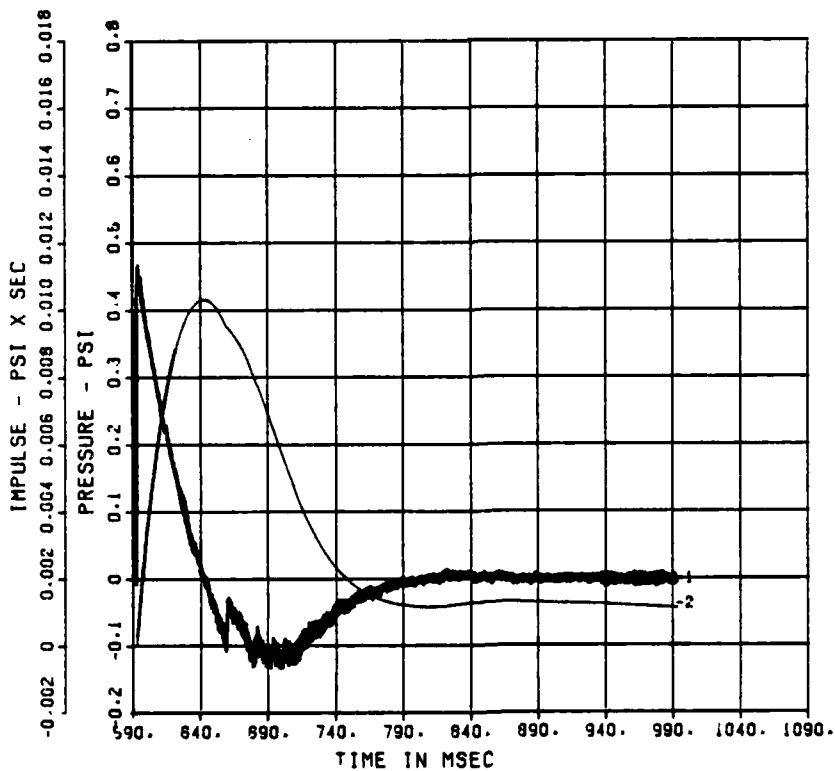


Chart E-42. Calibration Shot Air Blast Record at 740 Feet on Northwest Radial

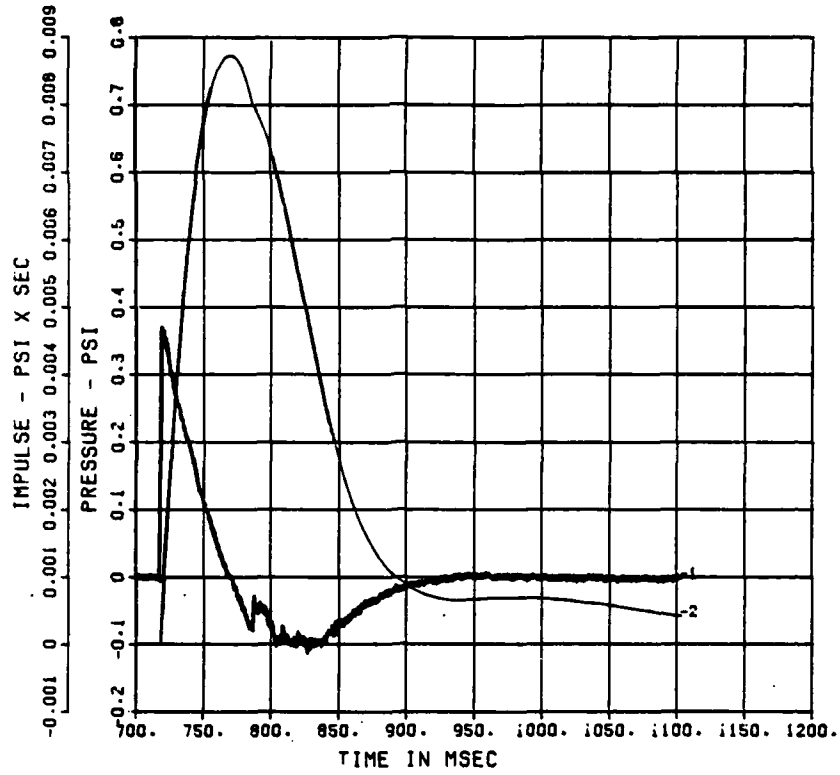


Chart E-43. Calibration Shot Air Blast Record at 880 Feet on Northwest Radial

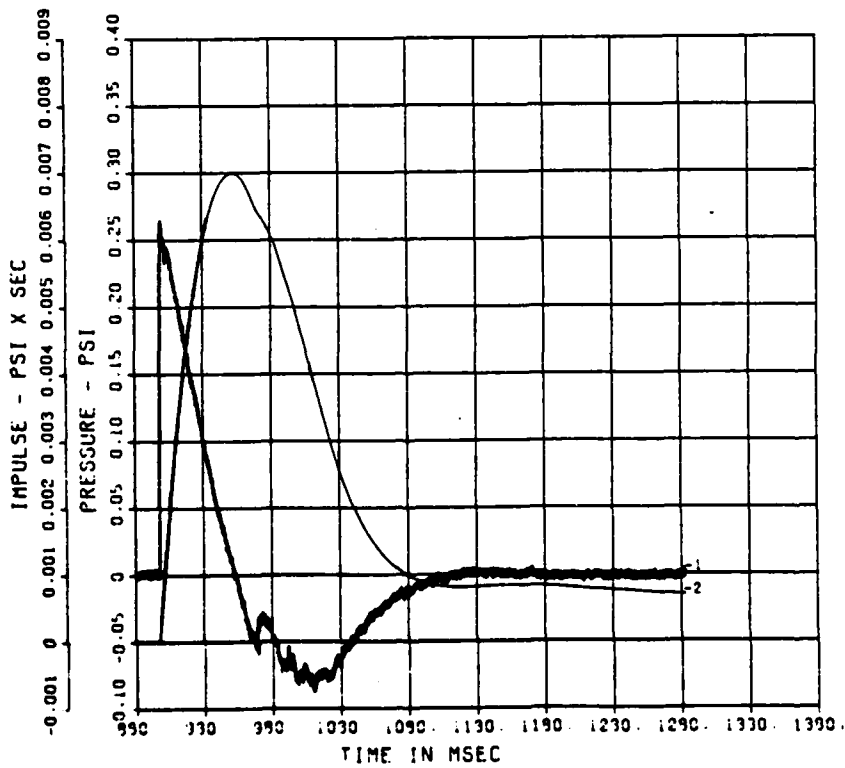


Chart E-44. Calibration Shot Air Blast Record at 1080 Feet on Northwest Radial

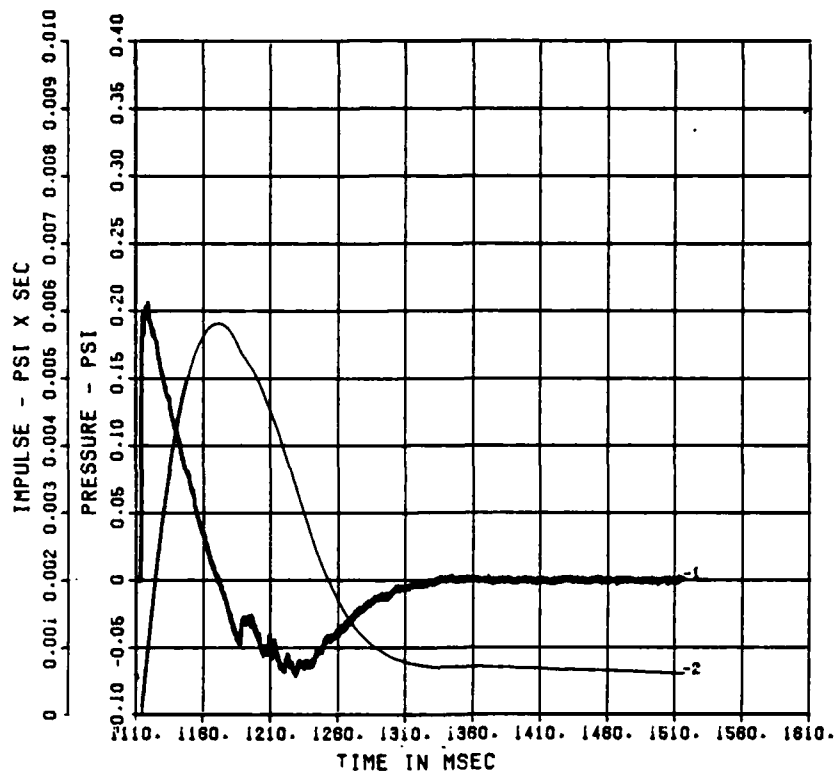


Chart E-45. Calibration Shot Air Blast Record at 1320 Feet on Northwest Radial

UNCLASSIFIED

SECURITY CLASSIFICATION OF THIS PAGE

REPORT DOCUMENTATION PAGE

1a. REPORT SECURITY CLASSIFICATION UNCLASSIFIED			1b. RESTRICTIVE MARKINGS			
2a. SECURITY CLASSIFICATION AUTHORITY			3. DISTRIBUTION/AVAILABILITY OF REPORT Approved for public release; distribution unlimited.			
2b. DECLASSIFICATION/DOWNGRADING SCHEDULE						
4. PERFORMING ORGANIZATION REPORT NUMBER(S) TRW Report 43597-6001-UT-00			5. MONITORING ORGANIZATION REPORT NUMBER(S) BMO-TR-84-17			
6a. NAME OF PERFORMING ORGANIZATION TRW Defense Systems Group		6b. OFFICE SYMBOL (If applicable)	7a. NAME OF MONITORING ORGANIZATION U.S. Air Force Ballistic Missile Office Air Force Systems Command			
6c. ADDRESS (City, State and ZIP Code) One Space Park Redondo Beach, CA 90278			7b. ADDRESS (City, State and ZIP Code) Norton Air Force Base, CA 92409			
8a. NAME OF FUNDING/SPONSORING ORGANIZATION		8b. OFFICE SYMBOL (If applicable) AWS	9. PROCUREMENT INSTRUMENT IDENTIFICATION NUMBER F04704-83-C-0045			
8c. ADDRESS (City, State and ZIP Code) Norton Air Force Base, CA 92409			10. SOURCE OF FUNDING NOS.			
			PROGRAM ELEMENT NO.	PROJECT NO.	TASK NO.	WORK UNIT NO.
11. TITLE (Include Security Classification) Peacekeeper Quantity-Distance Verification Program						
12. PERSONAL AUTHOR(S) Benjamin Sussholz						
13a. TYPE OF REPORT Final Report		13b. TIME COVERED FROM _____ TO _____		14. DATE OF REPORT (Yr., Mo., Day) 1984 June - 1 (A)		15. PAGE COUNT 336 14
16. SUPPLEMENTARY NOTATION						
17. COSATI CODES			18. SUBJECT TERMS (Continue on reverse if necessary and identify by block number)			
FIELD	GROUP	SUB. GR.	Airblast		Missiles	
			Explosions		Peacekeeper	
			Fragment hazards		Quantity-Distance	
19. ABSTRACT (Continue on reverse if necessary and identify by block number)						
<p>A detailed overview is presented of the test program and analytical investigations directed toward verification of the quantity-distance criteria associated with an accidental explosion of a Peacekeeper missile in a Minuteman silo. Three tests were conducted involving the detonation of Pentolite charges within scale model structures representative of a Wing V Minuteman silo. Measurements were made of airblast effects and structural debris and soil ejecta distributions. Calculations of airblast phenomena were made by means of a computer program for the purpose of establishing test predictions. Structural fragmentation characteristics were investigated with estimates established of fragment dimensions, number and</p>						
20. DISTRIBUTION/AVAILABILITY OF ABSTRACT UNCLASSIFIED/UNLIMITED <input checked="" type="checkbox"/> SAME AS RPT. <input type="checkbox"/> DTIC USERS <input type="checkbox"/>			21. ABSTRACT SECURITY CLASSIFICATION UNCLASSIFIED			
22a. NAME OF RESPONSIBLE INDIVIDUAL Lt. Steven F. Mattern			22b. TELEPHONE NUMBER (Include Area Code) (714) 382-4485		22c. OFFICE SYMBOL BMO/AWS	

UNCLASSIFIED

SECURITY CLASSIFICATION OF THIS PAGE

launch parameters. A debris scaling methodology was developed consisting of a statistical simulation technique and a trajectory limitation approach. Test data were analyzed in relation to scaling of airblast effects over the domain of the test results, and identification of significant properties of the structural debris and soil ejecta, such as dimensions, shape factor, sources, and density variation with range. Scaling evaluations were performed to determine appropriate quantity-distance values for airblast and hazardous fragments corresponding to a full-scale event.

UNCLASSIFIED

SECURITY CLASSIFICATION OF THIS PAGE

END

FILMED

10-84

DTIC